UNIVERSITÉ D'ORLÉANS

ÉCOLE DOCTORALE ENERGIE, MATERIAUX, SCIENCES DE LA TERRE ET DE L'UNIVERS

Institut des Sciences de la Terre d'Orléans

THÈSE présentée par :

Yann-Aurélien BRUGIER

soutenue le : **17 Juin 2016**

pour obtenir le grade de : **Docteur de l'université d'Orléans**

Discipline/ Spécialité : Sciences de la Terre et de l'Univers

Magmatologie du Piton de la Fournaise (Ile de la Réunion)

Approche Volcanologique, Pétrologique et Expérimentale

THÈSE dirigée par :

Michel PICHAVANT	Directeur de recherches, ISTO
Andréa DI MURO	Physicien, IPGP

RAPPORTEURS :

Julia HAMMER	Professeur, University of Hawaii (USA)
Patrick BACHELERY	Professeur, Université Blaise Pascal - Clermont-Ferrand

JURY :

Jean-Louis BOURDIER	Professeur, Université d'Orléans (Président du jury)
Julia HAMMER	Professeur, University of Hawaii (USA)
François FAURE	Professeur, Université de Lorraine - Nancy
Michel PICHAVANT	Directeur de recherches, ISTO
Andréa DI MURO	Physicien, IPGP
Patrick BACHELERY	Professeur, Université Blaise Pascal - Clermont-Ferrand

Cette thèse est dédiée
à ma grand-mère, Jacqueline TOUX.
La vie ne sera plus jamais
la même sans toi…

Remerciements

En tout premier lieu, je voudrais remercier mon directeur de thèse, Michel Pichavant. Sans sa confiance et son soutien sans faille et de tous les instants ce travail de thèse n'aurait jamais pu être mené à terme. Merci à toi Michel, de m'avoir accompagné dans cette découverte du monde de la recherche, de la pétrologie, le monde de l'expérimentale. Mes pensées vont bien entendu aussi à mon co-directeur de thèse Andréa Di Muro qui nous a toujours accueillis les bras ouverts à La Réunion : au sein de l'Observatoire où l'on squattait son bureau, lors des journées sur le terrain, tout comme chez lui pour des repas avec sa magnifique famille, merci pour tout, malgré la distance: merci. Je tiens à remercier aussi Jean-Louis Bourdier pour ses compétences sur le terrain, j'ai appris autant en 1 mois de terrain avec lui qu'en 5 ou 6 ans. Une pensée aussi pour les stagiaires qui ont pu être encadrés durant cette thèse : Pierre-Alain Jardinet et surtout Yannick le Moigne avec qui ce fut un plaisir de travailler. Je ne peux oublier Guillaume Boudoire aussi, avec qui les discussions ont toujours été un vrai plaisir !

Je souhaite ici prendre quelques lignes pour remercier les rapporteurs de ce manuscrit : Julia Hammer et Patrick Bachèlery, d'avoir accepté l'envoi en deux temps de cette thèse, qui m'a permis de survivre (et je pense que le mot est juste) au stade terminal de la rédaction. Merci bien sûr aussi à François Faure d'avoir accepté d'être examinateur de ce travail et de la soutenance.

Je voudrais tout d'abord remercier tous les membres de l'ISTO et de l'OSUC, tous ces gens qui ont fait partie de mon quotidien durant ces 3 ans et quelq… ces 4 ans. Je ne pourrai malheureusement pas citer tout le monde, et j'en oublierai sans doute certains, mais pourquoi ne pas essayer : merci à Rémi, à Esteban, Fred, au second Rémi, à tous les gars de l'atelier qui font miracle sur miracle dans ce labo et qui permettent à tous de pouvoir réaliser les manips, si vitales dans un labo de pétrologie expérimentale. Je n'oublie pas Juan qui est toujours là pour aider à monter les manips ; tout comme je n'oublie pas Olivier et Virginie pour le travail qu'ils abattent à gérer tous nos remboursements, nos ordres de mission qu'ils soient envoyés à l'avance ou le jour même ils font toujours de leur mieux pour nous, Nathalie aussi bien sûr, qui est capable de retrouver n'importe quelle obscure publication, et je pense aussi à Martine, Marlène ou encore Cathy qui depuis quelques temps déjà sont toujours là pour nous avec leur bonne humeur et leur disponibilité. Et bien sûr merci aux équipe de l'OVPF pour leur accueil, leurs soutien technique. Une pensée aux clermontois de DEGAZMAG aussi.
Ici, je voudrais avoir une pensée pour une personne en particulier, qui abat un travail monstrueux et ce pour tous les gens du laboratoire, qui se démultiplie chaque jour de chaque semaine et qui prends de tes nouvelles même à minuit quand tu passes la nuit devant la sonde: Grazie mille Ida !

Au gros morceau du labo maintenant, je voudrais remercier tous les doctorants qui sont passés au labo, qui y sont et ceux qui y seront encore une fois que j'aurai soutenu, merci pour tous ces petits moments, ces pauses café, ces repas de midi, ces V&B, ces soirées… Bref un grand merci à tout le monde : Dr Laumonnier, Alex, Giulia, La Praline, Val, ma co-bureau de choc Anne-Aziliz, Clément, Max, Chloé, Julien, Caro, Hugues, Eloise, Mohammed, Vincent, Julie, Pierangelo (on se retrouve bientôt sur une 3ème île d'Italie ?), à Zyneb (je sais, je sais, on va au V&B fêter ça) et à tous les autres merci du soutien. Ca fait toujours du bien de savoir qu'on est pas les seuls sur ce bateau. Je ne voudrais pas oublier aussi l'équipe du BRGM (Seb, Mathieu, Sarah) et de Variscan : à vous Mr Piko et ce bon vieux Jéjé, «mais oui c'est clair ! ».

Une pensée toute particulière pour La Villa : Leïla, Malky, Dada, Colin et Mamel, ça a été bref cette histoire et le Manoir l'a remporté aisément, mais que ce fut bon !
Je voudrais aussi remercier tout particulièrement Nounouille d'être toujours dispo, je suis allée l'embêter 36.000 fois pour de l'I.R. ou encore même récemment lui emprunter sa thèse. Je pense pouvoir dire, qu'après Michel elle aura été la personne sur laquelle je me suis le plus appuyé au labo et je n'aurais jamais pensé dire ça il y a 10 ans maintenant quand on était dans la même promo de Licence à Brest !
Bien sûr je pense très fort à mes Ananas et Pti Gui leur Pistache ; à Julie & Nico ; à Doudoum et à Kévin, à Hugo, à Flob, merci à tous, ces moments avec vous étaient géniaux, et seront encore géniaux !!
Je ne peux pas ne pas remercier tous les membres du Manoir que ce soit les anciens Léo, Papi, Rabi (et oui on est des rescapés vieux loup) ou encore Gwen et Olivier, comme les tous derniers arrivants mais qui me manqueront tout autant : Marie, Martin et Lucie, je n'aurais pas pu rêver mieux comme colocs… Ah mais oui faut pas que j'oublie notre 6ème coloc, la sorcière de Mayenne : merci pour tout Charlène !

A tous les amis de longue date comme ceux rencontrés durant ces années orléanaises, je veux dire à quel point c'est génial de savoir que même si on se voit qu'une ou deux fois certaines années, on saura qu'on passera toujours des moments inoubliables, donc pour tout ça un grand merci à Mon Amphibole, à ma Gran'ma (KGC For Ever !!), à ma coucougnette, mon Loulou, à La barrique et à sa famille, à Pépette, à Arthur, à la Miette bien sûr, à Sansan, à Jean-sé, Fab, Clément & Doriane, à Flo , à mes frangins de prénoms, à Coco, à la fratrie allemande d'Hélène et Robert, à Kévin & Lucile, ainsi qu'à Juju, Paulette, Marie, Bellec & Quentin's, Fredo, Steeve, Rooroo, Gégé boy. Merci aussi à Pédro de Miami, mon parrain, mon Arc en Ciel et à brendanou et Dani, même si on s'est pas beaucoup vu ces derniers temps.
Je voulais bien sûr garder les plus forts soutiens pour la fin : mes tantes, mon oncle, mes cousins d'être là. Merci à mon père, à Mumu, à Juju, à Gooly, Nini et Audrey, vous êtes tous importants à mes yeux, même si je vouls dis sans doute pas assez souvent.
Merci aussi à Gégé, Momo, Mick et Lucie (allez je mets la 2ème branche dans la belle-famille) pour m'avoir accepté aussi généreusement, aussi chaleureusement, j'ai vraiment trouvé une second famille avec vous et… vous êtes géniaux.

J'arrive à la fin de la deuxième page juste à temps pour remercier les deux femmes de ma vie, Maman je ne peux pas te remercier comme je devrais en quelques lignes mais sache que je sais tout ce que tu as fait pour moi, je t'en serai à jamais reconnaissant et je sais que si je suis l'homme que je suis aujourd'hui c'est grâce à toi…. Et aussi un peu grâce à ma petite Sahel, je ne sais pas ce que je ferai demain, ni où je serai mais je sais que tant que je serai avec toi, ça ne pourra que bien se passer. Merci pour tout, tu as supporté les 3 ans de thèse et pourtant tu es restée, je ne sais pas comment tu as fait, surtout à la fin mais encore mille fois Merci. Merci d'être qui tu es et d'être rentrée dans ma vie…

1 Table des matières

INTRODUCTION & PROBLEMATIQUE

La première référence à l'île de La Réunion dans les archives européennes de navigation remonte à 1502, sur le planisphère de Cantino (une compilation de différentes cartes du monde réalisée par des explorateurs portugais). Il est cependant très probable que l'île fut connue précédemment des navigateurs arabes, africains et indiens. Il aura fallu ensuite attendre plus d'un siècle, jusqu'à la colonisation de l'île (alors nommée l'île Bourbon) par les français entre 1642 et 1663, pour trouver trace de descriptions sommaires du volcan actif de l'île, le Piton de la Fournaise (*Lénat, 2016* et références incluses).

C'est à la lecture de documents publiés (ou non) à partir de 1755 que l'on peut trouver trace de descriptions précises et de dessins détaillés du Piton de la Fournaise et de ses activités éruptives, notamment avec le premier rapport d'une visite du sommet du PdF par Andoche Dolnet de Palmaroux, le 20 Septembre 1751 en compagnie d'un groupe de locaux et d'esclaves (d'après *d'Herguerty, 1755*). Les travaux d'autres auteurs comme *Crémont (1770)* ou *Guettard (1757)* ont été historiquement compilés par *A. Lacroix (1925, 1936, 1938)* ainsi que plus récemment (*Stieltjes & Moutou, 1989 ; Lénat, 2016* et références incluses). Un des plus reconnu de ces auteurs des 18$^{\text{ème}}$ et 19$^{\text{ème}}$ siècles fut Bory de Saint-Vincent dont le nom fut d'ailleurs donné à un des deux cratères principaux du cône actif, et à qui l'on doit une des premières cartes des alentours du PdF (*Bory de Saint-Vincent, 1804*), présentée ci-dessous (Figure 1).

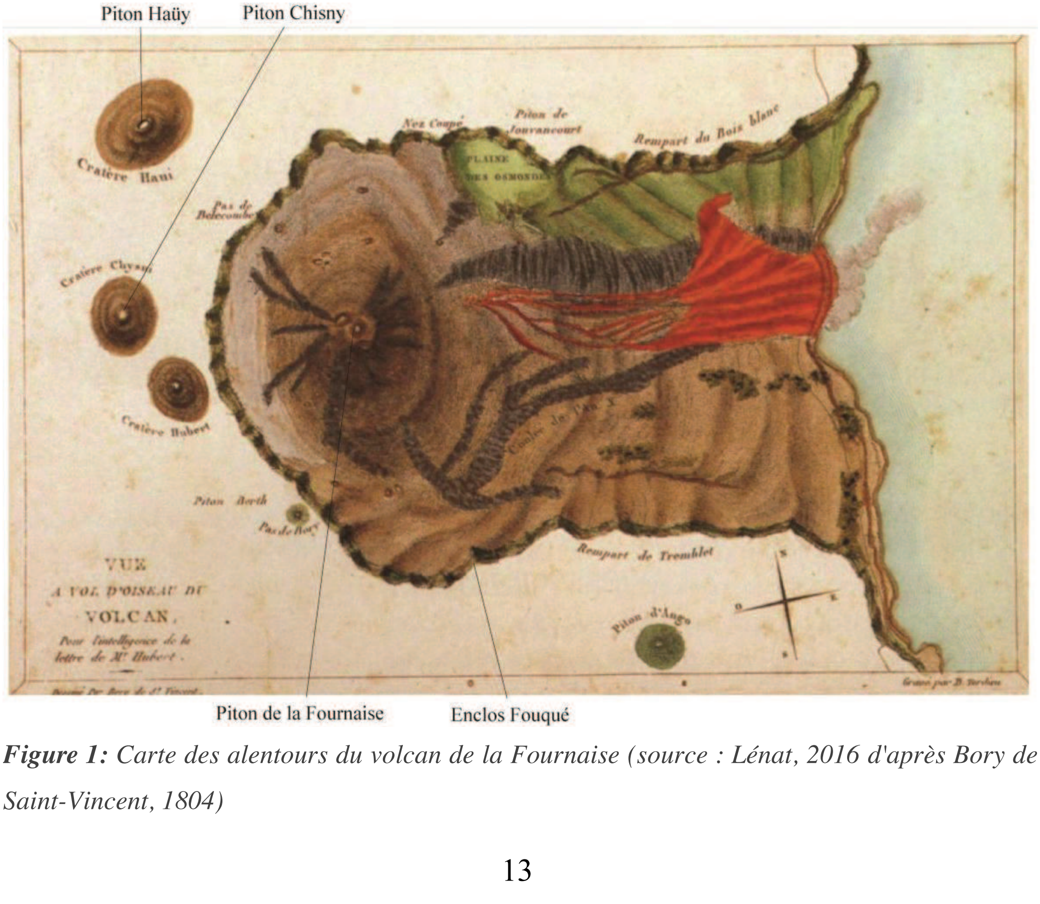

Figure 1: *Carte des alentours du volcan de la Fournaise (source : Lénat, 2016 d'après Bory de Saint-Vincent, 1804)*

On y voit notamment déjà décrits des édifices excentriques comme le Piton Chisny ou le Piton Haüy, ainsi que le tracé de la coulée de lave de l'éruption de 1802 au sein de l'Enclos Fouqué. De tels travaux, compilés régulièrement, permettent une connaissance partielle de l'histoire éruptive du Piton de la Fournaise entre 1755 et 1981, année de la première éruption décrite, surveillée et enregistrée par l'Observatoire Volcanologique du Piton de la Fournaise (*Bachèlery, 1981 ; Chevallier et al., 1981*). L'installation de l'observatoire à Bourg Murat (Plaine des Cafres, La Réunion) faisait en effet suite à l'éruption hors Enclos d'Avril 1977 dont les coulées de laves avaient partiellement détruit le village de Sainte Rose (Fig. 2).

Figure 2: *Photo d'archive de la coulée de 1977 atteignant l'église de Sainte Rose (www.manature974.canalblog.com)*

Cette éruption de 1977, dont les coulées ont pu atteindre le village de Sainte Rose et notamment l'église du village, que l'on voit ici être touchée par la coulée de lave (rebaptisée depuis « Notre Dame des Laves »), est symptomatique des risques liés aux éruptions hors Enclos du Piton de la Fournaise.

En effet, ces éruptions hors Enclos, malgré leur faible proportion (6 occurrences documentées en 1708, 1774, 1776, 1800, 1977 et 1998) dans l'activité moyenne du Piton de la Fournaise (1 à 2 éruptions annuelles), comportent les risques les plus importants pour les habitants des villages alentours et des infrastructures.

Malgré cet état de fait, connu et encore récemment démontré (voir *Di Muro, 2012 & 2015 ; Michon et al., 2015*), les éruptions (ainsi que l'activité des édifices) hors Enclos, donc excentrées par rapport au sommet du Piton de la Fournaise, restent relativement peu étudiées par rapport à celles qui interviennent régulièrement au sein de l'Enclos Fouqué.

Pourtant, les densités de cônes volcaniques, répertoriées dans la Figure 3, montrent bien que, tout le long de la structure orientée nord-ouest sud-est (la « NW-SE Rift Zone »), d'importants édifices se sont construits autour d'emplacements comme celui de la Plaine des Sables. En effet, cet ancien centre éruptif du Piton de la Fournaise, avant son déplacement vers l'est matérialisé par différentes structures d'effondrement comme celle ayant créé l'Enclos Fouqué (*Bachèlery, 1981 ; Lénat, 2016* et références incluses), est caractérisé par la présence de certains des plus gros édifices polygéniques observables sur le Piton de la Fournaise (à l'exception de l'édifice actuel), comme le Piton Haüy ou le Piton Chisny.

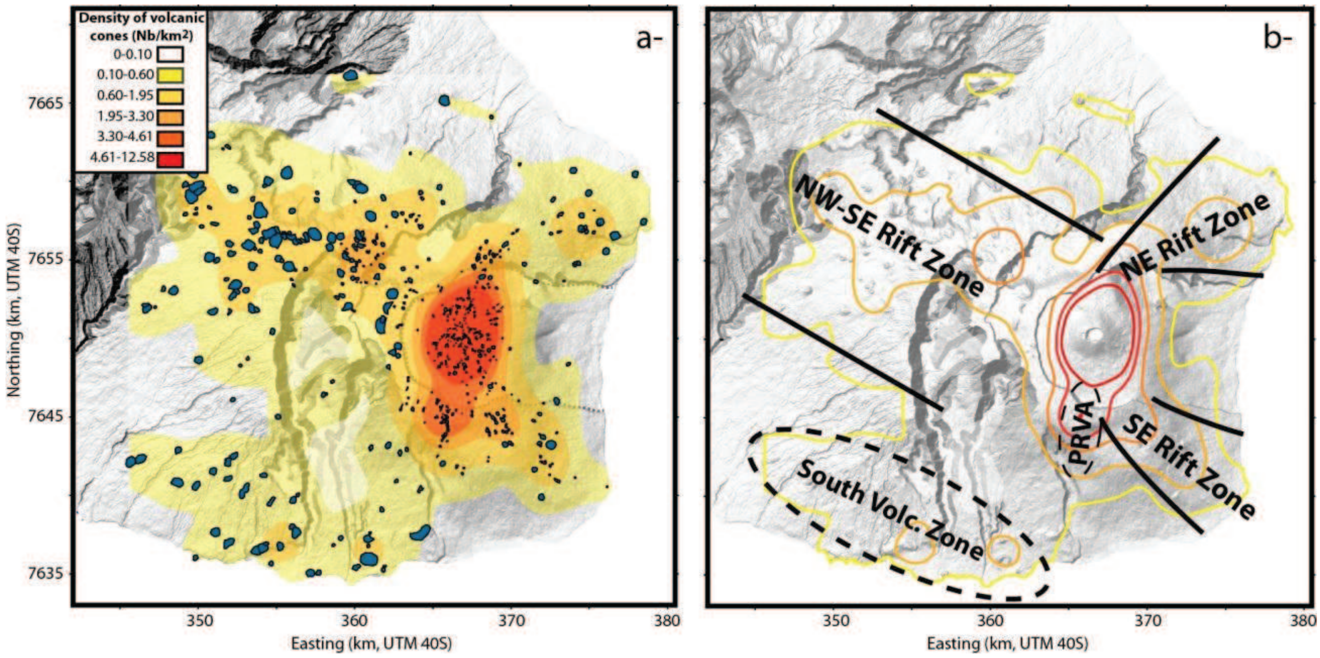

Figure 3: *Carte de concentrations des cônes volcaniques (a) et schéma structural des alentours du Piton de la Fournaise (b); d'après Michon et al. (2015)*

Ces édifices de gros volume sont associés à de nombreux dépôts de lapilli (*Bachèlery, 1981; Principe et al., 2016 ; Morandi et al., 2016*), lesquels recouvrent toute la Plaine des Sables et lui donnent son nom. Ce régime éruptif impliquant des fontaines de laves est bien plus violent que ce qui peut être observé habituellement au sein de l'Enclos (*Staudacher et al., 2016 et références incluses*). Il est aussi à noter que l'activité sismique la plus profonde a tendance à s'éloigner vers l'ouest par rapport au Piton de la Fournaise comme le montre la Figure 4 pour les éruptions d'Avril 2007 (Fig. 4a) et celles de Mai 2016 (Fig. 4b).

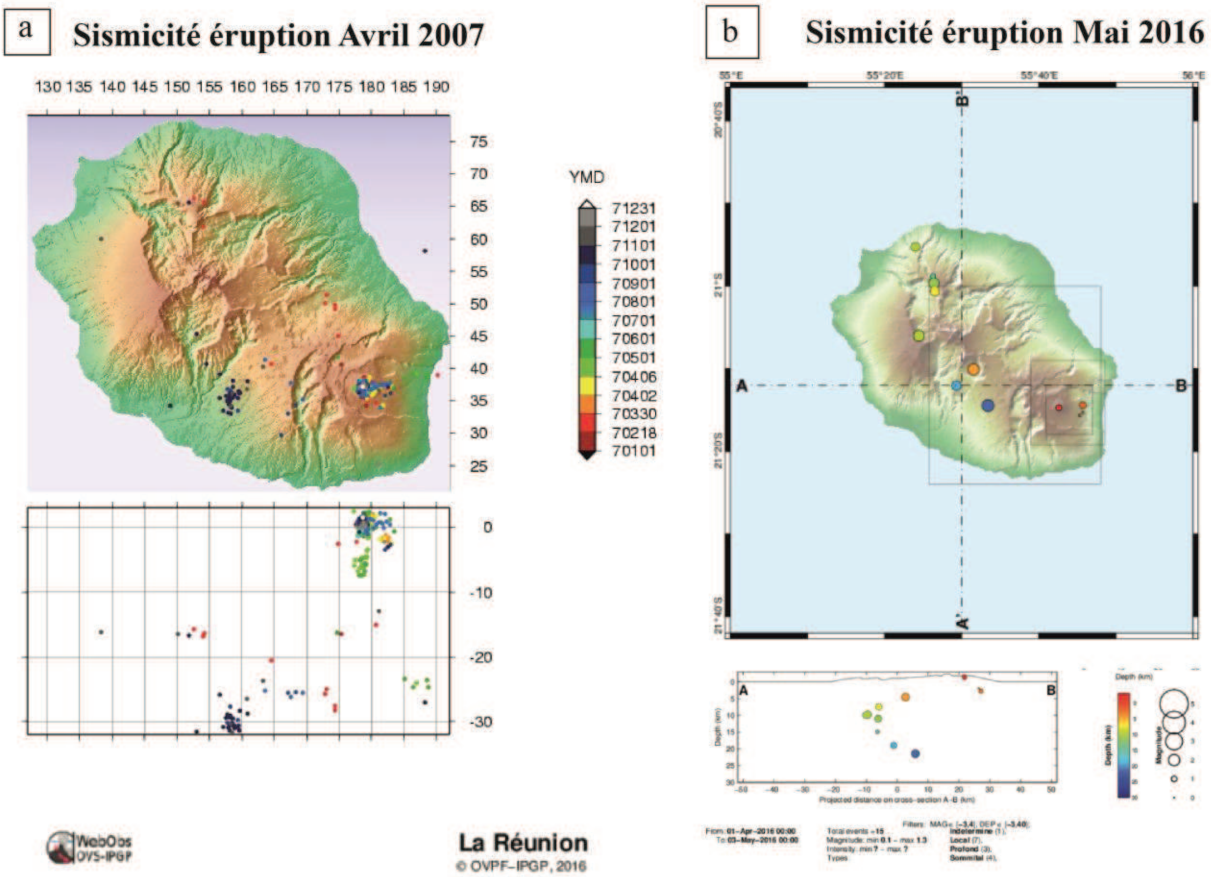

Figure 4: Sismicités associées aux éruptions du Piton de la fournaise datant d'Avril 2007 (a) et de Mai 2016 (b). source: WebObs (OVPF-IPGP)

En plus des observations sur la répartition des édifices (Fig. 3) et sur la sismicité (Fig.4), des différences de composition de produits éruptifs existent entre les éruptions au sein de l'Enclos et à l'extérieur de ce dernier. En effet, 4 groupes de compositions sont typiquement rencontrées dans les produits volcaniques sur l'île de La Réunion (Fig. 5). Le groupe des « Steady State Basalt » (SSB), globalement des basaltes transitionnels, domine l'activité récente du PdF (< 4000 ans) laquelle se traduit principalement par des éruptions à l'intérieur de l'Enclos. Le groupe des laves anormales (« Abnormal Group », AbG) montre des compositions chimiques spécifiques, très rarement observées à l'intérieur de l'Enclos Fouqué (cratère Hudson en 1998 d'après *Bureau et al., 1998a* et cratère Formica Léo d'après *Boudoire et al., in prep*), mais qui, par contre, caractérisent les produits émis hors Enclos le long de la NW-SE Rift Zone, et notamment sur la Plaine des Sables comme l'indique la composition pour le Piton Chisny sur la Figure 5.

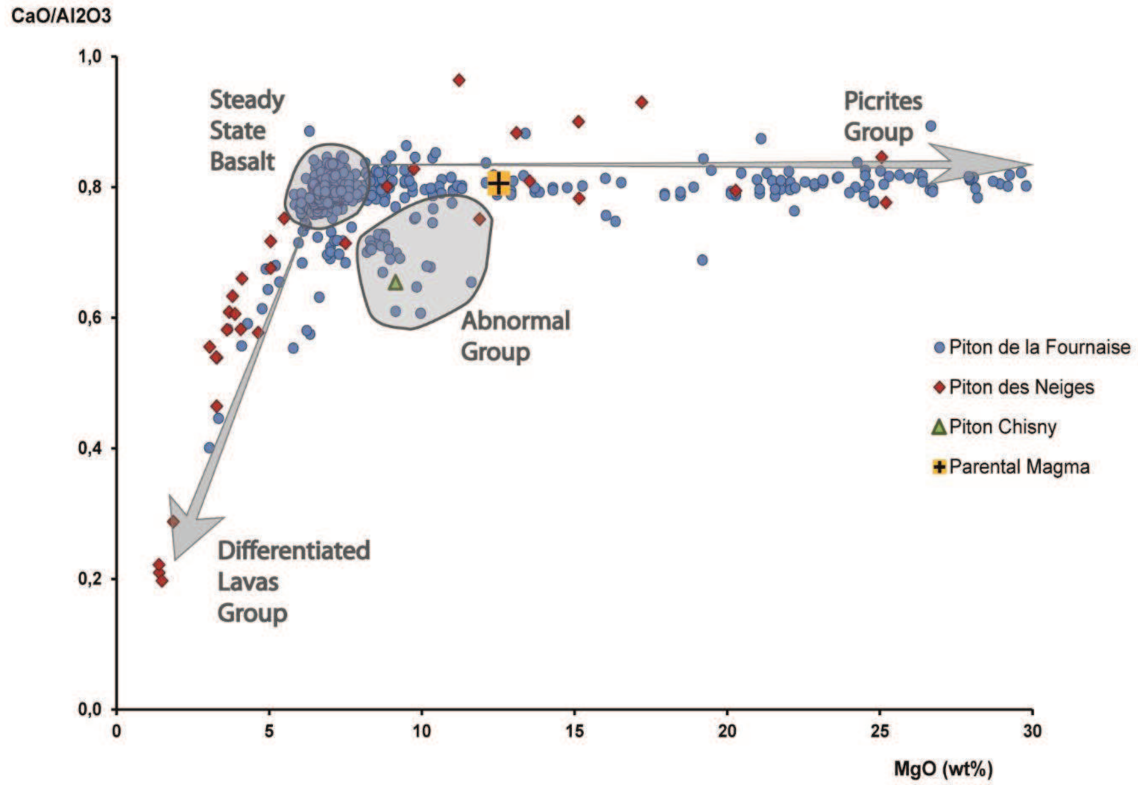

Figure 5: *Diagramme MgO vs CaO/Al2O3 pour des produits du Piton de la Fournaise ainsi que du Piton des Neiges, d'après Pichavant et al. (2016) et références incluses.*

Etant donné l'homogénéité isotopique des laves réunionnaises (*Fisk et al., 1988; Graham et al., 1990; Bosch et al., 2008 ; Vlastélic & Pietruszka, 2016*), les différences de composition entre les groupes de laves ont généralement été attribuées à des processus magmatiques intervenant au sein du système d'alimentation. Le cas des AbG suscite actuellement un grand intérêt et différents modèles ont été proposés pour expliquer ces compositions. Notons toutefois que les différents modèles font intervenir des concepts totalement différents. En effet, Kornprobst et al. (1984), puis Albarède et al. (1997) et Famin et al. (2009) ont proposé que de telles compositions proviennent d'un fractionnement profond de clinopyroxène (± olivine) au sein des magmas primitifs. Par contre, Villemant et al. (2009) et Salaün et al. (2010) interprètent le groupe des AbG comme le résultat d'un processus d'assimilation de cumulats à olivine par des liquides magmatiques plus ou moins différenciés.

Le seul cas des AbG souligne la nécessité de la réalisation d'études de pétrologie expérimentale sur des compositions du Piton de la Fournaise. Des études de ce type ont déjà porté sur des produits de La Réunion, principalement du Piton des Neiges. Cependant, elles ont été réalisées, soit à pression atmosphérique (*Tilley et al., 1971 ; Villeneuve, 2000*), soit à haute pression mais en absence de constituants volatils (H2O, CO2) ajoutés (*Fisk et al.,* *1988)*. La question se pose donc de l'applicabilité de telles expériences pour contraindre l'évolution des magmas réunionnais (*Pichavant et al., 2016*). Ce problème se pose tout particulièrement dans le contexte de fonctionnement d'un volcan actif qui demande d'intégrer au mieux les différents jeux de données (pétrologiques, géophysiques, géochimiques) dans une démarche globale de surveillance au service de la prévision.

C'est dans ce cadre que le travail de thèse a été réalisé. Il comprend trois objectifs principaux : (1) la réalisation d'une étude expérimentale représentative du système d'alimentation du PdF dans son ensemble, à partir d'un matériel de départ de composition typique de SSB et dans des conditions de pression, température, fO2, et de teneurs en volatils (H2O, CO2) réalistes ; (2) une étude pétrologique d'un échantillonnage représentatif de roches plutoniques réunionnaises pouvant servir de guide comparatif aux résultats expérimentaux et (3) l'obtention d'une base de données volcanologiques, pétrologiques et géochimiques significative sur le groupe des AbG permettant de confirmer son existence dans le système d'alimentation du PdF.

Les résultats seront présentés par type d'approche. Tout d'abord, l'étude volcanologique sera détaillée puis, dans un second temps, l'étude pétrologique des roches plutoniques. La présentation des résultats expérimentaux se fera en deux volets, correspondant chacun aux différents niveaux, superficiel ou profond, du système d'alimentation du Piton de la Fournaise.

CHAPITRE I : “Approche volcanologique - Etude volcano-stratigraphique et pétrologique d’édifices volcaniques de la Plaine des Sables et de leurs produits associés”

Résumé

Ce chapitre se présente sous la forme d'un article synthétisant les principaux résultats volcanologiques, volcano-stratigraphiques, pétrologiques et géochimiques obtenus lors de l'étude des édifices volcaniques polygéniques de la Plaine des Sables (PdS) : le Demi-Piton, le Piton Haüy et le Piton Chisny, ainsi que des produits hawaiiens récents (spatters, coulées et lapilli) qui leur sont associés. Les observations et descriptions présentées ici, ainsi que l'échantillonnage des produits éruptifs analysés, ont été réalisées durant deux missions de terrain (Octobre-Novembre 2013 et Février 2015) axées autour de cet ancien centre éruptif du volcan du Piton de la Fournaise qu'est la Plaine des Sables (île de La Réunion, Océan Indien). Une stratigraphie détaillée et mise à jour de chacun de ces 3 édifices polygéniques, faisant partie des plus volumineux observés sur le massif de la Fournaise avec le Piton de la Fournaise ss, a pu être proposée ainsi qu'une nouvelle version de la carte volcanologique de la Plaine des Sables récemment proposée par Principe et al. (2016). L'obtention de données géochimiques originales a permis de valider et de confirmer les nombreux épisodes éruptifs impliqués dans la construction de ces 3 spatter-ramparts, certains provenant clairement de magmas de compositions chimiques différentes. Les analyses en roche totale réalisées dans le cadre de cette étude montrent bien que les produits éruptifs de la Plaine des Sables ont des compositions distinctes des compositions généralement impliquées dans l'activité éruptive du Piton de la Fournaise. En effet, les produits de la PdS montrent de fortes teneurs en MgO (8-11%) ainsi que de relativement faibles rapports CaO/Al2O3 (0.65-0.78), ce qui, associé à des enrichissements en K2O et en éléments traces incompatibles, permet de les définir comme des magmas du groupe anormal (« Abnormal Group », AbG). Néanmoins, quelques échantillons avec des compositions de type « SSB », comparables à ceux généralement émis lors des éruptions modernes du PdF, ont été aussi rencontrés.

L'analyse des compositions des verres silicatés des différents dépôts de lapilli de la Plaine des Sables, que ce soit en éléments majeurs à la microsonde électronique ou en éléments traces au Laser ICP-MS, s'est révélée primordiale durant cette étude. En effet, en plus de permettre la validation et la confirmation des corrélations volcano-stratigraphiques effectuées à partir des observations et descriptions de terrain, les différentes compositions de verres silicatés obtenues ont pu être classées en 4 groupes compositionnels dont 3 correspondent à des compositions de verre silicatés encore inconnues ou très rarement rencontrées dans les produits réunionnais (Piton de la Fournaise et Piton des Neiges). Notamment, les lapilli du

Piton Chisny, émis lors d'un épisode de fontaine de lave très violent (un des plus violents de ceux du PdF), sont associés aux compositions de verre silicatés les plus primitives (8,55 à 8,74% MgO pour un rapport CaO/Al2O3 de 0,79-0,82) de celles analysées jusqu'alors dans les produits éruptifs du massif de la Fournaise. Des verres silicatés ayant des compositions typiques de l'AbG (6,55 à 8,29% MgO pour des rapports CaO/Al2O3 de 0,68 à 0,72) ont aussi été analysés. De telles compositions impliquent deux processus de fractionnement distincts : un fractionnement systématique de l'olivine et un fractionnement profond du clinopyroxène dans le cas des magmas de compositions caractéristiques de l'AbG.

L'analyse de tels verres silicatés de composition chimique typique du groupe AbG représente une avancée fondamentale pour la validation de l'existence (encore discutée par certains auteurs) de magmas de composition AbG au sein du système d'alimentation du Piton de la Fournaise, démontrant ainsi l'importance du fractionnement profond de clinopyroxène dans l'histoire magmatique de ce dernier, malgré la prédominance de l'olivine dans les produits éruptifs.

Compositional variability of basaltic spatters activity in the Plaine des Sables (Reunion island): Volcanological and Petrological constraints

Yann-Aurélien BRUGIER(1), Yannick LE MOIGNE(1), Michel PICHAVANT(1), Jean-Louis BOURDIER(1), Guillaume BOUDOIRE(2,3) & Andréa DI MURO(3,4)

(1) Institut des Sciences de la Terre d'Orléans (ISTO) : UMR 7327, Université d'Orléans, 45071 Orléans, France and ISTO, UMR 7327, CNRS, 45071 Orléans, France and ISTO, UMR 7327, BRGM, BP 36009 Orléans, France

(2) Laboratoire Géosciences Réunion, Université de La Réunion, Institut de Physique du Globe de Paris (IPGP), Sorbonne Paris-cité, UMR 7154 CNRS, F-97715 Saint-Denis, France

(3) Observatoire Volcanologique du Piton de la Fournaise (OVPF), Institut de physique du Globe de Paris (IPGP), Sorbonne Paris-Cité, UMR 7154 CNRS, Université Paris Diderot, Bourg Murat, France ; Plaine des Cafres, La Réunion (FR)

(4) Institut de Physique du Globe de Paris (IPGP), Sorbonne Paris-Cité, UMR 7154 CNRS, Université Paris Diderot, F-75005 Paris, France

Abstract The volcanostratigraphy and chemistry of recent products of the Plaine des Sables (PdS), a former eruptive center of Piton de la Fournaise (PdF) volcano in La Réunion Island (Indian Ocean), are described. New field observations combined with original geochemical data lead to the proposition of a revised and improved volcanological map and stress the specificity of magma series recently erupted on the PdS. Three of the most voluminous polygenetic volcanic edifices in the modern eruptive history of PdF belong to the PdS: Demi-Piton, Piton Haüy and Piton Chisny. The detailed stratigraphy of each of these 3 edifices has been worked out. The eruptive activity is typically Hawaiian, yielding the whole range of deposits from spatters, lava flows and lapilli. The 3 edifices were constructed as spatter-ramparts (or -cones). Their construction and evolution involve numerous eruptive episodes which tap several chemically distinct magma batches. Bulk rock major and trace element analyses show that the PdS products are atypical on the PdF. Most have high MgO (8-11 wt%) and low CaO/Al2O3 (0.65-0.78); enrichment in K2O and incompatible trace elements is marked, all these characteristics being diagnostic of the Abnormal Group (AbG) magma series. Few samples have bulk rock compositions similar to the Steady State Basalts (SSB) that dominate the present-day eruptions of PdF. Major and trace element analysis of glasses in lapilli samples defines 4 main compositional groups. Among these, 3 correspond to compositions so far unknown as glasses on the PdF. This includes AbG-type glasses (MgO = 6.55-8.29 wt%; CaO/Al2O3 = 0.68-0.72) from Piton Haüy and Piton Chisny, and primitive glasses (MgO = 8.55-8.74 wt% MgO; CaO/Al2O3 = 0.79-0.82) from Piton Chisny, these latter associated with a highly energetic lava fountaining episode. Olivine is the only phenocryst phase systematically present in PdS products. Yet, two fractionation mechanisms are identified from our data, one based on olivine and the other on clinopyroxene. Olivine fractionation is ubiquitous whereas cryptic clinopyroxene fractionation is associated with the AbG signature. The discovery of AbG-type glasses is decisive proof that the AbG series represent a specific magma type on the PdF.

Keywords: *Piton de la Fournaise, Plaine des Sables, volcanostratigraphy, AbG-type glasses, clinopyroxene fractionation*

1 Introduction

Since 400 ka until today, the Piton de la Fournaise has been highly active and is one of the best examples of basaltic shield volcanoes worldwide (Lénat, 2016 and references therein). In the recent activity (i.e., since the last ~ 40 ka), the most frequently erupted products are defined as "Steady State Basalts" (SSB). This *first* compositional group corresponds to transitional (tholeiitic to alkaline) basalts with a restricted compositional range (49-50 wt% SiO2; 5-7 wt% MgO; 0.75-0.85 CaO/Al2O3). In the same period, the second most abundant products emitted are olivine-rich basalts and picrites (44-45 wt% SiO2; 8-28 wt% MgO; 0.75-0.85 CaO/Al2O3), often associated with high magma production rates and large volume eruptions (e.g., in 2007). These lavas, named "Oceanites" when MgO > 20 wt% (Lacroix, 1923), are characterized by the presence of a variable but elevated (5-60%) proportion of olivine crystals and, consequently, by high whole-rock MgO contents. They are now consistently interpreted as reflecting the accumulation of olivine xenocrysts in a SSB-type liquid (Lacroix, 1923; Albarède, 1997; Villemant et al., 2009; Boivin & Bachèlery, 2009; Welsch et al., 2009). Both SSB and Picritic products are found emitted principally inside the Enclos Fouqué.

A *third* group occurs among products of the recent activity, the Abnormal Group (AbG). It is characterized by mixed geochemical characteristics (45-47 wt% SiO2; 8-11 wt% MgO; 0.60-0.80 CaO/Al2O3), with enrichments in Fe, Mg, Ti, Na, K, and depletions in Ca. Since Reunion lavas are isotopically very homogeneous (Albarède et al., 1997; Vlastélic et al., 2005; 2007; 2009; Bosch et al., 2008; Pietruzka et al., 2009; Vlastélic & Pietruszka, 2016), the different groups of PdF lavas above must be generated inside the volcano's plumbing system. Concerning the AbG group, various petrogenetic models have been proposed. AbG-type compositions have been suggested to result from clinopyroxene (+/- olivine) fractionation at depth (Kornprobst et al., 1979; Albarède et al., 1997; Famin et al., 2009). Alternatively, assimilation of olivine-rich cumulates by evolved melts (similar to the "Pintades" lavas) would yield AbG-type compositions (Villemant et al., 2009; Salaün et al., 2010). The main difference between these two models is that the former postulates the existence of AbG-type melts in the PdF plumbing system whereas, according to the latter, there is no need for exotic melt compositions since the evolved melts would represent fractionation products from SSB lavas. Another point is that the AbG group is still poorly documented, being represented by only a few eruptive products and a limited number of geochemical analyses (Bulk Rock analyses principally). The available data suggest that AbG-type products are rarely observed inside the Enclos Fouqué (e.g., Hudson eruption, early 1998 activity), but rather are found at eccentric cones outside the Enclos Fouqué and at recent cones west of the main central cone.

In this context, the aim of our study was first to complete the volcanological and petrological data characterization of the 3 main edifices of the PdS, and to propose a revised and improved volcanological stratigraphy and map, providing us a solid stratigraphic position of each deposit analyzed in this study. Indeed, in a second time, by studying these three edifices which all host AbG-type compositions, a mineralogical and geochemical database on AbG products has been developed. This has led to a more precise definition of this group of lavas and in particular to the demonstration of the existence of AbG-type melts on the PdF.

2 Geological setting & volcanological context

The La Reunion island is located in the south-west of Indian Ocean (21°10'S, 55°30'W), around 800 km off the Madagascar eastern coast (Fig.1a). La Réunion is a volcanic oceanic system situated at the end of a hotspot track (Duncan et al., 1989; Bonneville, 1990), which includes the Deccan flood basalts erupted 65 Ma ago (Chenet et al., 2007). The island's shape is that of an oval (50 km by 70 km) elongated in a northwest-southeast direction (Fig.1b). It represents the subaerial part (only 3% of the total volume, according to de Voogd et al. 1999) of a large volcanic edifice, 220-240 km in diameter and 7 km in height, sitting on the oceanic floor at 4 km below sea level (Lénat et al., 2016; and references therein).

Two juxtaposed volcanoes compose the island (Fig.1b): the Piton des Neiges to the NW and the Piton de la Fournaise to the SE (Lacroix, 1923; 1939). There is also an old hypovolcanic intrusive system buried under the eastern flank of the Piton de la Fournaise (Rançon et al, 1989) which has been attributed to a third volcano, named "Les Alizés" (Malengreau, 1995; Malengreau et al., 1999; Lénat et al., 2001; 2012a; Gailler et al., 2009; Gailler & Lénat, 2010; 2012; Smietana, 2011; Lénat, 2016). Some 3.3 Ma old pillow-lavas deposits have been associated with the Les Alizés volcano (Smietana et al., 2010). Yet, the existence of the Les Alizés volcano is still debated (Lebas, 2012; Salvany et al., 2012).

The Piton des Neiges activity began 5 Ma ago on the sea floor (Gillot et al., 1994). The oldest sub-aerial deposits are 2.2 Ma old (McDougall, 1971) and the activity ended 29 ka ago (McDougall, 1971; Quidelleur et al. 2010). A younger age has been obtained on pyroclastic deposits from Piton des Neiges (12 ± 3ka using the U-Th method; Deniel et al., 1992) but is not considered here as it appears questionable (see Salvany et al. 2012). An evolution from basaltic shield stage (between 2.2 and 0.4 Ma) to differentiated alkaline strato-volcano stage (between 350-400 and 29 ka) has been recognized in the eruptive history (Smietana, 2011; Lénat et al., 2016 and references therein). Since its last period of activity, the Piton des Neiges volcano has been deeply eroded, explaining the three 10 km-wide depressions named the Cilaos, Mafate and Salazie "Cirques".

The Piton de la Fournaise (PdF) has been active since 535 ka (Gillot & Nativel, 1989; Kluska, 1997). Its first stage of activity (530 to 400 ka) is characterized by the emission of feldspar-rich basalt to mugearite flows, grouped into the "Pintades" or "Plagioclase-Ultraphyric Basalts" lava unit (Bachèlery, 1981; Bachèlery and Mairine, 1990; Mairine and Bachèlery, 1997; Merle, 2010; Valer et al., 2015). The origin of these differentiated lavas is still debated, and they could represent alternatively either an initial alkaline phase of the Piton de la Fournaise or the last eruptive stage of the Les Alizés volcano (Smietana, 2010; Valer et al., 2015). Since 400 ka until today, the Piton de la Fournaise has been highly active and is one of the best examples of basaltic shield volcanoes worldwide (Lénat, 2016 and references therein). Its volcanological history is marked by a series of construction, destruction and deformation episodes (Bachèlery, 1981; Merle et al., 2010; Michon et al., 2016 and references therein).

The main structure of the present-day volcano is the U-shaped collapse caldera named “Enclos Fouqué”. This structure is thought to have originated from several caldera collapses associated with phreatomagmatic eruptions between 4880±35 BP and 2855±35 BP, as marked stratigraphically by the Bellecombe ash deposits (Bachèlery, 1981; Mohamed-Abchir, 1996; Upton et al., 2000; Ort et al., 2016; Morandi et al., 2016). The Enclos Fouqué collapse caldera actually delimits the currently active part of the PdF which includes the central cone and almost all recent eruptions (Fig.1b).

Westwards from the Enclos Fouqué, another collapse caldera, named “Rempart des Sables”, delimits the “Plaines des Sables” (PdS), the area which forms the subject of this paper (Fig.1c). The “Rempart des Sables” caldera is associated with the migration of the PdF volcanic center eastwards from its ancient (between 530 and 60 ka) to the actual location, around 60-40 ka ago (Bachèlery & Mairine, 1990; Gillot & Nativel, 1989; Merle et al., 2010; Staudacher & Allègre, 1993; Michon et al., 2016). The PdS, located 5 km west of the PdF summit, owes its name to a continuous thick (from 10 cm to 1 m) cover of basaltic lapilli, which contrasts with the generally effusive nature of PdF products. Several cones and associated lava flows outcrop in the PdS, especially three polygenic volcanic edifices aligned on a N30~40° axis (Fig.1c) that comprise AbG-type eruption products: the Piton Chisny, the Demi-Piton and the Piton Haüy (Bachèlery, 1981; Morandi et al., 2016; Principe et al., 2016).

Recent studies have proposed a first volcanological stratigraphy (Morandi et al., 2016) and volcanological map (Principe et al., 2016) of the PdS. A relative chronology of the main stratigraphic units has been defined using the Bellecombe ashes (from 4880±35 BP to 2855±35 BP) as the main depositional marker (Morandi et al., 2016; Principe et al., 2016). The “pre-Bellecombe” deposits include monogenic strombolian cones, in part covered by some Oceanite lava flows and by the Demi-Piton edifice, the latter covered by some reworked Bellecombe ashes. The post-Bellecombe deposits include the Piton Haüy products with lava flows and associated lapilli deposits, and the youngest edifice of the PdS, the Piton Chisny. The youngest deposits associated with Piton Chisny yield ages of 1105±60 BP (lava down the Langevin valley, Bachèlery, 1981; Tanguy et al., 2011) and 381±26 BP (the latest Chisny fall deposits, Morandi et al., 2016). The whole range of lava flow surface textures known at PdF are encountered at the surface of the PdS (Principe et al., 2016). Eruptive dynamics of Demi-Piton, Piton Haüy and Piton Chisny ranges from violent lava fountaining (lapilli falls covering the PdS) to long lasting effusive events (e.g. lava lake from the latest Chisny activity). Recent studies demonstrate that the PdS has been an area of frequent and sometimes violent eruptive activity a few hundred years ago. As the most voluminous eruptions occurred on the PdS have emitted lava flows able to reach inhabited areas, the PdS is considered as one of the most potentially hazardous area of the PdF massif (Di Muro, 2012; 2015; Morandi et al., 2016; Principe et al., 2016).

3 Methods

3.1 Field datas

Stratigraphical relations between volcanic deposits of the Plaine des Sables were determined on the basis of 75 outcrops descriptions and samples (see Table 1), obtained during 2 field missions. The main stratigraphical relations are summarized on volcano-stratigraphical sections (Fig.3, 4 & 5). GPS coordinates of these 75 sampling sites were measured. These coordinates were used to construct a volcanological map of the Plaines des Sables (Fig.2), with a Geographical Information System software (ArcGIS©).

3.2 Analytical techniques

Samples of spatters, scoriae and lava flows were examined in polished thin sections by optical microscopy. Lapilli were embedded in epoxy resin, and then polished for further examination and analysis. A few (REU 49, 50, 74) were subjected to mineral separations using the "float/sink" method with Bromoform ($\rho = 2.89$g.mL-1). In order to characterize the eruption products, different methods, summarized in Table 1 and detailed below, were implemented.

3.2.1 *Scanning electron microscopy*

Some representative samples were imaged with a scanning electron microscope (SEM) using the TESCAN Mira 3 XMU instrument at the ISTO-BRGM laboratory in Orléans.

3.2.2 *Bulk rock analyses*

Major and trace element bulk-rock analyses were carried out at the Centre de Recherches Pétrographiques et Géochimiques (CRPG-SARM) in Nancy (France) by inductively coupled plasma-optical emission spectrometry and -mass spectrometry (ICP-OES & ICP-MS, Carignan et al., 2001). A total of 29 samples covering the whole range of erupted products were analyzed (see Table 1).

3.2.3 *Electron microprobe analyses*

Major elements compositions of mineral phases (all samples) and matrix glasses (lapilli) were obtained with a CAMECA SX FIVE electron microprobe at the ISTO-BRGM laboratory. Analyses were performed under 15 kV acceleration voltage, 6 nA sample current, 10 s counting time on peak and 5 s counting time on background. Mineral phases were analyzed with a focused beam; for matrix glasses, a defocused beam (10µm) was used to minimize alkali migration (Di Carlo et al, 2006). Relative analytical errors are 1% (SiO2, MgO, CaO), 1-2% (Al2O3), 2-4% (FeO, Na2O) and 5-10% (TiO2, K2O). Chemical zonation in phenocrysts was documented either from spot (i.e., rim vs core) or scan (i.e., traverses with steps of 10-20 µm) analyses. Each matrix glass sample was analyzed twice, in order to constrain the internal compositional variability of each sample.

3.2.4 *LA-ICP-MS analyses*

Trace elements in matrix glasses were analyzed by laser ablation inductively coupled plasma-mass spectrometry (LA-ICP-MS). Analyses were performed at the Laboratoire des Domaines Océaniques (LDO-UMR6538) laboratory in Brest (France), using a 102-193 ArF Excimer laser ablation system (Compex Pro) coupled to an Element 2 (double focalization) ICP-MS system, with helium as the ablation gas for trace elements. Samples were analyzed using a laser repetition rate of 10Hz, a 60 µm laser spot diameters and a pulse energy of 100 mJ (15 J/cm). Measurements were calibrated against two basaltic standards (BIR-1 & BCR2) and one glass standard (NIST612), using CaO as the internal reference element. Between 2 to 5 measurements was obtained for each glass sample, depending of its crystallinity and vesicularity.

4 Results

Results presented below include, firstly, volcano-stratigraphic data on the PdS and, secondly, petrological and geochemical data on selected samples and deposits. Sample descriptions and types of analyzes performed are summarized on Table 1.

4.1 Volcanological and stratigraphic results

4.1.1 *Volcanological map*

A revised volcanological map of the PdS is proposed (Fig. 2). It draws on previous maps and correlations (Bachèlery, 1981; Morandi et al., 2016; Principe et al., 2016) and integrates our new field data, notably detailed volcano-stratigraphic informations and correlations on the Demi-Piton (Fig. 4), Piton Haüy (Fig. 5) and Piton Chisny (Fig. 6). The field-based informations have been greatly aided by glass chemical analyses (details provided below) which have been obtained systematically on lapilli samples. These served to crosscheck and confirm the stratigraphical attributions.

The PdS is largely covered by deposits associated with the "Piton Chisny" and "Aubert de la Rue" activity in the central to southern part of the studied area (Fig. 2). Erupted products includes spatters (units c1, 2, 3, 4, aub in Fig. 2), lava flows (c2a, b, c, d; c3a, b, c; aub1, aub2) and lapilli (c2lap, c3lap, rw). The whole range of deposits from Hawaiian-type activity, from explosive (lapilli deposits associated with violent lava fountaining) to effusive (thin .pahoehoe lava flows associated with long lasting effusive eruptions, see Fig. 3 for description .of typical deposits) is encountered. Drill cores in the western part of the PdS have found reworked lapilli over thicknesses exceeding 1 meter (Morandi et al., 2016). This reworked material comes from lava fountaining activity on Piton Chisny (units c2lap, c3lap).

The central part of the studied area is made principally of the Demi-Piton spatter-rampart (dp1, 2). This asymmetric structure is what remains after a syn- to post-depositional collapse event that has affected the edifice (see also Fig. 4). Lapilli associated with the upper deposits of the Demi-Piton (dp2 unit) have been sampled on the northern slopes of the rampart (sampling point #37 on Fig. 2), although this is the only example of lava fountaining activity found associated with the Demi-Piton. In the same way, no lava flow could be observed from the Demi-Piton, this type of activity being probably covered, either, on the east, by other pre-Bellecombe lava flows (oc1, 2) or, on the west, by Chisny lava flows (c2b,c; #c3a, b) and the reworked lapilli (rw).

In the north part of the studied area, the Haüy spatter-cone is relatively well preserved. Up to 3 spatter deposits can be distinguished (h1, 2, 3) despite a syn- to post-depositional collapse in the northwestern flank. Lapilli deposits associated with the stratigraphic unit h2 (h2lap) are found on the southwestern and southeastern slopes, as well as lava flows associated with the stratigraphic unit h3 (h3a). The collapse cirque contains a strombolian cone (h4) and small associated lava flows (h4a, b). The Haüy lava flows are probably in large part covered by the Chisny lava flows (c3a, b), and the reworked lapilli cover (rw), locally by lapilli deposits (c2lap).

All 3 polygenetic centers record syn- to post-depositional destabilization and/or collapse events as evidenced by the c1 and h1 units (respectively for Chisny and Haüy). Both correspond to tilted and displaced blocks of spatter, rafted by a syn-depositional flank collapse (Sumner, 1998). Moreover, 3 collapse cirques (for Chisny more a rock slide scarp) occur near the summit of each edifice.

There are 3 major lapilli deposits respectively associated with units h2, c2, c3. Among these, the c2lap deposit shows an important extension, being found on the slopes of Piton Haüy and so more than 1 km from a potential eruptive vent. This deposit marks the most violent lava fountain episode in the recent activity of the PdF. It has been used as a major stratigraphic marker in the PdS (Morandi et al., 2016; Principe et al., 2016).

Below, the detailed stratigraphic relations of the 3 main edifices are presented, from the oldest to the youngest.

4.1.2 *Demi-Piton: detailed stratigraphy*

Only the western flank of the Demi-Piton is preserved (Fig. 2). This particular structure offers a north-south cross-section inside the edifice (Fig. 4a, b). The basal spatter is covered by (1) post-Bellecombe deposits (oc1, 2), (2) the Bellecombe ash deposit (Bac) and (3) an important unit of reworked lapilli (rw, see Fig. 4b). Nevertheless, 2 lapilli deposits were found under the reworked layer. From base to top, this includes a lapilli deposit of unknown stratigraphic attribution (unsp, Fig. 4b; sample REU-01A, Table 1; 3) and a lapilli deposit which is associated (by making use of the glass chemical data) with the Chisny activity (c3lap; sample REU-01B; Table 1; 3).

The detailed stratigraphic section of the edifice is shown on Fig. 4c. It specifies the different types of spatter deposits encountered within the 2 main stratigraphic units, dp1, dp2. These are separated by a discontinuity level of altered lapilli with hints of paleo-soil (Fig. 4b, c). The dp1 unit (minimum thickness of 40 m) is mostly composed of hardened, welded and well compacted spatter deposits (Fig. 4d, e). One exception is a red tephra associated with lava fountaining observed just at the bottom of the discontinuity between dp1 and dp2 (Fig. 4j). The base of dp1 (thickness ~ 20 m) is made of a hardened, red spatter (sample REU-02, Table 1; 2) with coalesced spatter levels (Fig. 4f). This coalescence results from syn- to post-depositional compaction and welding of hot juvenile clasts during a rapid accumulation of spatter (Sumner, 1998). The transition between clasts outlines can be observed (Fig. 4f). At the top of this red coalesced spatter deposit, a black spatter (5-10 m thick) with numerous (0.5-2 m thick) coalesced spatter levels is described (Fig.4 d; e). These levels are continuous all along the edifice (Fig. 4e) and are named "clastogenic flows" since they are difficult to distinguish from intercalated lava flows (Sumner, 1998). The top part of the dp1 unit is composed of a welded, red spatter deposit (Fig. 4g), with some well compacted and stratified levels (Fig. 4i).

The dp2 unit is composed of sintered, fractured and fluidal clasts spatter deposits less agglomerated and compacted then the dp1 components (Fig. 4c). The upper deposits include a 1 m thick lapilli deposit (sample REU-37, Table 1; 3) with, on the top, a distinctive level of strongly welded red lapilli (Fig. 4k) that forms the surface of the main part of the western flank (sample REU-15, Table 1; 2). This is one of our two PdS samples where clinopyroxene phenocrysts are present (Table 4), and found crystallizing together with olivine phenocrysts. Dunitic xenoliths (Fig. 4h) occur all along the dp1 and dp2 units.

Overall, the structure of the polygenetic spatter-rampart with compacted and coalesced levels in the basal unit (dp1) and less welded and compacted upper deposits (dp2) is typical of large volume spatter edifices (Sumner, 1998).

4.1.3 *Piton Haüy: detailed stratigraphy*

Deposits associated with the Piton Haüy are divided in 4 stratigraphic units (h1, 2, 3, 4, Fig. 2). Deposits of unit h1, the first episode of construction of the edifice, are localized in the northern part of the PdS (Fig. 2; 5b, g). They are mainly composed of very oxidized, altered red spatters (sample REU-45; Table 1; 2). Typical outcrops of h1 deposits consist in spatter megablocks, most of them rafted during a syn-depositional flank collapse of the h1 edifice. These megablocks are the only remnants of the h1 products. This explains why, in the thalweg between Piton Haüy and Demi-Piton, Haüy deposits (unit h2) are observed directly above spatter deposits from the dp2 unit (Fig. 2; 5c-g).

Deposits of unit h2 are found mostly at the base of the main spatter cone edifice (Fig. 2). They consist of successive lapilli deposits and clastogenic flows (Fig. 5c). These h2 deposits are continuously observed from the foot of the eastern flank (Fig. 5h, i) to the thalweg between Piton Haüy and Demi-Piton (Fig. 5d-g). Lapilli deposits associated with the h2 unit can reach thicknesses of ~2-3 m (Fig. 5c, h). At least 3 episodes of lava fountaining with intercalations of "clastogenic flows" can be recognized (h2lap1, 2, 3, Fig. 5c). In each lapilli deposit, levels rich in bombs and fluidal clasts are observed (Fig. 3j), in relation with variations of the fountaining regime. The h2 lapilli directly cover the pre-Bellecombe oceanite lava flows (oc, Fig. 2) on the northeast part of the PdS near the foot of the eastern flank of Piton Haüy (Fig. 5i). Dunitic xenoliths (Fig. 3c) are found in the h2 deposits. The reworked lapilli cover (rw, Fig. 2) near Piton Haüy is made of h2 lapilli, either alone or mixed with c2 deposits (Fig. 3k).

The main topographic structure of Piton Haüy is the result of the construction of an important spatter-cone edifice associated with the h3 stratigraphic unit (Fig. 2). This spatter-cone is composed of several spatter episodes which are difficult to distinguish individually because their textures (fluidal clasts coalesced to clastogenic flows) are similar. In addition, the flanks of the edifice are affected by numerous fractures that result from post-depositional flank destabilizations and render correlations uncertain. The h3 spatters overlay the h2 deposits, as observed on the southern flank and up to the eastern flank of Piton Haüy (Fig. 5c-g).

A major cirque is observed on the western flank of the edifice (Fig. 2, 5a, b), a consequence of a syn to post-depositional flank collapse of the spatter-cone h3. The center of the cirque is occupied by a small strombolian cone (unit h4, Fig. 2; 5a, b; sample REU-30, Table 1, 2) which has emitted 2 lava flows (h4a, b, Fig. 2; sample REU-32B, Table 1, 2). These h4 deposits are interpreted to have originated from a post-collapse strombolian activity. The laminated pahoehoe h4 lava flow (Fig. 3n) is the second rock from our sample set that contains clinopyroxene phenocrysts (sample REU-32A, Table 1, 4). The reworked lapilli cover is encountered in the inner slopes of the cirque, as well as, locally, a lapilli layer belonging to the c2 unit (sample REU-32A, Table 1, 3).

4.1.4 *Piton Chisny & Aubert de la Rue : detailed stratigraphy*

Piton Chisny, with spatter deposits more than 100 m thick (Fig. 6c) is the main polygenetic center of the PdS (Fig. 2). As Piton Chisny corresponds to the last volcanic activity on the PdS, the Chisny deposits (spatters, lava flows, lapilli and reworked lapilli) cover the older deposits from either Demi-Piton or Piton Haüy. More than 2/3 of the PdS area (Fig. 2) is covered by the Piton Chisny edifice and its products. The complete spectrum of deposits associated with Hawaïan-type eruptions is encountered around Chisny (see Fig. 3). This polygenetic spatter-rampart is made of 4 stratigraphic units (c1, 2, 3, 4, Fig. 2, 6). The Aubert de la Rue spatter and lava field (aub, Fig. 2) forms a structure separate but close and which is considered as the fifth and last stage of activity of Piton Chisny.

At the foot of the northern and eastern flanks of Piton Chisny, spatter deposits associated with the c1 unit are observed (Fig. 3h; Fig. 6b, c, f, g). These are welded and stratified products with agglutinated fluidal clasts (Fig. 3h; sample REU-69A, Table 1, 2). Clasts of that type are associated with medium cooling (both ΔT and ΔT/t) and accumulation rates of magma fragments emitted from the inner to the outer portion of a basaltic lava fountain (Sumner et al., 2005). This unit includes intercalated (or clastogenic) lava flows; dunitic xenoliths are quite common (Fig. 6c). The spatter constructed during the c1 stage was largely dismantled by a syn-depositional collapse flank. Indeed, numerous rafted blocks of c1 spatter are found at the foot of the northern flank of Piton Chisny, embedded in lava flows from younger (c2 and c3) stratigraphic units (Fig. 2; Fig. 6g). Neither lava flow nor lapilli deposits of the c1 stage are found around Piton Chisny.

The spatter associated with the second unit c2 can be observed at the foot of the northern flank of Piton Chisny (Fig. 6d, e; sample REU-68, Table 1). It forms the base of the western flank of the spatter-rampart (sample REU-64A, Table 1; Fig. 2). These c2 spatter deposits consist of black brittle clasts (lapilli & bombs) barely compacted and agglomerated (Fig. 3f, g). Clasts of that type are associated with high cooling and medium accumulation rates of magma fragments emitted from the outer portion of a basaltic lava fountain (Sumner et al., 2005). Up to 4 lava flows were emitted during the c2 stage (c2a, b, c, d, Fig. 2). Texturally, they range from a thin pahoehoe (c2c in Fig. 2; Fig. 3l) to a chaotic lava flow rich in dunitic xenoliths (c2d in Fig. 2; Fig. 3o). A major lava-fountaining episode is also associated with c2 (c2lap in Fig. 2). In fact, lapilli deposited from that episode are observed all over the PdS: (i) at the foot of the north flank of Piton Chisny (sample REU-65, Fig.2; Table 1, 3), (ii) under c2 lava flows (sample REU-41, Fig.2; Table 1, 3), (iii) intercalated between c2 lava flows (REU-74, Fig. 2; Table 1-3), (iv) on the slopes of Piton Haüy (samples REU-32A, 34, 36 Fig.2; Table 1, 3) and (v) at the foot of the "Rempart des Sables" (samples REU-55, 70, Fig.2; Table 1, 3). From a petrographic point of view, the c2lap lapilli samples (e.g., REU-34) are characterized by micro-dunitic xenoliths and olivine macrocrysts. Field relationships (c2lap either covered by or intercalated between c2 lava flows) imply that lava fountains and lava flows were synchronous. The architecture of c2 products is consistent with an eruptive fissure oriented ~ N30° (in the alignment of the Chisny-Demi Piton-Haüy edifices) but fissures oriented N120° were also observed north of Piton Chisny (Fig. 2).

The main part of the Chisny edifice is made of spatter deposits associated with unit c3 (Fig. 2; Fig. 6b, c, e, g). This spatter corresponds to sintered, fractured and agglutinated fluidal red clasts (Fig. 3e; samples REU-60A, 61C, 71A, Table 1, 2). Clasts of that type are associated with medium cooling and accumulation rates of magma fragments emitted from the inner to the outer portion of a basaltic lava fountain (Sumner et al., 2005). An important clastogenic flow (c3b, Fig. 2) is described on the north-eastern flank, overlying the c1 spatter deposit (Fig. 2; Fig. 6a, b) and giving to the spatter-rampart Chisny its curved shape (Fig. 2; Fig. 6a, b). Intercalated lava flows (or clastogenic flows; sample REU-71B; Table 1, 2) are observed, as well as dunitic xenoliths and ballistic blocks (0.5-1 m size), some of them being doleritic (Fig. 3c, d). The numerous dense blocks found on the lower slopes of Piton Chisny (Fig. 3i) are interpreted as disaggregated and gravitationally entrained ballistics related to the c3 stage of activity. Up to 3 lava flows are emitted during the c3 stage (c3a, b, c). They cover important surfaces on the PdS, e.g. lava flow c3a extends up to the northern end of the PdS (Fig. 2). Lapilli belonging to the c3 unit are found either below the lava flows (c3b: samples REU-59A, REU-66, Table 1; c3c: samples REU-48, REU-57, Table 1) or intercalated between two of them. Therefore, the lava fountaining activity responsible for spatter construction and the emission of lava flows were synchronous.

At the summit of the Piton Chisny, a small spatter deposit (sample REU-62; Table 1, 2) with an intercalated lava flow (or a clastogenic flow; REU-63, Table 1) defines the c4 unit (c4; Fig. 2). This spatter is made of sintered and fractured fluidal clasts, barely agglutinated. Clasts are less altered and more reddish than the c3 spatter deposits. Ballistic blocks are absent; a few dunitic xenoliths were found. No other type of deposits (e.g., lava flows or lapilli deposits) has been observed within the c4 unit.

At the center of the curved spatter-rampart of Piton Chisny, a spatter characterized by black clasts with a fluidal texture is described (Fig. 2; Fig. 6a, b). This crater, named Aubert de la Rue (aub in Fig. 2), has contained an ancient lava lake (Bachèlery, 1981) and fed a lava field (aub1, 2, Fig. 2). It is considered as the last stage of activity of Piton Chisny. Spatter-cones of unit aub consist of agglutinated and partially coalesced splashed fluid clasts, e.g. cowpats (Fig. 3a, b; sample REU-75; Table 1, 2). Clasts of that type are associated with low cooling and low to medium accumulation rates of magma fragments issued from the inner portion of a basaltic lava fountain (Sumner et al., 2005). Among the 2 lava flows associated with the aub spatter, the oldest (aub1; Fig. 2) extends to the southern end of Demi-Piton toward the north, and to the end of the PdS toward the south. The youngest flow (aub2, Fig. 2; sample REU-58, Table 1) bypasses the northern flank of the aub spatter and follows the base of the eastern flank of Piton Chisny to the south scarf of the PdS (Fig. 6a, b). The aub lava flows cover the c3-related flows (Fig. 2).

The polygenetic Piton Chisny spatter-rampart shows many fractures (Fig. 2) and also rock slides (Fig. 6a, b) which indicate partial destabilization of its eastern flank, mainly constructed from deposits of the c3 unit. Nevertheless, Piton Chisny shows little evidence for collapse of the edifice. Syn- to post-depositional collapse is clearly more important on the Demi-Piton and Piton Haüy (e.g. the north-south cross-section of Demi-Piton and the collapse cirque at the summit of Piton Haüy).

4.2 Petrological and geochemical data

Selections of representative analyses are given in Table 2 (bulk-rock data), Table 3 (major and trace element compositions of matrix glasses) and Table 4 (mineral phases). The complete dataset used to construct Figures 7-9 is compiled in the Supplementary Data (Table S1).

4.2.1 *Bulk rock data*

Major and trace element bulk-rock analyses are available for 29 samples (Table 1 & S1). They encompass the different types of products (lapilli, lavas flows, spatter clasts), stratigraphic units and polygenetic centers on the PdS (2 samples from Demi-Piton; 4 from Piton Haüy; 19 from Piton Chisny). Only the h3 unit is missing from our dataset. Two samples from units with undetermined stratigraphic attribution (ol, pds, Fig. 2) have been also analyzed. Finally, 2 samples are from eruptions of PdF (within the Enclos Fouqué) in November and December 2009 (unit pdf2009). These are used below as reference for SSB lavas. Compared to these 2 reference compositions, the PdS samples are compositionally different. Most are enriched in Fe2O3(tot), MgO, K2O, TiO2, Ba, Ni, Sr, Cr, Zr and depleted in SiO2, CaO, Cu and Sc (Fig. 7a). Only the sample from the dp2 stratigraphic unit, which has low MgO and high CaO, as well as elevated Cu and Sc, approaches the 2009 (SSB) samples. However, both Cr and Ni are more strongly depleted in the dp2 sample than in the reference SSB (Table 1).

Apart from the low MgO (6.00-8.00 wt%) and high CaO (11.1-11.4 wt%) group which includes the two 2009 and the dp2 samples and is, by definition, representative of the SSB, the second group (which comprises most samples) has variable MgO (8.2-11.3 wt%) and low CaO (9.3-10.3 wt%), typical of the Abnormal Group (AbG). It can be subdivided in two subpopulations, one with low (8.2-9.4 wt%) and the other with high MgO (10.0-11.3 wt%), CaO being approximately constant. The two subpopulations include samples from the same units (e.g., c2, c3). Previous work has stressed the importance of olivine accumulation at PdF (Villemant et al., 2009) and it is most likely that the MgO dispersion in the bulk rock data (Fig. 7a) reflects (at least in part) such a mechanism (see for example the c3 data points).

In the Sc/Yb vs. CaO/Al2O3 diagram (Fig. 7b), the bulk rock data define a single variation trend. The 2009 samples have high CaO/Al2O3 (0.80-0.82) and Sc/Yb (~16) and they plot at the "primitive" end of the trend. The "evolved" end (CaO/Al2O3 = 0.65-0.68; Sc/Yb ~12) is defined by several samples from the 3 main edifices on the PdS. Such a trend of decreasing Sc/Yb with decreasing CaO/Al2O3 is indicative of clinopyroxene fractionation (Albarède et al., 1997). In the The La/Yb vs. CaO/Al2O3 diagram (not shown) which provides a complementary indication for clinopyroxene fractionation, the bulk rock data define a single slightly negative trend from the SSB samples at the lower end (La/Yb ~8) to samples from Demi-Piton, Piton Haüy and Piton Chisny samples at the higher end (La/Yb ~12-15). We conclude that the bulk rock data indicate different degrees of clinopyroxene fractionation between samples.

4.2.2 *Glass compositions*

Major and trace element compositions of matrix glasses have been determined on a total of 24 lapilli samples representative of the 3 main polygenetic centers and stratigraphic units on the PdS (1 dp2, 9 h2, 9 c2, 4 c3 and 1 sample from a stratigraphically unspecified lapilli deposit, unsp). Matrix glasses of the 2 pdf2009 scoriae have also been analyzed for reference. The data (Table 3) are plotted in Figure 8b-f. The SEM picture of a representative lapilli sample is shown (Fig. 8a) to document the crystallinity (proportion and size of crystals) of the analyzed products. In most cases, glass pools are large enough for LA ICP-MS analysis. The only exception is sample REU-37 (unit dp2, Table 3) whose glass Ni concentration markedly exceeds the whole-rock value (Table 2) suggesting some crystal contamination.

The MgO vs. CaO/Al2O3 plot (Fig. 8b) enables 4 compositional groups of glasses to be defined. (1) Glasses from the 2009 eruption have low MgO (6.14-6.29 wt%) and moderate CaO/Al2O3 (~0.80). In the other diagrams, the two 2009 glasses are specific, being characterized by low compatible and incompatible trace element concentrations (Fig. 8d, e), and also by the lowest La/Yb ratios (Fig. 8f). The dp2 glass plots close to the 2009 samples (Fig. 8b) although it has different incompatible trace element contents (Fig. 8e). It is also reminded that the dp2 glass analysis is somewhat uncertain because of crystal contamination.

(2) Glasses from the c2 unit form a tightly defined group with the highest MgO contents of the dataset (8.53-8.74 wt%) and moderate CaO/Al2O3 ratios (0.79-0.82). This group displays primitive characteristics on all diagrams such as high compatible elements (Fig. 8d), low incompatible elements (Fig. 8c, e) and La/Yb (Fig. 8f). (3) Glasses from the h2 and c3 units have the lowest CaO/Al2O3 ratios of the dataset (0.67-0.74) and are characterized by a significant dispersion in MgO contents (6.29-8.37 wt%). This group has the highest incompatible element concentrations (Fig. 8c, e) and the highest La/Yb ratios (Fig. 8f) of the dataset (the dp2 sample being excepted). It is also characterized by moderate to strong depletions in compatible elements (Fig. 8d) compared to group (2). (4) A single composition plots separate from all the others on several diagrams (sample REU-1B, Fig. 2; Table 3). It corresponds to the stratigraphically unspecified lapilli unit (unsp), at the base of the deposits covering the eastern flank of Demi-Piton (see Fig. 3b) and has the highest CaO/Al2O3 ratio (0.85) of the glass dataset.

Glasses from group (1) are, by definition, representative of the SSB lava group. They plot together with other glasses from 1998-2008 eruption products (Fig. 9a, b). However, the 3 other groups of glasses have strongly unusual compositions, so far unknown for glasses on the PdF. Glasses from group (2) have MgO clearly higher than SSB glasses from the 1998-2008 eruptions. In the same way, the group (4) glass has a CaO/Al2O3 ratio higher than all 1998-2008 glasses. But the most interesting group with respect to the existing glass database on the PdF is clearly group (3). With its low CaO/Al2O3, high MgO and K2O and high incompatible trace element contents, group (3) has attributes typical of the AbG group (Fig. 9). Therefore, this group provides the first examples of the existence of magmatic liquids with an AbG signature on the PdF.

As for the whole-rocks, the glass data provide evidence for two fractionation schemes, the first involving olivine and the second clinopyroxene. Evidence for the involvement of olivine (either fractionation or assimilation) comes from MgO, TiO2 as well as the compatible and incompatible elements (Fig. 8b-e). On those different diagrams, the glass data are found spread on a single trend. Group (2) glasses define the "primitive" and the 2009 and dp2 glasses the "evolved" end (although the 2009 glasses have particularly low Ba and the dp2 glass should be treated with caution for reasons given above). In the same way, evidence for the involvement of clinopyroxene comes from the La/Yb vs. CaO/Al2O3 plot (Fig. 8f). On this representation, the most "evolved" compositions, thus indicating a clear signature of clinopyroxene fractionation, is marked in the group (3) glasses whereas the 2009 and the groups (2) and (4) glasses show a minimal influence of clinopyroxene fractionation. It is emphasized that glasses with a clear clinopyroxene fractionation signature (group (3)) come from 2 of the main volcanic centers on the PdS (h2 from Piton Haüy and c3 from Piton Chisny). Therefore, this fractionation signature is neither specific of a particular volcanic structure nor of a period of activity.

4.2.3 *Mineral phases*

In all deposit types (spatters, flows, lapilli) on the PdS, the only phenocryst phase (size > 70-100 μm) is olivine. Phenocrysts of clinopyroxene (generally smaller in size) were observed in 2 deposits, in the welded lapilli at the top of Demi-Piton (REU-15, Table 1, 4) and in one lava flow associated with the h4 unit on Piton Haüy (REU-32B, Table 1, 4). Microphenocrysts of olivine, clinopyroxene and/or microlites of plagioclases were also observed in the lapilli (see Fig. 8a). Spinels occur as inclusions in olivine phenocrysts but also in isolation in the matrix. Representative compositions of these different mineral phases are given in Table 4.

4.2.3.1 Olivines

The olivine phenocryst data in Table 4 were obtained on 3 lapilli deposits: one associated with the c2 unit (REU-74, Table 1) and 2 with the h2 unit (REU-49, REU-50, Table 1). Mineral separation yielded olivine as the only silicate crystal. The Fo range (71.7-88.8, Table 4) matches that classically accepted for olivine on the PdF (69-87, see Boivin & Bachèlery, 2009). In detail, olivines from Piton Chisny (REU-74) have average Fo (~86±0.5) higher than olivines from Piton Haüy (average Fo 84~85). Olivine CaO contents are relatively high (~0.25 wt%), consistent with a magmatic origin. The Fe/Mg zonation is limited to +/- 0.2-1.5 Fo units. Ca and Ni zonations, either normal or inverse, and also a few normal Cr zonations, have been observed. Fe/Mg equilibrium between olivine and matrix glass has been evaluated for the 3 lapilli samples REU-74, REU-49 and REU-50 (Table 4) by using a Fe-Mg Kdol/liq of 0.33 (Brugier et al.,in prep) and a proportion of 18% Fe2O3 (Pichavant et al., 2016). In the 3 samples, the analyzed olivines have Fo contents both higher and lower than expected at equilibrium with the glass. These observations emphasize the variability of the olivine population in the same lapilli deposit. Olivines crystallized from a range of melt compositions, both more and less evolved than their corresponding matrix glass.

4.2.3.2 Clinopyroxenes

Clinopyroxene phenocrysts in REU-32B (Table 4) are augites with Mg# ranging from 74 to 79, variable Al2O3 (2.85-6.37 wt%) and TiO2 (1.47-2.97 wt%) and Cr2O3 (up to 0.29 wt%). Core-rim zonations (Mg, Fe, Al, Ti) have been observed. Such clinopyroxene compositions are similar to those analyzed in deposits associated with volcanic edifices in the N120 rift zone (Boudoire et al., in prep) and in werhlitic xenoliths on the PdS (Brugier et al., in prep). Microphenocrysts in REU-15 are compositionally similar (6, 7, Table 4). The microphenocryst analyzed in REU-49 (1, Table 4) is a subcalcic augite with a low Mg# (66.9) and high Al2O3 (10.43 wt%) and TiO2 (3.93 wt%), reflecting crystallization from an evolved melt. Calculated Mg# of clinopyroxene in equilibrium with REU-49 glass or REU-32B and REU-15 bulk rocks, based on an experimental Fe-Mg Kdcpx/liq of 0.28 (Brugier et al., in prep), are higher than the analyzed crystals (Table 4). This suggests that the analyzed clinopyroxenes crystallized from melts more evolved than the matrix glasses.

4.2.3.3 Plagioclases

Plagioclase microlites have been analyzed in the matrix of one lava flow from the h4 unit (REU-32B, Table 4). The 2 compositions given represent the compositional extrema, and they extend from labradorite (An60) to andesine (An45). They have K2O content increasing with decreasing An suggesting that the compositional range can be attributed to crystallization from a variably evolved magma. These plagioclase An contents agree with the data (Boivin & Bachèlery, 2009) for plagioclases in recent PdF lavas (An74 to An46).

4.2.3.4 Spinels

The 4 compositions given (Table 4) encompass the wide range of spinel compositions found in PdS deposits. One (5, REU-74, Table 4) has high Mg# (64.7), low Cr# (26.3) and TiO2 (1.54 wt%), typical of Mg-chromites found as inclusions in olivine phenocrysts. The 3 others represent spinels observed either as inclusions or microphenocrysts isolated in the matrix. They are characterized by lower Mg# (56 to 44) and higher Cr# (52 to 55) and TiO2 (2.46 to 4.25 wt%), suggesting that they crystallized from melts different (more evolved ?) than the Mg-chromites. Only weak core-rim zonations (86, Table 4) have been found.

5 Discussion

5.1 Volcanological evolution of the “Plaine des Sables”

The main volcanological achievements of this study include the production of detailed stratigraphic sections for each of the 3 main polygenic centers of the PdS (Fig. 4-6) and the proposition of a volcanological map (Fig. 2). These new data, although in general agreement with previously published volcanological reconstructions of the PdS (Bachèlery, 1981; Morandi et al., 2016; Principe et al., 2016), bring significant improvements that are underlined below.

Firstly, some stratigraphic attributions have been revised, such as for the deposits from the thalweg between Demi-Piton and Piton Haüy. The spatter deposit covering the north flank of Demi-Piton was previously associated with the first stage of activity of Piton Haüy (Principe et al., 2016). It is now forming part of the dp2 unit (Fig. 2). The succession of lapilli deposits – clastogenic flows, previously described as reworked alluvional deposits (Principe et al., 2016), is clearly associated with the h2 unit (Fig. 5c-g).

Secondly, the stratigraphy of Piton Chisny has been refined. Principe et al. (2016) have distinguished 1 “Proto-Chisny” and 3 Chisny eruptive phases, the Aubert de la Rue lava field (named “Gueules Rouges”) being the third and last episode. In comparison, in this study, the construction of the primary Chisny rampart is proposed to involve up to 4 stratigraphic units, and a fifth stage of activity is marked by the Aubert de la Rue spatter cone (see Fig. 2, 6). This new interpretation leads to changes in the stratigraphic attribution of deposits (especially lava flows) that are clearly visible in the new volcanological map. Essentially, the new model proposed for Piton Chisny is that the spatter-rampart is made from spatter deposits associated with 2 stratigraphic units, c2 and c3 (Fig. 2, 6). Previously, it was thought to be constructed from a single stratigraphic unit, the ”Proto-Chisny”, the eastern flank of the edifice being covered by spatter deposits associated with the “Gueules Rouges” unit (Principe et al., 2016). Such a covering of the eastern flank is not confirmed in this study and, globally, a minor importance is attributed to the fifth stage of Piton Chisny activity, the Aubert de la Rue spatter and lava field. The lava flow which extends to the northern limit of the PdS, previously attributed to the “Gueules Rouges” unit (Principe et al., 2016), is attributed to the Chisny unit c3a in the map (Fig. 2).

The lapilli deposits associated with the c2 unit (c2lap) originated from one of the most energetic lava-fountaining events on the PdF (Morandi et al., 2016). The demonstration, from the glass chemical data, that the c2lap unit extends up to the internal slopes of the Piton Haüy cirque (REU-32, Fig. 2) allows to push the limit of the c2lap deposit by more than 400 m to the north, compared to Morandi et al. (2016). In addition to its large extension, the c2lap deposit is apparently very homogeneous (always composed of non-altered cm-sized well-sorted black lapilli with relatively variable ash component), and the c2lap samples are chemically tightly grouped (Fig. 8b-f). Considering the large extension of c2lap deposits and their thickness (1.5-2 m at the base of Piton Chisny, REU-65, Fig. 2; 57 and 17 cm at distances of respectively 1.1 km and 1.7 km from the eruptive center, Morandi et al., 2016), the c2 lava-fountain can be compared with lava fountains on Hawaii such as during the Kilauea Iki eruption of 1959-1960. The 440 m high lava fountain of Kilauea Iki's 3rd eruptive phase has been associated with a 76 cm thick lapilli deposit located 900 m from the vent (Richter et al., 1970); the 580 m high lava fountain of the 15th eruptive phase produced the most extended deposits, with 30 cm thick deposits found at distances of more than 2 km from the vent (Parfitt, 1998). Even if such lapilli deposits are clearly dependent on local factors (topography, wind regimes), thus making such first-order comparisons risky, we estimate that the c2lap lava fountain was more than 400 m high and, as such, is comparable to the highest class of Hawaiian lava fountaining proposed by Houghton et al. (2016). Such high lava fountains have been described to be active for periods ranging from a few hours to more than a day (see Houghton et al., 2016 for a review). Therefore, our data confirm that the c2 lava fountaining event was the most (or one of the most) energetic, but also the most voluminous and probably the highest lava fountaining event on the PdF massif (Morandi et al., 2016; Principe et al., 2016). It is also noteworthy that the erupted melts were relatively primitive, since the group (2) has the highest MgO concentrations of the glass dataset (Fig. 9a).

5.2 Evolution of individual edifices

The 2 stratigraphic units defined for the Demi-Piton (dp1, dp2, Fig. 2, 4) show contrasted bulk rock compositions (Fig. 7). The dp1 sample has a typical AbG signature whereas the dp2 sample is similar to differentiated SSB (Fig. 9a). No lapilli sample was analyzed in the dp1 unit but the matrix glass in the dp2 lapilli (keeping in mind the contamination problem noted above) plots together with evolved glasses from the 1998-2008 eruptions (Fig. 8, 9), consistent with the evolved SSB signature of its corresponding bulk rock. Therefore, in the case of Demi-Piton, there is a good correlation between the volcanological observations and the chemical data. Both suggest 2 distinct periods of construction of the spatter-rampart, the first marked by AbG-type and the second by differentiated SSB-type magmas. Since an evolution from dp1 to dp2 compositions would be difficult to explain by crystal fractionation and/or assimilation of phenocryst phases in a single magma chamber (see the fractionation vectors in Fig. 9a), it is most probable that different magma batches were involved. Following eruption of the dp1 AbG-type unit, the Demi Piton feeding system was recharged with a slightly differentiated SSB-type magma, probably during the quiescence period marked by hints of a paleo-soil. Clinopyroxene fractionation is strongly marked in the dp1 composition (Fig. 7b). In contrast, the magma involved in the dp2 activity has high CaO/Al2O3 and Sc/Yb ratios, indicating a minimal importance of clinopyroxene fractionation. Clinopyroxene microphenocrysts in the REU-15 sample (Table 4) have lower Mg# than compositions at equilibrium with the matrix glass, suggesting that they crystallized from cold and differentiated parts of the shallow plumbing system.

In the case of Piton Haüy, the sequence of bulk rock compositions from the h1, h2 and h4 units shows similarities with the Demi-Piton. Indeed, the first (h1) unit is made of a typical AbG magma, chemically close to dp1 (Fig. 7). However, the other compositions differ from the typical SSB seen on Demi-Piton. Following the h1 unit, the Piton Haüy plumbing system was recharged with the primitive h2 magma batch (see Fig.7a, 9a). The relative positions of h2 bulk rock and matrix glasses suggest that accumulation of olivine partly controls the h2 whole rock composition (see the fractionation vectors in Fig. 9a). The h4 whole rock is intermediate between h1 and h2 illustrating the significant compositional variability of magmas on Piton Haüy. Both the h2 and h4 whole rocks are interpreted as representative of AbG magma series, despite their medium-high Sc/Yb, Fig. 7b; note that h2 has a low but h4 a very high La/Yb. This is mainly because the h2 matrix glasses, which are chemically evolved, record clear evidence for clinopyroxene (and also olivine) fractionation (Fig. 8b-f, 9b). We also note that the h2 whole-rock composition, although MgO-rich, does not plot on the picrite trend (Fig. 9a). Both the h2 and h4 samples contain clinopyroxene, as microlites in the former (REU-49, Table 4) and as phenocrysts in the latter (REU-32, Table 4), interpreted as crystallization products from cold shallow evolved melts. In the absence of analyses for the h3 unit, we conclude from the available data that Piton Haüy was constructed from a series of distinct AbG-type magma batches.

The h2 matrix glasses show a significant internal variability (Fig. 8b-e). If lapilli deposits are divided in different sub-units (e.g., h2lap 1, 2, 3, Fig. 5c), it appears that the chemical dispersion among h2 glasses is controlled by the stratigraphic position of lapilli samples within sub-units. Glass MgO concentrations systematically decrease from base to top. For example, REU-50 (7.97 wt% MgO) is below REU-51 (7.30 wt% MgO) in sub-unit h2lap 3 (Fig. 5c, Table 3). This chemical heterogeneity indicates a syn-eruptive change in magma composition, possibly driven by olivine crystallization and fractionation in the plumbing system. Lava fountains that produced the h2 lapilli deposits were of duration long enough for variations in glass chemistry to be recorded. This conclusion is corroborated by field observations indicating variations in the lava fountaining regime (Fig. 5h). In comparison, there is no indication for a differential influence of clinopyroxene fractionation in the h2 glass data. They all have nearly constant CaO/Al2O3 and La/Yb (Fig. 8b, f) and exhibit similar level incompatible trace element and K2O enrichments in comparison with the 1998-2008 SSB glasses (Fig. 8e, 9b).

Chemical dispersion is even more marked in the Piton Chisny than in the Piton Haüy. The 5 eruptive units clearly differ from SSB and they plot outside the picrite trend (Fig. 9a). They exhibit variably marked AbG characteristics, the strongest being for the c4 and aub samples (as well as for one c2), and the weakest for c2 and c3 samples (Fig. 7b; 8f). The chemical variability seen on Piton Chisny is mainly controlled by dispersion within eruptive units (see the c2 and c3 units). For bulk rock analyses, effects of olivine accumulation need to be taken into account (Fig. 7a). For the glass analyses, the contrast between the 2 main lapilli deposits c2 and c3 is remarkable. Piton Chisny is the only edifice on the PdS showing such a marked compositional contrast between glasses. The c3 glasses record an evolution similar to that defined for the h2 glasses, except that the latter extend to more MgO-rich compositions and, so, overall, olivine fractionation is more marked in the c3 than in the h2 glasses (Fig. 8b-e). However, both glasses have similar levels of K2O and incompatible element enrichments as well as comparable CaO/Al2O3 and La/Yb (Fig. 8e-f, 9b) and, therefore, they record similar extents of clinopyroxene fractionation. In contrast, clinopyroxene fractionation is much less marked in the c2 glass group (Fig. 8f, 9b) which has characteristics typical neither of AbG nor of SSB compositions. One interpretation consistent with the chemical data would be to associate the c2 group with SSB, the c2 data representing an example of primitive compositions uncommon among SSB glasses (Fig. 9a). However, the difficulty with this interpretation is that the c2 glasses belong to an eruptive unit which includes bulk rock samples with low CaO/Al2O3 and Sc/Yb, and high La/Yb, i.e., with clear AbG attributes (Fig. 7b, 9a and not shown). More work is needed to resolve the affiliation of the c2 glass group to PdF magma series.

In conclusion, the construction and evolution of polygenic volcanic centers on the PdS stress the importance of AbG magma series. The 3 main edifices detailed above bear the mark of AbG compositions being involved in their volcanological history. Clear indication for the involvement of typical SSB magmas is only seen on the Demi-Piton and, therefore, it is possible to contrast the role of SSB in the PdS (small importance) and inside l'Enclos Fouqué (major importance). Neither Oceanite nor Differentiated series appear to be involved. Each of the 3 main edifices resulted from several episodes involving discrete magma batches which bear the mark of complex petrogenetic processes including crystal fractionation and assimilation, cooling and differentiation as well as recharge by melts of chemically variable composition.

5.3 Implications for the origin of the Abnormal Group (AbG) magma series

The origin of the different magma series at PdF is a debated issue (Upton and Wadsworth, 1965; Ludden, 1978; Kornprobst et al., 1979, 1984; Albarède and Tamagnan, 1988; Fisk et al., 1988; Albarède et al., 1997; Fretzdorff and Haase, 2002; Vlastélic et al., 2005; Boivin et Bachèlery, 2009; Famin et al., 2009; Villemant et al., 2009; Salaün et al., 2010; Di Muro et al., 2014, 2015; Boudoire et al., in prep). Starting from the strong isotopic homogeneity of PdF lavas (Graham et al., 1990; Albarède et al., 1997; Fretzdorff & Haase, 2002; Bosch et al., 2008; Vlastélic et al., 2009), the present discussion focuses on mechanisms of intracrustal differentiation of a presumably single type of parental magma (Albarède et al., 1997; Famin et al., 2009; Villemant et al., 2009; Boudoire et al., in prep, Fig. 9a). There is agreement that the SSB magma series record a mechanism of olivine fractionation (Ludden, 1978; Kornprobst et al., 1979, 1984; Albarède and Tamagnan, 1988; Fisk et al., 1988; Albarède et al., 1997; Fretzdorff and Haase, 2002; Vlastélic et al., 2005; Boivin et Bachèlery, 2009; Famin et al., 2009; Di Muro et al., 2014, 2015; Pichavant et al, 2016). This trend is marked by a decrease in MgO associated with a relatively constant CaO/Al2O3 ratio (Fig. 9a). Evidence that this mechanism is of major importance on the PdF is provided by the SSB magma series which plot at the evolved end of the olivine control line passing through the postulated parental magma (Fig. 9a). In our dataset, olivine fractionation is the first of the two main evolutionary mechanisms identified (see above). Yet, most of our bulk rock compositions plot outside the "main" PdF trend (defined by the SSB and Oceanite magma series, Fig. 9a) and, in fact, only our pdf2009 and dp2 whole rock samples have compositions along this trend. The Differentiated series corresponds to compositions with < 6 wt% MgO decreasing together with CaO/Al2O3 (0.55-0.8) as a result of plagioclase +/- cpx fractionation (Kornprobst et al., 1984; Albarède and Tamagnan, 1988; Albarède et al., 1997; Boivin et Bachèlery, 2009; Famin et al., 2009). In our sample set, only the dp2 glass has a composition approaching that of the Differentiated series (Fig. 9a, b).

Another evolutionary trend based on early clinopyroxene fractionation has been recognized for some time on the PdF, as illustrated on Figure 9a (Kornprobst et al., 1984; Albarède et al., 1997; Boivin et Bachèlery, 2009; Famin et al., 2009; Boudoire et al., in prep). However, its petrogenetic significance and actual importance is still under discussion, mainly because the number of samples demonstrating this evolution was, until recently, limited (Albarède et al., 1997; Boivin et Bachèlery, 2009; Famin et al., 2009). This trend is characterized by a strong decrease of CaO/Al2O3 accompanied by a decrease in MgO (Fig. 9a). It is followed by an evolution at essentially constant (but low) CaO/Al2O3 and more strongly decreasing MgO which corresponds to the transition from clinopyroxene (+/- olivine) to olivine (+/- clinopyroxene) fractionation. As previously emphasized and shown on Figure 9a, most samples (whole rocks and glasses) of our dataset fall on this trend, clinopyroxene fractionation being the second of the two main fractionation mechanisms identified in this study. It is worth emphasizing here that SSB products show a minimal imprint of this mechanism. Therefore, and contrary to olivine fractionation which is marked in all magma series, clinopyroxene fractionation is exclusive of the AbG group.

Different models have been proposed for the origin of the AbG compositions on the PdF. Most are based on the crystallization of clinopyroxene as a liquidus phase in the deep parts of the feeding system (Kornprobst et al., 1979, 1984; Albarède et al., 1997; Boivin et Bachèlery, 2009; Famin et al., 2009; Boudoire et al., in prep). In those models, the evidence supporting clinopyroxene fractionation has mainly come from major and trace element bulk rock geochemical data (e.g., Albarede et al., 1997). This group of models leads to distinguish essentially between two main magma series on the PdF, a first with a strong imprint (the AbG series) and a second with a minimal imprint of clinopyroxene fractionation (SSB and Oceanite series). This conception has been, however, criticized and other types of models have explained the AbG compositions on the basis of a single magma series. In the model of Villemant et al. (2009), AbG compositions are generated as a result of assimilation of olivine xenocrysts by evolved melts from the Differentiated series. Indeed, one difficulty with the clinopyroxene fractionation model is that, until recently, experimental evidence showing the possibility to stabilize clinopyroxene on the liquidus of PdF magmas at reasonable pressures

(< 500 MPa) has been lacking (Fisk et al., 1988; Pichavant et al., 2016). However, recent experimental results obtained on a typical SSB in presence of volatiles have demonstrated a strong influence of pressure on phase equilibria (Brugier et al., in prep). Olivine was found to be the liquidus phase from 1 atm to ca. 350 MPa. Above that pressure, olivine was replaced on the liquidus by clinopyroxene. These experimental data (Brugier et al., in prep.), plus other recent analytical data on crystallization pressures of clinopyroxene from fluid inclusions (Boudoire et al., in prep), clearly strengthen the clinopyroxene fractionation model to explain the AbG magma series.

In this context, our analytical dataset bring new evidence to be considered in models for the origin of AbG magmas. On the one hand, our results indicate that AbG-type compositions are not accidental but, rather, can dominate in certain parts of the PdF such as the PdS. On the other hand, our data demonstrate the existence of AbG-type liquids on the PdF (Fig. 9). Therefore, not all AbG magmas can be viewed as heterogeneous magmatic mixtures (e.g., Villemant et al., 2009). Some clearly represent magmatic liquids whose origin needs to be determined. In this respect, the paucity of clinopyroxene phenocrysts in PdS products and on the PdF in general is one aspect of our results that warrants discussion. Indeed, the clinopyroxene fractionation model requires crystallization of clinopyroxene in the deep part of the plumbing system. Yet, clinopyroxene phenocrysts were found in only two of our samples, and a third contains clinopyroxene microlites. All clinopyroxenes analyzed in this study have Mg# lower than expected at equilibrium with their matrix glasses. Therefore, these clinopyroxenes represent late-crystallizing phases, as opposed to the early crystallizing clinopyroxenes expected to be involved in the clinopyroxene fractionation model. These observations stress the need for a mechanism of clinopyroxene resorption/assimilation to explain the disappearance of clinopyroxene phenocrysts in PdS products. In this regard, it is possible that some glasses in our dataset bear the mark of clinopyroxene assimilation (unsp, Fig. 9a).

6 Conclusions

The main conclusions of this study are the following:

- We have documented the volcanological history of the Plaine des Sables, an important episode in the recent activity of the Piton de la Fournaise. The volcanostratigraphy of the studied area has been revised and improved, and a new detailed (20m scale) map is proposed.

- Mechanisms of construction and evolution of the 3 main volcanic centers of the PdS (Demi-Piton, Piton Haüy, Piton Chisny), involve several discrete eruptive episodes. Each reflects multiple and complex magmatic processes such as crystal fractionation and/or assimilation and recharge of the plumbing system with chemically contrasted melts.
- The eruptive style inside the PdS is typically Hawaiian with the emission of spatters, lava flows and lapilli deposits from fountaining activity.
- The whole-rock and glass analyses demonstrate that the PdS products are strongly chemically variable. This diversity is marked both between and within the 3 main eruptive centers studied.
- The recent PdS products are characterized by the predominance of Abnormal Group magma series which are found to be present on the 3 main volcanic centers. Other magma series present on the PdF are either poorly represented (SSB) or totally absent (Oceanite, Differentiated magma series). The typology of PdS products is in strong contrasts with that recorded for the activity inside the Enclos Fouqué.
- Two main fractionation processes based on (1) olivine and (2) clinopyroxene have been identified in the erupted products. Olivine fractionation is ubiquitous whereas clinopyroxene fractionation is specific of AbG products. The clinopyroxene fractionation mechanism must be cryptic as clinopyroxene is typically absent as a phenocryst in the erupted products.
- The PdS products contain new types of glasses so far unrecognized on the PdF. This includes AbG compositions, and also compositions more primitive than glasses from SSB series.
- The existence of AbG-type glasses and their association with relatively primitive whole-rock compositions brings decisive support to the proposition that the AbG magma series represent a specific magma type on the PdF.

7 Acknowledgements

This work was supported by the DEGAZMAG (ANR 2011 Blanc SIMI 5-6 003) projects. Authors thank the OVPF Team for the reception and the technical support during field missions. Ida Di Carlo is acknowledged for her contribution to the electron microprobe analyses. We thank XX, XX and XX for their helpful reviews.

8 References cited

Albarède, F. & Tamagnan, V. (1988) Modelling the Recent Geochemical Evolution of the Piton de la Fournaise Volcano, Réunion Island, 1931-1986. Journal of Petrology 29, 997-1030.

Albarède, F., Luais, B., Fitton, G., Semet, M., Kaminski, E., Upton, B.G.J., Bachèlery, P. & Cheminée, J.L. (1997) The geochemical regimes of Piton de la Fournaise volcano (Réunion) during the last 530000 years. Journal of Petrology 38, 171-201.

Bachèlery, P. & Mairine, P. (1990) Evolution volcano-structurale du Piton de la Fournaise depuis 0.53 Ma. In : Lénat, J.F. (ed) *Le volcanisme de la Réunion*. Monographie : Centre de recherche en volcanologie, Clermont Ferrand, 213-242.

Bachèlery, P. (1981) Le Piton de la Fournaise (Ile de la Réunion): etude volcanologique, structural et pétrologique. PhD Thesis, Université Blaise Pascal, Clermont Ferrand, 215 pp.

Bonneville, A. (1990) Structure de la lithosphere. In : Lénat, J.F. (ed) *Le volcanisme de la Réunion*. Monographie : Centre de recherche en volcanologie, Clermont Ferrand, 1-18.

Boivin, P. & Bachèlery, P. (2009) Petrology of 1977 to 1998 eruptions of Piton de la Fournaise, La Réunion Island. Journal of Volcanological and Geothermal Research 184, 109-125.

Bosch, D., Blichert-Toft, J., Moynier, F., Nelson, B.K., Telouk, P., Gillot, P.Y. & Albarède, F. (2008) Pb, Hf and Nd isotope compositions of the two Réunion volcanoes (Indian Ocean): a tale of two small-scale mantle blobs. Earth and Planetary Science Letters 265, 748-768.

Boudoire, G., Brugier Y.A., Di Muro, A., Wörner, G., Métrich, N., Arienzo, I., Braukmüller, N., Kronz, A., Le Moigne, Y., Michon, L., Pichavant, M. & Zanon, V. (in prep) The deep plumbing system of volcanic islands : new insights from recent activity of the NW Rift Zone (NWRZ) of Piton de la Fournaise (La Réunion Island, Indian Ocean).

Brugier, Y.A., Boudoire, G., Pichavant, M., Le Moigne, Y., Di Muro, A., Clague, D., Bachèlery, P. & Bourdier, J.L. (2016b) Petrological and mineralogical characteristics of plutonic rocks from the Plaine des Sables (Piton de la Fournaise volcano, La Réunion Island) - Implications for crystallization processes of Réunion lavas.

Brugier, Y.A., Pichavant, M. & Di Muro, A. (2016c) Petrology of Steady State Basalt from Piton de la Fournaise volcano: A Volatiles-present Experimental Study of the shallow feeding system.

Carignan, J.,Hild, P., Mevelle, G.,Morel, J., and Yeghicheyan, D. (2001) Routine analyses of trace elements in geological samples using flow injection and low pressure on-line liquid chromatrography coupled to ICP-MS: a study of geochemical reference materials BR, DR-N, UB-N, AN-G and GH. Geostandards Newsletter 25 (2-3), 187-198.

Chenet, A.L., Quidelleur, X., Fluteau, F., Courtillot, V. & Bajpaic, S. (2007) ^{40}K-^{40}Ar dating of the Main Deccan large igneous province : further evidence of KTB age and short duration. Earth and Planetary Science Letters 263, 1-15.

de Voogd, B., Palome, S., Hirn, A., Charvis, P., Gallart, J., Rousset, D., Danobeitia, J. & Perroud, H. (1999) Vertical movements and material transport during hotspot activity: seismic reflection profiling offshore La Reunion. Journal of Geophysical Research 104, 2855-2874.

Deniel, C., Kieffer, G. & Lecointre, J. (1992) New ^{230}Th/^{238}U and ^{14}C age determinations from Piton des Neiges Volcano, Réunion – a revised chronology for the differentiated series. Journal of Volcanological and Geothermal Research 51, 253-267.

Di Carlo, I., Pichavant, M., Rotolo, S. G., and Scaillet, B. (2006) Experimental crystallization of a high-K arc basalt: the golden pumice, Stromboli volcano (Italy). Journal of Petrology 47, 1317-1343.

Di Muro, A. (2012 & 2015) Evaluation de l'aléa volcanique à La Réunion. Rapport final-année I et II. Projet BRGM/IPGP.

Di Muro, A., Métrich, N., Vergani, D., Rosi, M., Armienti, P.,Fougeroux, T., Deloule, E., Arienzo, I. & Civetta, L. (2014) The Shallow Plumbing System of Piton de la Fournaise Volcano (La Réunion Island, Indian Ocean) revealed by the Major 2007 Caldera-Forming Eruption. Journal of Petrology 55, 1287-1315.

Di Muro, A., Staudacher, T., Ferrazzini, V., Métrich, N., Besson, P., Garofalo, C. & Villemant, B. (2015) Shallow Magma Storage at Piton de la Fournaise Volcano After 2007 Summit Caldera Collapse Tracked in Pele's Hairs. In: Carey, R., Cayol, V., Poland, M. & Weis, D. (eds) *Hawaiian Volcanoes: From Source to Surface*. AGU Chapman Conference (Hawaii, 2012) Book. John Wiley & Sons.

Duncan, R.A., Backman, J. & Peterson, L. (1989) Reunion hotspot activity through tertiary time: initial results from the ocean drilling program, Leg 115. Journal of Volcanological and Geothermal Research 36, 193-198.

Famin, V., Welsch, B., Okumura, S., Bachèlery, P. & Nakashima, S. (2009) Three differentiation stages of a single magma at Piton de la Fournaise (Réunion hotspot). Geochemistry Geophysics Geosystems 10, Q01007.

Fisk, M.R., Upton, B.G.J., Ford, C.E. & White, W.M. (1988) Geochemical and Experimental Study of the Genesis of Magmas of reunion Island, Indian Ocean. Journal of Geophysical Research 93, 4933-4950.

Fretzdorff, S. & Haase, K.M. (2002) Geochemistry and petrology of lavas from the submarine flanks of Réunion Island (western Indian Ocean): implications for magma genesis and the mantle source. Mineralogy and Petrology 75, 153-184.

Gailler, L.S. & Lénat, J.F. (2010) Three-dimensional structure of the submarine flanks of La Reunion inferred from geophysical data. Journal of Geophysical Research-Solid Earth 115, B12105.

Gailler, L.S. & Lénat, J.F. (2012) Architecture of La Réunion inferred from geophysical data. Bulletin of Volcanology 51, 355-378.

Gailler, L.S., Lénat, J.F., Lambert, M., Levieux, G., Villeneuve, N. & Froger, J.L. (2009) Gravity structure of Piton de la Fournaise volcano and inferred mass transfer during the 2007 crisis. Journal of Volcanological and Geothermal Research 184, 31-48.

Gillot, P.Y. & Nativel, P.E. (1989) Eruptive history of the Piton de la Fournaise volcano, Réunion Island, Indian Ocean. Journal of Volcanological and Geothermal Research 36, 53-65.

Gillot, P.Y., Lefèvre, J.C. & Nativel, P.E. (1994) Model for the structural evolution of the volcanoes of Réunion Island. Earth and Planetary Science Letters 122, 291-302.

Graham, D., Lupton, J., Albarède, F. & Condomines, M. (1990) Extreme temporal homogeneity of helium isotopes at Piton de la Fournaise, Réunion Island. Nature 347, 545-548.

Kluska, J.M. (1997) Evolution magmatique et morphostructurale du Piton des Neiges au cours des derniers 500 000 ans. PhD Thesis, Université Paris Sud, Orsay, 95 pp.

Kornprobst, J., Boivin, P. & Bachèlery, P. (1979) L'alimentation des eruptions récentes du Piton de la Fournaise (Ile de la reunion, Océan Indien): degree d'évolution et niveau de segregation des laves émises. C.R. Acad. Sc. Paris, t.288, 1691-1694.

Kornprobst, J., Boivin, P., Lénat, J.F., Bachèlery, P., Bonneville, A., Dupont, P., Lecointre, J., Seidel, J.L., Thomas, P. & Vincent, P. (1984) Le Piton de la Fournaise, Ile de la Réunion. Colloque PIRPSEV 1984, Clermont-Ferrand.

Lacroix, A. (1923) Océanites. Minéralogie de Madagascar, vol. III, Paris, 49-50.

Lacroix, A. (1939) Les transformations récentes du sommet du volcan actif (Piton de la Fournaise) de l'Ile de la Réunion. Notes, Mémoires et Rapports de Volcanologie, 1-18.

Lebas, E. (2012) Processus de démantèlement des édifices volcaniques au cours de leur évolution : application à La Réunion et Montserrat et comparaison avec d'autres édifices. PhD Thesis, Paris Diderot, Paris, 407pp.

Lénat, J.F., Gibert-Malengreau, B. & Galdeano, A. (2001) A new model for the evolution of the volcanic island of Réunion (Indian Ocean). Journal of Geophysical Research-Solid Earth 106, 8645-8663.

Lénat, J.F., Bachèlery, P. & Merle, O. (2012a) Anatomy of Piton de la Fournaise volcano (La Reunion, Indian Ocean). Bulletin of Volcanology 74, 1945-1961.

Lénat, J.F. (2016) Construction of La Réunion. In: Bachèlery, P., Lénat, J.F., Di Muro, A. & Michon, L. (eds) *Active volcanoes of the southwest Indian Ocean: Piton de la Fournaise and Karthala*. Active volcanoes of the world. Springer, Berlin.

Ludden, J.N. (1978) Magmatic evolution of the basaltic shield volcanoes of Réunion Island. Journal of Volcanology and Geothermal Research 4, 171-198.

Mairine, P. & Bachèlery, P. (1997) Un grand épisode érosionnel dans l'histoire ancienne du Piton de la Fournaise. Comptes Rendus Académie Sciences Paris 325, 243-249.

Malengreau, B. (1995) Structure profonde de la Réunion d'après les données magnétiques et gravimétriques. PhD Thesis, Université Blaise Pascal Clermont Ferrand, 366 pp.

Malengreau, B., Lénat, J.F. & Froger, J.L. (1999) Structure of Reunion Island (Indian Ocean) inferred from the interpretations of gravity anomalies. Journal of Volcanological and Geothermal Research 88, 131-146.

McDougall, I. (1971) The geochronology and evolution of young volcanic island of Réunion, Indian Ocean. Geochimica et Cosmochimica Acta 35, 261-288.

Merle, O., Mairine, P., Michon, L., Bachèlery, P. & Smietana, M. (2010) Calderas, landslides and paleo-canyons on Piton de la Fournaise volcano (La Réunion Island, Indian Ocean). Journal of Volcanological and Geothermal Research 189, 131-142.

Michon, L., Ferrazzini, V., Di Muro, A., Villeneuve, N. & Famin, V. (2015) Rift zones and magma plumbing system of Piton de la Fournaise volcano : how do they differ from Hawaii and Etna. Journal of Volcanological and Geothermal Research 303, 112-129.

Michon, L., Lénat, J.F., Bachèlery, P. & Di Muro, A. (2016) Geology and Morphostructural Evolution of Piton de la Fournaise. In: Bachèlery, P., Lénat, J.F., Di Muro, A. & Michon, L. (eds) *Active volcanoes of the southwest Indian Ocean: Piton de la Fournaise and Karthala*. Active volcanoes of the world. Springer, Berlin.

Mohamed-Abchir, A. (1996) Les Cendres de Bellecombe: un évènement majeur dans le passé recent du Piton de la Fournaise, Ile de la Réunion. PhD Thesis, Université Paris VII, 248 pp.

Morandi, A., Di Muro, A., Principe, C., Michon, L., Leroi, G., Norelli, F. & Bachèlery, P. (2016) Pre-historic explosive activity at Piton de la Fournaise volcano. In: Bachèlery, P., Lénat, J.F., Di Muro, A. & Michon, L. (eds) *Active volcanoes of the southwest Indian Ocean: Piton de la Fournaise and Karthala*. Active volcanoes of the world. Springer, Berlin.

Ort, M.H., Di Muro, A., Michon, L. & Bachèlery, P. (2016) Explosive eruptions from the interaction of magmatic and hydrothermal systems during flank extension: the Bellecombe Tephra of Piton de la Fournaise (La Réunion Island). Bulletin of Volcanology 78, 1-14.

Pichavant, M., Brugier, Y. & Di Muro, A. (2016) Petrological and experimental constraints on the evolution of Piton de la Fournaise Magmas. In: Bachèlery, P., Lénat, J.F., Di Muro, A. & Michon, L. (eds) *Active volcanoes of the southwest Indian Ocean: Piton de la Fournaise and Karthala*. Active volcanoes of the world. Springer, Berlin.

Pietruszka, A.J., Hauri, E.H. & Blichert-Toft, J. (2009) Crustal contamination of mantle-derived magmas within Piton de la Fournaise volcano, Réunion island. Journal of Petrology 50, 661-684.

Principe, C., Morandi, A., Di Muro, A. & Michon, L. (2016) Volcanological Map of the Plaine des Sables, Piton de la Fournaise. In: Bachèlery, P., Lénat, J.F., Di Muro, A. & Michon, L. (eds) *Active volcanoes of the southwest Indian Ocean: Piton de la Fournaise and Karthala*. Active volcanoes of the world. Springer, Berlin.

Quidelleur, X., Holt, J.W., Salvany, T. & Bouquerel, H. (2010) The double structureof the Reunion geomagnetic event based on new K-Ar ages from the type locality, massif de la Montagne, Réunion Island (Indian Ocean) and assessment of the global context. Geophysical Journal International 182, 699-710.

Rançon, J.P., Rocher, P., Augé, T. & Nativel, P. (1989) Pétrologie de deux complexes intrusifs lités de l'île de la Réunion. Implications volcano-structurales. Géologie de la France 2-3, 135-156.

Salaün, A., Villemant, B., Semet, M.P. & Staudacher, T. (2010) Cannibalism of olivine-rich cumulate xenoliths during the 1998 eruption of Piton de la Fournaise (La Reunion hotspot): Implications for the generation of magma diversity. Journal of Volcanological and Geothermal Research 198, 187-204.

Salvany, T., Lahitte, P., Nativel, P. & Gillot, P.Y. (2012) Geomorphic evolution of the Piton des Neiges volcano (Réunion Island, Indian Ocean): Competition between volcanic construction and erosion since 1.4 Ma. Geomorphology 136, 132-147.

Smietana, M. (2011) Pétrologie, géochrnologie (K-Ar) et géochimie élémentaire et isotopique (Sr, Nd, Hf, Pb) des laves anciennes de La Réunion. Implications sur la construction de l'édifice volcanique. PhD Thesis, Université de La Réunion, 362 pp.

Smietana, M., Bachèlery, P. & Hémond, C. (2010) Heterogeneity in the mantle source of La Réunion Island. In: Geochimica et Cosmochimica Acta, Goldschmidt conference 2010 abstract, vol74, pp. A972.

Staudacher, T. & Allègre, C. (1993) Ages of the second caldera of Piton de la Fournaise volcano (Réunion) determined by cosmic ray produced ^{3}He and ^{21}Ne. Earth and Planetary Science Letters 119, 395-404.

Staudacher, T., Peltier, A., Ferrazzini, V., Di Muro, A., Boissier, P., Catherine, P., Kowalski, P., Lauret, F. & Lebreton, J. (2016) Fifteen Years of Intense Eruptive Activity (1998-2013) at Piton de la Fournaise Volcano : A Review. In: Bachèlery, P., Lénat, J.F., Di Muro, A. & Michon, L. (eds) *Active volcanoes of the southwest Indian Ocean: Piton de la Fournaise and Karthala*. Active volcanoes of the world. Springer, Berlin.

Sumner, J.M. (1998) Formation of clastogenic lava flows during fissure eruption and scoria cone collapse: the 1986 eruption of Izu-Oshima Volcano, eastern Japan. Bulletin of Volcanology 60, 195-212.

Sumner, J.M., Blake, S., Matela, R.J. & Wolff, J.A. (2005) Spatter. Journal of Volcanological and Geothermal Research 142, 49-65.

Tanguy, J.C., Bachèlery, P. & Le Goff, M. (2011) Archeomagnetism of Piton de la Fournaise: bearing on volcanic activity at La Réunion Island and geomagnetic secular variation in Southern Indian Ocean. Earth and Planetary Science Letters 303, 361-368.

Upton, B.G.J. & Wadsworth, W.J. (1965) The Basalts of Réunion Island, Indian Ocean. IAV International Symposium on Volcanology (New Zealand), scientific session of November.

Upton, B.G.J., Semet, M. & Joron, J.L. (2000) Cumulate clasts in the Bellecombe Ash Member, Piton de la Fournaise, Réunion Island, and their bearing on cumulative processes in the petrogenesis of the Réunion lavas. Journal of Volcanological and Geothermal Research 104, 297-318.

Valer, M., Schiano, P. & Bachèlery, P. (2015) Insights into the origin of magmas from the adventive cones of Piton de la Fournaise volcano (La Réunion Island). In: Geochimica et Cosmochimica Acta, Goldschmidt conference 2015 abstract 3219.

Villemant, B., Salaün, A. & Staudacher, T. (2009) Evidence for a homogeneous primary magma at Piton de la Fournaise (La Réunion) : A geochemical study of matrix glass, melt inclusions and Pelé's hairs of the 1998-2008 eruptive activity. Journal of Volcanological and Geothermal Research 184, 79-92.

Vlastélic, I. & Staudacher, T. (2005) Rapid change of lava composition from 1998 through 2002 at Piton de la Fournaise (Réunion Island) inferred from Pb isotopes and trace elements: evidence for variable crustal contamination. Journal of Petrology 46, 79-107.

Vlastélic, I., Peltier, A. & Staudacher, T. (2007) Short-term (1998-2006) fluctuations of Pb isotopes at Piton de la Fournaise volcano (Réunion Island): origins and constraints on the size and shape of the magma reservoir. Chemical Geology 244, 202-220.

Vlastélic, I., Deniel, C., Bosq, C., Télouk, P., Boivin, P., Bachèlery, P., Famin, V. & Staudacher, T. (2009) Pb isotope geochemistry of Piton de la Fournaise historical lavas. Journal of Volcanological and Geothermal Research 184, 63-78.

Vlastélic, I. & Pietruszka, A.J. (2016) A Review of the Recent Geochemical Evolution of Piton de la Fournaise Volcano (1927-2010). In: Bachèlery, P., Lénat, J.F., Di Muro, A. & Michon, L. (eds) *Active volcanoes of the southwest Indian Ocean: Piton de la Fournaise and Karthala*. Active volcanoes of the world. Springer, Berlin.

Welsch, B., Faure, F., Bachèlery, P. & Famin, V. (2009) Microcrysts Record Transient Convection at Piton de la Fournaise Volcano (La Réunion Hotspot). Journal of Petrology 50, 2287-2305.

Welsch, B., Faure, F., Famin, V., Baronnet, A. & Bachèlery, P. (2013) Dendritic Crystallization: A Single Process for all the Textures of Olivine in Basalts? Journal of Petrology 54, 539-574.

9 Figure captions

Fig.1. **(a)** Location of La Réunion island in the Indian Ocean. **(b)** Map of La Réunion island, based on satellite pictures. The blue line represents the coastal limit of the island. The white dashed line separates the two main volcanoes on the island: the Piton des Neiges (inactive and largely eroded) and the Piton de la Fournaise (active since 535.000 years, *Gillot & Nativel, 1989*). The orange line marks the collapse caldera named "Enclos Fouqué", which contains the Piton de la Fournaise volcano and the majority of young deposits (< 40.000 years) associated with its activity. The 3 main "rift zones" are indicated. The "North East" (N10-25°) and the "South East Rift Zone" (N160-180°) are similar to Hawaiian rift zones (*Michon et al 2015*). The "N120 Rift Zone" connects the Piton de la Fournaise and Piton des Neiges volcanoes. The red rectangle defines the studied area ("Plaine des Sables", PdS). **(c)** Detailed DEM (Digital Elevation Model, courtesy of OVPF) of the main morphostructural features of the PdS. The studied area, slightly colored in red, is limited by two collapse calderas: the "Rempart des Sables" at the west (black line) and the "Enclos Fouqué" at the east (orange line). The northern and southern borders of the PdS are 2 slope-breaks (black dashed lines). The 3 main studied volcanic edifices of the PdS are identified: Piton Haüy, Demi-Piton and Piton Chisny from North to South. The "Aubert de la Rue" spatter (and lava field associated) is the last stage of Piton Chisny activity (*Principe et al, 2016*).

Fig.2. Volcanological and structural map of the PdS. Stratigraphy and units contours are constructed on basis of field observations and GPS coordinates, represented on a detailed DEM. Field-based informations have been crosschecked and confirmed by chemical analyses of glasses in lapilli samples. Numbers indicated refer to lapilli samples (e.g. "32" for sample REU-32, Table 1) and the color coding gives the stratigraphic attribution (e.g. numbers 20, 23, 24, 25, 44, 49, 50/51, labelled in blue, indicate lapilli samples that all belong to the h2 unit).

Fig.3. Spectrum of deposits encountered on the PdS. **(a)** The "Aubert de la Rue" spatter edifice (stratigraphical unit aub, Fig. 2). This spatter is composed of agglutinated to partially coalesced splashed fluid clasts, e.g. cowpats. **(b)** Detailed texture of the splashed fluid clasts agglutination forming the aub spatter described in **(a)** (sample REU-75, Table 1). Hammer for scale. **(c)** Dunitic xenolith in spatter deposit from Piton Chisny (unit c1, Fig. 2). Basaltic coating is present. Coin for scale. **(d)** Ballistic doleritic block surrounded by spatter deposit

associated with (unit c3, Fig. 2). Hammer for scale. **(e)** Spatter deposit from unit c3 (Fig. 2) composed of sintered, fractured and agglutinated scoria clasts. The red colour is due to syn- to post-depositional thermal alteration. Hammer for scale. **(f)** Spatter deposit (unit c2, Fig. 2; sample REU-68, Table 1). This deposit is composed of brittle clasts (bombs and lapilli) very slightly compacted. The upper level is stratified and composed of bombs. The main part of the deposit, below the upper level, is composed of barely compacted lapilli, described in **(g)**. Hammers for scale. **(g)** Detailed texture of the lower part of the deposit described in **(f)** showing black lapilli agglomerated and barely compacted (sample REU-68, Table 1). Hammer for scale. **(h)** Spatter deposit (unit c1, Fig. 2; sample REU-69A, Table 1) with in particular reworked lapilli (sample REU-69B, Table 1) below the spatter deposit. Hammer for scale. **(i)** Ballistic block with basaltic coating. Such blocks are found distributed all around the spatter edifice on the slopes of Piton Chisny (unit c3, Fig. 2). Hammer for scale. **(j)** Lapilli and fluid clasts deposit from Piton Haüy (sample REU-44, Table 1) showing the transition between lapilli at the base and fluidal clasts (i.e. the big cowpat at the center). Hammer for scale. **(k)** Typical lapilli cover on the PdS showing a ~ 50cm thick black lapilli layer (unit c2, Fig. 2; sample REU-36, Table 1) on top of older reworked lapilli (unit h2, Fig. 2). Hammer for scale. **(l)** Thin pahoehoe lava flow (unit c2, Fig. 2; sample REU-73, Table 1). Reworked lapilli are found below the lava flow. Hammer for scale. **(m)** Detail of a thin pahoehoe olivine-rich lava flow (unit ol, Fig. 2). Coin for scale. **(n)** Laminated pahoehoe lava flows (unit h4, Fig. 2; sample REU-32B, Table 1). Some tunnels are visible. Hammer for scale. **(o)** Lava flow rich in dunitic xenoliths (white circles, unit c2, Fig. 2). Hammer for scale. **(p)** Pahoehoe lava flow (unit aub1, Fig. 2) covering the spatter deposit from unit c3.

Fig.4. **(a)** Panoramic view of the Demi-Piton. Several stratigraphic levels can be traced from north to south. **(b)** Schematic interpretation of the panoramic view **(a)**. The red dashed line marks the discontinuity between the 2 dp1 and dp2 units. **(c)** Stratigraphic cross-section of the Demi-Piton. Note that the base is not visible. The discontinuity between dp1 and dp2 is represented by a red dashed line. Samples from Demi-Piton deposits (e.g. REU-02, Table 1) are localized in the section. Letters in italics (from d to k) indicate the locations of pictures **(d)** **to (k)** which describe the spectrum of spatter deposits encountered. **(d)** Intercalated massive level, either an intercalated lava flow or a "coalesced" spatter level. Hammer for scale. **(e)** North to south view demonstrating the continuity of "coalesced" spatter levels inside the edifice. Slopes of deposits (~35-40° dip) approach the structural inclination (~30-35°). The basal stratigraphic units are covered by reworked lapilli. **(f)** Detailed view of a "coalesced"

spatter level showing deformed agglutinate with flattening of clasts. Clasts outlines are well preserved at the base and partially erased in the upper part of the deposit. Pencil for scale. **(g)** Spatter deposit with sintered, fractured and agglutinated scoria clasts. The red colour is due to syn- to post-depositional thermal alteration. Hammer for scale. **(h)** Dunitic xenolith in spatter deposit. Basaltic coating is present. Pencil for scale. **(i)** Alternating scoria spatter deposit (top of the picture in **(g)**) and agglutinated lapilli levels. Deposits are strongly bedded. Hammer for scale. **(j)** Fluidal clasts. Hammer for scale. **(k)** Level of strongly welded red lapilli forming the upper part of the dp2 deposit. A projected dense block (ballistic) is inserted. Hammer for scale.

Fig.5. **(a)** Panoramic view from the southeast of the inner part of Piton Haüy. The volcanic edifice forms a major cirque, indicating a syn- to post-depositional collapse of the structure. The center of this collapse cirque is occupied by a strombolian cone and associated lava flows. **(b)** Schematic interpretation of the panoramic view **(a)**. The collapsed spatter-cone corresponds to a unique stratigraphic unit (h3). The internal deposits (strombolian cone and associated lava flows) define the youngest unit (h4). The reworked lapilli deposit (rw) is seen at the foot of the southern flank of the cirque together with a small c2lap deposit. Sampling sites are localized (see Table 1). **(c)** Stratigraphic section of Piton Haüy as defined in the thalweg between Demi-Piton and Piton Haüy (see pictures **(d)** to **(g)**). The northern flank of Demi-Piton (dp2 deposits) is overlaid by 8-10 m of alternating lapilli and lava flows from unit h2. The contact between dp2 and h2 is exposed; note the lack of h1 deposits at this location. Spatter deposits associated with h3 unit are observed at the top of the section. The stratigraphic position of samples is indicated (see Table 1). **(d) to (g):** Pictures and schematic interpretations of deposits encountered in the thalweg between Piton Haüy and Demi-Piton (see **(c)**). **(d)** Picture of the eastern part of the thalweg. Spatter deposits at the west of the view belong to Piton Haüy. The main surface observed is a lava flow from Piton Haüy which fits closely on the slope of Demi-Piton at the east. **(e)** Schematic interpretation of **(d)**. Lapilli deposits (h2 unit, REU-20, Table 1) overlay a spatter deposit associated with the dp2 unit. The spatter deposits of unit h3 are found above the alternating lapilli and lava flows of unit h2. **(f)** Picture of the western part of the thalweg showing a lava flow overlying a lapilli deposit itself covered by a spatter edifice. **(g)** Schematic interpretation of **(f)** showing the h2lap lapilli deposited on a spatter deposit belonging to the dp2 unit, the h2 lava flow above h2lap and the h3 spatter above the h2 lava flow. A small lapilli deposit of unit c2 is observed at the foot of the h3 spatter (sample REU34, see Table 1). In the background, reworked lapilli

(rw) are observed and also rafted blocks of h1 spatter deposits. **(h)** Stratified lapilli and bombs deposit covered by a lava flow, northeastern flank of Piton Haüy. Hammer for scale. **(i)** Schematic cross section of **(h)**. Unit h2 is formed by alternating lapilli deposits and lava flows, as in the thalweg between Demi-Piton and Piton Haüy. An older oceanite lava flow (unit oc) is overlaid by the h2 unit. The stratigraphic position of samples is indicated (see Table 1).

Fig.6. (a) Panoramic view of the Piton Chisny eastern flank. The center of the picture corresponds to the Aubert de la Rue (aub) spatter-cone and associated lava flows. The summit of the Piton de la Fournaise volcano can be seen in the extreme background of the picture. **(b)** Schematic interpretation of the panoramic view **(a)**. The curved spatter-rampart edifice is made of deposits associated with the c3 unit (forefront). Deposits associated with the c1 unit occur at the base of the edifice. The lava flow aub1 is directed toward the north. The lava flow aub2 bypasses the northern flank of the aub spatter and follows the base of the spatter-rampart to the south part of the lava field. One older lava flow (oc1) and strombolian cones (sc) are seen in the background. Sampling sites for Piton Chisny deposits (e.g. REU-58; see Table 1) are localized. **(c)** stratigraphic section of Piton Chisny. The volcanic edifice is around 100 m thick. This includes at least 30 m for the bottom unit c1 (the base is not observable) and around respectively 20 and 40 m for units c2 and c3. The top unit c4 is the thinnest (< 3 m). Note that the aub products are not represented on the stratigraphic section; aub deposits correspond to the last stage of the activity of Piton Chisny. Samples strictly associated with Piton Chisny deposits (e.g. REU-60; see Table 1) are localized on the stratigraphic section. **(d) to (g):** Pictures and schematic interpretations of some outcrops on the western flank of Piton Chisny. **(d)** Picture of the northwest flank of Piton Chisny. A spatter deposit is observed in the foreground, covered by reworked lapilli. In the background, the spatter-rampart belongs to the c3 unit. **(e)** Schematic interpretation of **(d)**. The spatter in the foreground is associated with the c2 unit (Fig. 3f, g). Note the importance of reworked lapilli in the foreground. **(f)** Area between northern flank of Piton Chisny and southern flank of Demi-Piton. In the foreground, a lava flow and some tilted blocks of spatter deposits are observed. In the background, the c3 spatter rampart is seen. **(g)** Schematic interpretation of **(f)**. A c2 lava flow encloses several tilted blocks of spatter deposits from the c1 unit ("rafted blocks", *Sumner, 1998*). In the foreground, outcrops of unrafted c1 spatter deposits are observed.

Fig.7. Major elements from bulk rock analysis of PdF deposits (pdf09) and some Demi-Piton (dp1 & 2), Piton Haüy (h1,2 & 4) and Piton Chisny (c1,2,3,4 & aub) deposits. **(a)** MgO (wt%) vs CaO (wt%) diagram evidencing 3 compositional groups, classically defined at PdF. Steady State Basalts (MgO 6~8 wt% and CaO~11wt%) composed of pdf09 and dp2 deposits; some Picrites (MgO 10~11wt% and CaO 9,4~10,2wt%) composed of Haüy (h2 & h4) and Chisny (c1,c2 & c3) deposits; and compositions of the Abnormal Group (MgO 8,2~9,4wt% and CaO 9,4~10 wt%) containing Demi-Piton (dp1), Piton Haüy (h1) and Chisny (c1,c2,c3,c4 and aub) deposits. **(b)** CaO/Al_2O_3 vs Sc/Yb plot shows a positive correlation between this 2 ratios: c3 and pdf09 deposits showing the highest CaO/Al_2O_3 and Sc/Yb ratios whereas dp1, h1 and c2 characterized the lowest CaO/Al_2O_3 & Sc/Yb ratios. All the others deposits seems to be transitional between these 2 poles.

Fig.8. Matrix glass compositions. Analytical data in Table 3 and Table S1. **(a)** SEM picture of lapilli REU-49 (Table 1, 3) showing olivine (30-50 µm) and clinopyroxene (< 20 µm) microphenocrysts, plagioclase microlites and spinels (3-5µm). The size of the glass pool is larger than the laser ablation pit (60 µm). (b) to (f) major and trace element plots. Sample provenance is indicated (see also Fig. 2). The two SSB reference samples (pdf09) are the same as in Fig. 7. (b) to (e) MgO variation diagrams. **(b)** CaO/Al2O3 plot showing the 4 groups of glass compositions. **(c)** TiO2 plot showing the negative correlation between incompatible major elements and the glass MgO. **(d)** Ni plot showing the positive correlation between compatible trace elements and the glass MgO. **(e)** Ba plot showing the negative correlation between incompatible trace elements and the glass MgO. **(f)** Negative correlation between La/Yb and CaO/Al2O3 showing different extents of clinopyroxene fractionation between samples.

Fig.9. CaO/Al2O3 vs. MgO plot showing the bulk rock and matrix glass compositions from the PdS and other eruptions from PdF. PdS samples, pdf09, dp1, dp2, h1, h2, h4, c1, c2, c3, c4, aub, data from this study (Table 2, 3), bulk-rock and glass data are distinguished; bulk rock compositions of Réunion lavas, data from Albarède et al., 1997; Villemant et al., 2009; Salaün et al., 2010; Di Muro et al., 2015; matrix glasses of products erupted between 1998 and 2008, data from Boivin & Bachèlery, 2009; Villemant et al., 2009; Salaün et al., 2010; Welsch et al., 2013; Di Muro et al., 2015). **(a)** CaO/Al2O3 vs MgO plot. Three groups of Reunion lavas, SSB, Picrites, Differentiated lavas are marked in grey and the fourth group (AbG) in blue. The parental magma composition is from Villemant et al. (2009).

Fractionation trends for olivine and clinopyroxene, represented as black arrows, are experimentally constrained (Brugier et al., in prep). **(b)** K2O vs. MgO (wt%) plot showing compositions of matrix glasses from this study compared to matrix glasses from the 1998-2008 eruptions. Olivine, clinopyroxene and plagioclase fractionation trends are indicated.

Figure 1

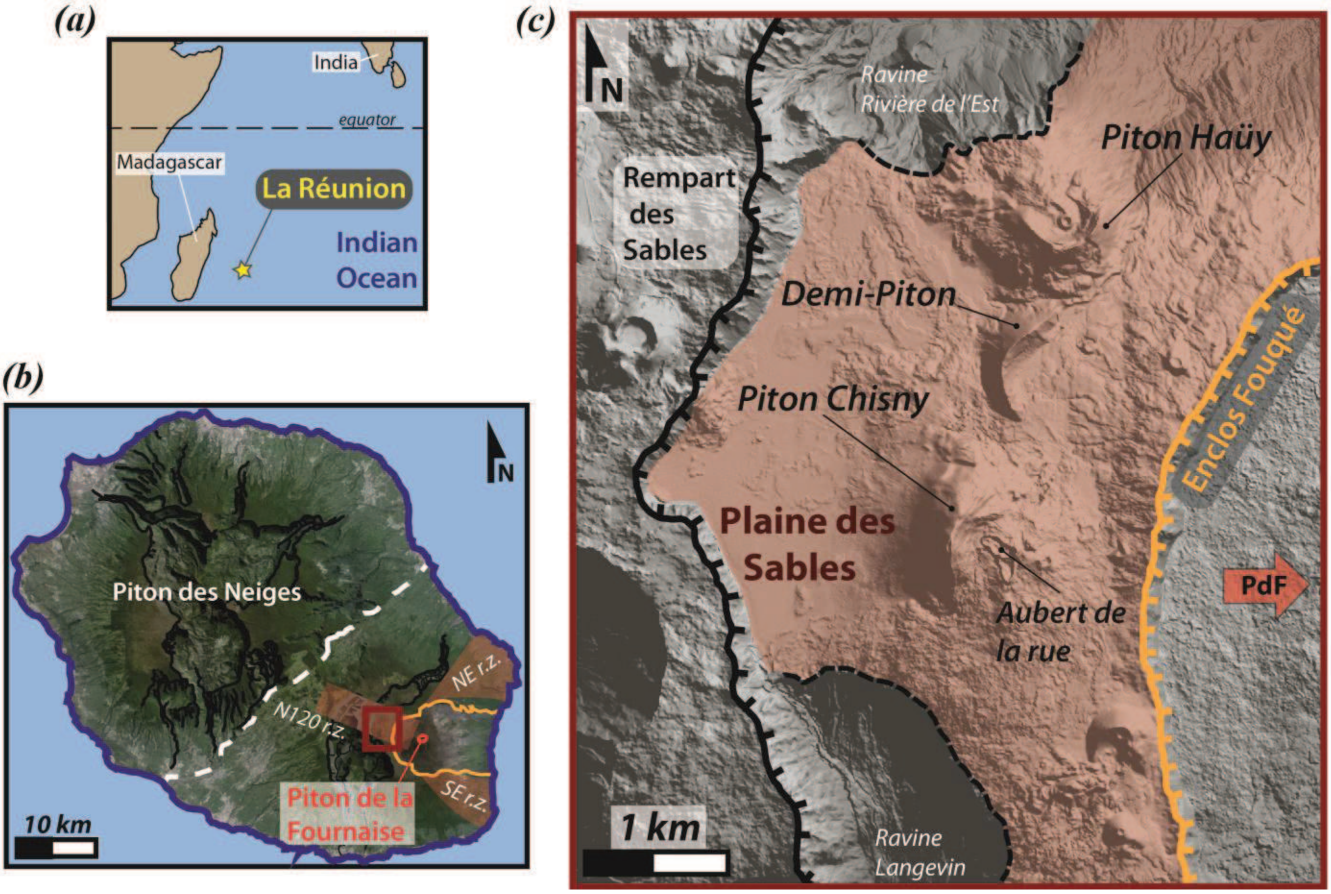
(a)
India
equator
Madagascar
La Réunion
Indian
Ocean
(b)
N
Piton des Neiges
NE r.z.
N120 r.z.
SE r.z.
Piton de la
Fournaise
10 km
(c)
N
Ravine
Rivière de l'Est
Rempart
des
Sables
Piton Haüy
Demi-Piton
Piton Chisny
Plaine des
Sables
Aubert de
la rue
Enclos Fouqué
PdF
1 km
Ravine
Langevin

Figure 2

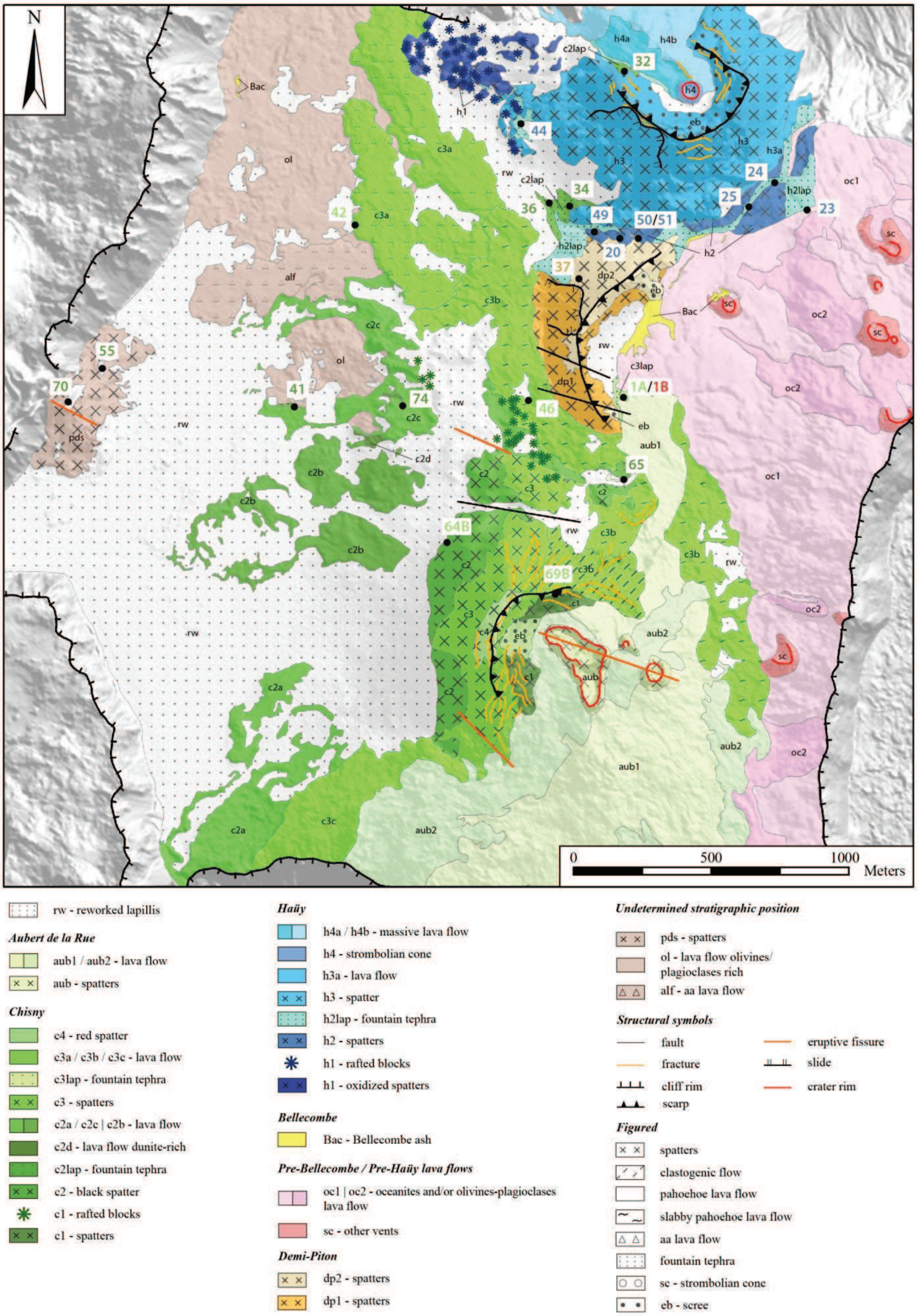
N
Bac
ol
alf
h1
c3a
c2lap
h4a
h4b
32
h4
eb
h3
h3a
44
rw
24
25
h2lap
23
oc1
sc
42
34
36
49
50/51
20
h2
37
dp2
c3b
eb
Bac
oc2
c2c
55
70
41
74
46
1A/1B
c3lap
dp1
pds
c2d
c2b
c2
c3
65
aub1
64B
69B
c1
c4
aub2
aub
c2a
c3c
0
500
1000
Meters
rw - reworked lapillis
Aubert de la Rue
aub1 / aub2 - lava flow
aub - spatters
Chisny
c4 - red spatter
c3a / c3b / c3c - lava flow
c3lap - fountain tephra
c3 - spatters
c2a / c2c | c2b - lava flow
c2d - lava flow dunite-rich
c2lap - fountain tephra
c2 - black spatter
c1 - rafted blocks
c1 - spatters
Haüy
h4a / h4b - massive lava flow
h4 - strombolian cone
h3a - lava flow
h3 - spatter
h2lap - fountain tephra
h2 - spatters
h1 - rafted blocks
h1 - oxidized spatters
Bellecombe
Bac - Bellecombe ash
Pre-Bellecombe / Pre-Haüy lava flows
oc1 | oc2 - oceanites and/or olivines-plagioclases lava flow
sc - other vents
Demi-Piton
dp2 - spatters
dp1 - spatters
Undetermined stratigraphic position
pds - spatters
ol - lava flow olivines/ plagioclases rich
alf - aa lava flow
Structural symbols
fault
fracture
cliff rim
scarp
eruptive fissure
slide
crater rim
Figured
spatters
clastogenic flow
pahoehoe lava flow
slabby pahoehoe lava flow
aa lava flow
fountain tephra
sc - strombolian cone
eb - scree

Figure 3a

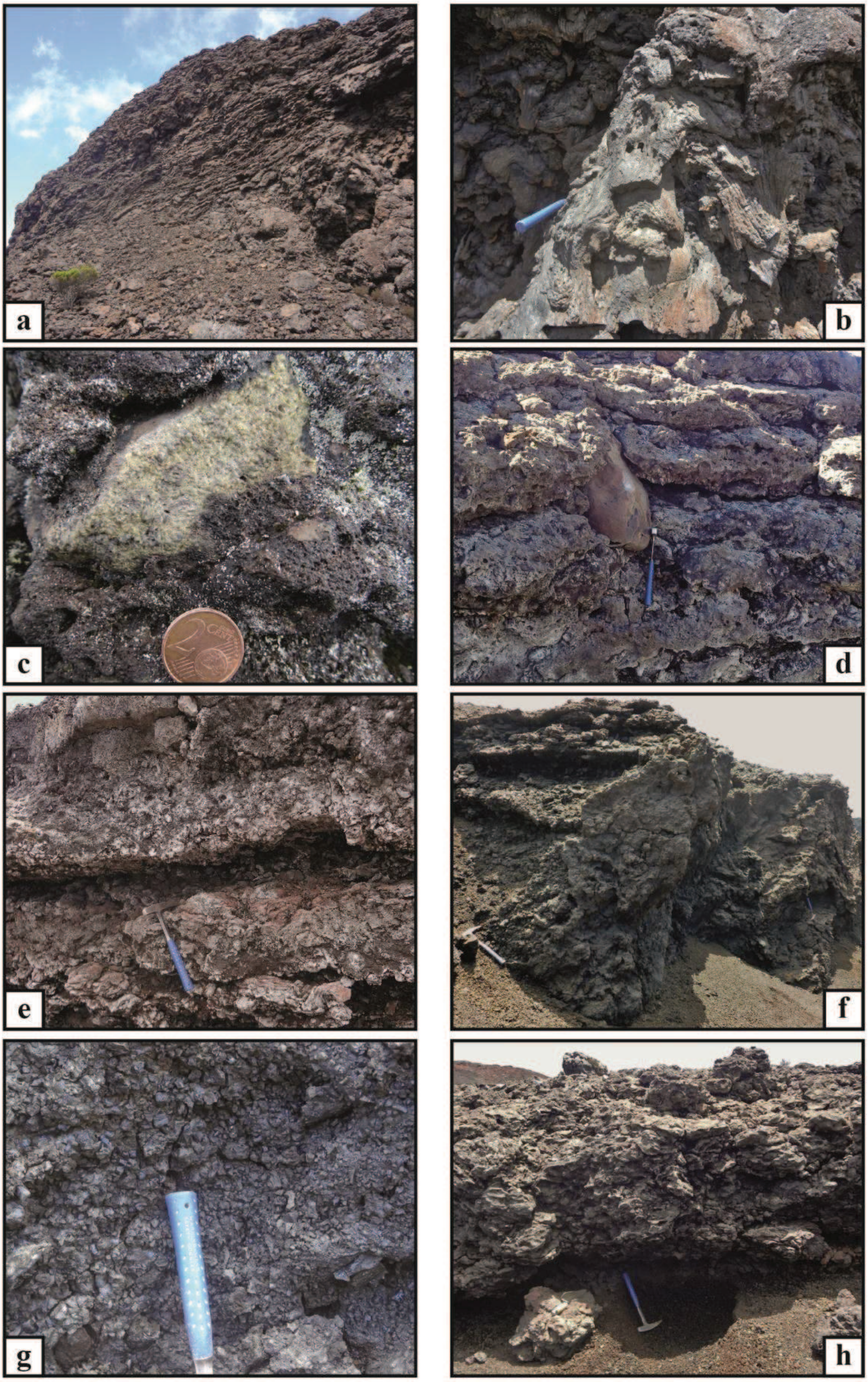

Figure 3b

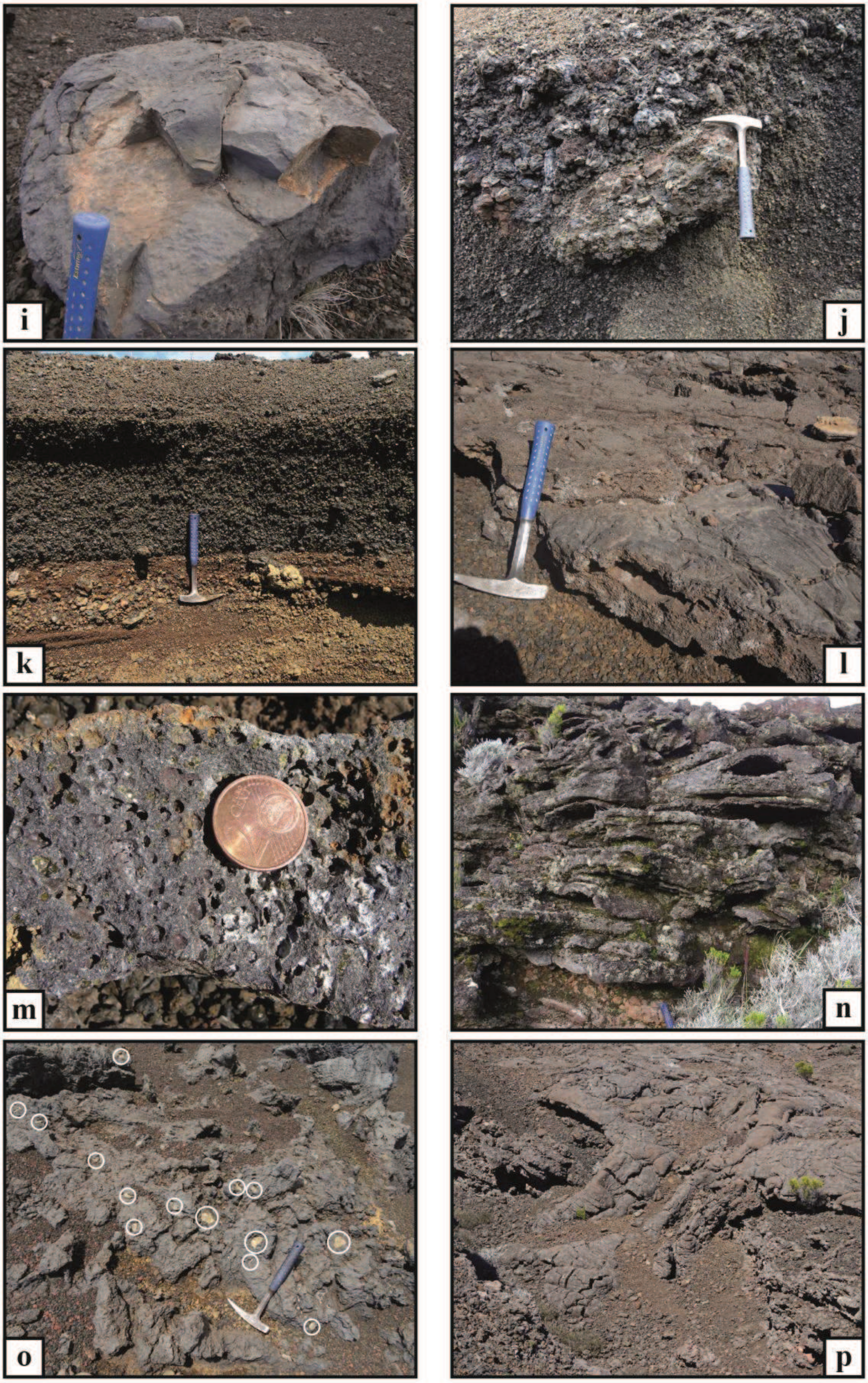

Figure 4

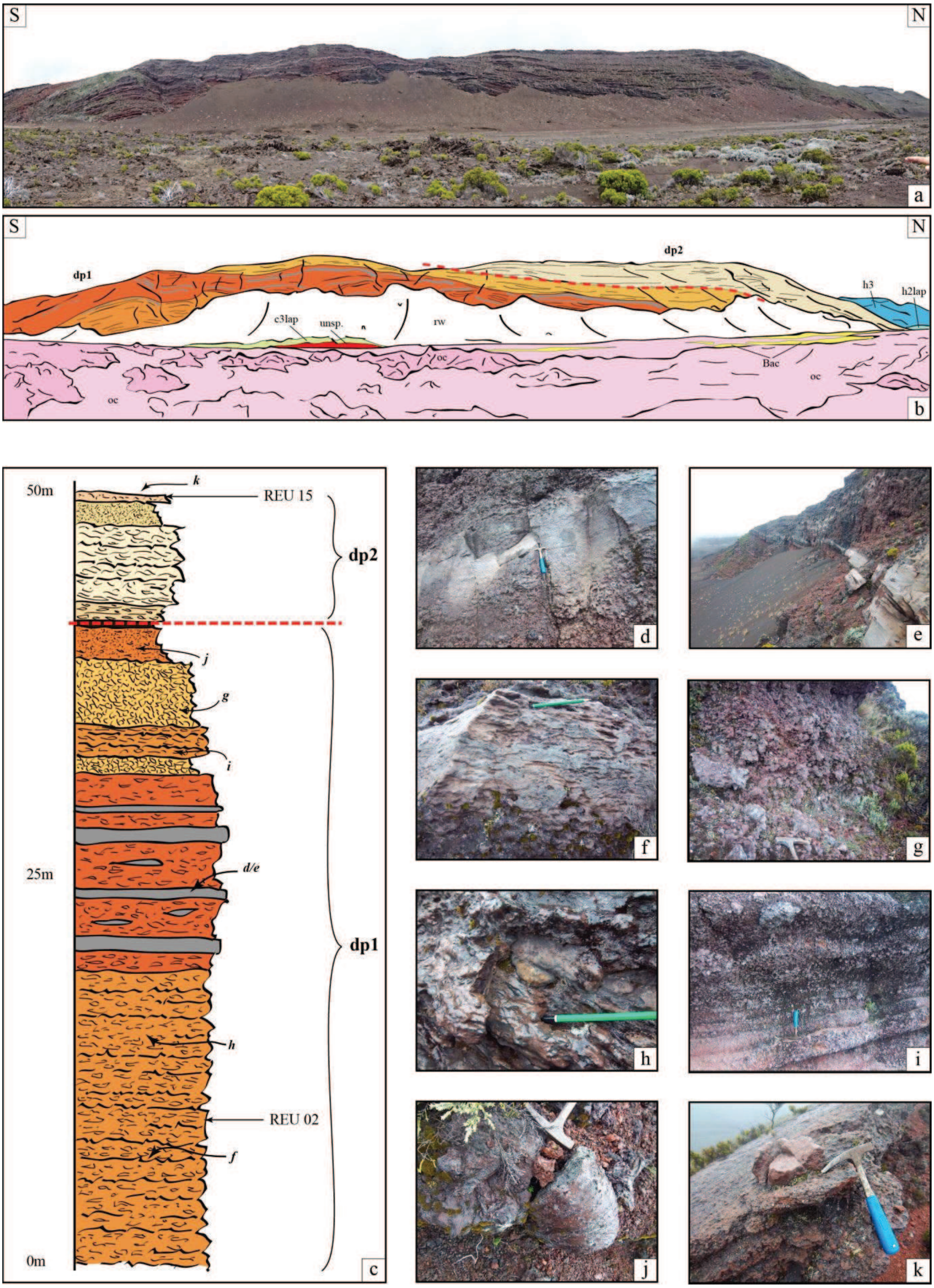
S
N
a
S
N
dp1
dp2
h3
h2lap
c3lap
unsp.
rw
oc
oc
Bac
oc
b
50m
25m
0m
k
REU 15
dp2
j
g
i
d/e
dp1
h
REU 02
f
c
d
e
f
g
h
i
j
k

Figure 5

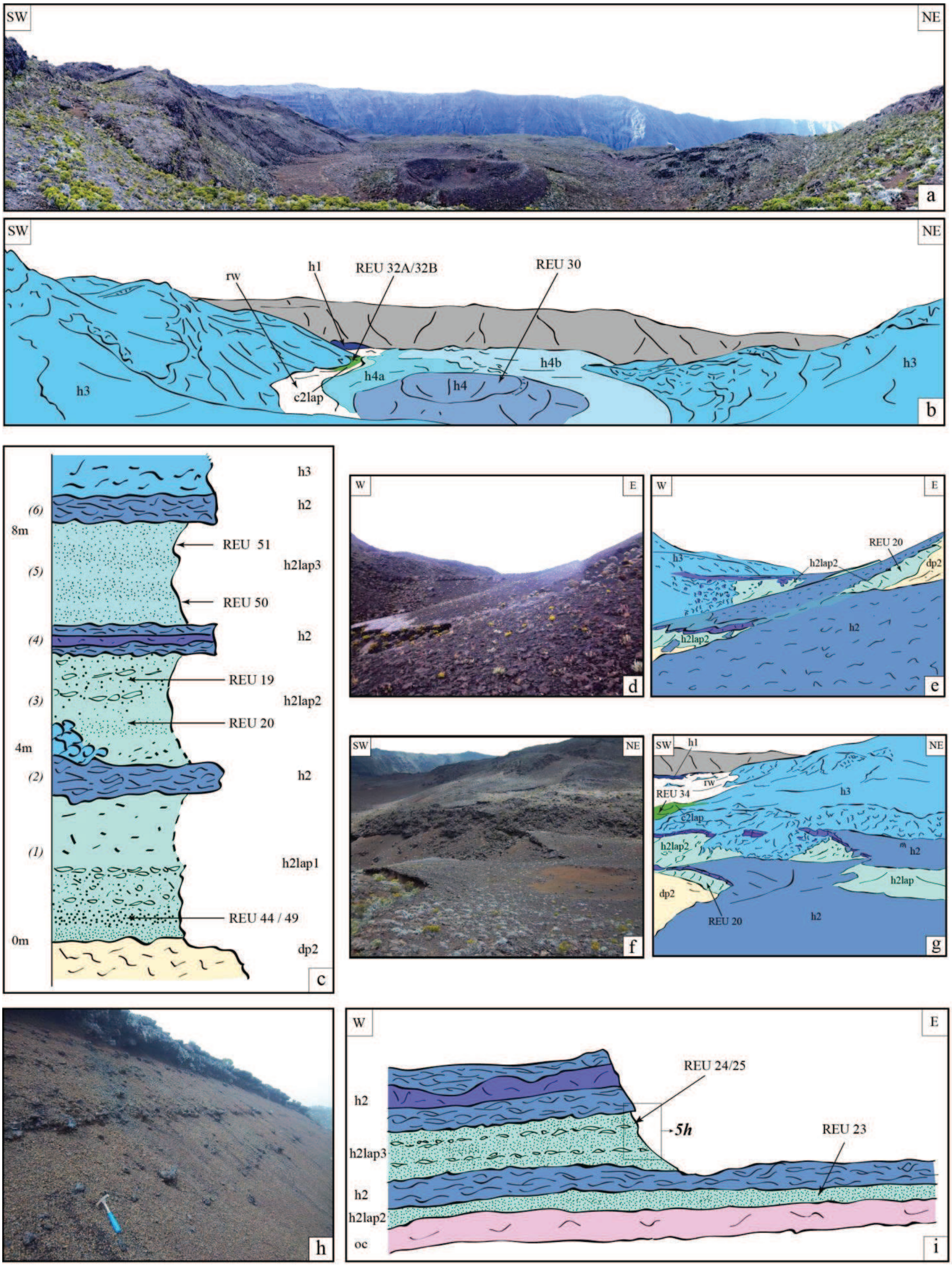
SW
NE
a
SW
NE
rw
h1
REU 32A/32B
REU 30
h4b
h4a
h4
h3
c2lap
h3
b
h3
(6)
h2
8m
REU 51
(5)
h2lap3
REU 50
(4)
h2
REU 19
(3)
h2lap2
REU 20
4m
(2)
h2
(1)
h2lap1
REU 44 / 49
0m
dp2
c
W
E
d
W
E
h3
REU 20
h2lap2
dp2
h2lap2
h2
e
SW
NE
f
SW
h1
NE
rw
REU 34
h3
c2lap
h2lap2
h2
h2lap
dp2
REU 20
h2
g
h
W
E
REU 24/25
h2
5h
REU 23
h2lap3
h2
h2lap2
oc
i

Figure 6

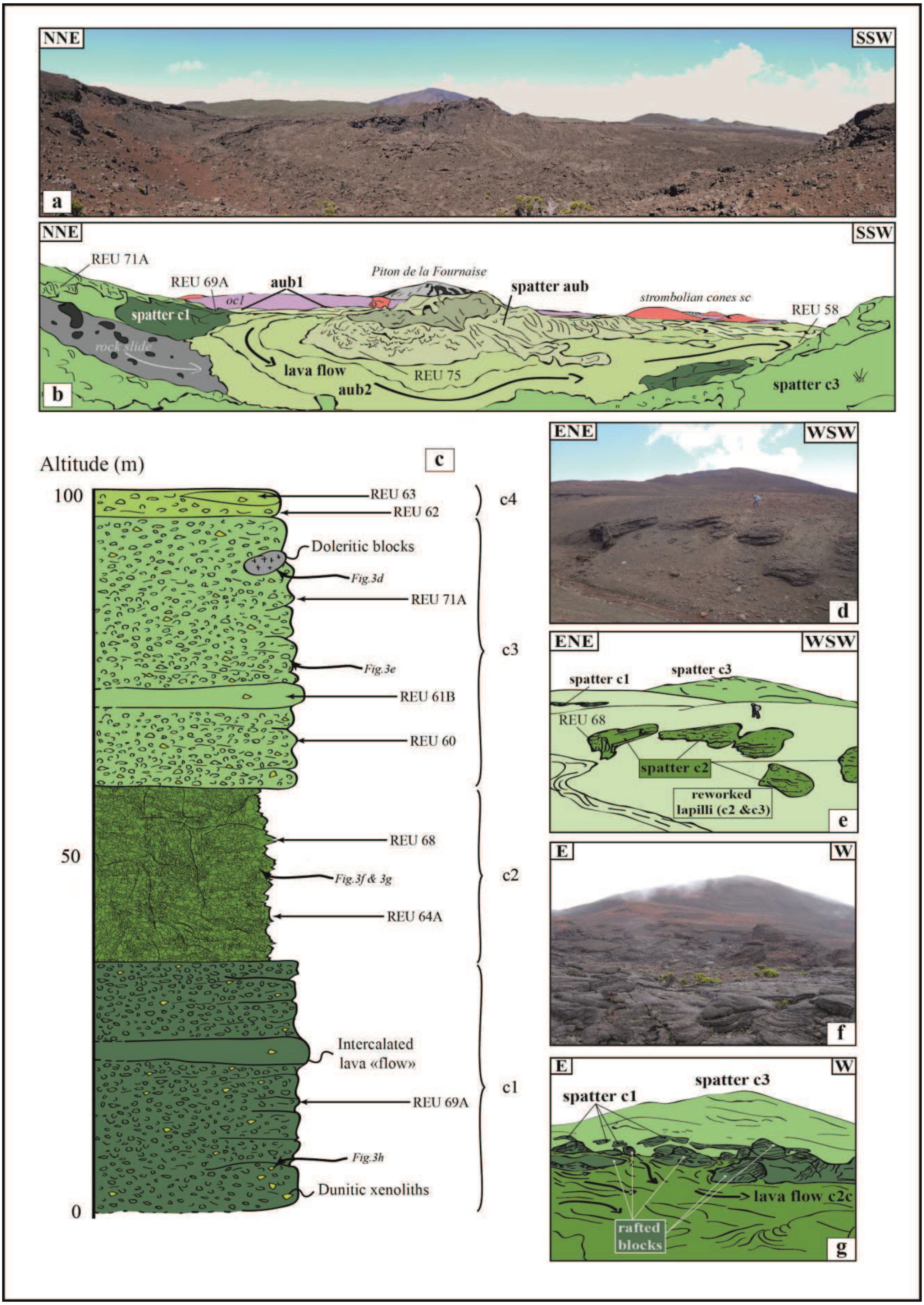
NNE
SSW
a
NNE
SSW
REU 71A
REU 69A
aub1
Piton de la Fournaise
spatter aub
strombolian cones sc
ocl
spatter c1
REU 58
rock slide
lava flow
REU 75
aub2
spatter c3
b
Altitude (m)
c
100
50
0
REU 63
REU 62
c4
Doleritic blocks
Fig.3d
REU 71A
c3
Fig.3e
REU 61B
REU 60
REU 68
Fig.3f & 3g
c2
REU 64A
Intercalated lava «flow»
REU 69A
c1
Fig.3h
Dunitic xenoliths
ENE
WSW
d
ENE
WSW
spatter c1
spatter c3
REU 68
spatter c2
reworked lapilli (c2 &c3)
e
E
W
f
E
W
spatter c1
spatter c3
lava flow c2c
rafted blocks
g

Figure 7

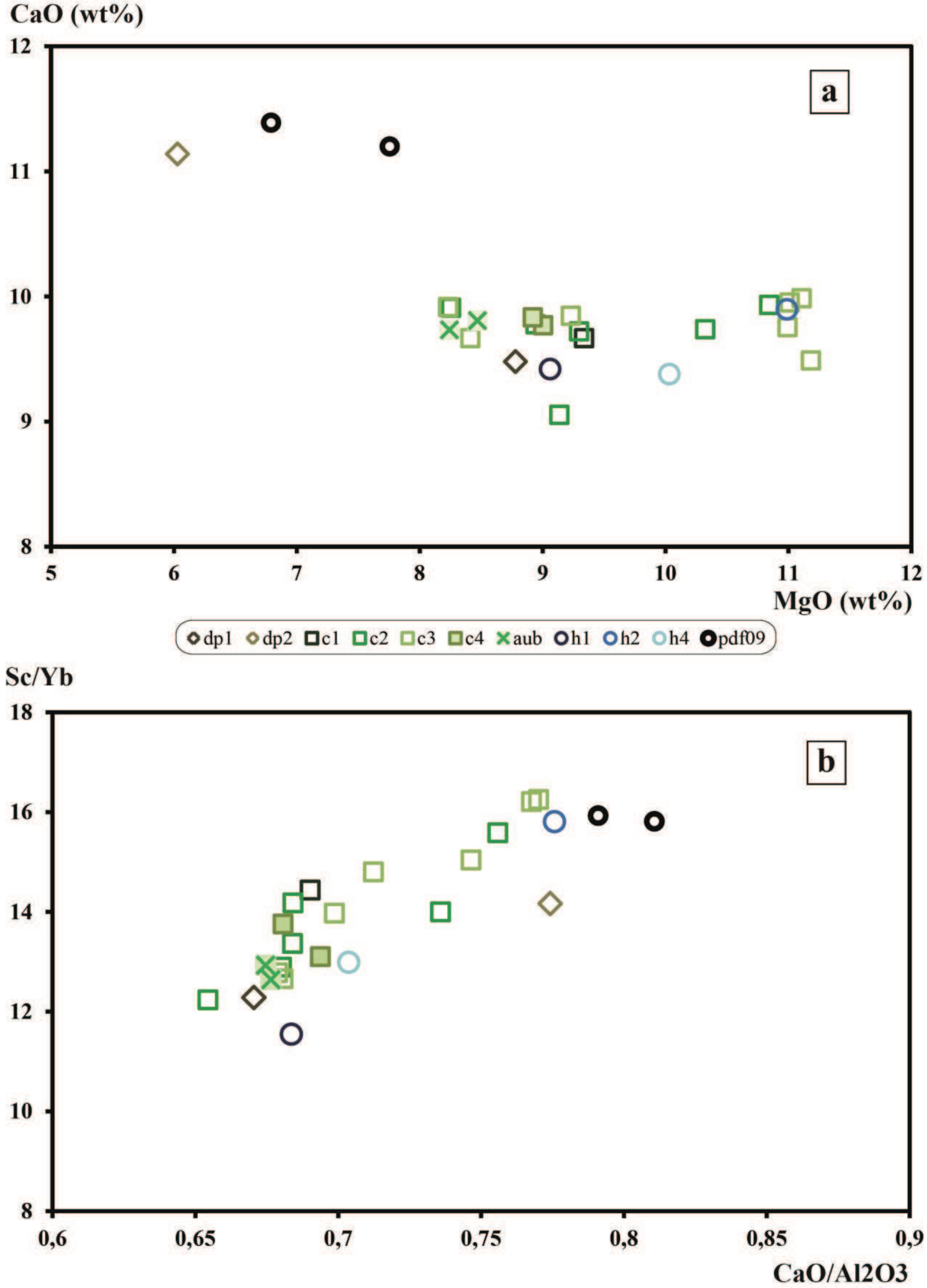
CaO (wt%)
12
11
10
9
8
5
6
7
8
9
10
11
12
MgO (wt%)
a
dp1
dp2
c1
c2
c3
c4
aub
h1
h2
h4
pdf09
Sc/Yb
18
16
14
12
10
8
0,6
0,65
0,7
0,75
0,8
0,85
0,9
CaO/Al2O3
b

Figure 8

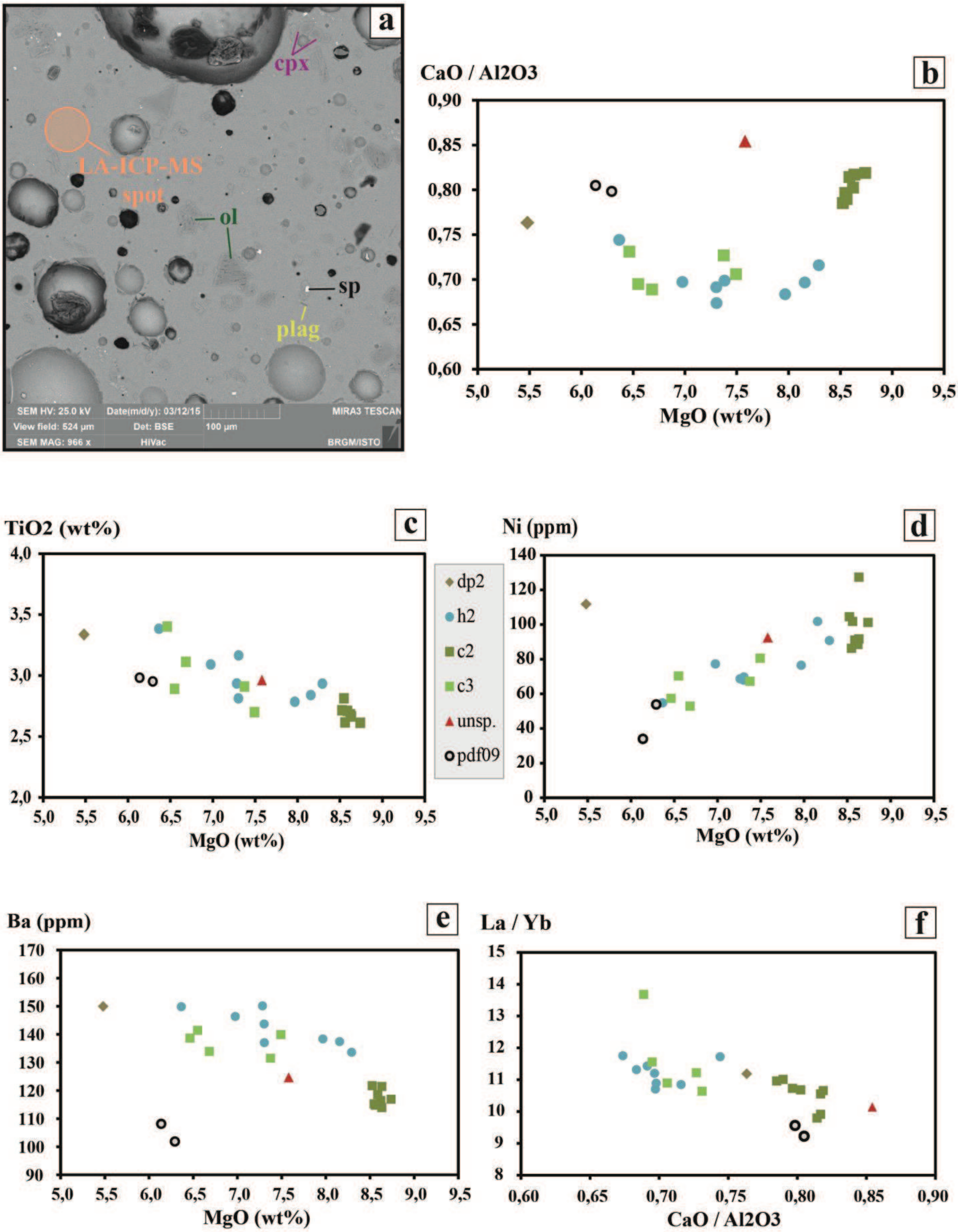
a
cpx
LA-ICP-MS
spot
ol
sp
plag
SEM HV: 25.0 kV
Date(m/d/y): 03/12/15
MIRA3 TESCAN
View field: 524 µm
Det: BSE
100 µm
SEM MAG: 966 x
HiVac
BRGM/ISTO
b
CaO / Al2O3
0,90
0,85
0,80
0,75
0,70
0,65
0,60
5,0
5,5
6,0
6,5
7,0
7,5
8,0
8,5
9,0
9,5
MgO (wt%)
c
TiO2 (wt%)
4,0
3,5
3,0
2,5
2,0
MgO (wt%)
dp2
h2
c2
c3
unsp.
pdf09
d
Ni (ppm)
140
120
100
80
60
40
20
0
MgO (wt%)
e
Ba (ppm)
170
160
150
140
130
120
110
100
90
MgO (wt%)
f
La / Yb
15
14
13
12
11
10
9
8
0,60
0,65
0,70
0,75
0,80
0,85
0,90
CaO / Al2O3

Figure 9

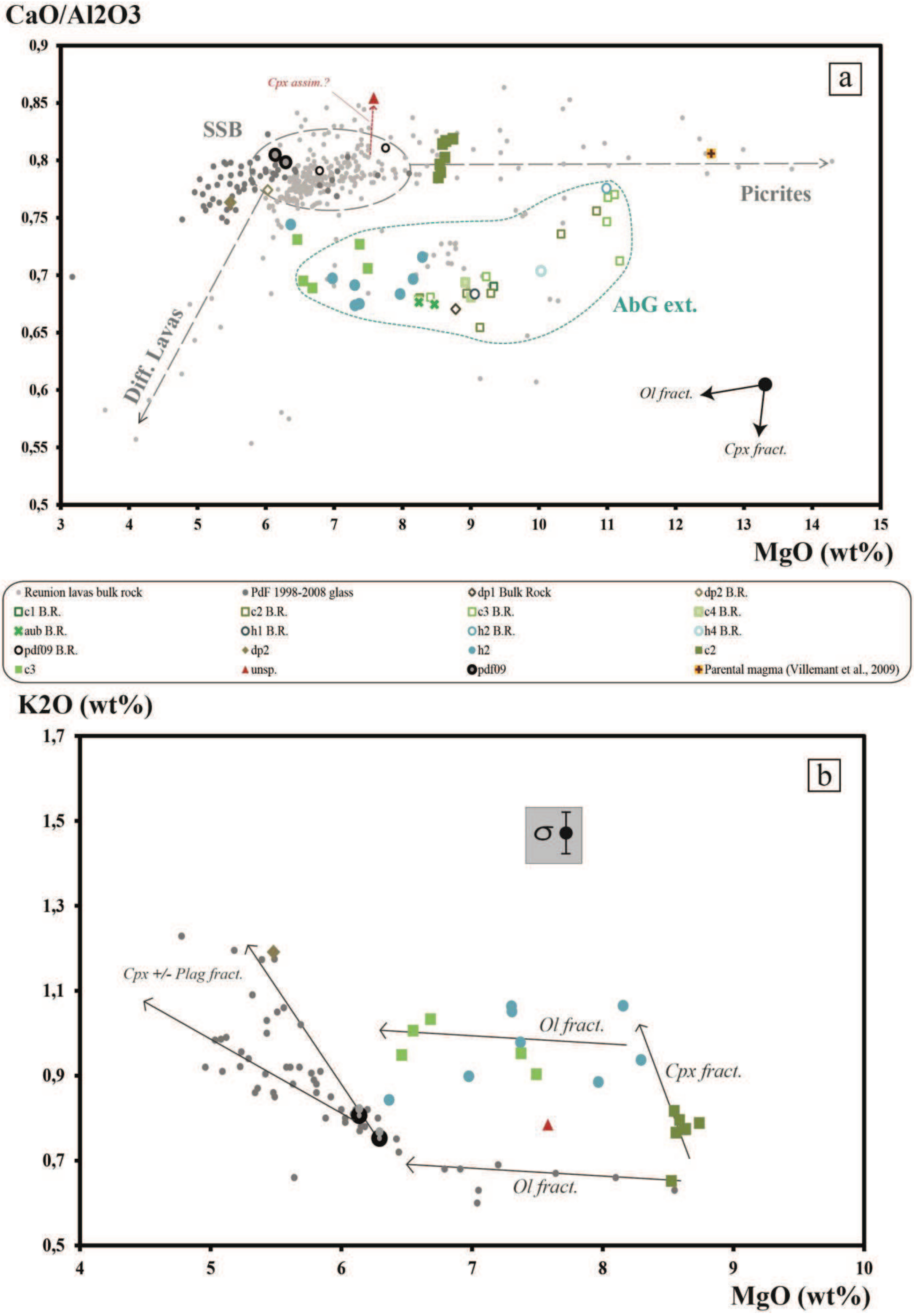
CaO/Al2O3
a
Cpx assim.?
SSB
Picrites
AbG ext.
Diff. Lavas
Ol fract.
Cpx fract.
0,9
0,85
0,8
0,75
0,7
0,65
0,6
0,55
0,5
3
4
5
6
7
8
9
10
11
12
13
14
15
MgO (wt%)
Reunion lavas bulk rock
PdF 1998-2008 glass
dp1 Bulk Rock
dp2 B.R.
c1 B.R.
c2 B.R.
c3 B.R.
c4 B.R.
aub B.R.
h1 B.R.
h2 B.R.
h4 B.R.
pdf09 B.R.
dp2
h2
c2
c3
unsp.
pdf09
Parental magma (Villemant et al., 2009)
K2O (wt%)
b
σ
Cpx +/- Plag fract.
Ol fract.
Cpx fract.
Ol fract.
1,7
1,5
1,3
1,1
0,9
0,7
0,5
4
5
6
7
8
9
10
MgO (wt%)

Table 1. Sample details.

Location	Strat. Unit	Reference	Description	Analyses
Lower east side of Demi-Piton	c3	REU - 1A	Lapilli	EMPA(a) / ICPMS
	unsp.	REU - 1B	Lapilli	EMPA(a) / ICPMS
Demi Piton - east cliff	dp1	REU - 02	Welded spatter	WR / EMPA(b)
Demi Piton - top	dp2	REU - 15	Accretionary lapilli with dense blocks	WR / EMPA(b)
Talweg between Demi-Piton and Piton Haüy	h2	REU - 20	Lapilli	EMPA(a) / ICPMS
100m of the junction of forest road and road leading to the cottage volcano	h2	REU - 23	Lapilli	EMPA(a) / ICPMS
Piton Haüy - bottom of the eastern flank	h2	REU - 24a	Lapilli	EMPA(a) / ICPMS
	h2	REU - 24b	Lapilli	WR
	h2	REU - 25	Lapilli	EMPA(a) / ICPMS
Piton Haüy - strombolian cone	h4	REU - 30	Scoria	WR
Piton Haüy - northwestern flank	c2	REU - 32A	Lapilli	EMPA(a) / ICPMS
	h4	REU - 32B	Lava flow	WR / EMPA(b) / SEM
Piton Haüy - southwestern flank	c2	REU - 34	Lapilli with dunitic inclusions	EMPA(a) / ICPMS
Talweg between Demi-Piton and Piton Haüy	c2	REU - 36	Lapilli	EMPA(a) / ICPMS
	dp2	REU - 37	Black lapilli	EMPA(a) / ICPMS
50m in the north of the forest road before Piton Chisny	c2	REU - 41	Lapilli under pahoehoe lava flow	EMPA(a) / ICPMS
West of Demi-Piton	c3	REU - 42	Lapilli under red chaotic lava flow	EMPA(a) / ICPMS
Southwest of Piton Haüy	c3	REU - 43	Lapilli under pahoehoe lava flow rich in olivine	EMPA(a) / ICPMS
Piton Haüy - northwestern flank	h2	REU - 44	Lapilli	EMPA(a) / ICPMS
Piton Haüy - western flank	h1	REU - 45	Oxidized spatter	WR
Between Demi-Piton and Piton Chisny	c3	REU - 46	Lapilli	EMPA(a) / ICPMS
West of Demi-Piton	c3	REU - 48	Chaotic pahoehoe lava flow	SEM
Talweg between Demi-Piton and Piton Haüy	h2	REU - 49	Lapilli	EMPA(a,b) / SEM / ICPMS
	h2	REU - 50	Lapilli	EMPA(a,b) / SEM / ICPMS
	h2	REU - 51	Lapilli	EMPA(a) / ICPMS
Pas des Sables	c2	REU - 55	Lapilli	EMPA(a) / ICPMS
West of Piton Chisny	c2	REU - 56	Pahoehoe lava flow	WR / SEM
Southwest of Piton Chisny	c3	REU - 57	Pahoehoe lava flow	WR
South of Piton Chisny	aub	REU - 58	Pahoehoe lava flow	WR / SEM
Northeast of Piton Chisny	c3	REU - 59A	Slabby lava flow	WR
North of Piton Chisny	c3	REU - 60A	Red spatter with dense blocks	WR
	c3	REU - 60B	Red spatter with dense blocks	WR
Piton Chisny - north flank	c3	REU - 61C	Lava flow intercalated in red spatter	WR
Piton Chisny - top	c4	REU - 62	Spatter with dense blocks	WR
	c4	REU - 63	Lava flow intercaled in a spatter	WR
Piton Chisny - nortwestern flank	c2	REU - 64A	Lava flow intercalated in black spatter	WR
	c3	REU - 64B	Lapilli	EMPA(a) / ICPMS
North of Piton Chisny	c2	REU - 65	Lapilli	EMPA(a) / ICPMS
	c3	REU - 66	Pahoehoe lava flow	WR
	c2	REU - 67	Pahoehoe lava flow	WR / SEM
Piton Chisny - western flank	c2	REU - 68	Black spatter	WR / SEM
Piton Chisny - eastern flank	c1	REU - 69A	Spatter	WR
	c3	REU - 69B	Lapilli	EMPA(a) / ICPMS
Pas des Sables	c2	REU - 70A	Lapilli	EMPA(a) / ICPMS
	pds	REU - 70B	Spatter	WR
Piton Chisny - northern flank	c3	REU - 71A	Spatter	WR
	c3	REU - 71B	Block of degazed lava	WR
West of Piton Chisny	ol	REU - 72	Pahoehoe lava flow, rich in ol and with plag	WR / SEM
	c2	REU - 73	Pahoehoe lava flow	WR / SEM
West of Demi-Piton	c2	REU - 74	Lapilli	WR / EMPA(a,b) /SEM / ICPMS
East of Piton Chisny / Aubert de la Rue lava field	aub	REU - 75	Spatter	WR / SEM
Piton de la Fournaise - summital activity - Dec. 2009 "SSB-type" eruptions[1]	pdf 09	REU - 76	Lappili	WR / EMPA(a,b) /SEM / ICPMS
	pdf 09	REU - 77	Lappili	WR / EMPA(a,b) /SEM / ICPMS

WR: whole-rock analysis; SEM: sample examined by scanning electron microscopy

EMPA: electron microprobe analysis of (a) glass and (b) mineral phases; ICPMS: glass laser ablation inductively coupled plasma mass spectrometry;

Samples from O.V.P.F.

Table 2. Whole-rock analyses.

Samples	**REU 02**	**REU 15**	**REU 45**	**REU 24B**	**REU 32B**	**REU69A**	**REU 67**	**REU 74**	**REU 56**	**REU 60A**	**REU 67**	**REU 62**	**REU 75**	**REU 76**	**REU 77**
Strat. Unit	*dp1*	*dp2*	*h1*	*h2*	*h4*	*c1*	*c2*	*c2*	*c2*	*c3*	*c3*	*c4*	*aub*	*pdf 2009*	*pdf 2009*
Type	*spatter*	*spatter*	*spatter*	*lapilli*	*flow*	*spatter*	*flow*	*lapilli*	*flow*	*spatter*	*flow*	*spatter*	*spatter*	*lapilli*	*lapilli*
Major elements (%)															
SiO_2	46,41	46,44	46,70	46,44	45,54	46,63	47,70	46,70	46,36	46,89	46,78	46,72	47,60	48,75	49,37
Al_2O_3	14,14	14,39	13,78	12,76	13,33	14,01	14,57	13,83	13,23	12,97	14,20	14,35	14,54	13,82	14,40
Fe_2O_3	12,91	13,50	13,20	13,14	12,94	13,44	13,13	13,20	13,39	13,50	13,17	13,35	13,11	11,78	11,98
MnO	0,17	0,18	0,18	0,18	0,18	0,18	0,18	0,18	0,18	0,18	0,18	0,18	0,18	0,16	0,17
MgO	8,78	6,03	9,06	10,99	10,03	9,34	8,26	9,14	10,32	11,11	8,41	9,00	8,47	7,76	6,79
CaO	9,48	11,14	9,42	9,90	9,38	9,67	9,91	9,05	9,74	9,99	9,67	9,77	9,81	11,20	11,39
Na_2O	2,95	2,51	2,86	2,45	2,75	2,74	3,15	2,90	2,64	2,55	3,03	2,52	3,08	2,57	2,71
K_2O	1,04	0,77	0,90	0,73	1,06	0,83	0,94	0,91	0,77	0,73	0,91	0,74	0,94	0,67	0,71
TiO_2	2,86	3,08	2,76	2,50	2,70	2,91	2,91	2,68	2,74	2,67	2,91	2,93	2,88	2,48	2,64
P_2O_5	0,42	0,36	0,38	0,30	0,49	0,38	0,44	0,39	0,35	0,33	0,44	0,39	0,44	0,29	0,32
L.O.I.	-0,65	0,32	-0,40	-0,73	0,15	-0,24	-0,78	-0,39	-0,73	-0,60	-0,72	-0,03	-0,66	-0,87	-0,79
Total	98,50	98,73	98,83	98,65	98,55	99,87	100,40	98,59	99,00	100,31	98,96	99,92	100,37	98,61	99,69
CaO/Al_2O_3	0,67	0,77	0,68	0,78	0,70	0,69	0,68	0,65	0,74	0,77	0,68	0,68	0,67	0,81	0,79
Trace elements (ppm)															
As	< L.D.	< L.D.	< L.D.	< L.D.	< L.D.	< L.D.	< L.D.	< L.D.	< L.D.	< L.D.	< L.D.	< L.D.	< L.D.	< L.D.	< L.D.
Ba	183,1	166,2	173,3	133,0	234,3	153,3	180,6	166,1	155,5	136,9	181,3	170,3	179,0	120,7	119,1
Be	1,4	1,2	1,3	1,1	1,4	1,1	1,3	1,3	1,1	0,9	1,3	1,2	1,3	1,0	1,1
Bi	< L.D.	< L.D.	< L.D.	< L.D.	< L.D.	< L.D.	< L.D.	< L.D.	< L.D.	< L.D.	< L.D.	< L.D.	< L.D.	< L.D.	< L.D.
Cd	0,4	0,4	0,2	0,1	0,2	0,2	0,2	0,1	0,2	0,2	0,2	0,3	0,2	0,2	0,2
Ce	56,1	50,2	50,9	42,2	63,9	48,5	57,9	50,4	49,2	44,1	58,8	50,7	57,1	39,9	39,8
Co	52,2	47,3	55,4	58,1	56,4	53,9	49,3	50,9	61,7	60,3	51,4	55,8	51,0	45,5	39,7
Cr	394,7	33,6	453,4	664,1	493,4	413,1	336,6	411,0	563,1	590,9	384,2	410,4	364,1	465,5	230,6
Cs	0,4	0,2	0,3	0,3	0,4	0,2	0,3	0,3	0,2	0,2	0,3	0,2	0,3	0,3	0,2
Cu	71,2	98,3	76,3	94,0	77,4	69,6	72,0	73,4	84,8	87,4	74,9	22,1	78,4	118,4	125,4
Dy	5,6	5,8	5,7	4,8	5,5	5,1	5,6	5,4	5,4	4,9	5,7	5,5	5,6	5,2	5,2
Er	2,6	2,7	2,7	2,2	2,4	2,4	2,6	2,5	2,5	2,3	2,7	2,7	2,6	2,5	2,5
Eu	2,4	2,4	2,4	2,0	2,5	2,1	2,4	2,3	2,2	2,0	2,4	2,2	2,3	2,1	2,1
Ga	22,1	22,9	22,3	20,3	22,1	21,5	22,6	20,7	22,2	20,5	22,5	22,1	22,5	22,2	21,4
Gd	6,6	6,6	6,5	5,7	6,7	5,9	6,4	6,5	6,1	5,6	6,6	6,3	6,4	6,2	6,1
Ge	1,5	1,6	1,7	1,2	1,5	1,4	1,5	1,2	1,6	1,5	1,6	1,5	1,5	1,3	1,2
Hf	5,5	5,1	5,3	4,3	6,1	4,7	5,4	5,1	4,8	4,5	5,6	4,9	5,5	4,4	4,4
Ho	1,1	1,2	1,2	0,9	1,0	1,0	1,1	1,0	1,0	1,0	1,1	1,1	1,1	0,9	0,9
In	0,1	0,1	0,1	0,0	0,1	< L.D.	0,1	0,0	0,1	0,1	0,1	0,2	0,1	0,1	0,0
La	26,4	23,1	22,8	18,5	29,4	20,9	25,4	22,2	21,6	19,0	25,9	21,9	25,4	17,2	17,2
Lu	0,3	0,4	0,4	0,3	0,3	0,3	0,3	0,3	0,3	0,3	0,3	0,3	0,3	0,3	0,3
Mo	1,4	0,9	1,2	1,1	1,4	1,1	1,3	1,4	1,1	1,0	1,3	1,2	1,4	1,2	1,1
Nb	26,5	24,8	24,6	17,6	32,3	21,1	24,4	21,0	20,9	18,7	24,9	21,7	24,4	16,1	15,8
Nd	31,1	29,1	29,4	24,5	34,5	26,9	31,5	28,8	27,4	25,1	31,6	28,6	30,8	24,0	24,0
Ni	203,8	62,6	221,5	295,2	266,0	215,7	172,1	213,2	283,9	302,2	183,1	217,1	183,4	142,2	91,9
Pb	3,1	1,8	2,0	1,7	2,8	1,8	2,7	2,7	2,8	2,1	2,5	3,6	2,2	1,7	1,6
Pr	7,5	6,8	6,9	5,4	8,4	6,3	7,5	6,4	6,4	5,8	7,5	6,6	7,4	5,2	5,2
Rb	26,7	17,7	23,3	17,6	30,0	21,2	24,9	22,1	21,1	18,2	24,7	17,1	25,5	16,2	16,0
Sc	26,1	31,6	26,3	29,8	25,8	28,9	28,4	26,1	29,3	31,0	28,0	29,4	28,2	33,5	33,4
Sb	< L.D.	< L.D.	< L.D.	< L.D.	< L.D.	< L.D.	< L.D.	< L.D.	< L.D.	< L.D.	< L.D.	< L.D.	< L.D.	< L.D.	< L.D.
Sm	7,2	7,1	6,9	5,8	7,6	6,3	7,2	6,6	6,5	5,9	7,3	6,7	7,1	6,0	6,0
Sn	6,2	4,2	4,3	1,6	6,1	2,0	2,0	1,8	2,3	1,8	2,2	1,5	3,1	2,2	3,8
Sr	455,7	417,4	417,4	322,3	511,6	381,3	438,2	367,5	385,3	349,1	433,1	399,6	440,3	328,9	320,5
Ta	2,1	1,9	1,9	1,6	2,5	1,8	2,1	1,9	1,8	1,6	2,1	1,8	2,1	1,4	1,4
Tb	1,0	1,0	1,0	0,9	1,0	0,9	1,0	1,0	0,9	0,8	1,0	1,0	1,0	0,9	0,9
Th	3,2	2,8	2,8	2,0	3,8	2,4	3,0	2,4	2,4	2,2	2,9	2,5	2,9	1,8	1,8
Tm	0,3	0,4	0,4	0,3	0,3	0,3	0,3	0,3	0,3	0,3	0,4	0,3	0,3	0,3	0,3
U	0,8	0,7	0,7	0,5	0,9	0,6	0,8	0,6	0,6	0,6	0,8	0,6	0,7	0,5	0,5
V	274,9	335,1	270,5	279,2	257,3	286,5	282,4	218,7	307,0	281,8	287,4	298,1	283,6	296,1	280,6
W	0,6	0,4	0,5	0,3	0,6	0,4	0,5	0,4	0,4	0,3	0,5	0,4	0,5	0,3	0,3
Y	27,2	28,1	27,9	23,4	26,0	25,5	27,5	26,5	26,5	24,2	28,1	27,9	27,6	26,4	25,8
Yb	2,1	2,2	2,3	1,9	2,0	2,0	2,2	2,1	2,1	1,9	2,2	2,1	2,2	2,1	2,1
Zn	121,6	127,8	125,1	118,6	120,5	120,0	123,0	119,5	127,9	117,5	126,1	148,5	124,3	110,6	105,9
Zr	224,8	201,8	204,4	152,5	262,2	196,3	227,6	183,1	194,2	160,7	230,4	183,1	226,8	156,7	154,6
Sc/Yb	12,3	14,2	11,5	15,8	13,0	14,4	12,9	12,2	14,0	16,3	12,7	13,8	12,9	15,8	15,9
Ce/Yb	26,4	22,5	22,3	22,4	32,2	24,2	26,3	23,7	23,5	23,2	26,6	23,8	26,2	18,8	19,0

Table 3. Glass laser ICPMS analyses.

Samples	REU 37	REU 20	REU 23	REU 24A	REU 25	REU 44	REU 49	REU 50	REU 51	REU 65	REU 70	REU 74	REU 32	REU 34	REU 36	REU 41	REU 55	REU 1A	REU 42	REU 46	REU 64B	REU 69B	REU 1B [2]	REU 76	REU 77
Strat. Unit	*dp2*	*h2*	*h2*	*h2*	*h2*	*h2*	*h2*	*h2*	*h2*	*c2*	*c2*	*c2*	*c2*	*c2*	*c2*	*c2*	*c2*	*c3*	*c3*	*c3*	*c3*	*c3*	*unsp.*	*pdf 2009*	*pdf 2009*
Major elements (%)[1]																									
SiO2	47,32	49,51	48,24	48,21	47,90	47,86	47,75	47,66	48,03	48,11	47,98	48,18	47,96	47,32	47,30	47,96	47,78	48,40	48,39	47,94	48,68	48,14	48,38	49,75	49,83
TiO2	3,34	3,38	2,93	2,84	3,17	2,87	3,09	2,78	2,81	2,61	2,62	2,72	2,66	2,68	2,71	2,66	2,81	2,70	2,91	3,40	2,89	3,11	2,96	2,98	2,95
Al2O3	13,61	14,04	13,77	14,08	14,28	14,67	14,19	14,25	14,21	13,22	13,53	13,58	13,27	13,65	13,40	13,27	13,36	14,18	14,47	14,56	14,57	14,67	13,50	13,66	13,84
Fe2O3	13,10	11,05	11,37	11,42	10,99	11,33	11,07	11,39	11,13	10,91	11,24	11,45	10,94	10,95	11,10	10,94	10,90	11,09	10,73	12,03	11,08	10,96	11,53	10,71	10,44
MnO	0,25	0,20	0,12	0,18	0,26	0,04	0,20	0,15	0,19	0,25	0,21	0,22	0,13	0,05	0,02	0,13	0,17	0,20	0,12	0,14	0,20	0,19	0,22	0,07	0,19
MgO	5,48	6,37	8,29	8,16	7,31	7,37	6,98	7,97	7,30	8,74	8,56	8,53	8,63	8,62	8,59	8,63	8,55	7,49	7,37	6,46	6,55	6,68	7,58	6,14	6,29
CaO	10,39	10,45	9,86	9,81	9,62	9,90	9,89	9,74	9,82	10,81	10,69	10,66	10,84	10,95	10,91	10,84	10,64	10,01	10,52	10,64	10,12	10,11	11,53	11,00	11,05
Na2O	3,07	1,81	3,01	2,94	3,01	2,98	2,93	3,03	3,16	2,37	2,76	2,68	2,46	2,64	2,61	2,46	2,72	3,24	2,96	2,88	3,32	3,33	2,69	2,76	2,86
K2O	1,19	0,84	0,94	1,06	1,05	0,98	0,90	0,89	1,06	0,79	0,77	0,65	0,77	0,77	0,80	0,77	0,82	0,90	0,95	0,95	1,01	1,03	0,78	0,81	0,75
P2O5	0,46	0,37	0,30	0,45	0,74	0,57	0,53	0,48	0,28	0,36	0,34	0,22	0,36	0,29	0,37	0,36	0,31	0,38	0,36	0,28	0,26	0,27	0,39	0,21	0,32
Cr2O3	0,03	0,01	0,01	0,07	0,07	0,01	0,06	0,05	0,02	0,08	0,04	0,05	0,02	0,09	0,05	0,02	0,08	0,04	0,06	0,04	0,04	0,04	0,04	0,01	0,02
NiO	0,00	0,12	0,15	0,07	0,00	0,16	0,11	0,17	0,02	0,00	0,02	0,00	0,16	0,00	0,01	0,16	0,00	0,00	0,01	0,00	0,00	0,09	0,00	0,00	0,02
Total	98,24	98,14	99,01	99,29	98,38	98,74	97,69	98,54	98,03	98,25	98,75	98,93	98,22	98,01	97,85	98,22	98,15	98,63	98,84	99,31	98,72	98,63	99,61	98,09	98,58
K2O/TiO2	0,36	0,25	0,32	0,37	0,33	0,34	0,29	0,32	0,38	0,30	0,29	0,24	0,29	0,29	0,29	0,29	0,29	0,33	0,33	0,28	0,35	0,33	0,26	0,27	0,26
CaO/Al2O3	0,76	0,74	0,72	0,70	0,67	0,68	0,70	0,68	0,69	0,82	0,79	0,79	0,82	0,80	0,81	0,82	0,80	0,71	0,73	0,73	0,69	0,69	0,85	0,80	0,80
Trace elements (ppm)[3]																									
B	1,6	4,7	1,1	1,5	1,4	1,6	1,5	1,4	1,7	1,1	2,0	1,1	1,3	1,4	1,2	1,3	1,3	1,2	1,1	1,2	1,1	1,0	1,2	0,9	12,7
Ba	149,9	149,8	133,6	137,4	137,0	150,2	146,3	138,4	143,7	116,9	114,8	121,7	113,9	116,5	118,6	121,4	115,3	139,9	131,5	138,7	141,4	133,9	124,7	108,2	101,9
Be	0,6	0,4	0,8	0,9	0,9	0,8	0,8	0,7	0,8	0,8	0,7	0,8	0,6	0,6	0,7	0,7	0,5	0,9	0,8	0,7	1,0	1,3	0,9	0,7	1,7
Ce	44,3	43,2	38,4	39,4	39,1	42,5	42,2	40,0	40,7	35,1	34,2	36,9	34,1	34,8	35,2	36,7	34,6	40,2	39,1	39,7	42,0	40,6	37,0	35,0	30,2
Co	46,4	32,9	36,9	41,5	35,1	36,4	38,0	37,9	36,0	39,2	38,3	40,6	39,7	39,6	40,5	45,7	37,3	37,3	36,8	34,0	34,7	25,2	36,3	29,1	33,6
Cr	226,5	187,2	241,4	266,0	212,6	210,4	206,4	229,3	221,1	297,0	308,8	300,4	312,8	313,5	285,3	308,9	302,6	215,0	216,4	183,9	248,0	173,4	319,6	78,5	197,4
Cs	0,2	0,6	0,2	0,4	0,4	0,2	0,2	0,4	0,4	0,2	0,2	0,2	0,3	0,3	0,2	0,2	0,3	0,3	0,2	0,2	0,3	0,3	0,2	0,2	2,3
Dy	4,2	4,0	4,3	4,1	4,0	4,5	4,5	4,0	4,0	3,9	3,5	3,8	3,5	3,7	4,0	4,0	3,6	4,4	4,0	4,3	4,4	3,7	4,5	3,9	3,6
Er	2,0	1,9	2,0	1,9	1,9	2,2	2,2	1,9	1,9	1,9	1,6	1,8	1,7	1,7	1,9	1,9	1,7	2,1	1,9	2,1	2,1	1,8	2,2	1,9	1,8
Eu	1,8	1,7	1,6	1,6	1,6	1,8	1,8	1,6	1,7	1,5	1,4	1,5	1,4	1,5	1,6	1,6	1,5	1,7	1,6	1,7	1,7	1,6	1,7	1,6	1,3
Gd	4,8	4,7	5,0	4,7	4,6	5,3	5,2	4,7	4,7	4,5	4,0	4,4	4,1	4,3	4,7	4,6	4,2	5,1	4,7	5,0	5,0	4,5	5,2	4,5	4,1
Hf	3,9	3,5	4,0	3,8	3,6	4,4	4,4	3,6	3,8	3,5	3,0	3,4	3,0	3,2	3,7	3,7	3,2	4,1	3,7	4,1	4,1	3,7	4,0	3,3	3,3
Ho	0,7	0,7	0,8	0,7	0,7	0,8	0,8	0,7	0,7	0,7	0,6	0,7	0,6	0,7	0,7	0,7	0,7	0,8	0,7	0,8	0,8	0,7	0,8	0,7	0,7
La	19,2	18,6	17,7	17,5	17,4	19,4	19,0	17,4	18,0	15,8	14,8	16,0	14,7	15,3	15,9	15,9	15,0	18,3	17,5	17,9	18,9	19,0	17,4	14,5	13,7
Li	5,4	247,8	4,6	4,4	4,0	5,1	5,0	4,5	4,5	5,1	30,2	4,2	4,0	3,9	4,1	4,3	3,9	4,9	4,5	2,1	5,1	7,1	4,6	4,3	1518,0
Lu	0,2	0,2	0,2	0,2	0,2	0,2	0,3	0,2	0,2	0,2	0,2	0,2	0,2	0,2	0,2	0,2	0,2	0,2	0,2	0,2	0,2	0,2	0,2	0,2	0,2
Nb	22,6	22,6	20,0	20,9	21,0	21,6	21,8	21,0	21,3	18,3	17,5	18,7	17,2	18,0	17,7	18,2	17,9	21,2	20,5	20,0	21,6	21,4	18,7	16,8	14,1
Nd	24,1	23,1	21,8	21,6	21,2	23,9	23,5	21,5	21,9	19,9	18,6	20,0	18,4	19,2	20,2	20,5	19,0	22,6	21,7	22,4	23,1	21,8	21,9	19,4	17,3
Ni	111,8	54,8	90,7	101,8	69,7	66,7	77,2	76,5	67,9	101,2	101,8	104,5	91,7	88,4	91,0	127,3	86,2	80,5	67,2	57,4	70,3	52,8	92,5	34,1	53,9
Pb	1,0	16,0	0,9	1,0	0,9	1,1	1,0	0,9	1,2	1,2	4,3	0,9	1,0	1,0	0,8	0,8	0,8	1,0	0,9	0,9	0,9	1,0	1,0	0,7	11,7
Pr	5,6	5,4	4,9	5,0	4,9	5,5	5,4	5,0	5,1	4,5	4,3	4,6	4,3	4,4	4,6	4,7	4,4	5,1	5,0	5,1	5,3	5,2	4,8	4,5	3,9
Rb	18,1	16,7	16,5	16,9	16,9	18,0	17,5	16,8	17,8	13,9	13,4	15,2	13,6	13,8	13,5	14,7	12,7	18,1	16,6	15,2	18,2	16,2	14,5	13,4	17,6
Sm	5,3	5,4	5,1	5,0	4,8	5,5	5,5	4,9	5,0	4,6	4,3	4,6	4,2	4,4	4,8	4,8	4,4	5,3	5,0	5,2	5,3	5,0	5,2	4,7	4,2
Sr	305,1	337,1	292,0	298,6	290,1	320,4	315,6	293,3	301,2	272,0	262,0	277,5	255,3	267,7	274,9	278,7	263,7	306,8	291,1	327,2	302,6	306,3	286,6	241,9	386,2
Ta	1,3	1,4	1,2	1,2	1,2	1,4	1,4	1,2	1,3	1,1	1,0	1,1	1,0	1,1	1,2	1,2	1,1	1,3	1,2	1,3	1,3	1,2	1,2	1,0	0,9
Tb	0,8	0,7	0,8	0,7	0,7	0,8	0,8	0,7	0,7	0,7	0,6	0,7	0,6	0,7	0,7	0,7	0,6	0,8	0,7	0,7	0,8	0,7	0,8	0,7	0,6
Th	2,2	2,2	2,1	2,0	2,0	2,4	2,3	2,0	2,1	1,9	1,7	1,8	1,7	1,7	1,9	1,9	1,7	2,2	2,1	2,2	2,2	2,1	2,1	1,6	2,2
U	0,5	0,5	0,4	0,4	0,4	0,4	0,4	0,4	0,4	0,4	0,3	0,4	0,4	0,4	0,3	0,4	0,4	0,4	0,4	0,4	0,4	0,4	0,4	0,3	0,4
Y	20,2	18,9	21,5	20,3	19,5	22,1	21,6	19,5	20,0	19,3	17,1	18,7	17,1	18,4	19,6	18,6	17,5	21,7	19,5	20,5	21,5	19,4	22,7	19,0	19,0
Yb	1,7	1,6	1,6	1,6	1,5	1,8	1,8	1,5	1,6	1,5	1,3	1,5	1,4	1,4	1,6	1,6	1,4	1,7	1,6	1,7	1,6	1,4	1,7	1,6	1,4
Zr	154,1	144,1	165,9	157,3	156,9	172,5	168,5	152,5	158,4	143,2	125,3	140,9	125,7	135,4	139,2	135,0	129,9	171,9	147,5	154,3	168,5	170,4	163,9	132,8	130,7
La/Yb	11,2	11,7	10,8	11,2	11,8	10,9	10,7	11,3	11,4	10,7	11,0	11,0	10,6	10,7	9,8	9,9	10,7	10,9	11,2	10,6	11,6	13,7	10,1	9,2	9,6
Ce/Yb	25,8	27,2	23,5	25,2	26,4	24,0	23,8	26,0	25,9	23,7	25,5	25,2	24,4	24,2	21,6	22,9	24,7	23,9	25,1	23,6	25,8	29,2	21,6	22,3	21,1

average of 2 analyses on each glass sample

unspecified stratigraphic attribution

average of 2~5 analyses on each glass sample (except REU37: 1 analysis)

Table 4. Electron microprobe analyses.

Mineral	**Olivine**	**Olivine**	**Olivine**	**Olivine**	**Olivine**	**Olivine**	**Olivine**	**Olivine**	**Olivine**	**Clinopyroxene**	**Clinopyroxene**	**Clinopyroxene**[1]	**Clinopyroxene**[1]	**Clinopyroxene**[1]	**Plagioclase**[1]	**Plagioclase**[1]	**Spinel**	**Spinel**	**Spinel**	**Spinel**
Reference	13	13	5	15	15	8	8	12	4	8	8	*1*	*6*	*7*	*2*	*5*	*86*	*86*	*5*	*3*
Location	*core*	*rim*	*core*	*core*	*rim*	*core*	*rim*	*core*	*core*	*core*	*rim*	-	-	-	-	-	*core*	*rim*	*ol incl.*	*ol incl.*
Sample	*REU74*	*REU74*	*REU74*	*REU49*	*REU49*	*REU49*	*REU49*	*REU50*	*REU50*	*REU32*	*REU32*	*REU49*	*REU15*	*REU15*	*REU32*	*REU32*	*REU74*	*REU74*	*REU74*	*REU49*
Strat. Unit	*c2*	*c2*	*c2*	*h2*	*h2*	*h2*	*h2*	*h2*	*h2*	*h4*	*h4*	*h2*	*dp2*	*dp2*	*h4*	*h4*	*c2*	*c2*	*c2*	*h2*
Oxides (%)																				
SiO2	41,10	41,13	39,56	39,83	40,48	38,03	38,35	41,16	38,19	51,05	48,75	44,57	47,47	49,09	55,87	52,03	0,06	0,03	0,28	0,02
TiO2	0,06	0,00	0,00	0,05	0,03	0,17	0,07	0,02	0,00	1,47	2,97	3,93	2,63	2,07	0,32	0,23	2,46	2,49	1,54	4,25
Al2O3	0,03	0,04	0,00	0,00	0,06	0,05	0,00	0,02	0,00	2,85	6,37	10,43	6,52	3,52	26,73	28,48	21,07	19,12	35,88	17,78
FeO	11,53	11,71	17,07	12,33	13,38	24,96	23,82	10,80	19,61	7,52	7,65	11,26	7,67	9,31	0,50	0,51	26,31	26,27	23,65	35,63
MnO	0,24	0,16	0,31	0,37	0,19	0,21	0,39	0,01	0,38	0,30	0,25	0,12	0,20	0,28	0,00	0,13	0,23	0,34	0,11	0,18
MgO	47,04	46,90	42,34	46,49	46,59	35,43	36,50	48,23	40,30	15,82	12,19	12,84	13,51	13,66	0,04	0,12	12,40	12,04	15,18	9,97
CaO	0,27	0,22	0,19	0,21	0,21	0,44	0,40	0,18	0,11	21,24	20,81	15,05	20,99	20,50	9,27	12,23	0,04	0,09	0,06	0,04
Na2O	0,00	0,00	0,06	0,01	0,00	0,00	0,00	0,03	0,00	0,31	0,65	0,87	0,29	0,32	5,79	4,22	0,03	0,00	0,00	0,01
K2O	0,00	0,00	0,04	0,03	0,01	0,00	0,00	0,00	0,06	0,00	0,13	0,20	0,05	0,06	0,46	0,35	0,00	0,04	0,00	0,00
P2O5	0,07	0,05	0,09	0,00	0,01	0,01	0,13	0,05	0,00	0,00	0,03	0,39	0,00	0,07	0,04	0,00	0,07	0,12	0,04	0,02
Cr2O3	0,11	0,00	0,51	0,09	0,02	0,00	0,02	0,00	0,02	0,29	0,00	0,10	0,19	0,03	0,03	0,00	33,49	35,33	19,10	28,56
NiO	0,24	0,59	0,08	0,20	0,34	0,27	0,01	0,60	0,00	0,05	0,00	0,03	0,00	0,00	0,00	0,00	0,15	0,11	0,30	0,00
Total	100,68	100,79	100,25	99,63	101,33	99,57	99,69	101,12	99,67	100,91	99,79	99,80	99,52	98,90	99,03	98,30	96,32	95,98	96,13	96,47
Fo / Mg#	**87,9**	**87,7**	**81,6**	**87,1**	**86,1**	**71,7**	**73,2**	**88,8**	**78,6**	**79,0**	**74,0**	**66,9**	**75,8**	**72,3**			**56,4**	**55,7**	**64,7**	**44,3**
En										**44,8**	**38,8**	**42,8**	**41,1**	**40,6**						
Fs										**11,9**	**13,7**	**21,1**	**13,1**	**15,5**						
Wo										**43,2**	**47,6**	**36,1**	**45,9**	**43,8**						
An															**45,7**	**60,3**				
Ab															**51,7**	**37,6**				
Or															**2,7**	**2,0**				
Cr#																	**51,6**	**55,3**	**26,3**	**51,9**
Fo / Mg# th.[2]	*82,56*	*82,56*	*82,56*	*80,02*	*80,02*	*80,02*	*80,02*	*81,63*	*81,63*	*84,83*	*84,83*	*82,52*	*79,13*	*79,13*						

[1] microphenocryst (REU49) or microlites; all other analyses refer to phenocrysts.

theoretical Fo or Mg# calculated for olivine (Kd=0,33 after *Brugier et al., in prep*) or clinopyroxene (Kd=0,28 after *Brugier et al., in prep*) phase in equilibrium with analyzed glass sample (or Bulk Rock for sample REU15 & REU32)

Fo=100*at. Mg/(Mg+Fe) in olivine; Mg#=100* at. Mg/(Mg+Fe) in clinopyroxene, En=100*at. Mg/(Mg+Fe+Ca) in cpx, Fs=100*at. Fe/(Mg+Fe+Ca) in cpx, Wo=100*at. Ca/(Mg+Fe+Ca) in cpx; An=100*at. Ca/(Ca+Na+K) in plagioclase, Ab=100*at. Na/(Ca+Na+K) in plag, Or=100*at. K/(Ca+Na+K) in plag; Cr#=100*at. Cr/(Cr+Al) in spinel.

CHAPITRE II : “Approche pétrologique - Etude pétrologique et minéralogique de roches plutoniques réunionnaises”

Résumé

Dans ce second chapitre, rédigé sous forme d'article, les résultats d'une étude pétrologique réalisée sur des enclaves plutoniques ultra-mafiques (dunites et wehrlites) à mafiques (gabbros à olivine ; gabbros et dolérites) de la Plaine des Sables, sont présentés. L'échantillonnage a été complété avec l'étude d'un gabbro du massif de Salazie, et d'une enclave de gabbro dans une ignimbrite, les deux étant associés au Piton des Neiges. L'objectif de ce travail était de contraindre la ou les séquences de cristallisation enregistrées dans les roches plutoniques de façon à pouvoir les comparer avec les résultats de l'étude de pétrologie expérimentale réalisée durant ce travail de thèse et présentée dans les Chapitres 3 et 4.

Les compositions modales, relations texturales ainsi que les compositions chimiques des phases minérales ont permis de définir, pour la plupart des échantillons, la séquence de cristallisation suivante : olivine, clinopyroxène, plagioclase, le spinelle cristallisant durant toute la séquence, suivi de la magnétite. En plus de ces phases minérales principales, des phases minérales secondaires, rarement décrites dans les roches ignées réunionnaises, comme l'apatite, la sanidine, l'ilménite ou encore la phlogopite, apparaissent dans les derniers stades de la cristallisation. Des inclusions de kaersutite ont été trouvées dans les clinopyroxènes de l'enclave de gabbro de l'ignimbrite. Les données augmentent fortement les gammes de compositions des phases minérales dans les roches ignées de La Réunion. Les olivines ont des teneurs en Fo qui peuvent descendre jusqu'à 27 et les feldspaths des teneurs en K2O jusqu'à 7,8 wt% dans la dolérite. Les clinopyroxènes interstitiels des dunites (Mg# jusqu'à 90,2%, 1,25wt% Al2O3) sont les plus primitifs des clinopyroxènes des produits magmatiques réunionnais. L'orthopyroxène (accompagné de pigeonite dans un échantillon), le spinelle et l'ilménite apparaissent en exsolution dans les clinopyroxènes de gabbros. Les températures d'équilibre entre les différents pyroxènes, obtenues avec le logiciel QUILF (1033 ± 41°C) sont interprétées comme la température minimale d'apparition du plagioclase dans l'assemblage gabbroïque ol+cpx+plag. Les températures et fO2 calculées à partir de l'équilibre entre ilménite et magnétite varient de 790±73°C (enclave de gabbro dans l'ignimbrite) à 965±2°C (dolérite), cette dernière étant cohérente avec les températures (900±100°C) déduites à partir de la position du solvus des feldspaths. Des fO2 assez réductrices ont été obtenues pour les dernières étapes de la cristallisation (ΔFMQ = -1.2 à -0.7 dans la dolérite).

La séquence de cristallisation définie à partir de ce travail est en adéquation avec celle classiquement attribuée au groupe des SSB. Elle n'apporte pas de preuve de cristallisation précoce de clinopyroxène. Cependant, la séquence de cristallisation déterminée sur l'enclave de gabbro (avec notamment l'amphibole cristallisant avant et/ou avec le clinopyroxene) est très différente de celle de tous les autres échantillons étudiés. Elle témoigne ainsi de l'existence de plusieurs séquences de cristallisation possibles pour les magmas réunionnais. La possibilité d'un fractionnement précoce de clinopyroxène ne peut donc être exclue à La Réunion sur la base de notre étude. Ceci met bien en relief les limites de l'approche basée sur des roches plutoniques naturelles (nombre limité, origine incertaine) pour déterminer les séquences de cristallisation.

Petrological and mineralogical characteristics of plutonic rocks from the Plaine des Sables (La Réunion island) – Implications for crystallization of Réunion lavas

Y.A. BRUGIER, G. BOUDOIRE, M. PICHAVANT, A. DI MURO, Y. LE MOIGNE & J-L. BOURDIER

Abstract A suite of ultra-mafic and mafic xenoliths from the Plaine des Sables, complemented by other representative plutonic and crystal-rich samples from La Réunion island, has been investigated with the objective to constrain igneous crystallization sequences for the Piton de la Fournaise volcanic series. The modal, textural and compositional data obtained on dunites, wehrlites, gabbros and a dolerite suggest a crystallization sequence in the order olivine, clinopyroxene, plagioclase for most samples. Spinel crystallizes all along this sequence, followed by magnetite. Mineral phases rarely described in La Réunion igneous rocks, such as sanidine, apatite and ilmenite, are associated with the latest crystallization stages. Phlogopite is locally present as a late-magmatic phase. Kaersutite occurs as inclusions in clinopyroxene in a gabbroic enclave from a Piton des Neiges ignimbrite. Mineral chemistry data on these plutonic samples extend the range of compositions known in La Réunion igneous rocks. Olivines with Fo as low as 27 and feldspars with K2O contents as high as 7.8 wt% K2O have been found in the dolerite. The interstitial diopsides in the dunitic cumulates record the most primitive clinopyroxene compositions (Mg# = 90.2, Al2O3 = 1.25 wt%) on the La Réunion island. Clinopyroxenes in gabbros host mineral exsolutions of orthopyroxene (± pigeonite), spinel and ilmenite, crystallizing as solid state re-equilibration products and postdating plagioclase crystallization. Pyroxene equilibration temperatures show that plagioclase appears in primitive spinel-bearing olivine gabbros at a minimum of 1033 ± 41°C. Ilmenite-magnetite equilibration temperatures are lower (790±73°C to 965±2°C), consistent with the oxide crystallization sequence. Particularly reducing fO2 (ΔFMQ = -1.2 to -0.7) characterize final crystallization stages under closed-system conditions. The determined crystallization sequence is consistent with the olivine fractionation mechanism classically proposed for the Steady State Basalts. There is no indication in the plutonic samples studied for early clinopyroxene fractionation, as previously suggested for the Abnormal Group series. However, the kaersutite-bearing Piton des Neiges gabbro has mineralogical attributes which imply an alternative crystallization sequence, colder and more hydrous than for all the other plutonic samples. Olivine fractionation should not be considered as the only possible differentiation mechanism taking place in La Réunion magmas.

***Keywords**: Piton de la Fournaise, Piton des Neiges, ultra-mafic cumulates, olivine gabbros, dolerites, crystallization sequence, orthopyroxene exsolutions, equilibrium temperature*

1 Introduction

In volcanic islands, plutonic rocks are rarely observable, unless erosion reaches the lowest internal parts of ancient, inactive volcanoes, e.g. Haleakala and Kauai on Hawaiian islands (Karatson et al., 1999 and references therein) or Tahiti-Nui island (Hildenbrand et al., 2008). When exposed, such deep plutonic rocks provide important information on the structure of fossil volcanic feeding systems. When exposures of plutonic massifs are not available, plutonic xenoliths occurring in volcanic deposits constitute alternative objects of study. Textural and mineralogical studies of such plutonic xenoliths have been frequently carried out to constrain crystallization and/or fractionation processes inside volcanic feeding systems. Such studies have been applied to various geodynamic settings including oceanic islands (Hawaiian: Bohrson and Clague, 1988; Fodor and Vandermeyden, 1988; Clague and Bohrson, 1991; Canary: Borley et al., 1971; Klügel et al., 2005) and island arcs (Aeolian: Laiolo and Cigolini, 2006).

La Réunion island (Indian Ocean) makes no exception to this rule. The ultra-mafic and mafic xenoliths that occur in volcanic products on the island have been investigated since more than 50 years (Lacroix, 1936; Babkine et al., 1966; Upton and Wadsworth, 1972; Ludden, 1978a; Mohamed-Abchir, 1996; Upton et al., 2000; Ort et al., 2016). In addition, plutonic bodies occur in erosion canyons cutting the Piton des Neiges (PdN), the old inactive volcano that forms the north-western part of the island (Upton and Wadsworth, 1972). More recently, drilling in the south-eastern part of the Piton de la Fournaise (PdF), the presently active volcano on the island, has encountered an important layered plutonic complex (Lerebour, 1987). However, and despite the favourable situation of La Réunion island, plutonic have been little studied in comparison with volcanic rocks, and only a few have been subjected to petrologic studies (Babkine et al., 1966; Upton and Wadsworth, 1972; Ludden, 1978a; Augé et al., 1989; Upton et al., 2000).

The La Réunion lavas are isotopically very homogeneous (e.g., Bosch et al., 2008) and, so, the chemical variability between erupted lavas is classically attributed to shallow-level processes occurring in the feeding system rather than to source-related processes (Ludden et al., 1978b; Fisk et al;, 1998; Albarède et al., 1997; Famin et al., 2009; Pietruszka et al., 2009; Welsch et al, 2009; Boudoire et al., in prep; Brugier et al., 2016a). Up to 4 magmatic series have been recognized to erupt on the PdF. The most abundant, the Steady State Basalts (SSB) have MgO = 5-8wt% and CaO/Al2O3 = 0.75-0.85 and are interpreted to result from olivine fractionation at shallow depths (Albarède et al., 1997; Boivin et Bachèlery, 2009; Welsch et al., 2009). Lavas from the Abnormal Group (AbG) have MgO = 8-11 wt% and CaO/Al2O3 = 0.60-0.80, and their origin is still debated. Deep clinopyroxene fractionation has been suggested to account for the characteristic geochemical features of the AbG lava group (Kornprobst et al., 1984; Albarède et al., 1997; Famin et al., 2009; Boudoire et al., in prep; Brugier et al., 2016a). Alternative models involving mixing between differentiated lavas and olivine-rich cumulates have also been proposed (Salaün et al., 2010).

Studies of plutonic rocks offer the opportunity to document igneous crystallization sequences and intensive parameters and to identify fractionation mechanisms such as proposed to explain the different magmatic series on La Réunion island. In this context, a comprehensive suite of ultra-mafic and mafic xenoliths from La Réunion has been investigated. The rocks come mainly from the Plaine des Sables (PdS) area, the site of relatively recent hawaiian to strombolian activity. To complete our set of La Réunion plutonic rocks, additional older xenoliths and one inclusion in a PdN ignimbrite have also been analyzed, as well as one sample from the massive plutonic body from PdN. In this paper, we describe the textural relations and provide a geochemical and mineralogical database for the studied samples. Results enable crystallization sequences to be defined and intensive parameters to be determined.

2 Geological and volcanological context

La Réunion island is situated in the Southwest Indian Ocean (Fig. 1a). The island (50 km by 70 km) is an oceanic volcanic system, composed of 2 juxtaposed volcanoes (Lacroix, 1923; 1939). It is located at the end of the hotspot track associated with the Deccan flood basalts eruption ~ 65 Ma ago (Duncan et al., 1989; Chenet et al., 2007). The two volcanoes which compose the island are the Piton des Neiges to the NW (presently inactive) and the Piton de la Fournaise to the SE (Fig. 1b). A drill core in the “Grand Brûlé” area (“GB” site in Fig. 1b) has revealed an hypovolcanic intrusive system under the eastern flank of the Piton de la Fournaise (Rançon et al, 1989). This plutonic complex has been attributed to a third older volcano, named “Les Alizés” (Malengreau, 1995; Malengreau et al., 1999; Lénat et al., 2001; 2012a; Smietana, 2011; Lénat, 2016), whose existence is still debated (Lebas, 2012; Salvany et al., 2012).

The Piton des Neiges (PdN) activity began 5 Ma ago with eruptions on the ocean floor (Gillot et al., 1994). The oldest subaerial deposits have been dated to 2.2 Ma (McDougall, 1971) and the youngest to 29 ka (McDougall, 1971; Quidelleur et al., 2010). The 12 ± 3ka age obtained on pyroclastic deposits from Piton des Neiges (Deniel et al., 1992) is not considered further here as it appears questionable (see Salvany et al. 2012). During the PdN sub-aerial eruptive history (2.2 Ma to 29 ka), evolution from a “basaltic shield” stage (between 2.2 and 0.4 Ma) to a “differentiated alkaline strato-volcano” stage (between 350-400 and 29 ka) has been documented (Smietana, 2011; Lénat, 2016 and references therein). Since its last period of activity, the Piton des Neiges volcano has been deeply eroded, leading to three 10 km-wide canyons named “Cirques”. In these Cilaos, Mafate and Salazie Cirques, gabbroic intrusions occur, such as the layered gabbro of the Salazie Cirque (“SAL” and “PN” in Fig. 1b; Upton and Wadsworth, 1972; Fisk et al., 1988). These intrusions form deep igneous bodies interpreted to represent the plutonic roots of the PdN feeding system (Upton and Wadsworth, 1965, 1972; Famin and Michon, 2010; Chaput et al., 2014a; b).

The Piton de la Fournaise (PdF) is active since 535 ka (Gillot and Nativel, 1989; Kluska, 1997). The first stage of activity (530 to 400 ka) is characterized by the emission of feldspar-rich basalt to mugearite flows, grouped into the “Pintades” or “Plagioclase-Ultraphyric Basalts” lava unit (Bachèlery, 1981; Bachèlery and Mairine, 1990; Mairine and Bachèlery, 1997; Merle et al., 2010; Valer et al., 2015). However, the origin of these differentiated lavas is still debated: they could represent the initial alkaline phase of the Piton de la Fournaise or the last eruptive stage of the Les Alizés volcano (Smietana, 2011; Valer et al., 2015), alternatively. Deposits associated with this stage come from walls of deep erosion canyons cuttings the plains between the PdN and the PdF (see “Pint” in Fig. 1b). The PdF volcanological history comprises several edifice deformation, construction and destruction episodes marked by major caldera collapses (Bachèlery, 1981; Merle et al., 2010; Michon et al., 2016 and references therein). The last collapse event (between 4880±35 BP and 2855±35 BP) is responsible for the main structure of the present-day volcano. It generated the U-shaped collapse caldera named “Enclos Fouqué” which delimits the currently active part of the PdF (Fig. 1b). Explosive phreatomagmatic eruptions, collectively defined as the “Bellecombe Tephra”, are associated with the collapse event that led to the Enclos Fouqué caldera (Bachèlery, 1981; Mohamed-Abchir et al., 1998; Upton et al., 2000; Ort et al., 2016;

Morandi et al., 2016). The Bellecombe Tephra unit, which is composed of few stratified ash deposits (Ort et al., 2016), is rich in lithic clasts of various types, including mafic cumulates and disaggregated olivine (Ol) or clinopyroxene (Cpx) single crystals (Mohamed-Abchir, 1996; Upton et al., 2000). The wehrlitic and gabbroic cumulates from the Bellecombe Tephra could witness the existence of a network of anastomosed sills, dykes and plutons at shallow depths (1.5 to 5 km) inside the volcanic edifice (Lénat et al., 2012a; Boudoire et al., in prep). Westwards from the Enclos Fouqué, the "Plaines des Sables" area (PdS) is delimited on its west by another collapse caldera, named the "Rempart des Sables" (Fig. 1c). The "Rempart des Sables" caldera resulted from the eastwards migration of the PdF volcanic center from its ancient (530-60 ka) location (approximately in the present PdS) to the actual one, around 60-40 ka ago (Bachèlery & Mairine, 1990; Gillot & Nativel, 1989; Merle et al., 2010; Staudacher & Allègre, 1993; Michon et al., 2016). Several cones, spatters and associated lava flows outcrop in the PdS which includes three major polygenic volcanic edifices: the Demi-Piton, the Piton Haüy and the Piton Chisny (Bachèlery, 1981; Morandi et al., 2016; Principe et al., 2016; Brugier et al., 2016a). The latter is associated with the youngest deposits (381+-26 BP) on the PdS (Morandi et al., 2016). Basaltic deposits encountered on the PdS range from violent lava fountaining (lapilli fall-outs) to long lasting effusive events (spatters and pahoehoe lava flows). The presence of numerous dunitic and wehrlitic xenoliths is documented in all these deposits (Upton et al., 1972; Bachèlery, 1981; Upton et al., 2000; Morandi et al., 2016; Principe et al., 2016; Boudoire et al., in prep; Brugier et al., in prep). Gabbroic xenoliths occur more rarely. In addition, some dolerites have been described either as xenoliths (Upton et al., 2000) or as ballistic blocks associated with Piton Chisny (Brugier et al., 2016a). The ultramafic to mafic xenoliths are generally considered as witnesses of the feeding system that is responsible for the activity on the PdS (Bachèlery, 1981; Mohamed-Abchir, 1996; Upton et al, 2000; Welsch et al., 2013) and the dolerites as products of basaltic liquids extensively crystallized inside the feeding system (Upton et al., 2000).

3 Samples

Most samples examined in this study are plutonic xenoliths. These are rocks typically centimetric in size encountered at the surface of the PdS. Our samples come from the Piton Chisny and Piton Haüy deposits; they have been collected on the slopes of Piton Chisny and in the thalweg between Demi-Piton and Piton Haüy (Fig. 1c). The xenoliths are generally coated by basaltic material. Petrographically, they range from dunite and wehrlite (PdS1 to

PdS10 in Fig.1c) to gabbro (PdS11-12-13 in Fig. 1c). Other crystal-rich samples from Piton Chisny such as dolerites (PdS14-18 in Fig. 1c) and basaltic ballistic blocks (PdS20-21 in Fig. 1c) have also been included in our sample set. Since our gabbroic xenoliths have not been previously described, one gabbroic xenolith from the Bellecombe Tephra (PdS19 in Fig. 1c) has been added for comparison. In addition to PdS samples, other representative plutonic rocks from the La Réunion have been included in this study, mainly for comparative purposes. Sample IGN (Fig. 1b) is a gabbroic inclusion in an ignimbrite from the explosive activity of the PdN. Sample SAL comes from the Salazie Cirque massive layered gabbro (Fig. 1b). All samples studied have been collected during 2012-2015 except gabbro PdS11 which comes from P. Bachèlery's collection and ultramafic xenolith samples PdS??? from D. Clague. The additional samples that are used below to complement our whole-rock analytical database are distinguished on Fig. 1b and c.

4 Methods

Major and trace element bulk-rock analyses were carried out at the Centre de Recherches Pétrographiques et Géochimiques (CRPG-SARM) in Nancy (France) by inductively coupled plasma-optical emission spectrometry and -mass spectrometry (ICP-OES & ICP-MS, Carignan et al., 2001). A total of 7 samples (doleritic blocks and basaltic bombs) from Piton Chisny were analyzed (see Table 2). Whole-rock analyses of plutonic xenoliths (dunite, wehrlite, gabbros) were taken from the literature.

Detailed mineralogical characterization of the samples was performed by various methods. Rocks were sawed and polished thin sections prepared for analyses. Modal compositions of 10 samples (1 dunite, 2 wehrlites, 6 gabbros and 1 dolerite) were determined by point-counting with step lengths of 0.4-0.5 mm along lines separated by 0.4-0.5 mm. The total of points varied from 579 to 1591. Textures of 8 representative samples were imaged with the TESCAN Mira 3 XMU scanning electron microscope (SEM) from the joint ISTO-BRGM laboratory in Orléans. Major element compositions of mineral phases, interstitial (or matrix) glasses and glass inclusions, and sulfide inclusions were obtained with a CAMECA SX FIVE electron microprobe at the ISTO-BRGM laboratory (Orléans) and either a CAMECA SX FIVE or a SX-50 at the CAMPARIS laboratory (Paris). Silicate phase analyses were performed under 15 kV acceleration voltage, 6 nA sample current, 10 s counting time on peak and 5 s counting time on background. Mineral phases were analyzed with a focused beam whereas, for interstitial glasses, a defocused beam (10 µm) was used to minimize alkali migration (Di Carlo et al, 2006). Relative analytical errors are 1% (SiO2, MgO, CaO), 1-2% (Al2O3), 2-4% (FeO, Na2O) and 5-10% (TiO2, K2O). Chemical zonation in phenocrysts was documented either from spot (i.e., rim vs core) or transect analyses (rim-core-rim or core-rim with steps of 2-3, 10, 20, 35 or 40 µm). S, Ni, Cu, Co, Fe and Pb in sulfides were analyzed under 20 kV acceleration voltage, 20 nA sample current, 10 s counting time on peak and 5 s counting time on background. X-ray distribution maps of Al, Ti, Cr, Ca, Fe, Mg were obtained for selected clinopyroxene crystals and a specific zone in a dolerite sample. These were carried out with the CAMECA SX FIVE electron microprobe at the ISTO-BRGM laboratory operated under an accelerating voltage of 15 kV, a beam current of 50 nA, a focused beam and a dwell time of 130 ms.

5 Results

Results below include petrographical descriptions, whole-rock analytical data and the presentation of a detailed dataset for mineral phases and glasses in La Réunion plutonic and associated rocks.

5.1 Modal compositions

Point-counting data for the 10 thin sections studied are presented on Table 1. Samples PdS1, PdS9 and PdS10 are ultramafic xenoliths with high Ol (92% to 58.7%) and Sp (4.4 to 2.4%) contents. The Cpx proportion underlines the transition from dunite (PdS1, 0.6% interstitial Cpx) to wehrlites (PdS9, 10, Cpx up to 36.8%). These 3 samples also have very little interstitial glass present (< 0.6%). In comparison, all the 7 other samples contain feldspar and therefore display a gabbroic assemblage. Concerning the nomenclature, four are xenoliths of olivine gabbro (PdS11, 12, 13, 19), SAL a massive olivine gabbro, PdS14 an olivine dolerite and IGN (the only olivine-free sample) a gabbroic inclusion. Cpx proportions are relatively constant (20-33%, Table 1) but Ol and Plag show important variations, from 0 to 51.2% and 14.1 to 63.1% respectively (Table 1). Sp drops to < 1.5% and both the proportion of glass and the vesicularity (counted as voids) increase in the gabbroic samples, the exception being the massive gabbro SAL. The dolerite (PdS14) has the highest vesicularity (12.4%). Two gabbroic xenolith samples (PdS11, 13) contain significant amounts of orthopyroxene (0.9 to 1.2%) as exsolutions in Cpx. Proportions of Fe-Ti oxides (ilmenite and magnetite, distinguished from Sp on textural grounds) reach significant amounts (> 3%). Note the presence of mineral phases rarely encountered in La Réunion igneous rocks, such as phlogopite in SAL.

5.2 Whole-rock analyses

Major and trace element bulk-rock analyses, covering the whole range of rock types mentioned in this work, are presented in Table 2. In addition to the 4 new bulk-rock analyzes from this study (PdS14, 17, 20, 21), data from previous studies have been used to provide a comprehensive picture of the whole compositional range. The dunite sample from the drill core in the Grand Brûlé area has a very high MgO (43 wt%) and, generally, MgO and Ni concentrations are good proxies for the olivine modal proportion (see GB for an example of olivine-rich rock and PdS14 for an example of olivine-poor rock, Table 1). The very high CaO/Al2O3 in wehrlites are consistent with Cpx being present, although in variable amounts. For gabbros, the major (Mg, Ca, and Al) and trace (Ce, Cr, Ni, Sr) element variability is controlled by the Ol, Cpx and Plag modal proportions (see Table 1). The new data for dolerites (PdS14, 17) show higher Mg, Co, Cr, Ni, V and lower Al and Sr than previous analyses for La Réunion dolerites (Upton et al., 2000). However, some of the older dolerite analyses (HUB1) are in fact close to plagioclase ultraphyric basalts (RR32, Table 2). The Piton Chisny ballistic blocks have compositions representative of basalts erupted on the PdS (Brugier et al., 2016a) although their elevated Mg, Cr, Ni and low Ca suggest a partially olivine-cumulative character.

5.3 Petrography and Mineralogy

5.3.1 *Textures*

Representative textures of the different rock types encountered are presented through thin sections photomicrographs and SEM back-scattered electron images, respectively (Fig. 2; 3). Dunitic (Fig. 2a) and wehrlitic (Fig. 2b; c) samples show characteristic cumulative textures marked by rounded olivines, low porosity and near absence of interstitial glass (Fig.3 a; b; c), consistent with the modal data (Table 1). Spinels appear as interstitial crystals or as inclusions in either Ol or Cpx (Fig. 3a; b; c). The main textural difference between dunites and wehrlites concerns Cpx. In dunites, this phase is either absent or, when present, typically interstitial (Fig. 3a). In wehrlites, Cpx appears either as small (< 1 mm) rounded crystals forming layers or bands (Fig. 3b) or as individual large (several mm) euhedral crystals (Fig. 3c). This demonstrates that clinopyroxene is second to olivine in the crystallization sequence.

Various textures are noted in the gabbroic samples (Fig. 2; 3). The main differences between samples relate to (1) variations in glass and vesicle proportions, (2) variable proportions and (3) specific textures of the main cumulus phases (Ol, Cpx, Plag) and (4) the presence of remarkable mineral inclusions. The Bellecombe Tephra xenolith PdS19 is the type example of glass- and vesicle-rich gabbros, also showing embayed Cpx and Ol (Fig. 2h). By opposite, the massive gabbro SAL is nearly holocrystalline (Fig. 2f). In this sample, phlogopite was found as anhedral crystals in late-stage microfractures (Fig. 2e). Except the gabbro inclusion IGN which is olivine-free, Ol, Plag and Cpx are present in variable proportions in all the other gabbros, and they mostly display typical cumulative textures characteristic of igneous crystallization. Plagioclase shows a range of habits and sizes as, for example, in PdS11, the gabbroic xenolith sample the richest in Plag, where both large euhedral and small granular crystals are observed (Fig. 2d). In other samples (SAL), plagioclase occurs as inclusions in Cpx (Fig. 2f). The Haüy gabbroic xenolith PdS12 is particularly rich in large (cm-sized) plagioclase crystals. Exsolution textures include oxide (either ilmenite or spinel) mineral exsolutions which are responsible for darkening of the host phase, usually Cpx, as observed in the gabbroic inclusion from the PdN ignimbrite (Fig. 2g) and also, although only partially, in the Haüy gabbroic xenoliths (Fig. 2i; j; k; see also below). Pyroxene (mainly orthopyroxene, more rarely pigeonite) exsolutions also characterize the Chisny and Haüy gabbros (Fig. 3d; e; see also below). Dolerite PdS14 has the highest vesicularity (Fig. 3f) and displays the classical intersertal texture with small numerous Plag (Fig. 2l). Both ilmenite and magnetite crystallize as large skeletal phases in the matrix (Fig. 3f).

5.3.2 *Olivines*

Representative compositions of olivines are presented in Table 3. The wide Fo range (Fo88.2 to Fo27.0) is detailed through Fo histograms for each sample (Fig. 4). The highest Fo (Fo88.2-83) are associated with olivines from dunites, where a bimodal Fo (87, 84) distribution is observed. Fo contents decrease from dunites to wehrlites (84-80), and an unimodal distribution appears (Fig. 4). Fo contents in olivines from gabbros range from 85 to 72. No correlation exists between the Fo content and the modal amount of olivine in gabbros. The widest range of Fo content is recorded in the dolerites, from Fo73.4 to 27. However, most compositions are between 65 and 73.4 and they correspond to cores and mantles of zoned crystals (Fig. 6e; f). Fo contents between 65 and 27 are associated with inner and outer rims, enriched in Fe, as described in the Fe distribution map (Fig. 6e). As a reference, olivines in recent PdF eruption products have Fo mostly between 83 and 84 (Boivin and Bachèlery, 2009) and mostly between 85 and 86 for the Piton Chisny and Piton Haüy eruptive activity (Brugier et al., 2016a).

If now the entire database is considered, different compositional groups, lithologically controlled and with a restricted Fo variability, emerge (i.e., Fo75, Fo82-85, Fo86-88, Fig. 5). Within each compositional group, the trace element (Ca, Mn, Ni) concentrations show large variations. For example, olivines from dunites record a wide range of CaO contents (e.g., from 0 to 0.4 wt%) at nearly fixed Fo (~ Fo87, Fig. 5). These variations in CaO reflect either normal or inverse core-rim zonation (e.g., ol3 in PdS8, ol1 in PdS9, Table 3). Both MnO and NiO show patterns similar to those observed for CaO. Superimposed to these trace element variations within each group, there are progressive variations in trace element concentrations with Fo. These are best revealed by the dolerite sample which has the largest Fo range and shows that both CaO and MnO increase (respectively up to nearly 1 wt% and 1.2 wt%) and NiO decreases (although the resolution is poor) with decreasing Fo (Fig. 5).

In dunites, wehrlites and gabbros, CaO contents in olivine can reach very low values, below 0.1 wt% (Fig. 5a). These CaO concentrations are classically associated with compositions of mantle olivines. Nevertheless, the fact that some low Fo (Fo76) gabbroic olivines have concentrations in this range is clearly inconsistent with a mantle origin and so alternative explanations have to be sought for. We interpret the very low CaO content in olivines analyzed in this study to result from a process of diffusive re-equilibration of Ca in olivine (Bohrson & Clague, 1988) specific to cumulate samples with long residence times in volcanic plumbing systems. In support to this interpretation, we note that the dolerite is the only sample in our dataset to have "normal" (0.4-0.5 wt%) and grouped CaO concentrations in olivine (Fig. 5a). The "within group" variations in MnO and NiO concentrations (Fig. 5b; c) are interpreted in the same way.

5.3.3 *Clinopyroxenes*

Representative analyses of clinopyroxenes are given in Table 4. The interstitial Cpx in dunites have the highest Mg# (90.2) and they define the primitive end-member (Wo49.4-44.8 En49.3-44.6 Fs7.2-5) of the Cpx database (Fig. 7). With evolution from dunite, wehrlite, gabbro to dolerite, Cpx compositions progressively change from diopside to augite (Wo45.2-38.9 En45.6-25.1 Fs31.2-10.8; Fig. 7). Interstitial Cpx in dunites have the lowest Al2O3 (1.1-2.7 wt%, Fig. 8a) and the highest Cr2O3 (0.6-1.4 wt%, Fig. 8b) contents. With decreasing

Mg# from dunite, wehrlite, gabbro to dolerite, Cr2O3 progressively decreases in Cpx (Fig. 8b). Nevertheless, Al2O3 follows a more complex evolution. Indeed, there is a general tendency for Al2O3 to decrease with decreasing Mg#, especially when the Cpx compositions in dolerite are considered, but at the same time we note that the most primitive Cpx compositions (interstitial crystals in dunite) also have very low Al (Fig. 8a). Thus, our results do not confirm previous suggestions that the most primitive (and considered the deeper) Cpx on the PdF are Al-rich (Fisk et al., 1988; Fretzdorff & Haase, 2002; Boivin & Bachèlery, 2009).

In detail, the Al2O3 variations are dominated by separate trends, lithologically controlled, of increasing Al2O3 at slightly decreasing Mg#. For example, Cpx in wehrlites show a strong Al2O3 enrichment (up to 5.4 wt%) associated with a modest decrease of Mg# (from 90 to ~ 85, Fig. 8a). The gabbroic samples follow broadly similar trends, although at lower Mg#: Cpx in the Chisny gabbroic xenolith (PdS11) have Al2O3 increasing up to ~ 5.5 wt% for Mg# decreasing to ~ 77. A similar slightly negative trend is also apparent in the Cpx database of D. Clague (Fig. 8a). Systematic differences appear between the different gabbros analyzed. Cpx in some samples (PdS13) overlap with Cpx in wehrlites whereas, others (IGN) have specific, low Mg# (74-72) compositions. Heterogeneous Cpx populations are also found (PdS19, Fig. 8a).

These Al2O3 variations mainly reflect compositional zonations at the crystal scale. The EMPA transect and Al distribution map for Cpx5 in wehrlite PdS9 reveals a complex core-rim zonation, with an Al-rich (4.0-4.5 wt% Al2O3) double core and Al-poor mantles and rims (2.5-3 wt% Al2O3, Fig. 9a). A similar zonation appears in the EPMA transect for Cpx1 in Chisny gabbro PdS11 where the core but also the outer rim are Al-rich, indicating a complex history. Sector zoning was found in Cpx from the Bellecombe gabbro PdS19 which is characterized by multiple Cpx populations on Fig. 8a. EPMA transects in sector zoned crystals clearly contrast the dark (Al-rich) and light (Al-poor) sectors (Fig. 9c; d). In those EMPA transects, Al is usually correlated with Ti and anti-correlated with Cr (Fig. 9c) but co-correlation between these 3 elements was also found (Fig. 9d). High Mg# Cr-rich Cpx cores as observed on the element distribution maps for the dolerite (Fig. 6d; f).

Comparing with previous studies, Cpx compositions in our gabbroic samples cover and largely extend the fields for gabbro in PdN (Ludden, 1978a) and for xenoliths in Bellecombe Tephra (Upton et al., 2000). There is quite a good match between our dataset and the field for dunites and wehrlites from D. Clague (Fig. 8a). Our Cpx data in dolerite largely extends the Cpx compositional range toward lower Mg# and Al2O3. Cpx in dolerite and in PUB overlap

(Smietana, 2011). Cpx in dolerite also have higher at. Ti (for a given at. Al) than the other samples (Fig. 8c).

Two compositional trends (one for Mg-rich augite and the other for augite) have been previously defined for Cpx in 1977-1998 PdF eruption products on the basis of at. Al/Ti (Boivin & Bachèlery, 2009). Cpx compositions from this study tend to cover the whole range of Al/Ti ratios (Fig. 8c) and, therefore, the subdivision proposed for the "volcanic" Cpx does not seem to apply to our "plutonic" Cpx.

5.3.4 *Feldspars*

Representative analyses of feldspars in gabbros and dolerites are given in Table 5. Only plagioclases (An25-85) occur in gabbroic samples (Fig. 10). They cover and extend the range of plagioclase compositions in 1977-1998 PdF eruption products (An45-80, Boivin & Bachèlery, 2009). In contrast, the dolerite sample shows a remarkably wide feldspar compositional range, extending from plagioclase to sanidine and limited by feldspar solvi for temperatures in the range 800-1000°C (Fig. 10). Apatite inclusions have been found in feldspars from the dolerite. Sanidine in dolerite has K2O increasing up to 7.8 wt% (Fig. 11a). Note that the only case of K-rich feldspar so far described in La Réunion concerns the core (6.9 wt% K2O) of a sanidine phenocryst in a PdN trachyte (Nativel, 1978). Zonation at the crystal scale account for a significant part of the feldspar compositional range in the dolerite (Fig. 6b; c). Most gabbroic samples plot on the same K2O-enrichment trend as the dolerite with the Bellecombe gabbro PdS19 at the high An end (An85) of the trend (Fig. 11b). However, plagioclases in the IGN gabbroic inclusion follow a second trend marked by little or no K2O enrichment with decreasing An (Fig. 11b). Such a trend, and the low An compositions (An65-25), suggests crystallization conditions for IGN plagioclases different than for the other gabbros.

5.3.5 *Spinels*

Representative analyses of spinels are given in Table 6. No dependence with textural type (i.e., inclusions vs. interstitial spinels) was found. Three groups emerge from the Cr# vs. Mg# compositional variations (Fig. 12a). The first (group I), characterized by relatively high and constant Cr# (55-65) for Mg# ranging from 57 to 38, mainly corresponds to spinels from dunites and wehrlites and more rarely from gabbros. The second (group II) is marked by a slightly negative correlation between Cr# (increasing from 43 to 58) and Mg# (decreasing from 58 to 33). Spinels in this group mainly come from wehrlites and gabbros and a few from dunites. The third group (III), entirely composed of spinels from gabbros, is defined by lower Cr# (31-50) while Mg# varies from 48 to 41 (Fig.12a). Our spinel compositions are in broad agreement with the data for the Chisny and Haüy lavas (Brugier et al., 2016a) and with the few analyses available for xenoliths in Bellecombe Tephra (Upton et al., 2000). On the TiO2 vs. Mg# plot (Fig. 12b), group I is marked by relatively homogeneous and low TiO2 contents (1.8-3.8 wt%) uncorrelated with Mg#. Group II shows a positive correlation between TiO2 (increasing from 2.8 to 5.2 wt%) and Mg# (increasing from 37 to 57). The third group, mostly marked by a significant TiO2 enrichment (from 4.5 to 12 wt%) with little variations in Mg#, suggest spinel crystallization in progressively more evolved melts.

5.3.6 *Ilmenites, magnetites*

Representative analyzes of ilmenites and magnetites are given in Table 7 and 8 respectively. For ilmenite, two compositional groups can be distinguished depending on textural type. The first group corresponds to ilmenite crystallized in the matrix of the dolerite sample PdS14 and present as the sole Fe-Ti oxide (either interstitial or as inclusions) in the massive gabbro SAL (Table 7). Those Ilm are relatively poor in Mn, Mg and Cr (Table 7). Ilm in dolerites have the lowest MnO (0.57 wt%) and MgO (0.5 wt%) contents. In the SAL gabbro, Ilm is comparatively slightly enriched in Mn and Cr. The second group corresponds to Ilm exsolutions in gabbros PdS12 and IGN, more fully described texturally below. These exsolved Ilm are characterized by high MgO (6.5-6.6 wt% in PdS12, 0.7-3.21 in IGN; Table 7) and also high Al2O3 and Cr2O3. Compositions from this group are similar to Ilm in Bellecombe xenoliths (Upton et al., 2000).

Magnetites crystallize both as inclusions in Cpx and Plag and as an interstitial phase in gabbros PdS12 and IGN, and in the matrix in dolerite PdS14. There are significant compositional variations in Ti, Al, Mg and Cr concentrations between samples (Table 8). Mt in the PdS12 gabbro have the lowest TiO2 (15.7-16.5 wt%) and the highest Al2O3 (3.9-4.4 wt%), MgO (5.73-6.02 wt%) and Cr2O3 (1.66-3.20 wt%). The dolerite sample PdS14 records the highest TiO2 contents (21.7-28.3 wt%) as well as low Al2O3 (0.5-1.2wt%), Mg and Cr. Magnetite in IGN has intermediate characteristics. In our dataset, only magnetites from the Haüy gabbro PdS12 approach compositions in Bellecombe xenoliths (4.3-6.3 wt% Al2O3, Upton et al., 2000).

In summary, ilmenite and magnetite coexist in 2 gabbros (IGN and PdS12) and in the dolerite PdS14. Textural relations compatible with equilibration between the two Fe-Ti oxides are especially clear for the dolerite PdS14 (both Fe-Ti oxides are found crystallizing in the matrix). Yet, and although the textural relations are less favourable for the gabbros (ilmenite exsolutions vs. magnetite inclusions), conditions of Fe-Ti oxide equilibration have been calculated for these two samples as well as for the dolerite (see below).

5.3.7 *Sulphides*

Small sulphides globules (1-2 μm) trapped in Ol and Cpx crystals have been observed in each rock type (dunites, wehrlites, gabbros and dolerites). Nevertheless, these globules are too small for analysis. Only a few 10-20 μm sized sulphide globules hosted in Cpx crystals from the Chisny gabbro PdS11 have been analyzed (Table 9). These sulphides are iron sulphides, Cu- (up to 8.12 wt%) and Ni- (up to 4.55 wt%) rich, comparable to the sulphides analyzed by Upton et al. (2000) in Bellecombe xenoliths. They differ from the second type of sulphides described by Collins et al. (2012) which is characterized by lower Ni (~1.2 wt%) and Cu contents (~1.5wt%).

5.3.8 *Accessory minerals*

Two types of accessory minerals have been observed in our PdN gabbroic samples: phlogopites crystallized in fractures (Fig. 2e) in SAL and amphibole inclusions in Cpx (Fig. 15b) in IGN. Results of EPMA analyses of these minerals are presented in Table 10. The phlogopites are relatively Ti-rich (3.28-4.48 wt% TiO2) and aluminous, with Phlog contents ranging from 69.1 to 76.2% and Mg# between 75 and 80. The amphibole inclusions are kaersutites (TiO2 = 5.80-6.00 wt%; Mg# = 62-64). Although unfrequent mineral phases in La Réunion igneous rocks, similar phlogopites have been described in one gabbro from the plutonic complex drilled in the Grand Brûlé area (Lerebour, 1987). In addition, kaersutite has been described previously in some PdN gabbros (Nativel, 1978).

5.3.9 *Glasses*

Some samples such as wehrlite PdS10 and or gabbros PdS12, 13, 19 contain interstitial glasses in sufficient amounts for electron microprobe analysis (Table 11). Inclusions/ embayments in Ol and Cpx have been also analyzed in PdS13 and PdS19. Results are plotted on Fig. 13 together with data for interstitial glasses in Bellecombe gabbros (Upton et al., 2000) and for Bellecombe ash (Ort et al., 2016). Interstitial glasses in gabbroic xenoliths from Piton Chisny and Piton Tremblet (Ludden, 1978b) are much more evolved (54.30-58.94 wt% SiO2; 1.81-3.21 wt% MgO; 1.89-4.39 wt% K2O) than our glass compositions and are not plotted on Fig. 13. The analyzed glasses have relatively high MgO (5.2-6.7 wt%) and high CaO/Al2O3 (0.61-0.83; Fig. 13a). The data for our Bellecombe xenolith (PdS19) have the highest MgO contents so far recorded for Bellecombe gabbros (Upton et al., 2000). Analyzed glasses are well grouped on a sample basis and inclusions/embayments have compositions similar to their respective interstitial glasses. With the exception of the wehrlite glass which has a very high CaO/Al2O3 (0.83), the data define a single CaO/Al2O3 vs. MgO trend that includes the literature glass data and is classical for progressive basalt differentiation. In the K2O vs. SiO2 diagram (Fig. 13b), the analyzed glasses separate in 2 groups: one wholly basaltic with SiO2 between 48.5 and 50.5 wt% and the other basaltic to more evolved with SiO2 contents between 51 and 53.7 wt%. K2O enrichment follows the SiO2 evolution (Fig. 13b).

5.3.10*Mineral exsolutions*

Mineral exsolutions have been observed in Cpx from gabbros and are described apart to emphasize their remarkable textural characteristics. They concern exsolutions of orthopyroxene and pigeonite in the Chisny gabbro PdS11 and of orthopyroxene in the Haüy gabbro PdS13. Representative analyses of exsolved pyroxenes are given in Table 12 and their compositions are plotted in Fig. 7. Two types of exsolution textures have been observed, lamellar and granular (Fig. 14; 15a). Both SEM images and element distribution maps clearly demonstrate crystallographic control by the host Cpx of the distribution and orientation of mineral exsolutions (Fig. 14; 15a). The distribution maps also reveal the existence of chemical halos in the host Cpx around the granular exsolutions (Fig. 14a; b).

Pyroxene exsolutions can occur in isolation or be accompanied by exsolution of oxide phases. In the Haüy gabbro PdS13, the Opx exsolutions are associated with exsolutions of spinels (analysis sp2, PdS13, Table 6) also distributed conformably with the crystallographic directions of the host Cpx, both parallel and orthogonal to the Opx exsolutions (Fig. 15a). In this sample, the exsolved Opx coarsens as the Cpx-Ol interface is approached and also inside the Ol crystal (Fig.15a).

Ilmenite also form mineral exsolution phases as found in Cpx from the Haüy gabbro PdS12 (Fig. 2i; j) and from the gabbroic inclusion IGN (Fig. 2g; 15b). Such oxide exsolutions lead to darkening of the host Cpx (Fig. 2g; 15b) and are also crystallographically controlled (Fig. 15b). Note the Ilm-free halos around the amphibole inclusions (Fig. 15b).

6 Discussion

6.1 Crystallization sequence of Piton de la Fournaise magmas

Textural and compositional results obtained on the studied ultramafic and mafic xenoliths provide clear evidence on the crystallization sequence of PdF magmas. This is a critical issue since, on the PdF, crystallization processes at depth are considered to control the composition of erupted magmas and to influence eruptive processes (Albarède et al., 1997; Famin et al., 2009; Pichavant et al., 2016; Di Muro et al., 2014, 2015; Boudoire et al., in prep; Brugier et al., 2016a). From our results, a crystallization sequence consistent for all samples studied (except IGN, see below) can be proposed. It is in the order olivine, clinopyroxene, plagioclase. Spinel crystallizes throughout the sequence, followed by magnetite. Orthopyroxene and pigeonite come in as later phases as is also the case for ilmenite and spinel exsolutions. The last stage of igneous crystallization is marked by the occurrence of sanidine together with apatite and ilmenite. Phlogopite can be involved in very late local crystallization episodes.

Concerning the main mineral phases, this proposed crystallization sequence is supported by textural and chemical evidence, combined. Ol crystallizing as an essential phase in dunites has compositions the most primitive, i.e., with the highest Fo (88). From dunite to dolerite, Fo progressively decreases (Fo88 to Fo27, Fig. 5) as crystallization proceeds and new phases enter the cumulus assemblage. Cpx changes from interstitial in dunite (Fig. 3a) to large euhedral crystals in wehrlites (Fig. 2b, c; Fig. 3b, c), concomittantly with a decrease in Mg# from 90 to ~ 85 (Fig. 7; 8a) and a drop in Cr concentrations (Fig. 8b). The appearance of plagioclase in gabbros goes along with a general decrease of Fo and Mg# in coexisting Ol (Fig. 4; 5) and Cpx (Fig. 7; 8), respectively, when compared to Ol and Cpx in wehrlites. The wide range of plagioclase compositions up to sanidine in dolerites (Fig. 10; 11) reflects crystallization of feldspar from melts becoming progressively more evolved. K-rich residual melts or fluids is also indicated by the crystallization of phlogopite either as a late-magmatic or a secondary phase in the PdN gabbro SAL (Fig. 2e).

Concerning the minor phases, apart from mineral exsolutions, spinel is systematic as an inclusion or an interstitial phase in dunites, wehrlites and gabbros. Spinel compositions progressively changes as crystallization progresses (Fig. 12). Magnetite is comparatively less abundant than spinel, and textural evidence (magnetite inclusions, interstitial crystals) suggests that magnetite comes in later than spinel and is associated with more advanced stages of crystallization of the "cotectic" Ol + Cpx + Plag assemblage. Apart from mineral exsolutions, ilmenite is confined as a late interstitial phase in dolerite, where it marks the final stages of magmatic crystallization together with sanidine and apatite.

Several mineral exsolutions have been identified in Cpx. These are new for La Réunion products and provide additional constraints on the crystallization sequence. Exsolutions include orthopyroxene and pigeonite in the Chisny gabbro (PdS11; Fig. 14), orthopyroxene and spinel exsolutions in one Haüy gabbro (PdS13; Fig. 15a) and ilmenite exsolutions in both one Haüy gabbro (PdS12; Fig. 2i; j) and the IGN inclusion (Fig. 15b). Orthopyroxene has been mentioned only very rarely in PdF products (Kornprobst & Bachèlery, 1984) and this study is the first to document in detail modes of Opx occurrence and compositions. Textural indications (Fig. 14; 15) strongly suggest that Opx does not crystallize from a melt as the other "cotectic" phases but rather is a product of solid state reequilibration of Cpx during cooling and residence in the feeding system. This interpretation is supported by the morphology of Opx exsolutions and their distribution within the Cpx host which demonstrate a strong crystallographic control. Some textures (transition from lamellar to granular, Fig. 14; coarsening of exsolutions, Fig. 15) are qualitatively consistent with the morphology and size of the exsolutions being controlled by chemical diffusion in Cpx and also Ol. A similar origin from solid state processes can be inferred from the textural relations of spinel and ilmenite exsolutions (Fig. 15a). However, the important point is that Opx postdates the crystallization of its Cpx host. Opx exsolutions are not encountered in all gabbros and have not been found in wehrlites. Therefore, the available evidence suggests that they appear later than the beginning of crystallization of plagioclase in the "cotectic" Ol+Cpx+Plag assemblage.

The kaersutite-bearing phase assemblage found in IGN is specific. Note that this sample comes from the PdN and that kaersutite gabbros from the PdN have been previously described (Nativel, 1978). The textural evidence (kaersutite inclusions in Cpx, Fig. 15b) would imply a relatively early rather than a late origin for the amphibole. It is also worth reminding that IGN is the only olivine-free gabbro in our sample set. Plagioclases in IGN have compositions that follow a trend different from all the other samples studied and extend to unusually low K2O at low An contents (Fig. 10; 11). All these arguments indicate colder and hydrous magmatic conditions for the IGN gabbroic inclusion, different from all the other samples (Sisson & Grove, 1993; Pichavant et al., 2002). This is consistent with the provenance of IGN from an ignimbritic eruption.

The IGN sample serves to caution that the crystallization sequence proposed above should not be viewed as necessary unique for all La Réunion magmas. Indeed, different types of fractionation (hence of crystallization) mechanisms have been suggested to account for the diversity of PdF eruptive products (Kornprobst et al., 1919, 1984; Albarède et al., 1997; Famin et al., 2009; Pichavant et al., 2016; Boudoire et al., in prep; Brugier et al., 2016a). For example, Steady-State Basalts (SSB) have been interpreted to result mainly from Ol fractionation whereas Abnormal Group (AbG) products would record a stage of high pressure Cpx fractionation (Kornprobst and Bachèlery, 1984; Albarède et al., 1997; Famin et al., 2009; Boudoire et al., in prep; Brugier et al., 2016a). Concerning this issue, it is worth emphasizing that only one type of crystallization sequence has been identified on our PdS samples, and another one on the PdN sample IGN. Although it is impossible to associate our plutonic rocks with a volcanic series, either SSB or AbG, the crystallization sequence recorded in the PdS plutonic xenoliths is clearly consistent with the one postulated for SSB lavas. Nevertheless, our results do not rule out the fractionation mechanism proposed for the AbG, given the limitations inherent to our sample set (number, provenance, depth).

The sequence proposed here (i.e., Cpx before Plag) has been classically used as evidence for high-pressure crystallization on the PdF (Albarède et al., 1997). This is because, according to the volatile-free experiments of Fisk et al. (1988), pressures > 250-500 MPa would be necessary for Cpx to crystallize as the second phase after Ol (see also Pichavant et al., 2016). However, recent experimental results in presence of volatiles (Brugier et al., 2016c) and results of MELTS calculations (Welsch et al., 2009) both demonstrate that clinopyroxene can persist as the second phase at pressures as low as 50-100 MPa. Therefore, the crystallization sequence proposed in this study carries no particular implication for magma crystallization depths within the PdS. We also stress that constraints on mineral equilibration pressures are limited on our plutonic xenolith samples. Fluid inclusions trapped in olivines and clinopyroxenes from 4 wehrlites samples, 2 from our sample set (PdS8 and PdS10), have yielded pressures (calculated at 1200°C after Bureau et al., 1998a) of 200-450 MPa and 100-350 MPa for inclusions in Ol and Cpx respectively (G. Boudoire, personnal communication). This pressure range overlaps with the pressures estimated for the “sills and dykes” network below the PdS (between 50 and 200 MPa, Lénat et al., 2012a), supposedly the site of origin of the plutonic rocks studied.

6.2 Constraints on intensive parameters (T, fO2)

The occurrence of Opx (+ Pig in PdS11) exsolved in Cpx crystals in 2 of our gabbro xenoliths (PdS11 and PdS13) offers the possibility to calculate temperatures of equilibration between the 2 (or the 3 if Pig is considered) pyroxenes using the software QUILF (Andersen et al., 1993). Results of these calculations are presented in Table 13. For PdS11, equilibration temperatures change only little by considering Pig (Table 13) and a similar range of temperatures is obtained for PdS11 and PdS13 (Fig. 16). Average equilibration temperatures and uncertainties are nearly identical for the two samples: 1031±39°C for PdS11 and 1036±43°C for PdS13. These results define minimum temperatures for the crystallization of a gabbroic assemblage in these 2 samples since, as pointed out above, Opx must come in later than Plag. The above data are consistent with the observation that Plag joins the Ol+Cpx phase assemblage at temperatures below ~ 1100°C in the 50 MPa experiments of Brugier et al. (2016c), and also with the temperatures implied by MELTS calculations at 100 MPa (Welsch et al., 2009). This temperature range (1050-1100°C) is interpreted to reflect crystallization of primitive olivine gabbros in the PdS, i.e., of the group of gabbros having Fo > 80 in Ol, Mg# > 80 in Cpx and Sp as the only oxide phase.

Pyroxene equilibration temperatures can be compared with temperatures deduced from Ilm-Mt pairs. These have been calculated for 3 samples (PdS12, IGN PdS14) and, for consistency, with QUILF (Table 14). The average temperatures calculated for these samples (PdS12: 858 ±52°C; IGN: 790 ±73°C; PdS14: 965 ±2°C) are lower than the pyroxene equilibration temperatures. This is consistent with pyroxene exsolution in gabbros being associated with Sp (Fig. 15a) and the observation that Mt crystallizes later than Sp. Consequently, temperatures calculated for Mt- should be lower than those for Sp-bearing assemblages. However, gabbro PdS12, which lacks pyroxene but has Ilm exsolutions, has very low Ilm-Mt temperatures (858 ±53°C).

Our Ilm-Mt results confirm that the gabbro inclusion IGN belongs to a different magmatic series characterized by relatively low crystallization temperatures (790 ±73°C) compatible with hydrous conditions and a more explosive eruptive style (ignimbrite). The Ilm-Mt temperatures calculated for the dolerite PdS14 (965 ±2°C) are both relatively high and very tightly grouped. Such temperature is remarkably consistent with temperatures defined by feldspar solvi (800~1000°C, see Fig.10). These are interpreted to mark the final stages of crystallization of small mafic magma batches in the PdS, most probably under closed-system conditions compatible with extreme incompatible (e.g., K2O) enrichment. For comparison, 3

Ilm-Mt temperatures are available for the Bellecombe gabbros (Upton et al., 2000). They range between 879 and 1017°C, overlapping with but lower than pyroxene equilibration temperatures, and are similar to results for gabbro PdS12 and dolerite PdS14.

Equilibrium fO2 recorded in these 3 samples range from ΔFMQ (deviation from the FMQ equilibrium calculated at the same P and T) = -1.2 to + 0.7 (Table 14). The data for gabbro PdS12 differ from the other two samples by being by far the most oxidizing (ΔFMQ ~ + 0.7). This, and the abnormally low temperature results above, could indicate possible equilibration problems between Ilm and Mt in this sample. The two other samples record fO2 below FMQ (IGN: ΔFMQ = -0.9 to -0.3; PdS14: ΔFMQ -1.2 to -0.7, Table 14), such reducing conditions being consistent with the occurrence of Ilm in these 2 samples. In contrast, results for the Bellecombe gabbros range from ΔFMQ = 0 to +1.1 (Upton et al., 2000), and so are in a more oxidizing range. Although more work is needed to resolve these discrepancies, the data on the Chisny dolerite have the lowest errors and can be viewed as the most significant (Table 14). It is interesting to note that the fO2 range implied is significantly more reducing (by 1.4 to 0.9 log unit) than proposed for the PdF lavas (ΔFMQ ~ + 0.2, Pichavant et al., 2016) and this probably relates to locally very H2O-poor conditions during final crystallization of the dolerite.

6.3 Implications for plutonic rocks on the La Réunion island

Our results bring new data on plutonic rocks from La Réunion island which have long attracted attention (Upton and Wadsworth, 1972; Ludden, 1978a; Nativel, 1978; Lerebour, 1987; Augé et al., 1989; Mohamed-Abchir et al., 1998; Upton et al., 2000). It is recalled that our sample set includes rocks mainly coming from the recent activity on the PdS (Piton Chisny and Piton Haüy) but also gabbros from the Bellecombe Tephra, from a PdN ignimbrite and from a PdN plutonic body which are representative of additional plutonic "end-members" on the island. Although not strictly a plutonic rock, the Chisny dolerite completes the spectrum of crystal-rich rocks investigated.

Our dataset extends previous results concerning mineral compositions. Ol analyzes in PdS xenoliths include the highest Fo (Fo 88.2, Fig. 4) recorded in ultra-mafic cumulates from the La Réunion island (compare with Fo 87.2 in the dunitic part of the Grand Brûlé intrusive complex, Augé et al., 1989). Zoned olivines in the dolerite sample have the lowest Fo (27; Fig. 4) in La Réunion PdF products, either volcanic or plutonic. Previously, the lowest Fo (48) were associated to Ol microlites in PUB lavas (Smietana, 2011). Cpx compositional end-members also occur in our analytical database. Interstitial Cpx in dunite xenoliths have the highest Mg# and Cr2O3 contents (Fig. 8b) and Cpx in the dolerite sample the lowest Mg# and Al2O3 contents in La Réunion products (Fig. 8a). Interstitial diopside had been previously described in a layer of dunitic cumulate within the Grand Brûlé plutonic body (Augé et al., 1989) but with lower MgO (15.1-15.8 wt%) and Cr2O3 (0.7-1 wt%) than in PdS xenoliths. Plagioclases in our gabbroic samples cover exceptionally wide An and K2O ranges. The whole An range is larger than that for gabbros in the Grand Brûlé drill core (An53.4 to 80.6, K2O < 0.25 wt%, Augé et al., 1989). To cover our whole feldspar dataset, it is necessary to include compositions from PUB lavas (Smietana, 2011, Fig. 11a) and from PdN gabbros (Nativel, 1978). The K-rich feldspars analyzed in the dolerite sample have the lowest An contents and the highest K2O contents (7.8 wt%) in La Réunion products.

Phase assemblages and compositions, combined with textural data, enables grouping of the La Réunion plutonic rocks to be proposed. The ultra-mafic group, best illustrated by PdS dunites and wehrlites, is clearly defined by cumulative textures, ultra-mafic phase assemblages (Ol + Sp ± Cpx) and compositions with primitive attributes (Fo > 85, Mg# > 85). The olivine gabbros can be divided in two groups. One, corresponding to the PdS11 and PdS13 samples, has relatively high Fo contents (78 to 86) and Mg# contents in Cpx (Mg# >80, Fig. 8a), and it includes spinel as the only oxide phase. Opx exsolutions also characterize this group. The second group corresponds to the olivine gabbro xenolith PdS12 and the massive PdN gabbro SAL. Indeed, these two samples share similarities such as lower Fo contents (73-77), occurrence of augite and of plagioclase with similar compositions and presence of Fe-Ti oxides. Textures with Plag inclusions in Cpx are also specific of these 2 samples, in contrast with the first group. Although there are obvious differences between the two samples (porosity, interstitial glass contents and phase assemblage, i.e., presence of phlogopite in late micro-fractures in SAL), these could all be attributed to a volume difference between, on the one hand, a large plutonic body (SAL) and a small cumulate formed inside the sills and dykes network below the PdS.

The 3 other studied samples (PdS14, 19, IGN) are each representative of a specific rock type, either plutonic or crystal-rich. Olivine gabbro PdS19 illustrates the specificities of the Bellecombe gabbroic xenoliths. These include Cpx zonations, Ol and Cpx embayments, and high interstitial glass contents and vesicularities (see also Upton et al., 2000). Such textures, and the complex eruptive history at the origin of the Bellecombe Tephra, lead to separate these clasts from the other and presumably younger PdS gabbros. The gabbroic inclusion sampled in the PdN ignimbritic deposit (IGN) is also highly specific. It has the most evolved

Cpx of our gabbroic samples (Fig. 8a) and plagioclase compositions spread along a specific trend (Fig. 10; 11b). Olivine misses from the phase assemblage and, instead, an hydrous phase, kaersutite occurs as inclusions in Cpx (Fig. 15b). The magmatic evolution is dominated by crystallization under relatively cold and hydrous conditions, consistent with the provenance of the sample from an ignimbritic eruption. Finally, the dolerite sample possesses several distinguishing features such as marked chemical zonations in Ol and Cpx (Fig. 6), wide range of feldspars and unusually K2O-rich compositions (Fig. 11a), presence of Fe-Ti oxides (Ilm in particular) and high vesicularities. These features are consistent with cooling and crystallization of the dolerite parental liquid without any replenishment or re-heating under essentially "closed-system" conditions.

7 Conclusions

The main conclusions of this study are the following:

- A comprehensive suite of plutonic (dunite, wehrlite and gabbro xenoliths, massive gabbro, gabbroic inclusion) and crystal-rich (dolerite) rocks has been investigated with the objective to reconstruct the crystallization sequence of La Réunion magmas.
- The crystallization sequence is in the order: olivine, clinopyroxene, plagioclase. Spinel crystallizes throughout the sequence, followed by Fe-Ti oxides. Later crystallization stages involve sanidine, apatite and ilmenite, locally phlogopite.
- Orthopyroxene ± pigeonite, spinel and ilmenite mineral exsolutions in Cpx crystals occur in gabbros but are absent from wehrlites. Their appearance postdates the beginning of crystallization of plagioclase in the "cotectic" Ol+Cpx+Plag assemblage and predates the transition between spinel and magnetite in gabbros.
- The crystallization sequence above supports the olivine fractionation mechanism proposed to control the composition of Piton de la Fournaise SSB lavas. However, it should not be viewed as necessary applicable to all La Réunion magmas. Alternative crystallization sequences such as the one proposed to explain the origin of AbG magmas can not be excluded from our data.
- Pyroxene equilibration temperatures based on mineral exsolutions yield an average of 1033 ± 41°C, interpreted as the minimum temperature for plagioclase crystallization in the group of primitive olivine gabbros.
- Ilmenite-magnetite equilibration temperatures are in the range 790±73 to 965±2°C depending on sample and correspond to more advanced crystallization stages than

recorded by pyroxenes. Oxygen fugacity straddles the FMQ equilibrium. The reducing conditions (ΔFMQ = -1.2 to -0.7) found for the dolerite are consistent with ilmenite crystallization.

- The textural and mineralogical data enable to group La Réunion plutonic rocks in 3 main categories. These include (1) ultra-mafic cumulates (dunites and wehrlites), (2) primitive olivine gabbros and (3) evolved olivine gabbros.
- On a more local scale, there are significant differences between gabbros from the phreatomagmatic Bellecombe Tephra eruption and the other PdS gabbros which presumably come from a younger feeding system. The Chisny dolerites are products of protracted cooling and crystallization under “closed-system” conditions.
- The gabbroic inclusion in an ignimbrite from the Piton des Neiges, characterized by a specific mineral assemblage and compositions, demonstrates the possibility of hydrous and relatively cold magmatic conditions on the La Réunion island.

8 Acknowledgements

This work was supported by the DEGAZMAG (ANR 2011 Blanc SIMI 5-6 003) projects. Authors thank the OVPF Team for the reception and the technical support during field missions. David Clague and Patrick Bachèlery are acknowledged for their contributions to this paper by gracefully sending samples and analytical datasets. Ida Di Carlo is acknowledged for her contribution to the electron microprobe analyses.

9 References cited

Albarède, F., Luais, B., Fitton, G., Semet, M., Kaminski, E., Upton, B.G.J., Bachèlery, P. & Cheminée, J.L. (1997) The geochemical regimes of Piton de la Fournaise volcano (Réunion) during the last 530000 years. Journal of Petrology 38, 171-201.

Andersen, D.J., Lindsley, D.H. & Davidson, P.M. (1993) QUILF: A Pascal program to assess equilibria among Fe-Mg-Mn-Ti oxides, pyroxenes, olivine, and quartz. Computers & Geosciences 19, 1333-1350.

Augé, T., Lerebour, P. & Rançon, J.-P. (1989) The Grand Brûlé exploration drilling : new data on the deep framework of the Piton de la Fournaise volcano. Part III: mineral chemistry of the cumulate rocks. Journal of the volcanological and geothermal research 36, 139-151.

Babkine, J., Conquère, F. & Vilminot, J.-C. (1966) Nodules de péridotite et cumulats d’olivine. Bulletin de la Société Française de Minéralogie et Cristallographie 89, 262-268.

Bachèlery, P. (1981) Le Piton de la Fournaise (Ile de la Réunion): etude volcanologique, structural et pétrologique. PhD Thesis, Université Blaise Pascal, Clermont Ferrand, 215 pp.

Bachèlery, P. & Mairine, P. (1990) Evolution volcano-structurale du Piton de la Fournaise depuis 0.53 Ma. In : Lénat, J.F. (ed) *Le volcanisme de la Réunion*. Monographie : Centre de recherche en volcanologie, Clermont Ferrand, 213-242.

Bohrson, W.A. & Clague, D.A. (1988) Origin of ultramafic xenoliths containing exsolved pyroxenes from Hualalai Volcano, Hawaii. Contributions to Mineralogy and Petrology 100, 139-155.

Boivin, P. & Bachèlery, P. (2009) Petrology of 1977 to 1998 eruptions of Piton de la Fournaise, La Réunion Island. Journal of Volcanological and Geothermal Research 184, 109-125.

Borley, G.D., Suddaby, P. & Scott, P. (1971) Some xenoliths from the alkaline rocks of Tenerife, Canary islands. Contribution to Mineralogy and Petrology 31, 102-114.

Bosch, D., Blichert-Toft, J., Moynier, F., Nelson, B.K., Telouk, P., Gillot, P.Y. & Albarède, F. (2008) Pb, Hf and Nd isotope compositions of the two Réunion volcanoes (Indian Ocean): a tale of two small-scale mantle blobs. Earth and Planetary Science Letters 265, 748-768.

Boudoire, G., Brugier Y.A., Di Muro, A., Wörner, G., Métrich, N., Arienzo, I., Braukmüller, N., Kronz, A., Le Moigne, Y., Michon, L., Pichavant, M. & Zanon, V. (*in prep*) The deep plumbing system of volcanic islands : new insights from recent activity of the NW Rift Zone (NWRZ) of Piton de la Fournaise (La Réunion Island, Indian Ocean).

Brugier, Y.A., Le Moigne, Y., Pichavant, M., Bourdier, J.L., Boudoire, G. & Di Muro, A. (2016a) Compositional variability of basaltic spatters activity in the Plaine des Sables (Reunion island): Volcanological and petrological constraints.

Brugier, Y.A., Pichavant, M. & Di Muro, A. (2016c) Petrology of Steady State Basalt from Piton de la Fournaise volcano: A Volatiles-present Experimental Study of the shallow feeding system.

Bureau, H., Métrich, N., Pineau, F. & Semet M.P. (1998) Magma-conduit interaction at Piton de la Fournaise volcano (Réunion Island) : a melt and fluid inclusion study. Journal of Volcanological and Geothermal Research 84, 39-60.

Chaput, M., Famin, V. & Michon, L. (2014a) Deformation of basaltic shield volcanoes under cointrusive stress permutations. Journal of Geophysical Research: Solid Earth 119, 274-301.

Chaput, M., Pinel, V., Famin, V., Michon, L. & Froger, J.-L. (2014b) Cointrusive shear displacement by sill intrusion in a detachment: A numerical approach. Geophysical Research Letters 41, 1937-1943.

Chenet, A.L., Quidelleur, X., Fluteau, F., Courtillot, V. & Bajpaic, S. (2007) ^{40}K-^{40}Ar dating of the Main Deccan large igneous province : further evidence of KTB age and short duration. Earth and Planetary Science Letters 263, 1-15.

Clague, D.A. & Bohrson, W.A. (1991) Origin of xenoliths in the trachyte at Puu Waawaa, Hualalai Volcano, Hawaii. Contributions to Mineralogy and Petrology 108, 439-452.

Collins, S.J., Maclennan, J., Pyle, D.M., Barnes, S.J. & Upton, B.G.J. (2012) Two phases of sulphide saturation in Réunion magmas : Evidence from cumulates. Earth and Planetary Sciences Letters (2012), 104-113.

Deniel, C., Kieffer, G. & Lecointre, J. (1992) New ^{230}Th/^{238}U and ^{14}C age determinations from Piton des Neiges Volcano, Réunion – a revised chronology for the differentiated series. Journal of Volcanological and Geothermal Research 51, 253-267.

Di Carlo, I., Pichavant, M., Rotolo, S. G., & Scaillet, B. (2006) Experimental crystallization of a high-K arc basalt: the golden pumice, Stromboli volcano (Italy). Journal of Petrology 47, 1317-1343.

Di Muro, A., Métrich, N., Vergani, D., Rosi, M., Armienti, P.,Fougeroux, T., Deloule, E., Arienzo, I. & Civetta, L. (2014) The Shallow Plumbing System of Piton de la Fournaise Volcano (La Réunion Island, Indian Ocean) revealed by the Major 2007 Caldera-Forming Eruption. Journal of Petrology 55, 1287-1315.

Di Muro, A., Staudacher, T., Ferrazzini, V., Métrich, N., Besson, P., Garofalo, C. & Villemant, B. (2015) Shallow Magma Storage at Piton de la Fournaise Volcano After 2007 Summit Caldera Collapse Tracked in Pele's Hairs. In: Carey, R., Cayol, V., Poland, M. & Weis, D. (eds) *Hawaiian Volcanoes: From Source to Surface*. AGU Chapman Conference (Hawaii, 2012) Book. John Wiley & Sons.

Duncan, R.A., Backman, J. & Peterson, L. (1989) Reunion hotspot activity through tertiary time: initial results from the ocean drilling program, Leg 115. Journal of Volcanological and Geothermal Research 36, 193-198.

Famin, V., Welsch, B., Okumura, S., Bachèlery, P. & Nakashima, S. (2009) Three differentiation stages of a single magma at Piton de la Fournaise (Réunion hotspot). Geochemistry Geophysics Geosystems 10, Q01007.

Famin, V. & Michon, L. (2010) Volcano destabilization by magma injections in a detachment. Geology 38, 219-222.

Fisk, M.R., Upton, B.G.J., Ford, C.E. & White, W.M. (1988) Geochemical and Experimental Study of the Genesis of Magmas of reunion Island, Indian Ocean. Journal of Geophysical Research 93, 4933-4950.

Fodor, R.V. & Vandermeyden, H.J. (1988) Petrology of gabbroic xenolith from Mauna Kea volcano, Hawaii. Journal of Geophysical Research 93, 4435-4452.

Fretzdorff, S. & Haase, K.M. (2002) Geochemistry and petrology of lavas from the submarine flanks of Réunion Island (western Indian Ocean): implications for magma genesis and the mantle source. Mineralogy and Petrology 75, 153-184.

Gillot, P.Y. & Nativel, P.E. (1989) Eruptive history of the Piton de la Fournaise volcano, Réunion Island, Indian Ocean. Journal of Volcanological and Geothermal Research 36, 53-65.

Gillot, P.Y., Lefèvre, J.C. & Nativel, P.E. (1994) Model for the structural evolution of the volcanoes of Réunion Island. Earth and Planetary Science Letters 122, 291-302.

Hildenbrand, A., Gillot, P.-Y. & Marlin, C. (2008) Geomorphological study of long-term erosion on a tropical volcanic ocean island: Tahiti-Nui (French Polynesia). Geomorphology 93, 460-481.

Karatson, D., Thouret, J.-C., Moriya, I. & Lomoschitz, A. (1999) Erosion calderas: origins, processes, structural and climatic control. Bulletin of Volcanology 61, 174-193.

Klügel, A., Hansteen, T.H. & Galipp, K. (2005) Magma storage and underplating beneath Cumbre Vieja volcano, La Palma (Canary Islands). Earth and Planetary Science Letters 236, 211-226.

Kluska, J.M. (1997) Evolution magmatique et morphostructurale du Piton des Neiges au cours des derniers 500 000 ans. PhD Thesis, Université Paris Sud, Orsay, 95 pp.

Kornprobst, J., Boivin, P. & Bachèlery, P. (1979) L'alimentation des eruptions récentes du Piton de la Fournaise (Ile de la reunion, Océan Indien): degree d'évolution et niveau de segregation des laves émises. C.R. Acad. Sc. Paris, t.288, 1691-1694.

Kornprobst, J. & Bachèlery, P. (1984) Les assemblages à orthopyroxène dans les gabbros du Piton de la Fournaise, Ile de la Réunion. Colloque PIRPSEV 1984, Clermont-Ferrand.

Kornprobst, J., Boivin, P., Lénat, J.F., Bachèlery, P., Bonneville, A., Dupont, P., Lecointre, J., Seidel, J.L., Thomas, P. & Vincent, P. (1984) Le Piton de la Fournaise, Ile de la Réunion. Colloque PIRPSEV 1984, Clermont-Ferrand.

Lacroix, A. (1923) Océanites. Minéralogie de Madagascar, vol. III, Paris, 49-50.

Lacroix, A. (1936) Le volcan actif de l'île de la Réunion et ses produits. Paris, Gauthier-Villars.

Laiolo, M. & Cigolini, C. (2006) Mafic and ultramafic xenoliths in San Bartolo lava field : New insights on the ascent and storage of Stromboli magmas. Bulletin of Volcanology 68, 653-670.

Lebas, E. (2012) Processus de démantèlement des édifices volcaniques au cours de leur évolution : application à La Réunion et Montserrat et comparaison avec d'autres édifices. PhD Thesis, Paris Diderot, Paris, 407pp.

Lénat, J.F., Gibert-Malengreau, B. & Galdeano, A. (2001) A new model for the evolution of the volcanic island of Réunion (Indian Ocean). Journal of Geophysical Research-Solid Earth 106, 8645-8663.

Lénat, J.F., Bachèlery, P. & Merle, O. (2012a) Anatomy of Piton de la Fournaise volcano (La Reunion, Indian Ocean). Bulletin of Volcanology 74, 1945-1961.

Lénat, J.F. (2016) Construction of La Réunion. In: Bachèlery, P., Lénat, J.F., Di Muro, A. & Michon, L. (eds) *Active volcanoes of the southwest Indian Ocean: Piton de la Fournaise and Karthala*. Active volcanoes of the world. Springer, Berlin.

Lerebour, P. (1987) Etude du forage du Grand Brûlé (Piton de la Fournaise, Ile de la Réunion) : Lithostratigraphie, Pétrologie, Minéralogies primaire et secondaire. PhD Thesis, Université Paris Sud-Orsay, Paris, 198pp.

Ludden, J.N. (1978a) Magmatic evolution of the basaltic shield volcanoes of Réunion Island. Journal of Volcanology and Geothermal Research 4, 171-198.

Ludden, J.N. (1978b) Fractionation trends defined by residual glasses in the lavas and xenoliths of Piton de la Fournaise, Reunion island. Canadian Mineralogist 16, 265-276.

Mairine, P. & Bachèlery, P. (1997) Un grand épisode érosionnel dans l'histoire ancienne du Piton de la Fournaise. Comptes Rendus Académie Sciences Paris 325, 243-249.

Malengreau, B. (1995) Structure profonde de la Réunion d'après les données magnétiques et gravimétriques. PhD Thesis, Université Blaise Pascal Clermont Ferrand, 366 pp.

Malengreau, B., Lénat, J.F. & Froger, J.L. (1999) Structure of Reunion Island (Indian Ocean) inferred from the interpretations of gravity anomalies. Journal of Volcanological and Geothermal Research 88, 131-146.

McDougall, I. (1971) The geochronology and evolution of young volcanic island of Réunion, Indian Ocean. Geochimica et Cosmochimica Acta 35, 261-288.

Merle, O., Mairine, P., Michon, L., Bachèlery, P. & Smietana, M. (2010) Calderas, landslides and paleo-canyons on Piton de la Fournaise volcano (La Réunion Island, Indian Ocean). Journal of Volcanological and Geothermal Research 189, 131-142.

Michon, L., Lénat, J.F., Bachèlery, P. & Di Muro, A. (2016) Geology and Morphostructural Evolution of Piton de la Fournaise. In: Bachèlery, P., Lénat, J.F., Di Muro, A. & Michon, L. (eds) *Active volcanoes of the southwest Indian Ocean: Piton de la Fournaise and Karthala*. Active volcanoes of the world. Springer, Berlin.

Mohamed-Abchir, A. (1996) Les Cendres de Bellecombe: un évènement majeur dans le passé recent du Piton de la Fournaise, Ile de la Réunion. PhD Thesis, Université Paris VII, 248 pp.

Mohamed-Abchir , A., Semet, M.P., Boudon, G., Ildefonse, P., Bachèlery, P. & Clocchiatti, R. (1998) Huge Hydrothermal Explosive Activity on Piton de la Fournaise, Réunion Island : The Bellecombe Ash Member, 2700BC, The European Laboratory Volcanoes. In: Proceedings of the Second Workshop, Santorini, Greece, 2 to 4 May 1996: Volcanic Risk: Luxembourg: Office for Official publications of the European Communities, European communities, 447-455.

Morandi, A., Di Muro, A., Principe, C., Michon, L., Leroi, G., Norelli, F. & Bachèlery, P. (2016) Pre-historic explosive activity at Piton de la Fournaise volcano. In: Bachèlery, P., Lénat, J.F., Di Muro, A. & Michon, L. (eds) *Active volcanoes of the southwest Indian Ocean: Piton de la Fournaise and Karthala*. Active volcanoes of the world. Springer, Berlin.

Nativel, P. (1978) Volcans de la Réunion, pétrologie, faciès zeolites, sublimes. PhD Thesis, Université Paris Sud, Paris, 510pp.

Ort, M.H., Di Muro, A., Michon, L. & Bachèlery, P. (2016) Explosive eruptions from the interaction of magmatic and hydrothermal systems during flank extension: the Bellecombe Tephra of Piton de la Fournaise (La Réunion Island). Bulletin of Volcanology 78, 1-14.

Pichavant, M., Martel, C., Bourdier, J.-L. & Scaillet, B. (2002) Physical conditions, structure, and dynamics of a zoned magma chamber : Mount Pelée (Martinique, Lesser Antilles Arc). Journal of Geophysical Research 107, ECV1-28.

Pichavant, M., Brugier, Y.A. & Di Muro, A. (2016) Petrological and experimental constraints on the evolution of Piton de la Fournaise Magmas. In: Bachèlery, P., Lénat, J.F., Di Muro, A. & Michon, L. (eds) *Active volcanoes of the southwest Indian Ocean: Piton de la Fournaise and Karthala*. Active volcanoes of the world. Springer, Berlin.

Pietruszka, A.J., Hauri, E.H. & Blichert-Toft, J. (2009) Crustal contamination of mantle-derived magmas within Piton de la Fournaise volcano, Réunion island. Journal of Petrology 50, 661-684.

Principe, C., Morandi, A., Di Muro, A. & Michon, L. (2016) Volcanological Map of the Plaine des Sables, Piton de la Fournaise. In: Bachèlery, P., Lénat, J.F., Di Muro, A. & Michon, L. (eds) *Active volcanoes of the southwest Indian Ocean: Piton de la Fournaise and Karthala*. Active volcanoes of the world. Springer, Berlin.

Quidelleur, X., Holt, J.W., Salvany, T. & Bouquerel, H. (2010) The double structure of the Reunion geomagnetic event based on new K-Ar ages from the type locality, massif de la Montagne, Réunion Island (Indian Ocean) and assessment of the global context. Geophysical Journal International 182, 699-710.

Rançon, J.P., Rocher, P., Augé, T. & Nativel, P. (1989) Pétrologie de deux complexes intrusifs lités de l'île de la Réunion. Implications volcano-structurales. Géologie de la France 2-3, 135-156.

Salaün, A., Villemant, B., Semet, M.P. & Staudacher, T. (2010) Cannibalism of olivine-rich cumulate xenoliths during the 1998 eruption of Piton de la Fournaise (La Reunion hotspot): Implications for the generation of magma diversity. Journal of Volcanological and Geothermal Research 198, 187-204.

Salvany, T., Lahitte, P., Nativel, P. & Gillot, P.Y. (2012) Geomorphic evolution of the Piton des Neiges volcano (Réunion Island, Indian Ocean): Competition between volcanic construction and erosion since 1.4 Ma. Geomorphology 136, 132-147.

Sisson, T.W. & Grove, T.L. (1993) Experimental investigations of the role of H2O in calc-alkaline differentiation and subduction zone magmatism. Contributions to Mineralogy and Petrology 113, 143-166.

Smietana, M. (2011) Pétrologie, géochrnologie (K-Ar) et géochimie élémentaire et isotopique (Sr, Nd, Hf, Pb) des laves anciennes de La Réunion. Implications sur la construction de l'édifice volcanique. PhD Thesis, Université de La Réunion, 362 pp.

Staudacher, T. & Allègre, C. (1993) Ages of the second caldera of Piton de la Fournaise volcano (Réunion) determined by cosmic ray produced ^{3}He and ^{21}Ne. Earth and Planetary Science Letters 119, 395-404.

Upton, B.G.J. & Wadsworth, W.J. (1965) The Basalts of Réunion Island, Indian Ocean. IAV International Symposium on Volcanology (New Zealand), scientific session of November.

Upton, B.G.J. & Wadsworth, W.J. (1972) Peridotitic and Gabbroic Rocks Associated with the Shield-Forming Lavas of Réunion. Contribution to Mineralogy and Petrology 35, 139-158.

Upton, B.G.J., Semet, M. & Joron, J.L. (2000) Cumulate clasts in the Bellecombe Ash Member, Piton de la Fournaise, Réunion Island, and their bearing on cumulative processes in the petrogenesis of the Réunion lavas. Journal of Volcanological and Geothermal Research 104, 297-318.

Valer, M., Schiano, P. & Bachèlery, P. (2015) Insights into the origin of magmas from the adventive cones of Piton de la Fournaise volcano (La Réunion Island). In: Geochimica et Cosmochimica Acta, Goldschmidt conference 2015 abstract 3219.

Welsch, B., Faure, F., Bachèlery, P. & Famin, V. (2009) Microcrysts Record Transient Convection at Piton de la Fournaise Volcano (La Réunion Hotspot). Journal of Petrology 50, 2287-2305.

Welsch, B., Faure, F., Famin, V., Baronnet, A. & Bachèlery, P. (2013) Dendritic Crystallization: A Single Process for all the Textures of Olivine in Basalts? Journal of Petrology 54, 539-574.

Wen, S. & Nekvasil, H. (1994) SOLVCALC: an interactive graphics program package for calculating the ternary feldspar solvus and for two-feldspar geothermometry. Computers & Geosciences 20, 1025-1040.

10 Figure captions

Fig.1. **(a)** Location of La Réunion island in the Indian Ocean. **(b)** Schematic map of La Réunion island. The dark line represents the coastal limit. The grey dashed line separates the two main volcanoes: the Piton des Neiges (presently inactive and largely eroded) and the Piton de la Fournaise (active since 535.000 years, *Gillot & Nativel, 1989*). The yellow area marks the collapse caldera named "Enclos Fouqué", which contains the Piton de la Fournaise volcano and the majority of young deposits (< 40.000 years). The 3 main "rift zones" are represented. The black rectangle defines our main sampling area, the "Plaine des Sables" (PdS). Locations and numbering of samples from previous studies are indicated in grey. Locations and numbering of samples from this study are indicated in green and blue. **(c)** Detailed DEM (Digital Elevation Model, courtesy of OVPF) of the PdS. The PdS is limited (1) by two collapse calderas (black lines): the "Rempart des Sables" at the west and the "Enclos Fouqué" at the east and (2) by two slope-breaks (black dashed lines) at the north and south. The 3 polygenic spatter-ramparts or cones are, from north to south, the Piton Haüy, the Demi-Piton and the Piton Chisny (*Bachèlery, 1987*). The "Aubert de la Rue" edifice corresponds to the last stage of activity of Piton Chisny (*Principe et al, 2015; Brugier et al., 2016a*). Detailed localization and numbering of PdS samples (PdS1 to PdS21) are indicated in green and blue. Note that most samples are associated with Piton Chisny. Samples PdS12 and 13 are associated with Piton Haüy and PdS19 with the Bellecombe Tephra (*Ort et al., 2016*).

Fig.2. Photomicrographs of representative thin sections of the different rock types. **(a)** Cumulative texture of rounded olivine (Ol) in dunite xenolith PdS1 (PAL). Note the interstitial Cr-spinels (Sp). **(b)** Clinopyroxene (Cpx)-rich vein in banded wehrlite PdS10 (PAL). **(c)** Large (cm size) Cpx in wehrlite PdS9 (PAL). **(d)** Gabbroic xenolith from Piton Chisny (PdS11) showing both large and granular plagioclase (Plag) coexisting with Cpx and Ol (PAL). **(e)** Phlogopite (Biot)-bearing vein in the Piton des Neiges massive gabbro SAL (PL). **(f)** Texture of massive gabbro SAL showing zoned Cpx with Plag inclusions (PAL). **(g)** Gabbroic inclusion (IGN) from a Piton des Neiges ignimbrite showing a Cpx- and Plag-bearing, Ol-free, mineral assemblage (PL). Cpx are strongly fractured and darkened by ilmenite exsolutions (see Fig. 15). **(h)** Gabbroic xenolith from the Bellecombe Tephra (PdS19) showing embayed Cpx and Plag and high amounts of interstitial glass and vesicles (PL). **(i)** Gabbroic xenolith from Piton Haüy (PdS12) showing large Ol and Cpx with areas darkened by ilmenite (Ilm) exsolutions (PL). **(j)** Detail of sample PdS12 showing the Plag

inclusions in Cpx and the crystallographically-oriented ilmenite exsolutions (PAL). **(k)** Cpx phenocrysts strongly darkened by Cr-spinel exsolutions in gabbroic xenolith PdS13 (PL). The sample also contains important fractions of interstitial glass and vesicles. **(l)** Numerous Plag and Cpx, and rare Ol, in the dolerite sample PdS14 (PL). PL: polarized light; PAL: polarized and analyzed light.

Fig.3. SEM back-scattered electron images of representative rock textures. **(a)** Cumulative texture in dunite PdS1. Note the interstitial Cpx and the occurrence of Sp, both interstitial and as inclusions in Ol. **(b)** Aligned Cpx in banded wehrlite sample PdS10. **(c)** Large euhedral Cpx in wehrlite PdS9. **(d)** Texture of the Plag-, Cpx- and Ol-bearing gabbroic xenolith from Piton Chisny (PdS11) emphasizing the vesicularity and showing the emplacement of the orthopyroxene and pigeonite (Opx) granular exsolutions. **(e)** Texture of the Piton Haüy gabbroic xenolith PdS13 showing chemically zoned Ol inclusions in Cpx and the location of the Opx exsolutions (both lamellar and granular). Note the occurrence of spinels both as inclusions in Ol and as exsolutions in Cpx (not visible). Silicate glass and vesicles are interstitial. **(f)** Doleritic texture in PdS14 showing numerous Plag and Cpx and few Ol. Numerous Ilm and Mt occur as 100 µm-sized dendritic crystals. The vesicularity is high.

Fig.4. Fo histograms for each type of sample: dunites, wehrlites, gabbros (including gabbroic xenoliths and massive gabbros) and dolerites. Number of analyzes is indicated in italics. Fo contents are the highest (89-84) in dunites and decrease in wehrlites (85-81). In gabbroic samples, a wider range of Fo contents (86-73) is recorded. An unimodal distribution is observed for each sample (e.g. Fo ~ 76 in sample SAL). Note the strong dispersion of Fo contents (74 to 27) in the dolerite sample where Fo 70 – 74 correspond to cores and the Fo < 70 compositions to rims of zoned Ol (see Figure 13).

Fig.5. Trace element concentrations plotted as a function of Fo for olivines from dunites, wehrlites, gabbros and dolerites. **(a)** CaO content (wt%). **(b)** MnO content (wt%). **(c)** NiO content (wt%). Note (1) the existence of different compositional groups, (2) the general decrease of Fo from dunite, wehrlite to gabbro, (3) the large variability of trace element concentrations within the different groups for Fo > 75 (e.g., the group with Fo ~ 87 has CaO ranging from 0.01 to 0.3 wt%) and (4) the important variability in Fo for the dolerite sample, correlated with either increases (CaO, MnO) or a decrease (NiO) of the trace element concentration.

Fig.6. Mineral zonations in dolerite sample PdS14. **(a)** SEM back-scattered image showing the main mineral phases present (Ol, Cpx, Plag). **(b)** Al distribution map. **(c)** Ca distribution map. **(d)** Cr distribution map. **(e)** Fe distribution map. **(f)** Mg distribution map. Notice in (b) and (c) the normal core-rim zonations in plagioclase and the growth bands in Cpx crystals marked in (b), (d) and (e). Both Cpx and Ol show normal Fe-Mg zonation. Note the strong Fe enrichment in Ol rims especially when in contact with a dendritic magnetite crystal (inside the dashed rectangle).

Fig.7. Ternary pyroxene diagram for dunites, wehrlites, gabbros and dolerites. Cpx show a continuous range of compositions from interstitial diopside in dunite, wehrlite and gabbro to augite in gabbro and dolerite. Compositions of pyroxene exsolutions in gabbros (either orthopyroxene, pigeonite or clinopyroxene exsolutions) are also shown. Limits of pyroxene fields and nomenclature after Morimoto et al. (1988).

Fig.8. Clinopyroxene compositions in dunites, wehrlites, gabbros and dolerites. **(a)** Al_2O_3 content (wt%) vs Mg# (= wt% MgO / (MgO + FeO) in Cpx, with FeO = FeO total) showing 3 main compositional groups. The first (Mg# = 85-90) corresponds to dunite, wehrlite and gabbro, the second (Mg# = 80-85) to gabbros and the third (Mg# < 80) to gabbros and dolerite. Al_2O_3 contents generally decrease with decreasing Mg# from group 1 to 3. The slightly positive variations in Al_2O_3 with decreasing Mg# (groups 1 and 2) reflect chemical zonations within individual crystals (see Figure 8). Literature data: Ludden (1978): gabbros; Upton et al. (2000): wehrlites, gabbros; Smietana (2011): Differentiated Lavas (“Pintades”); Clague (unpub.): dunites, wehrlites. **(b)** Cr_2O_3 content (wt%) vs Mg#. Notice the continuous and progressive decrease of the Cr_2O_3 content in Cpx from dunites to dolerites. **(c)** Al vs Ti (atomic concentrations) diagram (after *Boivin and Bachélery, 2009*). The two correlation lines describe the covariation between Al and Ti in the two sub-groups of Cpx (Mg-rich augite and augite) defined in the 1977-1998 eruptions of Piton de la Fournaise (*Boivin and Bachélery, 2009*) and are shown for comparison.

Fig.9. Results of EPMA transects on Cpx. **(a)** Variations of Al_2O_3, TiO_2 and Cr_2O_3 contents (wt%) along a rim-core-rim transect (AB) of a Cpx (Cpx5) in a wehrlite (PdS9). A SEM image of Cpx5 is shown and the location of the transect AB is specified on the Al distribution map. Notice the internal zonation of the crystal with a low-Al rim and a complexly zoned Al-

rich core. On the transect, note the similar behavior of Al2O3 and TiO2 and the antagonistic behavior of Cr2O3. **(b)** Variations of Al_2O_3, TiO_2 and Cr_2O_3 contents (wt%) along a rim-core transect (CD) of a Cpx (Cpx1) in the gabbroic xenolith from Piton Chisny (PdS11). A SEM image of Cpx1 is shown together with the location of the transect CD. The transect describes another complex rim-core zonation with Al-rich core and outer rim. TiO2 is correlated with Al2O3 and uniform Cr2O3 concentrations are observed. **(c)** Variations of Al_2O_3, TiO_2 and Cr_2O_3 contents (wt%) a transect (EF) in a sector-zoned Cpx (Cpx5) from a gabbroic xenolith from Bellecombe Tephra (PdS19). A photomicrograph of Cpx5 is provided (LPA) as well as the location of the transect. The dark sector is characterized by higher Al2O3 and TiO2 contents than the light sector. Cr2O3 concentrations are very low. **(d)** Variations of Al_2O_3, TiO_2 and Cr_2O_3 contents (wt%) along the core-rim transect (GH) of another Cpx (Cpx6) from PdS19. The photomicrograph (LPA) shows the GH transect through the complexly zoned (sector-zoned ?) crystal. The light zones are associated with low-Al and the dark zones with high-Al contents. Al2O3, TiO2 and Cr2O3 contents exhibit the same behavior.

Fig.10. Ternary feldspar diagram for gabbros and dolerites. Feldspars in gabbroic samples are plagioclases, mostly bytownites and labradorites. Andesines and oligoclases are restricted to sample IGN. Feldspars in the doleritic sample PdS14 cover a wide compositional range from plagioclase, anorthoclase to sanidine. Limits of feldspar solvi are calculated for a pressure of 50 MPa at 800, 900, 1000 and 1100°C (*Wen & Nekvasil, 1994*).

Fig.11. K2O (wt%) vs An in feldspars from gabbros and dolerites. **(a)** Plot for all feldspars emphasizing the negative correlation between K2O and An and the extreme enrichments in K2O in feldspars from the dolerite. **(b)** Detailed plot for plagioclases and K2O contents < 1 wt%. An ranges from ~ 85 to ~ 50 if the IGN sample is excluded. The highest An contents (> 80) are for gabbro PdS19 (Bellecombe Tephra). Below An 50, two trends appear, one leading to K2O-poor oligoclases and andesines specific of the IGN sample and the other, specific of the dolerite sample, marked by a strong K2O enrichment. Literature data: Upton et al. (2000): wehrlites, gabbros; Smietana (2011): Differentiated Lavas ("Pintades").

Fig.12. Compositions of Cr-spinels in dunites, wehrlites and gabbros (PdS 11, 13, 19). **(a)** Cr# vs Mg# plot defining 3 different spinel groups. Group I (fixed Cr# ~ 60%; Mg# ranging from 45 to 57) mostly comes from dunites and to a lesser extent from wehrlites and gabbros. Group II is defined by a slightly negative Mg# vs Cr# correlation and is mostly found in werhlites

and gabbros and to a lesser extent in dunites. Group III has Mg# contents of 48-41 and exhibits the lowest Cr# (30-44) of our dataset; it corresponds uniquely to gabbroic spinels. **(b)** TiO2 (wt%) vs Mg# plot emphasizing the low TiO2 in the group I spinels and the overall negative correlation between TiO2 contents and Mg#.

Fig.13. Major element compositions of interstitial glasses and glass embayments/inclusions in a wehrlite and gabbroic samples. Only inclusions hosted in Ol and Cpx are considered and no attempt was made to correct their compositions for post-entrapment crystallization. All data normalized to 100% (Table 12). **(a)** CaO/Al2O3 vs MgO (wt%) plot. Note (1) the relatively elevated MgO concentrations, (2) the progressive decrease of CaO/Al2O3 with decreasing MgO and (3) the overlap between interstitial glasses and glass inclusions/embayments. **(b)** K2O (wt%) vs SiO2 (wt%) plot. Note (1) the wide range of SiO2 concentrations from basalt to basaltic andesite, (2) the general progressive increase of K2O with SiO2 and (3) the similar behavior between glass inclusions/embayments and interstitial glasses in sample PdS13. Literature data: Upton et al. (2000): Bellecombe gabbros; Ort et al. (2016): Bellecombe ash.

Fig.14. Pyroxene exsolution textures in Cpx crystal from the Piton Chisny gabbroic xenolith PdS11. **(a)** zone I. **(b)** zone II. For both zones, large-scale textural relations are shown on the SEM back-scattered image and major elements (Al, Ca, Fe, Mg) distribution maps are provided for the Cpx host crystal. At smaller scale, two exsolution textures are distinguished: granular and lamellar. The lamellar exsolutions are clearly controlled by the crystallographic directions of the host Cpx. Exsolution phases include orthopyroxene and pigeonite compositions (Table 9) but both are collectively designated as Opx on the SEM images since the distinction between the two phases is difficult on the distribution maps. Notice the chemical halos in the host Cpx around the granular exsolutions, either in Ca (zone I, Ca depletion) or in Al (zone II, Al enrichment).

Fig.15. Pyroxene and oxide exsolution textures in Cpx from gabbroic samples. **(a)** Exsolutions of orthopyroxene and spinel in the Piton Haüy gabbro PdS13. SEM pictures of Cpx4 (1) and Cpx5 (2, 3) crystals. Note the remarkable orientation of the exsolution textures of Opx and Sp, which are orthogonal and suggest control of the exsolution process by the crystallographic directions of the host Cpx. Note also the elongated habit of Sp (analysis Sp2, PdS13, Table 6). In 2 and 3, notice the change from lamellar to granular exsolution when the Ol interface is approached and also the overall crystallographic control on the orientation of

exsolution products. In 3, granular Opx exsolutions clearly intrude Ol. **(b)** LP photomicrographs of Cpx1 from the gabbroic inclusion IGN. The Cpx1 is darkened by numerous ilmenite exsolutions (4, Table 7). At a higher magnification (5), the crystallographic control on the orientation of the exsolutions is apparent. In addition, kaersutite inclusions (Table 11) are hosted in Cpx1, some surrounded by an ilmenite-free halo (5).

Fig.16. Histograms of pyroxene equilibration temperatures for the two gabbros PdS11 and PdS13. The calculations use compositions of orthopyroxene (± pigeonite) exsolutions in clinopyroxene and are performed with the QUILF software, see Table 13 for details. Note the similar range of temperatures for the 2 samples (between 950°C and 1175°C). Sample PdS13 shows slightly more dispersed temperatures whereas temperatures for sample PdS11 cluster between 975 and 1000°C.

Figure 1

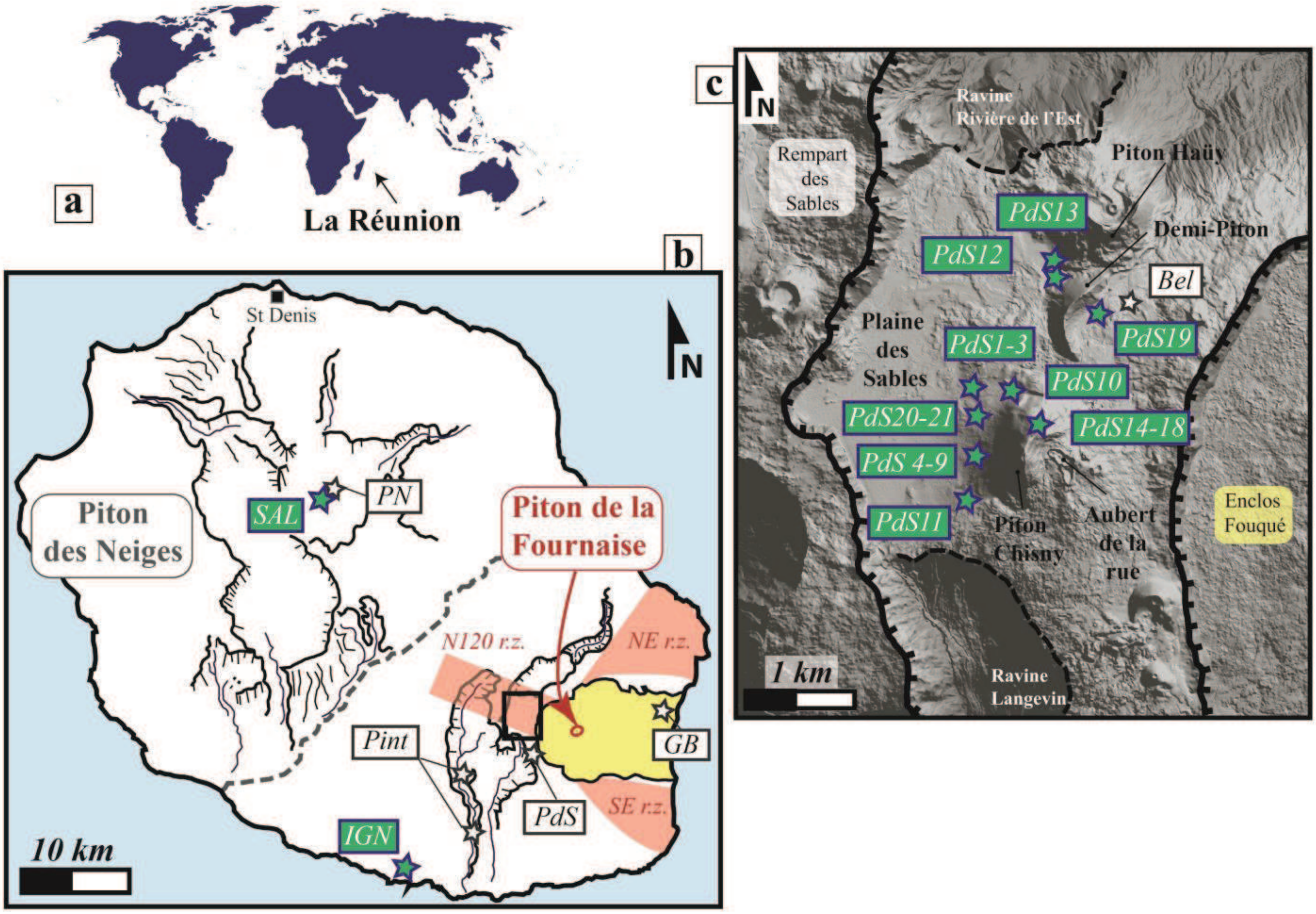
a
La Réunion
b
St Denis
N
Piton des Neiges
SAL
PN
Piton de la Fournaise
N120 r.z.
NE r.z.
SE r.z.
Pint
PdS
GB
IGN
10 km
c
N
Ravine Rivière de l'Est
Rempart des Sables
Piton Haüy
Demi-Piton
PdS13
PdS12
Bel
PdS19
Plaine des Sables
PdS1-3
PdS10
PdS20-21
PdS14-18
PdS 4-9
PdS11
Piton Chisny
Aubert de la rue
Enclos Fouqué
1 km
Ravine Langevin

Figure 2

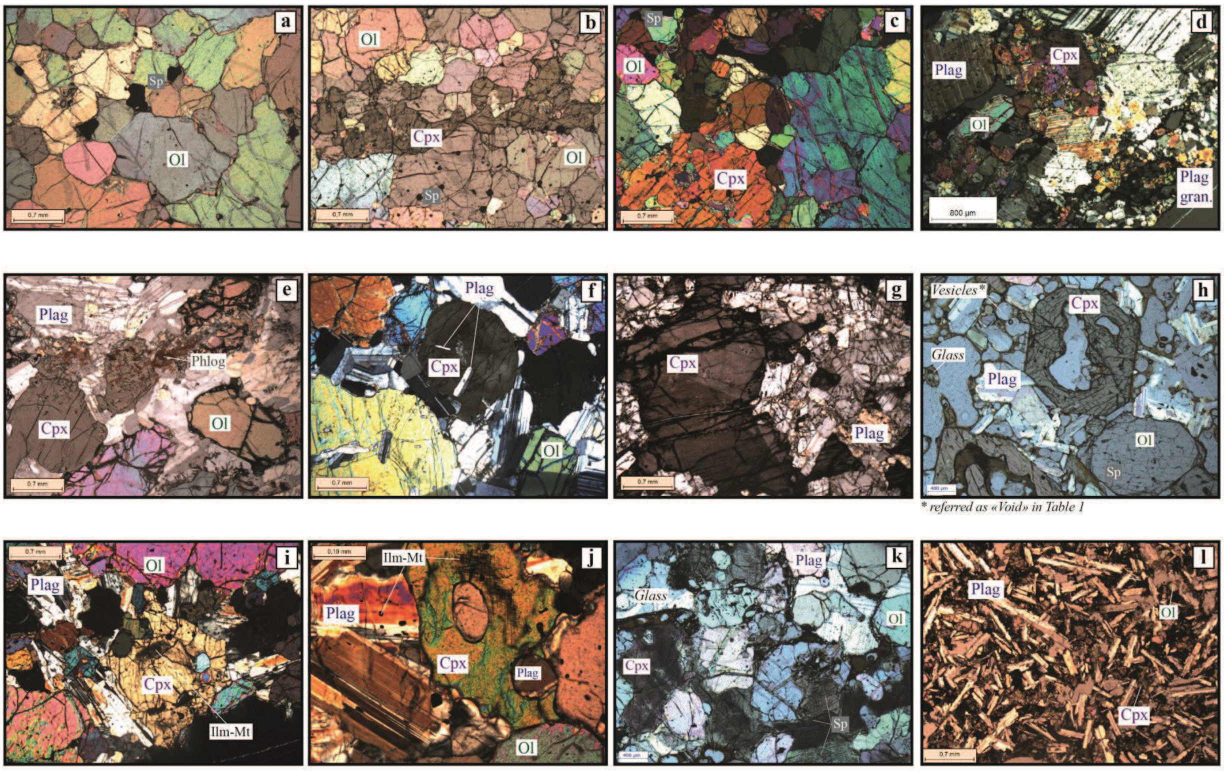

** referred as «Void» in Table 1*

Figure 3

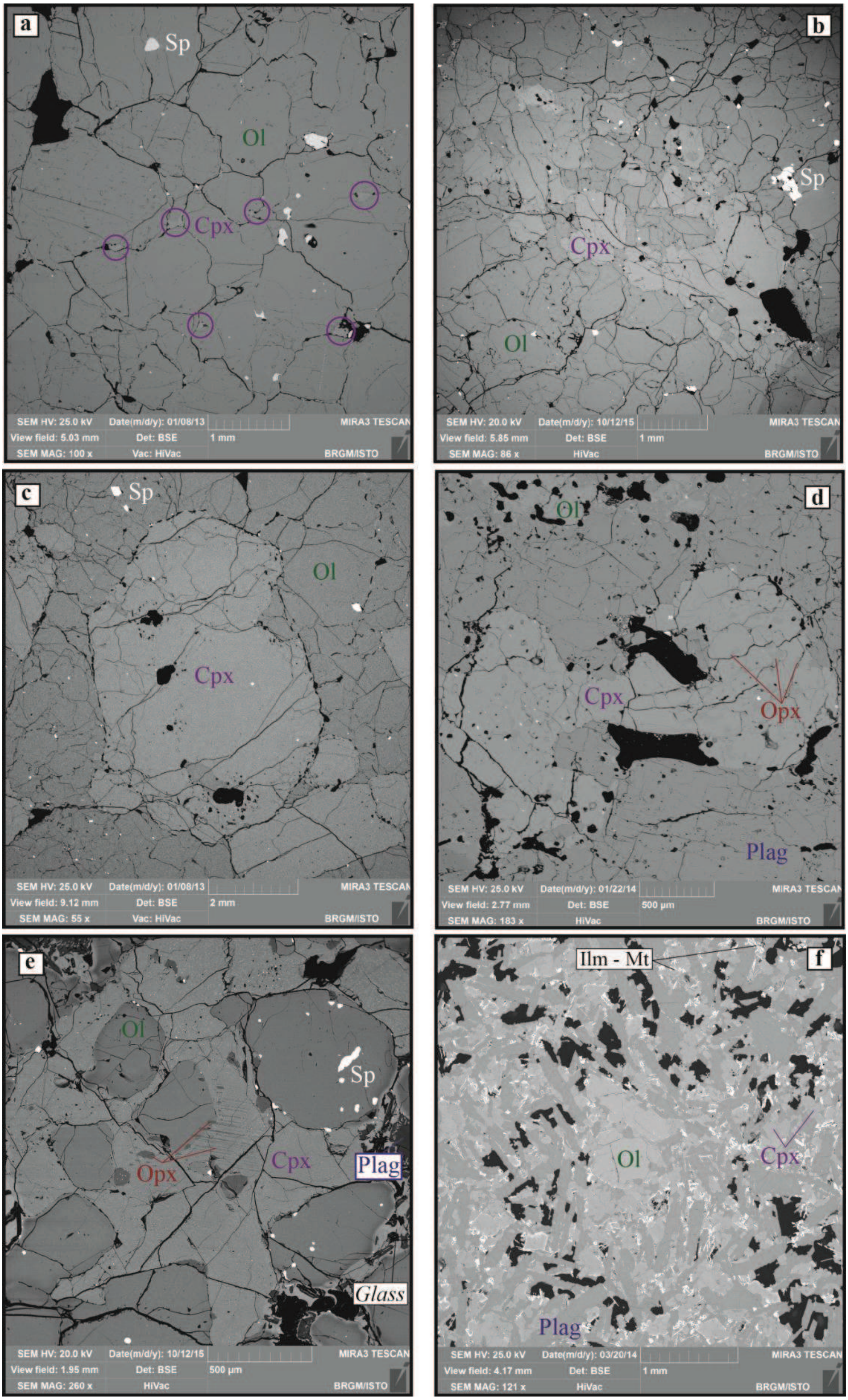
a
Sp
Ol
Cpx
SEM HV: 25.0 kV
Date(m/d/y): 01/08/13
MIRA3 TESCAN
View field: 5.03 mm
Det: BSE
1 mm
SEM MAG: 100 x
Vac: HiVac
BRGM/ISTO
b
Sp
Cpx
Ol
SEM HV: 20.0 kV
Date(m/d/y): 10/12/15
MIRA3 TESCAN
View field: 5.85 mm
Det: BSE
1 mm
SEM MAG: 86 x
HiVac
BRGM/ISTO
c
Sp
Ol
Cpx
SEM HV: 25.0 kV
Date(m/d/y): 01/08/13
MIRA3 TESCAN
View field: 9.12 mm
Det: BSE
2 mm
SEM MAG: 55 x
Vac: HiVac
BRGM/ISTO
d
Ol
Cpx
Opx
Plag
SEM HV: 25.0 kV
Date(m/d/y): 01/22/14
MIRA3 TESCAN
View field: 2.77 mm
Det: BSE
500 µm
SEM MAG: 183 x
HiVac
BRGM/ISTO
e
Ol
Sp
Opx
Cpx
Plag
Glass
SEM HV: 20.0 kV
Date(m/d/y): 10/12/15
MIRA3 TESCAN
View field: 1.95 mm
Det: BSE
500 µm
SEM MAG: 260 x
HiVac
BRGM/ISTO
f
Ilm - Mt
Ol
Cpx
Plag
SEM HV: 25.0 kV
Date(m/d/y): 03/20/14
MIRA3 TESCAN
View field: 4.17 mm
Det: BSE
1 mm
SEM MAG: 121 x
HiVac
BRGM/ISTO

Figure 4

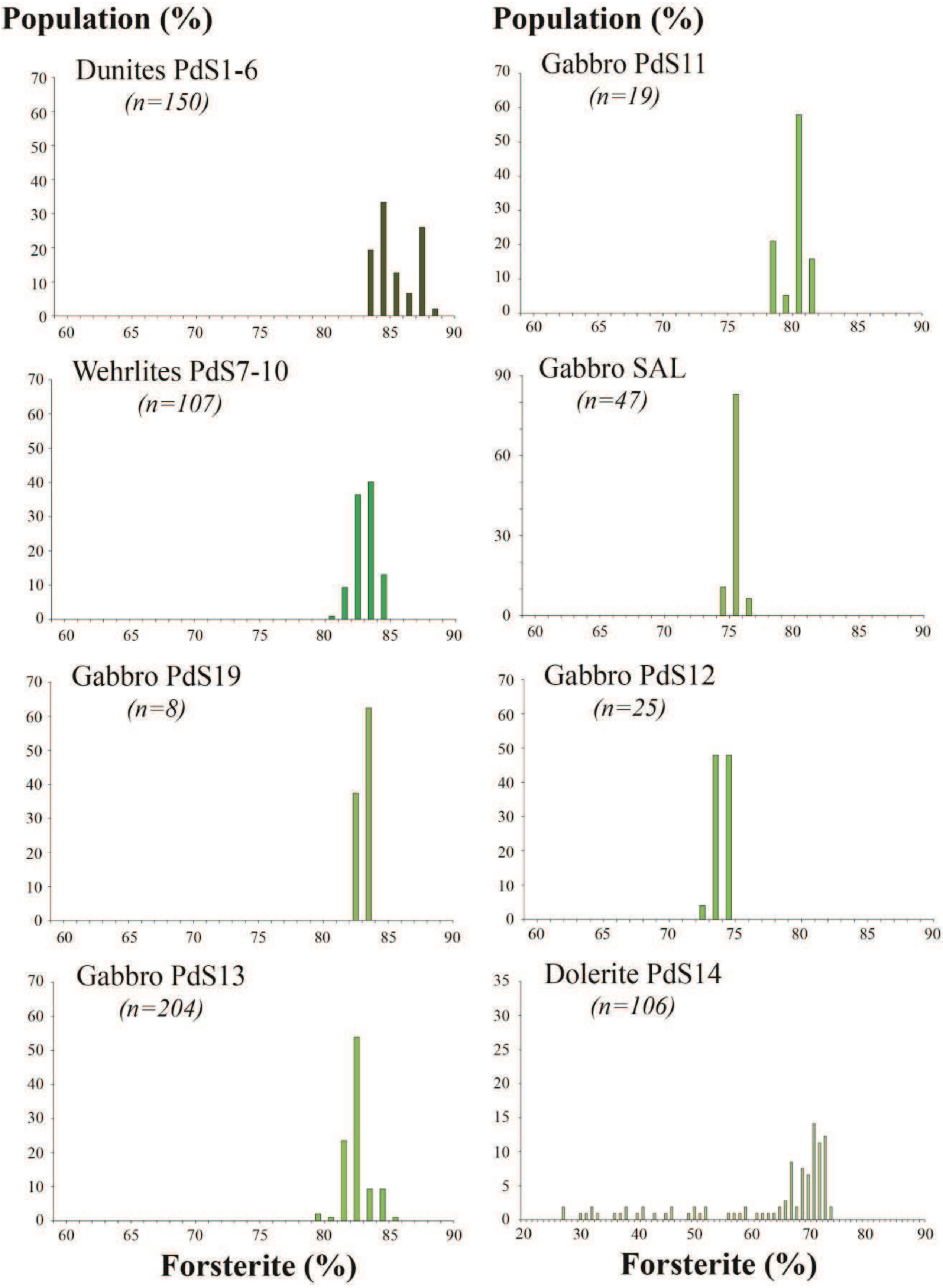
Population (%)
Population (%)
Dunites PdS1-6
(n=150)
Gabbro PdS11
(n=19)
Wehrlites PdS7-10
(n=107)
Gabbro SAL
(n=47)
Gabbro PdS19
(n=8)
Gabbro PdS12
(n=25)
Gabbro PdS13
(n=204)
Dolerite PdS14
(n=106)
0
10
20
30
40
50
60
70
90
5
15
25
35
60
65
70
75
80
85
90
20
30
40
50
Forsterite (%)
Forsterite (%)

Figure 5

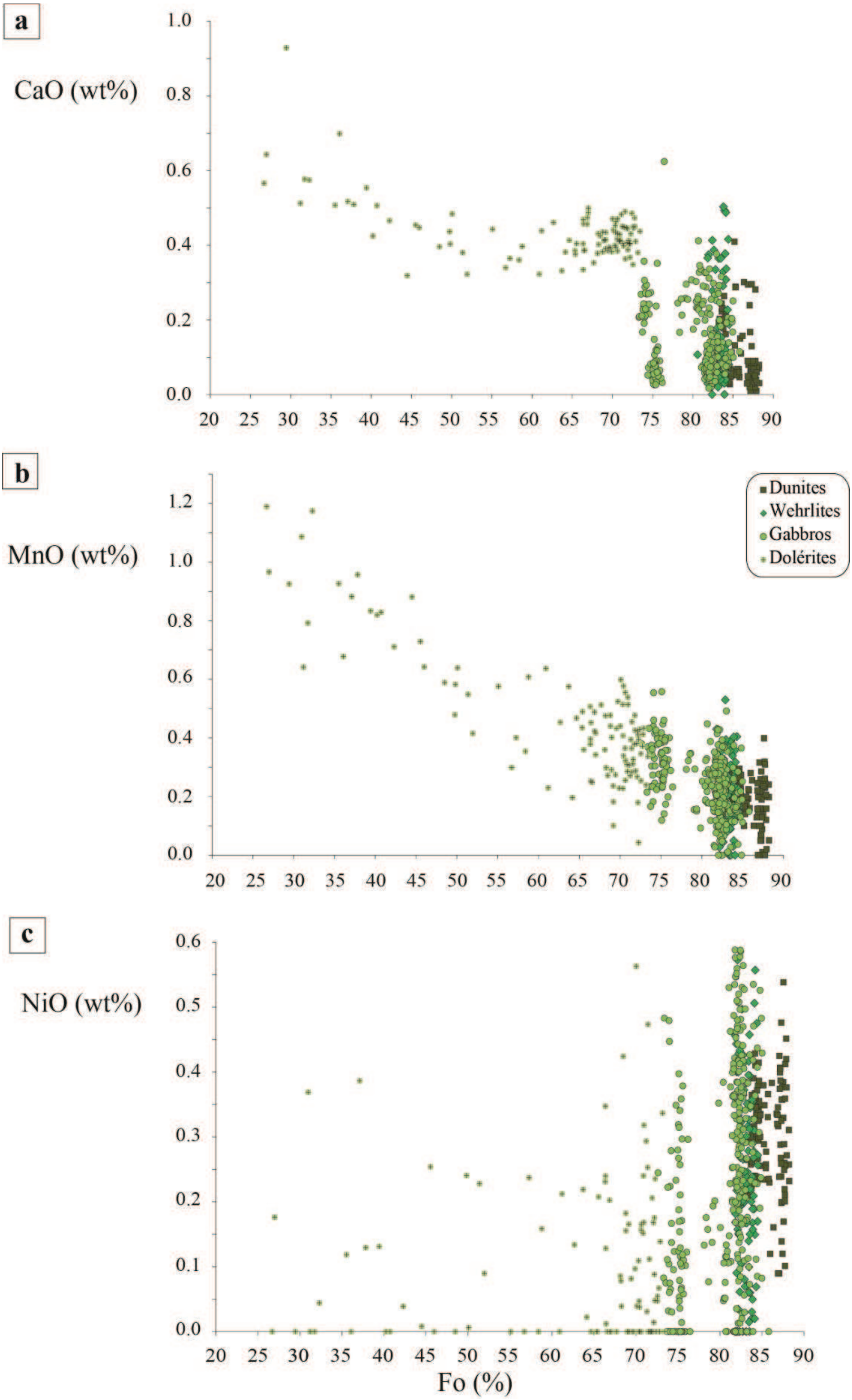
a
CaO (wt%)
1.0
0.8
0.6
0.4
0.2
0.0
20 25 30 35 40 45 50 55 60 65 70 75 80 85 90
b
MnO (wt%)
1.2
1.0
0.8
0.6
0.4
0.2
0.0
20 25 30 35 40 45 50 55 60 65 70 75 80 85 90
Dunites
Wehrlites
Gabbros
Dolérites
c
NiO (wt%)
0.6
0.5
0.4
0.3
0.2
0.1
0.0
20 25 30 35 40 45 50 55 60 65 70 75 80 85 90
Fo (%)

Figure 6

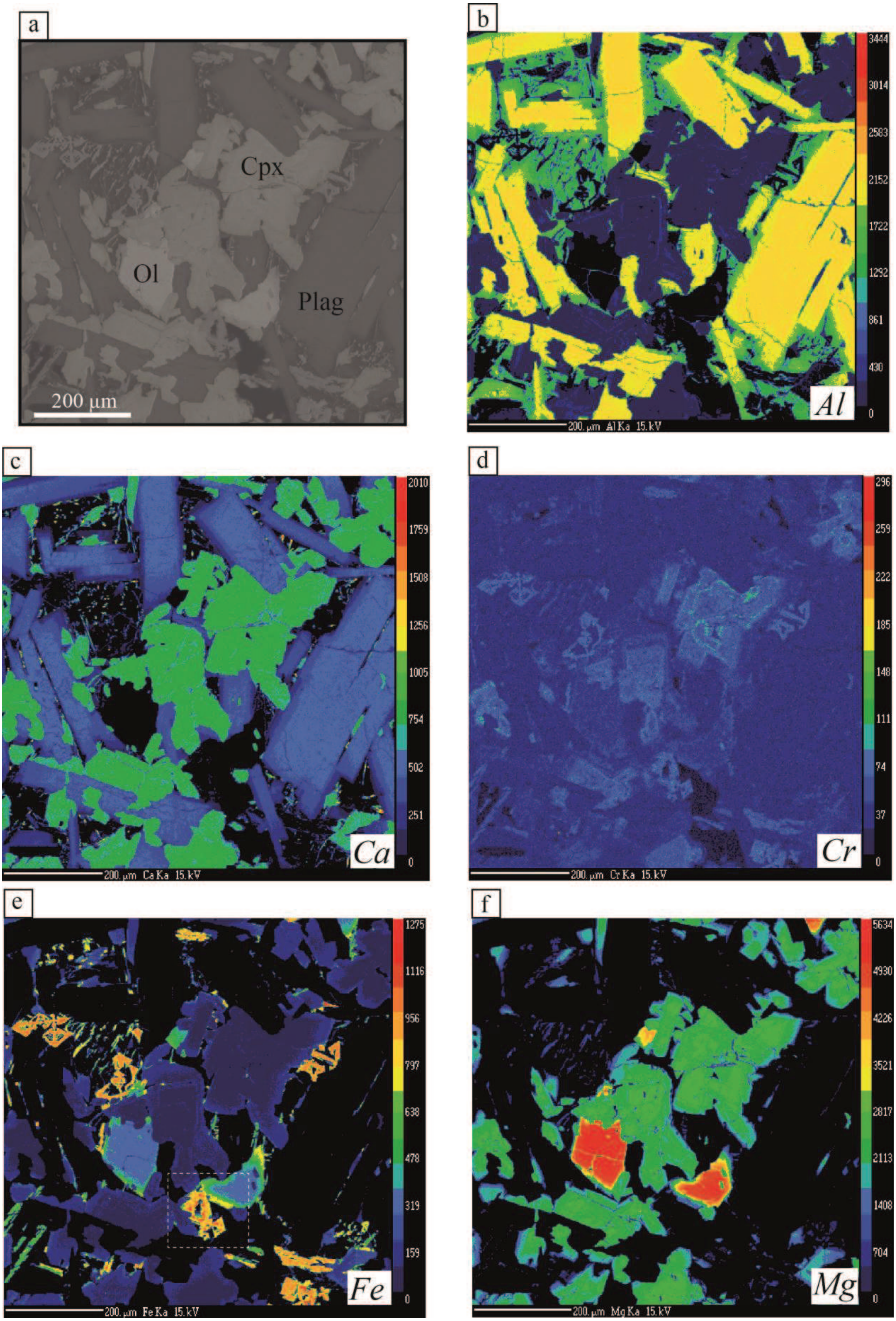
a
Cpx
Ol
Plag
200 μm
b
3444
3014
2583
2152
1722
1292
861
430
0
Al
200 μm Al Ka 15 kV
c
2010
1759
1508
1256
1005
754
502
251
0
Ca
200 μm Ca Ka 15 kV
d
296
259
222
185
148
111
74
37
0
Cr
200 μm Cr Ka 15 kV
e
1275
1116
956
797
638
478
319
159
0
Fe
200 μm Fe Ka 15 kV
f
5634
4930
4226
3521
2817
2113
1408
704
0
Mg
200 μm Mg Ka 15 kV

Figure 7

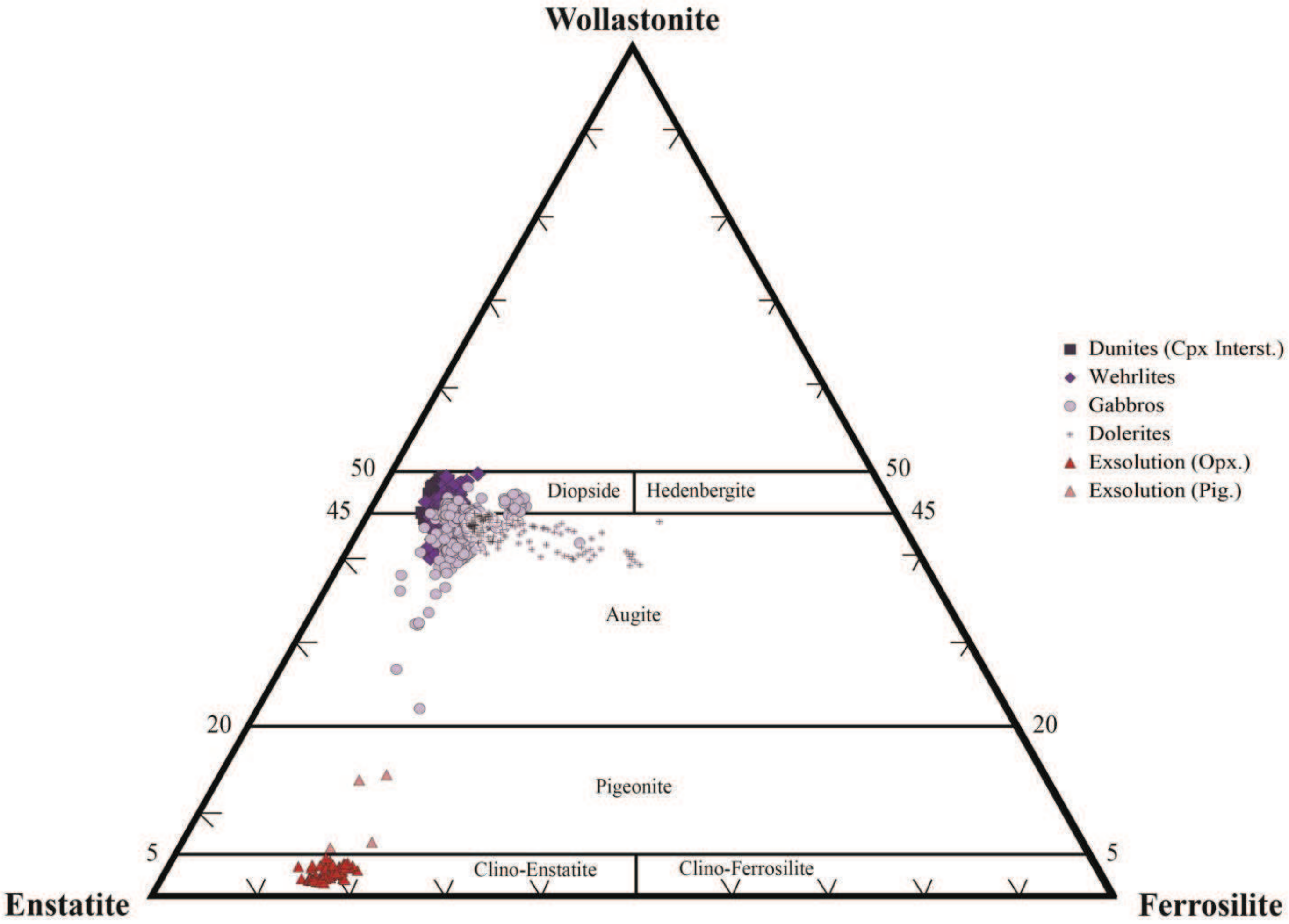
Wollastonite
Enstatite
Ferrosilite
50
50
45
45
20
20
5
5
Diopside
Hedenbergite
Augite
Pigeonite
Clino-Enstatite
Clino-Ferrosilite
■ Dunites (Cpx Interst.)
◆ Wehrlites
● Gabbros
+ Dolerites
▲ Exsolution (Opx.)
▲ Exsolution (Pig.)

Figure 8

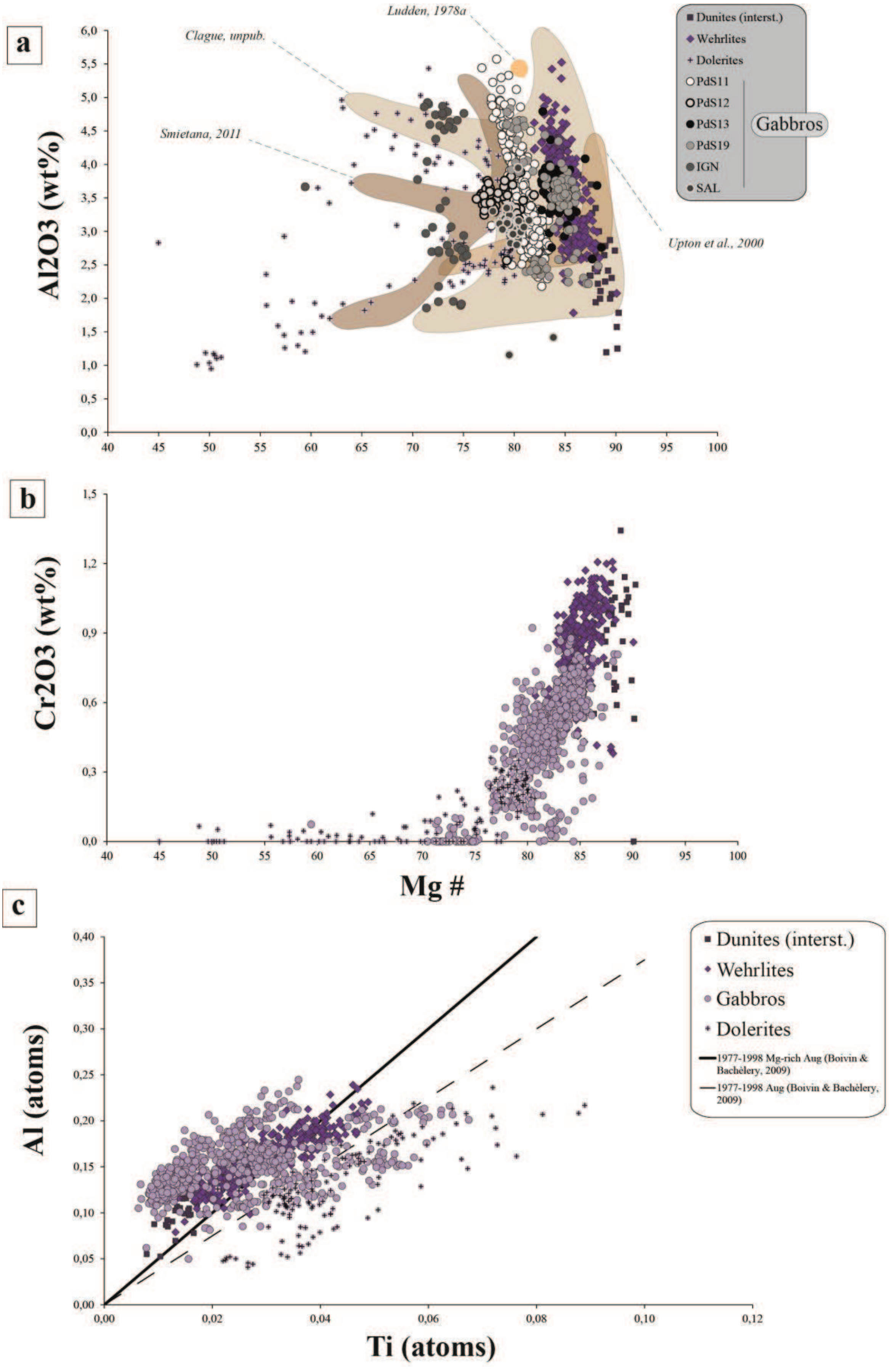
a
Al2O3 (wt%)
6,0
5,5
5,0
4,5
4,0
3,5
3,0
2,5
2,0
1,5
1,0
0,5
0,0
40
45
50
55
60
65
70
75
80
85
90
95
100
Ludden, 1978a
Clague, unpub.
Smietana, 2011
Upton et al., 2000
■ Dunites (interst.)
◆ Wehrlites
+ Dolerites
○ PdS11
○ PdS12
● PdS13
● PdS19
● IGN
● SAL
Gabbros
b
Cr2O3 (wt%)
1,5
1,2
0,9
0,6
0,3
0,0
40
45
50
55
60
65
70
75
80
85
90
95
100
Mg #
c
Al (atoms)
0,40
0,35
0,30
0,25
0,20
0,15
0,10
0,05
0,00
0,00
0,02
0,04
0,06
0,08
0,10
0,12
Ti (atoms)
■ Dunites (interst.)
◆ Wehrlites
● Gabbros
+ Dolerites
1977-1998 Mg-rich Aug (Boivin & Bachèlery, 2009)
1977-1998 Aug (Boivin & Bachèlery, 2009)

Figure 9

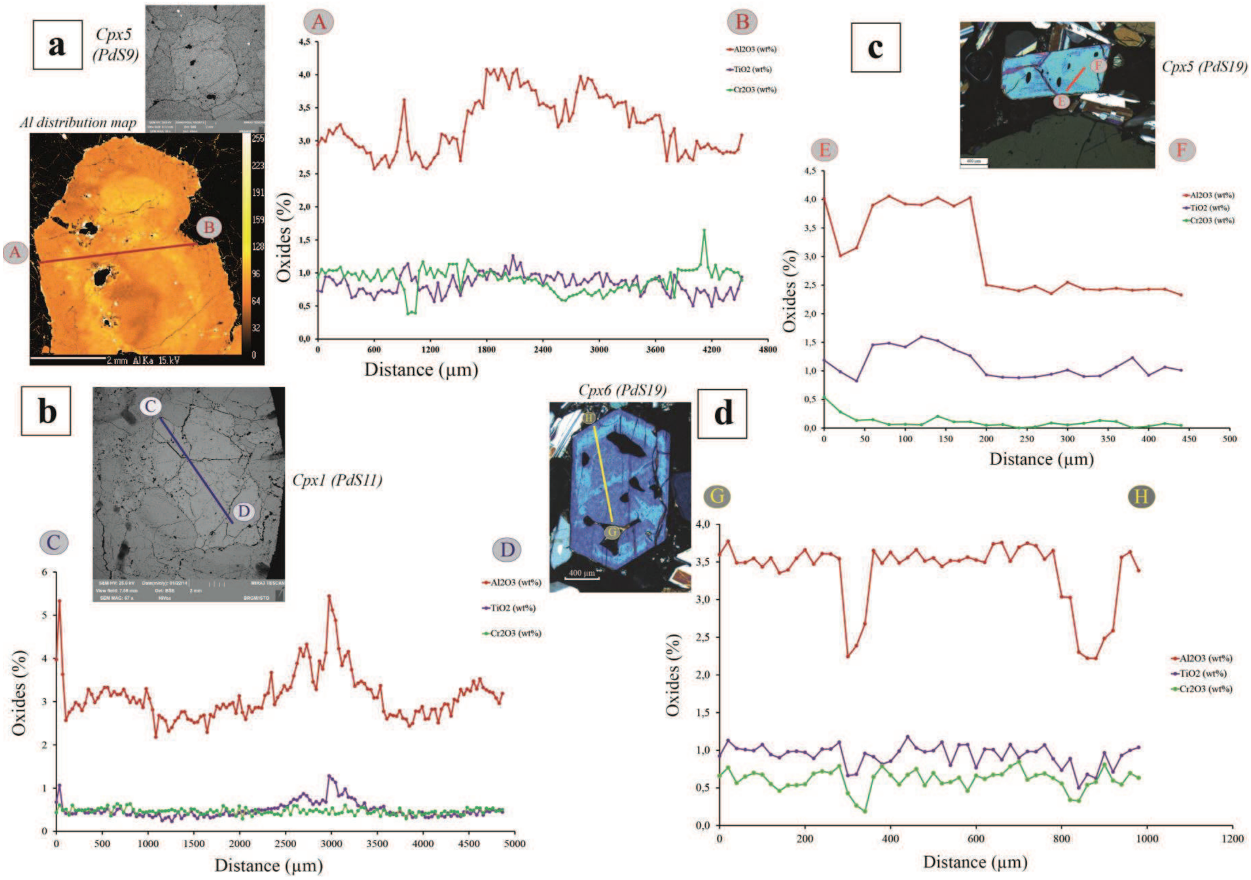
a
Cpx5 (PdS9)
Al distribution map
A
B
2 mm Al Ka 15 kV
255
223
191
159
128
96
64
32
0
Al2O3 (wt%)
TiO2 (wt%)
Cr2O3 (wt%)
Oxides (%)
Distance (µm)
b
Cpx1 (PdS11)
C
D
c
Cpx5 (PdS19)
E
F
d
Cpx6 (PdS19)
G
H
400 µm

Figure 10

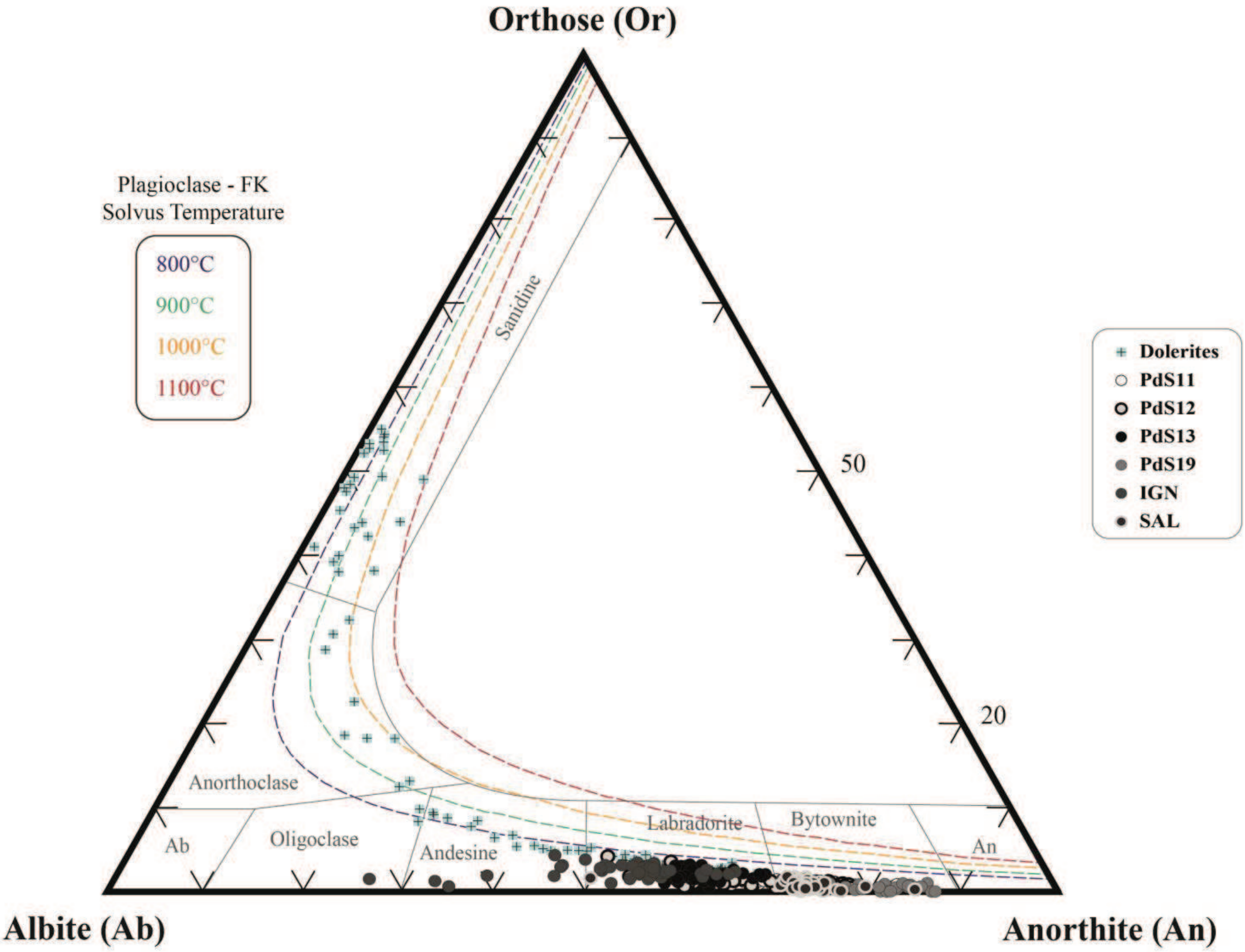
Orthose (Or)
Plagioclase - FK
Solvus Temperature
800°C
900°C
1000°C
1100°C
Sanidine
50
20
Anorthoclase
Ab
Oligoclase
Andesine
Labradorite
Bytownite
An
Dolerites
PdS11
PdS12
PdS13
PdS19
IGN
SAL
Albite (Ab)
Anorthite (An)

Figure 11

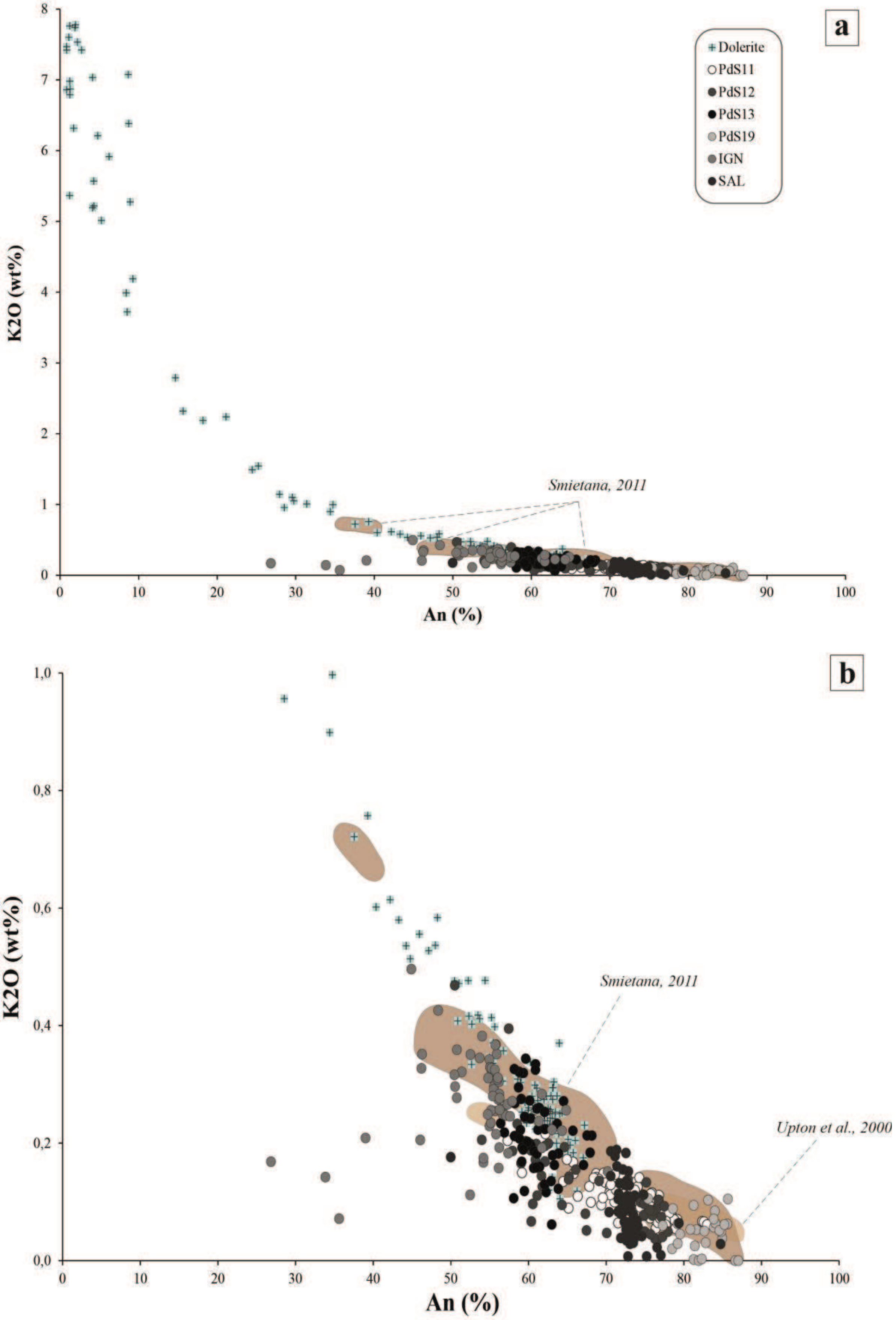
a
K2O (wt%)
An (%)
8
7
6
5
4
3
2
1
0
0
10
20
30
40
50
60
70
80
90
100
Dolerite
PdS11
PdS12
PdS13
PdS19
IGN
SAL
Smietana, 2011
b
K2O (wt%)
An (%)
1,0
0,8
0,6
0,4
0,2
0,0
0
10
20
30
40
50
60
70
80
90
100
Smietana, 2011
Upton et al., 2000

Figure 12

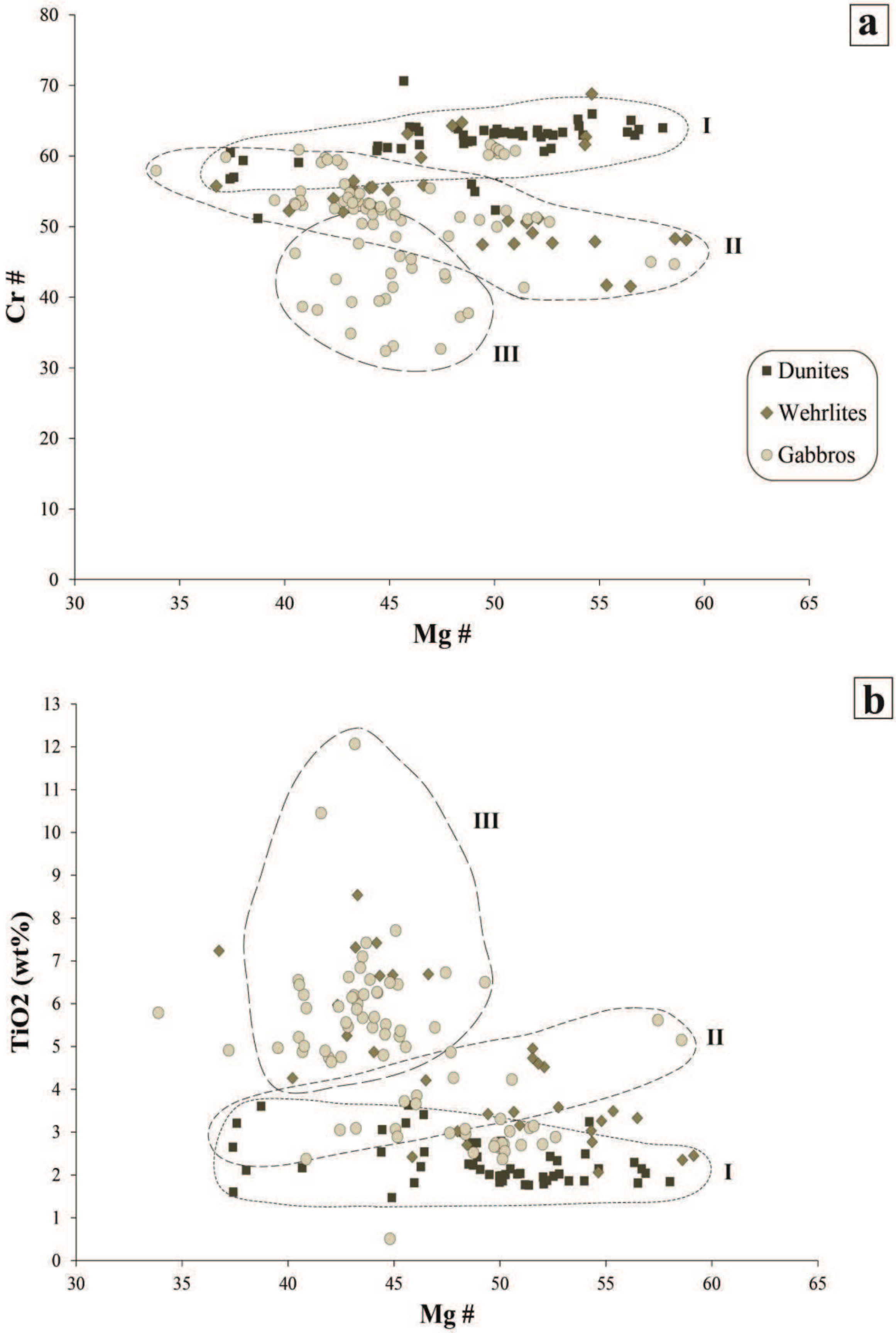
a
Cr #
80
70
60
50
40
30
20
10
0
30
35
40
45
50
55
60
65
Mg #
I
II
III
■ Dunites
◆ Wehrlites
● Gabbros
b
TiO2 (wt%)
13
12
11
10
9
8
7
6
5
4
3
2
1
0
30
35
40
45
50
55
60
65
Mg #
III
II
I

Figure 13

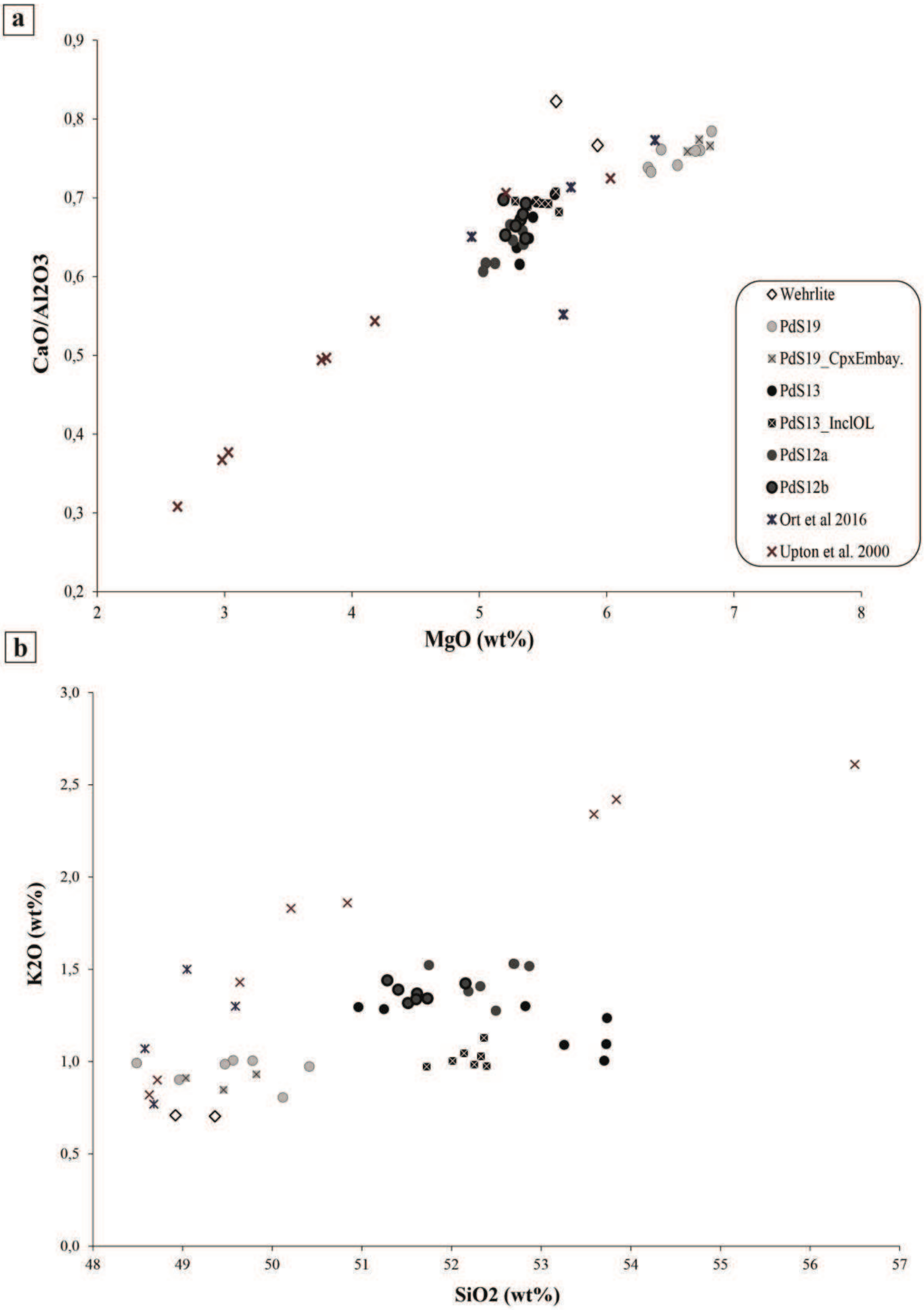
a
0,9
0,8
0,7
0,6
0,5
0,4
0,3
0,2
CaO/Al2O3
2
3
4
5
6
7
8
MgO (wt%)
◇ Wehrlite
● PdS19
× PdS19_CpxEmbay.
● PdS13
⊠ PdS13_InclOL
● PdS12a
● PdS12b
✖ Ort et al 2016
× Upton et al. 2000
b
3,0
2,5
2,0
1,5
1,0
0,5
0,0
K2O (wt%)
48
49
50
51
52
53
54
55
56
57
SiO2 (wt%)

Figure 14

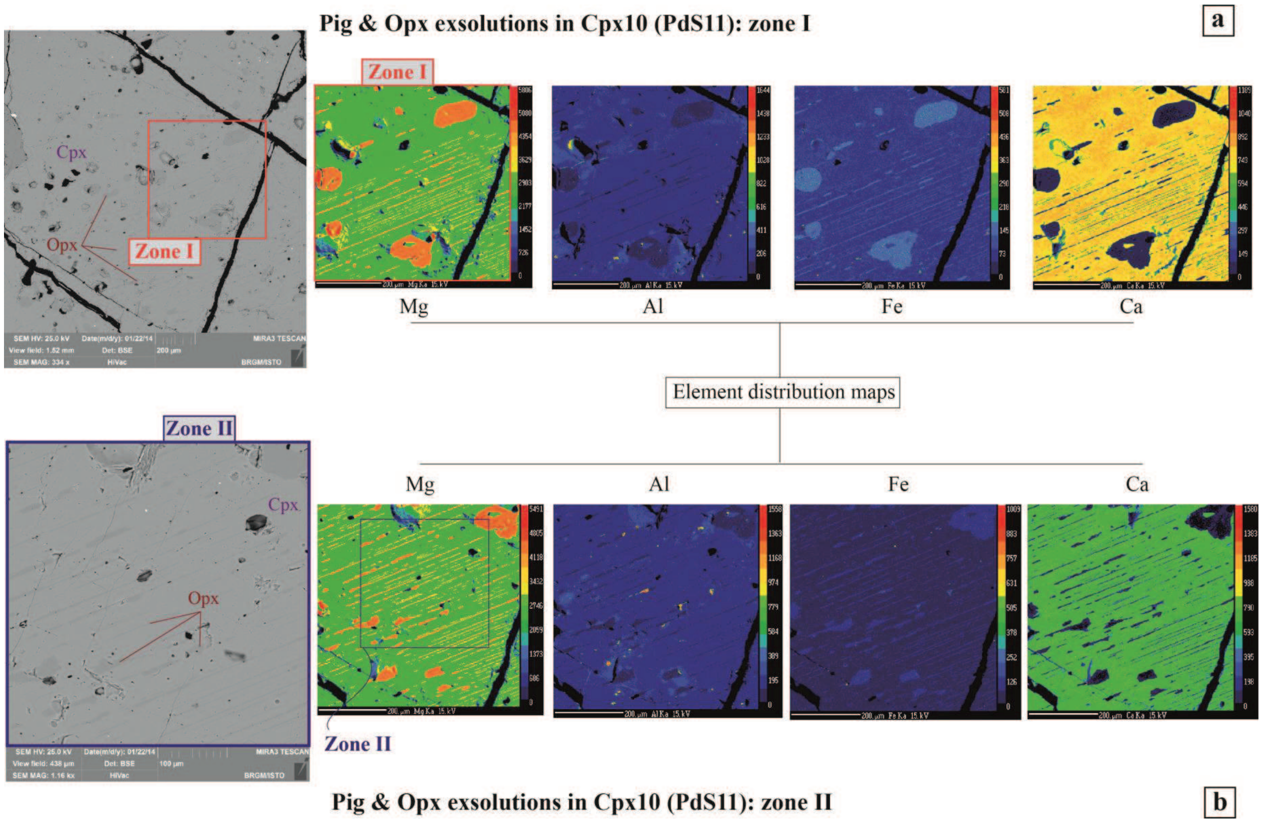

Pig & Opx exsolutions in Cpx10 (PdS11): zone I

Pig & Opx exsolutions in Cpx10 (PdS11): zone II

Figure 15

Opx - Sp exsolutions in Cpx4 and 5 (PdS13)

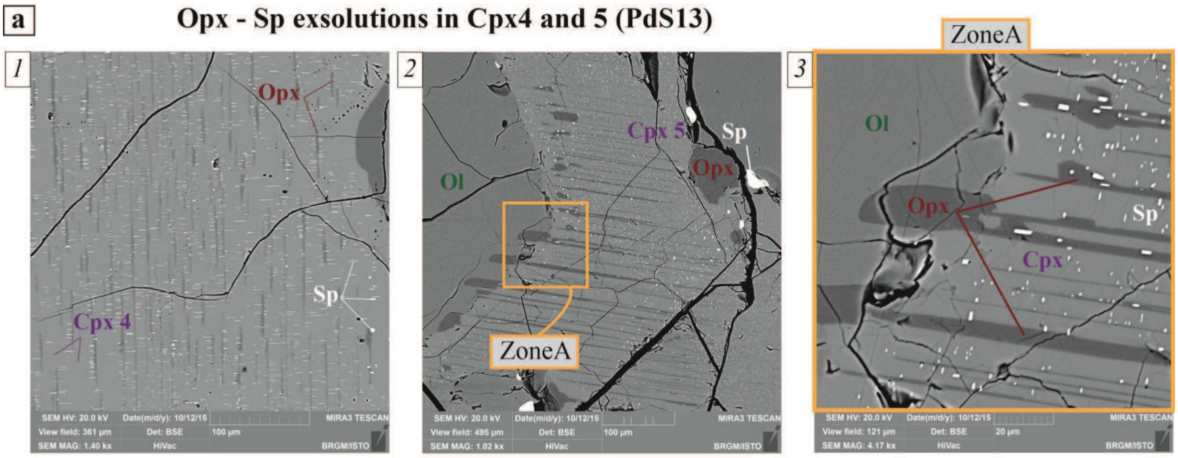

Ilm exsolutions in Cpx1 (IGN)

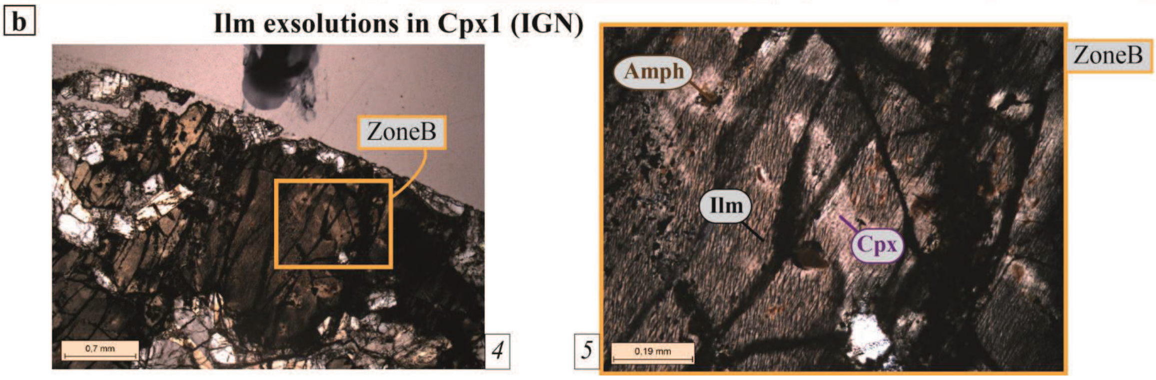

Figure 16

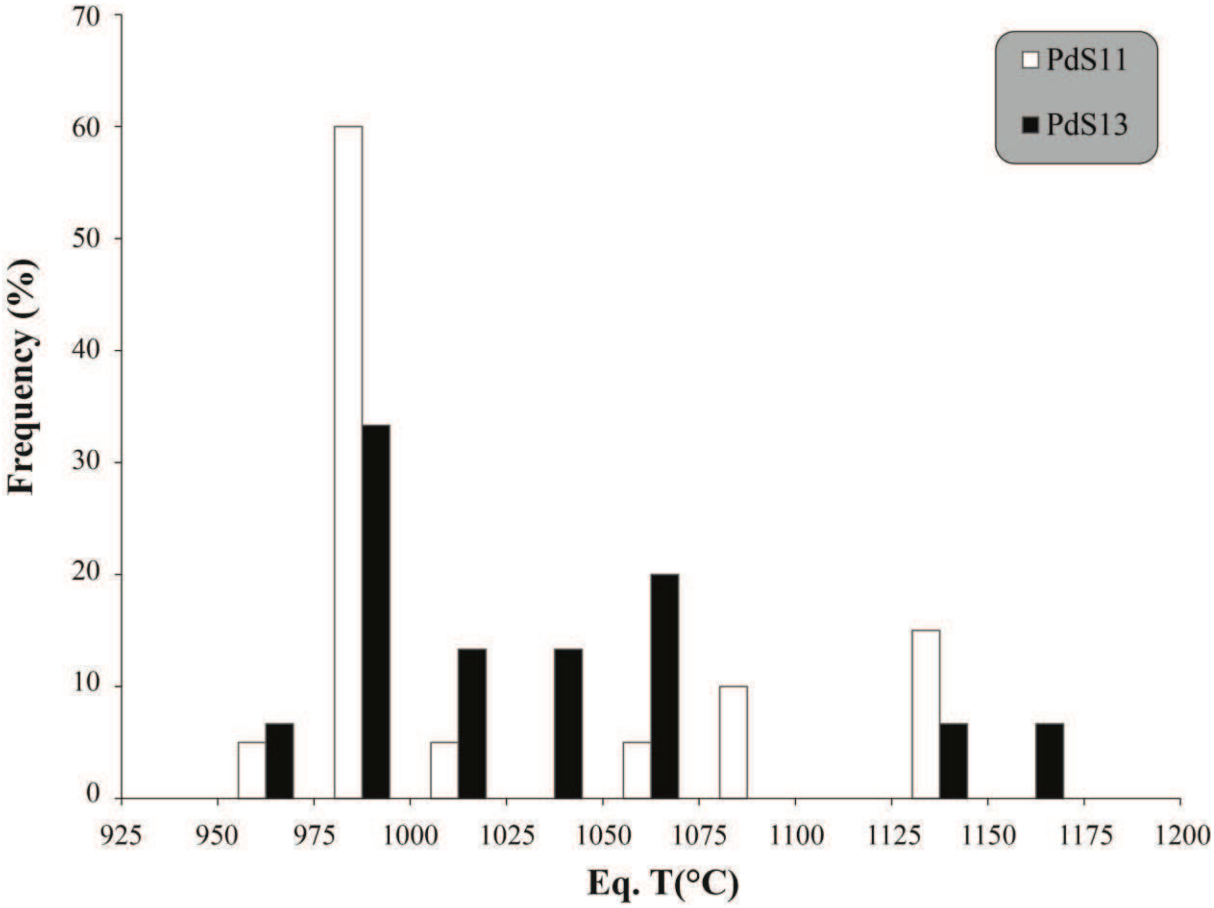
Frequency (%)
0
10
20
30
40
50
60
70
925
950
975
1000
1025
1050
1075
1100
1125
1150
1175
1200
Eq. T(°C)
□ PdS11
■ PdS13

Table 1. Modal compositions

Sample	**PdS1**	**PdS10**	**PdS9**	**PdS11**	**PdS12**	**PdS13**	**PdS19**	**IGN**	**SAL**	**PdS14**
Rock Type	*dunite*	*banded wehrlite*	*wehrlite*	*ol-gabbro*	*ol-gabbro*	*ol-gabbro*	*ol-gabbro*	*gabbro*	*ol-gabbro*	*dolerite*
Phases (%)										
Ol	92	67,9	58,7	5,9	33	51,7	25,2	-	20,2	4,7
Cpx	*0,6* [1]	26,4	36,8	25,4	23,1	20,6	22	33,1	29	29,4
Plag	-	-	-	*63,1* [2]	35	14,1	33,2	52	45,7	48,1
Opx	-	-	-	1,2	-	0,9	-	-	-	-
Sp	4,4	4,2	2,4	0,9	1,1	1,2	0,8	-	0,8	-
Ilm + Mag	-	-	-	-	3,8	2,5	0,2	6,8	0,2	3,9
Glass	0,1	0,3	0,6	0,9	2,1	4,7	8,7	2,6	0,1	1
Void	2,7	1,2	1,5	2,6	2	3	9,2	3,8	0,3	12,4
Other	0,3	-	-	0,2	-	1,3	0,8	1,7	*3,8* [3]	0,5
n	***1011***	***1079***	***1207***	***579***	***1070***	***948***	***1027***	***1082***	***1591***	***1081***

[1] *interstitial cpx*

[2] *includes 9 % granular plag*

[3] *includes 1,1 % phlogopite*

Table 2. Whole-rocks analyses

Provenance[1]	**GB**	**PdS**	**PN**	**PN**	**PdS**	**PdS**	**PdS**	**PdS**	**PdS**	**PdS**	**PdS**	**Pint**	**Pint**	**PdS**	**PdS**
Sample	GB15	94-G1	RE285	RE282	CB5	CB7	CB10	CB2	HUB 1	PdS14	PdS17	RR32	RR40	PdS20	PdS21
Rock type	Dunite	Wehrlite	Gabbro	Gabbro	Gabbro	Gabbro	Gabbro	Gabbro	Dolerite	Dolerite	Dolerite	P.U.B.[2]	P.U.B.[2]	Ballistic block	Ballistic block
Reference	*Lerebour (1987)*	*Upton et al. (2000)*	*Fisk et al. (1988)*	*Fisk et al. (1988)*	*Upton et al. (2000)*	*Upton et al. (2000)*	*Upton et al. (2000)*	*Upton et al. (2000)*	*Upton et al. (2000)*	*this work*	*this work*	*Smietana (2011)*	*Smietana (2011)*	*this work*	*this work*
Major elements (wt%)															
SiO2	39,20	45,74	39,63	47,61	41,83	41,87	45,74	47,24	49,78	47,81	47,78	47,27	45,81	46,26	46,63
Al2O3	0,89	3,55	4,42	14,73	3,92	7,04	16,02	18,18	21,29	14,88	14,67	19,79	14,11	12,89	13,30
FeO	14,60	10,39			14,77	15,18	6,60	7,53	6,05						
Fe2O3	1,30	11,55	20,96	6,91	16,41	16,87	7,33	8,37	6,72	12,70	12,97	11,03	16,22	13,29	13,43
MnO	0,24	0,16	0,25	0,11	0,21	0,22	0,11	0,12	0,08	0,17	0,18	0,09	0,13	0,18	0,18
MgO	43,00	23,78	25,01	11,32	30,71	24,07	10,29	7,21	4,50	6,74	6,67	3,55	4,72	10,75	10,19
CaO	0,44	13,62	7,78	16,53	6,62	8,58	15,85	13,06	11,95	11,64	11,53	11,55	9,94	9,86	9,90
Na2O	0,20	0,40	0,25	1,23	0,33	0,57	1,24	2,07	3,50	2,88	2,23	2,87	2,93	2,54	2,70
K2O	0,05	0,02	0,02	0,15	0,04	0,05	0,06	0,35	0,65	0,83	0,62	0,66	0,66	0,73	0,77
TiO2	0,10	0,80	1,35	0,79	0,46	0,83	0,94	1,30	1,21	2,89	2,98	3,30	5,48	2,65	2,76
P2O5	0,05	0,03	0,01	0,01	0,02	0,05	0,14	0,20	0,13	0,34	0,35	0,16	0,19	0,32	0,34
LOI	-0,01	-0,03	0,47	1,58	0,86	0,55	2,10	1,56	0,45	-0,48	0,08	0,14	0,96	-0,61	-0,84
TOTAL	100,06	99,62	99,21	97,81	101,41	100,70	99,82	99,66	100,26	100,39	100,05	100,27	100,19	98,87	99,36
CaO/Al2O3	0,49	3,84	1,76	1,12	1,69	1,22	0,99	0,72	0,56	0,78	0,79	0,58	0,70	0,76	0,74
Na2O+K2O	0,25	0,42	0,27	1,38	0,37	0,62	1,30	2,42	4,15	3,71	2,85	3,53	3,59	3,28	3,47
Trace elements (ppm)															
As										0	0			0	0
Ba		3	20	30	9	18	33	82	157	168	180	238	482	134	150
Be										1	1			1	1
Bi										0	0			0	0
Cd										0	0			0	0
Ce		5	0	0	5	3	17	27	33	44	48			43	48
Co*		*89*			*139*	*128*	*46*		*26*	44	46	21	27	58	60
Cr		3956	1802	1021	2355	1863	1010	271	30	198	193	35	31	607	551
Cs										0	0			0	0
Cu		19	190	57	23	94	32	54	56	81	18	-1	-8	75	85
Dy										5	5			5	5
Er										2	3			2	2
Eu*		*1*				*1*	*1*		*2*	2	2			2	2
Ga										22	23			20	21
Gd										6	6			5	6
Ge										2	2			1	2
Hf*		*1*			*1*	*1*	*2*		*3*	4	5			4	5
Ho										1	1			1	1
In										0	0			0	0
La		3	1	0	1	3	7	11	13	19	21			19	21
Lu										0	0			0	0
Mo										1	1			1	1
Nb		2	2	1	2	3	7	11	9	20	21			18	20
Nd		4	0	1	5	5	11	16	16	25	27			24	27
Ni		804	935	247	1267	794	184	133	65	85	88	0	0	296	269
Pb		1			1	2	2	3	3	2	2	0	0	2	4
Pr										6	6			6	6
Rb		1	2	5	1	1	1	9	14	20	23			18	21
Sb			35	49						36	35			30	30
Sc		71			28	30	52	36	20	0	0			0	0
Sm*		*2*			*1*	*2*	*3*		*3*	6	6			6	6
Sn										2	1			2	2
Sr		36	76	434	90	187	420	419	597	396	411	503	314	338	376
Ta*		*0*			*6*	*8*	*5*		*1*	2	2			2	2
Tb										1	1			1	1
Th		0	4	2	0	0	1	1	2	2	2			2	2
Tm										0	0			0	0
U										1	1			1	1
V		189	337	177	103	179	165	200	196	309	276			281	303
W*		*0*			*248*	*319*	*191*		*0*	0	0			0	0
Y		9	9	10	5	7	11	16	14	25	27			23	26
Yb*		*1*			*0*	*1*	*1*		*1*	2	2			2	2
Zn		75	138	37	113	114	46	64	48	115	127	77	82	124	124
Zr		28	19	22	18	32	58	92	102	175	191	150	108	157	173

[1] See Fig.1 for the detailed localization

Plagioclase-Ultraphyric Basalts

* Trace elements data either by XRF or by *INAA*

Table 3. Representative olivine analyses

Sample	**PdS1**	**PdS2**			**PdS5**				**PdS8**		**PdS9**					**PdS10**
Provenance	Piton Chisny	Piton Chisny			Piton Chsiny				Piton Chisny		Piton Chisny					Piton Chisny
Rock Type	Dunite	Dunite			Dunite				Wehrlite		Wehrlite					Banded wehrlite
Crystal	*ol9*	*ol2*	*ol2*	*ol2*	*ol9*	*ol10*	*ol10*	*ol10*	*ol3*	*ol3*	*ol1*	*ol1*	*ol4*	*ol4*	*ol7*	*ol7*
Analysis		*rim*	*core*	*rim*	*-*	*rim*	*core*	*rim*	*core*	*rim*	*core*	*rim*	*core*	*rim*	*-*	*-*
Oxides (wt%)																
SiO2	40,25	39,88	40,33	40,64	40,41	40,41	40,38	40,51	41,08	40,86	40,05	39,34	39,73	40,42	39,65	39,72
TiO2	0,04	0,00	0,03	0,00	0,09	0,06	0,07	0,00	0,09	0,00	0,00	0,00	0,06	0,02	0,02	0,00
Al2O3	0,05	0,05	0,00	0,06	0,00	0,07	0,01	0,00	0,00	0,02	0,12	0,05	0,00	0,04	0,02	0,00
FeO	12,28	12,62	11,21	11,68	15,69	15,14	15,24	15,43	16,23	16,90	15,56	15,34	16,62	15,68	14,52	17,44
MnO	0,05	0,00	0,05	0,26	0,14	0,19	0,20	0,17	0,10	0,11	0,03	0,26	0,09	0,11	0,21	0,44
MgO	47,37	47,60	47,22	46,84	43,61	43,98	44,22	44,34	43,69	43,54	45,32	44,25	44,75	44,68	44,40	43,99
CaO	0,13	0,24	0,03	0,05	0,19	0,19	0,20	0,23	0,11	0,03	0,05	0,29	0,12	0,09	0,10	0,05
Na2O	0,01	0,00	0,00	0,01	0,01	0,01	0,00	0,00	0,00	0,00	0,00	0,02	0,05	0,00	0,00	0,00
K2O	0,00	0,00	0,00	0,08	0,00	0,00	0,01	0,00	0,00	0,00	0,00	0,01	0,00	0,02	0,01	0,03
P2O5	0,00	0,00	0,13	0,01	0,00	0,03	0,00	0,00	0,00	0,00	0,10	0,09	0,00	0,00	0,06	0,20
Cr2O3	0,02	0,00	0,00	0,00	0,00	0,08	0,00	0,01	0,00	0,00	0,00	0,00	0,00	0,00	0,02	0,04
NiO	0,24	0,09	0,23	0,20	0,27	0,26	0,23	0,30	0,20	0,16	0,17	0,20	0,27	0,40	0,27	0,00
TOTAL	100,44	100,48	99,23	99,83	100,42	100,43	100,56	101,00	101,50	101,62	101,40	99,85	101,69	101,46	99,28	101,91
Fo	**87,3**	**87,1**	**88,2**	**87,7**	**83,2**	**83,8**	**83,8**	**83,7**	**82,8**	**82,1**	**83,9**	**83,7**	**82,8**	**83,6**	**84,5**	**81,8**

Table 3. (*continued)*

Sample	**PdS11**			**PdS19**		**PdS12**		**PdS13**			**SAL**		**PdS14**	
Provenance	Piton Chisny			Bellecombe		Thalweg DP-PH		Thalweg DP-PH			Cirq. Salazie		Chisny	
Rock Type	Ol gabbro			Ol gabbro		Ol gabbro		Ol gabbro			Ol gabbro		Dolerite	
Crystal	*ol2*	*ol4*	*ol5*	*ol4*	*ol4*	*ol1*	*ol1*	*ol19*	*ol19*	*ol19*	*ol5*	*ol5*	*ol4*	*ol4*
Analysis	*-*	*-*	*hosted in Plag19*	*rim*	*core*	*rim*	*core*	*rim*	*core*	*rim*	*core*	*rim*	*core*	*rim*
Oxides (wt%)														
SiO2	39,88	39,81	39,17	39,64	39,13	38,41	38,36	38,60	39,99	39,80	37,43	37,28	37,99	31,60
TiO2	0,05	0,00	0,03	0,00	0,06	0,08	0,00	0,00	0,00	0,01	0,10	0,00	0,09	0,16
Al2O3	0,10	0,05	0,05	0,00	0,00	0,00	0,04	0,04	0,00	0,02	0,00	0,01	0,00	0,03
FeO	17,75	17,68	17,89	15,79	16,03	24,65	23,71	17,26	13,57	15,30	22,19	23,51	23,69	54,64
MnO	0,29	0,26	0,25	0,15	0,14	0,22	0,44	0,28	0,15	0,16	0,40	0,43	0,33	0,96
MgO	41,87	43,16	42,08	44,32	44,75	37,96	37,99	43,06	46,00	44,82	38,46	38,31	36,68	11,33
CaO	0,33	0,25	0,23	0,25	0,29	0,21	0,21	0,29	0,12	0,08	0,06	0,05	0,43	0,64
Na2O	0,00	0,02	0,00	0,00	0,00	0,00	0,04	0,02	0,01	0,01	0,03	0,02	0,01	0,02
K2O	0,00	0,00	0,02	0,02	0,00	0,00	0,00	0,00	0,00	0,00	0,00	0,00	0,00	0,01
P2O5	0,13	0,09	0,06	0,00	0,00	0,00	0,00	0,00	0,07	0,01	0,00	0,20	0,01	0,25
Cr2O3	0,02	0,00	0,00	0,03	0,00	0,00	0,00	0,12	0,21	0,00	0,00	0,00	0,02	0,00
NiO	0,12	0,11	0,13	0,11	0,18	0,08	0,23	0,41	0,00	0,42	0,12	0,00	0,00	0,18
TOTAL	100,54	101,45	99,92	100,30	100,57	101,61	101,01	100,07	100,11	100,64	98,77	99,80	99,26	99,82
Fo	**80,8**	**81,3**	**80,7**	**83,3**	**83,3**	**73,3**	**74,1**	**81,6**	**85,8**	**83,9**	**75,6**	**74,4**	**73,4**	**27,0**

Fo = 100.Mg/(Mg+Fe) at.

Table 4. Clinopyroxenes analyses

Sample	**PdS1**		**PdS7**		**PdS9**					**PdS10**			**PdS11**							
Provenance	Chisny		Chisny		Chisny					Chisny			Chisny							
Rock Type	Dunite		Wehrlite		Wehrlite					Banded wehrlite			Ol gabbro							
Crystal	*Cpx3*	*Cpx6*	*Cpx1*	*Cpx1*	*Cpx2*	*Cpx2*	*Cpx5*	*Cpx5*	*Cpx5*	*Cpx3*	*Cpx3*	*Cpx3*	*Cpx1*	*Cpx1*	*Cpx1*	*Cpx2*	*Cpx2*	*Cpx2*	*Cpx10a*	*Cpx22*
Analysis	*Interst.*	*Interst.*	*core*	*rim*	*core*	*rim*	*rim*	*interm.*	*core*	*rim*	*core*	*rim*	*rim*	*core*	*rim*	*rim*	*core*	*rim*	*-*	*Opx-hosted*
Oxides (wt%)																				
SiO2	53,45	52,12	48,26	48,06	51,19	51,99	51,35	51,19	50,79	50,28	49,70	50,62	51,37	51,91	53,01	52,22	50,62	52,47	51,86	51,27
TiO2	0,28	0,78	1,64	1,67	0,74	0,79	0,57	0,97	0,92	0,82	1,70	0,97	0,92	1,15	0,40	0,67	1,27	0,50	0,39	0,91
Al2O3	1,25	2,86	5,43	5,33	2,56	2,38	2,76	3,19	4,02	4,22	4,98	3,49	4,23	5,21	2,84	3,94	5,40	2,94	3,13	4,17
FeO	3,35	3,64	4,74	5,00	3,88	5,47	4,48	7,10	5,02	5,06	5,43	5,38	7,33	7,32	6,63	6,85	7,89	6,83	6,04	7,75
MnO	0,03	0,10	0,22	0,11	0,13	0,35	0,09	0,17	0,07	0,00	0,20	0,10	0,18	0,12	0,18	0,19	0,21	0,15	0,07	0,03
MgO	17,21	16,22	14,67	14,41	16,56	17,13	16,15	16,73	16,39	16,37	15,21	16,25	15,45	14,48	15,80	15,97	14,67	15,63	16,26	16,69
CaO	23,94	24,09	22,86	22,94	22,97	21,80	22,60	20,35	20,85	22,03	21,82	22,09	18,53	18,95	20,42	18,86	18,47	20,21	20,48	19,75
Na2O	0,48	0,58	0,44	0,64	0,29	0,33	0,31	0,44	0,25	0,34	0,46	0,34	0,47	0,47	0,43	0,45	0,62	0,55	0,46	0,47
K2O	0,02	0,00	0,00	0,01	0,00	0,00	0,00	0,00	0,05	0,03	0,03	0,05	0,00	0,01	0,01	0,00	0,01	0,00	0,00	0,04
P2O5	0,00	0,00	0,08	0,10	0,00	0,18	0,00	0,01	0,00	0,00	0,00	0,31	0,02	0,03	0,04	0,00	0,04	0,02	0,04	0,02
Cr2O3	0,53	0,89	0,91	0,93	0,94	0,48	1,00	0,63	0,90	0,93	0,85	0,72	0,48	0,57	0,42	0,43	0,40	0,47	0,50	0,31
NiO	0,04	0,09	0,06	0,14	0,04	0,00	0,04	0,03	0,16	0,48	0,15	0,00	0,01	0,04	0,05	0,00	0,01	0,09	0,00	0,00
TOTAL	100,01	100,39	98,34	98,27	98,32	100,42	98,31	100,15	98,36	100,55	100,52	100,32	98,50	99,65	99,76	99,15	99,19	99,30	99,22	101,39
Fs	**5,2**	**6,9**	**7,9**	**8,3**	**6,2**	**8,6**	**7,2**	**11,3**	**8,2**	**8,1**	**9,0**	**8,6**	**12,5**	**12,8**	**10,9**	**11,5**	**13,7**	**11,3**	**9,9**	**12,3**
En	**47,4**	**46,4**	**43,5**	**42,8**	**47,0**	**47,8**	**46,3**	**47,3**	**47,9**	**46,7**	**44,8**	**46,3**	**47,0**	**45,0**	**46,2**	**47,9**	**45,3**	**46,0**	**47,3**	**47,4**
Wo	**47,4**	**46,7**	**48,7**	**48,9**	**46,8**	**43,7**	**46,5**	**41,4**	**43,8**	**45,2**	**46,2**	**45,2**	**40,5**	**42,3**	**42,9**	**40,6**	**41,0**	**42,7**	**42,8**	**40,3**
Mg#	**90,2**	**87,1**	**84,7**	**83,7**	**88,4**	**84,8**	**86,5**	**80,8**	**85,3**	**85,2**	**83,3**	**84,3**	**79,0**	**77,9**	**81,0**	**80,6**	**76,8**	**80,3**	**82,7**	**79,3**
Name [1]	***chromian diopside***	***chromian diopside***	***aluminian diopside***	***aluminian diopside***	***chromian diopside***	***augite***	***chromian augite***	***chromian augite***	***chromian augite***	***chromian augite***	***chromian augite***	***chromian augite***	***augite***	***chromian augite***	***augite***	***augite***	***aluminian augite***	***augite***	***augite***	***augite***

Table 4. (*continued*)

Sample	**PdS19**					**PdS12**	**PdS13**		**IGN**		**SAL**		**PdS14**					
Provenance	Bellecombe					thalweg DP-PH	thalweg DP-PH		Ignimbrite quarry		Cirq. Salazie		Chisny					
Rock Type	Ol gabbro					Ol gabbro	Ol gabbro		Gabbro		Ol gabbro		Dolerite					
Crystal	*Cpx2*	*Cpx2*	*Cpx2*	*Cpx5 sector zoned*		*Cpx2*	*Cpx6*	*Cpx6*	*Cpx1*	*Cpx5*	*Cpx1*	*Cpx1*	*Cpx1*	*Cpx1*	*Cpx2*	*Cpx2*	*Cpx21*	*Cpx21*
Analysis	*rim*	*core*	*rim*	*dark*	*light*	-	*rim*	*core*	-	-	*rim*	*core*	*rim*	*core*	*rim*	*core*	*rim*	*core*
Oxides (wt%)																		
SiO2	49,90	50,81	50,62	49,67	51,83	49,50	51,78	51,15	48,08	51,46	50,68	49,86	47,55	49,80	45,95	48,72	49,09	50,64
TiO2	1,07	1,06	0,75	1,52	1,07	1,69	0,65	1,01	2,22	0,68	0,97	1,14	0,75	0,87	3,17	2,09	1,81	1,12
Al2O3	4,36	3,60	3,78	4,01	2,45	3,60	3,31	3,89	4,81	1,89	3,93	3,06	2,86	1,14	4,93	3,58	3,98	2,70
FeO	5,20	5,22	5,38	6,72	6,00	7,72	7,35	4,87	8,39	8,43	6,61	7,05	17,02	17,56	12,58	9,26	7,41	6,62
MnO	0,20	0,10	0,17	0,10	0,21	0,14	0,22	0,14	0,16	0,20	0,31	0,32	0,31	0,10	0,16	0,10	0,08	0,10
MgO	15,71	16,02	15,96	15,21	16,65	14,99	19,71	15,63	12,68	13,98	15,19	15,53	7,81	10,06	12,03	14,25	14,16	15,54
CaO	22,64	22,15	22,45	21,68	21,52	21,45	15,74	21,14	21,78	22,40	21,15	20,82	19,05	18,47	19,76	20,05	21,03	20,96
Na2O	0,27	0,31	0,28	0,36	0,25	0,40	0,37	0,54	0,57	0,48	0,42	0,35	0,74	0,33	0,56	0,37	0,36	0,28
K2O	0,00	0,00	0,00	0,00	0,00	0,00	0,00	0,00	0,01	0,00	0,08	0,03	1,03	0,05	0,06	0,06	0,06	0,04
P2O5	0,09	0,06	0,00	0,00	0,00	0,00	0,01	0,00	0,02	0,03	0,05	0,00	3,93	0,15	0,00	0,03	0,00	0,00
Cr2O3	0,75	0,69	0,83	0,20	0,11	0,27	0,55	0,70	0,03	0,00	0,16	0,22	0,00	0,05	0,00	0,07	0,22	0,18
NiO	0,09	0,25	0,19	0,00	0,00	0,25	0,18	0,42	0,00	0,14	0,00	0,00	0,00	0,25	0,11	0,00	0,26	0,00
TOTAL	100,26	100,25	100,39	99,46	100,08	100,01	99,88	99,50	98,76	99,69	99,55	98,38	101,04	98,82	99,31	98,58	98,46	98,18
Fs	**8,4**	**8,4**	**8,6**	**10,9**	**9,5**	**12,5**	**11,7**	**8,1**	**14,2**	**13,6**	**10,9**	**11,5**	**30,8**	**29,7**	**21,2**	**15,3**	**12,4**	**10,8**
En	**45,0**	**45,9**	**45,5**	**44,0**	**46,9**	**43,2**	**56,1**	**46,6**	**38,4**	**40,2**	**44,6**	**45,1**	**25,2**	**30,3**	**36,1**	**42,1**	**42,4**	**45,3**
Wo	**46,6**	**45,7**	**45,9**	**45,1**	**43,6**	**44,4**	**32,2**	**45,3**	**47,4**	**46,2**	**44,6**	**43,4**	**44,1**	**40,0**	**42,7**	**42,6**	**45,2**	**43,9**
Mg#	**84,4**	**84,5**	**84,1**	**80,1**	**83,2**	**77,6**	**82,7**	**85,1**	**72,9**	**74,7**	**80,4**	**79,7**	**45,0**	**50,5**	**63,0**	**73,3**	**77,3**	**80,7**
Name [1]	***aluminian diopside***	***aluminian diopside***	***aluminian diopside***	***aluminian augite***	***augite***	***aluminian augite***	***chromian augite***	***chromian augite***	***aluminian augite***	***augite***	***aluminian augite***	***aluminian augite***	***aluminian augite***	***aluminian augite***	***aluminian augite***	***aluminian augite***	***aluminian augite***	***aluminian augite***

[1] After *Morimoto et al., 1988*

Fs = 100.Fe/(Fe+Mg+Ca) at.

En = 100.Mg/(Fe+Mg+Ca) at.

Wo = 100.Ca/(Fe+Mg+Ca) at.

Mg# = 100.Mg/(Mg+Fe) at.

All Fe as Fe^{2+}.

Table 5. Feldspars analyses

Sample	**PdS11**						**PdS19**				**PdS12**				**PdS13**		**IGN**			
Provenance	Chisny						Belecombe				Thalweg DP-PH				Thalweg DP-PH		Ignimbrite quarry			
Rock Type	Ol gabbro						Ol gabbro				Ol gabbro				Ol gabbro		Gabbro			
Crystal	*Plag1*	*Plag5*	*Plag7*	*Plag7*	*Plag23*	*Plag23*	*Plag3*	*Plag3*	*Plag4*	*Plag4*	*Plag1*	*Plag1*	*Plag5*	*Plag5*	*Plag8*	*Plag8*	*Plag5*	*Plag5*	*Plag8*	*Plag9*
Analysis	-	-	*core*	*rim*	*core*	*rim*	*core*	*rim*	*core*	*rim*	*rim*	*core*	*rim*	*core*	*rim*	*core*	*rim*	*core*	-	-
Oxides (xt%)																				
SiO2	47,71	49,63	48,68	50,03	49,54	51,07	46,27	46,20	48,65	45,33	51,62	48,34	48,52	53,37	52,67	51,71	51,92	49,35	53,24	58,00
TiO2	0,00	0,03	0,09	0,10	0,04	0,08	0,01	0,00	0,04	0,14	0,12	0,01	0,00	0,10	0,14	0,06	0,14	0,00	0,10	0,10
Al2O3	33,97	31,68	32,75	31,55	32,42	32,06	33,08	32,75	31,70	33,07	29,39	31,43	31,53	28,29	28,14	29,43	29,00	30,49	28,24	24,84
FeO	0,37	0,46	0,40	0,43	0,47	0,70	0,42	0,57	0,51	0,44	0,86	0,51	0,83	0,63	0,67	0,21	0,43	0,25	0,46	0,51
MnO	0,02	0,00	0,00	0,06	0,00	0,00	0,00	0,01	0,00	0,00	0,08	0,00	0,06	0,00	0,03	0,00	0,06	0,00	0,00	0,00
MgO	0,05	0,09	0,03	0,09	0,05	0,07	0,11	0,12	0,23	0,09	0,11	0,09	0,12	0,10	0,20	0,12	0,02	0,05	0,13	0,04
CaO	16,53	13,84	15,71	14,28	14,73	14,24	17,80	17,74	15,80	18,10	13,20	15,86	16,04	11,99	11,94	13,14	12,33	14,88	11,69	7,54
Na2O	1,70	2,85	2,21	2,87	2,85	3,25	1,37	1,57	2,47	1,35	4,07	2,60	2,52	4,90	4,38	3,77	4,51	3,01	5,18	7,23
K2O	0,07	0,13	0,07	0,13	0,12	0,13	0,00	0,05	0,11	0,00	0,17	0,05	0,13	0,21	0,23	0,25	0,26	0,15	0,11	0,14
P2O5	0,01	0,03	0,08	0,03	0,00	0,00	0,08	0,00	0,00	0,02	0,00	0,04	0,00	0,08	0,00	0,15	0,07	0,00	0,01	0,05
Cr2O3	0,00	0,00	0,06	0,00	0,00	0,01	0,01	0,00	0,00	0,00	0,00	0,05	0,00	0,00	0,01	0,00	0,00	0,00	0,00	0,00
NiO	0,01	0,06	0,06	0,00	0,05	0,00	0,14	0,15	0,00	0,00	0,00	0,00	0,00	0,00	0,00	0,00	0,00	0,05	0,00	0,00
Total	100,43	98,75	100,03	99,55	100,22	101,62	99,32	99,15	99,51	98,53	99,60	98,98	99,74	99,66	98,42	98,84	98,73	98,22	99,16	98,46
Ab(%)	**17,0**	**28,8**	**21,8**	**28,3**	**27,6**	**31,0**	**13,4**	**14,9**	**23,6**	**13,0**	**37,5**	**24,6**	**23,6**	**44,2**	**41,4**	**35,6**	**41,3**	**28,4**	**46,5**	**64,9**
An(%)	**82,4**	**69,9**	**77,4**	**70,5**	**71,2**	**67,8**	**86,6**	**84,6**	**75,4**	**87,0**	**60,9**	**75,0**	**75,2**	**54,0**	**56,4**	**62,1**	**56,4**	**70,2**	**52,5**	**33,8**
Or (%)	**0,7**	**1,3**	**0,7**	**1,2**	**1,2**	**1,2**	**0,0**	**0,5**	**1,0**	**0,0**	**1,6**	**0,5**	**1,2**	**1,8**	**2,2**	**2,4**	**2,3**	**1,4**	**1,0**	**1,3**

Table 5. ***(continued)***

Sample	**SAL**				**PdS14**												
Provenance	Cirq. Salazie				Chisny												
Rock Type	Ol gabbro				Dolerite												
Crystal	*Plag3*	*Plag3*	*Plag4*	*Plag4*	*Plag2*	*Plag2*	*Plag6*	*Plag8*	*Plag16*	*Plag16*	*Plag17*	*Plag17*	*Plag18*	*Plag19*	*Plag19*	*Plag20*	*Plag20*
Analysis	*rim*	*core*	*core*	*rim*	*rim*	*core*	*core*	*rim*	*rim*	*rim*	*rim*	*rim*	*rim*	*core*	*rim*	*rim*	*core*
Oxides (xt%)																	
SiO2	48,18	48,64	48,23	48,47	53,36	62,46	50,62	49,58	64,68	66,67	65,49	65,52	65,82	52,67	57,59	59,37	59,62
TiO2	0,07	0,25	0,03	0,13	0,20	0,26	0,04	0,14	0,17	0,05	0,05	0,11	0,05	0,00	0,11	0,06	0,14
Al2O3	31,17	31,02	31,97	31,40	26,92	21,89	29,18	30,01	18,23	18,30	18,28	18,69	18,66	28,04	25,32	23,81	24,40
FeO	0,49	0,53	0,54	0,56	1,27	1,00	0,45	0,77	1,03	0,91	0,72	0,72	0,35	0,93	1,00	0,77	0,77
MnO	0,00	0,00	0,05	0,13	0,06	0,03	0,12	0,01	0,00	0,18	0,00	0,12	0,05	0,00	0,00	0,10	0,08
MgO	0,04	0,04	0,03	0,05	0,16	0,03	0,14	0,13	0,03	0,00	0,01	0,04	0,02	0,17	0,06	0,04	0,04
CaO	15,15	14,92	14,50	14,53	11,35	3,90	13,53	14,01	0,34	0,24	0,32	1,18	0,53	11,46	7,92	6,43	6,80
Na2O	2,86	2,64	2,64	2,84	4,98	8,17	3,69	3,19	6,00	7,28	6,52	6,58	6,11	4,53	6,66	7,16	6,98
K2O	0,19	0,07	0,05	0,18	0,47	2,32	0,10	0,23	7,62	6,90	7,52	7,05	7,68	0,41	0,90	1,13	1,05
P2O5	0,00	0,00	0,00	0,00	0,00	0,09	0,03	0,00	0,10	0,00	0,03	0,21	0,00	0,00	0,04	0,00	0,04
Cr2O3	0,04	0,00	0,00	0,00	0,01	0,00	0,08	0,03	0,00	0,00	0,00	0,00	0,00	0,00	0,01	0,02	0,01
NiO	0,00	0,00	0,41	0,00	0,04	0,00	0,00	0,00	0,00	0,00	0,00	0,00	0,00	0,19	0,00	0,22	0,08
Total	98,19	98,13	98,45	98,28	98,81	100,15	97,98	98,10	98,19	100,52	98,94	100,21	99,27	98,39	99,59	99,11	99,99
Ab(%)	**26,9**	**26,0**	**26,6**	**27,6**	**44,8**	**65,7**	**35,0**	**30,6**	**43,5**	**50,9**	**45,9**	**46,3**	**43,5**	**42,5**	**57,8**	**62,2**	**61,1**
An(%)	**71,3**	**73,4**	**72,9**	**70,6**	**51,1**	**15,7**	**64,1**	**67,2**	**1,2**	**0,8**	**1,1**	**4,1**	**1,9**	**53,7**	**34,4**	**27,9**	**29,8**
Or (%)	**1,7**	**0,6**	**0,5**	**1,8**	**4,2**	**18,7**	**1,0**	**2,2**	**55,3**	**48,2**	**53,0**	**49,6**	**54,6**	**3,8**	**7,8**	**9,9**	**9,2**

Ab = 100.Na/(Na+K+Ca) at.
An = 100.Ca/(Na+K+Ca) at.
Or = 100.K/(Na+K+Ca) at.

Table 6. Spinels analyses

Sample	**PdS1**		**PdS4**		**PdS7**		**PdS10**	**PdS11**		**PdS19**		**PdS13**			
Provenance	Chisny		Chisny		Chisny		Chisny	Chisny		Bellecombe		thalweg DP-PH			
Rock Type	Dunite		Dunite		Wehrlite		Banded wehrlite	Ol gabbro		Ol gabbro		Ol gabbro			
Crystal	*sp5*	*sp8*	*sp2*	*sp4*	*sp4*	*sp4*	*sp2*	*sp11*	*sp6*	*sp2*	*sp4*	*sp2*	*sp10*	*sp11*	*sp27*
Analysis					*rim*	*core*	-								
Host	*Ol*	*Cpx*	*Ol*	-	*Ol*	*Ol*	*Ol*	*Cpx*	*Opx*	*Ol*	*Ol*	*Cpx*	*Cpx5*	*Cpx5*	*Ol*
Oxides (wt%)															
SiO2	0,02	0,03	0,03	0,00	0,05	0,00	0,11	0,12	0,23	0,09	0,00	0,18	0,20	0,14	0,07
TiO2	2,29	2,04	2,65	2,99	2,35	2,77	7,24	2,89	4,87	2,88	2,70	5,46	4,97	5,45	10,45
Al2O3	12,71	14,16	16,26	13,43	21,88	15,07	11,95	21,18	15,88	18,42	15,35	20,08	16,62	13,05	9,58
FeO	34,64	31,09	38,80	35,91	28,78	29,48	44,20	37,73	49,18	34,26	32,11	31,73	35,55	44,05	42,83
MnO	0,07	0,17	0,00	0,00	0,20	0,35	0,34	0,21	0,25	0,23	0,14	0,29	0,26	0,24	0,33
MgO	11,79	12,14	8,07	10,60	13,13	11,80	8,32	11,34	9,12	11,21	10,83	13,82	10,99	8,60	8,89
CaO	0,02	0,06	0,03	0,03	0,00	0,07	0,42	0,32	0,08	0,08	0,01	0,25	0,43	0,58	0,17
Na2O	0,00	0,00	0,00	0,00	0,01	0,00	0,17	0,00	0,00	0,00	0,00	0,00	0,02	0,02	0,05
K2O	0,00	0,01	0,00	0,00	0,00	0,01	0,00	0,00	0,00	0,00	0,06	0,00	0,00	0,06	0,00
P2O5	0,00	0,03	0,03	0,06	0,00	0,00	0,04	0,00	0,00	0,00	0,07	0,02	0,01	0,00	0,00
Cr2O3	32,81	37,16	31,82	35,37	30,47	37,79	22,43	22,29	14,92	28,66	35,68	24,17	25,75	22,61	21,31
NiO	0,44	0,33	0,19	0,25	0,12	0,21	0,01	0,33	0,24	0,64	0,00	0,34	0,36	0,25	0,42
TOTAL	94,77	97,22	97,89	98,64	96,94	97,47	95,22	96,41	94,76	96,49	96,95	96,34	95,17	95,04	94,09
Host Fo	86,4		84,2	82,06	84,21	84,21				82,60	83,07				79,07
Mg#	**56,3**	**56,9**	**37,4**	**48,3**	**58,6**	**54,4**	**36,7**	**51,4**	**40,9**	**51,6**	**50,0**	**58,6**	**49,3**	**39,5**	**37,2**
Cr#	**63,4**	**63,8**	**56,8**	**63,8**	**48,3**	**62,7**	**55,7**	**41,4**	**38,7**	**51,1**	**60,9**	**44,7**	**51,0**	**53,7**	**59,9**

Mg# = 100.Mg/(Mg+Fe^{2+}) at.

Cr# = 100.Cr/(Cr+Al) at.

Table 7. Ilmenites analyses

Sample	**IGN**				**PdS12**				**SAL**			**PdS14**		
Provenance	Ignimbrite quarry				Thalweg DP-PH				Cirq.Salazie			Chisny		
Rock Type	Gabbro				Ol gabbro				Ol gabbro			Dolerite		
Crystal	*ilm2*	*ilm5*	*ilm6*	*ilm7*	*ilm1*	*ilm1*	*ilm1*	*ilm1*	*ilm1*	*ilm1*	*ilm1*	*ilm1*	*ilm4*	*ilm5*
Analysis					*rim*			*core*	*rim*	*core*	*rim*			
Oxides (wt%)														
SiO2	0,03	0,16	0,04	0,48	0,02	0,05	0,03	0,07	0,01	0,01	0,07	0,49	0,06	0,24
TiO2	47,92	48,07	48,96	48,83	46,46	47,00	45,63	46,54	47,29	47,29	47,78	44,78	48,84	48,68
Al2O3	0,09	0,25	0,02	0,13	0,53	0,58	0,54	0,54	0,06	0,10	0,08	0,34	0,09	0,08
FeO	44,80	42,98	48,12	43,65	40,44	41,55	41,78	42,54	47,10	49,78	48,16	46,29	47,30	46,00
MnO	0,79	0,97	1,31	1,34	0,33	0,30	0,26	0,31	1,01	0,84	1,59	0,57	0,74	0,61
MgO	2,79	3,21	0,81	0,70	6,63	6,60	6,65	6,54	1,04	1,07	0,74	0,50	1,70	1,17
CaO	0,28	0,21	0,03	0,18	0,30	0,19	0,32	0,31	0,11	0,09	0,14	0,26	0,34	0,48
Na2O	0,04	0,00	0,03	0,09	0,02	0,01	0,02	0,06	0,00	0,02	0,00	0,00	0,00	0,00
K2O	0,03	0,04	0,00	0,07	0,00	0,00	0,00	0,03	0,00	0,00	0,00	0,10	0,00	0,00
P2O5	0,01	0,00	0,04	0,00	0,04	0,00	0,00	0,00	0,00	0,00	0,00	0,05	0,00	0,00
Cr2O3	0,03	0,01	0,00	0,07	0,41	0,45	0,39	0,31	0,28	0,33	0,31	0,00	0,04	0,01
NiO	0,00	0,33	0,00	0,00	0,39	0,00	0,01	0,00	0,19	0,44	0,00	0,00	0,27	0,00
Total	96,81	96,24	99,37	95,54	95,57	96,73	95,61	97,24	97,08	99,96	98,87	93,38	99,39	97,26
X Ilm	**0,91**	**0,93**	**0,93**	**0,97**	**0,88**	**0,88**	**0,86**	**0,86**	**0,92**	**0,89**	**0,91**	**0,91**	**0,92**	**0,94**

X Ilm = Ti/(Ti+Fe^{3+}/2) at.

Table 8. Magnetites analyses

Sample	**IGN**			**PdS12**				**PdS14**				
Provenance	Ignimbrite quarry			Thalweg DP-PH				Chisny				
Rock Type	Gabbro			Ol gabbro				Dolerite				
Crystal	*mt1*	*mt1*	*mt2*	*mt2*	*mt4*	*mt5*	*mt6*	*mt7*	*mt8*	*mt9*	*mt10c*	*mt10r*
Analysis	*core*	*rim*	-	-	-	-	-	-	-	-	*core*	*rim*
Oxide (wt%)												
SiO2	0,05	0,63	0,22	0,06	0,50	0,13	0,11	0,10	0,20	0,26	0,05	0,13
TiO2	19,48	18,62	19,16	16,35	15,76	16,54	16,47	23,81	21,65	22,46	23,71	28,28
Al2O3	2,82	3,09	2,81	4,40	4,27	3,93	4,13	1,08	0,65	0,50	1,18	0,83
FeO	67,91	69,56	68,33	64,03	64,12	64,91	66,11	67,51	71,93	69,73	68,91	67,02
MnO	0,66	0,38	0,33	0,22	0,47	0,42	0,37	0,90	0,72	0,58	0,69	0,47
MgO	2,93	3,11	2,68	5,73	6,02	5,73	5,81	0,52	0,75	0,45	0,96	1,08
CaO	0,62	0,82	0,75	0,25	0,56	0,18	0,40	0,09	0,14	0,46	0,06	0,13
Na2O	0,00	0,03	0,01	0,00	0,00	0,00	0,00	0,00	0,00	0,02	0,00	0,02
K2O	0,00	0,01	0,00	0,00	0,05	0,06	0,03	0,04	0,01	0,05	0,00	0,04
P2O5	0,05	0,00	0,00	0,18	0,00	0,01	0,00	0,00	0,00	0,00	0,00	0,00
Cr2O3	0,02	0,05	0,03	3,20	2,22	2,29	1,66	0,00	0,05	0,00	0,03	0,10
NiO	0,00	0,00	0,00	0,14	0,12	0,17	0,00	0,00	0,00	0,00	0,05	0,00
Total	94,53	96,29	94,31	94,57	94,09	94,36	95,09	94,05	96,12	94,51	95,64	98,10
X Mt	**0,37**	**0,38**	**0,37**	**0,38**	**0,40**	**0,41**	**0,42**	**0,27**	**0,36**	**0,32**	**0,28**	**0,17**

X Mt = Fe^{3+}/(Fe^{3+}+Ti) at. in the B site.

Table 9. Sulphides analyses

Sample	**PdS11**			
Provenance	Chisny			
Rock Type	Ol gabbro			
Crystal	*s1*	*s1*	*s5*	*s5*
Analysis	*core*	*rim*	*core*	*rim*
Host	*Cpx13*	*Cpx13*	*Cpx2*	*Cpx2*
Wt %				
S	32,21	36,41	35,37	37,97
Fe	50,37	53,66	51,78	52,28
Co	0,00	0,00	0,00	0,00
Ni	2,32	4,55	3,80	4,45
Cu	8,12	0,12	3,82	1,00
Pb	0,00	0,24	0,00	0,00
Total	93,01	94,98	94,78	95,71
At %				
S	48,44	52,16	51,19	53,54
Fe	43,49	44,14	43,02	42,32
Co	0,00	0,00	0,00	0,00
Ni	1,91	3,56	3,00	3,43
Cu	6,16	0,08	2,79	0,71
Pb	0	0,053	0	0
Total	100	100	100	100
Cu/(Cu+Ni) at.	**0,76**	**0,02**	**0,48**	**0,17**
Ni/(Ni+Fe) at.	**0,04**	**0,07**	**0,07**	**0,07**

Table 10. Secondary minerals analyses

Sample	**SAL**							**IGN**		
Provenance	Cirq. Salazie							Ignimbrite quarry		
Rock Type	Ol gabbro							Gabbro		
Crystal Analysis	*Phlog1*	*Phlog2*	*Phlog2*	*Phlog3*	*Phlog4*	*Phlog5*	*Phlog6*	*Amph1*	*Amph2*	*Amph3*
Oxides (xt%)										
SiO2	37,87	37,87	37,89	37,69	37,83	37,01	37,88	40,17	40,42	39,15
TiO2	3,28	3,66	3,49	4,27	4,32	4,48	3,85	5,92	5,80	6,00
Al2O3	14,05	13,76	14,63	13,83	13,75	13,71	13,91	11,99	11,97	11,61
FeO	8,64	8,40	8,93	8,83	10,24	10,79	9,82	12,02	12,15	13,18
MnO	0,01	0,19	0,12	0,12	0,15	0,00	0,01	0,00	0,24	0,12
MgO	19,96	20,25	19,57	19,12	18,33	17,97	19,30	12,17	12,23	11,90
CaO	0,07	0,06	0,01	0,02	0,02	0,00	0,05	11,83	11,56	12,00
Na2O	1,12	1,12	1,29	0,92	0,64	0,60	0,81	2,76	2,74	2,68
K2O	8,23	8,57	8,64	9,20	9,31	8,99	9,04	0,41	0,49	0,90
P2O5	0,00	0,05	0,02	0,03	0,00	0,02	0,00	0,02	0,04	0,00
Cr2O3	0,02	0,10	0,00	0,30	0,14	0,13	0,15	0,00	0,00	0,00
NiO	0,00	0,03	0,00	0,27	0,27	0,05	0,05	0,11	0,00	0,00
Total	93,25	94,04	94,58	94,59	94,99	93,74	94,87	97,41	97,63	97,53
Phlog	**74,9**	**76,2**	**73,5**	**73,7**	**70,4**	**69,1**	**72,6**			
Ann	**18,2**	**17,7**	**18,8**	**19,1**	**22,1**	**23,3**	**20,7**			
East	**5,6**	**4,9**	**6,1**	**5,7**	**5,7**	**5,7**	**5,2**			
Sid	**1,4**	**1,1**	**1,6**	**1,5**	**1,8**	**1,9**	**1,5**			
total	**100**	**100**	**100**	**100**	**100**	**100**	**100**			
Amph Mg#								**0,64**	**0,64**	**0,62**
Name [1]								**Kaersutite**	**Kaersutite**	**Kaersutite**

[1] After *Leake et al., 1997*

Table 11. Glass analyses

Sample	**PdS10**		**PdS12**						**PdS13**				**PdS19**					
Provenance	Chisny		Thalweg DP-PH						Thalweg DP-PH				Bellecombe					
Rock Type	Wehrlite		Ol gabbro						Ol gabbro				Ol gabbro					
Glass	*Interstitial*		*Interstitial*		*Interstitial*		*Interstitial*		*Interstitial*		*Inclusion*		*Interstitial*		*Interstitial*		*Inclusion*	
Host											*Ol*						*Cpx*	
n [1]	***2***	***σ***	***7***	***σ***	***3***	***σ***	***4***	***σ***	***7***	***σ***	***7***	***σ***	***4***	***σ***	***3***	***σ***	***3***	***σ***
Oxides (%) [2]																		
SiO2	49,14	*0,31*	52,43	*0,38*	51,80	*0,33*	51,48	*0,16*	52,78	*1,19*	52,17	*0,24*	49,65	*0,85*	49,41	*0,41*	49,44	*0,39*
TiO2	3,59	*0,08*	4,10	*0,24*	4,09	*0,07*	4,18	*0,18*	3,79	*0,13*	3,87	*0,23*	2,94	*0,16*	3,01	*0,03*	2,93	*0,19*
Al2O3	13,92	*0,26*	13,82	*0,27*	13,79	*0,08*	13,56	*0,24*	13,52	*0,15*	13,18	*0,12*	14,82	*0,25*	14,86	*0,11*	14,75	*0,13*
FeO	11,77	*0,49*	9,82	*0,34*	10,25	*0,19*	10,60	*0,35*	10,25	*0,73*	10,91	*0,30*	9,98	*0,62*	10,27	*0,36*	10,42	*0,35*
MnO	0,23	*0,01*	0,13	*0,07*	0,23	*0,10*	0,20	*0,07*	0,17	*0,11*	0,14	*0,13*	0,18	*0,10*	0,11	*0,09*	0,24	*0,02*
MgO	5,77	*0,23*	5,20	*0,13*	5,32	*0,04*	5,28	*0,09*	5,40	*0,10*	5,48	*0,12*	6,65	*0,22*	6,44	*0,11*	6,73	*0,09*
CaO	11,06	*0,35*	8,78	*0,16*	9,13	*0,17*	9,23	*0,11*	8,92	*0,41*	9,14	*0,09*	11,27	*0,13*	11,07	*0,13*	11,30	*0,21*
Na2O	3,16	*0,03*	3,27	*0,23*	3,07	*0,08*	3,25	*0,23*	3,03	*0,18*	2,93	*0,08*	3,02	*0,11*	3,12	*0,14*	2,76	*0,18*
K2O	0,71	*0,00*	1,45	*0,10*	1,36	*0,06*	1,38	*0,04*	1,19	*0,12*	1,02	*0,06*	0,94	*0,09*	0,96	*0,05*	0,90	*0,04*
P2O5	0,59	*0,28*	0,94	*0,27*	0,94	*0,20*	0,79	*0,37*	0,86	*0,12*	1,01	*0,20*	0,48	*0,20*	0,65	*0,03*	0,39	*0,18*
Cr2O3	0,04	*0,06*	0,01	*0,02*	0,02	*0,02*	0,00	*0,00*	0,04	*0,03*	0,03	*0,02*	0,07	*0,01*	0,06	*0,03*	0,00	*0,00*
NiO	0,01	*0,02*	0,06	*0,08*	0,00	*0,00*	0,05	*0,10*	0,05	*0,08*	0,12	*0,09*	0,01	*0,02*	0,03	*0,04*	0,15	*0,14*
Total	100,29		99,00		98,29		98,71		98,49		99,54		98,36		98,79		98,18	

[1] Average of multiple analyses, n is the number of analyses performed.

[2] Concentrations are normalized to 100%; Total is unnormalized.

Table 12. Exsolutions analyses

Sample	**PdS11**										**PdS13**			
Provenance	Piton Chisny										Thalweg DP-PH			
Rock Type	Ol gabbro										Ol gabbro			
Crystal	*Pig1*	*Pig2*	*Pig3*	*Pig4*	*Opx2*	*Opx8*	*Opx17*	*Opx18*	*Opx19*	*Opx21*	*Opx4*	*Opx6*	*Opx9 rim*	*Opx9 core*
Exsolution texture [1]	*gran.*	*gran.*	*gran.*	*lam.*	*lam.*	*lam.*	*lam.*	*lam.*	*lam.*	*gran.*	*lam.*	*lam.*	*gran.*	*gran.*
Host	*Cpx1*	*Cpx1*	*Cpx1*	*Cpx10*	*Cpx1*	*Cpx9*	*Cpx10*	*Cpx10*	*Cpx10*	*Cpx8*	*Cpx2*	*Cpx5*	*Cpx6*	*Cpx6*
Oxides (wt%)														
SiO2	54,25	52,26	54,05	55,00	54,58	55,57	55,14	55,68	55,67	55,47	50,39	55,33	54,51	54,63
TiO2	0,51	0,66	0,83	0,12	0,26	0,14	0,14	0,20	0,12	0,11	0,85	0,53	0,24	0,28
Al2O3	3,34	3,60	4,92	2,34	2,49	2,30	1,97	2,12	2,01	2,03	2,30	1,54	2,12	1,96
FeO	10,93	10,63	12,02	9,66	12,92	12,49	11,09	10,52	11,10	11,29	12,82	8,98	10,55	10,42
MnO	0,16	0,25	0,24	0,31	0,31	0,27	0,21	0,23	0,41	0,55	0,34	0,11	0,19	0,18
MgO	24,18	21,58	25,18	26,18	28,00	29,25	29,82	30,10	30,45	29,68	29,62	30,74	29,60	30,41
CaO	7,01	10,86	2,99	6,94	1,51	1,04	2,14	1,84	1,06	1,27	1,00	1,77	2,30	0,99
Na2O	0,13	0,22	0,60	0,17	0,03	0,04	0,09	0,06	0,05	0,05	0,02	0,04	0,05	0,05
K2O	0,01	0,02	0,20	0,01	0,00	0,00	0,03	0,03	0,00	0,06	0,00	0,00	0,04	0,00
P2O5	0,00	0,00	0,00	0,09	0,03	0,00	0,00	0,00	0,00	0,00	0,00	0,00	0,00	0,00
Cr2O3	0,28	0,24	0,19	0,23	0,17	0,21	0,25	0,23	0,25	0,14	1,60	0,28	0,41	0,30
NiO	0,00	0,06	0,05	0,00	0,11	0,04	0,00	0,00	0,03	0,15	0,18	0,15	0,00	0,00
TOTAL	100,80	100,36	101,26	101,06	100,40	101,36	100,85	101,00	101,15	100,81	99,12	99,47	100,01	99,22
Fs	**17,3**	**16,9**	**19,8**	**14,8**	**19,9**	**18,9**	**16,6**	**15,8**	**16,6**	**17,1**	**19,2**	**13,6**	**15,9**	**15,8**
En	**68,4**	**61,1**	**73,9**	**71,6**	**77,1**	**79,0**	**79,4**	**80,6**	**81,3**	**80,4**	**78,9**	**83,0**	**79,6**	**82,3**
Wo	**14,2**	**22,1**	**6,3**	**13,6**	**3,0**	**2,0**	**4,1**	**3,5**	**2,0**	**2,5**	**1,9**	**3,4**	**4,4**	**1,9**
Mg#	**79,8**	**78,4**	**78,9**	**82,9**	**79,4**	**80,7**	**82,7**	**83,6**	**83,0**	**82,4**	**80,5**	**85,9**	**83,3**	**83,9**
Name [2]	***Pigeonite***	***Augite***	***Pigeonite***	***Pigeonite***	***Enstatite***	***Enstatite***	***Enstatite***	***Enstatite***	***Enstatite***	***Enstatite***	***Enstatite***	***Enstatite***	***Enstatite***	***Enstatite***

gran. = granular ; lam. = lamellar. See text and Figures 14-15.

Fs = 100.Fe/(Fe+Mg+Ca) at.

En = 100.Mg/(Fe+Mg+Ca) at.

Wo = 100.Ca/(Fe+Mg+Ca) at.

Mg# = 100.Mg/(Mg+Fe) at.

After *Morimoto et al., 1988*.

Table 13. Results of pyroxene thermometry

Sample	**PdS11**												
Provenance	Piton Chisny												
Rock type	Ol gabbro												
P (bars)	*500*	*1000*	*500*	*500*	*500*	*500*	*500*	*500*	*500*	*500*	*500*	*500*	*500*
Phases in equilibrium													
Augite	Cpx1a	Cpx1a	Cpx1b	Cpx1d	Cpx2a	Cpx4b	Cpx10a	Cpx10d	Cpx10e	Cpx1c	Cpx1c	Cpx10b	Cpx10a
Orthopyroxene	Opx2	Opx2	Opx2	Opx4	Opx5	Opx32	Opx18	Opx15	Opx11	Opx3	Opx4	Opx19	Opx18
Pigeonite										Pig3	Pig3	Pig4	Pig4
T calc (°C)	**1078**	**1080**	**1068**	**981**	**995**	**987**	**1137**	**991**	**989**	**976**	**971**	**1004**	**1149**
σ	*47*	*47*	*8*	*52*	*31*	*22*	*88*	*28*	*43*	*25*	*28*	*49*	*41*

Sample	**PdS13**												
Provenance	Piton Haüy												
Rock type	Ol gabbro												
P (bars)	*500*	*500*	*500*	*500*	*500*	*500*	*500*	*500*	*500*	*500*	*500*	*500*	*500*
Phases in equilibrium													
Augite	Cpx1b	Cpx2a	Cpx2b	Cpx5a	Cpx5b	Cpx6a	Cpx6b	Cpx6c	Cpx6c	Cpx8a	Cpx8b	Cpx8b	Cpx9
Orthopyroxene	Opx1	Opx4	Opx4	Opx5	Opx6	Opx8	Opx9a	Opx9c	Opx9d	Opx12a	Opx12a	Opx12c	Opx13
Pigeonite													
T calc (°C)	**1044**	**987**	**1013**	**1074**	**1163**	**982**	**1149**	**1069**	**1005**	**990**	**986**	**962**	**1055**
σ	9	*36*	88	47	55	21	18	54	64	50	13	41	71

Table 14. Conditions of Fe-Ti oxide equilibration

Sample	**PdS14**							
Provenance	Piton Chisny							
Rock Type	Dolerite							
Oxide pairs	Ilm4a-Mt8	Ilm4a-Mt7	Ilm4a-Mt9	Ilm4b-Mt9	Mt10r-Ilm5	Mt10c-Ilm5	Mt10c-Ilm6	Mt10r-Ilm6
P (bars)	*500*	*500*	*500*	*500*	*500*	*500*	*500*	*500*
calc T(°C)	**894**	**968**	**933**	**933**	**1095**	**900**	**900**	**1095**
1 σ	0	0	0	0	9	0	0	9
calc log (fO2)	**-13,442**	**-12,278**	**-12,808**	**-12,808**	**-10,735**	**-13,716**	**-13,716**	**-10,735**
1 σ	0	0	0	0	0,073	0	0	0,073
ΔFMQ	***-0,733***	***-0,852***	***-0,804***	***-0,804***	***-1,167***	***-1,133***	***-1,133***	***-1,167***

Table 14. *(continued)*

Sample	**IGN**				**PdS12**	
Provenance	Ignimbrite Quarry				Piton Haüy	
Rock Type	Gabbro				Ol gabbro	
Oxide pairs	Ilm1-Mt2	Ilm1-Mt1c	Ilm1-Mt1	Ilm1-Mt1	Ilm1_Mt5	Ilm1_Mt4
P (bars)	*500*	*500*	*500*	*1000*	*500*	*500*
calc T(°C)	**771**	**765**	**813**	**813**	**860**	**857**
1 σ	60	54	89	89	52	53
calc log (fO2)	**-16,123**	**-16,249**	**-14,63**	**-14,628**	**-12,656**	**-12,708**
1 σ	0,793	0,718	1,08	1,077	0,59	0,585
ΔFMQ	***-0,912***	***-0,902***	***-0,35***	***-0,398***	***0,689***	***0,699***

CHAPITRE III : “Approche expérimentale – Simulation du système d’alimentation superficiel du Piton de la Fournaise par l’étude expérimentale des équilibres de phases d’un Steady State Basalt”

Résumé

Les résultats de l'étude de pétrologie expérimentale menée durant cette thèse et réalisée sur une composition de SSB du Piton de la Fournaise (émise durant l'éruption de Décembre 2009), seront présentés séparément en fonction de la zone du système d'alimentation que ces expériences simulent. Ce premier des deux Chapitres détaille les expériences réalisées à des pressions qui sont celles du système d'alimentation superficiel (0.1 et 50 MPa). Les résultats des expériences réalisées à plus haute pression sont présentés dans le Chapitre 4.

Ce chapitre, rédigé sous forme d'article, présente les résultats expérimentaux obtenus sur un produit de départ (REU0912-04) de composition typique de SSB au PdF (7,8 % MgO; 11,2% CaO; 13,8% Al2O3). Les expériences de cristallisation ont été réalisées à 0.1 et à 50 MPa en partant d'un verre obtenu à partir de l'échantillon REU0912-04. A 0.1 MPa, deux séries d'expériences ont été menées selon la fO2 (NNO et NNO-0,5). A 50 MPa, les expériences ont été conduites en présence de volatils (fluides H2O-CO2) et pour des fO2 modérément réductrices entre NNO et NNO-1.7. Les observations texturales et les calculs des coefficients de partage minéral-liquide montrent que l'équilibre a été globalement atteint et que le problème de la perte de fer a été dans l'ensemble maîtrisé. Les assemblages de phases et les compositions ne montrent que de faibles variations entre les deux pressions explorées. L'olivine (Fo74-86) est systématiquement la phase cristalline au liquidus. A 0.1 MPa, elle est suivie du plagioclase puis du clinopyroxène (NNO) ou par un assemblage plag+cpx (NNO-0,5). A 50 MPa, le clinopyroxène (En_{38-53} Wo_{38-45} Fs_{7-18}) est la seconde phase dans la séquence de cristallisation, suivi du plagioclase (An_{57-69} Ab_{30-40} Or_{1-5}). Les volatils dissous dans les verres expérimentaux (analyses FTIR et estimations par différence) varient entre 0,7-1,4% H2O et 128-551 ppm CO2, en accord avec les données d'inclusions vitreuses. Le bon accord entre les assemblages de phases naturels et expérimentaux, ainsi qu'entre les compositions (phases minérales et verres), indique que les expérimentations réalisées simulent de façon satisfaisante le système d'alimentation superficiel du PdF. La séquence de cristallisation définie pour une composition de SSB, à 50 MPa et pour une concentration en H2O dissoute de ~1%, montre l'apparition de l'olivine à 1175°C, suivie du clinopyroxène à 1150°C et du plagioclase autour de 1110°C.

Ces données expérimentales, obtenues en présence de volatils, sont radicalement différentes des résultats des expérimentations réalisées sans volatils. Elles conduisent à proposer des

pressions beaucoup plus superficielles pour le stockage des magmas. Les séquences de cristallisation obtenues démontrent que les fractionnements à l'origine des compositions de SSB peuvent opérer à de faibles pressions au sein du système d'alimentation du PdF, en accord avec les données géophysiques. Le fractionnement de l'olivine est le mécanisme évolutif principal à l'origine des SSB.

Petrology of a Steady State Basalt from Piton de la Fournaise volcano (Reunion Island): experimental insights on the shallow feeding system.

YANN-AURELIEN BRUGIER, MICHEL PICHAVANT & ANDREA DI MURO

Abstract Experimental phase equilibria have been determined for a Steady State Basalt (7.8 wt% MgO, 11.2 wt% CaO, 13.8 wt% Al2O3) erupted from Piton de la Fournaise volcano on La Réunion island. The experiments were performed both at 0.1 MPa under volatile-free conditions and at 50 MPa in presence of H2O-CO2 fluid mixtures. They simulate the shallowest part of the feeding system of the volcano. Redox conditions were kept slightly to moderately reducing, either at NNO or NNO-0.5 in the 0.1 MPa experiments and in the range NNO to NNO-1.7 in the 50 MPa experiments. All experiments were of crystallization type and attainment of equilibrium was monitored from textural data (scanning electron microscope imaging) and crystal-melt partitioning data (electron microprobe analyses of mineral and glass phases). Glass H2O and CO2 concentrations were measured by FTIR and the data complemented from "by difference" estimations. Experimental phase assemblages and compositions are similar for the two pressures investigated. Olivine (Fo74-86) is the liquidus phase at both pressures. At 50 MPa, it is followed by clinopyroxene (En_{38-53} Wo_{38-45} Fs_{7-18}) and then plagioclase (An_{57-69} Ab_{30-40} Or_{1-5}). At 0.1 MPa, plagioclase comes in second in the crystallization sequence, either alone (NNO) or together with clinopyroxene (NNO-0.5), and cotectic olivine+clinopyroxene+plagioclase crystallization starts at 1168°C (NNO-0.5) and 1160°C (NNO). The 50 MPa glasses have H2O (0.7-1.4 wt%) and CO2 (128-551 ppm) concentrations, in the same range as natural glass inclusions. For a melt H2O content of ~1 wt%, olivine appears at 1175°C, clinopyroxene at 1150°C and plagioclase at 1110°C. The experimental data demonstrate that, on the PdF, basalt magma crystallization in the sequence olivine, clinopyroxene, plagioclase is a mechanism possible at low pressures. Differences with previous high pressure experimental results are emphasized and are the consequence of experiments from this study being conducted in presence of volatiles. For melt H2O contents < 2 wt%, temperatures of crystallization, especially for plagioclase, are lowered and the crystallization sequence is modified, clinopyroxene crystallizing before plagioclase at low pressures. Our data imply magma fractionation levels much shallower than previously thought at Piton de la Fournaise, in better agreement with geophysical data.

Keywords: *Piton de la Fournaise, shallow feeding system, Steady State Basalts, experimental phase equilibria, volatiles*

1 Introduction

La Réunion, situated in the southwest of the Indian Ocean, is a volcanic island associated with the "Mascareignes hotspot" (Duncan et al., 1989; Bonneville, 1990; Chenet et al., 2007). The island has an oval shape of 50 by 70 km and is composed of two juxtaposed volcanic edifices. (1) The "Piton des Neiges" volcano (PdN) active since 5 Ma (Gillot et al., 1994) and until 29 ka ago (McDougall, 1971; Quidelleur et al., 2010) makes up most of the northwestern part of the island. It is now eroded by three km-deep erosion canyons. (2) The "Piton de la Fournaise" volcano (PdF) is one of the most active basaltic volcanoes on Earth (1-2 eruptions per year; Staudacher et al., 2016). Located in the southeastern part of the island, its activity has started 535 ka ago (Gillot & Nativel, 1989). The existence of a third volcano, named "les Alizés" (Malengreau, 1995; Malengreau et al., 1999; Lénat et al., 2001; Smietana, 2011; Lénat, 2016) is still debated (Lebas, 2012; Salvany et al., 2012). The volcanic history of the PdF is marked by several caldera-collapse events associated with progressive displacements of the active center (Bachèlery, 1981; Merle et al., 2010; Michon et al., 2016). Presently, the active part of the volcano which includes the Dolomieu crater at its center is contained in a major U-shaped collapse caldera named "Enclos Fouqué" (Lénat, 2016 and references therein). This structure is thought to have resulted from phreatomagmatic eruptions between 4880±35BP and 2855±35BP stratigraphically marked by the Bellecombe Tephra (Bachèlery, 1981; Mohamed-Abchir, 1996; Upton et al., 2000; Ort et al., 2016; Morandi et al., 2016). The Enclos Fouqué caldera actually delimits almost all eruptions in the modern activity, i.e., younger than 4700 years (Lacroix, 1923; Ludden, 1978a; Bachèlery, 1981; Kornprobst et al., 1984; Staudacher & Allègre, 1993; Peltier, 2007; Lénat, 2016; Staudacher et al., 2016 and references therein).

The PdF volcanic products are classically distributed in 4 different groups (see Pichavant et al., 2016 and references therein). (1) The Steady State Basalts (SSB) are transitional basalts with a narrow range of compositions (MgO = 5-8 wt%; CaO/Al2O3 = 0.75-0.85; see Albarède et al., 1997; Famin et al., 2009; Lénat et al., 2012). These are the dominant lavas emitted during the modern activity. (2) The picritic lavas, named "Oceanites" (Lacroix, 1936), are emblematic of the volcanic activity at La Réunion with their high fraction (> 50%; Vlastélic et al., 2005) of mm- to cm-sized olivine phenocrysts. Oceanites represent the second most important group of lavas erupted during the modern history of the PdF. Most workers (Albarède et al., 1997; Vlastélic et al., 2005; Welsch et al., 2009; Famin et al., 2009 ; Pichavant et al., 2016) now consider oceanites as SSB-type lavas having incorporated olivine xenocrysts at relative shallow depths inside the feeding system. This explains their wide range of bulk-rock MgO contents (8-28 wt%) and their CaO/Al2O3 (0.85-0.75) similar to SSB. (3) The Differentiated Lavas are characterized by a strong decrease in MgO (2-6 wt%) and CaO as well as by an increase in Al2O3 compared to the other groups, leading to low CaO/Al2O3 (from 0.8 to 0.2). They correspond to lavas erupted near the end of the activity of the PdN (Upton & Wadsworth, 1966) and during the early stages of activity of the PdF (Bachèlery, 1981; Albarède et al., 1997; Merle et al., 2010). Some authors have associated this differentiated stage with les Alizés volcano (Smietana, 2011; Valer et al., 2015) rather than with PdF. (4) The fourth group, named the Abnormal Group (AbG), differs clearly in compositions from the 3 others. It shows an enrichment in MgO (8-11 wt%) and in Fe, Ti, Na, K relative to SSB, and is depleted in CaO. CaO/Al2O3 (0.6-0.8) are lower than in SSB. AbG-type lavas are very rarely observed inside the Enclos Fouqué (e.g., Formica Léo or Hudson cones, Villemant et al., 2009; Salaün et al., 2010; Boudoire et al., in prep) and they mostly occur at eccentric vents more or less distant of the active center and belonging to the "North-West South-East" rift zone (Di Muro, 2012; 2015; Michon et al., 2014; Boudoire et al., in prep), or in areas such as the "Plaine des Sables" (Morandi et al., 2016; Principe et al., 2016; Brugier et al., 2016a; Boudoire et al., in prep).

La Réunion lavas (PdN and PdF products) are isotopically homogeneous (Fisk et al., 1988; Graham et al., 1990; Vlastélic & Pietruszka, 2016) despite small changes in trace elements and Pb, Sr, Nd, Hf isotopic ratios (Albarède et al., 1997; Valstélic et al., 2005, 2007, 2009; Bosch et al., 2008; Pietruszka et al., 2009). Therefore, the different groups of erupted compositions must originate from processes taking place inside the feeding system (Pichavant et al. 2016 and references therein). Indeed, deep clinopyroxene (± olivine) fractionation has been proposed to generate AbG compositions (Kornprobst et al., 1979, 1984; Albarède et al., 1997) whereas olivine fractionation would be responsible for the genesis of SSB. The other groups (Oceanites and Differentiated Lavas) would derive from SSB-type melts through processes taking place at shallow levels in the feeding system, respectively assimilation of olivine xenocrysts (Welsch et al., 2009) and magma differentiation (Upton & Wadsworth, 1966; Albarède et al., 1997).

Knowledge of the physico-chemical conditions of magmas is a prerequisite for modeling igneous systems and volcanic eruptions. Possible approaches to reach this goal include geothermometry and geobarometry on phenocryst assemblages and cumulate rocks (Upton et al., 2000; Boudoire et al., in prep.; Brugier et al., 2016b), glass inclusion studies (Bureau et al., 1998a; b; Famin et al., 2009; Di Muro et al., 2014) and experimental simulations (Di Carlo et al., 2006; Pichavant et al., 2009; 2014). Pichavant et al. (2016) has recently emphasized the paucity of experiments on Piton de la Fournaise compositions and especially the lack of high pressure experimental data in presence of volatiles. Several investigations of La Réunion magmas have been carried out at 0.1 MPa (Tilley et al., 1971; Fisk et al., 1988; Villeneuve, 2000). However, only one high pressure study is available and it was performed under volatile-free conditions (Fisk et al., 1988). Pichavant et al. (2016) noted problems with the application of the high pressure experiments of Fisk et al. (1988) to the PdF. In particular, the Fisk et al. (1988) data imply relatively deep magma fractionation, in a pressure range difficult to reconcile with the presence of shallow crustal storage zones beneath the PdF. Determination of (1) the pressure of the transition from clinopyroxene to olivine as the liquidus phase and (2) the lower pressure limit for clinopyroxene to crystallize before plagioclase, both in presence of H2O and CO2, were identified as critical experimental objectives for constraining the structure of the feeding system at Piton de la Fournaise (Pichavant et al., 2016).

This paper details an experimental study on a Steady State Basalt from Piton de la Fournaise in presence of volatiles. The main objective is to determine SSB crystallization sequences under conditions representative of the magmatic conditions on the PdF. The pressure range explored in this paper is deliberately chosen to be < 50 MPa, to simulate processes taking place in the shallowest part of the feeding system. Experimental results obtained at higher pressures are presented in a companion study (Brugier et al., 2016d).

2 Experimental approach and starting sample selection

The sample used in this paper (REU0912-04) comes from the eruptive activity of PdF in December 2009. Fissures opened on the southern flank of the volcano, running parallel to the Dolomieu crater. The eruption emitted 0.16 Mm^3 of nearly aphyric relatively Mg-rich basalts belonging to the SSB series (Staudacher et al., 2016). The sampling (performed by A. Di Muro) yielded cm-sized fresh scoria. Olivine is the only mineral phase present, rarely appearing as a proper phenocryst (A. Di Muro, personal communication); clinopyroxenes and feldspars plagioclases could be described as micro-phenocryst and/or microliths.

Both volatile-free and volatile-bearing high pressure experiments were performed at 0.1 MPa and 50 MPa, respectively on REU0912-04 (Table 1) and, so, our experimental results are applicable to SSB lava series erupting on the PdF. The 0.1 MPa experiments were conducted at two fO2 (NNO, NNO-0.5 where NNO is the fO2 of the Ni-NiO equilibrium) and at various temperatures (from 1215°C to 1160°C). The choice of such a T-fO2 range follows a recent compilation of magmatic temperatures and oxygen fugacities for PdF lavas (Pichavant et al., 2016). Although volatile-free experiments are not directly applicable to PdF lavas which contain dissolved volatiles, they provide reference informations for petrological interpretations as well as for monitoring activities, such as magmatic temperatures.

The pressure of the volatile-bearing experiments (50 MPa) was chosen to be representative of the "shallow feeding-system" (Lénat et al., 2012a; Di Muro et al., 2014; Michon et al. 2015) and of the potential magmatic storage zone defined by Peltier et al. (2009). Both are estimated at depths of 1.5 to 2.5 km (50-60 MPa). The choice of volatile compositions for the high pressure experiments was guided by previous observations and analyses of melt and/or fluid inclusions in olivines (Bureau et al. 1998a; 1998b; Famin et al., 2009; Welsch et al;, 2013; Di Muro et al., 2014) and clinopyroxenes (Boudoire et al, in prep). These data show that H2O and CO2 are the most important volatile components in the PdF magmatic system and, consequently, the 50 MPa experiments were performed under fluid-present conditions (H2O-CO2 mixtures). Glass inclusions show a wide range of volatile concentrations, e.g., H2O from 0.1 to 1.55 wt% and CO2 from < 100 ppm to 0.32 wt% corresponding to a wide range (from 0.2 to 420 MPa) of fluid-melt saturation pressures (Bureau et al., 1998 a; b). The 50 MPa experiments are thus expected to simulate the shallowest part of the plumbing system which feeds most recent eruptions.

3 Experimental methods

3.1 Starting material

REU0912-04 was ground in an agate mortar and fused in air at 1400°C, 0.1 MPa in a Pt crucible. Two cycles of melting (3-4h each), with grinding in between, were performed, yielding a homogeneous glass whose composition was checked by electron microprobe (Table 1). The glass was then crushed and stored in an oven.

3.2 0.1 MPa experiments

These were carried out in a vertical gas-mixing furnace using the wire-loop method. Two series of experiments were performed at NNO (the fO2 of the Ni-NiO equilibrium) and NNO-0.5, as controlled by CO-CO_2 gas mixtures (Deines et al., 1974). Experimental temperatures, monitored with Pt-PtRh thermocouples, ranged from 1215°C to 1160°C in each fO2 series (Table 2). The experiments were quenched electrically in air. To minimize Fe loss from the charge to the suspension wire, experiments were repeated under constant T-fO_2 conditions during 3 cycles of ~4 h (each starting with fresh glass) to progressively saturate the same suspension wire with Fe. Intermediates charges were quenched then dissolved in HF whereas the charge from the last cycle was retained for detailed study.

3.3 50 MPa experiments

$Au_{80}Pd_{20}$ capsules (length 15-25 mm, internal diameter 2.5 mm, wall thickness 0.2 mm) were used as containers. These were loaded with about 30 mg of REU0912-04 glass powder plus the fluid components (H2O and CO2). H2O was introduced as distilled demineralized water with a syringe and CO2 as $Ag_2C_2O_4$ powder. H_2O and $Ag_2C_2O_4$ were weighed so as to generate charges with variable $XH_2O_{in.}$ [initial molar $H_2O/(H_2O+CO_2)$] while keeping the $(H_2O+CO_2)/(H_2O+CO_2+glass)$ mass ratio constant at ~10%. In this study, $XH_2O_{in.}$ ranged from 1 to 0 which corresponds to CO2-free and nominally H2O-free conditions, respectively. In a few cases, when the $XH_2O_{in.}$ was too small, the mass of glass powder was increased to allow the mass of H2O to be more precisely weighted. All capsules were sealed by arc welding or by PUK, keeping them in a liquid nitrogen bath to prevent water loss. Once sealed, they were put in an oven for several hours and reweighted to check for leaks.

The phase equilibrium experiments were carried out in 2 identical internally heated pressure vessels, working vertically and pressurized with Ar-H_2 mixtures obtained by sequential loading of H_2 and Ar at room temperature (Scaillet et al., 1992). Initial H_2 pressures were fixed at 3 bar. Total pressure was recorded by a transducer calibrated against a Heise Bourdon tube gauge (uncertainty ± 20 bar). A double winding Mo furnace was used, allowing near-isothermal conditions in the 2-3cm long hot-spot (gradient < 2-3°C cm^{-1}). Temperature was measured by two thermocouples (type S) and was recorded continuously (total uncertainty ±5°C). Run durations ranged from 1.5 to 18h, and all of them were drop-quenched, resulting in nearly isobaric quench rates of ~100°C s^{-1} (Di Carlo et al., 2006).

Attempts were made to calibrate the fH2 in our phase equilibrium experiments from fH2 sensor experiments. These consisted in separate experiments in which sensor capsules (made of CoPd-CoO + H2O mixtures, Taylor et al., 1992) were equilibrated in the same temperature range and for the same initial H2 pressure and total pressure than the phase equilibrium experiments. The sensor experiments lasted for 3-5 days, sufficient to allow the CoPd alloys to equilibrate. They were carried out at 1200°C, 1150°C and 1100°C. Analysis of the composition of the CoPd alloy allows the fO_2 of the sensor capsule to be determined (Pownceby & O'Neill, 1994). The fH_2 of the sensor experiment is then obtained from the water dissociation equilibrium using the determined fO_2, the dissociation constant of water (Robie et al., 1979) and the fugacity of pure water at the experimental P and T (Holloway, 1987). However, the 1200°C sensor experiments failed and only two fH2 values are available, one at 1150°C (1.8 bar) and the other at 1100°C (5.23 bar, Table 3). Therefore, our initial objective to calibrate the fH2 in our phase equilibrium experiments was not entirely successful. For temperatures without a corresponding sensor experiment, fH2 were estimated equal to 3 bar (Table 3).

Several capsules with different $XH_2O_{in.}$ were run together in the same experiment (i.e., under constant P-T-fH_2). For each capsule, the fH2O was determined from the H2O content of the quenched glass, using the thermodynamic model for H2O solution in multicomponent melts of Burnham (1969). The fO2 of each charge is then calculated from the water dissociation equilibrium, using the fH2 and fH2O determined above, and the dissociation constant of water (Robie et al., 1979). Uncertainties on our log fO2 values are of the order of 0.5 log units, i.e., higher than in studies of the same type (e.g. Martel et al., 1999; Costa et al., 2004; Pichavant et al., 2002) mainly because our fH2 are known less precisely. In this study, fO2 are expressed as deviations from the NNO buffer, calculated at the experimental P and T (ΔNNO values in Table 3).

At the end of the experiment, capsules were weighed to check for leaks and then opened. For each capsule, fragments of the run product were mounted in epoxy and polished for scanning electron microprobe observations and electron microprobe analyses. Glass chips from selected charges were prepared for FTIR analyses. The metallic pellets in the sensor capsule were recovered, mounted in epoxy, polished and then analyzed by electron microprobe.

Special care was paid to mitigate the Fe loss problem in our experiments, given our relatively Fe-rich melt compositions and reducing fO2. Apart from the use of AuPd alloys as capsule materials (Kawamoto & Hirose, 1994; Hall et al., 2004; Di Carlo et al., 2006; Barr & Grove, 2010; Balta et al., 2011), both the "capsule Fe pre-saturation" (Grove, 1982) and the "Fe pre-enrichment” methods (Brugier et al., 2015) were tested. Difficulties were encountered with the “capsule Fe pre-saturation” method, such as uncertainties in the definition of conditions needed to saturate the AuPd alloy with the proper amount of Fe (see Balta et al., 2011). In addition, long durations are needed for the preparation of chemically homogeneous Fe-noble metal alloys at high temperatures (Gaillard et al., 2003) and for the dissolution of Fe doping materials. In fH2-buffered experiments as in this study, fO2 change between capsules in the same experiment and this would in principle require the preparation of different capsule materials. Consequently, “capsule Fe pre-saturation” was considered impracticable. The “Fe pre-enrichment” method was developed later than the initiation of this study (Brugier et al., 2015) and, so, was not applied to the 50 MPa experiments presented here but tested in higher pressure experiments (Brugier et al., 2016d).

4 Analytical methods

All charges were systematically examined by SEM under back-scattered electron mode (TESCAN Mira 3 XMU instrument, joint laboratory ISTO-BRGM) to confirm the identification of mineral phases and check for quench crystallization. Electron microprobe analyses were performed with a CAMECA SX FIVE electron microprobe at the ISTO-BRGM laboratory (Orléans) and either a CAMECA SX FIVE or a SX-50 at the CAMPARIS laboratory (Paris). Analyses were performed under 15 kV acceleration voltage, 6 nA sample current, 10 s counting time on peak and 5 s counting time on background. The Co-Pd alloys used as sensors were analyzed under 20 kV and 20 nA. For mineral phases, the electron beam was focused whereas, for interstitial glasses, a defocused beam (10 µm) was used to minimize alkali migration (Di Carlo et al., 2006). Relative analytical errors are 1% (SiO_2, MgO, CaO), 1-2% (Al_2O_3), 2-4% (FeO, Na_2O) and 5-10% (TiO_2, K_2O). Phase proportions and Fe losses were calculated for each charge using a least-squares mass-balance routine computed after Albarède (1995), using the electron microprobe compositions of the glass starting material and of all solid phases coexisting in the charge. The regression was based on nine major oxides, excluding MnO and P_2O_5.

For crystal-free or crystal-poor charges, H_2O and CO_2 in experimental glasses were analyzed by FTIR, using a Thermo Fisher instrument comprising a Nicolet 6700 spectrometer attached to a Continuum microscope. Spectra were acquired between 650 and 7000 cm^{-1} on doubly polished glass wafers (thicknesses between 50 and 100 µm, measured with an automated petrographic microscope) using an IR light source, a KBr beamsplitter and a liquid nitrogen cooled MCT/A detector. Between four and six spots (aperture mostly 50 µm) were analyzed on each sample. Concentrations of H_2O and CO_2 were determined from the Beer-Lambert law. Densities of analyzed glasses were calculated from the density of the volatile-free starting glass measured at room conditions (REU0912-04: 2.7365 ± 0,007), and using a partial molar volume of H_2O of 12 cm^3mol^{-1} (Richet et al., 2000) to compute the density of hydrous glass samples (Pichavant et al., 2009; 2014). H_2O concentrations were obtained from the absorbance of the 3510-3530 cm^{-1} band, with a linear baseline drawn between 3800 and 2500 cm^{-1}, and using an extinction coefficient (ε_{3530}) of 63 L mol^{-1} cm^{-1} (Mercier et al., 2010). For CO_2, the absorbance of the 1515 cm^{-1} band was measured on background-subtracted spectra (Dixon et al., 1995). An extinction coefficient (ε_{1515}) of 398 L mol^{-1} cm^{-1} was used (Bureau et al., 1998a). For crystal-rich charges, the "by-difference" method was used to estimate the concentration of dissolved H_2O (e.g. Devine et al., 1995). During each electron microprobe session, the difference to 100% of glass electron microprobe analyses was calibrated against the dissolved H2O content, using glasses of known H_2O concentrations (i.e., those previously analyzed by FTIR) as secondary standards. The "by-difference" method was applied to the few CO2-free as well as to the CO_2-bearing charges because, in this study, glass CO_2 concentrations are always < 0.1 wt%. Therefore, the overestimation in H_2O concentration introduced by the presence of dissolved CO_2 (which increases the difference to 100%) is negligible.

5 Experimental results

Experimental conditions and results are detailed in Tables 2 and 3, and experimental compositions in Tables 4 and 5 respectively for the 0.1 and 50 MPa charges. In total, 14 0.1 MPa and 23 50 MPa charges (corresponding to 6 experiments) are reported. All experimental charges were equilibrated under slightly to moderately reduced redox conditions. ΔNNO values of the 0.1 MPa (0 to -0.5) and 50 MPa (0 to -1.7) experiments overlap.

5.1 Fe loss and evaluation of equilibrium

The importance of Fe loss (relative values) can be evaluated from the mass-balance calculations (Tables 2 and 3). In the 0.1 MPa experiments, only two charges have significant (i.e., > 5%) Fe losses (one has > 10%), indicating that this problem has been efficiently counteracted. In the 50 MPa experiments, eight charges have > 10% Fe loss and two > 20%. Fe loss affects mainly the highest temperature (1170 and 1200°C) charges: five of these nine charges have > 10% Fe loss, including the two charges with > 20% Fe loss (Re049_II and Re043_III, Table 3). At lower temperatures (1150, 1125, 1101°C), only three of the fourteen charges have > 10% Fe loss. On average, the Fe loss is < 10% (8.5%) for the 23 high pressure charges and we conclude that this problem was kept at a relatively low level. No systematic differences in phase assemblages or compositions were found between charges having contrasted Fe losses.

All charges in this study are of crystallization type (e.g., starting from glass), whether performed under volatile-free (0.1 MPa experiments) or in presence of H2O-CO2 mixtures (50 MPa experiments). Although no reversals have been performed, the following lines of evidence allow to test the approach toward equilibrium in our experiments.

(1) The high pressure experiments lasted for 1.5 to 18h, sufficient for equilibrium crystallization of hydrous basaltic melts on the basis of previous studies (Barclay & Carmichael, 2004; Di Carlo et al., 2006; Pichavant & Macdonald, 2007; Pichavant et al., 2014). The 3-4h long 0.1 MPa cycles yielded phase assemblages and crystal proportions that are mutually consistent and evolve predictably with temperature (Tables 2).

(2) Crystals have equant, euhedral or tabular morphologies and their distribution is homogeneous in the charges. Crystal settling was not encountered and no quench crystals were detected by SEM.

(3) Sums of residuals from mass-balance calculations ($\sum R^2$) are ≤ 0.5 for 12 0.1 MPa charges. Only 2 charges (those with the highest Fe losses) have $\sum R^2 > 1$. This indicates excellent balance of silicate components between coexisting phases. In the 50 MPa charges, $\sum R^2$ are more variable, a consequence of higher Fe losses but also of additional analytical problems (Na loss) and heterogeneity of mineral phases. However, 6 charges have $\sum R^2 \leq 0.5$ and 10 charges have $\sum R^2 < 1$.

(4) Silicate glasses are chemically homogeneous as no compositional gradient has been detected from electron microprobe analyses.

(5) Compositions of olivines are rather homogeneous. If olivine compositions are averaged for a given charge, tightly grouped olivine-melt Fe-Mg exchange coefficients (K_d Ol-l) are obtained (Tables 2, 3 and see below), in the range expected for olivine-liquid equilibrium (Di Carlo et al., 2006; Pichavant & Macdonald, 2007; Pichavant et al., 2014). Nevertheless, a zoned olivine has been recognized by SEM (see below). Olivine Ca contents are relatively dispersed and there are significant variations in

olivine Fe contents (and so in Fo) within a given charge (Tables 4-5), implying small chemical heterogeneities.

(6) Clinopyroxenes are relatively chemically homogeneous. In some charges (7, Table 4; Re046_I, Table 5), they can be rather heterogeneous. For some crystals, core-rim zonations have been recognized by SEM. Analytical problems due to the small size of the crystals (commonly < 10-15 µm) also contribute to the chemical dispersion. This explains why clinopyroxene-liquid Fe-Mg exchange coefficients (K_d Cpx-l) are relatively dispersed, ranging from 0.22 to 0.57 (Tables 2-3). However, the average K_d Cpx-l data (see below) is consistent with literature values for clinopyroxene-liquid equilibrium (Di Carlo et al., 2006; Pichavant & Macdonald, 2007; Pichavant et al., 2014).

(7) Plagioclases are chemically sub-homogeneous (Tables 4-5).

(8) For a number of charges, negative phase proportions have been obtained from the mass balance calculations (Tables 2-3). In the 0.1 MPa charges, these negative values are mostly < 1% absolute, in the same range as the uncertainty on calculated proportions ($\pm$ 1%). However, some 50 MPa charges have larger negative proportions (Re048_V, Re046_III, Table 3), a consequence of the heterogeneities in phase compositions noted above.

Despite chemical heterogeneities noted above for the experimental phases, we conclude that crystal-liquid equilibrium was globally closely approached in both the 0.1 and 50 MPa experiments.

5.2 Phase equilibria

Olivine, clinopyroxene and plagioclase are the three major mineral phases crystallizing in the experiments. These are accompanied by Cr-spinel, systematically in the 0.1 MPa and occasionally in the 50 MPa experiments. Although olivine is the most frequent mineral phase (being present in 24 on a total of 37 charges), the maximum olivine proportion is only 6% (Tables 2-3). In comparison, both clinopyroxene and plagioclase can reach higher proportions (e.g., 15.9 and 16.3% respectively in the 1100°C, 50 MPa charge Re046_V, Table 3).

At 0.1 MPa, phase assemblages are similar for the two fO2 investigated (NNO-0.5 and NNO), even if crystallization sequences and crystallization temperatures differ between the two experimental series (Fig. 1). Olivine is the liquidus phase in both series. It appears at a lower temperature (between 1182 and 1177°C) at NNO than at NNO-0.5 (between 1205 and

1182°C; Fig.1). Crystallization of olivine is followed either by plagioclase plus clinopyroxene (appearing together between 1172 and 1168°C) at NNO-0.5 or by plagioclase appearing as the second phase (between 1172 and 1165°C) followed by clinopyroxene as the third phase (between 1165 and 1160°C) at NNO (Fig. 1). The NNO experimental series systematically record lower crystallization temperatures than the NNO-0.5 series. "Cotectic" (Ol+Cpx+Plag) crystallization starts between 1172 and 1168°C at NNO-0.5, and between 1165 and 1160°C at NNO (Fig. 1). In both series, spinel is present at all experimental temperatures although in variable amounts between charges.

At 50 MPa, five temperatures have been investigated from 1100 to 1200°C. The sequence of appearance of mineral phases on the liquidus is clearly established by the T-$XH_2O_{in.}$ data (Table 3 and Figure 2a). They show that, upon lowering $XH_2O_{in.}$, olivine comes in first as the liquidus phase followed by clinopyroxene and then plagioclase (Fig. 2a). The succession from melt (L), olivine- (L+Ol) to clinopyroxene-bearing (L+Ol+Cpx) phase assemblages is demonstrated at 1175, 1150 and 1125°C, and the succession from L+Ol+Cpx to plagioclase-bearing (L+Ol+Cpx+Plag) assemblages at 1100°C. Note that one 1150°C charge (Re048_IV) plotting in the L+Ol+Cpx domain lacks clinopyroxene and so is inconsistent with the others. Experimental phase relations are also shown on a T-H_2O in melt diagram (Fig. 2b) constructed from the determined glass H2O concentration data (Table 3). At 1200°C, the highest experimental temperature explored, all charges are supra-liquidus even for melt H2O contents as low as 0.5 wt%. It is worth mentioning that the H2O in melt region < 0.5 wt% (grey field in Fig. 2b) is excluded because reduction of the relatively Fe3+ rich starting glass by H2 from the pressure medium generates a minimum of ~0.5 wt% H2O in the charge. At 1170°C, olivine appearance on the liquidus is bracketed by charges Re040_III and Re040_IV (0.8-1 wt% H2O, Table 3) and, at 1150°C, by charges Re048_I and Re048_II (1.2-1.2 wt% H2O, Table 3). At temperatures of 1125 and 1100°C, only sub-liquidus charges were obtained. Both the olivine and plagioclase saturation curves were drawn by taking into account all experimental charges. However, for the clinopyroxene saturation curve (Fig. 2b), two charges were ignored (Re048_IV at 1150 and Re043_I at 1170°C; Table 3; Fig. 2b). These inconsistencies are due to difficulties with the determination of glass H2O concentrations. FTIR data are available only for 11 charges and the "by difference" method has a sensitivity of ± 0.5 wt% absolute, i.e., it is very imprecise for glass H2O concentrations < 2 wt% as in this study. These factors, and the generation of H2O during the experiment (see above), explain the uncertainty on the location of the clinopyroxene saturation curve (Fig. 2b).

In summary, our experimental data on REU0912-04 demonstrate that liquidus temperatures are below 1200°C and that olivine is the liquidus phase both at 0.1 MPa for the two fO2 series and at 50 MPa. Crystallization sequences are more variable depending on experimental conditions. Clinopyroxene is the second phase in the crystallization sequence at 50 MPa in presence of volatiles. At 0.1 MPa volatile-free, it crystallizes second (together with plagioclase) at NNO-0.5 whereas, at NNO, clinopyroxene is replaced by plagioclase as the second crystallizing phase.

5.3 Composition of crystalline phases

5.3.1 *Olivines*

Olivines in the 0.1 MPa experiments have Fo between 81.7 and 86.4, around 84 on average (84.2 for the NNO and 83.9 for the NNO-0.5 series, Table 4). Olivines in the 50 MPa experiments exhibit a larger Fo range, from 74.6 to 86.4 (Table 5), 85.1 on average. The average Fo decreases with temperature from 84.8 (1170°C), 84.6 (1150°C), 82.6 (1125°C) to 78.4 (1100°C, Table 5). In the same way, Fo decreases with decreasing XH_2O_{init} in a given experiment, e.g., charges in run Re046 have Fo (averaged on each charge) progressively decreasing from 80.6 to 75.4 (Table 3; 5). Nevertheless, olivines from a given charge can have variable Fo contents (Tables 4-5). These variations (±1-2 Fo units) are the consequence of variable Fe concentrations which raises the possibility of a dispersion of analytical nature.
Compositions of experimental olivines are plotted on Figure 3a and b, respectively, for the 0.1 and 50 MPa charges. Our experimental olivines and olivines from the 1977-1998 PdF lavas (Boivin & Bachèlery, 2009) overlap. Compositions of olivine in the December 2009 eruption from where our starting sample comes from are also quite well reproduced experimentally, either at 0.1 or at 50 MPa. Nevertheless, experimental olivines are more CaO-rich than natural olivines. They evolve along "vertical" trends (Fig. 3a; b) suggesting CaO dispersion. The three 1170°C olivine compositions that are identical to the December 2009 data points (Fig. 3b) correspond to core analyses of the only zoned olivine found in this study (Table 3).

The olivine –liquid Fe-Mg exchange coefficient (Kd Ol-liq) calculated by averaging the data for the 24 ol-bearing charges (at 0.1 and 50MPa, Tables 2-3) is 0.31±0.03, in agreement with literature values for hydrous basaltic experiments (0.27-0.33, Sisson & Grove, 1993; 0.25-0.39, Righter & Carmichael, 1996; 0.32±0.04, Pichavant & Macdonald; 0.34±0.05, Pichavant et al., 2014). This Kd Ol-liq uses melt FeO contents calculated from glass compositions (Kress & Carmichael, 1991) for P-T-fO2 conditions specific of each charge (Tables 2-3).

Average Kd Ol-liq are 0.29±0.02 in the 0.1 MPa volatile-free experiments and 0.32±0.02 in the 50 MPa fluid-present experiments.

5.3.2 *Clinopyroxenes*

Clinopyroxenes are augites with 38-53% En, 38-45% Wo, 7-18% Fs (Tables 4-5) and Mg# (calculated with total Fe as Fe2+) between 68 and 87 (Fig. 4a). They contain 2.24 to 11.05 wt% Al2O3 (Fig. 4a), 0.67 to 4.37 wt% TiO2 and 0 to 1.15 wt% Cr2O3 (Tables 4-5). Both the 0.1 and 50 MPa clinopyroxenes have similar compositions (Fig. 4a; b). Mg# increases with temperature and similar trends of Al2O3 enrichment with decreasing Mg# are observed at the different temperatures (Fig. 4a). Experimental compositions are in good agreement with natural clinopyroxenes from the 1977-1998 PdF lavas (Fig. 4a; b). On the Al-Ti plot (Fig. 4b), our experimental clinopyroxene compositions are quite dispersed. They show a slight tendency to follow the "Mg-rich augites" trend (Boivin and Bachèlery, 2009), marked by a higher Al(at.) for a given Ti(at.), but the experimental dataset also comprise compositions poor in Al that plot right of the two regression lines. Part of the dispersion in Al content is due to variations within crystals as chemical zonations were detected by SEM in some charges. The average Fe-Mg clinopyroxene-liquid exchange coefficient (Kd Cpx-liq), calculated with Fe as Fe2+ in both phases, is 0.31±0.10 (averaging all the data from Tables 2-3). If extreme values from charges 13 (series NNO), 14 (series NNO-0.5, Table 2) and Re046_I (Table 3) are filtered out, the average Kd Cpx-liq becomes 0.27±0.03, in excellent agreement with literature values for hydrous basaltic compositions (0.26-0.31, Sisson & Grove, 1993; 0.29±0.08, Pichavant & Macdonald, 2007; 0.27±0.06, Pichavant et al., 2014).

5.3.3 *Plagioclases*

Plagioclases in the 0.1 and 50 MPa experiments are labradorites with 57-69% An, 30-40% Ab and 1-5% Or (Tables 2-3), similar to plagioclases in the 1977-1998 PdF lavas (Boivin & Bachèlery, 2009). The average Na-Ca plagioclase-liquid coefficient is close to 1 (0.94±0.10), i.e. relatively low, but consistent with plagioclase-liquid partitioning data for low H2O melt concentrations (e.g., Pichavant et al., 2002) as in this study.

5.3.4 *Spinels*

Spinels in the 50 MPa experiments could be analyzed in only a few charges. These are Cr-spinels with Mg# ranging from 46 to 52%, high Cr# values (66-67%), ~25 wt% FeO, Al2O3 contents of ~14 wt% and Cr2O3 contents around 43 wt%. The oxides analyzed in the 0.1 MPa charges were glass-contaminated because of their small size, but they have higher FeO (32 to 45 wt%) andlower Cr2O3 (16.5 to 27 wt%) than in the 50 MPa charges, and various Al2O3 contents (13 to 24 wt%).

5.4 Melt compositions

Compositions of experimental glasses in the 0.1 and 50 MPa charges (Tables 4-5) are shown in Figure 5 and compared, on the one hand, with the composition of the starting glass and, on the other hand, with interstitial glasses in the 1977-1998 PdF lavas. Experimental compositions and trends depend on the phase assemblage. Glasses from supra-liquidus charges have the highest MgO contents (8.4-7.3 wt%) and steady CaO/Al2O3 (0.84-0.78, Fig. 5a), and they cluster around the composition of the starting glass. Glasses in equilibrium with olivines show a slight MgO decrease (8.1-7.5) at constant CaO/Al2O3 (0.81). The largest compositional variations are for glasses from L+Ol+Cpx and L+Ol+Cpx+Plag charges which are associated with the lowest temperatures and highest proportions of crystals. L+Ol+Cpx melts record a strong decrease of MgO contents from 8.1 to 6.1 wt% with CaO/Al2O3 decreasing from 0.81 to 0.71 (Fig. 5a), and L+Ol+Cpx+Plag melts from 5.9-5.4 wt% MgO with CaO/Al2O3 decreasing from 0.68 to 0.66. Glass K2O contents slightly increase with progressive crystallization from 0.67 to ~1 wt% K2O for melts in equilibrium with plagioclase (Fig. 5b). Although the 0.1 and 50 MPa glasses overlap, the 0.1 MPa data are less variable than the 50 MPa compositions because crystallinities are kept higher in the former (maximum crystal proportions 12%, Table 2) than in the latter charges (maximum crystal proportions 38%, Table 3), and most of the glass variability is in fact assumed by the 50 MPa charges.

The high-MgO end of experimental glasses and matrix glasses from the 1977-1998 PdF lavas (Boivin & Bachèlery, 2009) overlap (Fig. 5a). Glasses from the L+Ol+Cpx+Plag and most of the L+Ol+Cpx charges have CaO/Al2O3 lower than their natural counterparts (Fig. 5a). This implies that clinopyroxene and/or plagioclase fractionation is not marked in the chemistry of matrix glasses from the 1977-1998 activity. This is consistent with the observation that the phenocryst mineralogy of PdF lavas is largely dominated by olivine (Lacroix, 1923; Albarède et al., 1997; Boivin & Bachèlery, 2009; Welsch et al., 2013). In fact, clinopyroxene and plagioclase are very rarely found as phenocrysts in lavas.

5.5 Glass volatile concentrations

The H_2O and CO_2 concentration data for the 50 MPa glasses (Table 3) are illustrated in Figure 6. Glass H2O contents range from 0.7 to 1.4 wt% and CO2 from 128 to 551 ppm. The data cluster near the VOLATILECALC model 50 MPa isobar (Newman and Lowenstern, 2002) despite two points showing significantly higher CO2 concentrations. Overall, the experimental data are consistent with the natural glass inclusion data. Both group of data overlap although there is a tendency for experimental glasses to plot at slightly higher H2O concentrations. Therefore, our 50 MPa experiments adequately simulate natural volatile concentration regimes as recorded in the glass inclusions.

6 Discussion

6.1 Validation of experimental results

Before discussing the implications of the experimental results for the shallow feeding system of Piton de la Fournaise, it is first necessary to test their applicability. This is done below by comparing our synthetic charges with the mineralogical and petrological characteristics of PdF eruption products.

In our experiments, mineral phases, assemblages and compositions typical of SSB erupted in the modern history of PdF have been obtained (Albarède et al., 1997). The occurrence of olivine as the liquidus phase both at 0.1 and 50 MPa is consistent with olivine being by far the main phenocryst phase in PdF products (Lacroix, 1923; Upton & Wadsworth, 1972; Kornprobst et al., 1984; Albarède et al., 1997; Fretzdorff & Haase, 2002; Boivin and Bachèlery, 2009; Welsch et al., 2009). Experimental olivine compositions (Fo74-86) match the composition of olivines in December 2009 products and in products erupted during the 1977-1998 activity (Boivin & Bachèlery, 2009; Fig. 3), which are mainly SSB. In this respect, the bimodal Fo values at 84 and 82 often proposed for SSB (Boivin & Bachèlery, 2009) corresponds to a Fo range well covered in the experimental charges. Experimental clinopyroxenes and plagioclases closely reproduce their respective natural compositions in 1977-1998 PdF lavas (Albarède et al., 1997; Boivin & Bachèlery, 2009; Di Muro et al., 2014;

Fig. 4) and also in plutonic ultra-mafic and mafic xenoliths (Ludden, 1978a; Upton et al., 2000; Brugier et al., 2016b). It is also important to note that melt compositions agree with matrix glasses from PdF eruption products (Fig. 5), and that glass volatile concentrations in the 50 MPa experiments are close to natural concentrations in glass inclusions (Fig. 6). We conclude that our experiments closely simulate the evolution of relatively evolved crystal-poor SSB-like basaltic magmas on the PdF such as those erupted during the 1977-1998 period and more recently.

6.2 Comparison with previous experimental studies

Our experiments bring new results applicable to La Réunion magmas. However, before discussing them, it is useful to compare our results with previous experimental studies on La Réunion products (Tilley et al., 1971; Fisk et al., 1988; Villeneuve, 2000; see Pichavant et al., 2016 for a review).

Different phase assemblages were obtained in the previous 0.1 MPa volatile-free studies. Certain compositions yielded olivine as the liquidus phase (Tilley et al., 1971; Fisk et al., 1988; Villeneuve, 2000) whereas, for others, olivine was replaced by plagioclase on the liquidus (Tilley et al., 1971; Villeneuve 2000). Liquidus temperatures (1178-1522°C, Tilley et al., 1971; T > 1206°C, Fisk et al., 1988; from < 1200 to > 1250°C, Villeneuve, 2000) equal or higher than in this study (1205 and 1182°C, Fig. 1) were obtained. Both Fisk et al. (1988) and Villeneuve (2000) crystallized olivine plus plagioclase phase assemblages. Such differences between experimental results can be explained by the wide diversity of starting compositions used in previous studies, which ranged from SSB-type lavas, olivine-rich “oceanites” to differentiated lavas, the latter from PdN. It is also worth emphasizing that some experiments were performed in air or under an Ar atmosphere (Tilley et al., 1971), i.e., under too oxidized conditions, whereas others were run at the iron-wüstite buffer, i.e., under too reduced conditions (Fisk et al., 1988). Three SSB-type compositions from the PdF were investigated at NNO by Villeneuve (2000). Either olivine or plagioclase were found to crystallize on the liquidus at temperatures between 1200 and 1250°C and between 1175 and 1200°C, respectively, close to liquidus temperatures from this study. By opposite, clinopyroxene never preceded plagioclase in the crystallization sequence (compare with Fig. 1). “Cotectic” (Ol+Cpx+Plag) crystallization was initiated at 1162.5°C and 1150°C (Villeneuve, 2000), close to our “cotectic” temperature range (< 1168°C for NNO-0.5 and < 1160°C for NNO, Fig. 1). We conclude to a good agreement between our 0.1 MPa results and those of

Villeneuve (2000) especially considering that starting materials were slightly different between the two studies.

Only one high pressure experimental study has been previously carried out on La Réunion products. Fisk et al. (1988) investigated a total of 6 compositions, all coming from the PdN, at between 0.1 and 2000 MPa under volatile-free conditions and fO2 close to iron-wüstite (see Pichavant et al., 2016). The results were used to define a general crystallization sequence for La Réunion magmas. The synthetic diagram constructed by Pichavant et al. (2016) on the basis of their results for the 11 wt% MgO composition shows olivine to be the liquidus phase between 0.1 and 800 MPa for liquidus temperatures systematically >1250°C. Plagioclase crystallizes as the second phase in the sequence between 0.1 and 300 MPa at temperatures > 1200°C. In this pressure range, clinopyroxene is the third phase, and it becomes the second to crystallize in the sequence between 300 and 800 MPa. If it is assumed that Piton de la Fournaise magmas crystallize in the sequence olivine-clinopyroxene-plagioclase (Albarède et al., 1997; Welsch et al., 2009; Brugier et al., 2016b), then the Fisk et al. (1988) experimental results would lead to the conclusion that magma fractionation takes place for the most part at > 300 MPa, near the base of the crust (Pichavant et al., 2016).

6.3 Liquidus phase equilibria

Our 50 MPa experimental results obtained in presence of volatiles differ drastically from Fisk et al. (1988). Indeed, according to their study, olivine should crystallize as the liquidus phase below 1275°C, followed by plagioclase crystallizing below 1210°C and then clinopyroxene below 1175°C. In comparison, our experimental results for a melt H2O content of ~1wt% yield olivine appearing on the liquidus at 1170°C, followed by clinopyroxene below 1150°C and plagioclase as the third crystallizing phase below 1110°C. Although starting compositions differ between the two studies (8 vs. 11 wt% MgO in this study and Fisk et al., 1988), comparison of the results shows that (1) temperatures of crystallization of olivine and plagioclase are severely reduced and (2) the order of crystallization is modified, clinopyroxene replacing plagioclase as the second phase in the crystallization sequence. These modifications on crystallization temperatures and crystallization sequence are interpreted to be due to the presence of volatiles (H2O and CO2) in our experiments. Addition of H2O is known to strongly affect basalt phase equilibria in suppressing plagioclase crystallization and promoting early fractionation of ferromagnesian silicates (Yoder, 1965; Sisson and Grove, 1993; Pichavant and Macdonald, 2007). Our experimental results show that the effect of volatiles is significant even at relatively low concentrations (< 2 wt% H_2O, Table 3). We conclude that the important differences between this study and Fisk et al. (1988) are due to differences in experimental conditions, mainly concerning volatiles. The fluid-present experiments from this study enable the phase equilibria of basaltic melts with volatile concentrations similar to natural glass inclusions to be determined. Results provide constraints directly applicable to the PdF.

6.4 Implications for the shallow feeding system of the PdF

At Piton de la Fournaise, the different groups of erupted products are generally proposed to originate from magmatic processes occurring inside the feeding system. For example, the Abnormal Group has been explained either by deep clinopyroxene fractionation (Kornprobst et al., 1989; Albarède et al., 1997; Famin et al., 2009; Brugier et al., 2016a; d) or by a mechanism of assimilation ("cannibalism") of dunitic cumulates by slightly differentiated melts (Villemant et al., 2009; Salaün et al., 2010). In the case of SSB, olivine fractionation has been classically proposed (Lacroix, 1923; Upton & Wadsworth, 1972; Albarède et al., 1997; Upton et al., 2000; Famin et al., 2009), and this mechanism is actually supported by our experimental results. Indeed, olivine is the liquidus phase at the two experimental pressures explored. Our liquidus temperatures (1205-1177°C at 0.1 MPa and <1200°C at 50 MPa) are consistent with temperatures of PdF lavas (~1200°C, Pichavant et al., 2016). The chemistry of SSB matrix glasses is compatible with olivine fractionation (Fig. 5). The good match between our experimental and natural fO_2 (Boivin & Bachèlery, 2009; Pichavant et al., 2016), on the one hand, and between experimental and natural volatile concentrations (Bureau et al., 1998a; b; Famin et al., 2009; Di Muro et al., 2014), on the other hand, is emphasized. We conclude that most small volume eruptions of SSB composition on the PdF have petrological and geochemical features adequately experimentally simulated in this study. Liquids have ~1 wt% dissolved H_2O, 6-8 wt% MgO, CaO/Al_2O_3 of ~0.8 and their geochemical characteristics are controlled by low-pressure olivine-liquid equilibrium. Our experimental results, which attribute a low pressure origin to the fractionation mechanism at the origin of SSB, enable to better reconcile the petrological and geophysical constraints. The latter provide independent evidence for a low-pressure magma evolution inside the shallow feeding system of the PdF. A dykes and sills network with locally small storage zones has been imaged from near the surface to the base of the volcanic edifice (Lénat et al., 2012a; Lénat, 2016 and references therein). Alternatively, a magma reservoir could reside at the interface between the volcanic edifice and the oceanic crust (Peltier et al., 2009). Therefore, agreement is emerging between the various approaches concerning pressures of magma fractionation on the PdF.

Nevertheless, pressures deduced from certain melt inclusions hosted in olivine (up to 400-500 MPa; Bureau et al., 1998a; b) clearly indicate that olivine fractionation is not limited to shallow pressures but can occur deeper inside the feeding system. This observation could explain certain matrix glass compositions analyzed in 1977-1998 PdF lavas (Boivin & Bachèlery, 2009). These show a strong decrease in MgO (from ~8.7 to ~4.5 wt%), associated with only a modest decrease in CaO/Al2O3 (0.81 to ~0.70), which is more important than in our 50 MPa experimental glasses. These glasses could bear the mark of several olivine fractionation episodes during the magma "raising & storage" history whereas our experimental glasses record only one fractionation process.

The 50 MPa experimental glasses clearly show that most matrix glasses in 1977-1998 PdF lavas (Boivin & Bachèlery, 2009) never experienced plagioclase fractionation. This is an important conclusion because petrologic studies on the PdF have overestimated the role of the plagioclase. Indeed, cotectic Ol+Plag fractionation has been frequently suggested to explain SSB compositions (Ludden, 1978a; Tilley et al., 1971; Fisk et al., 1988), an interpretation that is not supported by our results. Conversely, the role of clinopyroxene has been underestimated, probably because it occurs third in the Fisk et al. (1988) crystallization sequence. Yet, there is geochemical evidence for cryptic clinopyroxene fractionation in PdF products (Kornprobst et al., 1984; Albarède et al., 1997; Brugier et al., 2016a), and petrologic evidence for clinopyroxene being involved in the deep part of the feeding system is growing (Upton et al., 2000; Boudoire et al., in prep; Brugier et al., 2016b; d).

7 Conclusions

The main conclusions of this study are the following:

- Experimental phase equilibria have been determined for one composition typical of Steady State Basalts from Piton de la Fournaise under T-fO2-P-H2O melt conditions representative of the shallow feeding system.
- Both volatile-free 0.1 MPa experiments at NNO and NNO-0.5 and volatile-bearing 50 MPa experiments in presence of H2O and CO2 at NNO to NNO-1.7 have been performed. All experiments were of crystallization type and attainment of equilibrium was globally closely approached.

- Olivine is systematically the liquidus phase at both 0.1 and 50 MPa. Clinopyroxene crystallizes as the second phase in the sequence at 50 MPa, followed by plagioclase. At 0.1 MPa, depending on fO2, plagioclase is the second phase, either alone or accompanied by clinopyroxene.
- Liquidus temperatures are below 1200°C both at 0.1 and 50 MPa, consistent with temperatures inferred for SSB lavas but significantly lower than derived from previous high pressure volatile-free experiments. At 0.1 MPa, cotectic olivine+clinopyroxene +plagioclase crystallization starts < 1168°C (NNO-0.5) and < 1160 (NNO), in agreement with previous 0.1 MPa studies. At 50 MPa and for a melt H2O content consistent with natural concentrations (~1 wt% in glass inclusions), olivine appears at 1175°C, clinopyroxene at 1150°C and plagioclase at 1110°C.
- Experimental assemblages and mineral and glass compositions are in agreement with natural assemblages and compositions in SSB-type lavas. H2O (0.7-1.4 wt%) and CO2 (128-551 ppm) concentrations in experimental glasses are in the same range than in glass inclusions.
- Olivine-liquid, clinopyroxene-liquid and plagioclase-liquid exchange coefficients have been determined for PdF magma compositions thus providing constraints for petrological calculations and models.
- Differences between our experimental results and previous high pressure data are the consequence of the addition of volatiles on phase equilibria. Temperatures of crystallization are strongly lowered, the crystallization sequence is modified and the role of plagioclase needs to be downplayed.
- Our experiments closely simulate the shallow level magmatic evolution of SSB basalts that feed the PdF eruptions. They provide an experimental basis to confirm that magma crystallization in the sequence olivine, clinopyroxene, plagioclase is possible at low pressures. Magma fractionation at Piton de la Fournaise takes place at levels much shallower than previously thought.

8 Ackowledgements

This work was supported by the DEGAZMAG (ANR 2011 Blanc SIMI 5-6 003) projects. Ida Di Carlo is acknowledged for her contribution to the electron microprobe analyses. We thank XX, XX and XX for their helpful reviews.

9 References cited

Albarède, F. (1995) *Introduction to Geochemical Modeling*. Cambridge University Press, 543p.

Albarède, F., Luais, B., Fitton, G., Semet, M., Kaminski, E., Upton, B.G.J., Bachèlery, P. & Cheminée, J.L. (1997) The geochemical regimes of Piton de la Fournaise volcano (Réunion) during the last 530000 years. Journal of Petrology 38, 171-201.

Bachèlery, P. (1981) Le Piton de la Fournaise (Ile de la Réunion): etude volcanologique, structural et pétrologique. PhD Thesis, Université Blaise Pascal, Clermont Ferrand, 215 pp.

Balta, J.B., Beckett, J.R., and Asimow, P.D. (2011) Thermodynamic properties of alloys of gold-74/palladium-26 with variable amounts of iron and the use of Au-Pd-Fe alloys as containers for experimental petrology. American Mineralogist, 96, 1467-1474.

Barr, J. and Grove, T.L. (2010) AuPdFe ternary solution model and applications to understanding the fO_2 of hydrous, high-pressure experiments. Contributions to Mineralogy and Petrology, 160, 631-643.

Boivin, P. & Bachèlery, P. (2009) Petrology of 1977 to 1998 eruptions of Piton de la Fournaise, La Réunion Island. Journal of Volcanological and Geothermal Research 184, 109-125.

Bosch, D., Blichert-Toft, J., Moynier, F., Nelson, B.K., Telouk, P., Gillot, P.Y. & Albarède, F. (2008) Pb, Hf and Nd isotope compositions of the two Réunion volcanoes (Indian Ocean): a tale of two small-scale mantle blobs. Earth and Planetary Science Letters 265, 748-768.

Boudoire, G., Brugier Y.A., Di Muro, A., Wörner, G., Métrich, N., Arienzo, I., Braukmüller, N., Kronz, A., Le Moigne, Y., Michon, L., Pichavant, M. & Zanon, V. (*in prep*) The deep plumbing system of volcanic islands : new insights from recent activity of the NW Rift Zone (NWRZ) of Piton de la Fournaise (La Réunion Island, Indian Ocean).

Bureau, H., Pineau, F., Métrich, N., Semet M.P. & Javoy, M. (1998a) A melt and fluid inclusion study of the gas phase at Piton de la Fournaise volcano (Réunion Islanf). Chemical Geology 147, 115-130.

Bureau, H., Métrich, N., Pineau, F. & Semet M.P. (1998b) Magma-conduit interaction at Piton de la Fournaise volcano (Réunion Island) : a melt and fluid inclusion study. Journal of Volcanological and Geothermal Research 84, 39-60.

Burnham, C.W. (1979) The importance of volatile constituents. In: Yoder, H. S., Jr (ed.) *The evolution of Igneous Rocks*. Priceton University Press, pp. 439-482.

Brugier, Y.A., Alletti, M. & Pichavant, M. (2015) Fe pre-enrichment: A new method to counteract iron loss in experiments on basaltic melts. American Mineralogist 100, 2106-2111.

Brugier, Y.A., Le Moigne, Y., Pichavant, M., Bourdier, J.L., Boudoire, G. & Di Muro, A. (2016a) Compositional variability of basaltic spatters activity in the Plaine des Sables (Reunion island): Volcanological and petrological constraints.

Brugier, Y.A., Boudoire, G., Pichavant, M., Le Moigne, Y., Di Muro, A., Clague, D., Bachèlery, P. & Bourdier, J.L. (2016b) Petrological and mineralogical characteristics of plutonic rocks from the Plaine des Sables (Piton de la Fournaise volcano, La Réunion Island) - Implications for crystallization processes of Réunion lavas.

Brugier, Y.A., Pichavant, M. & Di Muro, A. (2016d) Marked pressure-induced changes in phase equilibria for a Piton de la Fournaise volcano (La Réunion island) lava – implications for the deep feeding system.

Costa, F., Scaillet, B. & Pichavant, M. (2004) Petrological and experimental constraints on the pre-eruption conditions of Holocene dacite from Volcan San Pedro (36°S, Chilean Andes) and the importance of sulphur in silicic subduction-related magmas. Journal of Petrology, 45, 855-881.

Deines, P., Nafziger, R.H., Ulmer, G.C., and Woermann, E. (1974) Temperature-oxygen fugacity tables for selected gas mixtures in the system C-H-O at one atmosphere total pressure. Bulletin of the Earth and Mineral Sciences Experiment Station, Number 88, Pennsylvania State University.

Devine, J.D., Gardner, J.E., Brack, H.P., Layne, G.D. & Rutherford, M.J. (1995) Comparison of microanalytical methods for estimating H2O contents of volcanic glasses. American Mineralogist 80, 319-328.

Di Carlo, I., Pichavant, M., Rotolo, S. G., and Scaillet, B. (2006) Experimental crystallization of a high-K arc basalt: the golden pumice, Stromboli volcano (Italy). Journal of Petrology 47, 1317-1343.

Di Muro, A. (2012 & 2015) Evaluation de l'aléa volcanique à La Réunion. Rapport final-année I et II. Projet BRGM/IPGP.

Di Muro, A., Métrich, N., Vergani, D., Rosi, M., Armienti, P.,Fougeroux, T., Deloule, E., Arienzo, I. & Civetta, L. (2014) The Shallow Plumbing System of Piton de la Fournaise Volcano (La Réunion Island, Indian Ocean) revealed by the Major 2007 Caldera-Forming Eruption. Journal of Petrology 55, 1287-1315.

Dixon, J.E., Stolper, E.M. & Holloway, J.R. (1995) An experimental study of water and carbon dioxide solubilities in mid-ocean ridge basaltic liquids. Part I: calibration and solubility models. Journal of Petrology 36, 1607-1631.

Famin, V., Welsch, B., Okumura, S., Bachèlery, P. & Nakashima, S. (2009) Three differentiation stages of a single magma at Piton de la Fournaise (Réunion hotspot). Geochemistry Geophysics Geosystems 10, Q01007.

Fisk, M.R., Upton, B.G.J., Ford, C.E. & White, W.M. (1988) Geochemical and Experimental Study of the Genesis of Magmas of reunion Island, Indian Ocean. Journal of Geophysical Research 93, 4933-4950.

Fretzdorff, S. & Haase, K.M. (2002) Geochemistry and petrology of lavas from the submarine flanks of Réunion Island (western Indian Ocean): implications for magma genesis and the mantle source. Mineralogy and Petrology 75, 153-184.

Gaillard, F., Pichavant, M., and Scaillet, B. (2003) Experimental determination of activities of FeO and Fe_2O_3 components in hydrous silicic melts under oxidizing conditions. Geochimica et Cosmochimica Acta, 67, 4389-4409.

Hall, L.J., Brodie, J., Wood, B.J., and Carroll, M.R. (2004) Iron and water losses from hydrous basalts contained in $Au_{80}Pd_{20}$ capsules at high pressure and temperature. Mineralogical Magazine, 68, 75-81.

Holloway, J.R. (1987) Igneous fluids. In: Eugster, H.P. & Carmichael, I.S.E. (eds) *Thermodynamic Modeling of Geological Materials: Minerals, Fluids and Melts. Mineralogical Society of America, Reviews in Mineralogy* 17, 211-233.

Kawamoto, T. and Hirose, K. (1994) Au-Pd sample containers for melting experiments on iron and water-bearing systems. European Journal of Mineralogy 6, 381-385.

Kornprobst, J., Boivin, P. & Bachèlery, P. (1979) L'alimentation des eruptions récentes du Piton de la Fournaise (Ile de la reunion, Océan Indien): degree d'évolution et niveau de segregation des laves émises. C.R. Acad. Sc. Paris, t.288, 1691-1694.

Kornprobst, J., Boivin, P., Lénat, J.F., Bachèlery, P., Bonneville, A., Dupont, P., Lecointre, J., Seidel, J.L., Thomas, P. & Vincent, P. (1984) Le Piton de la Fournaise, Ile de la Réunion. Colloque PIRPSEV 1984, Clermont-Ferrand.

Lacroix, A. (1923) Océanites. Minéralogie de Madagascar, vol. III, Paris, 49-50.

Lacroix, A. (1936) Les transformations récentes du sommet du volcan actif (Piton de la Fournaise) de l'Ile de la Réunion. Notes, Mémoires et Rapports de Volcanologie, 1-18.

Lebas, E. (2012) Processus de démantèlement des édifices volcaniques au cours de leur évolution : application à La Réunion et Montserrat et comparaison avec d'autres édifices. PhD Thesis, Paris Diderot, Paris, 407pp.

Lénat, J.F., Gibert-Malengreau, B. & Galdeano, A. (2001) A new model for the evolution of the volcanic island of Réunion (Indian Ocean). Journal of Geophysical Research-Solid Earth 106, 8645-8663.

Lénat, J.F., Bachèlery, P. & Merle, O. (2012a) Anatomy of Piton de la Fournaise volcano (La Reunion, Indian Ocean). Bulletin of Volcanology 74, 1945-1961.

Lénat, J.F. (2016) Construction of La Réunion. In: Bachèlery, P., Lénat, J.F., Di Muro, A. & Michon, L. (eds) *Active volcanoes of the southwest Indian Ocean: Piton de la Fournaise and Karthala*. Active volcanoes of the world. Springer, Berlin.

Ludden, J.N. (1978a) Magmatic evolution of the basaltic shield volcanoes of Réunion Island. Journal of Volcanology and Geothermal Research 4, 171-198.

Malengreau, B. (1995) Structure profonde de la Réunion d'après les données magnétiques et gravimétriques. PhD Thesis, Université Blaise Pascal Clermont Ferrand, 366 pp.

Malengreau, B., Lénat, J.F. & Froger, J.L. (1999) Structure of Reunion Island (Indian Ocean) inferred from the interpretations of gravity anomalies. Journal of Volcanological and Geothermal Research 88, 131-146.

McDougall, I. (1971) The geochronology and evolution of young volcanic island of Réunion, Indian Ocean. Geochimica et Cosmochimica Acta 35, 261-288.

Martel, C., Pichavant, M., Holtz, F., Scaillet, B., Bourdier, J.L. & Traineau, H. (1999) Effects of fO2 and H2O on andesite phase relations between 2 and 4 kbar. Journal of Geophysical Research, 104, 29453-29470.

Mercier, M., Di Muro, A., Métrich, N., Giordano, D., Belhadj, O. & Mandeville C.W. (2010) Spectroscopic analysis (FTIR, Raman) of water in mafic and intermediate glasses and glass inclusions. Geochimica et Cosmochimica Acta 74, 5641-5656.

Merle, O., Mairine, P., Michon, L., Bachèlery, P. & Smietana, M. (2010) Calderas, landslides and paleo-canyons on Piton de la Fournaise volcano (La Réunion Island, Indian Ocean). Journal of Volcanological and Geothermal Research 189, 131-142.

Michon, L., Ferrazzini, V., Di Muro, A., Villeneuve, N. & Famin, V. (2015) Rift zones and magma plumbing system of Piton de la Fournaise volcano : how do they differ from Hawaii and Etna. Journal of Volcanological and Geothermal Research 303, 112-129.

Michon, L., Lénat, J.F., Bachèlery, P. & Di Muro, A. (2016) Geology and Morphostructural Evolution of Piton de la Fournaise. In: Bachèlery, P., Lénat, J.F., Di Muro, A. & Michon, L. (eds) *Active volcanoes of the southwest Indian Ocean: Piton de la Fournaise and Karthala*. Active volcanoes of the world. Springer, Berlin.

Mohamed-Abchir, A. (1996) Les Cendres de Bellecombe: un évènement majeur dans le passé recent du Piton de la Fournaise, Ile de la Réunion. PhD Thesis, Université Paris VII, 248 pp.

Morandi, A., Di Muro, A., Principe, C., Michon, L., Leroi, G., Norelli, F. & Bachèlery, P. (2016) Pre-historic explosive activity at Piton de la Fournaise volcano. In: Bachèlery, P., Lénat, J.F., Di Muro, A. & Michon, L. (eds) *Active volcanoes of the southwest Indian Ocean: Piton de la Fournaise and Karthala*. Active volcanoes of the world. Springer, Berlin.

Ort, M.H., Di Muro, A., Michon, L. & Bachèlery, P. (2016) Explosive eruptions from the interaction of magmatic and hydrothermal systems during flank extension: the Bellecombe Tephra of Piton de la Fournaise (La Réunion Island). Bulletin of Volcanology 78, 1-14.

Peltier, A., Bachèlery, P. & Staudacher, T. (2009) Magma transport and storage at Piton de la Fournaise (La Réunion) between 1972 and 2007: A review of geophysical and geochemical data. Journal of Volcanology and Geothermal Research 184, 93-108.

Pichavant, M., Martel, C., Bourdier, J.L. & Scaillet, B. (2002) Physical conditions , structure, and dynamics of a zoned magma chamber : Mount Pelée (Martinique, Lesser Antilles Arc). Journal of Geophysical Research 107, ECV 2 1-27.

Pichavant, M. & Macdonald, R. (2007) Crystallization of primitive basaltic magmas at crustal pressures and genesis of the calc-alkaline igneous suite: experimental evidence from St Vincent, Lesser Antilels arc. Contributions to Mineralogy and Petrology 154, 535-558.

Pichavant, M., Di Carlo, I., Le Gac, Y., Rotolo, S., and Scaillet, B. (2009) Experimental constraints on the deep magma feeding system at Stromboli volcano, Italy. Journal of Petrology 50, 601-624.

Pichavant, M., Scaillet,B., Pommier, A., Iacono-Marziano, G. & Cioni, R. (2014) Nature and Evolution of Primitive Vesuvius Magmas : an Expreimental Study. Journal of Petrology 55, 2281-2310.

Pichavant, M., Brugier, Y. & Di Muro, A. (2016) Petrological and experimental constraints on the evolution of Piton de la Fournaise Magmas. In: Bachèlery, P., Lénat, J.F., Di Muro, A. & Michon, L. (eds) *Active volcanoes of the southwest Indian Ocean: Piton de la Fournaise and Karthala*. Active volcanoes of the world. Springer, Berlin.

Pietruszka, A.J., Hauri, E.H. & Blichert-Toft, J. (2009) Crustal contamination of mantle-derived magmas within Piton de la Fournaise volcano, Réunion island. Journal of Petrology 50, 661-684.

Principe, C., Morandi, A., Di Muro, A. & Michon, L. (2016) Volcanological Map of the Plaine des Sables, Piton de la Fournaise. In: Bachèlery, P., Lénat, J.F., Di Muro, A. & Michon, L. (eds) *Active volcanoes of the southwest Indian Ocean: Piton de la Fournaise and Karthala*. Active volcanoes of the world. Springer, Berlin.

Pownceby, M. I. and O'Neill, H. St. C. (1994) Thermodynamic data from redox reactions at high temperatures. III. Activity-composition relations in Ni-Pd alloys from EMF measurements at 850-1250 K and calibration of the NiO + Ni-Pd assemblage as a redox sensor. Contributions to Mineralogy and Petrology 116, 327-339.

Quidelleur, X., Holt, J.W., Salvany, T. & Bouquerel, H. (2010) The double structureof the Reunion geomagnetic event based on new K-Ar ages from the type locality, massif de la Montagne, Réunion Island (Indian Ocean) and assessment of the global context. Geophysical Journal International 182, 699-710.

Rançon, J.P., Rocher, P., Augé, T. & Nativel, P. (1989) Pétrologie de deux complexes intrusifs lités de l'île de la Réunion. Implications volcano-structurales. Géologie de la France 2-3, 135-156.

Richet, P., Whittington, A. Hotlz, F., Behrens, H., Ohlhorst, S. & Wilke, M. (2000) Water and and the density of silicate glasses. Contributions to Mineralogy and Petrology 138, 337-347.

Robie, R. A., Hemingway, B. S., and Fisher, J. R. (1979) Thermodynamic properties of minerals and related substances at 298.15 K and 1 bar (10^5 pascals) pressure and at higher temperatures. US Geological Survey Bulletin 1452.

Salaün, A., Villemant, B., Semet, M.P. & Staudacher, T. (2010) Cannibalism of olivine-rich cumulate xenoliths during the 1998 eruption of Piton de la Fournaise (La Reunion hotspot): Implications for the generation of magma diversity. Journal of Volcanological and Geothermal Research 198, 187-204.

Salvany, T., Lahitte, P., Nativel, P. & Gillot, P.Y. (2012) Geomorphic evolution of the Piton des Neiges volcano (Réunion Island, Indian Ocean): Competition between volcanic construction and erosion since 1.4 Ma. Geomorphology 136, 132-147.

Scaillet, B., Pichavant, M., Roux, J., Humbert, G. & Lefèvre, A. (1992) Improvements of the Shaw membrane technique for measurements and control of fH2 at high temperatures and pressures. American Mineralogist, 77, 647-655.

Sisson, T.W. & Grove, T.L. (1993) Experimental investigations of the role of H2O in calc-alkaline differentiation and subduction zone magmatism. Contributions to Mineralogy and Petrology 113, 143-166.

Smietana, M. (2011) Pétrologie, géochrnologie (K-Ar) et géochimie élémentaire et isotopique (Sr, Nd, Hf, Pb) des laves anciennes de La Réunion. Implications sur la construction de l'édifice volcanique. PhD Thesis, Université de La Réunion, 362 pp.

Staudacher, T. & Allègre, C. (1993) Ages of the second caldera of Piton de la Fournaise volcano (Réunion) determined by cosmic ray produced ^{3}He and ^{21}Ne. Earth and Planetary Science Letters 119, 395-404.

Staudacher, T., Peltier, A., Ferrazzini, V., Di Muro, A., Boissier, P., Catherine, P., Kowalski, P., Lauret, F. & Lebreton, J. (2016) Fifteen Years of Intense Eruptive Activity (1998-2013) at Piton de la Fournaise Volcano : A Review. In: Bachèlery, P., Lénat, J.F., Di Muro, A. & Michon, L. (eds) *Active volcanoes of the southwest Indian Ocean: Piton de la Fournaise and Karthala*. Active volcanoes of the world. Springer, Berlin.

Taylor, J. R., Wall, V. J., and Pownceby, M. I. (1992) The calibration and application of accurate redox sensors. American Mineralogist, 77, 284-295.

Tilley, C.E., Thompson, R.N., Wadsworth, W.J. & Upton, B.G.J. (1971) Melting relations of some lavas of Réunion Island, Indian Ocean. Mineralogical Magazine 38, 344-352.

Upton, B.G.J. & Wadsworth, W.J. (1965) The Basalts of Réunion Island, Indian Ocean. IAV International Symposium on Volcanology (New Zealand), scientific session of November.

Upton, B.G.J. & Wadsworth, W.J. (1972) Peridotitic and Gabbroic Rocks Associated with the Shield-Forming Lavas of Réunion. Contribution to Mineralogy and Petrology 35, 139-158.

Upton, B.G.J., Semet, M. & Joron, J.L. (2000) Cumulate clasts in the Bellecombe Ash Member, Piton de la Fournaise, Réunion Island, and their bearing on cumulative processes in the petrogenesis of the Réunion lavas. Journal of Volcanological and Geothermal Research 104, 297-318.

Valer, M., Schiano, P. & Bachèlery, P. (2015) Insights into the origin of magmas from the adventive cones of Piton de la Fournaise volcano (La Réunion Island). In: Geochimica et Cosmochimica Acta, Goldschmidt conference 2015 abstract 3219.

Villeneuve, N. (2000) Apports multi-sources à une meilleure comprehension de la mise en place des coulées de lave et risques associés au Piton de la Fournaise: Géomorphologie quantitative en terrain volcanique. PhD Thesis, Institut de Physique du Globe de Paris, 378pp.

Villemant, B., Salaün, A. & Staudacher, T. (2009) Evidence for a homogeneous primary magma at Piton de la Fournaise (La Réunion) : A geochemical study of matrix glass, melt inclusions and Pelé's hairs of the 1998-2008 eruptive activity. Journal of Volcanological and Geothermal Research 184, 79-92.

Vlastélic, I. & Staudacher, T. (2005) Rapid change of lava composition from 1998 through 2002 at Piton de la Fournaise (Réunion Island) inferred from Pb isotopes and trace elements: evidence for variable crustal contamination. Journal of Petrology 46, 79-107.

Vlastélic, I., Peltier, A. & Staudacher, T. (2007) Short-term (1998-2006) fluctuations of Pb isotopes at Piton de la Fournaise volcano (Réunion Island): origins and constraints on the size and shape of the magma reservoir. Chemical Geology 244, 202-220.

Vlastélic, I., Deniel, C., Bosq, C., Télouk, P., Boivin, P., Bachèlery, P., Famin, V. & Staudacher, T. (2009) Pb isotope geochemistry of Piton de la Fournaise historical lavas. Journal of Volcanological and Geothermal Research 184, 63-78.

Vlastélic, I. & Pietruszka, A.J. (2016) A Review of the Recent Geochemical Evolution of Piton de la Fournaise Volcano (1927-2010). In: Bachèlery, P., Lénat, J.F., Di Muro, A. & Michon, L. (eds) *Active volcanoes of the southwest Indian Ocean: Piton de la Fournaise and Karthala*. Active volcanoes of the world. Springer, Berlin.

Yoder, H.S. jr (1965) Diopside-anorthite-water at five and ten kilobars and its bearing on explosive volcanism. Yearb Carnegie Inst Wash 64: 82-89.

Welsch, B., Faure, F., Bachèlery, P. & Famin, V. (2009) Microcrysts Record Transient Convection at Piton de la Fournaise Volcano (La Réunion Hotspot). Journal of Petrology 50, 2287-2305.

Welsch, B., Faure, F., Famin, V., Baronnet, A. & Bachèlery, P. (2013) Dendritic Crystallization: A Single Process for all the Textures of Olivine in Basalts? Journal of Petrology 54, 539-574.

10 Figure captions

Fig. 1. T-*f*O_2 phase diagram for REU0912-04 showing experimental data points (squares), saturation curves and phase assemblages. The diagram compiles data from the two 0.1 MPa experimental series. See Table 2 for experimental details. Liq, liquid (silicate melt); Ol, olivine; Plag, plagioclase feldspar; Cpx, clinopyroxene; Sp, spinel.

Fig. 2. 50 MPa phase diagrams. (**a**) T-XH2Oinit. phase diagram for REU0912-04 showing data points (squares), phase assemblages, saturation curves and stability fields determined from the fluid-present 50 MPa experiments. Details of the experiments are provided in Table 3. XH2O init. [initial molar $H_2O/(H_2O+CO_2)$] are directly calculated from weights of distilled water and silver oxalate loaded in each capsule. The saturation curve of clinopyroxene ignores one 1150°C charge in the L+Ol+Cpx field which lacks clinopyroxene. (**b**)T-H2O in melt phase diagram for REU0912-04 showing data points (squares), phase assemblages, saturation curves and stability fields determined from the fluid-present 50 MPa experiments. Details of the experiments are provided on Table 3. Melt H2O contents are determined either by µ-FTIR or the "by difference" method. The grey field drawn for H2O in melt < 0.5 wt% illustrates H2O concentration conditions that are not reachable with our experimental methodology (see text). Liq, liquid (silicate melt); Ol, olivine; Cpx, clinopyroxene; Plag, plagioclase feldspar; Sp, spinel.

Fig. 3. CaO (wt%) vs. Fo for experimental and natural olivines. (**a**) Experimental olivines from the 0.1 MPa experiments. (**b**) Experimental olivines from the 50 MPa experiments. Details about the experiments are given in Tables 2-3 and experimental compositions in Tables 4-5. Natural olivine compositions are from Boivin and Bachèlery (2009) for 1977-1998 PdF lavas and from Di Muro (personal communication) for the December 2009 eruption that erupted REU0912-04. Note that for the experimental olivines, individual analyses (and not averages for a given charge) are plotted.

Fig. 4. (**a**) Al2O3 (wt%) vs. Mg# (calculated with Fe2+ = Fetot) for experimental clinopyroxenes. The experimental data are distinguished by temperature for the 50 MPa series whereas, for the 0.1 MPa series, the different temperatures are grouped. Individual clinopyroxene analyses (and not averages for a given charge) are plotted. The grey field shows compositions of natural clinopyroxenes in 1977-1998 PdF lavas (Boivin and

Bachèlery, 2009). **(b)** Al vs. Ti diagram (atomic concentrations) comparing compositions of experimental clinopyroxenes from this study with the two trends previously proposed to describe the Al-Ti covariation in augites from 1977-1998 PdF lavas (Boivin & Bachèlery, 2009). Both the 0.1 and 50 MPa data are grouped and individual clinopyroxene analyses are plotted.

Fig. 5. MgO variation diagrams for experimental glasses from this study. Data from Tables 4-5 for the experimental glasses and from Table 1 for the glass starting composition. The 50 MPa experimental data points are distinguished by phase assemblage (L; L+Ol; L+Ol+Cpx; L+Ol+Cpx+Plag) whereas the 0.1 MPa data points are grouped. Matrix glass compositions for PdF lavas erupted from 1977 to 2008 [from Boivin and Bachèlery (2009), Villemant et al. (2009), Salaün et al. (2010), Welsch et al (2013) and Di Muro et al. (2014)] are also shown for comparison. **(a)** CaO/Al_2O_3 vs. MgO (wt%). **(b)** K_2O (wt%) vs. MgO (wt%). Note the widest compositional ranges of the 50 than of the 0.1 MPa glasses as well as the general trends, positive in **(a)** and negative in **(b)**. Liq, liquid (silicate melt); Ol, olivine; Cpx, clinopyroxene; Plag, plagioclase feldspar.

Fig. 6. H_2O and CO_2 concentrations in glasses from the 50 MPa fluid-present experiments. Experimental conditions and concentrations in Table 3. Data on natural glass inclusions from Di Muro et al. (2014), Famin et al. (2009) and Bureau et al. (1998a) for, respectively, the 2007 products, the 2005 oceanites and the 1998 lavas. The fluid-melt saturation isobars 10, 30, 50 and 100 MPa are calculated with VOLATILECALC (Newman and Lowenstern, 2002).

Figure 1

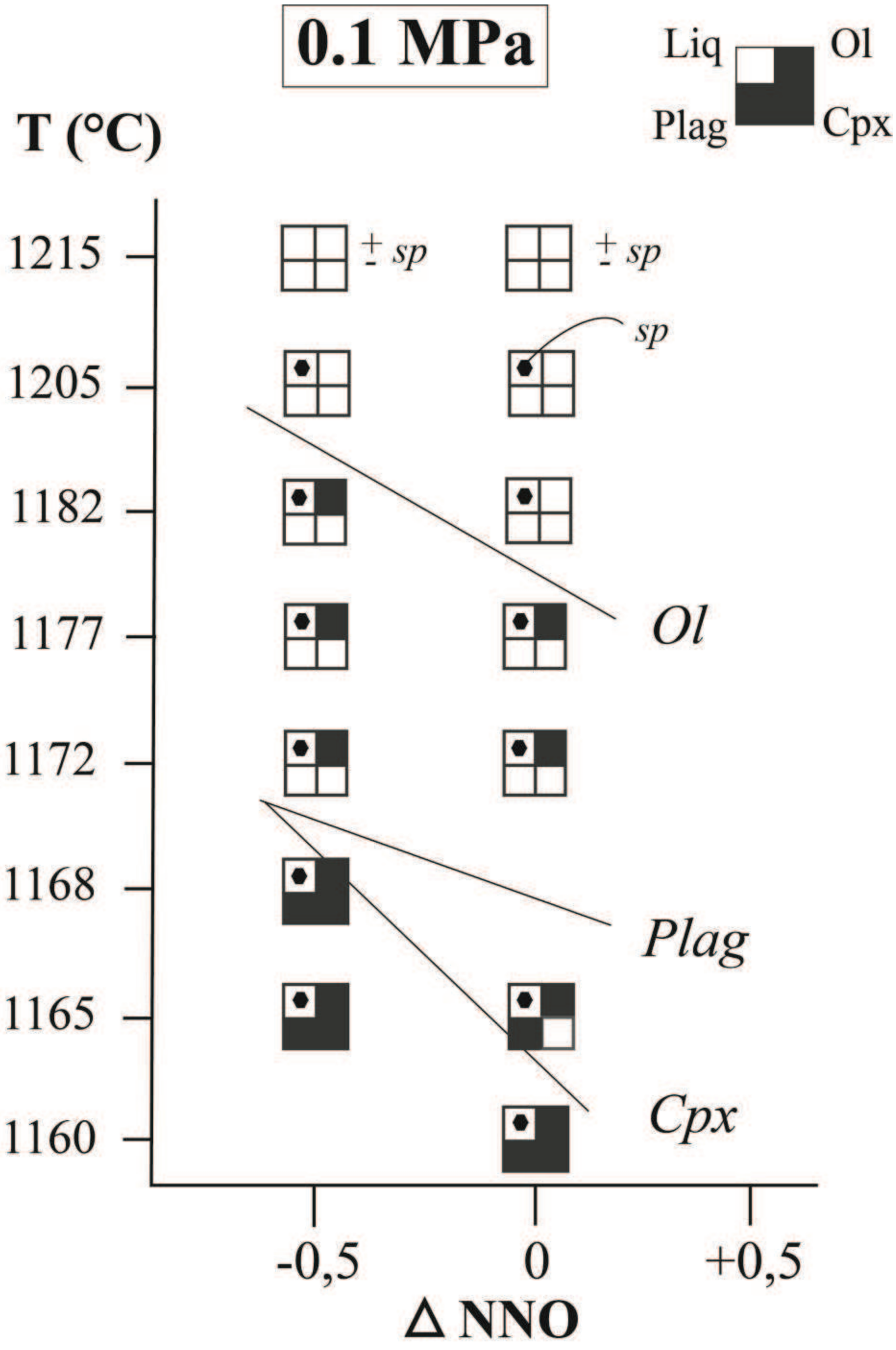
0.1 MPa
Liq
Ol
Plag
Cpx
T (°C)
1215
1205
1182
1177
1172
1168
1165
1160
± sp
± sp
sp
Ol
Plag
Cpx
-0,5
0
+0,5
Δ NNO

Figure 2

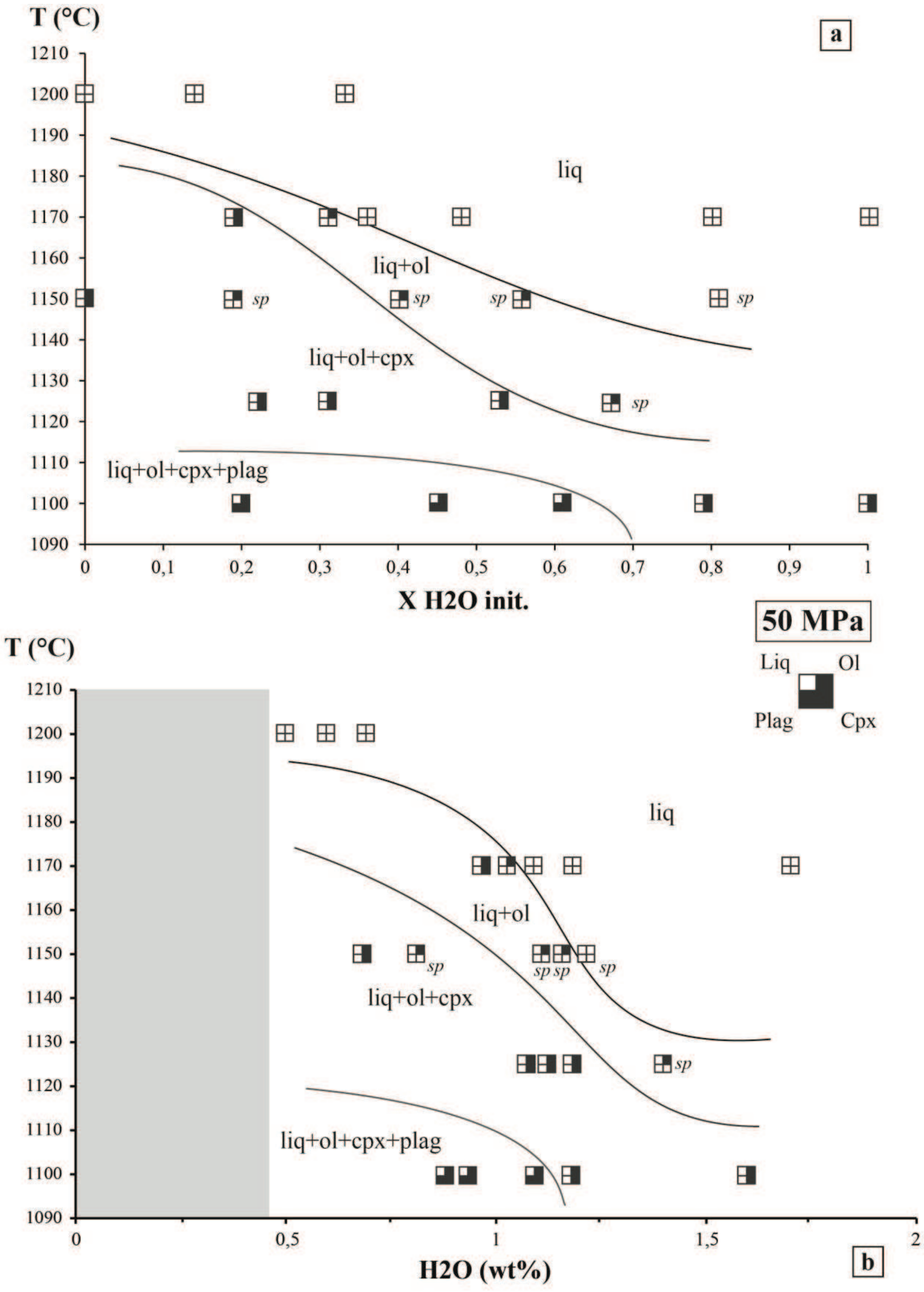
a
T (°C)
1210
1200
1190
1180
1170
1160
1150
1140
1130
1120
1110
1100
1090
0
0,1
0,2
0,3
0,4
0,5
0,6
0,7
0,8
0,9
1
X H2O init.
liq
liq+ol
liq+ol+cpx
liq+ol+cpx+plag
sp
50 MPa
Liq
Ol
Plag
Cpx
b
T (°C)
1210
1200
1190
1180
1170
1160
1150
1140
1130
1120
1110
1100
1090
0
0,5
1
1,5
2
H2O (wt%)
liq
liq+ol
liq+ol+cpx
liq+ol+cpx+plag
sp

Figure 3

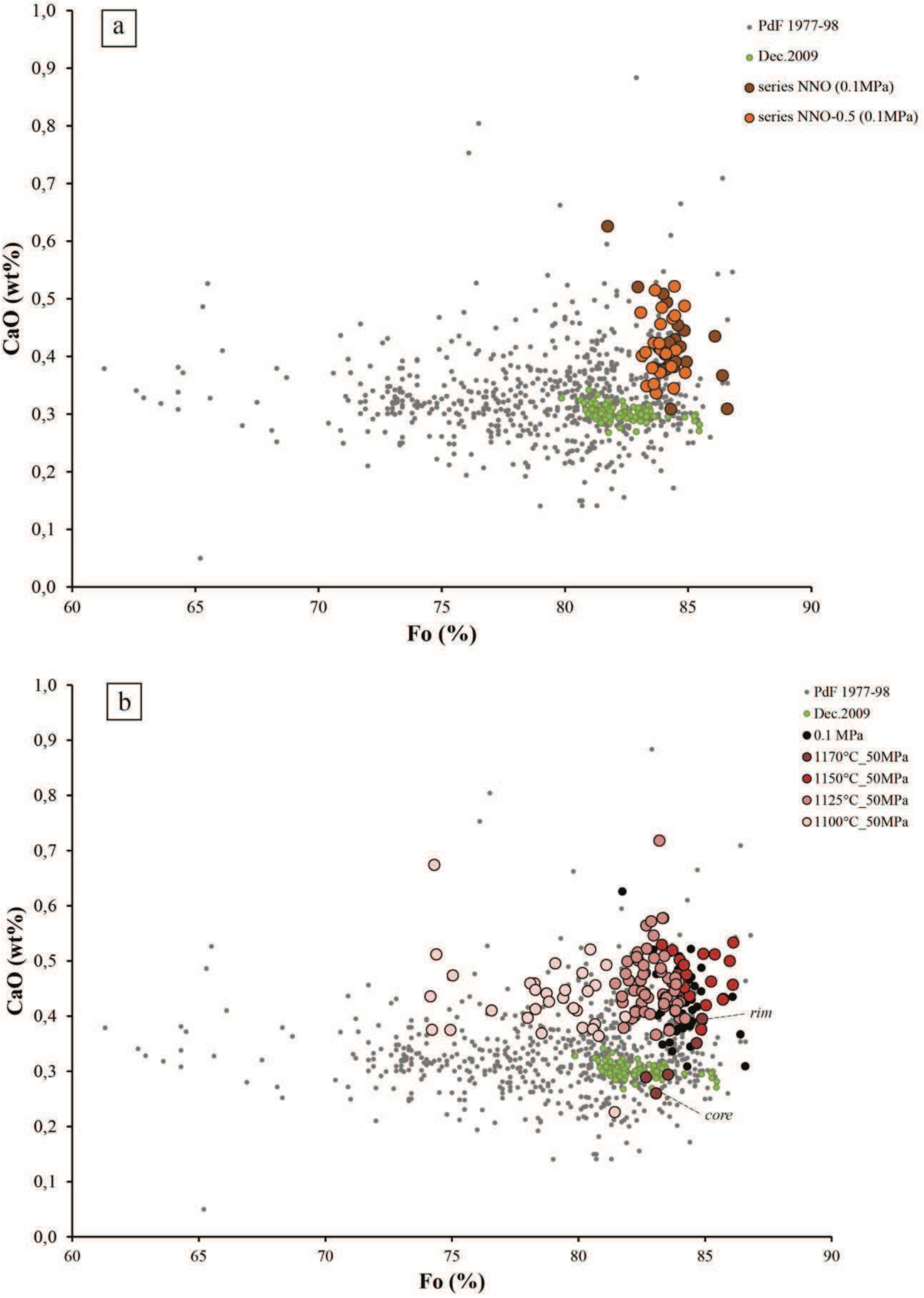
a
CaO (wt%)
Fo (%)
1,0
0,9
0,8
0,7
0,6
0,5
0,4
0,3
0,2
0,1
0,0
60
65
70
75
80
85
90
PdF 1977-98
Dec.2009
series NNO (0.1MPa)
series NNO-0.5 (0.1MPa)
b
CaO (wt%)
Fo (%)
PdF 1977-98
Dec.2009
0.1 MPa
1170°C_50MPa
1150°C_50MPa
1125°C_50MPa
1100°C_50MPa
rim
core

Figure 4

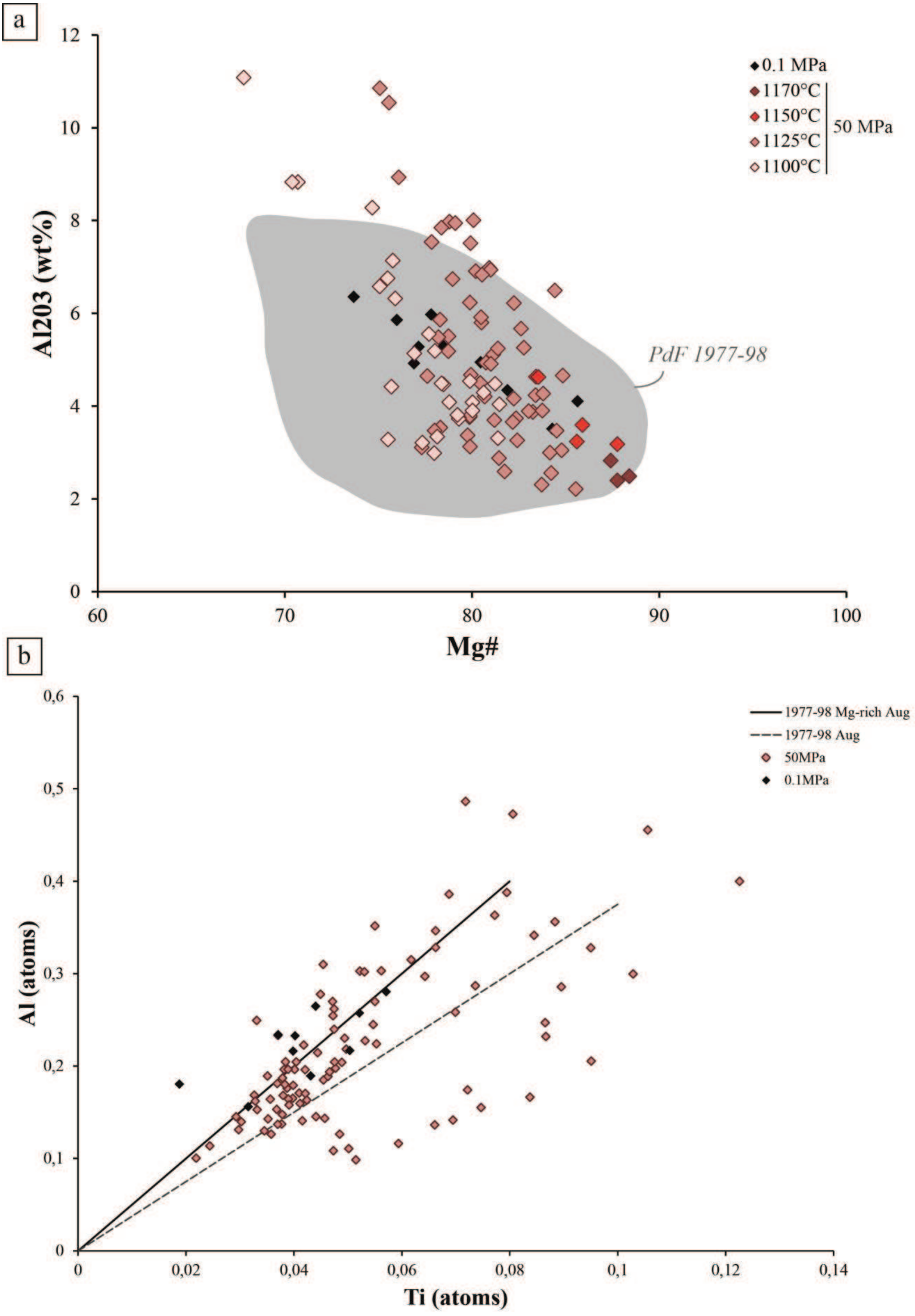
a
12
10
8
6
4
2
0
Al203 (wt%)
60
70
80
90
100
Mg#
◆ 0.1 MPa
◆ 1170°C
◆ 1150°C
◆ 1125°C
◇ 1100°C
50 MPa
PdF 1977-98
b
0,6
0,5
0,4
0,3
0,2
0,1
0
Al (atoms)
0
0,02
0,04
0,06
0,08
0,1
0,12
0,14
Ti (atoms)
1977-98 Mg-rich Aug
1977-98 Aug
◆ 50MPa
◆ 0.1MPa

Figure 5

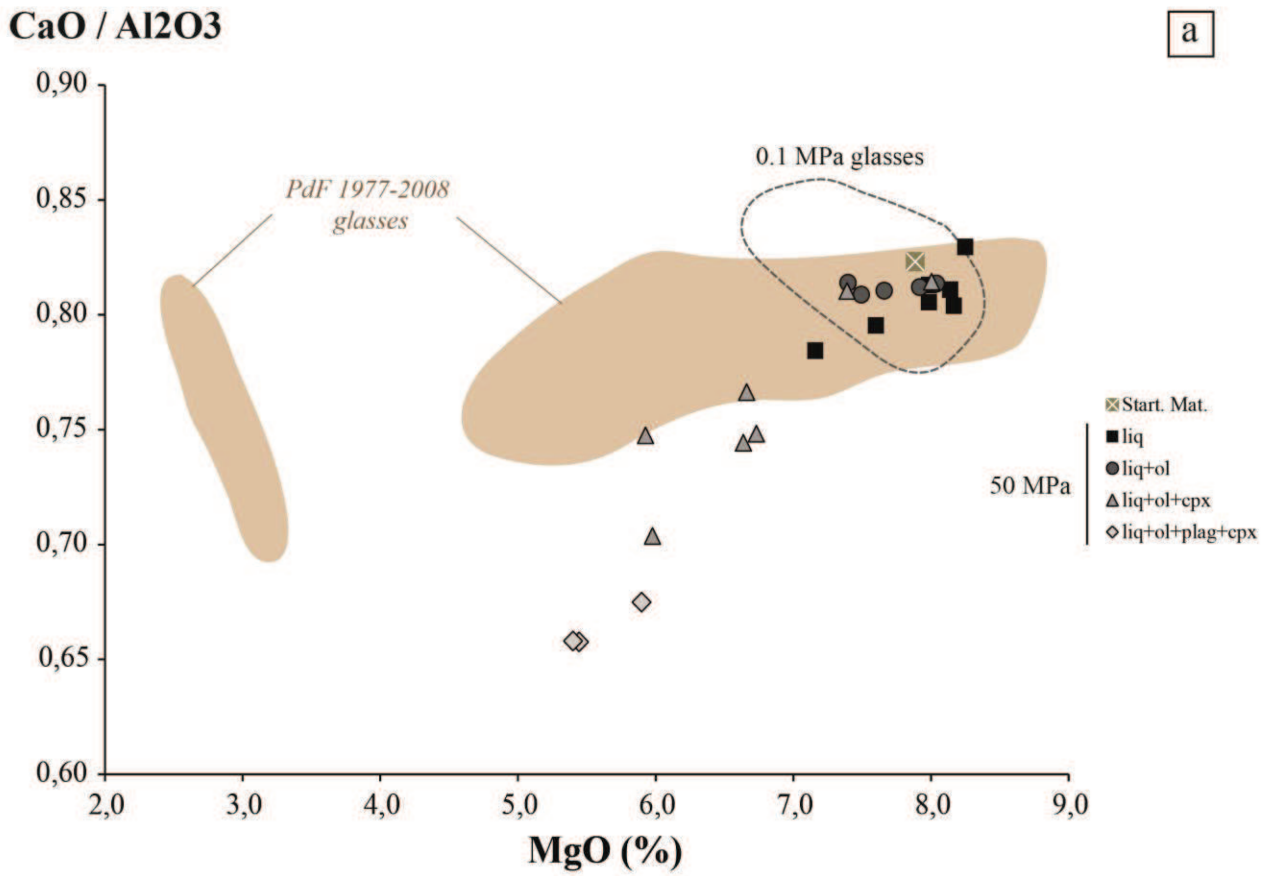
CaO / Al2O3
a
0,90
0,85
0,80
0,75
0,70
0,65
0,60
2,0
3,0
4,0
5,0
6,0
7,0
8,0
9,0
MgO (%)
PdF 1977-2008 glasses
0.1 MPa glasses
Start. Mat.
50 MPa
liq
liq+ol
liq+ol+cpx
liq+ol+plag+cpx

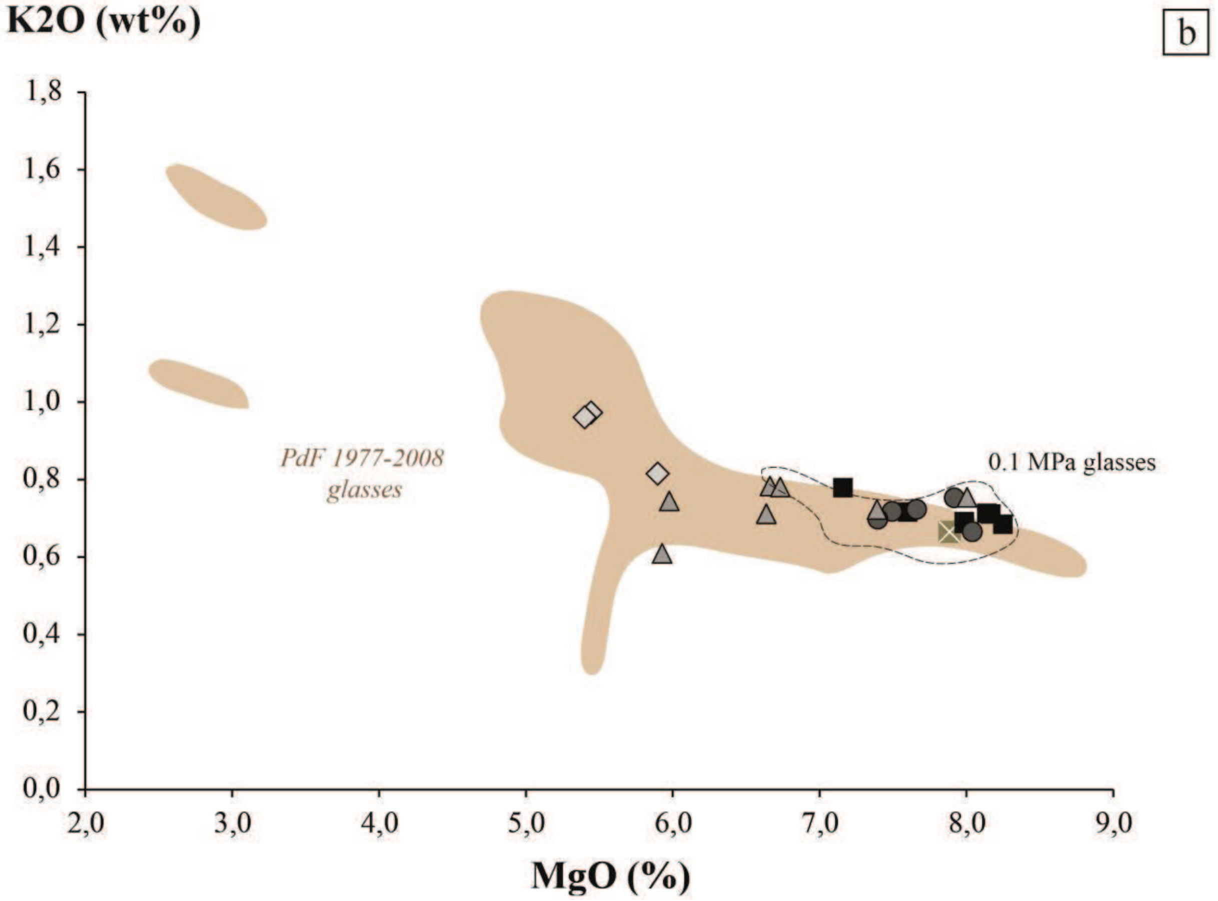
K2O (wt%)
b
1,8
1,6
1,4
1,2
1,0
0,8
0,6
0,4
0,2
0,0
2,0
3,0
4,0
5,0
6,0
7,0
8,0
9,0
MgO (%)
PdF 1977-2008 glasses
0.1 MPa glasses

Figure 6

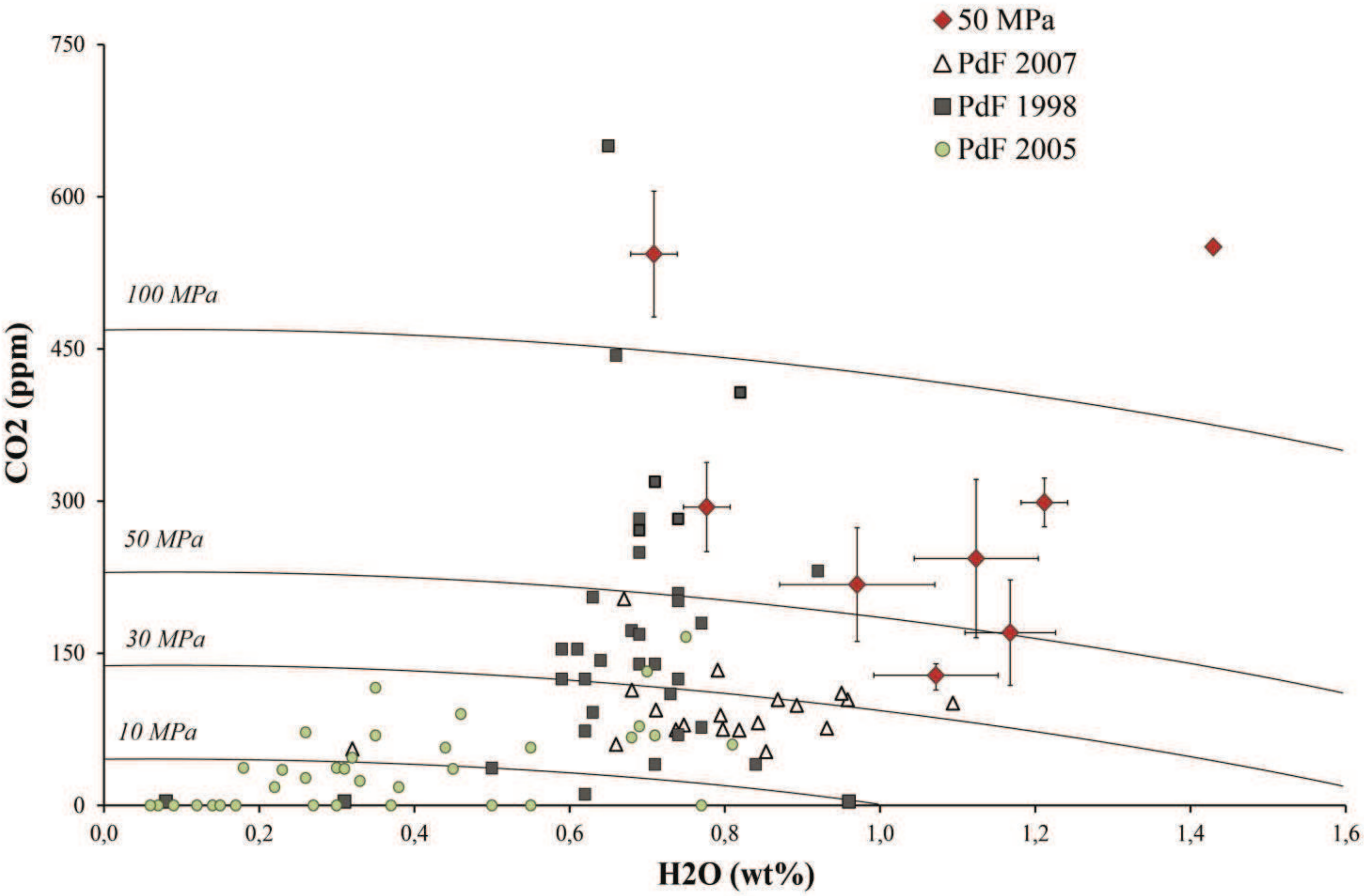

50 MPa
PdF 2007
PdF 1998
PdF 2005
CO2 (ppm)
H2O (wt%)
100 MPa
50 MPa
30 MPa
10 MPa
0
150
300
450
600
750
0,0
0,2
0,4
0,6
0,8
1,0
1,2
1,4
1,6

Table 1. Major element composition of the PdF starting sample

Sample	**REU0912-04**		
	Whole-rock	Glass[1]	*st.dev. 2*
Oxides (wt%)			
SiO2	48,75	49,24	*0,38*
TiO2	2,48	2,53	*0,06*
Al2O3	13,82	13,54	*0,22*
FeOt	11,78	12,26	*0,33*
MnO	0,16	0,16	*0,03*
MgO	7,76	7,87	*0,13*
CaO	11,20	11,14	*0,13*
Na2O	2,57	2,55	*0,16*
K2O	0,67	0,66	*0,01*
P2O5	0,29	0,34	*0,12*
Total	98,61	99,80	
Trace elements (ppm)			
Cr	466	365	
Ni	142	509	

[1] Average of 100 analyses

Table 2. 0,1MPa experiments

Charge	T (°C)	logfO2 (bar)	ΔNNO	Phase assemblage	$\sum R$	Fe loss %	Kd Fe-Mg *Ol-l*	Kd Na-Ca Plag-l	Kd Fe-Mg Cpx-l
NNO series, Starting Material = REU0912-04, Pt wire, CO-CO2 gas mixing furnace									
3	1215	-7,57	0,0	Gl(98,7), Sp(1,3)	1,24	-6,7			
4	1205	-7,68	0,0	Gl(99,8), Sp(0,2)	0,08	-0,9			
6	1182	-7,96	0,0	Gl(101), Sp(-1)	0,24	+1			
12	1177	-7,99	0,0	Gl(99,3), Ol(0,4), Sp(0,3)	0,51	-3,8	0,31		
10	1172	-8,05	0,0	Gl(97,9), Ol(0,4), Sp(1,7)	0,33	-2,2	0,28		
8	1165	-8,13	0,0	Gl(99), Ol(1,3), Plag(-0,4), Sp(0,1)	0,03	-0,1	0,3	1,01	
13	1160	-8,19	0,0	Gl(88), Ol(3,5), Plag(8), Cpx(2), Sp(-1,7)	0,5	+2,3	0,29	1,01	0,41
NNO-0,5 series, Starting Material = REU0912-04, Pt wire, CO-CO2 gas mixing furnace									
2	1215	-8,07	-0,5	Gl(96), Sp(4)	3,25	-11,7			
1	1205	-8,23	-0,5	Gl(99,7), Sp(0,3)	0,12	-2			
5	1182	-8,44	-0,5	Gl(99,7), Ol(0,6), Sp(-0,3)	0,01	+0,6	0,29		
11	1177	-8,49	-0,5	Gl(100,7), Ol(0,1), Sp(-0,8)	0,07	-0,5	0,3		
9	1172	-8,55	-0,5	Gl(96,8), Ol(1,2), Sp(2)	0,34	-2,2	0,31		
14	1168	-8,60	-0,5	Gl(94,5), Ol(3,2), Plag(4,3), Cpx(-0,8), Sp(-1,2)	0,29	+2,3	0,26	0,87	0,38
7	1165	-8,63	-0,5	Gl(98,9), Ol(2,1), Plag(0,9), Cpx(-1,4), Sp(-0,5)	0,12	0	0,28	0,89	0,29

Table 3 H_2O- and CO_2-bearing 50MPa experiments

Charge	xH_2O init.	H_2O melt wt%	CO_2 melt (ppm)	aH2O	logfO2 bar	ΔNNO bar	Phase assemblage	∑ *R*	Fe loss %	Kd Fe-Mg *Ol-l*	Kd Fe-Mg *Cpx-l*	Kd Na-Ca *Plag-l*
Re049, 510 bars, 1200°C, fH2 ≈ 3bars , 1.5 & 4h, AuPd capsules												
Re049_I	0,33	*0,7*		0,16	-8,90	-1,2	Gl(100)	1,71	-11,7			
Re049_II	0,14	*0,6*		0,12	-9,16	-1,4	Gl(100)	6,26	-24,4			
Re049_III	0	*0,5*		0,09	-9,41	-1,7	Gl(100)	1,63	-11,5			
Re043, 514 bars, 1170°C, fH2 ≈ 3bars , 14.5h, AuPd capsules												
Re043_I	0,19	**1,0**	218	0,26	-8,84	-0,8	Gl(102), Ol(3), Cpx(-5)	3,85	-17	0,32	0,22-0,27	
Re043_III	0,36	**1,2**	170	0,36	-8,56	-0,5	Gl(100)	14,45	-38,1			
Re040, 507 bars, 1170°C, fH2 ≈ 3bars , 18h, AuPd capsules												
Re040_I	1	**1,7**		0,65	-8,04	0,0	Gl(100)					
Re040_II	0,8	**1,1**	128	0,15	-9,29	-1,2	Gl(100)	0,77	-3,2			
Re040_III	0,48	**0,8**		0,23	-8,94	-0,9	Gl(100)	0,92	2,3			
Re040_IV	0,31	**1**		0,24	-8,91	-0,8	Gl(99,7), Ol(0,3)	0,9	2,4	0,28		
Re048, 511 bars, 1150°C, fH2 = 1,8 bars , 3.5h, xCo = 0,19 , AuPd capsules												
Re048_I	0,81	**1,2**	243	0,39	-8,31	0,0	Gl(99), Sp(1)	0,28	-3			
Re048_II	0,56	*1,2*		0,38	-8,32	0,0	Gl(99), Ol(0,1), Sp(0,9)	0,33	-4	0,36		
Re048_III	0,4	**1,2**	299	0,39	-8,31	0,0	Gl(97,8), Ol(0,9), Sp(1,3)	1,08	-7	0,35		
Re048_IV	0,19	**0,8**	294	0,18	-9,12	-0,8	Gl(96,9), Ol(1,7), Sp(1,4)	1,61	-10	0,36		
Re048_V	0	**0,7**	544	0,15	-8,97	-0,7	Gl(100,9), Ol(3,1), Cpx(-4)	2,78	-15	0,32	0,27-0,33	
Re045, 507 bars, 1125°C, fH2 ≈ 3 bars , 5h, AuPd capsules												
Re045_I	0,67	**1,4**	551	0,45	-8,94	-0,3	Gl(97,8), Ol(1,5), Sp(0,7)	0,64	-6	0,32		
Re045_II	0,53	*1,1*		0,39	-9,08	-0,5	Gl(95,6), Ol(3,1), Cpx(1,3)	1,27	-5,4	0,34	0,31-0,32	
Re045_III	0,31	*1,1*		0,31	-9,28	-0,7	Gl(93,8), Ol(3,3), Cpx(2,9)	1,58	-5,1	0,31	0,28-0,37	
Re045_IV	0,22	*1,2*		0,40	-9,05	-0,4	Gl(94,7), Ol(3,6), Cpx(1,7)	2,25	-11	0,34	0,31-0,39	
Re046, 506 bars, 1101°C, fH2 = 5,23 bars , 4.3h, xCo = 0,3 , AuPd capsules												
Re046_I	1	*1,6*		0,44	-9,82	-0,9	Gl(91), Ol(3,5), Cpx(5,5)	0,47	+0,5	0,31	0,57-0,51	
Re046_II	0,79	*1,2*		0,36	-9,99	-1,1	Gl(88,3), Ol(1,9), Cpx(9,8)	1,50	-6	0,29	0,27-0,21	
Re046_III	0,61	*0,9*		0,25	-10,29	-1,4	Gl(91,3), Ol(2,6), Cpx(9,6), Plag(-3,6)	0,49	-4	0,32	0,28-0,38	0,8
Re046_IV	0,45	*0,9*		0,54	-9,64	-0,7	Gl(70,6), Ol(4), Cpx(15,5), Plag(9,8)	0,21	-1,2	0,33	0,25-0,39	0,9
Re046_V	0,2	*1,1*		0,43	-9,84	-0,9	Gl(61,9), Ol(5,9), Cpx(15,9), Plag(16,3)	0,02	0,3	0,31	0,25-0,29	1,1

Bold = H2O contents measured by FTIR // *Italic* = H2O contents calculated with the "by difference" method

Approximated (see text)

Measured by sensors (see text)

Table 4 Compositions of experimental products: 0,1MPa experiments

Charge	Phase	SiO2	TiO2	Al2O3	FeO	MnO	MgO	CaO	Na2O	K2O	P2O5	Cr2O3	NiO	Total	Composition
NNO series															
3	Gl(3)	50,53	2,68	14,23	9,61	0,16	7,92	11,10	2,50	0,70	0,30	0,27	0,00	99,62	
4	Gl(3)	50,07	2,65	13,84	10,50	0,21	7,94	11,38	2,40	0,60	0,30	0,04	0,06	99,38	
6	Gl(7)	49,78	2,67	13,60	10,87	0,20	7,98	11,35	2,56	0,65	0,20	0,10	0,04	97,12	
12	Gl(7)	50,14	2,52	14,10	10,01	0,14	7,65	11,59	2,61	0,67	0,54	0,02	0,02	99,62	
	Ol core	40,07	0,15	0,05	14,85	0,03	44,70	0,31	0,02	0,04	0,35	0,00	0,21	100,78	Fo 84,3
	Ol rim	40,36	0,00	0,03	14,47	0,23	45,43	0,45	0,04	0,03	0,07	0,06	0,24	101,40	Fo 84,8
10	Gl(3)	51,03	2,59	14,16	9,62	0,15	7,51	11,32	2,65	0,71	0,25	0,00	0,01	98,28	
	Ol(3)	40,24	0,00	0,06	12,91	0,20	45,81	0,37	0,01	0,00	0,16	0,23	0,02	100,02	Fo 86,4
8	Gl(6)	50,57	2,57	13,97	10,41	0,13	7,14	11,57	2,55	0,70	0,26	0,08	0,05	97,60	
	Ol(7)	39,62	0,05	0,14	14,83	0,29	43,18	0,42	0,02	0,02	0,12	0,96	0,06	99,71	Fo 83,8
	Plag(2)	49,31	0,72	32,74	0,56	0,04	0,27	12,46	3,36	0,25	0,19	0,03	0,03	99,95	An63Ab34Or3
13	Gl(4)	49,13	3,01	13,50	11,70	0,20	6,70	11,28	2,76	0,81	0,68	0,04	0,18	99,35	
	Ol	38,88	0,12	0,23	17,02	0,31	42,71	0,63	0,07	0,00	0,34	0,01	0,06	100,36	Fo 81,7
	Plag(3)	51,15	0,83	24,85	3,23	0,05	1,66	13,01	3,54	0,35	0,19	0,03	0,05	98,93	An63Ab34Or3
	Cpx(4)	48,17	1,75	5,61	8,90	0,24	15,74	18,80	0,48	0,03	0,18	0,23	0,12	100,25	En46Wo39Fs15
NNO-0,5 series															
2	Gl(2)	51,61	2,55	14,14	8,33	0,23	8,29	11,44	2,53	0,66	0,14	0,04	0,01	98,73	
1	Gl(5)	50,03	2,62	13,84	10,34	0,08	8,07	11,36	2,48	0,77	0,26	0,08	0,07	98,91	
5	Gl (11)	50,29	2,58	13,83	10,67	0,17	7,39	11,29	2,57	0,72	0,22	0,19	0,07	98,51	
	Ol (3)	39,32	0,06	0,05	15,58	0,16	44,17	0,37	0,01	0,00	0,25	0,81	0,11	100,90	Fo 83,5
11	Gl(2)	49,76	2,61	13,94	10,65	0,31	7,68	11,20	2,62	0,61	0,53	0,03	0,07	99,55	
	Ol(5)	39,45	0,05	0,09	15,21	0,20	44,57	0,41	0,04	0,04	0,32	0,07	0,39	100,83	Fo 83,9
9	Gl(4)	51,06	2,69	14,15	9,43	0,08	7,16	11,45	2,89	0,74	0,25	0,07	0,03	98,43	
	Ol	39,98	0,06	0,19	14,07	0,36	44,21	0,49	0,03	0,00	0,17	0,31	0,04	99,90	Fo 84,9
	Ol	40,02	0,02	0,11	15,99	0,12	44,05	0,48	0,01	0,00	0,00	0,05	0,00	100,84	Fo 83,1
14	Gl(3)	49,34	2,72	13,60	11,35	0,28	7,18	11,64	2,57	0,72	0,61	0,00	0,00	99,05	
	Ol	39,57	0,05	0,00	14,29	0,39	45,02	0,37	0,07	0,05	0,19	0,00	0,36	100,36	Fo 84,9
	Ol	39,25	0,23	0,09	15,74	0,21	45,02	0,36	0,01	0,00	0,50	0,00	0,01	101,39	Fo83,6
	Plag	50,01	0,09	28,68	1,80	0,00	1,09	14,00	3,24	0,12	0,05	0,00	0,00	99,09	An68Ab31Or1
	Plag	50,43	1,45	20,87	6,58	0,10	3,73	12,37	3,39	0,54	0,21	0,00	0,00	99,66	An61Ab34Or5
	Cpx(2)	48,38	1,50	5,65	7,79	0,15	15,62	20,11	0,49	0,04	0,08	0,35	0,22	100,39	En45Wo42Fs13
7	Gl(5)	50,25	2,89	13,84	10,60	0,18	7,12	11,59	2,50	0,66	0,27	0,01	0,10	97,90	
	Ol(6)	39,41	0,06	0,19	14,99	0,21	43,43	0,45	0,02	0,01	0,10	0,62	0,07	99,56	Fo 83,8
	Plag	52,84	0,30	27,37	1,81	0,00	0,52	13,04	3,68	0,22	0,00	0,00	0,00	99,78	An63Ab35Or2
	Plag	50,82	0,23	28,86	1,22	0,00	0,45	14,31	3,19	0,16	0,02	0,17	0,05	99,47	An68Ab31Or1
	Cpx	48,55	1,42	4,91	7,32	0,25	16,91	19,15	0,31	0,02	0,00	0,19	0,28	99,32	En49Wo39Fs12
	Cpx	52,87	0,67	4,10	5,35	0,07	17,89	17,52	0,48	0,00	0,00	0,17	0,78	99,90	En53Wo38Fs9

Table 5 Compositions of experimental products: 50MPa experiments

Charge	Phase	SiO2	TiO2	Al2O3	FeO	MnO	MgO	CaO	Na2O	K2O	P2O5	Cr2O3	NiO	Total	Composition
Series "Re049" T=1200°C // P=510bars															
Re049_I	Gl(10)	51,14	2,61	14,00	8,81	0,18	8,14	11,35	2,57	0,71	0,28	0,05	0,15	97,98	
Re049_II	Gl(6)	51,97	2,68	14,26	7,64	0,13	8,17	11,46	2,61	0,71	0,30	0,03	0,05	98,36	
Re049_III	Gl(4)	50,96	2,65	13,90	8,81	0,12	8,25	11,53	2,56	0,68	0,26	0,07	0,22	98,54	
Series "Re043" T=1170°C // P=514bars															
Re043_III	Gl(15)	52,60	2,68	14,50	6,34	0,17	8,00	11,81	2,64	0,75	0,42	0,05	0,04	97,16	
Re043_I	Gl(15)	52,01	2,83	14,74	7,42	0,11	7,16	11,56	2,79	0,78	0,48	0,06	0,05	97,35	
	Ol	41,16	0,13	0,05	12,90	0,22	45,89	0,41	0,03	0,00	0,00	0,04	0,03	100,87	Fo86,4
	Ol	40,44	0,04	0,06	14,02	0,25	45,40	0,40	0,00	0,02	0,00	0,03	0,00	100,64	Fo85,2
	Cpx	52,42	1,73	2,87	4,49	0,14	17,48	21,07	0,25	0,00	0,00	1,15	0,02	101,61	En50Wo43Fs7
	Cpx	53,14	1,79	2,51	4,22	0,08	18,06	19,90	0,28	0,03	0,00	1,13	0,00	101,06	En52Wo41Fs7
Series "Re040" T= 1170°C // P=507bars															
Re040_II	Gl(7)	49,33	2,66	14,18	10,26	0,12	7,98	11,42	2,74	0,69	0,49	0,04	0,10	95,83	
Re040_III	Gl(8)	49,28	2,68	14,22	10,86	0,14	7,60	11,31	2,78	0,72	0,28	0,03	0,11	95,60	
Re040_IV	Gl(10)	50,18	2,81	14,52	8,88	0,17	8,04	11,81	2,51	0,67	0,34	0,04	0,03	96,94	
	Olr	39,40	0,09	0,06	14,53	0,24	45,75	0,40	0,05	0,00	0,03	0,00	0,06	100,59	Fo84,9
	Olc	38,72	0,00	0,08	16,72	0,31	44,73	0,29	0,03	0,00	0,19	0,09	0,32	101,48	Fo82,7
Series "Re048" T=1150°C // P=511bars															
Re048_I	Gl(10)	50,74	2,56	14,11	9,44	0,20	7,99	11,47	2,43	0,69	0,23	0,05	0,09	97,67	
Re048_II	Gl(5)	50,82	2,50	14,14	9,31	0,13	7,92	11,48	2,60	0,75	0,27	0,05	0,04	97,41	
	Ol	40,67	0,17	0,07	15,66	0,15	44,62	0,45	0,02	0,02	0,00	0,00	0,09	101,91	Fo83,6
	Ol	40,16	0,09	0,00	14,01	0,19	44,65	0,42	0,00	0,00	0,11	0,13	0,05	99,80	Fo85
Re048_III	Gl(5)	51,13	2,81	14,16	8,87	0,19	7,66	11,48	2,52	0,72	0,32	0,02	0,12	98,52	
	Ol	40,72	0,08	0,14	13,79	0,22	45,17	0,52	0,03	0,00	0,11	0,00	0,06	100,84	Fo85,4
	Ol	40,12	0,10	0,03	15,12	0,37	43,84	0,44	0,03	0,03	0,09	0,00	0,08	100,24	Fo83,8
Re048_IV	Gl(4)	51,26	2,82	14,40	8,51	0,16	7,49	11,65	2,52	0,72	0,35	0,04	0,10	98,45	
	Ol	39,82	0,10	0,09	14,61	0,36	43,88	0,47	0,00	0,00	0,00	0,26	0,07	99,66	Fo84,3
	Ol	39,20	1,16	0,28	15,53	0,33	43,59	0,58	0,00	0,05	0,03	0,04	0,15	100,93	Fo83,3
Re048_V	Gl(5)	51,43	2,82	14,49	8,17	0,14	7,39	11,74	2,59	0,72	0,25	0,06	0,20	99,82	
	Ol	40,53	0,07	0,09	12,99	0,13	45,17	0,53	0,01	0,00	0,03	0,00	0,04	99,58	Fo86,1
	Ol	39,92	0,50	0,20	13,45	0,24	45,23	0,43	0,00	0,00	0,00	0,00	0,05	100,03	Fo85,7
	Cpx	52,83	1,08	3,18	4,17	0,06	16,79	20,56	0,29	0,06	0,00	0,00	0,92	99,93	En49Wo44Fs7
	Cpx	51,85	1,44	4,64	5,53	0,12	15,61	19,88	0,27	0,08	0,07	0,05	0,77	100,31	En47Wo43Fs10

Table 5 ***Continued***

Series "Re045" T=1125°C // P=507bars															
Re045_I	Gl(5)	51,29	2,71	14,34	8,83	0,15	7,40	11,67	2,63	0,70	0,25	0,02	0,01	96,34	
	Ol	40,05	0,02	0,00	16,48	0,10	43,57	0,43	0,04	0,00	0,07	0,05	0,33	101,15	Fo82,5
	Ol	39,62	0,06	0,04	15,27	0,28	45,68	0,40	0,00	0,00	0,00	0,06	0,02	101,39	Fo84,2
Re045_II	Gl(5)	51,75	2,66	14,55	9,30	0,22	6,66	11,15	2,52	0,78	0,36	0,01	0,02	97,05	
	Ol	38,75	0,06	0,10	17,49	0,37	43,07	0,46	0,04	0,02	0,02	0,04	0,06	100,47	Fo81,4
	Ol	39,84	0,06	0,10	16,52	0,23	44,04	0,45	0,00	0,01	0,00	0,00	0,01	101,24	Fo82,6
	Cpx	49,33	4,37	9,09	6,96	0,18	12,43	18,17	0,60	0,22	0,00	0,40	0,00	101,75	En42Wo45Fs13
	Cpx	51,41	2,35	3,10	5,44	0,09	17,03	20,97	0,31	0,04	0,00	0,91	0,08	101,73	En48Wo43Fs9
Re045_III	Gl(2)	51,24	2,75	14,92	9,13	0,17	6,73	11,17	2,70	0,78	0,35	0,03	0,03	96,64	
	Ol	39,59	0,00	0,18	16,09	0,28	43,95	0,55	0,00	0,00	0,08	0,00	0,00	100,72	Fo83
	Ol	39,68	0,12	0,08	17,02	0,14	43,09	0,48	0,00	0,01	0,06	0,01	0,00	100,69	Fo81,9
	Cpx	50,34	1,32	3,11	8,32	0,28	15,91	19,97	0,24	0,00	0,03	0,42	0,12	100,06	En46Wo41Fs13
	Cpx	51,22	1,18	3,47	5,33	0,23	16,31	20,83	0,29	0,04	0,04	1,04	0,09	100,07	En47Wo44Fs9
Re045_IV	Gl(5)	52,17	2,82	14,88	8,81	0,15	6,64	11,08	2,51	0,71	0,23	0,01	0,00	96,96	
	Ol	39,54	0,18	0,10	17,37	0,18	43,53	0,44	0,00	0,01	0,10	0,03	0,22	101,70	Fo81,7
	Ol	39,65	0,00	0,05	15,57	0,24	45,34	0,46	0,00	0,01	0,00	0,00	0,07	101,37	Fo83,8
	Cpx	52,36	1,83	2,24	5,26	0,16	17,46	21,06	0,16	0,02	0,00	0,66	0,01	101,23	En49Wo43Fs8
	Cpx	50,00	3,76	10,35	6,38	0,09	11,07	15,48	0,17	0,54	n.a.	0,38	0,00	98,22	En43Wo43Fs14
Series "Re046" T=1100°C // P=506bars															
Re046_I	Gl(2)	49,35	2,59	14,31	9,51	0,04	5,93	10,69	3,04	0,61	0,24	0,05	0,11	96,47	
	Ol	40,00	0,01	0,10	17,73	0,30	42,67	0,50	0,00	0,04	0,04	0,00	0,09	101,48	Fo81,1
	Ol	39,13	0,09	0,03	18,72	0,18	41,82	0,41	0,00	0,05	0,03	0,00	0,00	100,45	Fo80
	Cpx	50,45	1,51	3,71	7,17	0,16	15,41	20,39	0,27	0,00	0,00	0,61	0,00	99,68	En45Wo43Fs12
	Cpx	47,90	2,56	11,05	9,01	0,30	10,64	16,89	0,66	0,31	0,25	0,16	0,00	99,73	En38Wo44Fs18
Re046_II	Gl(2)	52,20	2,74	14,92	10,20	0,24	5,98	10,50	2,30	0,74	0,17	0,01	0,00	96,71	
	Ol	40,22	0,00	0,06	16,77	0,36	42,42	0,40	0,00	0,00	0,04	0,00	0,07	100,33	Fo81,8
	Ol	39,26	0,09	0,07	19,21	0,17	42,59	0,42	0,01	0,00	0,00	0,00	0,01	101,82	Fo79,8
	Cpx	50,79	1,38	4,00	6,12	0,14	15,09	20,58	0,27	0,00	0,00	0,71	0,00	99,08	En45Wo45Fs10
	Cpx	49,20	1,90	5,17	7,75	0,10	15,42	19,20	0,31	0,06	0,07	0,40	0,00	99,58	En46Wo41Fs13
Re046_III	Gl(7)	50,62	3,00	15,58	9,88	0,21	5,90	10,51	3,00	0,82	0,45	0,01	0,02	96,24	
	Ol	39,53	0,05	0,04	18,99	0,20	41,24	0,45	0,00	0,02	0,00	0,02	0,12	100,66	Fo79,5
	Ol	38,80	0,06	0,04	20,35	0,27	41,08	0,47	0,00	0,00	0,21	0,00	0,20	101,47	Fo78,3
	Cpx	50,59	1,43	4,46	6,18	0,19	15,01	20,81	0,28	0,00	0,04	0,58	0,00	99,57	En45Wo45Fs10
	Cpx	50,82	1,60	6,31	7,84	0,06	13,85	18,05	0,47	0,26	0,06	0,38	0,18	99,88	En44Wo42Fs14
	Plag	50,65	0,13	29,66	0,86	0,00	0,26	14,16	3,03	0,07	0,00	0,00	0,00	98,83	An69Ab30Or1
	Plag	51,80	0,19	28,64	0,73	0,01	0,37	13,68	3,35	0,15	0,04	0,00	0,04	99,00	An66Ab32Or2
Re046_IV	Gl(4)	50,42	3,31	14,90	11,32	0,19	5,44	9,80	2,92	0,97	0,70	0,03	0,00	96,14	
	Ol	39,02	0,24	0,62	22,83	0,26	37,02	0,68	0,04	0,05	0,00	0,02	0,12	100,90	Fo74,3
	Ol	39,08	0,07	0,05	19,98	0,35	40,43	0,45	0,01	0,00	0,00	0,00	0,13	100,55	Fo78,3
	Cpx	50,76	1,50	3,87	6,81	0,24	15,31	20,03	0,29	0,02	0,00	0,37	0,00	99,20	En46Wo43Fs11
	Cpx	50,43	1,63	3,26	8,89	0,24	15,39	18,78	0,27	0,00	0,02	0,30	0,15	99,36	En45Wo40Fs15
	Plag	50,74	0,20	28,75	0,84	0,01	0,33	13,73	3,26	0,13	0,00	0,00	0,00	98,00	An67Ab32Or1
	Plag	52,50	0,67	26,82	1,51	0,00	0,39	12,00	4,20	0,33	0,02	0,01	0,00	98,44	An57Ab40Or3
Re046_V	Gl(3)	50,32	3,40	14,81	11,67	0,17	5,40	9,74	2,89	0,96	0,61	0,02	0,00	95,34	
	Ol	37,64	0,12	0,09	23,72	0,46	38,16	0,44	0,01	0,07	0,19	0,03	0,05	100,99	Fo74,1
	Ol	38,34	0,15	0,07	21,27	0,36	38,98	0,41	0,04	0,02	0,00	0,00	0,30	99,96	Fo76,6
	Cpx	50,33	1,66	4,40	8,22	0,04	14,36	19,53	0,43	0,07	0,00	0,42	0,15	99,61	En43Wo43Fs14
	Cpx	51,00	1,57	3,30	7,57	0,28	15,18	19,31	0,28	0,03	0,00	0,31	0,00	98,86	En46Wo41Fs13
	Plag	52,30	0,69	26,33	1,92	0,18	0,72	12,28	4,16	0,26	0,09	0,00	0,09	99,02	An58Ab39Or3
	Plag	52,38	0,42	26,73	1,35	0,04	0,56	12,52	4,06	0,21	0,00	0,00	0,00	98,26	An59Ab39Or2

CHAPITRE IV : “Approche expérimentale – étude des équilibres de phases haute pression d’un magma réunionnais et caractérisation des fractionnements profonds”

Résumé

Les résultats expérimentaux de simulation du système d'alimentation superficiel du Piton de la Fournaise ont été présentés au Chapitre 3. Ce Chapitre 4 détaille les expériences réalisées à plus haute pression (de 200MPa à 1GPa). L'objectif principal est d'apporter des contraintes expérimentales sur les parties les plus profondes du PdF. Pour ce faire, la composition de SSB REU0912-04 ayant fait l'objet du travail au Chapitre 3 sera à nouveau utilisée dans ce Chapitre afin de faciliter les comparaisons.

Dans ce Chapitre, rédigé sous forme d'article, certaines méthodologies expérimentales spécifiques aux expériences haute pression sont présentées. Un protocole de contrôle de la perte de fer a été systématiquement mis en œuvre. Ainsi, les expériences ont été menées, d'une part, sur le verre REU0912-04 et sur un matériau enrichi en fer (verre plus 4.2% FeO ajouté). Par ailleurs, des expériences avec olivine et/ou clinopyroxène ajoutés ont été réalisées pour forcer la saturation du liquide et s'approcher de la composition des liquides primitifs. Les expériences à 200, 300 et 400 MPa ont été effectuées en autoclave à chauffage interne et celle à 1 GPa en piston cylindre. Elles ont été conduites systématiquement en présence de volatils (fluides H_2O-CO_2) et dans deux gammes de fO_2, de NNO-1,5 à NNO d'une part et de NNO+0,5 à NNO+2, d'autre part. Les teneurs en H_2O dissoutes dans les verres (1-2 %) ont été estimées par différence. Les charges avec le matériau enrichi en fer se sont avérées être trop enrichies et la distribution en fer hétérogène au sein d'une même charge et d'une charge à l'autre. Ces problèmes ont conduit à traiter ces charges à part. Les observations texturales et les calculs des coefficients de partage minéral-liquide pour les charges avec le verre REU0912-04 et celles avec minéraux ajoutés indiquent une bonne approche de l'équilibre. Plusieurs changements notoires interviennent selon la pression dans les assemblages de phases expérimentaux. Premièrement, l'olivine, qui cristallise systématiquement à 200, 300 et 340 MPa pour les charges enrichies en fer, est remplacée par le clinopyroxène au liquidus à 400 MPa pour la composition REU0912-04. Nos expériences permettent donc de proposer pour la première fois la possibilité d'un fractionnement, à partir de 400 MPa, du clinopyroxène dans le système d'alimentation du PdF. La gamme de pression pour un tel fractionnement profond de clinopyroxène est cohérente avec le niveau de sous-plaquage identifié par les études géophysiques à l'interface croûte-manteau sous l'édifice réunionnais (Gallart et al., 1999). La démonstration expérimentale du clinopyroxène en phase liquidus dans les conditions du système d'alimentation profond permet de soutenir le

mécanisme de fractionnement de clinopyroxène qui a été proposé pour expliquer l'origine des compositions AbG (voir le Chapitre 1). Deuxièmement, l'olivine est instable dans l'expérience réalisée à 1 GPa, elle réagit pour donner de l'orthopyroxène et son influence est vraisemblablement très limitée > 500 MPa.

Les données obtenues à haute pression avec celles présentées dans le Chapitre 3 permettent de construire les lignes cotectiques ol+cpx à diverses pressions, en particulier pour 400 MPa. La comparaison avec les verres naturels, notamment les verres AbG présentés dans le Chapitre 1, montrent que ces derniers dérivent nécessairement d'un fractionnement à des pressions > 400 MPa, c'est-à-dire dans une gamme de pression dans le domaine du manteau supérieur. Ces résultats expérimentaux apportent donc des conclusions primordiales pour les processus pétrologiques profonds ayant lieu dans le système d'alimentation du PdF. Ils remettent notamment en cause les compositions proposées pour les magmas parentaux au PdF.

Pressure effect on liquidus phases for a Steady State Basalt from Piton de la Fournaise volcano (Reunion Island): experimental insights on deep Cpx fractionation.

YANN-AURELIEN BRUGIER, MICHEL PICHAVANT & ANDREA DI MURO

Abstract High pressure experimental phase equilibria have been determined for a Steady State Basalt (7.8 wt% MgO, 11.2 wt% CaO, 13.8 wt% Al2O3) from Piton de la Fournaise volcano on La Réunion island to determine the pressure of the transition from olivine to clinopyroxene on the liquidus and simulate the evolution of primitive magmas inside the deep feeding system. A second Fe enriched composition, obtained by addition of 4.2 wt% FeO to the starting glass, was also used to mitigate Fe loss. The experiments were carried out mostly between 200 and 400 MPa, and also at 1GPa, at temperatures from 1175°C to 1250°C and in presence of volatiles (H2O-CO2 mixtures). Redox conditions are estimated to between NNO-1.5 and NNO+2. Both crystallization and clinopyroxene- and/or olivine-added experiments were performed. Attainment of equilibrium was checked by SEM observations of experimental charges and mineral-melt partitioning data. Glass melt H2O contents were estimated using the "by difference" method. Difficulties were encountered with the Fe enrichment method and results of Fe enriched charges needed to be treated separately. At 1175°C, olivine crystallized in Fe enriched charges at 200 and 300 MPa. At 400 MPa, clinopyroxene is the sole liquidus phase. In the 1GPa, 1250°C clinopyroxene- and olivine-added charge, olivine partially reacted to orthopyroxene (Mg# = 85-88). Olivines are Fo-poor (Fo < 80) in charges with the Fe enriched starting material, and reach Fo88 in the Ol-added experiments. Experimental clinopyroxenes (En_{43-56} Wo_{30-47} Fs_{7-16}) are diopsides and augites and approach the composition of the most primitive crystals in ultra-mafic cumulates. Clinopyroxenes crystallized at 1 GPa have low CaO and significant Na2O (~0.5 wt%). Glasses in mineral-added charges extend the range of experimental melts toward primitive compositions (10-11 wt% MgO). The experimental data demonstrate for the first time the possibility for clinopyroxene to crystallize on the liquidus at pressures compatible with magma storage zones, thus supporting models of clinopyroxene fractionation in the deep feeding system. Comparison with experimental liquid compositions shows that natural glasses result from essentially two types of fractionation mechanisms, olivine-dominated and clinopyroxene-dominated, the latter taking place at pressures > 400 MPa, i. e., at or below the crust-mantle transition beneath the island.

Keywords: *Piton de la Fournaise; Steady State Basalts; high pressure experiments; phase equilibria; pressure effect; deep clinopyroxene fractionation*.

1 Introduction

La Réunion is a volcanic island of the southwest Indian Ocean, located around 800 km off the Madagascar eastern coast. Volcanic activity, associated with the Mascareignes hotspot (Duncan et al., 1989; Bonneville, 1990; Chenet et al., 2007), started 5 Ma ago (Gillot et al., 1994) and continues until now. Two juxtaposed volcanoes compose the island: the now deeply eroded Piton des Neiges (PdN) whose activity ended 29 ka ago (McDougall, 1971; Quidelleur et al., 2010), and the Piton de la Fournaise (PdF) volcano, one of the most active basaltic volcanoes on Earth (1-2 eruptions per year; Staudacher et al., 2016) and whose activity began 535 ka ago (Gillot & Nativel, 1989). The existence of a third volcano, named "les Alizés" (Malengreau, 1995; Malengreau et al., 1999; Lénat et al., 2001; Smietana, 2011; Lénat, 2016), is still debated (Lebas, 2012; Salvany et al., 2012).

Volcanic products erupted by the PdF are classically distributed in 4 different groups: "Steady State Basalts" (SSB), "Oceanites" (Oc), "Differentiated Lavas" (Diff. Lavas) and the "Abnormal Group" (AbG), see Albarède et al. (1997), Famin et al. (2009) and Pichavant et al. (2016). Two of these groups are clearly separated. (1) SSB, the dominant lavas in the modern activity (< 4000 years) of the PdF, are transitional basalts with a narrow range of compositions (MgO = 5-8 wt%; CaO/Al2O3 = 0.75-0.85; see Albarède et al., 1997; Famin et al., 2009; Lénat et al., 2012a). (2) The AbG group, which clearly differs from the 3 other groups, shows enrichments in MgO (8-11 wt%) as well as in Fe, Ti, Na, K, and depletions in CaO, leading to relatively low CaO/Al2O3 (0.6-0.8). AbG-type lavas are very rarely observed inside the present-day main eruptive site, the Enclos Fouqué (e.g., Formica Léo or Hudson cones, Villemant et al., 2009; Salaün et al., 2010; Boudoire et al., in prep). They mostly occur at eccentric vents more or less distant of the active center, either belonging to the North-West South-East rift zone (Di Muro, 2012; 2015; Michon et al., 2015; Boudoire et al., in prep) or in areas such as the "Plaine des Sables" (PdS, Morandi et al., 2016; Principe et al., 2016; Brugier et al., 2016a; Boudoire et al., in prep).

There is relatively broad agreement on the origin of SSB compositions, as well as of the related Oceanites and Differentiated Lavas (Bachèlery, 1981; Albarède et al., 1997; Vlastélic et al., 2005; Welsch et al., 2009; Famin et al., 2009; Villemant et al., 2009; Salaün et al., 2010; Smietana, 2011; Valer et al., 2015) and the magmatological discussion at the PdF now mainly focuses on mechanisms of generation of AbG-type compositions. The strong isotopic homogeneity of La Réunion lavas (Fisk et al., 1988; Graham et al., 1990; Vlastélic & Pietruszka, 2016), despite small changes in trace elements and Pb, Sr, Nd, Hf isotopic ratios (Albarède et al., 1997; Vlastélic et al., 2005, 2007, 2009; Bosch et al., 2008; Pietruszka et al., 2009), suggests that these two main magmatic groups originate from different fractionation mechanisms in the volcanic feeding system. Deep clinopyroxene (± olivine) fractionation has been proposed to generate AbG compositions (Kornprobst et al., 1979, 1984; Albarède et al., 1997; Famin et al., 2009; Brugier et al., 2016a; Boudoire et al., in prep) whereas olivine fractionation would be responsible for the genesis of SSB compositions (Albarède et al., 1997; Famin et al., 2009; Welsch et al., 2009; Brugier et al., 2016c).

To clarify these issues, an experimental study has been recently performed on a SSB-type composition, between 0.1 and 50 MPa and in presence of H2O-CO2 fluid mixtures (Brugier et al., 2016c). This study has closely simulated the shallow part of the feeding system (Peltier et al., 2009; Lénat et al., 2012a; Di Muro et al., 2014; Michon et al. 2015) and brought constraints on crystallization conditions and mechanisms (Brugier et al., 2016c). Liquidus phase equilibria were defined and the importance of olivine fractionation as a control of SSB lava diversity demonstrated. These experimental results have shown that clinopyroxene can crystallize second after olivine at low pressures (50 MPa), and this up to surface conditions for some fO2 (Brugier et al., 2016c).

This paper presents an extension of the experimental work of Brugier et al. (2016c) on a PdF Steady State Basalt. Higher experimental pressures (from 200 MPa to 1 GPa) have been considered to (1) determine the pressure of the transition from clinopyroxene to olivine as the liquidus phase under fluid-present conditions (Pichavant et al., 2016) and (2) simulate the evolution of primitive magmas inside the deep feeding system of the Piton de la Fournaise.

2 Selection of the starting sample and experimental approach

The sample used in this paper (REU0912-04) was erupted during the December 2009 PdF fissural activity, localized on the southern flank of the volcano, with fissures running parallel to the Dolomieu crater. The eruption had a volume of 0.16 Mm^3 and it yielded nearly aphyric, relatively Mg-rich basalts belonging to the SSB series (Staudacher et al., 2016). The cm-sized scoriae were sampled by A. Di Muro. Olivine is a rare phenocryst (A. Di Muro, personal communication); clinopyroxenes and plagioclases are found as microphenocrysts and/or microlites.

This sample is the same as used previously in 0.1 MPa volatile-free and 50 MPa volatile-bearing experiments (Brugier et al., 2016c). Those experiments were performed under experimental (T-P-fO2-melt H2O and CO2 contents) representative of the shallow feeding-system of the PdF (Lénat et al., 2012a; Di Muro et al., 2014; Michon et al., 2015; Brugier et al., 2016c). Nevertheless, higher pressure magmatic processes are recorded in PdF products. Geophysical studies have located potential magma storage zones at pressures of 120 to 200 MPa (Lénat et al., 2012a; Di Muro et al., 2014). Certain glass inclusions have volatile concentrations (up to 1.55 wt% H2O and to 0.32 wt% CO2) that imply fluid-melt saturation pressures up to 420 MPa (Bureau et al., 1998 a; b). A similar pressure range has been determined in certain fluid inclusions (Boudoire et al., in prep). Such high saturation pressures (400-450 MPa) coincide with the depth (12-15 km) of the underplating layer identified from geophysical studies at the interface between mantle and oceanic crust beneath La Réunion (Gallart et al., 1999), and interpreted as a wehrlitic crystal mush zone. In addition, a deep (> 400 MPa) mechanism of clinopyroxene (± olivine) fractionation has been proposed to generate the AbG compositions (Kornprobst et al., 1979, 1984; Albarède et al., 1997; Brugier et al., 2016a). All these petrological and geophysical data motivate the present experimental investigation which reports phase equilibrium data at pressures of 200, 300, 400 MPa and 1 GPa under fluid-present conditions, using H2O-CO2 mixtures.

The use of a relatively evolved SSB-type composition to simulate deep-seated processes (where magma compositions are presumably more primitive) might not be totally adequate. However, it allows direct comparison between experimental studies (this work and Brugier et al., 2016c) and so the effect of pressure can be unambiguously determined. In addition, there are no direct constraints on the composition of primitive magmas at La Réunion since primitive eruption products or glass inclusions are lacking. Therefore, instead of embarking in a necessarily ad hoc definition of primitive/parental magmas (e.g., Ludden, 1978; Famin et al., 2009; Villemant et al., 2009), an inverse approach will be applied here. The PdF differentiation sequence will be examined “uphill”, beginning with relatively evolved compositions (REU0912-04) to progressively approach the characteristics of primitive magmas.

3 Experimental methods

3.1 Starting material

REU0912-04 scoriae were ground in an agate mortar and fused in air at 1400°C, 0.1 MPa in a Pt crucible. Two cycles of melting (3-4h each), with grinding in between, were performed, yielding a homogeneous glass whose composition was checked by electron microprobe (Table 1). The glass was then crushed and stored in an oven.

Special care was paid to mitigate the Fe loss problem given our relatively Fe-rich melt compositions and reducing conditions in certain of our experiments. Apart from the use of AuPd alloys as capsule materials (Kawamoto & Hirose, 1994; Hall et al., 2004; Di Carlo et al., 2006; Barr & Grove, 2010; Balta et al., 2011), the "Fe pre-enrichment" method (Brugier et al., 2015) was systematically implemented. Brugier et al. (2015) have shown that the use of starting materials pre enriched in Fe can significantly reduce Fe loss in petrological experiments. Therefore, a second Fe enriched composition was used as starting material in this study. This was obtained by adding 4.2 wt% FeO to REU0912-04 glass and mixing the resulting powder mechanically in an agate mortar. The calculated composition of this Fe enriched starting mixture is presented in Table 1.

3.2 200-400 MPa experiments

$Au_{80}Pd_{20}$ capsules (length 15-25 mm, internal diameter 2.5 mm, wall thickness 0.2 mm) were used as containers. These were loaded with about 30-50 mg of either the Fe enriched mixture (HP2, HP3, HP4 series) or REU0912-04 (HP40, HP4b series) glass powder plus the fluid components (H_2O and CO_2). H_2O was introduced as distilled demineralized water with a syringe and CO_2 as $Ag_2C_2O_4$ powder. H_2O and $Ag_2C_2O_4$ were weighed so as to generate charges with variable $XH_2O_{in.}$ [initial molar $H_2O/(H_2O+CO_2)$] while keeping the $(H_2O+CO_2)/(H_2O+CO_2+glass)$ mass ratio constant at ~10%. In this study, $XH_2O_{in.}$ ranged from 0.4 to 0.1. In a few cases, when the $XH_2O_{in.}$ was too small, the mass of glass powder was increased to allow the mass of H2O to be more precisely weighted.

Either clinopyroxene- or olivine-added charges were prepared to force saturation with respect to these mineral phases under the experimental conditions. To do so, in experimental series HP2, HP3 and HP4, an additional capsule was loaded with a mixture of 50 mg of Fe-enriched powder plus 20% (~10 mg) of grounded and sieved (to 50-100 µm) clinopyroxenes hand-picked from the Plaine des Sables wehrlitic cumulates (see Table 1). In experimental series

HP43, both olivine and olivine plus clinopyroxene saturation were tested. Capsules were loaded with mixtures of 30 mg of REU0912-04 glass powder with, respectively, 10% (~3 mg) of grounded and sieved (to 50-100 µm) San Carlos olivine (Table 1), and 20% (~6 mg) of clinopyroxene plus 10% (~3 mg) of olivine. These crystal-rich capsules were all loaded with H_2O and $Ag_2C_2O_4$ to generate a $XH_2O_{in.}$ of 0.3. All capsules were sealed by arc welding or by PUK, keeping them in a liquid nitrogen bath to prevent water loss. Once sealed, they were put in an oven for several hours and reweighted to check for leaks.

The experiments were carried out in an internally heated pressure vessel working vertically and pressurized with either pure Ar (HP3, HP4, HP43 series) or Ar-H_2 mixtures (HP2 and HP40 series) obtained by sequential loading of H_2 and Ar at room temperature (Scaillet et al., 1992). Initial H_2 pressures were fixed at 4 bar. Total pressure was recorded by a transducer calibrated against a Heise Bourdon tube gauge (uncertainty ± 20 bar). A double winding Mo furnace was used, allowing near-isothermal conditions in the 2-3cm long hot-spot (gradient < 2-3°C cm^{-1}). Temperature was measured by two thermocouples (type S) and recorded continuously (total uncertainty ±5°C). Run durations ranged from 1.5 to 18h, and all of them were drop-quenched, resulting in nearly isobaric quench rates of ~100°C s^{-1} (Di Carlo et al., 2006).

At the end of the experiment, capsules were weighed to check for leaks and then opened. For each capsule, fragments of the run product were mounted in epoxy and polished for scanning electron microprobe observations and electron microprobe analyses.

3.3 1GPa experiments

An $Au_{80}Pd_{20}$ capsule (length 14 mm, internal diameter 2.5 mm, wall thickness 0.2 mm) was used as container and loaded with a mixture of 30 mg of REU0912-04 glass powder and 20% (~6 mg) of clinopyroxene plus 10% (~3 mg) of San Carlos olivine, plus the fluid components (H_2O and CO_2). H_2O was introduced as distilled demineralized water with a syringe and CO_2 as $Ag_2C_2O_4$ powder. H_2O and $Ag_2C_2O_4$ were weighed so as to generate a charge with a $XH_2O_{in.}$ of 0.3. This experiment was conducted in a piston cylinder with a ½” furnace assembly made of graphite and outer sleeves of pyrex and talc (Sifré et al., 2014). The sample was chemically isolated from the assembly by 2 alumina disks and an alumina tube. Temperature was read to within ± 5 °C. A 10% correction was applied on pressure, known to ± 0.1 GPa. The run lasted for 5 h and the sample was quenched in less than 10 s by shutting down the furnace power while manually maintaining the pressure as close as possible to the target pressure.

4 Analytical methods

Experimental charges were systematically examined by SEM under back-scattered electron mode (TESCAN Mira 3 XMU instrument, joint laboratory ISTO-BRGM) to confirm the identification of mineral phases and check for quench crystallization. Electron microprobe analyses were performed with a CAMECA SX FIVE electron microprobe at the ISTO-BRGM laboratory (Orléans), under 15 kV acceleration voltage, 6 nA sample current, 10 s counting time on peak and 5 s counting time on background. Mineral phases were analyzed with a focused electron beam whereas, for silicate glasses, a defocused beam (10 µm) was used to minimize alkali migration (Di Carlo et al., 2006). Relative analytical errors are 1% (SiO_2, MgO, CaO), 1-2% (Al_2O_3), 2-4% (FeO, Na_2O) and 5-10% (TiO_2, K_2O). Phase proportions and Fe losses were calculated for each charge using a least-squares mass-balance routine computed after Albarède (1995), using the electron microprobe compositions of the glass starting material (non Fe pre-enriched glass, Table 1) and of all solid phases coexisting in the charge. The regression was based on nine major oxides, excluding MnO and P_2O_5. X-ray distribution maps of Al, Cr, Ca, Fe, Mg were obtained for a few complex clinopyroxene crystals. These were carried out with the CAMECA SX FIVE electron microprobe at the ISTO-BRGM laboratory operated under an accelerating voltage of 15 kV, a beam current of 50 nA, a focused beam and a dwell time of 130 ms.

The "by-difference" method was used to estimate the concentration of dissolved H_2O (e.g. Devine et al., 1995). During each electron microprobe session, the difference to 100% of glass electron microprobe analyses was calibrated against the dissolved H2O content, using glasses of known H_2O concentrations (previously analyzed by FTIR, see Brugier et al., 2016c) as secondary standards. The "by-difference" method was applied to CO_2-bearing charges because, in this study, glass CO_2 concentrations should be always < 0.1 wt%. Therefore, the overestimation in H_2O concentration introduced by the presence of dissolved CO_2 (which increases the difference to 100%) is negligible.

5 Experimental results

Experimental conditions and results are detailed in Table 2 and experimental compositions in Table 3. In total, 25 high pressures charges (corresponding to 6 experiments performed in internally heated gas vessel and 1 experiment in piston cylinder) are reported. The gas vessel experiments were performed under variable redox conditions. From other experiments performed in the same laboratory and under the same pressure, temperature and initial H2 pressure conditions, the redox conditions of the HP2 and HP40 experiments (4 bar H2 initial) can be estimated in the range NNO-1.5 to NNO, and of the HP2, HP4, HP4b, HP43 experiments (no H2 initially added) in the range NNO+0.5 to NNO+2. Redox conditions in the piston-cylinder experiment are unknown.

5.1 Fe loss/gain

The importance of Fe loss/gain (relative values) can be evaluated from the mass-balance calculations on experimental charges without added crystals (Table 2). In the high pressure experiments performed with the Fe-enriched starting material (HP2, HP3 and HP4 series), most charges have gained Fe (Fe losses from +1.1% to +7.2% relative, Table 2) in comparison with REU0912-04 glass. Only one charge from the HP2 series has lost Fe (Fe loss of -5%). Overall, these data are consistent with addition of Fe from the Fe enriched starting material. However, the systematic Fe gains imply that, on average, a too high proportion of Fe has been added. Charges from the HP2 series show an inconsistent behavior with respect to Fe. Three have marked Fe gains and the fourth is the only one with Fe loss among experiments performed with the Fe enriched starting material. Yet, this experiment was performed with 4 bars of H2 initially added (Table 2). As the most reducing of the three HP2, HP3, HP4 experiments, HP2 charges would be expected to show either minimum Fe gains or maximum Fe losses (see Hall et al., 2004; Di Carlo et al., 2006; Barr & Grove, 2010; Balta et al., 2011; Brugier et al., 2015), which is not observed.

SEM examination of charges having started from the Fe enriched material reveals that Fe can be heterogeneously distributed (Fig. 1a), a consequence of the preparation of the Fe enriched starting material by mechanically mixing REU0912-04 glass and FeO. The distribution of silicate crystals also appears heterogeneous (olivine on one side and clinopyroxene on the other side, Fig. 1a). In one charge (HP2_II), a Fe oxide block (x 100 µm large) armoured from the glass by silicate crystals was found. Therefore, practical difficulties have been encountered with the Fe enrichment method (Brugier et al., 2015).

Fe losses calculated for experiments performed with REU0912-04 glass are relatively low for charges from the HP4b series (< 4.3%) but quite high in the HP40 series (> 24.4%), consistent with the respective initial H2 pressures and redox conditions of the two experiments (Table 2). The long duration of the HP40 experiment also worsened the Fe loss problem. Even if charges with contrasted Fe losses in the HP40 and HP4b series show no systematic differences in phase assemblages and compositions, the complex chemical zonations observed in clinopyroxenes (Fig. 1c; 3; 4) from some HP40 charges are attributed to progressive Fe loss from the charge toward the capsule in this long experiment.

We conclude that Fe loss to the container capsule has remained a persistent problem in this study and that efforts to mitigate this difficulty have not been completely successful. In fact, new difficulties, such as bulk and local Fe heterogeneities between charges, have been introduced.

5.2 Evaluation of equilibrium

In this study, all charges starting from glass were of crystallization type. Those starting from the Fe enriched mixture involved reaction between glass and FeO (mainly Fe dissolution) followed, or accompanied, by crystallization. No reversals have been performed. Yet, the following lines of evidence allow the approach toward equilibrium to be evaluated in our experiments.

(9) The high pressure experiments lasted for 5 to 17h, sufficient for equilibrium crystallization of hydrous basaltic melts on the basis of previous studies (Barclay & Carmichael, 2004; Di Carlo et al., 2006; Pichavant & Macdonald, 2007; Pichavant et al., 2014; Brugier et al., 2016c). This is valid only for experiments starting from glass as Fe heterogeneities were found in charges made with the Fe enriched material, even for durations > 10 h (Fig. 1a, Table 2).

(10) Crystals in charges starting from glass have equant, euhedral or tabular morphologies and their distribution is relatively homogeneous (Fig. 1a; 1d). Yet, differences in crystal sizes can occur in the same charge (Fig. 1b). Crystal settling was noticed only in the piston cylinder charge. Quench crystals were identified in two charges (Fig. 1f; h; i).

(11) Sums of residuals from mass-balance calculations ($\sum R^2$) are ≤ 1 for 10 out of the 19 calculated charges (the olivine- and clinopyroxene-added charges were excluded). Only 3 charges (those with the highest Fe losses) have $\sum R^2 > 10$. This indicates reasonable balance of silicate components between coexisting phases. Negative spinel proportions are systematically observed in some experiments performed with the Fe enriched starting material (HP3, Table 2), probably because of differences between nominal and effective Fe enrichment.

(12) Silicate glasses are mostly chemically homogeneous. Compositional gradients have been detected in only one charge. In the piston-cylinder charge HP10, glass in the crystal-poor top part is compositionally different from glass in the crystal-rich area (Fig. 1i). Chemical heterogeneities associated with the preparation of the Fe enriched composition can produce phase assemblages and distributions that locally vary (Fig. 1a) but glass compositions remain chemically homogeneous.

(13) Compositions of experimental olivines are quite homogeneous in a given charge (Table 3). In the HP2 charges, olivine-melt Fe-Mg exchange coefficients (K_d Ol-l, calculated with liquid FeO = FeOtotal, Table 2) are in the range expected for olivine-liquid equilibrium (Di Carlo et al., 2006; Pichavant & Macdonald, 2007; Pichavant et al., 2014). In the other charges, K_d Ol-l are lower, a difference related to the redox conditions, more oxidized in HP3, HP4, HP43 than in HP2. For the former charges, K_d Ol-l (Table 2) are minimum values because an appreciable proportion of Fe is present in the melt as Fe2O3.

(14) Clinopyroxenes can be grouped in two populations. The first comprises small crystals (< 10-20 μm, Fig. 1a; b; d), generally numerous and relatively chemically homogeneous (Table 3). These yield K_d Cpx-l (0.27 to 0.33; Table 2) consistent with literature values for clinopyroxene-liquid equilibrium (Di Carlo et al., 2006; Pichavant & Macdonald, 2007; Pichavant et al., 2014). The second corresponds to larger crystals that occur in some charges. Core-rim textural variations accompanied by chemical zonations (CpxA, Fig. 1b; Table 3) have be observed, sometimes complex (CpxB, Fig. 1c; 3) and indicating deviation from equilibrium crystallization.

We conclude that crystal-liquid equilibrium was globally closely approached in experiments performed with glass and with the Fe enriched material. Indications for non-equilibrium crystallization, which include heterogeneous phase assemblages and distributions and chemically heterogeneous clinopyroxenes, are overall of limited importance.

5.3 Olivine- and clinopyroxene-added charges

Experiments performed with clinopyroxene- and/or olivine-added charges involved complex reactions between minerals and glass, and crystallization. These yielded specific textures and phase assemblages, detailed below.

(1) Olivine persists as a residual anhedral phase (Ol R, Fig. 1e; f; g; Table 3) in the three charges where it was added. It is abundant in the HP43 charges but very rare in the HP10 charge despite identical amounts added in starting materials. In the two HP43 charges, residual olivines show strong core-rim normal Fo zonations from ~95 (cores) to ~88.7 (rims) and inverse Ca zonations from ~0.15 wt% (cores) to 0.30-0.40 wt% (rims). The presence of Fo95 (Fo91 in San Carlos olivines) indicates that residual olivine cores are being extensively reequilibrated under the experimental conditions. In the HP43_I charge, small euhedral olivines, presumably crystallized from the melt, have compositions (Fo88) approaching residual olivine rims. Kd Ol-l (calculated with liquid FeO = FeOtotal using rim compositions and crystals grown from the melt) are in the same range (0.23-0.24) as in the other oxidizing charges (see above, Table 3).

(2) Residual clinopyroxene also persisted in the 5 charges (3 performed with the Fe enriched starting material) where it was added. In the highest temperature, most reacted 1225°C charge (HP43_II), anhedral rounded oval clinopyroxene cores are surrounded by thick euhedral rims (Fig. 1f; g), indicating extensive dissolution-recrystallization. Core-rim chemical zonations, with Ca-rich (unreacted, see Table 1) cores and Al-, Fe- and Mg-enriched rims are systematically found (Table 3). For a given charge, residual clinopyroxene rims and clinopyroxene crystallized from the melt have the same range of compositions (Table 3). Kd Cpx-l (calculated with rim compositions and crystals grown from the melt) range from 0.28 to 0.32, in agreement with values calculated for the other charges (Table 3).

(3) Orthopyroxene was found to crystallize in the olivine- and clinopyroxene-added 1 GPa experiment. This, combined with the near disappearance of olivine as a residual phase (see above), indicates that orthopyroxene crystallizes following the reaction: olivine + melt = orthopyroxene. Olivine (Fo88.7, Table 3) is therefore interpreted to be unstable in the HP10 charge at 1 GPa. Orthopyroxene (Mg# = 85-88) grows as euhedral crystals of different size. It coexists with large zoned residual and smaller newly-formed clinopyroxenes, compositionally similar to residual clinopyroxene rims (Table 3). Both the Kd Cpx-l and Kd Opx-l (calculated with rim compositions and pyroxenes

crystallized from the melt) are in the range of equilibrium values (e.g., Pichavant and Macdonald, 2007), as is the case for the Kd Ol-l calculated using the composition of the residual olivine (Table 2).

Although bulk equilibrium is clearly not attained in these mineral-added charges (occurrence of zoned crystals, persistence of unreacted cores, olivine present at 1 GPa outside its stability domain), analysis of phase compositions and mineral-liquid partitioning data indicate that local equilibrium is reasonably well approached between mineral rims and the rest of the charge.

5.4 Phase equilibria

Presentation of the phase equilibria excludes the mineral-added charges, focusing on experiments performed with the REU0912-04 glass and the Fe enriched starting material. The Fe gains observed in the 3 experiments starting from the Fe enriched material as well as the practical difficulties mentioned above with the Fe enrichment methodology make difficult to compare directly results obtained with the two types of starting materials. So, the respective results will be discussed separately below.

Clinopyroxene and olivine are the two major mineral phases present, crystallizing from either the REU0912-04 glass or the Fe enriched starting material. Both are frequently accompanied by spinel. Olivine and clinopyroxene crystallize in a similar number of charges (6 Ol-bearing and 7 Cpx-bearing, Table 2). Olivine occurs at 200 and 300 MPa, sometimes accompanied by clinopyroxene (HP2, 3), whereas clinopyroxene is the only phase crystallizing at 400 MPa (HP4b and HP40). In the experiment ended at 340 MPa pressure, clinopyroxene is joined by olivine. Higher mineral phase proportions occur in clinopyroxene- than in olivine-bearing charges, the highest proportions (14 % clinopyroxene) being found in the HP40 experiment. Olivine proportions are 4 % maximum.

Experimental data obtained with the two types of starting materials are plotted together on the P-$XH_2O_{in.}$ isothermal phase diagram (Fig. 2a). The olivine and clinopyroxene saturation curves are constructed by using only the data on REU0912-04 glass starting material, either from this study at 400 MPa (HP40 and HP4b, Table 2) or from Brugier et al. (2016c) at 50 MPa, 1170°C. Olivine is the liquidus phase until ~300 MPa, and it is replaced by clinopyroxene on the liquidus for higher pressures (Fig. 2a). Note that results obtained with the Fe enriched starting material yield liquidus data in the order olivine and then olivine + clinopyroxene upon increasing pressure, i.e., in broad agreement with the data on REU0912-

04 glass. If the olivine + clinopyroxene cotectic assemblage crystallized in HP4_IV (Fe enriched material) is considered, the olivine and clinopyroxene saturation curves could cross at a pressure slightly higher than drawn (Fig. 2a). Two Cpx-added charges performed with the Fe enriched material crystallized olivine at 200 and 300 MPa, but olivine is absent from the equivalent charge at 340 MPa final pressure (Table 2), implying that olivine saturation becomes more difficult as pressure is increased above 300 MPa. The presence of small olivine inclusions in clinopyroxene from the 400 MPa charge HP40_III (Fig. 1d) indicates early olivine crystallization (probably during the pressure buildup period) followed by resorption and clinopyroxene crystallization as final conditions (400 MPa) are attained.

The phase relations are also shown on the P-H2O in melt isothermal phase diagram (Fig. 2b). The grey field drawn for H2O in melt < 0.5 wt% corresponds to H2O-poor concentration conditions difficult to reach with our experimental methodology because reduction of the relatively Fe3+ rich starting glass by H2 from the pressure medium would generate a minimum of ~0.5 wt% H2O in the charge. On this diagram, the location of the clinopyroxene saturation curve at 400 MPa is only estimated because of the poor sensitivity of the “by difference” method for H2O concentrations < 2 wt%.

5.5 Composition of crystalline phases

5.5.1 *Olivines*

Olivines crystallized in this study at 200, 300 and 340 MPa have relatively low Fo (< 80, Table 3). In comparison, those crystallized from REU0912-04 glass at 0.1 and 50 MPa have higher Fo (82-86, Brugier et al., 2016c). The low Fo olivines from this study reflect the addition of FeO to the starting material. Note that the influence of Fe enrichment is partially mitigated by the addition of Cpx in 2 charges of the series HP2 and HP3 which crystallize olivines with systematically slightly higher Fo (Table 3) than in the non Cpx-added charges, since partial dissolution of Cpx increases the melt Mg#. In the olivine-added, 1225°C charges, olivines in local equilibrium with the melt reach Fo between 88 and 89, i.e., much higher than in the 1175°C charges performed with the Fe enriched composition. This Fo range is identical to that of the residual metastable olivine (Fo88.7) in the 1 GPa experiment. The very high Fo (95) of residual olivines cores record an ongoing reequilibration process between the added crystals and the rest of the charge.

5.5.2 *Clinopyroxenes*

Clinopyroxenes are diopsides and augites with 43-56% En, 30-47% Wo, 7-16% Fs (Table 3) and Mg# (calculated with total Fe as Fe2+) between 71.5 and 88.5. Apart from the Cpx-added charges, discussed previously, there are only two clinopyroxene-bearing charges ran with the Fe enriched composition (Table 2), one yielding the most Fs-rich composition in our dataset (Table 3). Therefore, the new experimental clinopyroxene data mostly pertain to the non Fe enriched REU0912-04 composition. Generally, experimental crystals are chemically homogeneous in a given charge (average compositions given in Table 3). However, some larger clinopyroxenes display chemical zonations, such as CpxA (Fig. 1b), CpxB (Fig. 1c) and CpxC (Fig. 1g). Representative analyzes of these zoned crystals (core and rims for CpxA and C, z1, z2, z3 and z4 spots for CpxB) are detailed in Table 3 and element distribution maps illustrated for CpxB (Fig. 3). Compositions of experimental clinopyroxenes crystallized at 400 MPa (HP4b, HP40 and HP43 series) and at 1 GPa (HP10) are plotted on a Al2O3 vs. Mg# diagram (Fig. 4). Comparison is made with clinopyroxenes crystallized at 50 MPa (Brugier et al., 2016c) and with natural clinopyroxenes from ultra-mafic cumulates (Brugier et al., 2016b). Although a large part of the compositional range can be covered by variations in a single crystal, as shown by the data for the complexly zoned CpxB, the 400 and 50 MPa experimental clinopyroxene compositions overlap (Fig. 4). The 400 MPa data extend toward the "primitive" end of the diagram (high Mg# and low Al2O3) whereas the 50 MPa cover a wider compositional range, especially toward higher Al2O3 and lower Mg#. There is a good agreement between experimental (HP40 and HP43_II charges) and natural clinopyroxenes from dunites and wehrlites, although experimental crystals do not reach the maximum Mg# (~90) and minimum Al2O3 (1.5 wt%) of the natural range. The 1 GPa appear similar to the 400 MPa compositions yet their very low CaO (14-15 wt%) and small but detectable Na2O (~0.5 wt%, Table 3), render these clinopyroxenes different from all the others.

5.5.3 *Orthopyroxenes*

Orthopyroxene compositions in the 1 GPa experiment vary with textural type and location in the charge which is the one characterized by a slightly heterogeneous melt. Orthopyroxene crystals grown in the melt have slightly lower MgO and higher FeO (and so lower Mg# ~85) than crystals with chemistries locally influenced by the destabilization of olivine (Mg# = 87-88). CaO contents are, however, identical in both types (Table 3).

5.5.4 *Spinels*

Spinels cover a wide range of compositions, from Cr-rich (chromite) to Fe-rich (magnetite). They have Cr2O3 between 6 and 31 wt%, FeO between 33 and 65 wt% and Al2O3 between 16 and 7 wt% (Table 3). Cr# ranges from 35 to 55. Fe-rich spinels are mostly found in experimental charges performed with the Fe-enriched starting material. In the HP3 charges, spinels have FeO progressively decreasing and Cr2O3 increasing with decreasing XH2Oin (Table 3).

5.6 Melt compositions

Compositions of experimental glasses (Table 3) are plotted as a function of pressure and phase assemblage in a CaO/Al2O3 vs. Mg# diagram (Fig. 5). The two types of starting material used in this study lead to distinguish two compositionally distinct groups of glasses. Glasses from experiments performed with the Fe enriched starting material at 200, 300 and 340 MPa have Mg# between 45 and 55%, clearly lower than those from experiments performed at 400 MPa and 1 GPa with REU0912-04 glass (56-68%). Systematic enrichments in CaO/Al2O3 ratio appear in the Cpx-added charges, at 200, 300 and 400 MPa. The strong increase in glass CaO/Al2O3 in the 400 MPa, 1225°C Cpx-added charge is consistent with the extensive dissolution-recrystallization observed for the Cpx crystals (Fig. 1f). In the same way, glass Mg# markedly increases in the Ol-added 400 MPa, 1225°C as a result of partial olivine dissolution and reequilibration. Therefore, the 1225 and 1250°C mineral-added charges substantially extend the range of experimental melts towards more primitive (i.e., higher CaO/Al2O3 and Mg#) compositions. Effects of clinopyroxene (± olivine) fractionation (decrease of CaO/Al2O3 with decreasing Mg#) are apparent in the 340 MPa series and also in the two 400 MPa series although, in the latter, the effect of clinopyroxene fractionation partially obliterated by Fe loss (increase in Mg#).

6 Discussion

6.1 Validation of experimental results

Before discussing the implications of the experimental results for the deep feeding system of Piton de la Fournaise, it is first necessary to test their applicability. This is done below by comparing our synthetic charges with the mineralogical and petrological characteristics of PdF eruption products, plutonic rocks and comparable experimental studies.

In our experiments performed at pressures between 200 and 340 MPa, mineral phases and assemblages consistent with typical SSB products erupted during the modern history of PdF (e.g., ol ± cpx, Albarède et al., 1997) have been obtained. This is in agreement with previous experimental results obtained at lower pressures on the same SSB-type starting material (Brugier et al, 2016c). The occurrence of olivine as the liquidus phase at 200 and 300 MPa (Fig. 2) is consistent with (1) olivine being by far the main phenocryst in PdF volcanic products (Lacroix, 1923; Upton & Wadsworth, 1972; Kornprobst et al., 1984; Albarède et al., 1997; Fretzdorff & Haase, 2002; Boivin and Bachèlery, 2009; Welsch et al., 2009) and (2) crystallization sequences deduced from studies of plutonic cumulates which show that olivine is the first phase to appear (Brugier et al., 2016b). Therefore, results from this study confirm conclusions drawn from the 0.1 and 50 MPa data and show that crystallization in the order olivine - clinopyroxene is possible at 50, but also at 200 and 300 MPa. Nevertheless, experimental olivines in the 200 and 300 experiments have Fo (75-79) globally lower than natural olivine phenocrysts in SSB (Boivin and Bachèlery, 2009; Brugier et al., 2016c), a consequence of the addition of FeO to the starting material. Therefore, our 200 and 300 MPa experiments performed with the Fe enriched material reasonably but imperfectly simulate conditions in the PdF feeding system.

The experimental results at 400 MPa on REU0912-04 are marked by a drastic modification of liquidus phase relations, clinopyroxene replacing olivine as the liquidus phase (Fig. 2). It is worth stressing that direct evidence for primitive clinopyroxene-phyric lavas of deep provenance is presently lacking on the PdF. In the same way, crystallization sequences starting with clinopyroxene have not been identified from studies of plutonic cumulates (Brugier et al., 2016b). However, clinopyroxene fractionation is a major petrogenetic process recognized on the PdF (Albarède et al., 1997). A mechanism of deep clinopyroxene fractionation has been frequently invoked for the origin of the AbG lava group (Kornprobst et al., 1984; Albarède et al., 1997; Famin et al., 2009; Brugier et al., 2016a; b; Boudoire et al., in prep). The 400 MPa data, in demonstrating for the first time the possibility for clinopyroxene to crystallize on the liquidus at pressures compatible with the depth of the feeding system, clearly support such a mechanism.

The mineral-added charges, especially at the highest temperatures (1225 and 1250°C), explore magmatic conditions more primitive than in the shallow part of the feeding system. They yield Fo~88 olivines, higher than the maximum Fo (86) in olivines crystallized at 0.1 and 50 MPa (Brugier et al., 2016c), reaching the most primitive olivines in ultra-mafic cumulates (Fo88, Brugier et al., 2016b). Such a Fo range, however, stays lower than the maximum Fo for olivine on the PdF (90.6, Fretzdorff & Haase, 2002). Liquid compositions in mineral-added charges go beyond the range of glasses analyzed on the PdF and allows comparison with inferred parental magmas (Ludden, 1978; Famin et al., 2009; Villemant et al., 2009). The experiments, both on REU0912-04 glass and mineral-added, yield clinopyroxenes that closely approach the compositions of the most primitive crystals in plutonic ultra-mafic and mafic cumulates (Fig. 4). The occurrence of orthopyroxene in the 1 GPa charge, although consistent with general principles of basalt phase equilibria (Bender et al., 1978; Gust and Perfit, 1987; Pichavant et al., 2002), is mainly useful to show that olivine is not a stable phenocryst at this pressure and for the experimental conditions of this mineral-added charge (metastable equilibrium with Fo88 olivine). So far, orthopyroxene has been rarely found on the PdF. It can appear as late crystallization products in evolved rocks such as gabbros (Brugier et al., 2016b). We conclude that the mineral-added charges open a window into magmatic processes and compositions not commonly exposed on the PdF.

6.2 Improving the Fe-enrichment method

The Fe-enrichment method, recently proposed by Brugier et al. (2015) to counteract Fe loss in petrological experiments, has been tested in this study. Two main difficulties were encountered, (1) addition of a too high proportion of Fe (4.2% FeO) in our Fe enriched material and (2) chemical heterogeneities in the charges due to imperfect mechanical mixing between glass and FeO powders. The former problem is clearly borne out by the mass balance calculations which return systematic Fe gains (Table 2), and by phase compositions (olivines, clinopyroxenes, glasses), more Fe-rich than in equivalent experiments with the non Fe enriched material (see above). The latter difficulty is supported by SEM examinations of experimental charges (e.g., Fig. 1a), and practical improvements to the method are worth being suggested. The first major improvement would be the use of a Fe enriched glass rather than a mechanical mixture. Preparation of a Fe-doped glass under redox controlled conditions would clearly improve the chemical homogeneity of the Fe enriched starting material, thus allowing comparison between different charges using this starting material. As the second suggestion, we wish to stress the need to avoid a too large modification of the bulk composition. The amount of FeO to be added must be adjusted precisely, preferentially beginning with low, underestimated values. Our results suggest that the addition of only 1~1.5% FeO (instead of 4.2%) could have been sufficient to keep Fe loss at sufficiently low levels in our experiments.

6.3 Influence of pressure on phase equilibria

Comparison between the 400 MPa (clinopyroxene as the liquidus phase, Table 2) and the 0.1 and 50 MPa (olivine as the liquidus phase, Brugier et al., 2016c) results defines a strong isothermal (~1175°C) pressure effect on phase equilibria for the REU0912-04 composition investigated (Fig. 2). Pressure effects on basalt phase equilibria are well experimentally characterized under volatile-free conditions and, generally, they take place over a pressure range > 1 GPa, i.e., much larger than in this study (Bender et al., 1978; Gust and Perfit, 1987; Fisk et al. 1988; Pichavant et al., 2002; Whitaker et al., 2007). As a rule, olivine saturates at low pressures on the liquidus of basalt and is replaced by pyroxenes upon increasing pressure. For example, Fisk et al. (1988) report a systematic change in liquidus phase relations, from olivine to clinopyroxene, upon increasing pressure for several natural La Réunion compositions (see also Pichavant et al., 2016). The change occurs at 900 MPa for the 8.8 wt% MgO composition investigated and at 800 MPa for the 9.74 wt% MgO composition (Fisk et al., 1988). In the experiments of Whitaker et al. (2007), performed on an intra-plate basalt, olivine remains on the liquidus until the highest pressure investigated (950 MPa) but clinopyroxene comes in second before plagioclase above 800 MPa. In comparison, our results were obtained on a relatively evolved basalt and in presence of H2O-CO2 fluid mixtures. They demonstrate that a marked change in phase equilibria can take place at low pressures (< 500 MPa, Fig. 2). For comparison, Husen et al. (2016) have recently documented the effects of pressure (between 100 and 400 MPa) for small amounts of H2O (~0.5 wt%) on the phase relations of tholeiitic basalts. For the 3 compositions investigated, clinopyroxene was found to be the sole liquidus phase at 400 MPa, being either joined or replaced by an olivine+plagioclase assemblage at 200 MPa. Other recent volatile-bearing experimental studies on basalts (Di Carlo et al., 2006; Feig et al., 2006; Lanzo et al., 2016) have observed pressure-induced changes in phase equilibria of the same type, and in the same pressure range, as found for REU0912-04. Therefore, we conclude that the pressure effect evidenced in this study is typical of volatile-bearing basaltic melts. Apart from the clinopyroxene-olivine phase relations, we also stress that plagioclase was never found to appear in run products from this study (Table 2), thus confirming previous conclusions (Brugier et al., 2016c) attributing to H2O a critical role on plagioclase saturation in basaltic systems.

Until recently, the role of pressure on magma fractionation at the PdF was based on the volatile-free experiments of Fisk et al. (1988), as discussed by Albarède et al. (1997). Pichavant et al. (2016) noticed that the Fisk et al. (1988) data imply relatively deep magma fractionation, in a pressure range difficult to reconcile with depths of crustal magma storage zones beneath the PdF. However, the data presented in this study imply that the question should be totally reconsidered. Our results provide an experimental basis to allow clinopyroxene fractionation to take place from 300-350 MPa and deeper in the volcano's plumbing system. It is reminded that this mechanism is one of the most often proposed to explain the AbG compositions at the PdF (Kornprobst et al., 1984; Albarède et al., 1997; Famin et al., 2009; Brugier et al., 2016a; Boudoire et al;, in prep). The crust-mantle boundary beneath La Réunion is located at 12–15 km depths (Gallard et al. 1999; Lénat et al., 2012) or 320–400 MPa. Geophysical studies have interpreted the interplating level imaged at the crust-mantle boundary as a magma accumulation zone or crystal-rich wehrlitic mush (Gallart et al., 1999). This interpretation is clearly substantiated by our data.

The 1 GPa experiment demonstrates that Fo88 olivine becomes unstable as pressure is increased above 400 MPa. Although more Fo-rich olivines exist on the PdF, and so results of the 1 GPa experiment should be applied with caution, the instability of olivine is consistent with the reduced role generally attributed to olivine in the deep feeding system (Kornprobst et al., 1984; Albarède et al., 1997; Famin et al., 2009; Brugier et al., 2016a; Boudoire et al;, in prep). Our results suggest that, above 400-500 MPa, olivine would play only a limited role in magma fractionation. Olivine fractionation is mainly restricted to low pressures (< 300 MPa) at the PdF.

6.4 Constraints on magma fractionation and location of cotectics

Compositions of experimental liquids are compared with natural PdF glasses on the CaO-MgO diagram of Figure 6. To assist in petrological interpretations, firstly, magma fractionation trends need to constructed (Fig. 6a). The clinopyroxene fractionation trend is relatively well defined by the two 400 MPa HP4b and HP40 experimental series where clinopyroxene crystallizes as the sole liquidus phase. Both series enable an average, quite steep, clinopyroxene fractionation trend to be constructed. The olivine fractionation trend is determined from the Ol-added 1225°C 400 MPa charge HP43_I. In the same experiment, the Cpx- and Ol-added charge HP43_II is used to locate a clinopyroxene+olivine assimilation trend, whose slope is consistent (intermediate) between the two clinopyroxene and olivine fractionation trends (Fig. 6a).

Secondly, positions of olivine+clinopyroxene saturated cotectic liquids (designated as olivine+clinopyroxene cotectics) have a critical importance. Previous work has shown that they mainly depend on pressure, being relatively insensitive to temperature and melt H2O content (Pichavant et al., 2009; 2014; Lanzo et al., 2016). Both the 0.1 MPa and 50 MPa cotectics are well defined from the low pressure data Brugier et al., 2016c). They run parallel to each other, and their respective positions conform to the expected influence of pressure (i.e., the 0.1 MPa lies slightly above the 50 MPa cotectic, Fig. 6b). Note that the REU0912-04 glass composition plots in the olivine field relative to those two cotectics, consistent with phase relations (olivine as the liquidus phase) in this pressure range (Brugier et al., 2016c). The 200 and 300 MPa cotectics cannot be defined since charges made with REU0912-04 glass are lacking. At 400 MPa, the Cpx- and Ol-added charge HP43_II defines one point of the cotectic (Fig. 6b). The 400 MPa HP4b and HP40 glasses (at equilibrium with clinopyroxene) provide maximum CaO contents (for a given MgO) along the cotectic. These different constraints are taken together to locate the 400 MPa cotectic (Fig. 6b). At 1 GPa, no olivine+clinopyroxene cotectic can be defined since olivine is unstable but the two liquid compositions at equilibrium with clinopyroxene+orthopyroxene are shown. Compared to the 400 MPa cotectic, they plot at distinctly lower CaO contents for a given MgO, consistent with expansion of the clinopyroxene relative to the olivine field upon increasing pressure.

6.5 Interpretation of natural glass compositions

Experimental melts are compared with compositions of natural glasses from the PdF on Figure 6c. Natural compositions include matrix glasses from 1998 eruption products and glasses from lapilli deposits in the Plaine des Sables. The 1998 glasses comprise compositions that belong both to SSB and AbG magmatic groups (Villemant et al., 2009), and the Plaine des Sables glasses mostly to the AbG group (Brugier et al., 2016a). In addition, three potential parental compositions inferred for PdF magmas (Fisk et al., 1988; Famin et al., 2009;

Villemant et al., 2009) are shown together with experimental cotectics and fractionation trends. The 1998 PdF glasses plot left of the 400 MPa cotectic, extending to MgO concentrations < 6 wt%, in the range of the low pressure (0.1 and 50 MPa) cotectics (Fig. 6c). Their distribution is consistent with an origin for the natural glasses by olivine fractionation at low pressure, followed by clinopyroxene and plagioclase fractionation (see also Brugier et al., 2016c).

The group of glasses from the PdS is different. One first subgroup, with high CaO and relatively high MgO, plots right of the 400 MPa cotectic (Fig. 6c). This implies an origin for those glasses either from olivine or clinopyroxene fractionation, but at pressures necessarily > 400 MPa. In the former hypothesis, parental magmas would plot right of this subgroup, in the direction of the proposed parental compositions. In the latter, parental melts would need to plot away from the glass subgroup along the clinopyroxene fractionation vector. It is important to stress that these glasses have geochemical characteristics that reflect clinopyroxene fractionation (Brugier et al., 2016a). In addition, olivine fractionation is of limited importance above 400-500 MPa (see above) and, therefore, the latter hypothesis is preferred, even if it leads to call into question the range of parental magma compositions at the PdF.

The second subgroup, characterized by lower CaO and variable and increasing MgO, plots on both sides of the 400 MPa cotectic (Fig. 6c). The determined clinopyroxene fractionation vector shows that the high MgO end of this subgroup can derive from the first by clinopyroxene fractionation. However, such a fractionation mechanism would have to occur at pressures > 400 MPa given the location of the 400 MPa cotectic. The subgroup then follows a trend of slightly increasing CaO at decreasing MgO, nearly parallel to the olivine fractionation vector and the 1998 glass trend, interpreted to reflect a change in fractionation mechanism from clinopyroxene-dominated to olivine-dominated < 400 MPa. We conclude that the natural glasses, especially the recently discovered group of AbG-type glasses on the PdS (Brugier et al., 2016a) require an origin by fractionation at high pressures in the feeding system.

6.6 Broader implications

Our experimental results clearly support the proposition that deep clinopyroxene fractionation is an important mechanism taking place in the PdF feeding system and is at the origin of the AbG magma group (Kornprobst et al., 1984; Albarède et al., 1997; Famin et al., 2009; Brugier et al., 2016a; Boudoire et al., in prep). However, the pressure range for the fractionation mechanism implied by the experimental and the glass composition data (> 400 MPa, Fig. 6c), together with geophysical information on the structure of the La Réunion island, suggests that the evolution of PdF magmas must take place, at least in part, in the mantle section beneath the island. This stresses the importance of constraining compositions of primitive melts at pressures > 400 MPa. From the discussion above, compositions of magmas parental to the PdS AbG glasses would have higher CaO/Al2O3 than all parental magmas proposed to date (Fig. 6c). In this regard, melt compositions in the 1 GPa experiment (at equilibrium with a clinopyroxene+orthopyroxene assemblage) have the required characteristics. Despite their elevated MgO concentrations (10-11 wt% MgO), it is worth emphasizing that melts in that charge are at (metastable) equilibrium with Fo88 olivine. In other words, those melts are not at equilibrium with the most Fo-rich olivines on the PdF, either Fo89 (Bureau et al., 1998) or Fo90.6 (Fretzdorff & Haase, 2002). Therefore, only minimum bounds on parental melt compositions are provided by the 1 GPa experiment.

7 Conclusion

The main conclusions of this study are the following:

- Experimental phase equilibria have been investigated for a composition typical of Steady State Basalts from the Piton de la Fournaise between 200 MPa and 1 GPa and under conditions representative of the deep feeding system. To mitigate Fe loss, a Fe enriched starting material was also used.
- Experiments were mostly of crystallization-type. Clinopyroxene- and olivine-added experiments explored magmatic conditions more primitive than in the shallow part of the feeding system. Mineral-liquid equilibrium was globally closely approached but Fe loss remained as a persistent problem. Experiments with the Fe enriched material yielded too Fe-rich compositions and charges showed heterogeneous Fe distributions.
- Olivine crystallized at both 200 and 300 MPa in charges performed with the Fe enriched material. Charges with the non Fe enriched glass demonstrate an isothermal (1175°C) change in liquidus phase equilibria from olivine at 50 MPa to clinopyroxene at 400 MPa. In the 1 GPa experiment, olivine reacted to orthopyroxene.
- Experimental assemblages and mineral and glass compositions (except in charges with the Fe enriched material) are in relatively good agreement with natural assemblages and compositions in PdF volcanic and plutonic rocks. They demonstrate for the first

time the possibility for clinopyroxene to crystallize on the liquidus at pressures compatible with the deep feeding system. Olivines, clinopyroxenes and glasses in mineral-added charges reach relatively primitive compositions.

- Replacement of olivine by clinopyroxene on the liquidus is constrained to take place from 350-400 MPa and above at 1175°C, i.e., clinopyroxene becomes the liquidus phase in a pressure range significantly lower than previously inferred using volatile-free experiments. This range of pressures is in agreement with the internal structure of the La Réunion island. It supports interpretations of the underplating level geophysically identified at the crust-mantle interface as a magma accumulation and a wehrlitic crystal mush zone.
- Experimental melt compositions enable olivine and clinopyroxene fractionation trends and the pressure-dependence of clinopyroxene+olivine cotectics to be determined. Natural glasses record different fractionation mechanisms. AbG glasses originate by a clinopyroxene-dominated fractionation mechanism at > 400 MPa in the feeding system.
- Our results call into question the range of parental magma compositions previously proposed for the PdF and stress the possibility for the magmatic evolution to take place at least in part in the underlying mantle.

8 Acknowledgements

This work was supported by the DEGAZMAG (ANR 2011 Blanc SIMI 5-6 003) projects. Ida Di Carlo is acknowledged for her contribution to the electron microprobe analyses. We thank XX, XX and XX for their helpful reviews.

9 References cited

Albarède, F. (1995) *Introduction to Geochemical Modeling*. Cambridge University Press, 543p.

Albarède, F., Luais, B., Fitton, G., Semet, M., Kaminski, E., Upton, B.G.J., Bachèlery, P. & Cheminée, J.L. (1997) The geochemical regimes of Piton de la Fournaise volcano (Réunion) during the last 530000 years. Journal of Petrology 38, 171-201.

Bachèlery, P. (1981) Le Piton de la Fournaise (Ile de la Réunion): etude volcanologique, structural et pétrologique. PhD Thesis, Université Blaise Pascal, Clermont Ferrand, 215 pp.

Balta, J.B., Beckett, J.R., and Asimow, P.D. (2011) Thermodynamic properties of alloys of gold-74/palladium-26 with variable amounts of iron and the use of Au-Pd-Fe alloys as containers for experimental petrology. American Mineralogist, 96, 1467-1474.

Barclay, J. & Carmichael, I.S.E. (2004) A Hornblende Basalt from Western mexico: Water-saturated Phase Relations Constrain a Pressure-Temperature Window of Eruptibility. Journal of Petrology 45, 485-506.

Barr, J. and Grove, T.L. (2010) AuPdFe ternary solution model and applications to understanding the fO_2 of hydrous, high-pressure experiments. Contributions to Mineralogy and Petrology, 160, 631-643.

Bender, J.F., Hodges, F.N. & bence, A.E. (1978) Petrogenesis of basalts from the project famous area: experimental study from 0 to 15 kbars. Earth and Planetary Science Letters 41, 277-302.

Boivin, P. & Bachèlery, P. (2009) Petrology of 1977 to 1998 eruptions of Piton de la Fournaise, La Réunion Island. Journal of Volcanological and Geothermal Research 184, 109-125.

Bonneville, A. (1990) Structure de la lithosphere. In : Lénat, J.F. (ed) *Le volcanisme de la Réunion*. Monographie : Centre de recherche en volcanologie, Clermont Ferrand, 1-18.

Bosch, D., Blichert-Toft, J., Moynier, F., Nelson, B.K., Telouk, P., Gillot, P.Y. & Albarède, F. (2008) Pb, Hf and Nd isotope compositions of the two Réunion volcanoes (Indian Ocean): a tale of two small-scale mantle blobs. Earth and Planetary Science Letters 265, 748-768.

Boudoire, G., Brugier Y.A., Di Muro, A., Wörner, G., Métrich, N., Arienzo, I., Braukmüller, N., Kronz, A., Le Moigne, Y., Michon, L., Pichavant, M. & Zanon, V. (*in prep*) The deep plumbing system of volcanic islands : new insights from recent activity of the NW Rift Zone (NWRZ) of Piton de la Fournaise (La Réunion Island, Indian Ocean).

Bureau, H., Pineau, F., Métrich, N., Semet M.P. & Javoy, M. (1998a) A melt and fluid inclusion study of the gas phase at Piton de la Fournaise volcano (Réunion Islanf). Chemical Geology 147, 115-130.

Bureau, H., Métrich, N., Pineau, F. & Semet M.P. (1998b) Magma-conduit interaction at Piton de la Fournaise volcano (Réunion Island) : a melt and fluid inclusion study. Journal of Volcanological and Geothermal Research 84, 39-60.

Brugier, Y.A., Alletti, M. & Pichavant, M. (2015) Fe pre-enrichment: A new method to counteract iron loss in experiments on basaltic melts. American Mineralogist 100, 2106-2111.

Brugier, Y.A., Le Moigne, Y., Pichavant, M., Bourdier, J.L., Boudoire, G. & Di Muro, A. (2016a) Compositional variability of basaltic spatters activity in the Plaine des Sables (Reunion island): Volcanological and petrological constraints.

Brugier, Y.A., Boudoire, G., Pichavant, M., Le Moigne, Y., Di Muro, A., Clague, D., Bachèlery, P. & Bourdier, J.L. (2016b) Petrological and mineralogical characteristics of plutonic rocks from the Plaine des Sables (Piton de la Fournaise volcano, La Réunion Island) - Implications for crystallization processes of Réunion lavas.

Brugier, Y.A., Pichavant, M. & Di Muro, A. (2016c) Petrology of Steady State Basalt from Piton de la Fournaise volcano: A Volatiles-present Experimental Study of the shallow feeding system.

Chenet, A.L., Quidelleur, X., Fluteau, F., Courtillot, V. & Bajpaic, S. (2007) ^{40}K-^{40}Ar dating of the Main Deccan large igneous province : further evidence of KTB age and short duration. Earth and Planetary Science Letters 263, 1-15.

Devine, J.D., Gardner, J.E., Brack, H.P., Layne, G.D. & Rutherford, M.J. (1995) Comparison of microanalytical methods for estimating H2O contents of volcanic glasses. American Mineralogist 80, 319-328.

Di Carlo, I., Pichavant, M., Rotolo, S. G., and Scaillet, B. (2006) Experimental crystallization of a high-K arc basalt: the golden pumice, Stromboli volcano (Italy). Journal of Petrology 47, 1317-1343.

Di Muro, A. (2012 & 2015) Evaluation de l'aléa volcanique à La Réunion. Rapport final-année I et II. Projet BRGM/IPGP.

Di Muro, A., Métrich, N., Vergani, D., Rosi, M., Armienti, P.,Fougeroux, T., Deloule, E., Arienzo, I. & Civetta, L. (2014) The Shallow Plumbing System of Piton de la Fournaise Volcano (La Réunion Island, Indian Ocean) revealed by the Major 2007 Caldera-Forming Eruption. Journal of Petrology 55, 1287-1315.

Duncan, R.A., Backman, J. & Peterson, L. (1989) Reunion hotspot activity through tertiary time: initial results from the ocean drilling program, Leg 115. Journal of Volcanological and Geothermal Research 36, 193-198.

Famin, V., Welsch, B., Okumura, S., Bachèlery, P. & Nakashima, S. (2009) Three differentiation stages of a single magma at Piton de la Fournaise (Réunion hotspot). Geochemistry Geophysics Geosystems 10, Q01007.

Feig, S.T., Koepke, J. & Snow, J.E. (2006) Effect of water on tholeiitic basalt phase equilibria: an experimental study under oxidizing conditions. Contributions to Mineralogy and Petrology 152, 611-638.

Fisk, M.R., Upton, B.G.J., Ford, C.E. & White, W.M. (1988) Geochemical and Experimental Study of the Genesis of Magmas of reunion Island, Indian Ocean. Journal of Geophysical Research 93, 4933-4950.

Fretzdorff, S. & Haase, K.M. (2002) Geochemistry and petrology of lavas from the submarine flanks of Réunion Island (western Indian Ocean): implications for magma genesis and the mantle source. Mineralogy and Petrology 75, 153-184.

Gallart, J., Driad, L., Charvis, P., Sapin, M., Hirn, A., Diaz, J., de Voogd, B. & Sachpazi, M. (1999) Perturbation to the lithosphere along the hotspot track of La Réunion from an offshore-onshore seismic transect. Journal of Geophysical research 104, 2895-2908.

Gillot, P.Y. & Nativel, P.E. (1989) Eruptive history of the Piton de la Fournaise volcano, Réunion Island, Indian Ocean. Journal of Volcanological and Geothermal Research 36, 53-65.

Gillot, P.Y., Lefèvre, J.C. & Nativel, P.E. (1994) Model for the structural evolution of the volcanoes of Réunion Island. Earth and Planetary Science Letters 122, 291-302.

Graham, D., Lupton, J., Albarède, F. & Condomines, M. (1990) Extreme temporal homogeneity of helium isotopes at Piton de la Fournaise, Réunion Island. Nature 347, 545-548.

Gust, D.A. & Perfit, M.R. (1987) Phase relations of a high-Mg basalt from the Aleutian Island Arc: Implications for primary island arc basalts and high-Al basalts. Contributions to Mineralogy and Petrology 97, 7-18.

Hall, L.J., Brodie, J., Wood, B.J., and Carroll, M.R. (2004) Iron and water losses from hydrous basalts contained in $Au_{80}Pd_{20}$ capsules at high pressure and temperature. Mineralogical Magazine, 68, 75-81.

Husen, A., Almeev, R.R. & Holtz, F. (2016) The effect of H2O and pressure on multiple saturation and liquid lines of descent in basalt from the Shatsky Rise. Journal of Petrology 57, 309-344.

Kawamoto, T. and Hirose, K. (1994) Au-Pd sample containers for melting experiments on iron and water-bearing systems. European Journal of Mineralogy 6, 381-385.

Kornprobst, J., Boivin, P. & Bachèlery, P. (1979) L'alimentation des eruptions récentes du Piton de la Fournaise (Ile de la reunion, Océan Indien): degree d'évolution et niveau de segregation des laves émises. C.R. Acad. Sc. Paris, t.288, 1691-1694.

Kornprobst, J., Boivin, P., Lénat, J.F., Bachèlery, P., Bonneville, A., Dupont, P., Lecointre, J., Seidel, J.L., Thomas, P. & Vincent, P. (1984) Le Piton de la Fournaise, Ile de la Réunion. Colloque PIRPSEV 1984, Clermont-Ferrand.

Lacroix, A. (1923) Océanites. Minéralogie de Madagascar, vol. III, Paris, 49-50.

Lanzo, G., Di Carlo, I., Pichavant, M., Rotolo, S.G. & Scaillet, B. (2016) Origin of primitive ultra-calcic arc melts at crustal conditions – Experimental evidence on the La Sommata basalt, Vulcano, Aeolian Islands. Journal of Volcanology and Geothermal Research 321, 85-101.

Lebas, E. (2012) Processus de démantèlement des édifices volcaniques au cours de leur évolution : application à La Réunion et Montserrat et comparaison avec d'autres édifices. PhD Thesis, Paris Diderot, Paris, 407pp.

Lénat, J.F., Gibert-Malengreau, B. & Galdeano, A. (2001) A new model for the evolution of the volcanic island of Réunion (Indian Ocean). Journal of Geophysical Research-Solid Earth 106, 8645-8663.

Lénat, J.F., Bachèlery, P. & Merle, O. (2012a) Anatomy of Piton de la Fournaise volcano (La Reunion, Indian Ocean). Bulletin of Volcanology 74, 1945-1961.

Lénat, J.F. (2016) Construction of La Réunion. In: Bachèlery, P., Lénat, J.F., Di Muro, A. & Michon, L. (eds) *Active volcanoes of the southwest Indian Ocean: Piton de la Fournaise and Karthala*. Active volcanoes of the world. Springer, Berlin.

Ludden, J.N. (1978a) Magmatic evolution of the basaltic shield volcanoes of Réunion Island. Journal of Volcanology and Geothermal Research 4, 171-198.

Malengreau, B. (1995) Structure profonde de la Réunion d'après les données magnétiques et gravimétriques. PhD Thesis, Université Blaise Pascal Clermont Ferrand, 366 pp.

Malengreau, B., Lénat, J.F. & Froger, J.L. (1999) Structure of Reunion Island (Indian Ocean) inferred from the interpretations of gravity anomalies. Journal of Volcanological and Geothermal Research 88, 131-146.

McDougall, I. (1971) The geochronology and evolution of young volcanic island of Réunion, Indian Ocean. Geochimica et Cosmochimica Acta 35, 261-288.

Michon, L., Ferrazzini, V., Di Muro, A., Villeneuve, N. & Famin, V. (2015) Rift zones and magma plumbing system of Piton de la Fournaise volcano : how do they differ from Hawaii and Etna. Journal of Volcanological and Geothermal Research 303, 112-129.

Morandi, A., Di Muro, A., Principe, C., Michon, L., Leroi, G., Norelli, F. & Bachèlery, P. (2016) Pre-historic explosive activity at Piton de la Fournaise volcano. In: Bachèlery, P., Lénat, J.F., Di Muro, A. & Michon, L. (eds) *Active volcanoes of the southwest Indian Ocean: Piton de la Fournaise and Karthala*. Active volcanoes of the world. Springer, Berlin.

Peltier, A., Bachèlery, P. & Staudacher, T. (2009) Magma transport and storage at Piton de la Fournaise (La Réunion) between 1972 and 2007: A review of geophysical and geochemical data. Journal of Volcanology and Geothermal Research 184, 93-108.

Pichavant, M., Martel, C., Bourdier, J.L. & Scaillet, B. (2002) Physical conditions , structure, and dynamics of a zoned magma chamber : Mount Pelée (Martinique, Lesser Antilles Arc). Journal of Geophysical Research 107, ECV 2 1-27.

Pichavant, M. & Macdonald, R. (2007) Crystallization of primitive basaltic magmas at crustal pressures and genesis of the calc-alkaline igneous suite: experimental evidence from St Vincent, Lesser Antilels arc. Contributions to Mineralogy and Petrology 154, 535-558.

Pichavant, M., Di Carlo, I., Le Gac, Y., Rotolo, S., and Scaillet, B. (2009) Experimental constraints on the deep magma feeding system at Stromboli volcano, Italy. Journal of Petrology 50, 601-624.

Pichavant, M., Scaillet,B., Pommier, A., Iacono-Marziano, G. & Cioni, R. (2014) Nature and Evolution of Primitive Vesuvius Magmas : an Expreimental Study. Journal of Petrology 55, 2281-2310.

Pichavant, M., Brugier, Y. & Di Muro, A. (2016) Petrological and experimental constraints on the evolution of Piton de la Fournaise Magmas. In: Bachèlery, P., Lénat, J.F., Di Muro, A. & Michon, L. (eds) *Active volcanoes of the southwest Indian Ocean: Piton de la Fournaise and Karthala*. Active volcanoes of the world. Springer, Berlin.

Pietruszka, A.J., Hauri, E.H. & Blichert-Toft, J. (2009) Crustal contamination of mantle-derived magmas within Piton de la Fournaise volcano, Réunion island. Journal of Petrology 50, 661-684.

Principe, C., Morandi, A., Di Muro, A. & Michon, L. (2016) Volcanological Map of the Plaine des Sables, Piton de la Fournaise. In: Bachèlery, P., Lénat, J.F., Di Muro, A. & Michon, L. (eds) *Active volcanoes of the southwest Indian Ocean: Piton de la Fournaise and Karthala*. Active volcanoes of the world. Springer, Berlin.

Quidelleur, X., Holt, J.W., Salvany, T. & Bouquerel, H. (2010) The double structureof the Reunion geomagnetic event based on new K-Ar ages from the type locality, massif de la Montagne, Réunion Island (Indian Ocean) and assessment of the global context. Geophysical Journal International 182, 699-710.

Salaün, A., Villemant, B., Semet, M.P. & Staudacher, T. (2010) Cannibalism of olivine-rich cumulate xenoliths during the 1998 eruption of Piton de la Fournaise (La Reunion hotspot): Implications for the generation of magma diversity. Journal of Volcanological and Geothermal Research 198, 187-204.

Salvany, T., Lahitte, P., Nativel, P. & Gillot, P.Y. (2012) Geomorphic evolution of the Piton des Neiges volcano (Réunion Island, Indian Ocean): Competition between volcanic construction and erosion since 1.4 Ma. Geomorphology 136, 132-147.

Scaillet, B., Pichavant, M., Roux, J., Humbert, G. & Lefèvre, A. (1992) Improvements of the Shaw membrane technique for measurements and control of fH2 at high temperatures and pressures. American Mineralogist, 77, 647-655.

Sifré, D., Gardés, E., Massuyeau, M., Hashim, L., Hier-Majumber, S. & Gaillard, F. (2014) Electrical conductivity during incipient melting in the oceanic low-velocity zone. Nature 509, 81-85.

Sisson, T.W. & Grove, T.L. (1993) Experimental investigations of the role of H2O in calc-alkaline differentiation and subduction zone magmatism. Contributions to Mineralogy and Petrology 113, 143-166.

Smietana, M. (2011) Pétrologie, géochrnologie (K-Ar) et géochimie élémentaire et isotopique (Sr, Nd, Hf, Pb) des laves anciennes de La Réunion. Implications sur la construction de l'édifice volcanique. PhD Thesis, Université de La Réunion, 362 pp.

Staudacher, T., Peltier, A., Ferrazzini, V., Di Muro, A., Boissier, P., Catherine, P., Kowalski, P., Lauret, F. & Lebreton, J. (2016) Fifteen Years of Intense Eruptive Activity (1998-2013) at Piton de la Fournaise Volcano : A Review. In: Bachèlery, P., Lénat, J.F., Di Muro, A. & Michon, L. (eds) *Active volcanoes of the southwest Indian Ocean: Piton de la Fournaise and Karthala*. Active volcanoes of the world. Springer, Berlin.

Upton, B.G.J. & Wadsworth, W.J. (1972) Peridotitic and Gabbroic Rocks Associated with the Shield-Forming Lavas of Réunion. Contribution to Mineralogy and Petrology 35, 139-158.

Valer, M., Schiano, P. & Bachèlery, P. (2015) Insights into the origin of magmas from the adventive cones of Piton de la Fournaise volcano (La Réunion Island). In: Geochimica et Cosmochimica Acta, Goldschmidt conference 2015 abstract 3219.

Villemant, B., Salaün, A. & Staudacher, T. (2009) Evidence for a homogeneous primary magma at Piton de la Fournaise (La Réunion) : A geochemical study of matrix glass, melt inclusions and Pelé's hairs of the 1998-2008 eruptive activity. Journal of Volcanological and Geothermal Research 184, 79-92.

Vlastélic, I. & Staudacher, T. (2005) Rapid change of lava composition from 1998 through 2002 at Piton de la Fournaise (Réunion Island) inferred from Pb isotopes and trace elements: evidence for variable crustal contamination. Journal of Petrology 46, 79-107.

Vlastélic, I., Peltier, A. & Staudacher, T. (2007) Short-term (1998-2006) fluctuations of Pb isotopes at Piton de la Fournaise volcano (Réunion Island): origins and constraints on the size and shape of the magma reservoir. Chemical Geology 244, 202-220.

Vlastélic, I., Deniel, C., Bosq, C., Télouk, P., Boivin, P., Bachèlery, P., Famin, V. & Staudacher, T. (2009) Pb isotope geochemistry of Piton de la Fournaise historical lavas. Journal of Volcanological and Geothermal Research 184, 63-78.

Vlastélic, I. & Pietruszka, A.J. (2016) A Review of the Recent Geochemical Evolution of Piton de la Fournaise Volcano (1927-2010). In: Bachèlery, P., Lénat, J.F., Di Muro, A. & Michon, L. (eds) *Active volcanoes of the southwest Indian Ocean: Piton de la Fournaise and Karthala*. Active volcanoes of the world. Springer, Berlin.

Welsch, B., Faure, F., Bachèlery, P. & Famin, V. (2009) Microcrysts Record Transient Convection at Piton de la Fournaise Volcano (La Réunion Hotspot). Journal of Petrology 50, 2287-2305.

Welsch, B., Faure, F., Famin, V., Baronnet, A. & Bachèlery, P. (2013) Dendritic Crystallization: A Single Process for all the Textures of Olivine in Basalts? Journal of Petrology 54, 539-574.

Whitaker, M.L., Nekvasil, H., Lindsley, D.H. & Difrancesco, N. (2007) The role of pressure in producing compositional diversity in intraplate basaltic magmas. Journal of Petrology 48, 365-393.

10 Figure captions

Fig. 1. SEM back-scattered electron images of experimental charges and textures. **(a)** Charge HP4_IV showing 2 distinctive areas, one with large (> 100 µm) olivine (Ol) crystals associated with numerous Fe-rich spinels (Sp) and the second more extensively crystallized with small (< 10 µm) clinopyroxenes (Cpx). Such textures are interpreted to reflect chemical heterogeneities in the Fe enriched starting material (see text). Note the presence of large (200-300 µm) gas vesicles. **(b)** Charge HP4b_II showing small (< 10 µm) euhedral chemically homogeneous clinopyroxene (Cpx) coexisting with a large (> 30 µm) crystal (CpxA) zoned from core to rim (Table 3). Note the brighter ring inside CpxA with resorption (?) textures and spinel inclusions (Sp). **(c)** Complex clinopyroxene (CpxB) in charge HP40_III showing different compositional zones (z1, z2, z3, z4, see Fig. 3 and Table 3). **(d)** Another view of the same charge HP40_III showing clinopyroxene (Cpx) crystals smaller than in (**c**). Olivine (Ol) inclusions are present in 2 clinopyroxene crystals but absent elsewhere in the charge and never in direct contact with glass. **(e)** Olivine-added charge HP43_I showing the residual San Carlos olivines (Ol R) embedded in glass. Note the anhedral shape of the crystals and the core-rim zonations (Table 3). A few small euhedral olivine crystals could be crystallization products from the melt. **(f)** Olivine- and clinopyroxene-added charge HP43_II showing residual zoned San Carlos olivines (Ol R) and residual clinopyroxene crystals (Cpx R, detailed in (**g**)). Numerous small (< 10µm) clinopyroxenes (Cpx) crystallized from the melt are also present. Note the occurrence of quench crystals. **(g)** Detail of the same charge HP43_II showing residual olivines (Ol R), residual clinopyroxene cores (Cpx C core) and clinopyroxenes crystallized from the melt (Cpx). Note the euhedral shape of Cpx C rim which has a composition close to Cpx (Table 3). **(h)** Olivine- and clinopyroxene-added charge HP10 showing residual zoned clinopyroxene (Cpx R) and quench crystallization at their rims. Rare residual olivine crystals are present (not shown). Euhedral orthopyroxene (Opx) appear as large crystals. **(i)** Detail of the same charge HP10 showing euhedral orthopyroxene (Opx) of various sizes, small clinopyroxenes (Cpx) crystallized from the melt and residual clinopyroxenes. The location of the glass electron microprobe spot z2, close to the crystal-rich part of the charge, is indicated. The glass electron microprobe spot z1 (Table 3, not shown) is from elsewhere (crystal-free top part) in the charge.

Fig. 2. High-pressure phase diagrams for REU0912-04. (**a**) Isothermal P-XH2Oinit. phase diagram (temperature fixed at 1175°C) showing data points (squares), phase assemblages, saturation curves and stability fields. Data points obtained with REU0912-04 glass are shown in black and with the Fe enriched material in grey (see Table 2 for details about the experiments). The 50 MPa data are from Brugier et al. (2016c). Note that the saturation curves are constructed using only the results for REU0912-04 glass. (**b**) Isothermal P-H2O in melt phase diagram for REU0912-04 (temperature fixed at 1175°C) showing data points (squares), phase assemblages, saturation curves and stability fields determined from the same experimental charges as in (**a**). Melt H2O contents are determined either with the "by difference" method for experiments from this study or by FTIR for some of the 50 MPa charges (Brugier et al., 2016c). The charges obtained with Fe-enriched starting material (HP2, HP3 and HP4 experiments) are presented in grey but not considered in the construction of saturation curves. The location of the Cpx saturation curve at 400 MPa is estimated because the "by difference" method has a poor sensitivity for H2O concentrations < 2 wt%. The grey field drawn for H2O in melt < 0.5 wt% corresponds to H2O-poor concentration conditions that can not be reached with our experimental methodology (see text). The green field gives pressures of the underplating level, a wehrlitic layer geophysically imaged at the interface between the mantle and the oceanic crust below the La Réunion Island (Gallard et al., 1999). Liq, liquid (silicate melt); Ol, olivine; Cpx, clinopyroxene.

Fig. 3. Al, Ca, Cr, Fe and Mg distribution maps for the strongly zoned clinopyroxene from charge HP40_III (CpxB, Fig. 1). Compositions of the different electron microprobe analyzes (z1, z2, z3, z4) are given in Table 3.

Fig. 4. Al_2O_3 (wt%) vs. Mg# (calculated with Fe2+ = Fetot) for clinopyroxenes crystallized in the high-pressure experiments HP4b, HP40, HP43 and HP10. Experimental conditions in Table 2 and analytical data in Table 3. Individual clinopyroxene analyses (and not averages for a given charge) are plotted. The dashed field gives compositions of clinopyroxenes in the 50 MPa experiments on REU0912-04 (Brugier et al., 2016c). The brown field shows compositions of natural clinopyroxenes in dunitic and wehrlitic ultra-mafic cumulates from the PdS (Brugier et al., 2016b).

Fig. 5. CaO/Al_2O_3 vs. Mg# (calculated with Fe2+ = Fetot) plot showing experimental glass compositions. Data in Table 3. Charges are distinguished by pressure and phase assemblage. Compositions of REU0912-04 glass and of the Fe enriched starting material are shown. Note the lower glass Mg# for charges performed with the Fe enriched starting material. Note also the systematic deviations (toward higher CaO/Al2O3 and Mg#) of glasses from charges with added Cpx and/or Ol.

Fig. 6. Comparison between experimental liquid compositions and natural PdF glasses in a CaO (wt%) vs. MgO (wt%) diagram. Symbols and colours as in Fig. 5. Experimental liquid compositions (normalized to 100%) from Table 3. Natural glasses are from Villemant et al. (2009) and Salaün et al. (2010) for matrix glasses from 1998 PdF eruption products, and from Brugier et al. (2016a) for glassy lapilli on the PdS. (**a**) Experimental definition of mineral fractionation trends. The data points plotted are glasses from the 400 MPa (REU0912-04 glass and mineral-added charges) and from the 1 GPa (mineral-added charges) experiments. See Table 2 for experimental details. The clinopyroxene fractionation trend (black arrow) is determined as the average between the two trends defined by the HP40 and HP4b charges (Table 2). The Ol fractionation trend is the Ol assimilation trend, reversed, as defined by charge HP43_I. Charge HP43_II is used to define the combined Cpx + Ol assimilation trend. **(b)** Construction of olivine+clinopyroxene cotectics. The experimental data points plotted are the same as in (**a**). The 0.1 and 50 MPa cotectics are tightly defined from the experiments of Brugier et al. (2016c). The 400 MPa cotectic is constrained from charge HP43_II and also from the HP40 and HP4b charges. Compositions of low pressure glasses (0.1 and 50 MPa experiments of Brugier et al., 2016c) are also shown (pink fields). Notice the location of the two 1 GPa clinopyroxene+orthopyroxene saturated glass compositions. **(c)** Comparison between experimental and natural glasses. The experimental results (data points, cotectics, fractionation trends) are the same as in (**a**) and (**b**). Three compositions proposed to be parental to PdF magmas (Fisk et al., 1988; Famin et al., 2009; Villemant et al., 2009) are also plotted. Notice the respective location of PdS glasses (two light brown fields) and of 1998 matrix glasses (grey field) relative to the 400 MPa cotectic. See text for discussion.

Figure 1

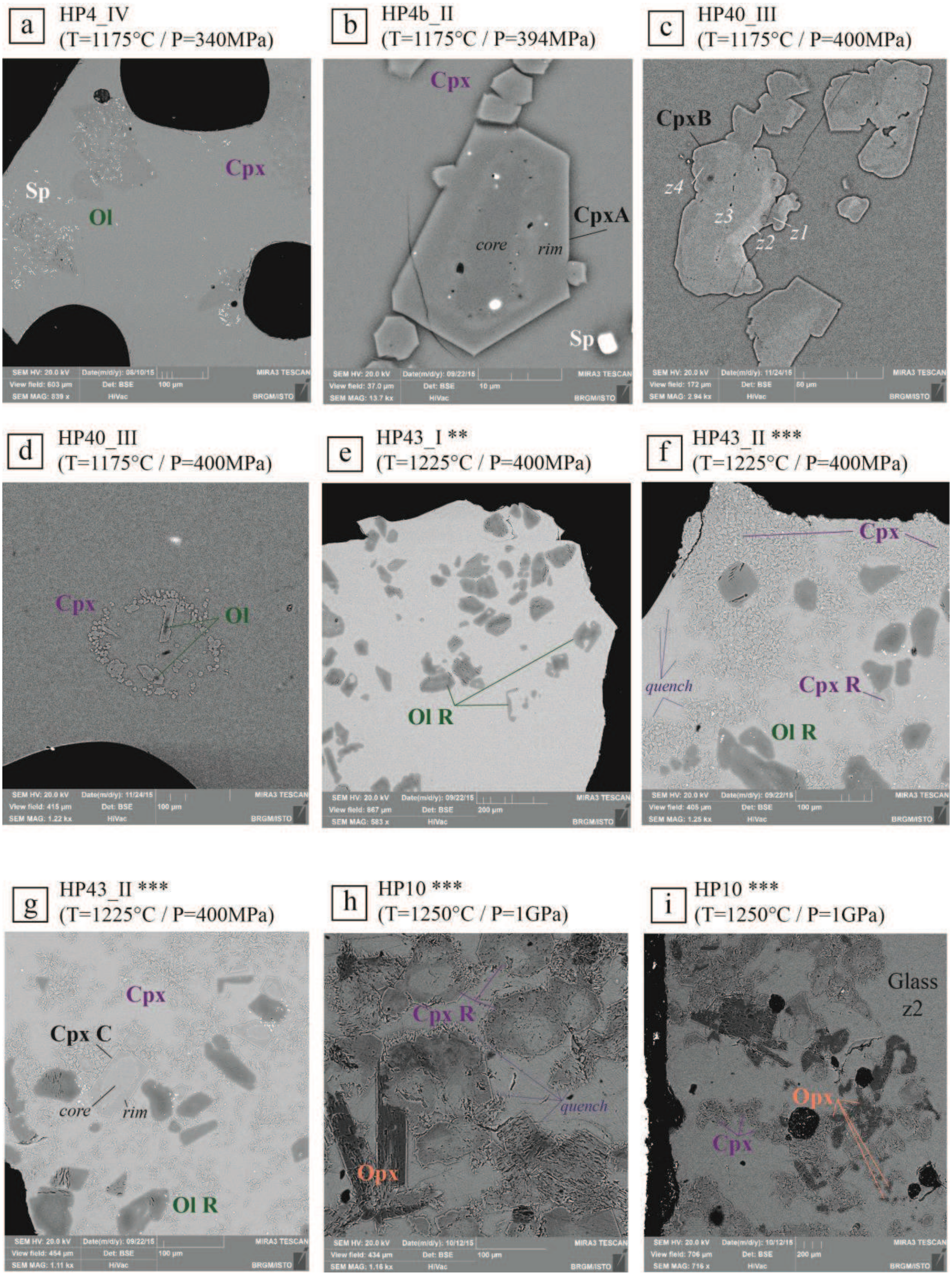
a
HP4_IV
(T=1175°C / P=340MPa)
Sp
Ol
Cpx
100 µm
b
HP4b_II
(T=1175°C / P=394MPa)
Cpx
CpxA
core
rim
Sp
10 µm
c
HP40_III
(T=1175°C / P=400MPa)
CpxB
z4
z3
z2
z1
50 µm
d
HP40_III
(T=1175°C / P=400MPa)
Cpx
Ol
100 µm
e
HP43_I **
(T=1225°C / P=400MPa)
Ol R
200 µm
f
HP43_II ***
(T=1225°C / P=400MPa)
Cpx
quench
Cpx R
Ol R
100 µm
g
HP43_II ***
(T=1225°C / P=400MPa)
Cpx
Cpx C
core
rim
Ol R
100 µm
h
HP10 ***
(T=1250°C / P=1GPa)
Cpx R
quench
Opx
100 µm
i
HP10 ***
(T=1250°C / P=1GPa)
Glass
z2
Opx
Cpx
200 µm

Figure 2

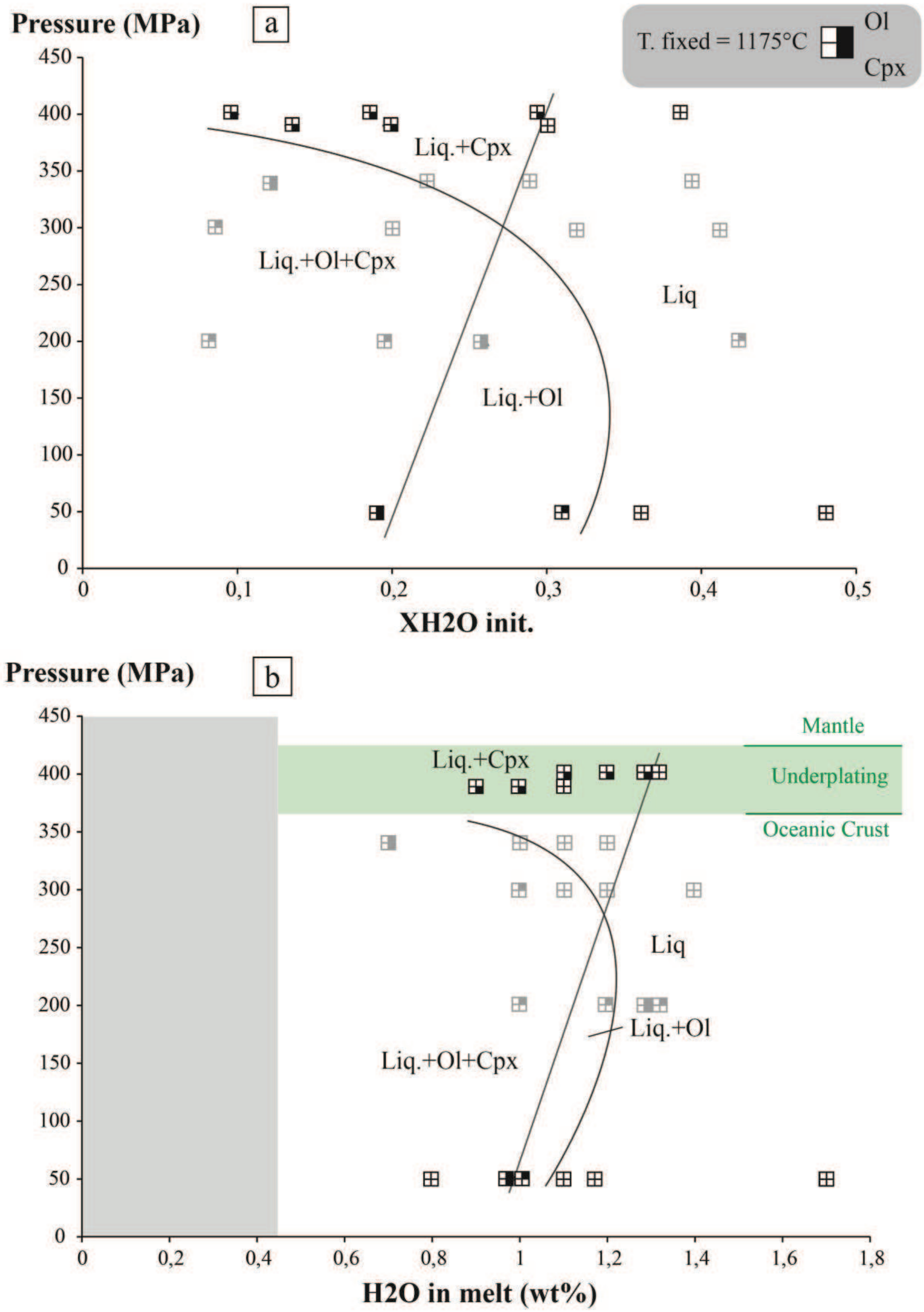
Pressure (MPa)
a
T. fixed = 1175°C
Ol
Cpx
450
400
350
300
250
200
150
100
50
0
Liq.+Cpx
Liq.+Ol+Cpx
Liq
Liq.+Ol
0
0,1
0,2
0,3
0,4
0,5
XH2O init.
Pressure (MPa)
b
Mantle
Underplating
Oceanic Crust
450
400
350
300
250
200
150
100
50
0
Liq.+Cpx
Liq
Liq.+Ol
Liq.+Ol+Cpx
0
0,2
0,4
0,6
0,8
1
1,2
1,4
1,6
1,8
H2O in melt (wt%)

Figure 3

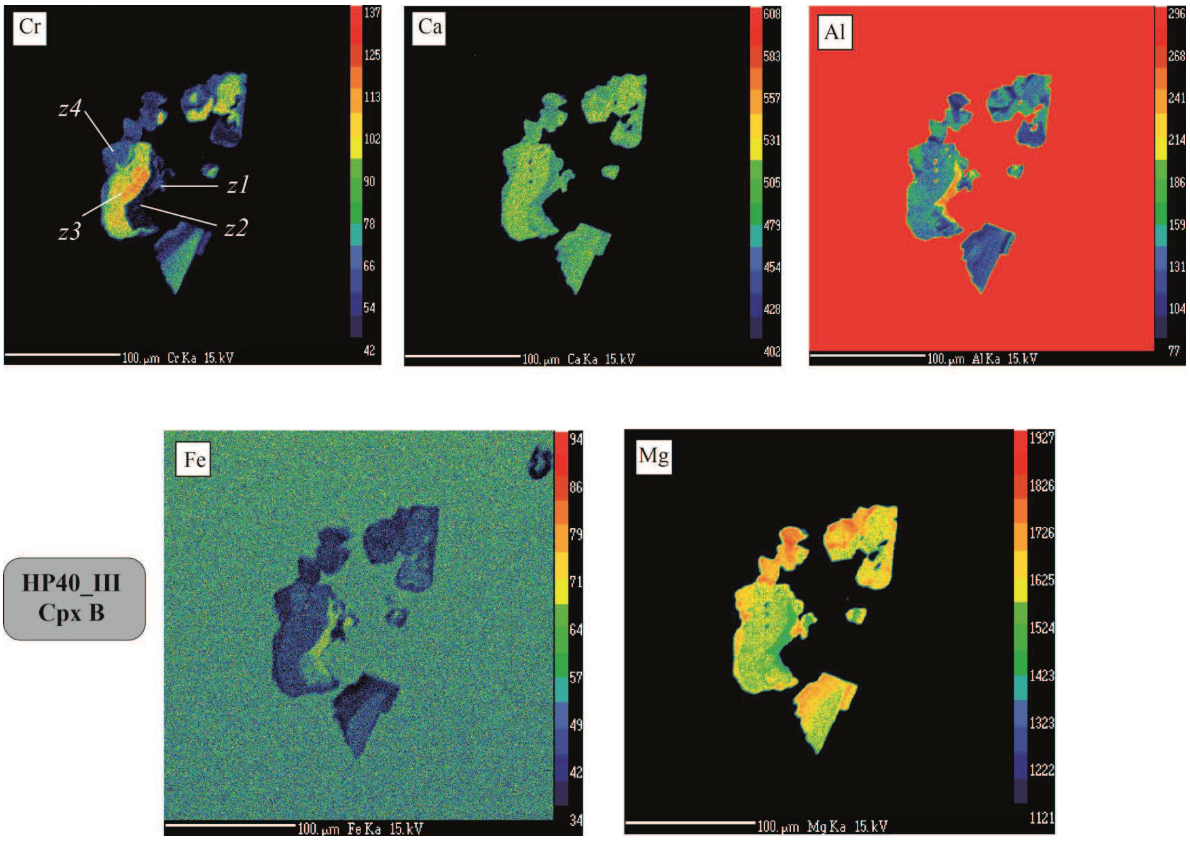
Cr
z4
z1
z3
z2
137
125
113
102
90
78
66
54
42
100 µm Cr Ka 15 kV
Ca
608
583
557
531
505
479
454
428
402
100 µm Ca Ka 15 kV
Al
296
268
241
214
186
159
131
104
77
100 µm Al Ka 15 kV
HP40_III
Cpx B
Fe
94
86
79
71
64
57
49
42
34
100 µm Fe Ka 15 kV
Mg
1927
1826
1726
1625
1524
1423
1323
1222
1121
100 µm Mg Ka 15 kV

Figure 4

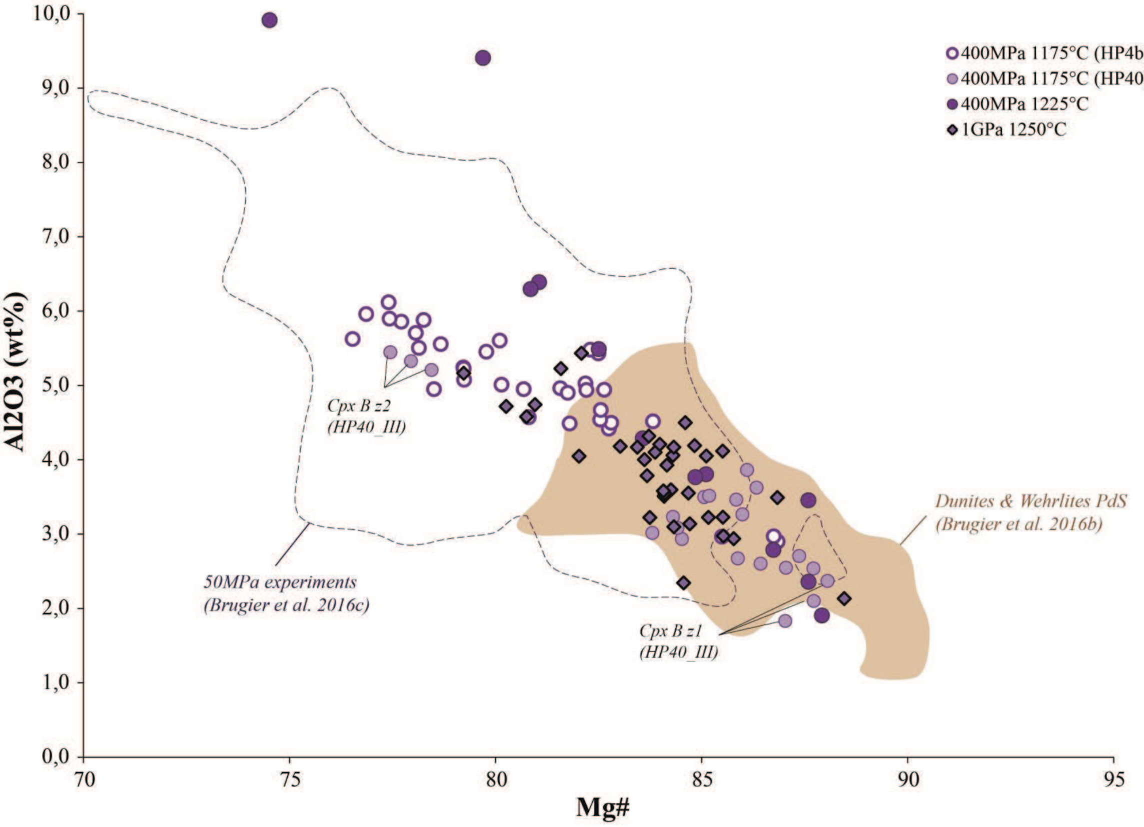
10,0
9,0
8,0
7,0
6,0
5,0
4,0
3,0
2,0
1,0
0,0
Al2O3 (wt%)
70
75
80
85
90
95
Mg#
400MPa 1175°C (HP4b)
400MPa 1175°C (HP40)
400MPa 1225°C
1GPa 1250°C
Cpx B z2
(HP40_III)
Cpx B z1
(HP40_III)
Dunites & Wehrlites PdS
(Brugier et al. 2016b)
50MPa experiments
(Brugier et al. 2016c)

Figure 5

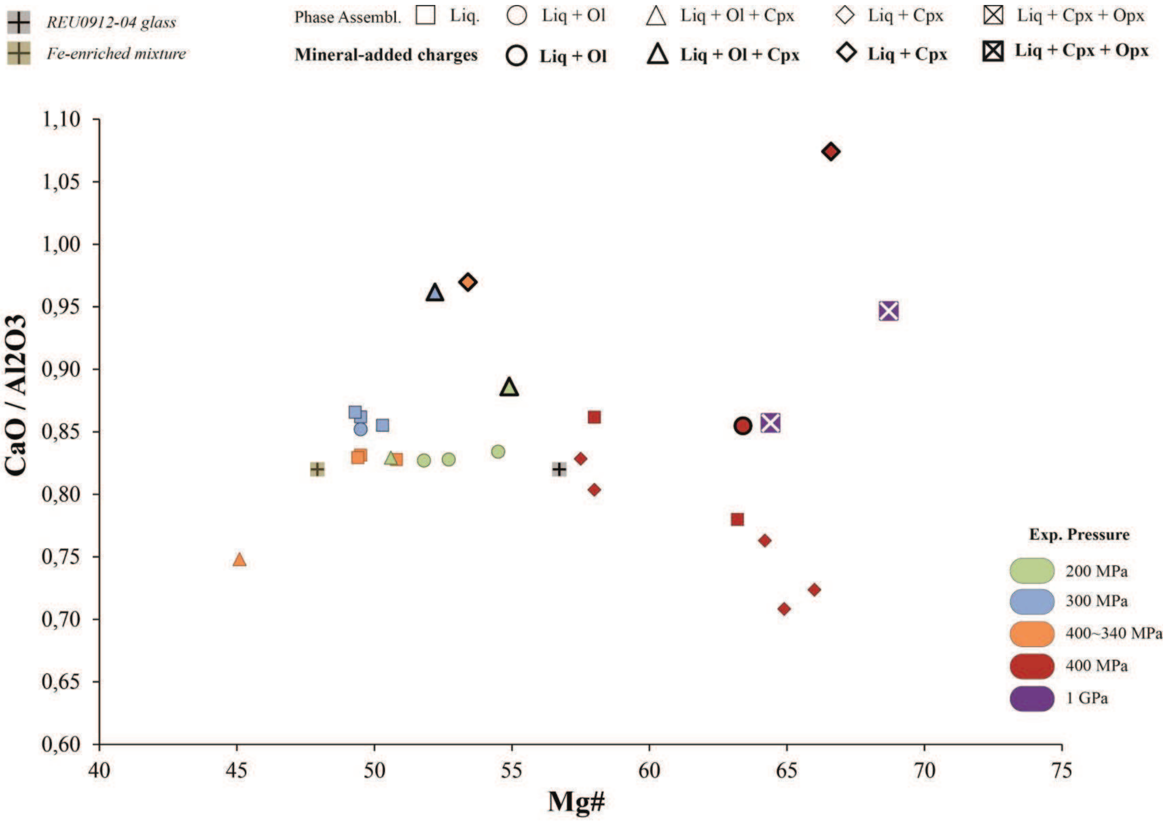
REU0912-04 glass
Fe-enriched mixture
Phase Assembl. Liq. Liq + Ol Liq + Ol + Cpx Liq + Cpx Liq + Cpx + Opx
Mineral-added charges Liq + Ol Liq + Ol + Cpx Liq + Cpx Liq + Cpx + Opx
CaO / Al2O3
1,10
1,05
1,00
0,95
0,90
0,85
0,80
0,75
0,70
0,65
0,60
Mg#
40
45
50
55
60
65
70
75
Exp. Pressure
200 MPa
300 MPa
400~340 MPa
400 MPa
1 GPa

Figure 6

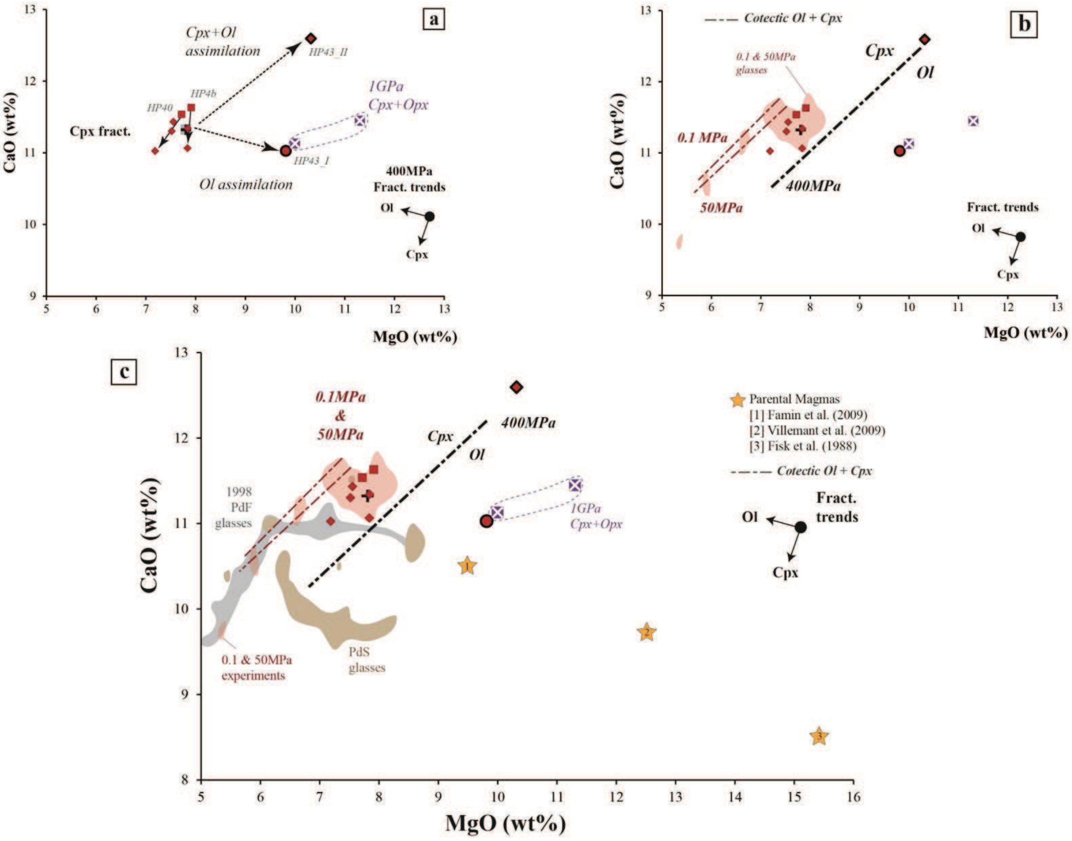
a
CaO (wt%)
MgO (wt%)
Cpx+Ol
assimilation
HP43_II
HP4b
HP40
Cpx fract.
1GPa
Cpx+Opx
HP43_I
Ol assimilation
400MPa
Fract. trends
Ol
Cpx
b
Cotectic Ol + Cpx
0.1 & 50MPa
glasses
Cpx
Ol
0.1 MPa
50MPa
400MPa
Fract. trends
Ol
Cpx
c
0.1MPa
&
50MPa
Cpx
Ol
400MPa
1998
PdF
glasses
1GPa
Cpx+Opx
0.1 & 50MPa
experiments
PdS
glasses
Parental Magmas
[1] Famin et al. (2009)
[2] Villemant et al. (2009)
[3] Fisk et al. (1988)
Cotectic Ol + Cpx
Fract.
trends
Ol
Cpx
1
2
3
13
12
11
10
9
8
5
6
7
8
9
10
11
12
13
14
15
16

Table 1. Major element composition of the PdF starting sample

Sample	**REU0912-04**			**Fe-enrich REU0912-04**	**Cpx**	**Ol**
	Piton de la Fournaise				*Wehrlite PdS*	*San Carlos*
	Whole-rock	Glass[1]	*st.dev. 2*	Start Mat.		
Oxides (wt%)						
SiO2	48,75	50,04	*0,38*	47,89	51,34	41,92
TiO2	2,48	2,59	*0,06*	2,47	0,74	0,01
Al2O3	13,82	13,81	*0,22*	13,21	3,03	0,02
FeOt	10,60	10,61	*0,33*	14,46	4,95	8,87
MnO	0,16	0,16	*0,03*	0,16	0,10	0,11
MgO	7,76	7,81	*0,13*	7,47	16,42	49,17
CaO	11,20	11,32	*0,13*	10,83	22,45	0,09
Na2O	2,57	2,55	*0,16*	2,44	0,10	0,01
K2O	0,67	0,67	*0,01*	0,65	0,19	0,01
P2O5	0,29	0,32	*0,12*	0,31	0,03	0,02
Total	98,61	98,36		100	100,26	100,65
Trace elements (ppm)						
Cr	466	371		362	5540	129
Ni	142	510		506	718	3110
Fo						**90,8**

[1] Average of 100 analyses

Fe-enriched starting material; REU0912-04 glass plus 4.2 wt% FeO added.

Table 2 H_2O- and CO_2-bearing high pressure experiments

Charge	XH2Oinit	H2O melt wt%	aH2O	Cpx	Ol	Phase assemblage [1]	∑ R²	Fe loss %	Kd Fe-Mg Ol-l	Kd Fe-Mg Cpx-l	Kd Fe-Mg Opx-l
HP2, 2028 bars, 1175°C, fH2 ≈ 4bars, 5h, Fe-rich starting material, AuPd capsules											
HP2_I	0,42	1,3	0,196			Gl(100,8), Ol(0,8), Sp(-1,6)	0,8	+5,9	0,29		
HP2_II	0,26	1,3	0,189			Gl(96,9), Ol(3,2), Cpx(1,1), Sp(-1,2)	0,57	+4,7	0,32	0,27	
HP2_III	0,20	1,2	0,182			Gl(96,5), Ol(2,3), Sp(1,2)	0,5	-4,8	0,31		
HP2_IV	0,08	1	0,117			Gl(98,8), Ol(2,4), Sp(-1,2)	0,47	+4,5	0,3		
HP2_X *	0,26	1,4	0,227	X		Gl, Ol, Cpx, Sp			0,29	0,24 ***- 0,24*** [2]	
HP3, 3067 bars, 1175°C, fH2 ≈ 0,5bars 16h, Fe-rich starting material, AuPd capsules											
HP3_I	0,41	1,4	0,197			Gl(103,8), Sp(-3,8)	0,6	+1,1			
HP3_II	0,32	1,2	0,151			Gl(105,2), Sp(-5,2)	1,28	+2,1			
HP3_III	0,20	1,1	0,132			Gl(105,3), Sp(-5,3)	1,89	+4			
HP3_IV	0,08	1	0,108			Gl(103,7), Ol(0,9), Sp(-4,6)	2,6	+7,2	0,26		
HP3_X *	0,31	1,5	0,230	X		Gl, Ol, Cpx, Sp			0,21	0,24 ***- 0,22***	
HP4, 4060->3400 bars, 1174°C, fH2 ≈ 0,5 bars, 13h, Fe-rich starting material, AuPd capsules											
HP4_I	0,39	1,2	0,130			Gl(104,5), Sp(-4,5)	0,46	+1,3			
HP4_II	0,29	1,1	0,116			Gl(105,4), Sp(-5,4)	0,84	+2,2			
HP4_III	0,22	1	0,099			Gl(106), Sp(-6)	1,2	+3,1			
HP4_IV	0,12	0,7	0,048			Gl(98,7), Ol(2,1), Cpx(5,6), Sp(-6,4)	1,41	+3,7	0,24	0,29	
HP4_X *	0,29	1,4	0,192	X		Gl, Cpx, Sp				0,28 ***- 0,23***	
HP4bis, 4007->3944 bars, 1175°C, fH2 ≈ 0,5 bars, 14.5h, AuPd capsules											
HP4b_I	0,30	1,1	0,104			Gl(98,8), Sp(1,2)	0,2	-1,2			
HP4b_II	0,20	1	0,087			Gl(99,5), Cpx(0,1), Sp(0,4)	0,03	-0,4		0,33	
HP4b_III	0,13	0,9	0,070			Gl(96,5), Cpx(1,9), Sp(1,6)	0,38	-4,3		0,32	
HP40, 3997 bars, 1175°C, fH2 ≈ 4bars, 17h, AuPd capsules											
HP40_I	0,39	1,3	0,119			Gl(100)	8,67	-24,4			
HP40_II	0,29	1,3	0,134			Gl(92,3), Cpx(7,7)	11,38	-28,9		0,27	
HP40_III	0,19	1,1	0,098			Gl(90), Cpx(10)	13,71	-31,7		0,29	
HP40_IV	0,10	1,2	0,114			Gl(86), Cpx(14)	15,6	-33,5		0,28	
HP43, 4072->4004 bars, 1225°C, fH2 ≈ 0,5 bars, 6h, AuPd capsules											
HP43_I **	0,30	1,3	0,148		X	Gl, Ol, Sp	-	-	0,24 ***- 0,23***		
HP43_II ***	0,33	1,2	0,152	X	X	Gl, Cpx, Sp, quench	-	-	***0,24***	0,31 ***- 0,32***	
HP10, 10 000 bars, 1250°C, 6h, AuPd capsule											
HP10_I ***	0,34	1,5	0,119	X	X	Gl, Cpx, Opx, quench	-	-	***0,24***	0,32 ***- 0,28***	0,33 ***- 0,24***

* Cpx-added charge, residual Cpx present (X)

** Ol-added charge, residual Ol present (X)

*** Cpx- and Ol-added charge, residual Ol and Cpx present (X)

[1] Refers to phases crystallized in the melt only

[2] Kd calculated by using the rim composition of residual Cpx or Ol; All the other Kd use compositions of phases crystallized in the melt

Table 3 Compositions of experimental products

Charge	Phase	SiO2	TiO2	Al2O3	FeO	MnO	MgO	CaO	Na2O	K2O	P2O5	Cr2O3	NiO	Total	Composition
Series "HP2" T=1175°C // P=2028bars															
HP2_I	Gl(23)	48,97	2,54	13,62	11,96	0,16	7,47	11,27	2,57	0,68	0,62	0,06	0,08	97,04	Mg# 52,7
	Ol(6)	39,29	0,03	0,05	19,59	0,19	41,64	0,35	0,02	0,02	0,04	0,05	0,06	101,32	Fo 79,1
HP2_II	Gl(18)	49,41	2,62	14,00	11,48	0,13	6,58	11,61	2,67	0,72	0,66	0,06	0,07	97,02	Mg# 50,6
	Ol(4)	38,23	0,08	0,04	22,43	0,24	39,53	0,44	0,02	0,01	0,17	0,03	0,05	101,29	Fo 75,9
	Cpx(8)	49,97	1,44	4,76	6,78	0,10	14,55	21,29	0,33	0,01	0,01	1,27	0,05	100,57	En43Wo46Fs11
	Cpx c	52,12	0,80	2,07	7,49	0,09	16,69	19,51	0,21	0,00	0,00	0,64	0,07	99,70	En48Wo40Fs12
	Cpx r	49,44	1,34	5,42	7,32	0,00	14,46	20,67	0,29	0,04	0,00	1,48	0,02	100,48	En43Wo45Fs12
	Sp	0,31	4,74	16,09	33,33	0,37	8,96	0,40	0,00	0,00	0,00	31,29	0,03	95,50	Cr# 57
HP2_III	Gl(19)	49,63	2,60	13,89	10,78	0,15	7,25	11,58	2,68	0,68	0,59	0,04	0,12	97,12	Mg# 54,5
	Ol(6)	39,02	0,06	0,06	19,26	0,20	41,73	0,41	0,01	0,00	0,07	0,04	0,08	100,93	Fo 79,4
HP2_IV	Gl(18)	49,30	2,63	13,86	11,56	0,19	6,96	11,46	2,64	0,66	0,63	0,04	0,07	97,80	Mg# 51,8
	Ol(9)	38,91	0,10	0,07	20,08	0,19	41,25	0,44	0,02	0,01	0,18	0,06	0,10	101,41	Fo 78,6
HP2_X *	Gl(40)	49,37	2,53	13,47	11,05	0,16	7,54	11,94	2,52	0,65	0,65	0,06	0,07	96,99	Mg# 54,9
	Ol (9)	39,02	0,08	0,12	18,39	0,18	41,58	0,53	0,02	0,02	0,21	0,06	0,10	100,31	Fo 80,1
	Cpx (3)	51,56	0,90	2,71	6,51	0,20	16,81	20,60	0,26	0,02	0,00	0,86	0,06	100,49	En48Wo42Fs10
	Cpx R r	51,24	0,85	2,58	6,36	0,32	16,39	21,43	0,23	0,01	0,02	0,86	0,00	100,30	En46Wo44Fs10
	Cpx R c	52,62	0,81	2,20	3,91	0,11	16,63	24,29	0,27	0,00	0,00	0,38	0,00	101,21	En46Wo48Fs6
Series "HP3" T=1175°C // P=3067bars															
HP3_I	Gl(18)	48,90	2,46	13,06	13,29	0,15	7,54	11,17	2,42	0,63	0,34	0,02	0,02	95,95	Mg# 50,3
	Sp(5)	0,14	3,57	7,20	64,98	0,20	7,15	0,28	0,00	0,01	0,01	5,90	0,25	89,68	Cr# 35
HP3_II	Gl(7)	48,33	2,47	12,86	13,85	0,23	7,61	11,08	2,41	0,68	0,39	0,02	0,07	96,80	Mg# 49,5
	Sp(4)	0,38	4,12	8,15	61,97	0,15	7,31	0,34	0,05	0,04	0,06	7,18	0,14	89,89	Cr# 37
HP3_III	Gl(11)	48,17	2,46	12,84	14,07	0,17	7,66	11,12	2,43	0,65	0,37	0,02	0,03	96,79	Mg# 49,3
	Sp(4)	0,25	4,37	11,27	52,88	0,12	7,78	0,37	0,02	0,02	0,01	13,35	0,07	90,50	Cr# 44
HP3_IV	Gl(16)	48,64	2,45	13,15	13,42	0,18	7,39	11,21	2,41	0,69	0,38	0,04	0,03	97,53	Mg# 49,5
	Ol(7)	39,13	0,07	0,08	18,89	0,18	40,59	0,44	0,03	0,02	0,07	0,03	0,13	99,66	Fo 79,3
	Sp(2)	0,75	4,09	13,79	44,56	0,19	8,56	0,42	0,02	0,05	0,11	19,67	0,21	92,43	Cr# 49
HP3_X *	Gl(13)	48,74	2,39	12,28	13,20	0,15	8,08	11,81	2,32	0,65	0,33	0,03	0,02	96,44	Mg# 52,2
	Ol	39,00	0,00	0,03	15,31	0,12	43,39	0,39	0,01	0,00	0,00	0,01	0,27	98,52	Fo 83,5
	Cpx	48,75	1,11	4,85	8,08	0,24	15,40	19,96	0,34	0,00	0,00	0,46	0,00	99,20	En45Wo42Fs13
	Cpx	51,46	0,923	3,166	4,897	0,219	16,036	22,432	0,28	0,021	0	1,036	0	100,469	En46Wo46Fs8
	Sp(5)	0,1738	3,4334	9,5624	52,1928	0,1432	8,2936	0,3542	0,0174	0,0242	0,0188	16,4336	0,0824	90,73	Cr# 54
	Cpx R r	50,661	0,598	3,562	6,916	0,173	16,244	20,276	0	0,377	0	0,556	0	99,362	En47Wo42Fs11
	Cpx R c	50,255	1,001	3,629	5,18	0,032	15,459	22,534	0,03	0,242	0,085	0,951	0	99,398	En45Wo47Fs8
Series "HP4" T= 1175°C // P=4060 ->3400bars															
HP4_I	Gl(20)	48,38	2,40	13,34	13,17	0,18	7,64	11,04	2,54	0,63	0,59	0,01	0,07	96,62	Mg# 50,8
	Sp(3)	0,28	4,05	8,40	62,99	0,34	7,71	0,31	0,00	0,05	0,11	9,71	0,10	94,04	Cr# 43
HP4_II	Gl(18)	47,78	2,50	13,14	13,94	0,16	7,66	10,93	2,54	0,62	0,60	0,03	0,11	97,48	Mg# 49,5
	Sp(3)	0,15	4,17	9,41	61,54	0,25	7,79	0,37	0,01	0,01	0,06	11,05	0,21	95,04	Cr# 44
HP4_III	Gl(20)	47,58	2,45	13,19	14,05	0,18	7,71	10,94	2,53	0,63	0,64	0,04	0,05	97,71	Mg# 49,4
	Sp	0,03	3,11	10,49	45,87	0,40	8,63	0,26	0,01	0,02	0,18	27,74	0,32	97,06	Cr# 64
	Sp(2)	0,26	4,74	10,52	56,37	0,25	7,84	0,30	0,04	0,02	0,05	12,92	0,10	93,41	Cr# 45
HP4_IV	Gl(11)	47,79	2,57	13,99	14,31	0,14	6,61	10,47	2,63	0,73	0,68	0,03	0,04	98,40	Mg# 45,1
	Ol(10)	38,22	0,06	0,09	20,95	0,18	40,81	0,40	0,03	0,02	0,06	0,04	0,13	100,98	Fo 77,6
	Cpx(5)	48,27	0,99	5,33	9,75	0,10	15,53	18,61	0,44	0,02	0,08	0,34	0,03	99,48	En45Wo39Fs16
	Sp(3)	0,34	5,22	12,60	54,88	0,25	8,04	0,27	0,02	0,04	0,01	12,99	0,04	94,70	Cr# 41
HP4_X *	Gl(24)	47,78	2,37	12,31	13,32	0,15	8,56	11,94	2,37	0,60	0,50	0,05	0,07	96,74	Mg# 53,4
	Cpx(9)	51,13	0,86	3,66	6,31	0,17	16,03	21,23	0,32	0,02	0,04	0,68	0,09	100,56	En46Wo44Fs10
	Cpx(6)	48,36	1,55	6,05	9,13	0,10	14,99	18,31	0,38	0,05	0,07	0,41	0,03	99,42	En45Wo40Fs15
	Cpx(9)	51,12	1,05	3,91	5,41	0,15	15,72	22,39	0,29	0,00	0,02	0,86	0,08	101,00	En45Wo46Fs9
	Sp(3)	0,21	3,52	10,35	51,11	0,20	9,31	0,42	0,01	0,03	0,02	17,77	0,26	93,21	Cr# 54
	Cpx R c	51,09	0,71	2,99	5,04	0,00	16,36	22,79	0,27	0,00	0,00	0,90	0,16	100,30	En46Wo46Fs8
	Cpx R r	50,63	0,60	3,45	6,36	0,25	16,83	21,30	0,32	0,02	0,00	0,68	0,22	100,65	En47Wo43Fs10

Table 3 *Continued*

Series "HP4bis" T=1175°C // P=4007->3944bars															
HP4b_I	Gl(10)	50,37	2,60	13,50	10,21	0,19	7,91	11,63	0,67	2,52	0,30	0,03	0,07	96,18	Mg# 58
	Sp(2)	0,22	2,30	12,08	43,81	0,15	10,60	0,36	0,03	0,03	0,03	21,66	0,23	91,50	Cr# 55
HP4b_II	Gl(7)	50,30	2,62	13,69	10,34	0,14	7,84	11,34	0,70	2,61	0,32	0,05	0,03	97,34	Mg# 57,5
	CpxA c	52,06	0,79	2,89	4,24	0,09	15,68	22,61	0,00	0,36	0,00	1,05	0,00	99,76	En46Wo47Fs7
	CpxA r	49,69	0,87	4,90	6,32	0,23	15,87	20,42	0,06	0,48	0,03	1,04	0,13	100,02	En47Wo43Fs10
	Cpx (10)	48,88	1,04	5,45	7,40	0,10	15,71	19,93	0,01	0,50	0,01	0,48	0,07	99,59	En46Wo42Fs12
	Sp	0,35	2,96	14,10	41,66	0,18	11,13	0,28	0,05	0,10	0,00	22,54	0,08	93,42	Cr# 52
HP4b_III	Gl(6)	50,67	2,70	14,06	9,70	0,11	7,52	11,30	0,72	2,62	0,49	0,05	0,07	97,30	Mg# 58
	Cpx (10)	49,88	0,99	4,94	6,69	0,11	16,22	19,24	0,04	0,44	0,03	0,90	0,03	99,52	En48Wo41Fs11
Series "HP40" T=1175°C // P=3997bars															
HP40_I	Gl(6)	50,86	2,74	14,79	8,00	0,14	7,72	11,54	0,73	2,82	0,48	0,02	0,17	94,63	Mg# 63,2
HP40_II	Gl(5)	51,27	2,78	14,99	7,50	0,14	7,55	11,43	0,79	2,90	0,52	0,02	0,11	94,83	Mg# 64,2
	Cpx	50,33	0,94	3,56	4,88	0,22	17,30	20,12	0,00	0,28	0,00	0,57	0,05	98,25	En50Wo42Fs8
HP40_III	Gl(10)	51,49	2,76	15,29	7,18	0,15	7,84	11,06	0,77	2,91	0,47	0,03	0,04	95,48	Mg# 66
	Cpx (3)	51,60	0,70	2,48	4,84	0,11	18,25	19,75	0,01	0,27	0,00	0,34	0,09	98,43	En52Wo40Fs8
	CpxB_z1 (2)	51,29	0,74	2,50	4,42	0,10	17,68	20,81	0,05	0,29	0,23	0,44	0,00	98,54	En50Wo43Fs7
	CpxB_z2 (2)	47,37	2,01	5,24	7,73	0,05	15,32	19,86	0,01	0,31	0,18	0,21	0,02	98,30	En45Wo42Fs13
	CpxB_z3 (2)	50,23	0,90	3,06	5,39	0,15	16,39	21,62	0,02	0,27	0,05	1,03	0,08	99,18	En47Wo44Fs9
	CpxB_z4 (2)	50,70	1,01	3,22	5,03	0,19	17,30	20,26	0,03	0,29	0,03	0,45	0,19	98,69	En50Wo42Fs8
HP40_IV	Gl(10)	51,94	2,91	15,57	6,94	0,17	7,19	11,03	0,78	2,99	0,38	0,03	0,08	94,91	Mg# 64,9
	Cpx (3)	52,28	0,59	2,07	4,59	0,11	18,40	19,98	0,03	0,28	0,00	0,25	0,03	98,61	En52Wo41Fs7
Series "HP43" T=1225°C // P=4072->4004bars															
HP43_I **	Gl(16)	50,01	2,60	12,90	10,11	0,12	9,81	11,03	0,67	2,32	0,26	0,06	0,11	96,94	Mg# 63,4
	Ol(6)	40,82	0,06	0,30	11,38	0,15	46,53	0,51	0,03	0,05	0,02	0,02	0,33	100,19	Fo 87,9
	Ol R c	42,38	0,07	0,00	4,51	0,15	51,92	0,15	0,01	0,01	0,00	0,00	0,31	99,50	Fo 95,3
	Ol R r	40,77	0,03	0,08	10,64	0,26	46,45	0,28	0,00	0,03	0,00	0,02	0,36	98,91	Fo 88,6
HP43_II ***	Gl(8)	50,54	2,30	11,72	9,21	0,12	10,32	12,59	0,54	2,19	0,30	0,08	0,07	97,16	Mg# 66,6
	Cpx(8)	51,58	1,07	4,85	5,85	0,12	17,27	17,94	0,06	0,42	0,02	0,59	0,09	99,88	En52Wo38Fs10
	CpxC c	51,88	0,69	2,86	4,52	0,28	16,09	22,55	0,00	0,38	0,00	1,01	0,05	100,30	En46Wo47Fs7
	CpxC r	51,89	0,85	3,76	4,84	0,25	17,66	19,37	0,06	0,37	0,00	1,07	0,00	100,11	En51Wo41Fs8
	Ol R c	42,75	0,00	0,01	5,23	0,00	52,29	0,16	0,05	0,03	0,00	0,00	0,44	100,97	Fo 94,7
	Ol R r	41,82	0,03	0,00	10,65	0,06	47,56	0,39	0,04	0,00	0,01	0,06	0,36	100,98	Fo 88,8
"HP10" T=1250°C // P=10,000bars															
HP10	Gl z1 (32)	50,09	2,31	12,09	9,17	0,15	11,30	11,45	2,47	0,58	0,22	0,12	0,06	96,94	Mg# 68,7
	Gl z2 (5)	49,55	2,46	12,98	9,84	0,12	10,00	11,13	2,88	0,71	0,21	0,07	0,05	96,40	Mg# 64,4
	Cpx(35)	51,66	0,70	3,87	6,63	0,15	19,38	15,81	0,52	0,02	0,02	0,50	0,05	99,32	En56Wo33Fs11
	Opx(15)	54,66	0,29	2,28	9,33	0,14	30,12	2,76	0,09	0,02	0,01	0,26	0,07	100,03	En81Wo5Fs14
	Ol R -> Opx c	53,80	0,27	2,53	7,88	0,17	31,65	2,74	0,07	0,02	0,03	0,93	0,19	100,27	En84Wo5Fs11
	Ol R -> Opx r	55,98	0,13	2,62	7,28	0,02	30,92	2,79	0,09	0,00	0,08	0,94	0,00	100,85	En83Wo5Fs13
	Ol R (20)	40,30	0,02	0,03	10,69	0,15	47,16	0,27	0,02	0,02	0,04	0,06	0,20	98,95	Fo 88,7
	Cpx R c	51,68	0,93	3,17	4,49	0,00	15,92	22,00	0,26	0,00	0,00	0,66	0,00	99,10	En47Wo46Fs7
	Cpx R r	50,81	1,13	6,62	7,14	0,04	19,70	14,02	0,51	0,04	0,03	0,39	0,00	100,43	En58Wo30Fs12

c: core composition; r: rim composition; R: residual phase, either Ol or Cpx

CpxA, B, C shown in Fig. 1

For CpxB, z1, z2, z3, z4 are electron microprobe spots located in Fig. 1 and Fig. 3

For the HP10 experiment, z1 and z2 are 2 different glass electron microprobe spots (z1=crystal-free zone in the top of the capsule, z2= at proximity of crystals and located in Fig. 1)

CONCLUSION & PERSPECTIVES

1 Rappel des principaux résultats

Le principal enjeu de ce travail de thèse était d'apporter des contraintes pétrologiques sur les deux groupes magmatiques les plus distinctifs identifiés dans les produits du PdF : les Steady State Basalts (SSB) et l'Abnormal Group (AbG), d'après *Ludden et al. (1978a); Kornprobst et al. (1984) Albarède et al (1997), Boivin & Bachèlery (2009) ; Famin et al. (2009), Villemant et al. (2009) ; Salaün et al. (2010) ; Pichavant et al. (2016).*

Pour ce faire une étude expérimentale portant sur les équilibres de phase d'une composition typique de SSB, en fonction de la pression, et conduite dans des conditions simulant le système d'alimentation du PdF dans son intégralité, a été réalisée. Cette première étude expérimentale haute-pression réalisée en présence de volatiles (H2O+CO2) pour une composition de La Réunion a fourni les résultats présentés dans les chapitres 3 et 4.

En parallèle, une étude volcanologique et pétrologique des produits et édifices volcaniques classiquement attribués au groupe AbG (Piton Chisny, Piton Haüy et Demi-Piton sur la Plaine des Sables d'après *Bachèlery, 1981; Albarède et al., 1997; Famin et al., 2009 ; Morandi et al., 2016 ; Principe et al., 2016 ; Boudoire et al., in prep*) a été menée dans le but de contraindre l'existence ou non de liquides magmatiques de composition AbG au sein du système d'alimentation récent du PdF, ainsi que de discriminer les différents processus à l'origine des deux groupes de magmas SSB-AbG. Cette étude allant de la stratigraphie volcanique des pitons de la Plaine des Sables à l'analyse en éléments majeurs et traces des verres de lapilli a été présentée dans le chapitre 1.

Enfin, une étude pétrologique complète d'une variété de roches grenues réunionnaises, allant des dunites aux gabbros et dolérites a été réalisée dans le but de définir la (ou les) séquence(s) de cristallisation pouvant avoir lieu au sein des liquides magmatiques présents dans le système d'alimentation du Piton de la Fournaise. Cett étude a fourni un guide comparatif aux résultats expérimentaux. Les résultats de l'étude des xénolithes de la Plaine des Sables, présentés dans le chapitre 2, viennent largement compléter les données existantes sur les roches plutoniques réunionnaises, jusque-là axées sur les corps plutoniques du Piton des Neiges (*Upton & Wadsworth, 1972 ; Nativel, 1978*), sur les résultats du forage du complexe hypovolcanique associé au volcan « Les Alizés » (*Lerebour, 1987 ; Augé et al., 1989*) ou sur les enclaves retrouvées dans les dépôts des éruptions phréato-magmatiques des « Cendres de Bellecombe » (*Mohamed-Abchir, 1998 ; Upton et al., 2000 ; Collins et al., 2012*).

La Figure 1, ci-dessous, présente certains des résultats les plus importants obtenus lors de ce travail, en comparant un état de l'art sommaire sur les données de verres silicatés disponibles avant le début de ce travail de thèse (Fig. 1a), et l'apport de ce travail de thèse en termes de compositions de verres silicatés, ainsi que de construction des vecteurs de fractionnement des principales phases minérales (olivine, clinopyroxene) et des conditions de saturation (cotectiques) olivine+clinopyroxene en fonction de la pression basées sur les données expérimentales (Fig.1b).

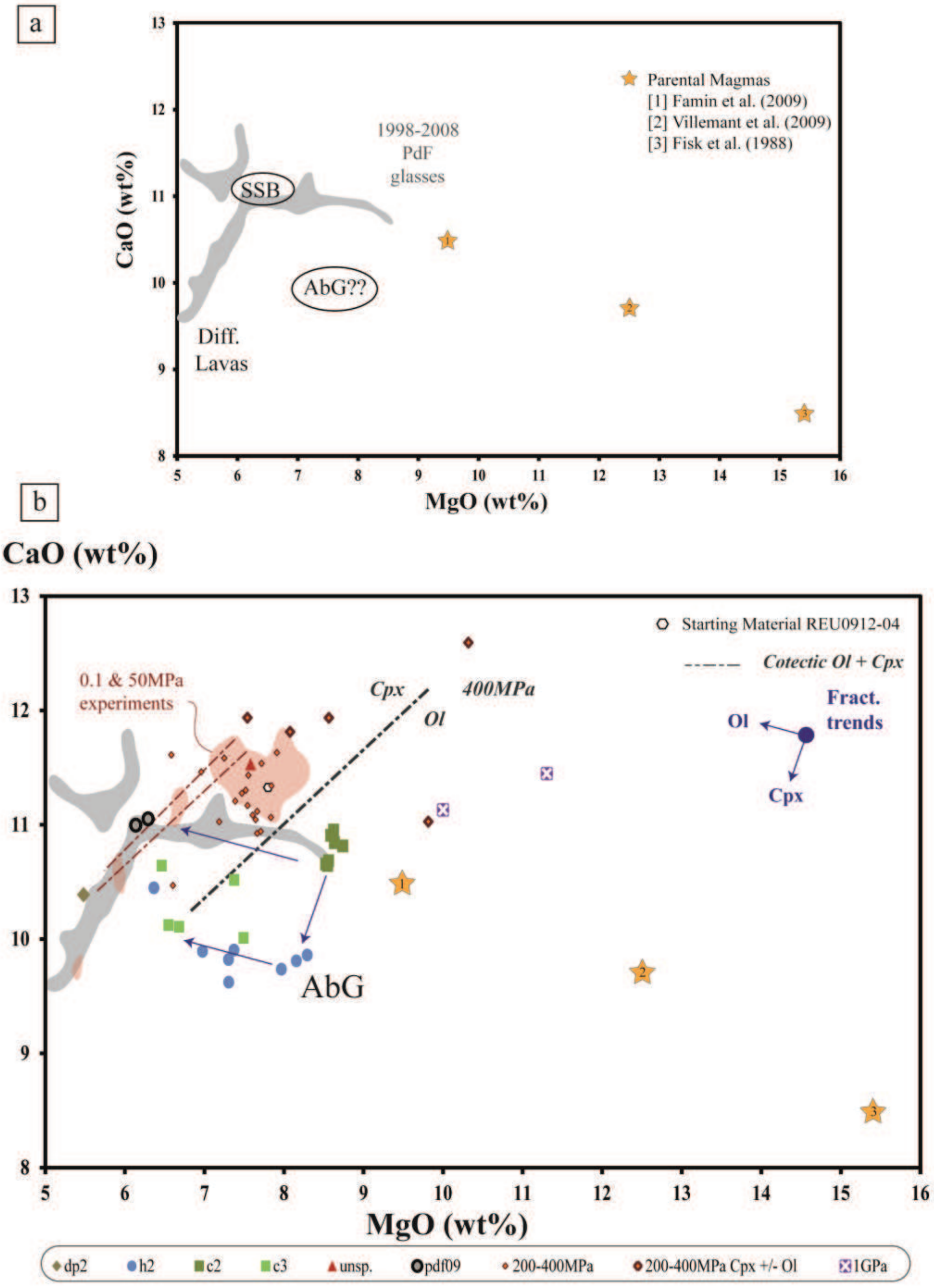

__Figure 6:__ Diagrammes MgO vs CaO synthétisant les données existantes (a) et l'apport des données de verres silicatés obtenus durant cette étude (b).

Les compositions des verres silicatés des lapilli obtenus lors de l'étude volcanologique et pétrologique des édifices de la Plaine des Sables (Chapitre 1) montrent clairement des compositions différentes des verres analysés jusqu'alors dans des produits éruptifs du Piton de la Fournaise (verres de matrice pour des produits émis entre 1998 et 2008, provenant de *Villemant et al., 2009 ; Welsch et al., 2009 ; Salaün et al., 2010 ; Di Muro et al., 2014*). Ces compositions des verres des lapilli sont globalement riches en MgO (6,5 à 8,7 %pds) et appauvries en CaO (9,6 à 11%pds) par rapport aux verres des SSB et trouvés en matrice des dépôts du PdF de 1998 à 2008 qui ont des compositions plus ou moins différenciées.

L'existence de liquides magmatiques de composition AbG a donc été validée durant ce travail de thèse. De plus, comme indiqué sur la Figure 6a (Chapitre 1), les compositions de ces verres AbG sont en accord avec un processus de fractionnement précoce de clinopyroxène (*Kornprobst et al., 1984 ; Albarède et al., 1997 ; Famin et al., 2009 ; Boudoire et al., in prep*), lequel est aussi soutenu par les données des éléments traces (Figs. 7 et 8, Chapitre1). L'apport des données expérimentales obtenues durant ce travail de thèse est ici primordial car la construction des lignes de saturation cotectiques, pour plusieurs pressions représentatives du système d'alimentation du PdF, permet de contraindre une pression minimum pour le fractionnement du clinopyroxene. En effet, les compositions les plus primitives de nos verres AbG, qui ne semblent pas avoir subi un fractionnement de clinopyroxène marqué, sont dans le champ de stabilité de l'olivine par rapport au cotectique à 400 MPa (Fig. 1b), ce qui implique une pression de fractionnement supérieure pour expliquer leurs compositions. Il est à rappeler que les points expérimentaux à 1GPa, qui caractérisent un domaine où l'assemblage cpx+opx est à l'équilibre et où l'olivine est instable, pourraient définir un modèle pour ces liquides primitifs.

Les données de verres expérimentaux obtenues ne peuvent pas être considérées comme des magmas parentaux potentiels étant donné le matériel de départ évolué utilisé dans nos expériences et leur composition. Cependant, les pentes des cotectiques ne variant que peu avec la temperature ou la teneur en H2O pour une pression donnée (Pichavant et al., 2009 ; Lanzo et al., 2016), l'existence de liquides primitifs enrichis en MgO et CaO à haute pression doit être prise en compte dans le mécanisme de fractionnement profond de clinopyroxène.

La figure 2 ci-dessous permet de synthétiser les différents résultats obtenus lors de ce travail de thèse, ainsi que les principaux points de cette conclusion, dans le contexte du système d'alimentation du Piton de la Fournaise, considéré dans son ensemble.

Ceci permet de définir un domaine de prédominance de l'olivine dans la partie crustale du système d'alimentation (de la surface jusqu'à 13-14km de profondeur). Un tel domaine est compatible avec (1) la séquence de cristallisation définie pour les roches plutoniques réunionnaises (*Upton & Wadsworth, 1972 ; Lerebour, 1987 ; Upton et al., 2000*, Chapitre2), (2) les différentes pressions expérimentales auxquelles l'olivine a été définie comme phase au liquidus (de 0,1 à 300 MPa, Chapitres 3, 4), ainsi que (3) le fait que l'olivine soit pratiquement le seul phénocristal observé dans les produits volcaniques du PdF (*Lacroix, 1936 ; Upton & Wadsworth, 1965 ; Ludden, 1978a ; Bachèlery, 1981 ; Kornprobst et al., 1984 ; Albarède et al., 1997 ; Bureau et al., 1998a,b ; Vlastèlic et al., 2005 ; Boivin & Bachèlery, 2009 ; Welsch et al., 2009 ; Di Muro et al., 2014 ;* Chapitre 1).

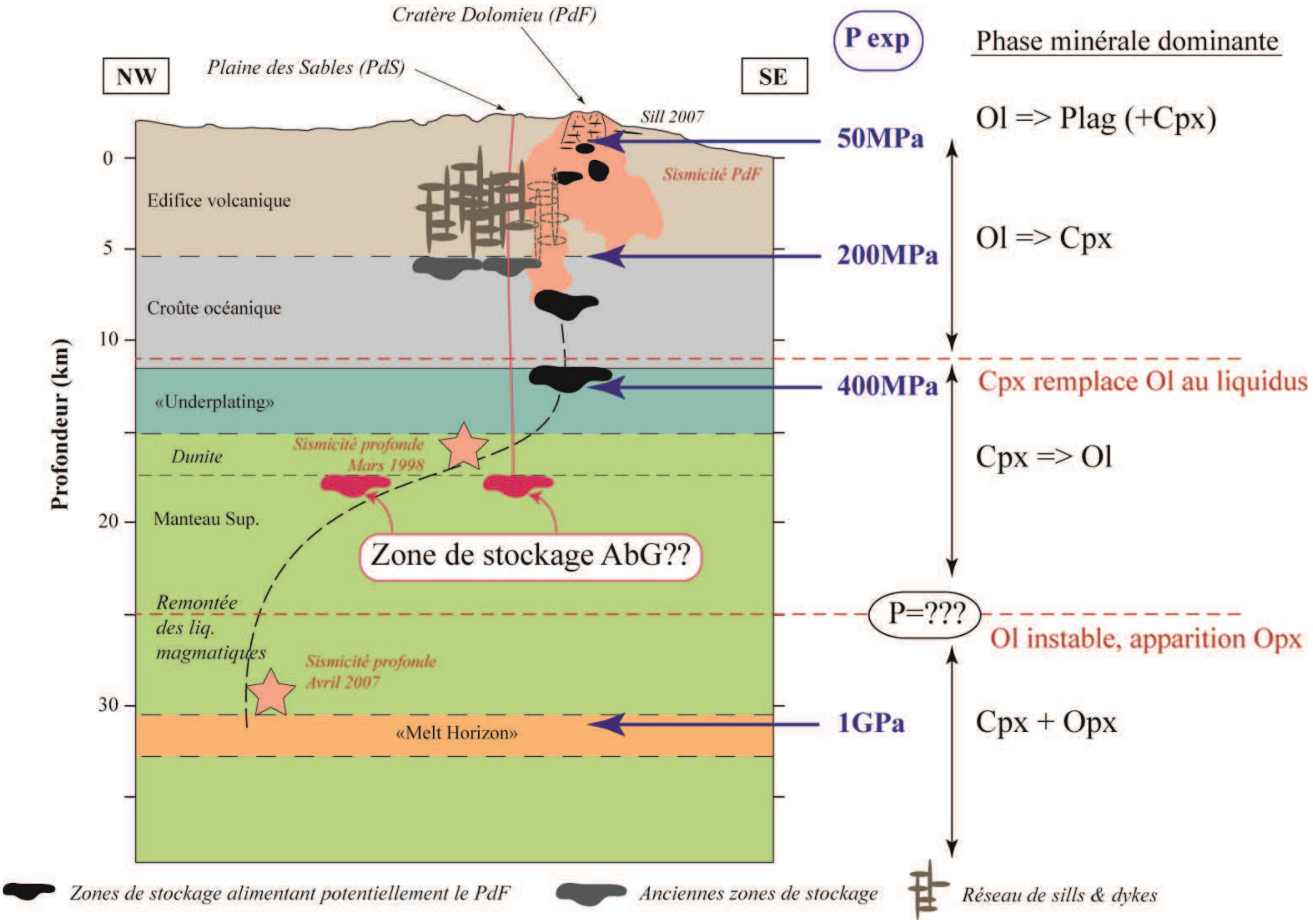

Figure 7: *Schéma représentant le système d'alimentation du Piton de la Fournaise (basé sur les donénes géophysiques existantes) ainsi que les domaines d'équilibres des principales phases expérimentales.*

Pour des pressions supérieures à 350~400MPa, l'olivine est remplacée par le clinopyroxène au liquidus (Fig. 2), ce qui en terme de pression correspond parfaitement à la localisation d'un niveau de sous-plaquage identifié par les données géophysiques à l'interface croûte-manteau (370~420MPa, *Gallart et al., 1999*) et interprété comme un réservoir magmatique cristallisant un assemblage wehrlitique. Etant donné que cette pression de 400 MPa a été définie comme une pression minimum à partir de laquelle le fractionnement de clinopyroxène précoce et profond, à l'origine du groupe de magmas de compositions AbG, intervient, il est clair qu'un tel processus se peut se dérouler que dans la partie la plus profonde du système d'alimentation du PdF, c'est-à-dire au sein du manteau supérieur. Le niveau de « Melt Horizon » (*Fontaine et al., 2015*) situé autour de 30 km de profondeur (~1GPa) pourrait définir une pression maximale pour le fractionnement du clinopyroxène précoce qui serait ainsi confiné à des pressions entre ~500 MPa et 1GPa (Fig. 2).

Des zones de stockage potentielles pour des magmas qui subiraient le fractionnement de clinopyroxène profond à l'origine des AbG ont été récemment proposées par *Boudoire et al. (in prep)*, à l'interface d'un niveau dunitique situé sous le sous-plaquage wehrlitique, et correspondant à des pressions de 500 à 600 MPa, ce qui semble être en adéquation avec nos résultats. Une remontée très rapide doit être envisagée pour limiter le refroidissement des magmas et le fractionnement d'olivine. Toutefois, une remontée aussi rapide des magmas devrait favoriser l'émission de laves de type ankaramite. Or, ceci n'est pas observé (une occurrence d'ankaramite a été répertoriée sur le massif de la Fournaise, d'après *A. Di Muro, comm.pers*.) malgré l'existence, dans de petits édifices monogéniques de composition AbG, de produits à pyroxène (*Boudoire et al., in prep*).

A plus haute pression, il est intéressant de noter que l'expérience réalisée à 1GPa pourrait être discutée dans le cadre du « melt horizon » (Fontaine et al., 2015) lequel, selon nos résultats, pourrait contenir des liquides silicatés profonds à l'équilibre avec un assemblage clinopyroxène+orthopyroxene, dont la composition s'approcherait des magmas parentaux potentiels du Piton de la Fournaise.

Avant de discuter des perspectives qui peuvent être envisagées à partir de ce travail de thèse, il paraît primordial de souligner ici que les résultats obtenus dans le volet expérimental de cette étude conduisent à une bien meilleure intégration entre les différents types de données, pétrologiques (produits naturels, assemblages de phases, inclusions vitreuses et fluides) et géophysiques, que l'étude expérimentale antérieure de Fisk et al. (1988) le permettait. Ce résultat est essentiellement dû à l'ajout de volatiles (H2O et CO2) dans nos expériences, ce qui permet d'approcher plus précisément les conditions d'évolution des magmas naturels et de proposer des simulations expérimentales plus directement applicables pour la surveillance.

2 Perspectives

S'il paraît clair, au vu de ce qui précède, que les principaux objectifs de ce travail de thèse ont été globalement atteints, plusieurs perspectives doivent être évoquées. Il apparaît tout d'abord nettement qu'une étude expérimentale et / ou de modélisation pour contraindre les potentielles compositions de magma parentaux alimentant le Piton de la Fournaise serait nécessaire. Au vu des faibles concentrations en volatils dans les verres expérimentaux rencontrées dans ce travail et attendues dans les études futures, il apparaît aussi comme nécessaire d'utiliser des protocoles expérimentaux spécifiques et systématiquement des méthodes d'analyse des teneurs en H2O et CO2 sensibles plutôt que les estimations par différence.

Une étude expérimentale sur un produit de départ ayant une composition typique d'AbG serait également tout à fait pertinente. Les données du Chapitre 1 permettent d'identifier certains lapillis, notamment les produits du Piton Haüy, comme de très bons candidats pour un tel matériel de départ. Cette étude porterait dans un premier temps sur la réalisation d'expériences d'équilibres de phases isobares dans des conditions de haute pression correspondant au système d'alimentation profond (de 200-300 MPa à 1 GPa), en présence de volatils. Une fois la séquence de cristallisation pour une composition de type AbG définie, suivraient des expériences de décompression qui simuleraient la remontée des magmas depuis la zone de stockage profond, et l'évolution de l'assemblage de phases au liquidus en réponse à la décompression. Ceci pourrait éventuellement permettre de définir les vitesses et durées nécessaires pour résorber les clinopyroxènes profonds. D'autres expériences d'équilibration de la composition AbG de départ avec un assemblage wehrlitique pourraient être aussi envisagées en complément.

Afin de compléter les données pétrologiques existantes sur les édifices pouvant être associés à des liquides d'origine profonde, une mission de terrain pourrait être envisagée pour réaliser une étude volcanologique et pétrologique des cônes situés dans la rift zone NO-SE et dont les produits contiennent des phénocristaux de clinopyroxène. Certaines cibles sont déjà identifiées et d'autres à définir avec l'OVPF (A. Di Muro, G. Boudoire).

Un tel projet permettrait d’apporter des contraintes volcanologiques, pétrologiques et expérimentales supplémentaire sur le groupe des AbG, sur les processus profonds régissant le volcanisme réunionnais, et à plus grande échelle sur le volcanisme des OIB.

Bibliographie

Albarède, F., Luais, B., Fitton, G., Semet, M., Kaminski, E., Upton, B.G.J., Bachèlery, P. & Cheminée, J.L. (1997) The geochemical regimes of Piton de la Fournaise volcano (Réunion) during the last 530000 years. Journal of Petrology 38, 171-201.

Augé, T., Lerebour, P. & Rançon, J.-P. (1989) The Grand Brûlé exploration drilling : new data on the deep framework of the Piton de la Fournaise volcano. Part III: mineral chemistry of the cumulate rocks. Journal of the volcanological and geothermal research 36, 139-151.

Bachèlery, P. (1981) Le Piton de la Fournaise (Ile de la Réunion): etude volcanologique, structural et pétrologique. PhD Thesis, Université Blaise Pascal, Clermont Ferrand, 215 pp.

Boivin, P. & Bachèlery, P. (2009) Petrology of 1977 to 1998 eruptions of Piton de la Fournaise, La Réunion Island. Journal of Volcanological and Geothermal Research 184, 109-125.

Bory de Saint-Vincent, J-B-G-M (1804) Voyage dans les quatre principales îles des mers d'Afrique, pendant lannées neuf et dix de la République (1801 et 1802), Marseille, Laffitte. Buisson F., Paris.

Bosch, D., Blichert-Toft, J., Moynier, F., Nelson, B.K., Telouk, P., Gillot, P.Y. & Albarède, F. (2008) Pb, Hf and Nd isotope compositions of the two Réunion volcanoes (Indian Ocean): a tale of two small-scale mantle blobs. Earth and Planetary Science Letters 265, 748-768.

Boudoire, G., Brugier Y.A., Di Muro, A., Wörner, G., Métrich, N., Arienzo, I., Braukmüller, N., Kronz, A., Le Moigne, Y., Michon, L., Pichavant, M. & Zanon, V. (*in prep*) The deep plumbing system of volcanic islands : new insights from recent activity of the NW Rift Zone (NWRZ) of Piton de la Fournaise (La Réunion Island, Indian Ocean).

Brugier, Y.A., Le Moigne, Y., Pichavant, M., Bourdier, J.L., Boudoire, G. & Di Muro, A. (2016a) Compositional variability of basaltic spatters activity in the Plaine des Sables (Reunion island): Volcanological and petrological constraints.

Brugier, Y.A., Boudoire, G., Pichavant, M., Le Moigne, Y., Di Muro, A., Clague, D., Bachèlery, P. & Bourdier, J.L. (2016b) Petrological and mineralogical characteristics of plutonic rocks from the Plaine des Sables (Piton de la Fournaise volcano, La Réunion Island) - Implications for crystallization processes of Réunion lavas.

Brugier, Y.A., Pichavant, M. & Di Muro, A. (2016c) Petrology of Steady State Basalt from Piton de la Fournaise volcano: A Volatiles-present Experimental Study of the shallow feeding system.

Bureau, H., Pineau, F., Métrich, N., Semet M.P. & Javoy, M. (1998a) A melt and fluid inclusion study of the gas phase at Piton de la Fournaise volcano (Réunion Islanf). Chemical Geology 147, 115-130.

Bureau, H., Métrich, N., Pineau, F. & Semet M.P. (1998b) Magma-conduit interaction at Piton de la Fournaise volcano (Réunion Island) : a melt and fluid inclusion study. Journal of Volcanological and Geothermal Research 84, 39-60.

Chevallier, L., Lalanne, F.-X., Bachèlery, P. & Vincent, P.M. (1981) L'éruption du mois de février 1981 au Piton de la Fournaise (Ile de La Réunion, Océan Indien). Phénoménologie et remarques structurales. Comptes rendus de l'académie des sciences de Paris 293, 187-190.

Collins, S.J., Maclennan, J., Pyle, D.M., Barnes, S.J. & Upton, B.G.J. (2012) Two phases of sulphide saturation in Réunion magmas : Evidence from cumulates. Earth and Planetary Sciences Letters (2012), 104-113.

d'Herguerty M. (1755) Observations sur le volcan de l'Ile Bourbon. Mémoires de la Société royale des sciences et belles-lettres de Nancy 3, 218-235.

de Crémont, H. (1770) Excursion au Volcan de la Fournaise en 1768. In: E-C. Fréron (ed) *L'Année littéraire vol.7,* Delalain, Paris,73-97.

Di Muro, A. (2012 & 2015) Evaluation de l'aléa volcanique à La Réunion. Rapport final-année I et II. Projet BRGM/IPGP.

Di Muro, A., Métrich, N., Vergani, D., Rosi, M., Armienti, P.,Fougeroux, T., Deloule, E., Arienzo, I. & Civetta, L. (2014) The Shallow Plumbing System of Piton de la Fournaise Volcano (La Réunion Island, Indian Ocean) revealed by the Major 2007 Caldera-Forming Eruption. Journal of Petrology 55, 1287-1315.

Duncan, R.A., Backman, J. & Peterson, L. (1989) Reunion hotspot activity through tertiary time: initial results from the ocean drilling program, Leg 115. Journal of Volcanological and Geothermal Research 36, 193-198.

Famin, V., Welsch, B., Okumura, S., Bachèlery, P. & Nakashima, S. (2009) Three differentiation stages of a single magma at Piton de la Fournaise (Réunion hotspot). Geochemistry Geophysics Geosystems 10, Q01007.

Fisk, M.R., Upton, B.G.J., Ford, C.E. & White, W.M. (1988) Geochemical and Experimental Study of the Genesis of Magmas of reunion Island, Indian Ocean. Journal of Geophysical Research 93, 4933-4950.

Fontaine, F. R., Barruol, G., Tkalčić, H., Wölbern, I., Rümpker, G., Bodin, T. & Haugmard, M. (2015). Crustal and uppermost mantle structure variation beneath La Réunion hotspot track. Geophysical Journal International 203, 107–126.

Fretzdorff, S. & Haase, K.M. (2002) Geochemistry and petrology of lavas from the submarine flanks of Réunion Island (western Indian Ocean): implications for magma genesis and the mantle source. Mineralogy and Petrology 75, 153-184.

Gallart, J., Driad, L., Charvis, P., Sapin, M., Hirn, A., Diaz, J., de Voogd, B. & Sachpazi, M. (1999) Perturbation to the lithosphere along the hotspot track of La Réunion from an offshore-onshore seismic transect. Journal of Geophysical research 104, 2895-2908.

Gillot, P.Y. & Nativel, P.E. (1989) Eruptive history of the Piton de la Fournaise volcano, Réunion Island, Indian Ocean. Journal of Volcanological and Geothermal Research 36, 53-65.

Gillot, P.Y., Lefèvre, J.C. & Nativel, P.E. (1994) Model for the structural evolution of the volcanoes of Réunion Island. Earth and Planetary Science Letters 122, 291-302.

Graham, D., Lupton, J., Albarède, F. & Condomines, M. (1990) Extreme temporal homogeneity of helium isotopes at Piton de la Fournaise, Réunion Island. Nature 347, 545-548.

Guettard, M. (1757) Mémoire sur plusieurs morceaux d'histoire naturelle tires du cabinet S.A.S.M le duc d'Orléans. Histoire de l'académie royale des sciences, année 1753 (Mémoires), 376-382.

Kornprobst, J., Boivin, P. & Bachèlery, P. (1979) L'alimentation des eruptions récentes du Piton de la Fournaise (Ile de la reunion, Océan Indien): degree d'évolution et niveau de segregation des laves émises. C.R. Acad. Sc. Paris, t.288, 1691-1694.

Kornprobst, J., Boivin, P., Lénat, J.F., Bachèlery, P., Bonneville, A., Dupont, P., Lecointre, J., Seidel, J.L., Thomas, P. & Vincent, P. (1984) Le Piton de la Fournaise, Ile de la Réunion. Colloque PIRPSEV 1984, Clermont-Ferrand.

Lacroix, A. (1925) Succession des éruptions et bibliographie du volcan actif de la réunion. Bulletin de volcanologie 1, 20-56.

Lacroix, A. (1936) Le volcan actif de l'île de la réunion et ses produits. Gauthier-Villars, Paris, 297pp.

Lacroix, A. (1938) Le volcan actif de l'île de la Réunion (supplément) et celui de la Grande-Comore. Gauthier-Villars, Paris, 57pp.

Lénat, J.F. (2016) A Brief History of the Observation of the Central Area of Piton de la Fournaise. In: Bachèlery, P., Lénat, J.F., Di Muro, A. & Michon, L. (eds) *Active volcanoes of the southwest Indian Ocean: Piton de la Fournaise and Karthala*. Active volcanoes of the world. Springer, Berlin.

Lénat, J.F. (2016) Construction of La Réunion. In: Bachèlery, P., Lénat, J.F., Di Muro, A. & Michon, L. (eds) *Active volcanoes of the southwest Indian Ocean: Piton de la Fournaise and Karthala*. Active volcanoes of the world. Springer, Berlin.

Lerebour, P. (1987) Etude du forage du Grand Brûlé (Piton de la Fournaise, Ile de la Réunion) : Lithostratigraphie, Pétrologie, Minéralogies primaire et secondaire. PhD Thesis, Université Paris Sud-Orsay, Paris, 198pp.

Ludden, J.N. (1978a) Magmatic evolution of the basaltic shield volcanoes of Réunion Island. Journal of Volcanology and Geothermal Research 4, 171-198.

Michon, L., Ferrazzini, V., Di Muro, A., Villeneuve, N. & Famin, V. (2015) Rift zones and magma plumbing system of Piton de la Fournaise volcano : how do they differ from Hawaii and Etna. Journal of Volcanological and Geothermal Research 303, 112-129.

Mohamed-Abchir , A., Semet, M.P., Boudon, G., Ildefonse, P., Bachèlery, P. & Clocchiatti, R. (1998) Huge Hydrothermal Explosive Activity on Piton de la Fournaise, Réunion Island : The Bellecombe Ash Member, 2700BC, The European Laboratory Volcanoes. In: Proceedings of the Second Workshop, Santorini, Greece, 2 to 4 May 1996: Volcanic Risk: Luxembourg: Office for Official publications of the European Communities, European communities, 447-455.

Morandi, A., Di Muro, A., Principe, C., Michon, L., Leroi, G., Norelli, F. & Bachèlery, P. (2016) Pre-historic explosive activity at Piton de la Fournaise volcano. In: Bachèlery, P., Lénat, J.F., Di Muro, A. & Michon, L. (eds) *Active volcanoes of the southwest Indian Ocean: Piton de la Fournaise and Karthala*. Active volcanoes of the world. Springer, Berlin.

Nativel, P. (1978) Volcans de la Réunion, pétrologie, faciès zeolites, sublimes. PhD Thesis, Université Paris Sud, Paris, 510pp.

Pichavant, M., Brugier, Y. & Di Muro, A. (2016) Petrological and experimental constraints on the evolution of Piton de la Fournaise Magmas. In: Bachèlery, P., Lénat, J.F., Di Muro, A. & Michon, L. (eds) *Active volcanoes of the southwest Indian Ocean: Piton de la Fournaise and Karthala*. Active volcanoes of the world. Springer, Berlin.

Pietruszka, A.J., Hauri, E.H. & Blichert-Toft, J. (2009) Crustal contamination of mantle-derived magmas within Piton de la Fournaise volcano, Réunion island. Journal of Petrology 50, 661-684.

Principe, C., Morandi, A., Di Muro, A. & Michon, L. (2016) Volcanological Map of the Plaine des Sables, Piton de la Fournaise. In: Bachèlery, P., Lénat, J.F., Di Muro, A. & Michon, L. (eds) *Active volcanoes of the southwest Indian Ocean: Piton de la Fournaise and Karthala*. Active volcanoes of the world. Springer, Berlin.

Salaün, A., Villemant, B., Semet, M.P. & Staudacher, T. (2010) Cannibalism of olivine-rich cumulate xenoliths during the 1998 eruption of Piton de la Fournaise (La Reunion hotspot): Implications for the generation of magma diversity. Journal of Volcanological and Geothermal Research 198, 187-204.

Staudacher, T., Peltier, A., Ferrazzini, V., Di Muro, A., Boissier, P., Catherine, P., Kowalski, P., Lauret, F. & Lebreton, J. (2016) Fifteen Years of Intense Eruptive Activity (1998-2013) at Piton de la Fournaise Volcano : A Review. In: Bachèlery, P., Lénat, J.F., Di Muro, A. & Michon, L. (eds) *Active volcanoes of the southwest Indian Ocean: Piton de la Fournaise and Karthala*. Active volcanoes of the world. Springer, Berlin.

Stieltjes, L. & Moutou, P. (1989) A statistical and probalistic study of the historic activity of Piton d ela Fournaise, Réunion Island. Journal of Volcanology and Geothermal Research 36, 67-86.

Tilley, C.E., Thompson, R.N., Wadsworth, W.J. & Upton, B.G.J. (1971) Melting relations of some lavas of Réunion Island, Indian Ocean. Mineralogical Magazine 38, 344-352.

Upton, B.G.J. & Wadsworth, W.J. (1972) Peridotitic and Gabbroic Rocks Associated with the Shield-Forming Lavas of Réunion. Contribution to Mineralogy and Petrology 35, 139-158.

Upton, B.G.J., Semet, M. & Joron, J.L. (2000) Cumulate clasts in the Bellecombe Ash Member, Piton de la Fournaise, Réunion Island, and their bearing on cumulative processes in the petrogenesis of the Réunion lavas. Journal of Volcanological and Geothermal Research 104, 297-318.

Villemant, B., Salaün, A. & Staudacher, T. (2009) Evidence for a homogeneous primary magma at Piton de la Fournaise (La Réunion) : A geochemical study of matrix glass, melt inclusions and Pelé's hairs of the 1998-2008 eruptive activity. Journal of Volcanological and Geothermal Research 184, 79-92.

Villeneuve, N. (2000) Apports multi-sources à une meilleure comprehension de la mise en place des coulées de lave et risques associés au Piton de la Fournaise: Géomorphologie quantitative en terrain volcanique. PhD Thesis, Institut de Physique du Globe de Paris, 378pp.

Vlastélic, I. & Pietruszka, A.J. (2016) A Review of the Recent Geochemical Evolution of Piton de la Fournaise Volcano (1927-2010). In: Bachèlery, P., Lénat, J.F., Di Muro, A. & Michon, L. (eds) *Active volcanoes of the southwest Indian Ocean: Piton de la Fournaise and Karthala*. Active volcanoes of the world. Springer, Berlin.

Welsch, B., Faure, F., Bachèlery, P. & Famin, V. (2009) Microcrysts Record Transient Convection at Piton de la Fournaise Volcano (La Réunion Hotspot). Journal of Petrology 50, 2287-2305.

Table des Figures (Introduction et Conclusion)

ANNEXES

1 Supplementary datas du Chapitre 1

Table S1 Whole-rock analyses.

Samples	**REU 02**	**REU 15**	**REU 45**	**REU 24B**	**REU 32B**	**REU69A**	**REU 67**	**REU 74**	**REU 56**	**REU64A**	**REU73**	**REU68**	**REU 60A**	**REU 67**	**REU57**	**REU59A**	**REU61C**	**REU66**	**REU60B**	**REU71A**	**REU71B**	**REU 62**	**REU63**	**REU 75**	**REU58**	**REU70B**	**REU72**	**REU 76**	**REU 77**
Strat. Unit	*dp1*	*dp2*	*h1*	*h2*	*h4*	*c1*	*c2*	*c2*	*c2*	*c2*	*c2*	*c2*	*c3*	*c3*	*c3*	*c3*	*c3*	*c3*	*c3*	*c3*	*c3*	*c4*	*c4*	*aub*	*aub (c5?)*	*pds*	*ol*	*pdf 2009*	*pdf 2009*
Type	*spatter*	*spatter*	*spatter*	*lapilli*	*flow*	*spatter*	*flow*	*lapilli*	*flow*	*flow*	*flow*	*spatter*	*spatter*	*flow*	*flow*	*flow*	*flow*	*flow*	*spatter*	*spatter*	*spatter*	*spatter*	*flow*	*spatter*	*flow*	*pds*	*ol*	*lapilli*	*lapilli*
Major elements (%)																													
SiO2	46,41	46,44	46,70	46,44	45,54	46,63	47,70	46,70	46,36	46,80	46,72	46,69	46,89	46,78	46,78	45,75	46,95	47,53	46,73	46,56	47,02	46,72	46,76	47,60	46,82	46,75	47,23	48,75	49,37
Al2O3	14,14	14,39	13,78	12,76	13,33	14,01	14,57	13,83	13,23	14,29	13,14	14,21	12,97	14,20	14,20	13,32	14,09	14,61	12,96	13,07	12,94	14,35	14,17	14,54	14,39	12,85	13,64	13,82	14,40
Fe2O3	12,91	13,50	13,20	13,14	12,94	13,44	13,13	13,20	13,39	13,41	13,58	13,61	13,50	13,17	13,17	13,67	13,44	12,93	13,53	13,52	13,40	13,35	13,39	13,11	12,98	13,79	13,51	11,78	11,98
MnO	0,17	0,18	0,18	0,18	0,18	0,18	0,18	0,18	0,18	0,18	0,18	0,18	0,18	0,18	0,18	0,18	0,18	0,18	0,18	0,18	0,18	0,18	0,18	0,18	0,18	0,18	0,18	0,16	0,17
MgO	8,78	6,03	9,06	10,99	10,03	9,34	8,26	9,14	10,32	8,94	10,84	9,30	11,11	8,41	8,41	11,18	9,23	8,23	11,01	10,99	10,79	9,00	8,92	8,47	8,24	10,41	10,36	7,76	6,79
CaO	9,48	11,14	9,42	9,90	9,38	9,67	9,91	9,05	9,74	9,78	9,93	9,72	9,99	9,67	9,67	9,49	9,85	9,92	9,95	9,75	10,19	9,77	9,83	9,81	9,73	9,80	9,65	11,20	11,39
Na2O	2,95	2,51	2,86	2,45	2,75	2,74	3,15	2,90	2,64	2,80	2,54	2,70	2,55	3,03	3,03	2,48	2,87	3,14	2,56	2,54	2,56	2,52	2,92	3,08	3,04	2,67	2,77	2,57	2,71
K2O	1,04	0,77	0,90	0,73	1,06	0,83	0,94	0,91	0,77	0,84	0,74	0,84	0,73	0,91	0,91	0,74	0,85	0,94	0,74	0,73	0,73	0,74	0,86	0,94	0,91	0,89	0,80	0,67	0,71
TiO2	2,86	3,08	2,76	2,50	2,70	2,91	2,91	2,68	2,74	2,94	2,73	2,95	2,67	2,91	2,91	2,73	2,92	2,85	2,69	2,69	2,66	2,93	2,94	2,88	2,86	3,18	2,72	2,48	2,64
P2O5	0,42	0,36	0,38	0,30	0,49	0,38	0,44	0,39	0,35	0,38	0,34	0,38	0,33	0,44	0,44	0,34	0,38	0,43	0,33	0,33	0,33	0,39	0,38	0,44	0,43	0,41	0,36	0,29	0,32
L.O.I.	-0,65	0,32	-0,40	-0,73	0,15	-0,24	-0,78	-0,39	-0,73	-0,55	-0,50	-0,32	-0,60	-0,72	-0,72	-0,21	-0,75	-0,89	-0,69	-0,42	-0,72	-0,03	-0,53	-0,66	-0,68	-0,43	-0,52	-0,87	-0,79
Total	98,50	98,73	98,83	98,65	98,55	99,87	100,40	98,59	99,00	99,80	100,24	100,26	100,31	98,96	98,96	99,68	100,01	99,86	99,99	99,94	100,09	99,92	99,81	100,37	98,91	100,49	100,70	98,61	99,69
CaO/Al2O3	0,67	0,77	0,68	0,78	0,70	0,69	0,68	0,65	0,74	0,68	0,76	0,68	0,77	0,68	0,68	0,71	0,70	0,68	0,77	0,75	0,79	0,68	0,69	0,67	0,68	0,76	0,71	0,81	0,79
Trace elements (ppm)																													
As	< L.D.	< L.D.	< L.D.	< L.D.	< L.D.	< L.D.	< L.D.	< L.D.	< L.D.	< L.D.	< L.D.	< L.D.	< L.D.	< L.D.	< L.D.	< L.D.	< L.D.	< L.D.	< L.D.	< L.D.	< L.D.	< L.D.	< L.D.	< L.D.	< L.D.	< L.D.	< L.D.	< L.D.	< L.D.
Ba	183	166	173	133	234	153	181	166	156	168	141	156	137	181	181	146	168	184	137	142	141	170	167	179	185	156	155	121	119
Be	1	1	1	1	1	1	1	1	1	1	1	1	1	1	1	1	1	1	1	1	1	1	1	1	1	1	1	1	1
Bi	< L.D.	< L.D.	< L.D.	< L.D.	< L.D.	< L.D.	< L.D.	< L.D.	< L.D.	< L.D.	< L.D.	< L.D.	< L.D.	< L.D.	< L.D.	< L.D.	< L.D.	< L.D.	< L.D.	< L.D.	0	< L.D.	1	< L.D.	< L.D.	< L.D.	1	< L.D.	< L.D.
Cd	0	0	0	0	0	0	0	0	0	0	0	0	0	0	0	0	0	0	0	0	0	0	0	0	0	0	0	0	0
Ce	56	50	51	42	64	48	58	50	49	52	46	50	44	59	59	45	50	59	44	46	45	51	53	57	59	57	48	40	40
Co	52	47	55	58	56	54	49	51	62	55	60	55	60	51	51	65	54	51	59	61	60	56	56	51	51	59	58	46	40
Cr	395	34	453	664	493	413	337	411	563	370	579	410	591	384	384	579	409	344	575	621	623	410	406	364	367	537	515	466	231
Cs	0	0	0	0	0	0	0	0	0	0	0	0	0	0	0	0	0	0	0	0	0	0	0	0	0	0	0	0	0
Cu	71	98	76	94	77	70	72	73	85	113	87	78	87	75	75	106	43	73	89	159	159	22	89	78	73	99	116	118	125
Dy	6	6	6	5	5	5	6	5	5	6	5	5	5	6	6	5	5	6	5	5	5	6	6	6	6	6	5	5	5
Er	3	3	3	2	2	2	3	2	3	3	2	3	2	3	3	2	3	3	2	2	2	3	3	3	3	3	2	2	2
Eu	2	2	2	2	2	2	2	2	2	2	2	2	2	2	2	2	2	2	2	2	2	2	2	2	2	2	2	2	2
Ga	22	23	22	20	22	21	23	21	22	23	21	22	21	23	23	22	22	23	20	21	21	22	23	23	23	22	21	22	21
Gd	7	7	7	6	7	6	6	7	6	6	6	6	6	7	7	6	6	7	6	6	6	6	7	6	7	7	6	6	6
Ge	2	2	2	1	2	1	1	1	2	1	1	1	1	2	2	2	2	2	1	1	2	1	2	1	1	1	1	1	1
Hf	6	5	5	4	6	5	5	5	5	5	5	5	4	6	6	5	5	6	4	4	4	5	5	5	6	6	5	4	4
Ho	1	1	1	1	1	1	1	1	1	1	1	1	1	1	1	1	1	1	1	1	1	1	1	1	1	1	1	1	1
In	0	0	0	0	0	< L.D.	0	0	0	0	0	< L.D.	0	0	0	0	0	0	0	< L.D.	0	0	0	0	0	0	0	0	0
La	26	23	23	18	29	21	25	22	22	23	20	22	19	26	26	19	22	26	19	20	19	22	23	25	26	24	21	17	17
Lu	0	0	0	0	0	0	0	0	0	0	0	0	0	0	0	0	0	0	0	0	0	0	0	0	0	0	0	0	0
Mo	1	1	1	1	1	1	1	1	1	1	1	1	1	1	1	1	1	1	1	1	1	1	1	1	1	1	1	1	1
Nb	27	25	25	18	32	21	24	21	21	22	19	22	19	25	25	21	22	25	19	19	19	22	23	24	25	23	20	16	16
Nd	31	29	29	25	35	27	32	29	27	29	26	28	25	32	32	26	28	32	25	26	26	29	30	31	31	32	27	24	24
Ni	204	63	222	295	266	216	172	213	284	205	293	219	302	183	183	335	212	170	296	309	281	217	206	183	173	282	268	142	92
Pb	3	2	2	2	3	2	3	3	3	2	2	3	2	2	2	2	2	3	2	3	3	4	3	2	3	3	4	2	2
Pr	7	7	7	5	8	6	7	6	6	7	6	6	6	8	8	6	7	8	6	6	6	7	7	7	8	7	6	5	5
Rb	27	18	23	18	30	21	25	22	21	22	19	22	18	25	25	20	21	25	19	20	19	17	23	26	25	23	21	16	16
Sc	26	32	26	30	26	29	28	26	29	29	31	29	31	28	28	30	29	28	31	30	32	29	29	28	28	30	29	34	33
Sb	< L.D.	< L.D.	< L.D.	< L.D.	< L.D.	< L.D.	< L.D.	< L.D.	< L.D.	< L.D.	< L.D.	< L.D.	< L.D.	< L.D.	< L.D.	< L.D.	< L.D.	< L.D.	< L.D.	< L.D.	0	< L.D.	< L.D.	< L.D.	< L.D.	< L.D.	< L.D.	< L.D.	< L.D.
Sm	7	7	7	6	8	6	7	7	7	7	6	7	6	7	7	6	7	7	6	6	6	7	7	7	7	7	6	6	6
Sn	6	4	4	2	6	2	2	2	2	9	2	4	2	2	2	6	2	2	2	6	2	1	2	3	2	2	2	2	4
Sr	456	417	417	322	512	381	438	368	385	400	355	381	349	433	433	364	396	454	346	344	352	400	415	440	443	394	369	329	321
Ta	2	2	2	2	3	2	2	2	2	2	2	2	2	2	2	2	2	2	2	2	2	2	2	2	2	2	2	1	1
Tb	1	1	1	1	1	1	1	1	1	1	1	1	1	1	1	1	1	1	1	1	1	1	1	1	1	1	1	1	1
Th	3	3	3	2	4	2	3	2	2	3	2	2	2	3	3	2	3	3	2	2	2	3	3	3	3	3	2	2	2
Tm	0	0	0	0	0	0	0	0	0	0	0	0	0	0	0	0	0	0	0	0	0	0	0	0	0	0	0	0	0
U	1	1	1	1	1	1	1	1	1	1	1	1	1	1	1	1	1	1	1	1	1	1	1	1	1	1	1	0	0
V	275	335	271	279	257	287	282	219	307	306	293	296	282	287	287	306	293	289	287	294	298	298	307	284	287	287	280	296	281
W	1	0	1	0	1	0	0	0	0	0	0	0	0	0	0	0	0	0	0	0	0	0	0	0	0	0	0	0	0
Y	27	28	28	23	26	25	28	27	26	27	25	26	24	28	28	25	26	28	24	25	25	28	28	28	28	27	26	26	26
Yb	2	2	2	2	2	2	2	2	2	2	2	2	2	2	2	2	2	2	2	2	2	2	2	2	2	2	2	2	2
Zn	122	128	125	119	121	120	123	120	128	126	121	123	118	126	126	132	125	125	117	123	123	149	128	124	127	129	126	111	106
Zr	225	202	204	153	262	196	228	183	194	203	166	198	161	230	230	194	198	232	160	166	163	183	208	227	232	229	190	157	155
Sc/Yb	12,3	14,2	11,5	15,8	13,0	14,4	12,9	12,2	14,0	13,4	15,6	14,2	16,3	12,7	12,7	14,8	14,0	12,8	16,2	15,0	15,9	13,8	13,1	12,9	12,6	14,4	14,0	15,8	15,9
Ce/Yb	26,4	22,5	22,3	22,4	32,2	24,2	26,3	23,7	23,5	24,3	23,2	24,0	23,2	26,6	26,6	22,6	24,2	26,5	23,2	22,8	22,8	23,8	23,9	26,2	26,3	27,2	23,1	18,8	19,0

2 Annexe n°2 : Pichavant et al. (2016) « Petrological and Experimental Constraints on the Evolution of Piton de la Fournaise Magmas »

Chapitre n°10 de l'ouvrage Springer «Active Volcanoes of the Southwest Indian Ocean », Bachèlery, P., Lénat, J.-F., Di Muro, A. & Michon, L. (Eds.).

3 Annexe n°3 : Brugier et al. (2015) « Fe pre-enrichment : A new method to counteract iron loss in experiments on basaltic melts »

Petrological and Experimental Constraints on the Evolution of Piton de la Fournaise Magmas

10

Michel Pichavant, Yann Brugier and Andrea Di Muro

Abstract

This chapter outlines essential petrological features of Piton de la Fournaise magmas. The main characteristics of the different magma types, and of their components (mineral and glass phases) are detailed. The available geophysical and petrological informations on the structure of the feeding system are combined and the magmatic conditions (temperature, volatile concentrations, redox state) summarized. Experimental modelling of the magmatic evolution is limited by the presently available database which concerns volatile-free compositions mostly from Piton des Neiges.

10.1 Piton de la Fournaise Magmas

10.1.1 Magma Types

Lavas and volcanic deposits of Piton de la Fournaise are distributed in 4 different compositional groups (Fig. 10.1; Table 10.1), which correspond to the activity inside, but also outside, the present-day Enclos Fouqué collapse caldera.

The Steady State Basalt (SSB) group is the most abundant in the recent activity of the volcano. SSB lavas are transitional basalts with a narrow range of compositions, from MgO = 5–8 wt% and CaO/Al_2O_3 = 0.75–0.85 (e.g., Albarède et al. 1997; Famin et al. 2009; Villemant et al. 2009; Salaün et al. 2010; Fig. 10.1). The SSB group is the point of convergence of 2 evolutive trends, one involving the Picrite group (MgO = 8–28 wt%, CaO/Al_2O_3 = 0.75–0.85) and the other the Differentiated Lavas group (MgO = 2–6 wt%, CaO/Al_2O_3 = 0.2–0.8, Fig. 10.1).

Picritic lavas, locally designated as oceanites (Lacroix 1936), are characteristic of the volcanic activity of La Réunion Island, being found at Piton de la Fournaise but also at Piton des Neiges. They contain millimetric to centimetric crystals of olivine embedded in a microcrystalline dark matrix. Much has been written on the petrology of La Réunion oceanites and their significance is still not completely clear. However, oceanite whole-rock compositions clearly plot on olivine control lines (e.g., Salaün et al.

M. Pichavant (✉) · Y. Brugier
ISTO, Orléans, France
e-mail: pichavan@cnrs-orleans.fr

A. Di Muro
IPGP-OVPF, La Réunion, France

P. Bachèlery et al. (eds.), *Active Volcanoes of the Southwest Indian Ocean*,
Active Volcanoes of the World, DOI 10.1007/978-3-642-31395-0_10

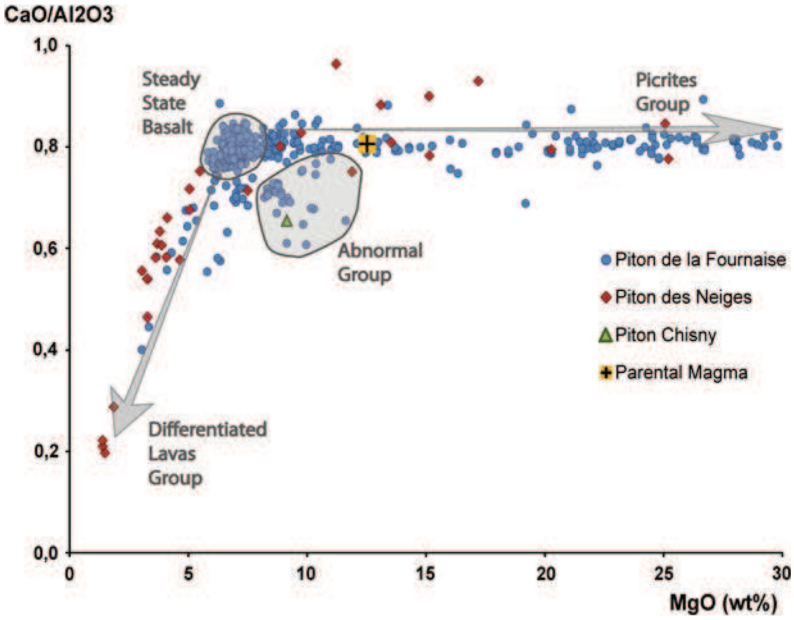

Fig. 10.1 CaO/Al_2O_3 versus MgO plot for Piton de la Fournaise and Piton des Neiges magmas. Data from Albarède et al. (1997), Boivin and Bachèlery (2009), Brugier et al. (2015), Bureau et al. (1999), Fisk et al. (1988), Peltier (2007), Salaün et al. (2010), Sobolev and Nikogosian (1994), Upton and Wadsworth (1972), Vigouroux et al. (2009), Villemant et al. (2009), Vlastélic et al. (2005, 2007), Welsch et al. (2013). The 4 different magma groups and one representative composition of parental magma (Villemant et al. 2009) are shown

2010; Fig. 9.1) suggesting that their chemistry reflects the proportion of olivine crystals present in the rock. In this context, an important observation is that the composition of matrix glasses in oceanites is nearly constant and similar to SSB bulk rocks (e.g., Welsch et al. 2009, see below). Most workers now consider that oceanites, instead of representing the product of crystallization of a picritic magmatic liquid at depth, result from a general mechanism of shallow incorporation of olivine crystals into a basaltic parental magma.

The Differentiated Lavas group, with a compositional evolution marked by strongly decreasing CaO and increasing Al_2O_3 at decreasing MgO, has been defined mainly from differentiated lavas erupted near the end of activity of Piton des Neiges (Upton and Wadsworth 1966). Differentiated alkaline lavas are found during the early stages of activity of the Piton de la Fournaise (Albarède et al. 1997) but are uncommon among recent products. This group includes chemically evolved terms such as hawaiites, mugearites and benmoreites and, in the recent activity, rare trachytic pumices (Vlastélic et al. 2011). Recent work (Smietana 2011) has suggested that these early differentiated alkaline lavas (the Pintades unit) in fact do not belong to the Piton de la Fournaise series but rather should be associated with the activity of the older Les Alizés volcano which forms the basement of the Piton de la Fournaise (Lénat et al. 2012).

The 4th lava group, the Abnormal Group (AbG) is compositionally different from the 3 others. It comprises lavas with MgO = 8–11 wt% and CaO/Al_2O_3 = 0.60–0.80, and shows enrichments in Fe, Mg, Ti, Na, K and a depletion in Ca relative to SSB basalts. AbG-type compositions are rarely observed inside the Enclos Fouqué caldera (e.g., Hudson eruption, early 1998 activity) being mostly found at eccentric vents or at recent vents west of the central cone (Lénat et al. 2012).

For example, the basaltic cones outside the Enclos Fouqué (Piton Chisny, Piton Haüy) have

Table 10.1 Representative major and trace element compositions of Piton de la Fournaise and Piton des Neiges magmas

	Piton de la Fournaise				Piton des Neiges				Parental magma
	SSB	Picrite	AbG	Diff.	SSB	Picrite	AbG	Diff.	
SiO_2 (wt %)	49.37	44.13	46.70	52.91	48.55	45.03	44.97	58.74	48.39
Al_2O_3	14.40	7.47	13.83	15.99	13.18	9.35	12.57	18.62	12.06
FeO	–	13.36	–	10.10	–	12.13	–	–	1.83
Fe_2O_3	11.98	–	13.20	–	12.72	–	12.84	6.71	10.09
MnO	0.17	0.19	0.18	0.19	0.18	0.17	0.17	0.17	0.19
MgO	6.79	25.30	9.14	3.04	9.74	20.28	11.89	1.40	12.52
CaO	11.39	6.10	9.05	6.41	10.91	7.43	9.44	3.90	9.72
Na_2O	2.71	1.35	2.90	5.04	2.44	1.62	2.61	5.97	2.26
K_2O	0.71	0.38	0.91	2.36	0.62	0.48	0.68	3.14	0.55
TiO_2	2.64	1.36	2.68	2.50	2.35	1.77	2.32	1.02	2.33
P_2O_5	0.32	0.15	0.39	0.92	0.28	0.29	0.25	0.39	0.06
L.O.I.	*−0.79*	–	*−0.39*	–	–	*−0.37*	–	*−0.44*	–
Sum	99.69	99.79	98.59	99.46	100.97	98.92	97.74	99.62	100.00
Ba (ppm)	119.10	69.50	166.10	430.20	144.00	74.00	170.00	648.00	102.00
Be	1.07		1.29						
Cd	0.16		0.14						
Ce	39.78	23.10	50.41	125.90	36.00	20.30	27.00	125.00	31.70
Co	39.68		50.93			76.00			59.00
Cr	230.60	1712.00	411.00	0.00	472.00		721.00	7.00	691.00
Cs	0.24	0.13	0.33	0.36		0.19			
Cu	125.40	66.30	73.38	11.40	98.00		75.00	8.00	
Dy	5.16	2.96	5.38	10.88	5.20	1.50			5.23
Er	2.47	1.36	2.50	5.48	2.60				2.66
Eu	2.08	1.05	2.27	4.15	1.90	1.63			1.64
Ga	21.41		20.71						
Gd	6.14	3.36	6.53	12.67	5.80				5.96
Ge	1.25		1.16						
Hf	4.40	2.55	5.10	11.72		3.00			4.24
Ho	0.94	0.54	0.96	2.03					0.93
La	17.17	9.90	22.19	56.30	18.00	12.99	14.00	50.00	14.20
Lu	0.31	0.17	0.31	0.63	0.31	0.18			0.29
Mo	1.13		1.38						
Nb	15.81	13.20	21.01	72.70	20.00	18.00	19.00	68.00	
Nd	23.99	13.50	28.76	65.10	20.00		17.00	45.00	18.80
Ni	91.93	1012.80	213.20	2.10	244.00	900.00	376.00	5.00	404.00
Pb	1.56	1.15	2.71	4.85					
Pr	5.22	2.96	6.40	15.71					4.64

(continued)

Table 10.1 (continued)

	Piton de la Fournaise				Piton des Neiges				Parental magma
	SSB	Picrite	AbG	Diff.	SSB	Picrite	AbG	Diff.	
Rb	16.00	9.50	22.08	59.70	14.00	13.00	19.00	100.00	12.80
Sc	33.42	19.60	26.05	13.20	35.00	21.00	29.00	3.00	27.00
Sm	5.96	3.07	6.62	13.29	5.60	1.10			5.38
Sn	3.84		1.81						
Sr	320.50	185.00	367.50	448.00	324.00	247.00	309.00	531.00	324.00
Ta	1.44		1.94			1.13			1.90
Tb	0.93	0.51	0.97	1.92		0.61			0.92
Th	1.82	0.96	2.40	7.50	3.00	1.44	3.00	10.00	1.62
Tm	0.33		0.34						
U	0.47	0.32	0.60	1.53		0.32			0.44
V	280.60	180.90	218.70	95.30	321.00		272.00	0.00	
W	0.32		0.40						
Y	25.80	14.60	26.52	57.80	26.00	20.00	25.00	28.00	
Yb	2.10	1.10	2.13	4.36	2.10	1.47			2.24
Zn	105.90	107.10	119.50	128.30	100.00		100.00	89.00	
Zr	154.60	99.50	183.10	493.10	168.00	129.00	145.00	543.00	
References	Brugier (2012)	Albarède et al. (1997)	Brugier (2012)	Albarède et al. (1997)	Fisk et al. (1988)	Sobolev and Nikogosian (1994)	Fisk et al. (1988)	Fisk et al. (1988)	Villemant et al. 2009

Data from Albarède et al. (1997), Brugier (2012), Fisk et al. (1988), Sobolev and Nikogosian (1994), Villemant et al. (2009)

whole-rock compositions typical of the AbG group, with relatively low CaO/Al_2O_3 at high MgO (Fig. 10.1). The AbG group has mixed geochemical features, some (e.g., high MgO) suggesting a primitive character and others (e.g., low CaO/Al_2O_3, high K_2O) indicating a differentiated evolution similar to that shown by the Differentiated Lavas group (Fig. 10.1). Nevertheless, it seems clear from Fig. 10.1 that the AbG group of lavas does not evolve directly from SSB-like parental liquids.

Piton de la Fournaise basalts range from tholeiitic to alkaline. The He, Nd and Sr isotopic homogeneity of La Réunion lavas has been emphasized (e.g., Fisk et al. 1988; Graham et al. 1990). More recent studies have deciphered small, but systematic, changes in trace element abundances and Pb, Sr, Nd, Hf isotope ratios (Albarède et al. 1997; Vlastélic et al. 2005, 2007, 2009; Bosch et al. 2008; Pietruszka et al. 2009). This geochemical variability has been interpreted to reflect melting of different source components intrinsic to La Réunion mantle plume, and superimposed crustal processes including magma contamination and fractionation. Clinopyroxene (+olivine) fractionation (“wehrlitic trend”) has been proposed to generate AbG compositions (Kornprobst et al. 1979, 1984) and to drive tholeiitic basalts in the field of alkaline basalts (Albarède et al. 1997). Evidence for an important petrogenetic role of clinopyroxene is globally clear from both major and trace elements variations (Figs. 10.1 and 10.2). However, clinopyroxene fractionation is commonly cryptic. For example, the early lavas from Piton Chisny bear a strong geochemical imprint of clinopyroxene

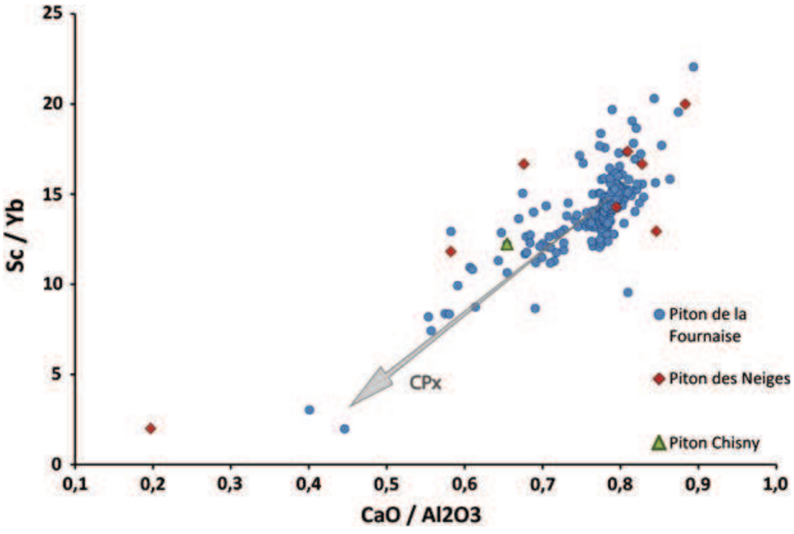

Fig. 10.2 Sc/Yb versus CaO/Al_2O_3 plot emphasizing the importance of clinopyroxene fractionation. Data from Albarède et al. (1997), Brugier et al. (2015), Fisk et al. (1988), Peltier (2007), Salaün et al. (2010), Sobolev and Nikogosian (1994)

fractionation (low Ca and Sc/Yb, Figs. 10.1 and 10.2), yet they contain olivine as the sole silicate phenocryst phase, clinopyroxene being found only in the ultramafic cumulate nodules (Upton and Wadsworth 1972). The genesis of more differentiated lavas such as those belonging to the prehistoric activity (Rempart series) has been modeled by crystal fractionation of a gabbroic assemblage ("gabbroic trend") dominated by clinopyroxene (30–70 %), plagioclase (20–40 %) and minor olivine (10 %, Albarède et al. 1997).

10.1.2 Magma Components

Olivine, clinopyroxene, plagioclase and Cr-spinel are found systematically in Piton de la Fournaise products. Ti-rich magnetite is also present, together with sulfides. Ilmenite and amphibole are rare (Albarède et al. 1997). In general, the four main crystalline phases are found in a variety of textural types, occurring as phenocrysts, microphenocrysts and microlites (Salaün et al. 2010; Welsch et al. 2009, 2013). However, the characteristics of the mineral phase assemblage are specific of the lava group.

SSB lavas host olivine, clinopyroxene, plagioclase and spinel (the latter mainly as inclusions in olivine) in variable but generally low proportions. For example, phenocryst contents range from 0 to 10 vol.% in 1985 lavas (Boivin and Bachèlery 2009, see also Salaün et al. 2010 for 1998 products). Textural evidence suggests that, in SSB, clinopyroxene and plagioclase crystallize together with olivine, this lava group being often designated as "cotectic". The olivine + clinopyroxene + plagioclase + spinel four phase assemblage is also typical of the AbG Group. Compared to SSB lavas erupted contemporaneously with AbG lavas during 1998, the latter (Hudson vent) are richer in olivine and poorer in clinopyroxene and plagioclase than the former (Kapor vent, see Salaün et al. 2010). Early AbG lavas from Piton Chisny are crystal-poor (<2 vol.%) and have only phenocrysts of olivine and Cr-spinel. Oceanite lavas from the Picrite group contain macrocrysts of olivine, mesocrysts of either olivine or an assemblage of clinopyroxene and plagioclase, and microcrysts of olivine + clinopyroxene + plagioclase + spinel ± Ti-magnetite (Welsch et al. 2009). The proportion of olivine macrocrysts in oceanite can reach ~50 vol.% (e.g., Salaün et al. 2010). Piton de la Fournaise basalts generally contain small amounts of plagioclase (but see Boivin and Bachèlery 2009 and Salaün et al. 2010 for exceptions). However, plagioclase is the dominant phase in the Differentiated Lava group from Piton des Neiges and early Piton de la

Fournaise (feldspar phyric hawaiites, mugearites and benmoreites, Upton and Wadsworth 1966; Albarède et al. 1997).

Olivine compositions at Piton de la Fournaise are rarely highly forsteritic. Histograms of Fo contents yield frequency maxima at 86 (early activity, Albarède et al. 1997), 81 and 84 (1977–1998 activity, Boivin and Bachèlery 2009), 81 and 84 (1998 activity, Villemant et al. 2009), 84 (2005 oceanite, Welsch et al. 2009), 85–86 (Chisny lavas, Brugier 2012) and 83 and 88 for both the Chisny ultramafic cumulate nodules (Brugier et al. 2015) and the dunite nodules analyzed by Sobolev and Nikogosian (1994). Bureau et al. (1999) found Fo contents as high as 89 in AbG lavas erupted from the Hudson vent, in agreement with the Fo88 compositions found by Salaün et al. (2010). This supports 89 as the maximum Fo content for Piton de la Fournaise olivines (Fisk et al. 1988; Albarède et al. 1997). However, the dataset of Sobolev and Nikogosian (1994) contains more forsteritic olivine compositions, up to Fo90.6 in an oceanite. Fretzdorff and Haase (2002) found olivines with Fo contents up to 90.6 in a suite of picritic submarine lavas dredged in the northeastern flank of the Réunion island. Normal core-rim zonation is commonly observed in olivine crystals, for example from Fo84 cores to Fo80 rims in oceanite (Welsch et al. 2009, see also Salaün et al. 2010). Olivine microphenocrysts and microlites have Fo contents lower than phenocrysts (or macrocrysts, Welsch et al. 2009). Texturally, the occurrence of deformed olivines has led to the proposition that many crystals at Piton de la Fournaise are xenocrysts derived from the mechanical disaggregation of earlier cumulates (e.g., Albarède et al. 1997). However, Welsch et al. (2013) have recently shown that the olivine macrocrysts from oceanite mostly originate from dendritic growth and ripening in suspension within the melt; since very few olivine macrocrysts have experienced intracrystalline deformation, they cannot be considered as xenocrysts.

Clinopyroxenecompositions are mostly augite, some extending into the fields of diopside and salite in the En-Fs-Wo diagram (Boivin and Bachèlery 2009; Welsch et al. 2009). Boivin and Bachèlery (2009) distinguished two pyroxene compositional groups, one with an average composition En49Fs9Wo42 (Mg-augitic) and the other En48Fs12Wo40 (augitic). They suggested that the former group, with higher Al/Ti ratios, crystallized at higher pressures than the latter. Fisk et al. (1988) mentioned the occurrence of aluminous augite crystals in lavas carrying Fo89 olivine. In the same way, Fretzdorff and Haase (2002) described Al-rich augites coexisting with Fo-rich olivines in the picritic submarine lavas. Clinopyroxene Mg/(Mg + Fe_t) is rather homogeneous, either for a given period of activity, within a single eruption, or between magma groups; core to rim variations are generally not very strong. However, clinopyroxene microlites may show more evolved (i.e., less calcic) compositions than phenocrysts (Boivin and Bachèlery 2009; Salaün et al. 2010).

Plagioclase in recent (1977–1998) Piton de la Fournaise products ranges from An45 to An80 (Boivin and Bachèlery 2009). Phenocrysts and microlites are only slightly compositionally different: the former have a frequency maximum at An70 (total range: An58–80) and the latter at An65 (total range: An45–76). The 1998 products have similar characteristics (Salaün et al. 2010). In contrast, plagioclase compositions were more calcic during the early activity of the volcano (frequency maximum at An84 in the Rempart series, Albarède et al. 1997).

Spinels (both inclusions in olivine and isolated crystals dispersed in the matrix) are mostly chromites with Cr/(Cr + Al) around 70 and Mg/(Mg + Fe_t) between 50 and 65. They have TiO_2 contents between 2 and 3 wt%, increasing with decreasing Mg/(Mg + Fe_t), and $Fe^{3+}/(Fe^{3+} + Al + Cr)$ of 10–15 % (Brugier 2012). Spinel compositions at Piton de la Fournaise do not show systematic variations with magma types (Sobolev and Nikogosian 1994; Albarède et al. 1997; Welsch et al. 2009; Brugier 2012). However, lavas from Piton Chisny contain unusual Mg-rich (Mg/(Mg + Fe_t) = 60–70) and Cr-poor (Cr/(Cr + Al) = 30) crystals, besides the normal compositions (Brugier 2012).

Data on matrix glasses concern the SSB and Picrite groups and, to a lesser extent, the AbG group. One difficulty resides in the microcrystallinity of the samples, especially those having cooled in air, because groundmass crystallization limits the size of the glass pools amenable to electron microprobe analysis. This has motivated the use of unconventional rapidly quenched glassy materials such as Pélé's hairs and tears to document changes in matrix glass compositions (Villemant et al. 2009). In first approximation, the composition of the matrix glass in most Piton de la Fournaise products is similar to SSB bulk rocks (MgO = 5.5–6 wt%, CaO/Al_2O_3 = 0.79–0.82), i.e., it is in equilibrium with olivines in the range Fo75–80 (Welsch et al. 2009). However, systematic compositional variations have been recently discovered. Matrix glasses with MgO contents as high as 8–9 wt% have been analyzed in 2007 products (Villemant et al. 2009). The 1998–2007 matrix glasses define a unique evolution trend starting from these high-MgO glasses and ending at ~5.5 wt% MgO, which corresponds to the evolved Hudson and Kapor matrix glasses (Villemant et al. 2009; Salaün et al. 2010). This evolution mimics that shown by whole rocks during the same period, if olivine-rich oceanites and AbG lavas are excepted. For more differentiated rocks, interstitial glasses from the Bellecombe cumulate xenoliths (Upton et al. 2000) and aphyric magmas from the early Piton de la Fournaise (Albarède et al. 1997) pursue the 1998–2007 evolution trend toward lower MgO (Salaün et al. 2010).

Melt inclusions are common in olivine crystals from Piton de la Fournaise. Primary inclusions are either glassy (ejected lapilli) or recrystallized (lava samples). Secondary inclusions are mainly fluid inclusions. These occur along healed fractures in olivine and are associated with glass and crystals in variable proportions (Sobolev and Nikogosian 1994; Bureau et al. 1998a; Famin et al. 2009). Compositions of primary glassy inclusions (recalculated for post-entrapment crystallization of olivine) range from 8 to 10 wt% MgO (Bureau et al. 1998a), 8–11.5 wt% MgO (Famin et al. 2009) to up to ~14 wt% MgO (Sobolev and Nikogosian 1994). Less magnesian compositions (5.5–7 wt% MgO) are reported by Villemant et al. (2009) for inclusions in 1998 and 2007 products. In 2005 oceanite, Welsch et al. (2009) emphasized the large variability of glass inclusion compositions in terms of K_2O, P_2O_5, K_2O/TiO_2 and CaO/Al_2O_3, especially when compared to the tightly grouped matrix glass compositions.

H_2O and CO_2 concentrations in glass inclusions are generally <1 wt% and <500 ppm (Bureau et al. 1998b; Famin et al. 2009). However, certain samples (Piton de Caille, Hudson) have H_2O and CO_2 concentrations largely exceeding these values, with H_2O up to ~1.6 wt% and CO_2 up to ~2800 ppm (Bureau et al. 1998b; 1999). The secondary fluid inclusions contain essentially pure CO_2 with a large range of densities, from 0 to 0.8 g/cm^3 (Bureau et al. 1998a; Famin et al. 2009).

There seems to exist overall agreement on the order of crystallization of silicate phases in Piton de la Fournaise magmas, excluding rocks from the Differentiated series. Albarède et al. (1997) suggested progressive crystallization in the order olivine-clinopyroxene-plagioclase. This sequence is consistent with data on the Chisny ultramafic cumulate nodules (Upton and Wadsworth 1972). These are dominated by dunites made of olivine and Cr-spinels; wehrlitic nodules are less abundant. In these, clinopyroxene is present in low amounts and the Fo content of olivine is lower than in dunitic nodules (83 vs. 87, Brugier et al. 2015). A minor proportion of gabbroic nodules also exists (Bachèlery, personal communication, 2013). Overall, these observations leave little doubt on the order of crystallization of the Chisny magmas. The fact that clinopyroxene precedes plagioclase in the crystallization sequence of Piton de la Fournaise basalts is also supported by recent textural studies and numerical runs using the MELTS software (Famin et al. 2009; Welsch et al. 2009, 2013).

10.2 Structure of the Magma Feeding System and Magmatic Conditions

10.2.1 Combined Geophysical and Petrological Constraints on the Structure of the Feeding System

The dense monitoring network on La Réunion island (OVPF/IPGP), coupled with the high eruption frequency, allows magma ascent at Piton de la Fournaise to be followed in real time. This provides constraints on the overall structure of the feeding system and three zones of magma storage are presently defined (see also the description in Michon et al. 2016, Chap. 7). For the *shallow* magma storage zone, models essentially divide into two groups. Lénat and Bachèlery (1990) suggested the presence of an array of sills and dykes between 0.5 and 1.5 km beneath the Dolomieu crater whereas Nercessian et al. (1996) and Peltier et al. (2007) favoured the existence of a single reservoir of about 0.3 km^3 at about 2.5 km depth. Whereas the structure of the magma chamber is still debated, it is worth stressing that seismic and deformation constraints essentially agree with petrological data on the depth of shallow magma storage. Most melt-fluid saturation pressures (calculated from H_2O and CO_2 concentrations in glass inclusions) are <50 MPa (<~1.9 km for a crustal density of 2.7 g/cm^3, Bureau et al. 1998b; Famin et al. 2009). For the fluid inclusions, entrapment pressures are either of a maximum of ~70 MPa (2.6 km, Famin et al. 2009) or <95 MPa (~3.6 km, Bureau et al. 1998b). The seismicity that preceeded the 1998 eruption, and also during 2005 and 2007, provide evidence that the magmas stored near the surface have ascended from a second reservoir located at *intermediate* crustal depths (Battaglia et al. 2005; Peltier et al. 2009). The root of the 1998 seismic swarms is located at about 200 MPa (7.6 km depth), which corresponds to the top of the oceanic crust beneath La Réunion island (Gallard et al. 1999). At greater depths, the intermediate velocity layer described in the southwestern part of La Réunion has been interpreted as underplating of the base of the crust by mantle magmas, followed by their crystallization and differentiation (Gallard et al. 1999). This layer has thus all attributes of a *deep* magma storage zone. It is located at 320–400 MPa (12–15 km depth), a pressure range consistent with melt-fluid saturation pressures computed for the Piton de Caille (190–420 MPa, Bureau et al. 1998b) and Hudson (<420 MPa, Bureau et al. 1999) glass inclusions. The CO_2-rich inclusions from the Piton de Caille and Chisny ultramafic nodules also yield high pressures, up to 500 and 350 MPa respectively (Bureau et al. 1998a).

10.2.2 Magma Temperature

Information on temperatures of Piton de la Fournaise magmas comes from different methods. First, optical pyrometry and thermocouple measurements in the field provide direct data on lava temperatures, from 872 °C and up to 1170 °C with a frequency maximum between 1100 and 1150 °C. The pyrometry is systematically higher than the thermocouple data because active parts of lava flows can be measured with that method (Boivin and Bachèlery 2009). Second, magma temperatures have been computed from olivine-liquid equilibrium. When applied to olivine phenocryst cores and their host bulk lava, grouped values are obtained, close to 1200 °C for the 1977–1998 products (Boivin and Bachèlery 2009). As a variant of this method, the MgO content of the melt (from the analysis of glass inclusions) at equilibrium with olivine yields temperatures (e.g., Helz and Thornber 1987) between 1170 and 1215 °C (Bureau et al. 1998a, b) and between 1192 and 1236 °C (Famin et al. 2009). It should be noted however that results with methods based on glass inclusion compositions depend on procedures adopted to correct for post-entrapment olivine crystallization. Third, thermometric measurements on melt inclusions have yielded homogeneization temperatures from

1170 to about 1215 °C (Bureau et al. 1998a, b). A markedly higher temperature range (1235–1345 °C) has been reported by Sobolev and Nikogosian (1994).

Except the field measurements which apparently give minimum values, the other methods define a consistent temperature range for the Piton de la Fournaise magmas, broadly centred on 1200 °C. The data of Sobolev and Nikogosian (1994) reach very high temperatures, but are consistent with their proposal of the existence of picritic (up to ~ 14 wt% MgO) melt inclusions in Piton de la Fournaise olivines. It is emphasized that the available temperature estimates concern mainly the SSB and Picrite lava groups. This 1200 °C value should best be viewed as an "average" or "steady-state" temperature for PTF lavas since magma temperatures would be expected to vary along with differentiation and depth of the tapped magma storage zone.

10.2.3 Oxygen Fugacity

Oxygen fugacities between NNO+0.7 to NNO-1.8 have been computed from the olivine-liquid equilibrium (Boivin and Bachèlery 2009). Most values are however <NNO, and so Piton de la Fournaise magmas evolve under moderately reducing conditions (Fig. 10.3). Similar results (from NNO+0.3 to NNO-1.8) were obtained (Brugier et al. 2015) from the analysis of FeO and Fe_2O_3 in 5 bulk rocks (2 SSB and 3 AbG), using the calibration of Kress and Carmichael (1991). Slightly more oxidizing log fO_2 values (from NNO+1 to NNO-0.5) have been obtained (Brugier et al. 2015) by taking the Fe_2+/Fe_3+ of spinels to calculate the FeO/Fe_2O_3 of magmatic liquids (Maurel and Maurel 1982; Danyuschevsky and Sobolev 1994; Kress and Carmichael 1991). In the same way, log fO_2 between NNO-0.3 and NNO-0.9 are reported by Bureau et al. (1998b) from spinel-melt equilibria calculated with the expression of Maurel and Maurel (1984). Finally, oxygen fugacities from NNO-0.4 to NNO-0.8 (Brugier et al. 2015) were calculated from the olivine-spinel oxybarometric expression of Ballhaus et al. (1991).

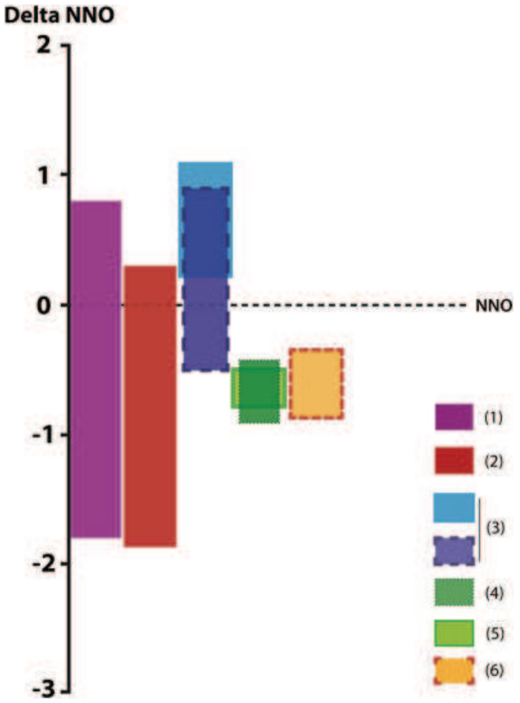

Fig. 10.3 Compilation of log fO_2 data (shown as deviations from the NNO buffer) obtained with different methods emphasizing the moderately reducing redox state of Piton de la Fournaise magmas. (1) olivine-liquid equilibrium (Boivin and Bachèlery 2009); (2) bulk rock analyses of FeO and Fe_2O_3 (Brugier et al. 2015); (3) calculated FeO and Fe_2O_3 of magmatic liquids based on Kress and Carmichael (1991) for two compositional groups of spinels (Brugier et al. 2015); (4) spinel-melt equilibria (Bureau et al. 1998b); (5) olivine-spinel oxybarometry (Brugier et al. 2015); (6) log fO_2 results for mantle source region obtained with V/Sc ratios in Piton de la Fournaise magmas, based on Lee et al. (2005) (Brugier et al. 2015). See also text

We conclude from these data that the fO_2 range of the Piton de la Fournaise magmas is reasonably well defined, around NNO-0.5. This makes the average Fe_2O_3/FeO of basaltic liquids at Piton de la Fournaise slightly higher than commonly assumed (the proportion of Fe_2O_3 is 18 % and not 15 %, e.g., Fisk et al. 1988).

10.3 Experimental Constraints

10.3.1 General

There are only a few experimental studies on magmatic products from La Réunion island. This includes the work of Tilley et al. (1971) and Fisk et al. (1988). In addition, Albarède et al. (1997) mentioned unpublished experimental results by Mesnil and Baker. First, it is important to stress that most of the samples investigated experimentally to date come from Piton des Neiges. There are in fact relatively few experimental data available on Piton de la Fournaise rocks. For example, on the total of 13 Réunion lavas worked experimentally by Tilley et al. (1971), only 6 come from Piton de la Fournaise. The 6 samples investigated by Fisk et al. (1988) all come from Piton des Neiges. Second, no experimental information is as yet available on La Réunion magmas in presence of volatile components, either H_2O or CO_2.

10.3.2 Results

Tilley et al. (1971) performed melting experiments under unbuffered redox conditions at 1 atm., either in argon or in air above 1230 °C. Liquidus temperatures ranged from 1522 °C (oceanite, about 27 wt% MgO) down to 1185 °C (hawaiite, 4.8 wt% MgO), decreasing progressively with decreasing bulk rock MgO. For rocks with bulk MgO higher than ~7 wt%, the order of crystallization is olivine, plagioclase and clinopyroxene. Olivine and plagioclase crystallized together on the liquidus of a 5 wt% MgO basalt whereas, for the hawaiite sample investigated, the liquidus phase was plagioclase.

Fisk et al. (1988) basically extended the work of Tilley et al. (1971). Some compositions used previously by Tilley et al. (1971) were re-investigated at 1 atm.; high pressure experiments were conducted mostly at 250–1000 MPa in gas vessel, and a few at 1500 and 2000 MPa in piston-cylinder. No volatile components were added to the starting materials. Redox conditions were mostly close to the iron-wustite buffer (Fisk et al. 1988), i.e., several log units more reducing than Piton de la Fournaise magmas. However, some 1 atm. experiments were also conducted closer to the natural fO_2 range. Although 6 rocks from 8.8 to nearly 27 wt% MgO were studied, the data mostly bear on 4 compositions that cover a more restricted range (8–13 wt% MgO). A high degree of internal consistency appears in results for the different samples and several general conclusions can be drawn (Fig. 10.4; see also Albarède et al. 1997, Fig. 21).

1. As expected, liquidus temperatures increase both with pressure (below 1000 MPa the gradient is about 4 °C/100 MPa) and, at a given pressure, with the MgO content of the starting material. For example, the 8 wt% MgO rock has liquidus temperatures from 1240 (1 atm.) to 1280 °C (1000 MPa) and the 13 wt% MgO rock from 1330 to 1370 °C.
2. The liquidus phase is always olivine at low pressures. Upon increasing pressure, it is replaced on the liquidus by clinopyroxene, this transition occurring at 800–1000 MPa for compositions with bulk MgO < 11 wt%, and at ~1800 MPa for the composition with 13 wt% MgO.

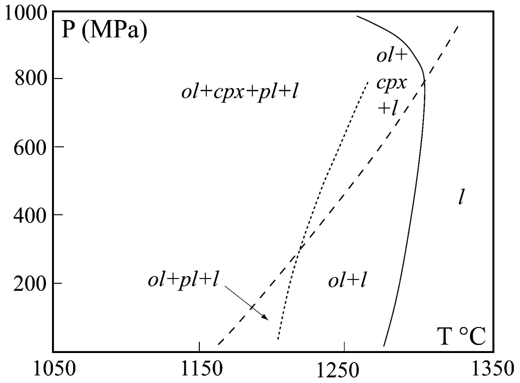

Fig. 10.4 Summary phase diagram for Piton de la Fournaise magmas based on the experimental data of Fisk et al. (1988). The diagram is constructed from experimental data mainly on a 11 wt% MgO oceanite from Piton des Neiges. *L* liquid; *ol* olivine; *cpx* clinopyroxene; *pl* plagioclase

3. The order of crystallization is (a) olivine-clinopyroxene-plagioclase below 800–1000 MPa (or below 1800 MPa for the 13 wt% MgO composition), and (b) olivine-plagioclase-clinopyroxene below 250–500 MPa, the latter sequence being in agreement with the experiments of Tilley et al. (1971).
4. Spinel is absent from most runs, being restricted to the few 1 atm. experiments performed at fO_2 around the natural range.
5. Orthopyroxene never occurs as an experimental phase.

Although compositions of experimental phases were not detailed, Fisk et al. (1988) give Fo, Mg/(Mg + Fe_t) and An contents of experimental olivine, clinopyroxene and plagioclase, respectively. Fo88 is the maximum olivine Fo content, consistent with the proposition that Piton de la Fournaise olivines have Fo < 89 (see above). However, the 27 wt% MgO composition was not studied at near-liquidus temperatures where it would have presumably crystallized olivines with Fo > 88. Clinopyroxenes have Mg/(Mg + Fe_t) equal or higher than olivine. The investigated sample with 11 wt% MgO (which is quite Ca-rich, CaO ~13 wt%) yields clinopyroxene Mg/(Mg + Fe_t) and plagioclase An contents up to 86 and 90 respectively (the highest of the experimental database), for a maximum olivine Fo content of 86.

10.3.3 Application to Piton de la Fournaise Magmas

Experiments by Fisk et al. (1988) have provided a framework for interpreting the genesis and evolution of Piton de la Fournaise magmas. In particular, these experimental data have been used to define pressures of magma fractionation (Albarède et al. 1997). The Fisk et al. (1988) data imply minimum pressures of 250–500 MPa for clinopyroxene to crystallize before plagioclase. Fractionation of olivine together with clinopyroxene would also require a minimum of 250–500 MPa from their data. Still higher crystallization pressures (a minimum of 800–1000 MPa for compositions <11 wt% MgO) would be necessary for fractionation of clinopyroxene alone.

Assuming that all Piton de la Fournaise primitive magmas crystallize in the sequence olivine-clinopyroxene-plagioclase (see above and Albarède et al. 1997; Welsch et al. 2009), then the Fisk et al. (1988) experimental results would lead to the conclusion that magma fractionation takes place for the most part at the base of the crust or in the mantle. The crust-mantle boundary beneath La Réunion is located at 12–15 km depths (Gallard et al. 1999; Lénat et al. 2012) or 320–400 MPa. Thus, the 250–500 MPa minimum pressures required by the Fisk et al. (1988) data makes it possible that crystallization of either olivine + clinopyroxene or olivine + clinopyroxene + plagioclase takes place at the base of the crust. Fractionation of a clinopyroxene-rich, olivine-poor assemblage was proposed by Albarède et al. (1997) to occur at mantle pressures (800–1000 MPa), consistent with the pressure (900 MPa) determined for the crystallization of aluminous augites (Fretzdorff and Haase 2002). Therefore, the Fisk et al. (1988) data implies relatively deep magma fractionation, in a pressure range difficult to reconcile with the presence of shallow crustal storage zones beneath Piton de la Fournaise (see above). It is worth noting that both melt and fluid inclusions are consistent with fluid-melt saturation and fluid entrapment at crustal pressures, and that petrological evidence for crystallization pressures above 400–500 MPa (Bureau et al. 1998b, 1999) is presently lacking.

These difficulties lead to an alternative interpretation of the Fisk et al. (1988) data, reminding that their experiments were performed under volatile-free conditions (see above). Recently, numerical runs using the MELTS software (Famin et al. 2009; Welsch et al. 2009) have been performed for a parental Piton de la Fournaise magma composition (see below), in presence of 1 wt% H_2O and 0.1 wt% CO_2, and for a fO_2 set at the FMQ buffer (about 0.7 log unit below NNO). They show that clinopyroxene crystallizes second after olivine at 100 MPa

(Welsch et al. 2009), i.e., at pressures much lower than the 250–500 MPa minimum pressure range found by Fisk et al. (1988).

These results open the possibility that magma fractionation at Piton de la Fournaise takes place at levels much shallower than previously thought. We conclude that there is a need for experiments on Piton de la Fournaise magmas in presence of volatile components, H_2O and CO_2. Determination of (1) the pressure of the transition from clinopyroxene to olivine as the liquidus phase and (2) the lower pressure limit for clinopyroxene to crystallize before plagioclase, both in presence of H_2O and CO_2, represent critical experimental objectives for constraining the structure of the feeding system at Piton de la Fournaise.

The lack of orthopyroxene (Fisk et al. 1988) implies that none of the rocks experimentally studied is saturated on its liquidus with an olivine-orthopyroxene phase assemblage. Therefore, none can be interpreted as a melt directly produced from either a peridotitic or harzburgitic source. It follows that Piton de la Fournaise melts must have suffered differentiation following extraction from their mantle source. On this basis, several studies have attempted to reconstruct the composition of Réunion parental magmas (Ludden 1978; Fisk et al. 1988; Sobolev and Nikogosian 1994; Fretzdorff and Haase 2002; Villemant et al. 2009; Dasgupta et al. 2010). In detail, results differ between studies, with substantial dispersions especially for SiO_2 (45–48.5 wt%), Al_2O_3 (10–12.5 wt%), MgO (12.5–20 wt%) and CaO (8–10 wt%). One representative composition of parental magma is shown in Table 10.1. The observation that the evolutionary trend for the AbG group intersects the olivine control line in Fig. 10.1 at about 11 wt% MgO indicates that 11 wt% MgO is actually a minimum for the parental magmas. Taking 89 as the maximum Fo in olivine (see above), an olivine-melt Fe–Mg partition coefficient of 0.306 (Fisk et al. 1988), an average total FeO of 11.74 wt% (Fisk et al. 1988) and a $Fe_2O_3/(Fe_2O_3 + FeO)$ proportion of 18 % (corresponding to NNO-0.5, see above), parental melts must have a maximum of 13.7 wt% MgO. Higher melt MgO concentrations are obtained by taking more Fo-rich olivine compositions (15–20 wt% MgO, Sobolev and Nikogosian 1994; 17 wt% MgO, Fretzdorff and Haase 2002). Therefore, there is agreement on the picritic nature of the Réunion parental melts. However, all reconstructions so far have assumed fractionation of only olivine at depth. This assumption may be correct if differentiation takes place for pressures and melt compositions where olivine is the sole liquidus phase. According to Fisk et al. (1988), this occurs at <800–900 MPa for melt MgO contents <11 wt%, and at <1800 MPa for 13 wt% MgO. However, clinopyroxene may precede/join olivine on the liquidus. Wehrlitic differentiation, either at crustal (Kornprobst et al. 1979, 1984) or mantle (Albarède et al. 1997; Fretzdorff and Haase 2002) depths, necessarily involves clinopyroxene fractionation. In this case, the reconstruction of parental Piton de la Fournaise magmas becomes more difficult because the composition of clinopyroxene must be known for reverse fractionation calculations to be reliably performed.

Acknowledgements The authors thank Didier Laporte for his constructive review. The project about the Piton de la Fournaise at Orléans is supported by the ANR DEGAZMAG. Ida Di Carlo and Michel Fialin provided assistance with electron microprobe analyses at Orléans and Paris.

References

Albarède F, Luais B, Fitton G, Semet M, Kaminski E, Upton BGJ, Bachèlery P, Cheminee JL (1997) The geochemical regimes of Piton de la Fournaise volcano (Réunion) during the last 530,000 years. J Petrol 38:171–201

Ballhaus C, Berry RF, Green DH (1991) High pressure experimental calibration of the olivine-orthopyroxene-spinel oxygen barometer: implications for the oxidation state of the upper mantle. Contrib Mineral Petrol 107:27–40

Battaglia J, Ferrazzini V, Staudacher T, Aki K, Cheminée JL (2005) Pre-eruptive migration of earthquakes at the Piton de la Fournaise Volcano (Réunion Island). Geophys J Int 161:549–558

Boivin P, Bachèlery P (2009) Petrology of 1977 to 1998 eruptions of Piton de la Fournaise, La Réunion island. J Volcanol Geotherm Res 184:109–125

Bosch D, Blichert-Toft J, Moynier F, Nelson BK, Télouk P, Gillot P-Y, Albarède F (2008) Pb, Hf and Nd isotope compositions of the two Réunion volcanoes

(Indian Ocean): a tale of two small-scale mantle blobs. Earth Planet Sci Lett 265:748–768

Brugier Y (2012) Pétrologie naturelle et expérimentale de laves du Piton de la Fournaise, La Réunion. Msc thesis, Université d'Orléans, 76 p

Brugier Y-A. Pichavant M. Di Muro A. (2015) Experimental determination of phase equilibria of a basalt from Piton de la Fournaise (La Réunion island): 1atm data and high pressure results in presence of volatiles. European Geosciences Union, General Assembly 2015

Bureau H, Métrich N, Pineau F, Semet M (1998a) Magma-conduit interaction at Piton de la Fournaise volcano (Réunion island): a melt and fluid inclusion study. J Volcanol Geotherm Res 84:39–60

Bureau H, Pineau F, Métrich N, Semet M, Javoy M (1998b) A melt and fluid inclusion study of the gas phase at Piton de la Fournaise volcano (Réunion island). Chem Geol 147:115–130

Bureau H, Métrich N, Semet M, Staudacher T (1999) Fluid-magma decoupling in a hot-spot volcano. Geophys Res Lett 26:3501–3504

Danyuschevsky LV, Sobolev AV (1994) Ferric-ferrous ratio and oxygen fugacity calculations for primitive mantle-derived melts: calibration of an empirical technique. Mineral Petrol 57:229–241

Dasgupta R, Jackson MG, Lee C-TA (2010) Major element chemistry of ocean island basalts—conditions of melting and heterogeneity of mantle source. Earth Planet Sci Lett 289:377–392

Famin V, Welsch B, Okumura S, Bachèlery P, Nakashima S (2009) Three differentiation stages of a single magma at Piton de la Fournaise volcano (Réunion hot spot). Geochem Geophys Geosyst 10. doi:10.1029/2008GC002015

Fisk MR, Upton BGJ, Ford CE, White WM (1988) Geochemical and experimental study of the genesis of magmas of Réunion island, Indian Ocea. J Geophys Res 93:4933–4950

Fretzdorff S, Haase KM (2002) Geochemistry and petrology of lavas from the submarine flanks of Réunion Island (western Indian Ocean): implications for magma genesis and the mantle source. Mineral Petrol 75:153–184

Gallard J, Driad L, Charvis Ph, Sapin M, Hirn A, Diaz J, de Voogd B, Sachpazi M (1999) Perturbation to the lithosphere along the hotspot track of La Réunion from an offshore-onshore seismic transect. J Geophys Res 104:2895–2908

Graham D, Lupton J, Albarède F, Condomines M (1990) Extreme temporal homogeneity of helium isotopes at Piton de la Fournaise, Réunion Island. Nature 347:545–548

Helz RT, Thornber CR (1987) Geothermometry of Kilauea Iki lava lake, Hawaii. Bull Volcanol 49:651–668

Kornprobst J, Boivin P, Bachèlery P (1979) L'alimentation des éruptions récentes du Piton de la Fournaise (Ile de la Réunion, Océan Indien): degré d'évolution et niveau de ségrégation des laves émises. CR Acad Sci 288:1691–1694

Kornprobst J, Boivin P, Lénat JF, Bachèlery P, Bonneville A, Dupont P, Lecointre J, Seidel JL, Thomas P, Vincent PM (1984) Le Piton de la Fournaise, île de la Réunion. Colloque Prévision et Surveillance des Eruptions Volcaniques. (C.N.R.S.–I.N.A.G.) Clermont-Ferrand, pp 75–82

Kress VC, Carmichael ISE (1991) The compressibility of silicate liquids containing Fe_2O_3 and the effect of composition, temperature, oxygen fugacity and pressure on their redox states. Contrib Mineral Petrol 108:82–92

Lacroix A (1936) Le volcan actif de l'île de la Réunion et ses produits. Gauthier et Villard, 297 p

Lee CTA, Leeman WP, Canil D, Li ZXA (2005) Similar V/Sc systematics in MORB and arc basalts: implications for the oxygen fugacities of their mantle source regions. J Petrol 46:2313–2336

Lénat JF, Bachèlery P (1990) Structure et fonctionnement de la zone centrale du Piton de la Fournaise. In: Lénat JF (ed) Le volcanisme de La Réunion. Centre de Recherches Volcanologiques, Clermont-Ferrand, pp 257–296

Lénat JF, Bachèlery P, Merle O (2012) Anatomy of Piton de la Fournaise volcano (La Réunion, Indian Ocean). Bull Volcanol 74:1945–1961

Ludden J (1978) Magmatic evolution of the basaltic shield volcanoes of Réunion island. J Volcanol Geotherm Res 4:171–198

Maurel C, Maurel P (1982) Etude expérimentale de l'équilibre Fe_2+–Fe_3+ dans les spinelles chromifères et les liquides silicatés basiques coexistant à 1 atm. CR Acad Sci 295:209–212

Maurel C, Maurel P (1984) Etude expérimentale de la distribution du fer ferrique entre spinelle chromifère et liquide silicaté basique. Bull Mineral 107:25–33

Michon L, Ferrazzini V, Di Muro A (2016) Magma paths at Piton de la Fournaise volcano. In: Bachèlery P, Lénat J-F, Di Muro A, Michon L (eds) Active volcanoes of the Southwest Indian Ocean: Piton de la Fournaise and Karthala. Active Volcanoes of the World (Chap. 7). Springer, Berlin, Heidelberg

Nercessian A, Hirn A, Lépine J-C, Sapin M (1996) Internal structure of Piton de la Fournaise volcano from seismic wave propagation and earthquakes distribution. J Volcanol Geotherm Res 70:123–143

Peltier A (2007) Suivi, modélisation et évolution des processus d'injections magmatiques au Piton de La Fournaise. PhD thesis, Université de La Réunion, 365 p

Peltier A, Staudacher T, Bachèlery P (2007) Constraints on magma transfers and structures involved in the 2003 activity at Piton de la Fournaise from displacement data. J Geophys Res 112. doi:10.1029/2006JB004379

Peltier A, Bachèlery P, Staudacher T (2009) Magma transport and storage at Piton de la Fournaise (La Réunion) between 1972 and 2007: a review of geophysical and geochemical data. J Volcanol Geotherm Res 184:93–108

Pietruszka AJ, Hauri EH, Blichert-Toft J (2009) Crustal contamination of mantle-derived magmas within Piton de la Fournaise volcano, Réunion Island. J Petrol 50:611–684

Salaün A, Villemant B, Semet M, Staudacher T (2010) Cannibalism of olivine-rich cumulate xenoliths during the 1998 eruption of Piton de la Fournaise (La Réunion hotspot): implications for the generation of magma diversity. J Volcanol Geotherm Res 198:187–204

Smietana, M (2011) Pétrologie, géochronologie (K–Ar) et géochimie élémentaire et isotopique (Sr, Nd, Hf, Pb) des laves anciennes de La Réunion. Implications sur la construction de l'édifice volcanique. PhD thesis, Université de La Réunion, 362 p

Sobolev AV, Nikogosian IK (1994) Petrology of long-lived plume magmatism: Hawaii, Pacific and Réunion islands, Indian Ocean. Petrology 2:111–144

Tilley CE, Thompson RN, Wadsworth WJ, Upton BGJ (1971) Melting relations of some lavas of Réunion island, Indian Ocean. Mineral Mag 38:344–352

Upton BGJ, Wadsworth WJ (1966) The basalts of Réunion island, Indian Ocean. Bull Volcanol 29:7–23

Upton BGJ, Wadsworth WJ (1972) Peridotitic and gabbroic rocks associated with the shield-forming lavas of Réunion. Contrib Mineral Petrol 35:139–158

Upton BGJ, Semet M, Joron J-L (2000) Cumulate clasts in the Bellecombe Ash Member, Piton de la Fournaise, Réunion Island, and their bearing on cumulative processes in the petrogenesis of the Réunion lavas. J Volcanol Geotherm Res 104:297–318

Vigouroux N, Williams-Jones AE, Wallace P, Staudacher T (2009) The November 2002 eruption of Piton de la Fournaise, Réunion: tracking the pre-eruptive thermal evolution of magma using melt inclusions. Bull Volcanol 71:1077–1089

Villemant B, Salaün A, Staudacher T (2009) Evidence for a homogeneous primary magma at Piton de la Fournaise (La Réunion): a geochemical study of matrix glass, melt inclusions and Pélé's hairs of the 1998–2008 eruptive activity. J Volcanol Geotherm Res 184:79–92

Vlastélic I, Staudacher T, Semet M (2005) Rapid change of lava composition from 1998 to 2002 at Piton de La Fournaise (Réunion) inferred from Pb isotopes and trace elements: evidence for variable crustal contamination. J Petrol 46:79–107

Vlastélic I, Peltier A, Staudacher T (2007) Short-term (1998–2006) fluctuations of Pb isotopes at Piton de la Fournaise volcano (Réunion Island): origins and constrains on the size and shape of the magma reservoir. Chem Geol 244:202–220

Vlastélic I, Deniel C, Bosq C, Télouk P, Boivin P, Bachèlery P, Famin V, Staudacher T (2009) Pb isotope geochemistry of Piton de la Fournaise historical lavas. J Volcanol Geotherm Res 184:63–78

Vlastélic I, Staudacher T, Bachèlery P, Télouk P, Neuville D, Benbakkar M (2011) Lithium isotope fractionation during magma degassing: Constraints from silicic differentiates and natural gas condensates from Piton de la Fournaise volcano (Réunion Island). Chem Geol 284:26–34

Welsch B, Faure F, Bachèlery P, Famin V (2009) Microcrysts record transient convection at Piton de la Fournaise volcano (La Réunion hotspot). J Petrol 50:2287–2305

Welsch B, Faure F, Famin V, Baronnet A, Bachèlery P (2013) Dendritic crystallization: a single process for all the textures of olivine in basalts? J Petrol 54:539–574

American Mineralogist, Volume 100, pages 2106–2111, 2015

INVESTIGATING PETROLOGIC INDICATORS OF MAGMATIC PROCESSES IN VOLCANIC ROCK

Fe pre-enrichment: A new method to counteract iron loss in experiments on basaltic melts†

YANN-AURELIEN BRUGIER[1,*], MARINA ALLETTI[1] AND MICHEL PICHAVANT[1]

[1]Université d'Orléans, ISTO, UMR 7327, 45071, Orléans, France; and CNRS/INSU, ISTO, UMR 7327, 45071 Orléans, France; and BRGM, ISTO, UMR 7327, BP 36009, 45060 Orléans, France

ABSTRACT

Capsule pre-saturation has been traditionally employed to circumvent Fe loss from the charge to the container in petrological experiments. However, the method is time-consuming and fraught with theoretical and practical difficulties. An alternative method, based on the use of starting materials pre-enriched in Fe, is presented. Test experiments on two natural basalts, both non Fe-enriched and Fe-enriched with the addition of Fe oxides, have been carried out at 1 atm and 50 MPa (H_2O-saturated), 1200 and 1250 °C, between NNO and NNO-1 and in Pt and $Au_{80}Pd_{20}$ capsules. Glasses and capsules were analyzed by electron microprobe. Fe-concentrations in the capsule near the glass interface strongly depend on the capsule material, being 5–10 times less for $Au_{80}Pd_{20}$ than for Pt. For non Fe-enriched compositions, Fe loss reaches –15% ($Au_{80}Pd_{20}$) and –60% (Pt). Increasing the level of Fe-enrichment reduces Fe loss, the amount of Fe alloyed with the capsule being compensated by the amount of Fe added to the starting composition. FeO_t concentrations in high-pressure glasses bracket the nominal FeO_t of the two starting basalts, demonstrating that Fe alloying has been successfully counteracted. Combination of AuPd containers with Fe pre-enriched starting materials offers excellent perspectives to solve the Fe loss issue in high-pressure experiments on basaltic compositions.

Keywords: Experiments, capsules, iron loss, pre-enrichment, basalts

INTRODUCTION

Fe loss from the charge to the container is one of the most difficult problems in experimental petrology. Classically, in a high-pressure experiment, the charge is contained in a chemically inert noble metal such as Pt, Au, or Ag (e.g., Chou 1986). For temperatures <1050 °C, Au capsules are commonly used. However, the relatively low melting point of Au makes it inappropriate for experiments on basaltic systems. The use of Pt enables working at temperatures >1050 °C, but Pt is known to interact strongly with the charge, leading to the formation of a PtFe alloy, which removes most of the Fe from the starting material (Stern and Wyllie 1975). Various methods have been proposed to mitigate Fe loss, the most commonly used being capsule Fe *pre-saturation* (see Grove 1982). This method involves the preparation at 1 atm of an alloy (PtFe in early studies) in equilibrium with the Fe-bearing charge at high temperature and pressure, and the use of that alloy as a container, instead of pure Pt (e.g., Ford 1978; Grove 1982). More recently, AuPd alloys have attracted much interest as a substitute to Pt because of their lower susceptibility to alloying with Fe (Kawamoto and Hirose 1994). However, large amounts of Fe can dissolve in AuPd alloys depending on f_{O_2} (Hall et al. 2004; Di Carlo et al. 2006; Barr and Grove 2010; Balta et al. 2011). Therefore, the Fe pre-saturation approach has been extended to AuPd capsules (Gaetani and Grove 1998; Barr and Grove 2010; Balta et al. 2011 and references therein).

There are however several theoretical and practical difficulties with the Fe pre-saturation method. Balta et al. (2011) emphasized that defining the conditions needed to saturate either Pt or AuPd with the proper amount of Fe for a high-pressure experiment is difficult. Even after the correct 1-atm pre-saturation conditions are determined for one high-pressure experiment, these conditions will differ from those needed for the next experiment in ways that are difficult to predict. In particular, one parameter that must be known precisely for the planning of the pre-saturation conditions is the f_{O_2} of the high-pressure experiment. For example, for a hydrogen buffered (i.e., constant f_{H_2}) gas vessel experiment with charges of different f_{H_2O} ran together (e.g., Di Carlo et al. 2006), f_{O_2} must vary between charges. Theoretically, for each charge, a specific alloy would need to be prepared if the pre-saturation method is to be used. Another major shortcoming of the pre-saturation method concerns the long durations necessary to prepare chemically homogeneous Fe-noble metal alloys even at high temperatures (Gaillard et al. 2003; see below). Dissolution of the Fe doping material following capsule pre-saturation can be also sluggish, the whole method being very time-consuming.

Difficulties with capsule Fe pre-saturation leave room for alternative approaches to reduce Fe loss in petrological experiments. In this paper, we present a new empirical method to mitigate Fe loss in high-pressure experiments on basaltic systems. The method is based on a new approach, i.e., the use of starting materials *pre-enriched* in Fe.

EXPERIMENTAL AND ANALYTICAL METHODS

The new method was developed within the framework of two experimental projects on natural basaltic melts that required Fe loss to be minimized. In the first project, S solubilities are measured at high temperatures (1200 °C) and pressures (200 MPa) under moderately reducing conditions (i.e., at $f_{O_2} \leq$ the Ni-NiO buffer,

---

* E-mail: yann-aurelien.brugier@cnrs-orleans.fr

† Special collection papers can be found on GSW at http://ammin.geoscienceworld.org/site/misc/specialissuelist.xhtml.

0003-004X/15/0010–2106$05.00/DOI: http://dx.doi.org/10.2138/am-2015-5166

NNO), using Pt capsules to prevent the formation of complex Pd-, S-bearing compounds (Pichavant et al. 2006). The second project is a phase equilibrium study at 50–400 MPa, 1100–1200 °C, and a f_{O_2} ~ NNO-0.5 on transitional basalts from La Réunion Island (Indian Ocean), with $Au_{80}Pd_{20}$ capsules used as containers (Brugier et al. in preparation). Both projects require Fe loss to be minimized. Initially, the Fe capsule pre-saturation method was attempted but difficulties of the type summarized above were encountered. Consequently, a new methodology based on specific experiments performed at 1 atm and 50 MPa was tested, in parallel with Pt and $Au_{80}Pd_{20}$ capsules.

A basaltic pumice from Stromboli (PST-9, Pichavant et al. 2011) and a basaltic scoria erupted in 2009 from the Piton de la Fournaise (REU-04) were used as starting materials. PST-9 has been previously experimentally investigated by Di Carlo et al. (2006) and Pichavant et al. (2009). The two samples were separately crushed, ground, and then fused at 1 atm, 1400 °C for 4 h in a large Pt crucible open to air to produce crystal- and volatile-free homogeneous glasses. Chips of each starting glass were mounted in epoxy and their composition checked by electron microprobe (Table 1), the rest ground and stored in an oven at 120 °C. An aliquot of each glass was used to prepare Fe-enriched (or Fe pre-enriched) starting materials by physically mixing with Fe oxide, either magnetite or hematite powders (chemical reagent grade purity). Iron enrichments are reported as wt% Fe added to the glass-oxide mixture (Tables 2 and 3).

1-atm experiments

The PST-9 and REU-04 starting compositions (either glass or glass-Fe oxide powders) were loaded, respectively, in Pt and $Au_{80}Pd_{20}$ tubes (diameter: 2.5 mm, length: 20–25 mm, wall thickness: 0.2 mm), previously welded at one end. Capsules were side by side and vertically held in an alumina tube that was suspended through a Pt wire in the furnace. A 1-atm vertical gas mixing furnace was used, both at 1200 °C (NNO and NNO-0.5) and 1250 °C (NNO-0.5). The f_{O_2} was controlled by CO-CO_2 gas mixtures monitored by certified electronic flowmeters (Deines et al. 1974). Temperature was read by an S-type thermocouple and is accurate to within 2 °C. The sample holder and thermocouple were both located in the hot spot of the furnace. The thermal gradient is less than 5 °C along the length of the capsules.

For the PST-9 experiments, two runs of ~100 h were conducted at 1200 and 1250 °C with three capsules corresponding to three Fe-enrichments (0, 5, and 13 wt% Fe added). The two 72 and 194 h REU-04 experiments (1200 °C), which started from a non Fe-enriched composition, were in fact classical pre-saturation experiments (Table 2). Charges were quenched by electrically fusing the Pt wire, resulting in the drop of the sample holder in the cold bottom part of the furnace.

TABLE 1. Composition of starting glasses

Oxide	PST-9	REU-04
SiO_2	50.6	50.5
TiO_2	0.88	2.56
Al_2O_3	16.2	13.8
FeO_t	7.95	10.6
MnO	0.13	0.14
MgO	7.16	7.63
CaO	12.1	11.3
Na_2O	2.38	2.64
K_2O	1.88	0.69
P_2O_5	0.61	0.17
Cr_2O_3	0.03	0.05
NiO	0.05	0.03
Total	99.7	99.1

Notes: Data are averages calculated on multiple (10–50) glass analyses. Concentrations are normalized to 100%; Total is unnormalized.

TABLE 2. Experimental conditions for 1-atm experiments

Charge no.	1	2	3	4	5	6	7	8
T (°C)	1200	1200	1200	1250	1250	1250	1200	1200
Log f_{O_2}	–8.2	–8.2	–8.2	–8.2	–8.2	–8.2	–7.7	–7.7
ΔNNO[a]	–0.5	–0.5	–0.5	–0.5	–0.5	–0.5	0	0
Capsule material	Pt	Pt	Pt	Pt	Pt	Pt	$Au_{80}Pd_{20}$	$Au_{80}Pd_{20}$
Wt% Fe added[b]	0	5	13	0	5	13	0	0
Duration (h)	110	110	110	100	100	100	72	194
Fe in capsule (at%)[c]	4	5–8	7–10	4–7	8–11	20–24	0.5	1.5
Glass	PST-9	PST-9	PST-9	PST-9	PST-9	PST-9	REU-04	REU-04

[a] Log f_{O_2} charge – Log f_{O_2} NNO at the same P and T. NNO equation from Pownceby and O'Neill (1994).

[b] Amount of Fe (metallic iron) added to the glass in wt%.

[c] Fe concentration in capsule at the glass interface.

TABLE 3. Experimental conditions for high-pressure experiments

Experiment	1200 °C, 485 bar, 42 h				1200 °C, 475 bar, 40 h			
Charge no.	HP1	HP2	HP3	HP4	HP5	HP6	HP7	HP8
Log f_{O_2}	–8.5	–8.5	–8.5	–8.5	–8.5	–8.5	–8.5	–8.5
ΔNNO[a]	–0.8	–0.8	–0.8	–0.8	–0.8	–0.8	–0.8	–0.8
Capsule material	Pt	Pt	Pt	$Au_{80}Pd_{20}$	Pt	Pt	$Au_{80}Pd_{20}$	$Au_{80}Pd_{20}$
wt% Fe added[b]	0	5	13	10	5	13	0	2
Fe in capsule (at%)[c]	24–25	26–27	30–33	3.2–3.4	26	38	4	2.9
Glass	PST-9	PST-9	PST-9	REU-04	PST-9	PST-9	REU-04	REU-04

[a] Log f_{O_2} charge – Log f_{O_2} NNO at the same P and T. NNO equation from Pownceby and O'Neill (1994).

[b] Amount of Fe (metallic iron) added to the glass in wt%.

[c] Fe concentration in capsule at the glass interface.

Capsules were mounted in epoxy and polished parallel to their axial plane (Fig. 1), so that they could be analyzed at different positions (top, i.e., the closest to the gas atmosphere, middle, bottom, i.e., the closest to the welded end) along their length.

High-pressure experiments

Pt (for PST-9) and $Au_{80}Pd_{20}$ (REU-04) capsules were used in the high-pressure experiments similarly to those at 1 atm, apart from being welded shut. About 5 mg distilled-deionized water and ~50 mg of either glass or glass-Fe oxide mixture were loaded so as to yield H_2O-saturated conditions. Both non-Fe-enriched and Fe-enriched compositions were investigated (Table 3). Two similar experiments were performed at 50 MPa, 1200 °C in a rapid-quench internally heated pressure vessel operating vertically and pressurized with an Ar-H_2 gas mixture (Di Carlo et al. 2006). Total pressure was recorded by a transducer calibrated against a Heise Bourdon tube gauge (uncertainty ±2.0 MPa). The double-winding molybdenum furnace allowed a near-isothermal hot-spot zone of 2–3 cm length, with a gradient of <3 °C/cm. Temperature was monitored by two S-type thermocouples with an uncertainty of ±5 °C. H_2 and Ar, loaded sequentially at room temperature, were used to pressurize the vessel and to control the f_{O_2}, the two experiments being performed with the same initial H_2 pressure (3 bar). Experimental f_{H_2} (i.e., the f_{H_2} at 50 MPa, 1200 °C) was measured by CoO-CoPd sensors (Taylor et al. 1992) in separate capsules. A f_{O_2} of NNO-0.8 was determined for all high-pressure capsules (calculations performed with K_{water} from Robie et al. 1979, f_{H_2O} from Burnham et al. 1969, the NNO equation from Pownceby and O'Neill 1994, and the CoPd sensor calibration of Taylor et al. 1992). Run durations were in both cases ~40 h, longer than most experiments with hydrous basaltic melts but approaching the duration of the 1-atm series. The experiments were terminated by drop-quenching the sample

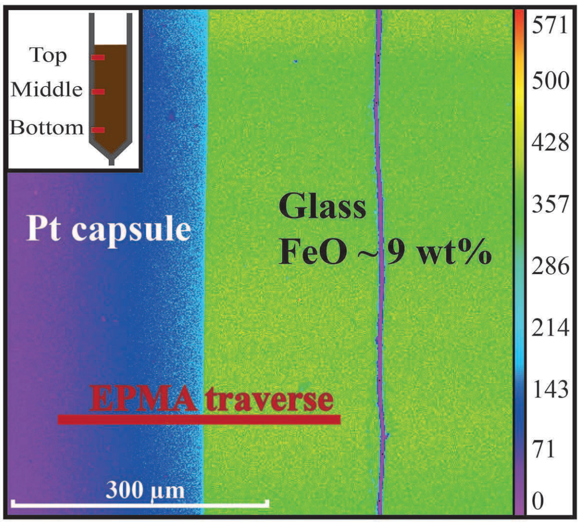

FIGURE 1. Distribution of Fe (Fe*K*α intensity map, 15 kV acceleration voltage) in 1-atm charge 5 (experimental conditions in Table 2) illustrating the chemically homogeneous glass layer and the progressive decrease in Fe concentration in the Pt capsule from the glass interface toward its external rim.

holder (Di Carlo et al. 2006). Capsules were then weighed and checked for possible leaks. Only capsules that did not show any change in weight were retained and mounted in the same way as the 1-atm capsules.

Electron microprobe analyses

The experimental products were analyzed with a Cameca SX Five electron microprobe at ISTO, Orléans. Analyses mainly were performed along traverses several hundred micrometers long positioned across and perpendicular to the glass-capsule interface (Fig. 1). Analytical conditions were set, for experimental glasses, at 15 kV (acceleration voltage), 6 nA (sample current), 10 s (counting time on peak), and 5 s (counting time on background). Capsules were analyzed for Fe under the same conditions except for capsules HP4, HP5, HP7, and HP8, which were analyzed at 15 kV, 30 nA, 30 s, and 5 s. CoPd sensor alloys were analyzed separately under higher acceleration voltage (20 kV) and a 20 nA sample current. Relative analytical errors are 1% (SiO_2, MgO, CaO), 1–2% (Al_2O_3), 2–4% (FeO, Na_2O), and 5–10% (TiO_2, K_2O) for glasses. For capsules, the detection limit for Fe is around 4500 ppm, corresponding to 1.5 at% Fe, except for HP4, HP5, HP7, and HP8 (detection limit around 270 ppm, corresponding to 0.08 at% Fe). For sensors, the error on the alloy composition is ±1–2 at%.

RESULTS

1-atm experiments

Fe concentrations in capsules at the glass interface, obtained from the analytical traverses, depend markedly on the capsule material (Table 2). At 1200 °C and NNO-0.5, they range between 4 and 10 at% Fe for Pt (reaching 24 at% Fe at 1250 °C), but barely exceed the limit of detection for $Au_{80}Pd_{20}$ at 1200 °C, NNO (0.5–1.5 at% Fe). The Fe distribution within $Au_{80}Pd_{20}$ capsules could not be precisely evaluated due to low Fe-capsule concentrations and the elevated Fe detection limit. Charges in Pt capsules define a positive correlation between the Fe interface concentration and the level of Fe-enrichment (Table 2). Capsule Fe concentrations progressively decrease toward their external rim (Fig. 1), emphasizing the lack of bulk chemical equilibrium in our experiments. An equilibrium Fe distribution between capsule and melt is only attained near the capsule-glass interface. This stresses the long durations needed to homogenize Fe concentrations in Pt capsules of "normal" thickness (0.2 mm).

The REU-04 glasses have $\Delta FeO_t < 5\%$ [$\Delta FeO_t = 100 \cdot (FeO_t$ glass – FeO_t starting glass)/(FeO_t starting glass), see Table 4] indicating that no significant Fe loss occurred, consistent with the low Fe interface concentrations observed in $Au_{80}Pd_{20}$ capsules. In comparison, the PST-9 glasses exhibited a complex behavior in Pt capsules. Although glasses along a given traverse are chemically homogeneous, a systematic vertical stratification of glass compositions inside capsules is present. As a result, the glass data have been distinguished as a function of the position of the analytical traverse in the capsule (either top, middle, or bottom, Table 4). For a given capsule and from bottom to top, glass FeO_t, MgO, and CaO decrease, and SiO_2, Al_2O_3, Na_2O, and K_2O increase. The same type of trends were observed both in non Fe-enriched and Fe-enriched charges. This compositional stratification makes difficult to evaluate the pre-enrichment method. For example, for a given capsule, large differences in Fe loss (ΔFeO_t) occur between bottom and top glasses (e.g., –2% and –31%, respectively, for bottom and top in experiment 2, 5 wt% added Fe, Table 4). We attribute the observed zonations mainly to the persistence of a redox gradient inside capsules, the bottom part of the melt layer keeping oxidizing conditions (since the starting glasses were synthesized in air), only the top part of the melt layer being equilibrated with the f_{O_2} of the gas mixture.

High-pressure experiments

Fe-concentrations in the capsules near the glass interface range between 24 and 38 at% Fe for Pt and 3 and 4 at% Fe for $Au_{80}Pd_{20}$ capsules (Fig. 2), higher than in the corresponding 1-atm charges and in general positively correlated with the Fe-enrichment (Table 3). Both Pt and $Au_{80}Pd_{20}$ capsules display heterogeneous Fe distributions, with Fe concentrations progressively decreasing from the glass interface toward the capsule external rim. For capsules analyzed under specific analytical conditions, the data show that Fe concentrations >1.5 at% extend to distances longer in $Au_{80}Pd_{20}$ than in Pt (Fig. 2). Contrasting with the 1-atm glasses, the high-pressure glasses are chemically homogeneous at the scale of the entire charge. For the non-enriched starting compositions, ΔFeO_t values are elevated. They differ with the capsule material, reaching –60% (Pt) and –15% ($Au_{80}Pd_{20}$, Table 5). Upon increasing the level of Fe-enrichment, ΔFeO_t progressively evolves from negative (Fe loss) to positive (Fe gain). For PST-9 in Pt capsules, ΔFeO_t from –60%, –1%, +10%, +106% to +138% are obtained and, for REU-04 in $Au_{80}Pd_{20}$ capsules, of –15%, –6%, and +12% (Table 5). Results of representative glass traverses obtained on the two starting compositions with different Fe-enrichments are illustrated on Figure 3. For both compositions and types of capsule

TABLE 4. Composition of representative 1-atm experimental glasses

Oxide	1	2	2	3	3	4	5	5	6	6	7	8
SiO_2	50.2	49.9	53.8	49.3	54.3	51.1	49.3	51.7	46.2	52.4	48.8	49.7
TiO_2	1.00	1.03	1.06	0.90	0.93	0.85	0.89	0.82	0.79	0.80	2.53	2.52
Al_2O_3	16.6	16.3	17.0	16.4	17.0	17.3	16.7	17.1	15.7	16.9	13.6	13.7
FeO_t	7.54	7.79	5.48	9.86	6.30	7.24	9.95	7.89	15.2	9.95	10.8	10.6
MnO	0.20	0.16	0.13	0.17	0.12	nd	nd	nd	nd	nd	0.17	0.18
MgO	7.25	7.72	6.44	6.65	5.45	6.40	6.31	5.82	6.31	4.7	8.22	7.91
CaO	11.5	11.4	9.62	10.9	8.75	12.2	11.9	11.7	11.69	9.53	12.4	12.2
Na_2O	2.77	2.60	2.88	2.73	3.12	2.57	2.56	2.55	2.14	2.80	2.53	2.26
K_2O	2.30	2.40	2.77	2.34	3.23	1.94	1.89	1.97	1.52	2.47	0.65	0.55
P_2O_5	0.67	0.65	0.71	0.71	0.70	0.49	0.50	0.51	0.48	0.48	0.31	0.29
Cr_2O_3	0.04	0.04	0.05	0.05	0.04	nd	nd	nd	nd	nd	0.03	0.03
NiO	0.02	0.01	0.02	0.01	0.01	nd	nd	nd	nd	nd	0.01	0.06
Total	97.7	97.0	97.6	97.6	97.0	97.7	96.9	100	97.6	97.7	95.7	97.8
wt% Fe added[a]	0	5	5	13	13	0	5	5	13	13	0	0
ΔFeO_t (% relative)	–5	–2	–31	+24	–21	–9	+25	–1	+91	+25	+2	0
Position	bottom	bottom	top	bottom	top	bottom	bottom	top	bottom	top	middle	middle
Glass	PST-9	PST-9	PST-9	PST-9	PST-9	PST-9	PST-9	PST-9	PST-9	PST-09	REU-04	REU-04

Notes: Charge no. as in Table 2. Data are averages calculated on multiple (10–50) glass analyses. Concentrations are normalized to 100%; Total is unnormalized. $\Delta FeO_t = 100 \cdot (FeO_t$ glass – FeO_t starting glass)/(FeO_t starting glass).

[a] Amount of Fe (metallic iron) added to the glass in wt%.

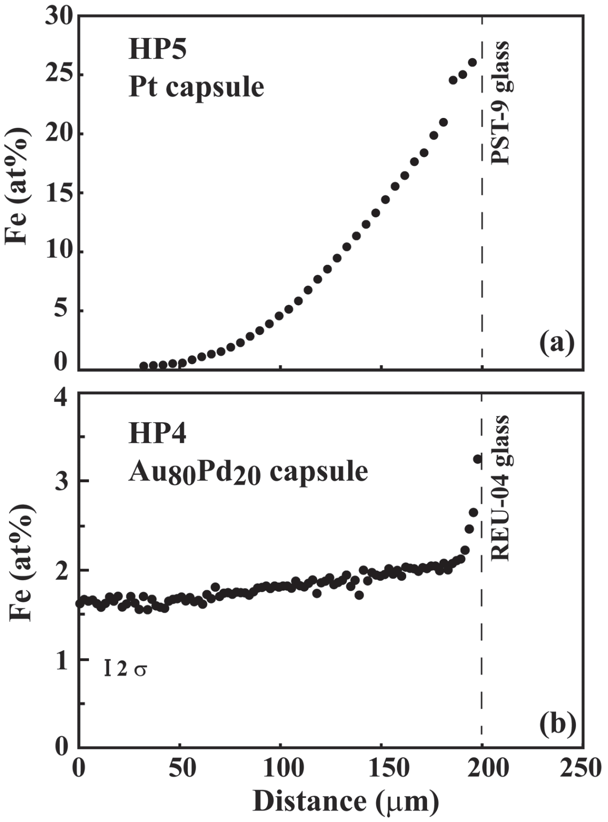

FIGURE 2. Representative electron microprobe traverses through different capsules from the same high-pressure experiment. Fe concentrations in capsules (at%) are plotted against distance (μm). Experimental conditions in Table 3. (**a**) Pt capsule, charge HP5. Error bars are smaller than symbols. (**b**) $Au_{80}Pd_{20}$ capsule, charge HP4. Melt compositions and Fe enrichments in Table 5. Note the heterogeneity in the Fe distribution inside capsules, especially in **a**, the difference in Fe interface concentrations between Pt and $Au_{80}Pd_{20}$ and the longer Fe diffusion distances in $Au_{80}Pd_{20}$ than in Pt.

materials, the nominal FeO_t of the starting basalt is bracketed by the glass FeO_t concentrations, demonstrating that Fe loss toward the capsule has been effectively counteracted. The 5 wt% Fe added PST-9 composition (HP2, Table 5) illustrates the case of an optimum level of Fe pre-enrichment, defined as the amount of Fe added that yields <5% Fe loss/gain.

DISCUSSION

Our tests establish the potential of the pre-enrichment method to circumvent the Fe loss problem in experiments with basaltic melts. Working with starting materials enriched in Fe enables the influence of Fe alloying with the capsule material to be counteracted. The method has been successfully tested on both Pt and $Au_{80}Pd_{20}$ capsules, at a pressure of 50 MPa, relatively high temperatures (1200 °C) and moderately reducing f_{O_2} (from NNO to NNO-1). Under more reducing conditions, more Fe would alloy with capsule materials but the method should still be applicable in principle. It is important to stress that the proposed pre-enrichment method is empirical and should be adjusted for each particular set of starting compositions and experimental conditions. In particular, the experimental duration should be considered as a variable since equilibrium between melt and capsule is not attained in experiments of a few days on basaltic melts and, therefore, Fe loss is expected to increase with experimental duration, all other parameters being equal.

TABLE 5. Composition of representative high-pressure experimental glasses

Oxide	HP1	HP2	HP3	HP4	HP5	HP6	HP7	HP8
SiO_2	53.2	51.0	46.5	49.6	49.8	44.3	51.3	50.5
TiO_2	0.98	0.87	0.79	2.59	0.90	0.79	2.61	2.55
Al_2O_3	17.3	17.2	15.0	14.2	16.9	14.8	14.0	13.7
FeO_t	3.15	7.84	16.4	11.9	8.76	18.9	8.96	9.92
MnO	0.14	0.16	0.13	0.11	0.15	0.15	0.16	0.19
MgO	6.90	6.51	5.87	7.23	6.47	5.90	7.92	8.08
CaO	13.0	11.9	10.7	11.4	12.0	10.6	11.8	11.7
Na_2O	2.45	2.06	2.14	1.93	2.46	2.20	2.43	2.57
K_2O	2.21	2.01	1.96	0.73	2.06	1.78	0.62	0.59
P_2O_5	0.67	0.52	0.53	0.36	0.49	0.46	0.21	0.20
Cr_2O_3	0.01	0.00	0.00	0.02	0.01	0.01	0.03	0.04
NiO	0.01	0.00	0.00	0.00	0.04	0.04	0.07	0.05
Total	92.7	93.5	93.6	92.7	94.1	95.1	96.0	95.4
wt% Fe added[1]	0	5	13	10	5	13	0	2
ΔFeO_t (% relative)	−60	−1	+106	+12	+10	+138	−15	−6
Position	middle	middle	middle	all	bottom	bottom	all	all
Glass	PST-9	PST-9	PST-9	REU-04	PST-9	PST-9	REU-04	REU-04

Notes: Charge no. as in Table 3. Data are averages calculated on multiple (10–50) glass analyses. Concentrations are normalized to 100%; Total is unnormalized. $\Delta FeO_t = 100 \cdot (FeO_t \text{ glass} - FeO_t \text{ starting glass})/(FeO_t \text{ starting glass})$.
[a] Amount of Fe (metallic iron) added to the glass in wt%.

In our experiments, the additional Fe was introduced as Fe oxide. This has the advantage of simplicity and flexibility, since Fe enrichments can be sensitively adjusted. Results show that changing the type of Fe oxide (magnetite vs. hematite) does not influence the final glass compositions. Fe oxides rapidly dissolve in basaltic melts under our experimental conditions. The vertical stratification of glass compositions in the 1-atm Pt charges is not the result of Fe oxide sedimentation. In contrast with the 1-atm charges, the high-pressure glass layers are chemically homogeneous indicating that Fe diffuses rapidly in the melt. However, our tests were conducted at high temperatures, above the liquidus and for hydrous melts. Other procedures might be needed if the pre-enrichment method is to be used at lower temperatures (or under H_2O-poor conditions), because (1) Fe oxide dissolution might take more time and (2) Fe might diffuse less rapidly in the melt. It is important to recognize that the success of the approach is based on a marked diffusivity contrast between Fe in capsule (slow) and Fe (bulk) in the melt (fast). Use of Fe-enriched glasses instead of glass-Fe oxide mixtures would eliminate the oxide dissolution step. However, we caution that the method needs further testing under conditions leading to slow bulk melt Fe diffusivities.

In addition to the pre-enrichment methodology, several aspects of this study are worth being emphasized. First, our results confirm the quite good performance of $Au_{80}Pd_{20}$ capsule materials with respect to alloying with Fe. At 1200 °C, Fe concentrations (at the glass-capsule interface) are 0.5–1.5 at% Fe in the 1-atm NNO experiments, increasing to 2–4 at% Fe in the high-pressure NNO-0.8 experiments. These Fe concentrations are consistent with the measurements of Balta et al. (2011), noticing that their $Au_{74}Pd_{26}$ alloys were equilibrated with pure Fe oxide and with their calculations for equilibration with a Kilauea basalt. We stress that, for experiments on basaltic melts at around NNO,

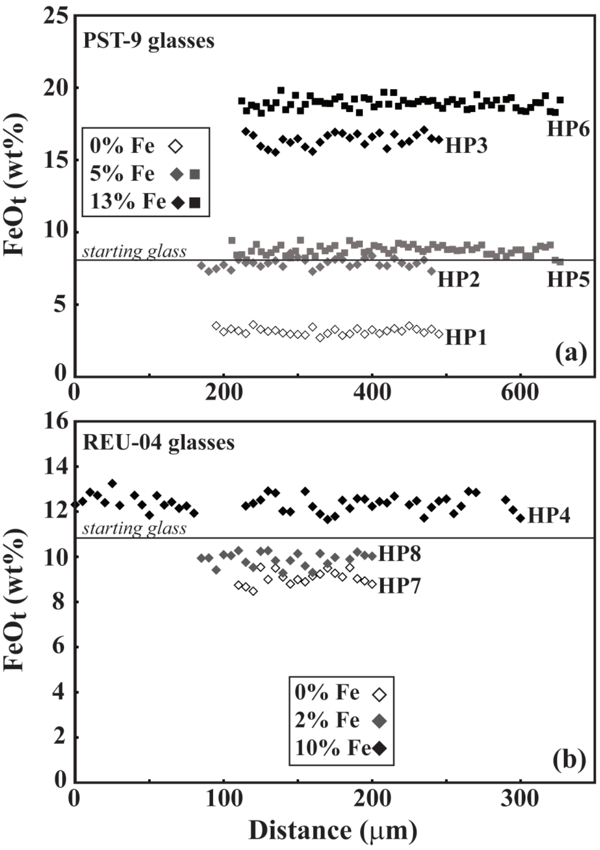

Figure 3. Results of electron microprobe traverses showing glass FeO_t concentrations (wt%, normalized to 100%) plotted against distance (μm) for the high-pressure charges. Experimental conditions in Table 3. Glass averages in Table 5. Data points are distinguished with Fe pre-enrichments expressed as wt% Fe added to the glass. (**a**) PST-9 charges ran in Pt capsules. (**b**) REU-04 charges ran in $Au_{80}Pd_{20}$ capsules. The horizontal lines mark the FeO_t of the starting PST-9 and REU-04 glasses (Table 1). In **a**, the starting PST-9 glass composition is bracketed by charges HP2 and HP5 (both with 5% Fe added) and, in **b**, the REU-04 by charges HP8 (2 wt% Fe) and HP4 (10 wt% Fe).

Fe interface concentrations for AuPd alloys are 5–10 times less than for Pt. Yet, these concentrations are sufficient to affect the FeO_t concentration of the encapsulated melt. In addition to differences in interface concentrations between capsule materials, Fe diffuses to longer distances in $Au_{80}Pd_{20}$ than in Pt capsules. In our high-pressure experiments at NNO-0.8, Fe losses with $Au_{80}Pd_{20}$ capsules are –15% (Table 5). Comparable Fe losses (–13% on average) were reported by Di Carlo et al. (2006) despite f_{O_2} (between NNO-0.1 and NNO+2.3) being on average higher than in this study. Although these Fe losses are significant, the use of $Au_{80}Pd_{20}$ instead of Pt (Fe loss of –60%, HP1, Table 5) clearly represents a major improvement. We conclude that the combination of AuPd containers and Fe pre-enriched starting materials offers excellent perspectives to solve the Fe loss issue in high-pressure experiments on basaltic compositions, when sulfur is not involved. Indeed, Au-Pd alloys tend to react with S to form complex Pd- and S-bearing compounds (Pichavant et al. 2006), weakening the capsule walls and falsifying the composition of the resulting glasses. Second, the melt zonation problem encountered provides an additional illustration of the difficulty to apply 1-atm methodologies to high-pressure experiments. In our 1-atm experiments, chemical stratification of the melt prevented precise evaluation of Fe gains/losses and so our tests remain inconclusive. Furthermore, chemical gradients in the melt affected all major oxides in addition to FeO_t, thus introducing a bias on melt composition that is not limited to Fe. More work is needed if the pre-enrichment method is to be applied to 1-atm experiments. Third, compared to the traditional capsule pre-saturation, the pre-enrichment method presents important advantages. Capsule preparation at 1 atm prior to the high-pressure experiment (synthesis of alloy, removal of Fe-doping material, cleaning) is totally avoided, which saves time. Fe incorporation to the capsule takes place in situ during the high-pressure experiment and, so, no estimation of the alloy composition under high-pressure conditions (e.g., Barr and Grove 2010) is needed. Overall, the proposed method is fast, easy to implement, and robust even if the optimum level of Fe pre-enrichment is left to be empirically determined.

IMPLICATIONS

We have presented a new methodology to counteract Fe loss from experimental charges to capsule materials in high-temperature/high-pressure experimental studies. The method is based on the use of starting materials pre-enriched in Fe. During the experiment, Fe alloys with the capsule material but the amount of Fe lost to the capsule is compensated by the amount of Fe added to the starting composition. Fe pre-enrichment has been demonstrated to work at high pressure (50 MPa), high temperature (1200 °C), moderately reducing f_{O_2} (NNO-0.8) and for both Pt and $Au_{80}Pd_{20}$ capsule materials. The method is empirical, i.e., an optimum level of Fe enrichment must be determined for each particular set of starting compositions and experimental conditions, the latter including the run duration. Although tested on hydrous basaltic melts, the method offers potential for other types of experimental conditions and compositions, and is highly adaptable. Compared to the traditional pre-saturation, Fe pre-enrichment eliminates the need to prepare appropriate container capsules at 1 atm prior to high-pressure experiments; estimating the alloy composition in the high-pressure experiment becomes unnecessary. For high-pressure experiments on basaltic compositions under moderately reducing f_{O_2} such as volatiles solubility and phase equilibria, the combination of AuPd containers and Fe pre-enriched starting materials provides excellent perspectives to solve the Fe loss problem.

ACKNOWLEDGMENTS

This work was supported by the VUELCO (FP7 EC) and DEGAZMAG (ANR 2011 Blanc SIMI 5-6 003) projects. Ida Di Carlo is acknowledged for her contribution to the electron microprobe analyses. We thank Brian Balta, Etienne Médard, and Thomas Shea for their helpful reviews.

REFERENCES CITED

Balta, J.B., Beckett, J.R., and Asimow, P.D. (2011) Thermodynamic properties of alloys of gold-74/palladium-26 with variable amounts of iron and the use of Au-Pd-Fe alloys as containers for experimental petrology. American Mineralogist, 96, 1467–1474.

Barr, J., and Grove, T.L. (2010) AuPdFe ternary solution model and applications to understanding the f_{O_2} of hydrous, high-pressure experiments. Contributions to Mineralogy and Petrology, 160, 631–643.

Burnham, C.W., Holloway, J.R., and Davis, N.F. (1969) Thermodynamic properties of water to 1000°C and 10000 bars. The Geological Society of America Special Paper 132, 96 p.

Chou, I.-M. (1986) Permeability of precious metals to hydrogen at 2 kb total pressure and elevated temperatures. American Journal of Science, 286, 638–658.

Deines, P., Nafziger, R.H., Ulmer, G.C., and Woermann, E. (1974) Temperature-oxygen fugacity tables for selected gas mixtures in the system C-H-O at one atmosphere total pressure. Bulletin of the Earth and Mineral Sciences Experiment Station, Number 88, Pennsylvania State University.

Di Carlo, I., Pichavant, M., Rotolo, S.G., and Scaillet, B. (2006) Experimental crystallization of a high-K arc basalt: The golden pumice, Stromboli volcano (Italy). Journal of Petrology, 47, 1317–1343.

Ford, C.E. (1978) Platinum-iron alloy sample containers for melting experiments on iron-bearing rocks. Mineralogical Magazine, 42, 271–275.

Gaetani, G.A., and Grove, T.L. (1998) The influence of water on melting of mantle peridotite. Contributions to Mineralogy and Petrology, 131, 323–346.

Gaillard, F., Pichavant, M., and Scaillet, B. (2003) Experimental determination of activities of FeO and Fe_2O_3 components in hydrous silicic melts under oxidizing conditions. Geochimica et Cosmochimica Acta, 67, 4389–4409.

Grove, T.L. (1982) Use of FePt alloys to eliminate the iron loss problem in 1 atmosphere gas mixing experiments: theoretical and practical considerations. Contributions to Mineralogy and Petrology, 78, 298–304.

Hall, L.J., Brodie, J., Wood, B.J., and Carroll, M.R. (2004) Iron and water losses from hydrous basalts contained in $Au_{80}Pd_{20}$ capsules at high pressure and temperature. Mineralogical Magazine, 68, 75–81.

Kawamoto, T., and Hirose, K. (1994) Au-Pd sample containers for melting experiments on iron and water-bearing systems. European Journal of Mineralogy, 6, 381–385.

Pichavant, M., Scaillet, B., Di Carlo, I., Rotolo, S., and Métrich, N. (2006) Sulfur in hydrous, oxidized basaltic magmas: phase equilibria and melt solubilities. American Geophysical Union, Fall Meeting 2007, abstract #V41C-02.

Pichavant, M., Di Carlo, I., Le Gac, Y., Rotolo, S., and Scaillet, B. (2009) Experimental constraints on the deep magma feeding system at Stromboli volcano, Italy. Journal of Petrology, 50, 601–624.

Pichavant, M., Pompilio, M., D'Oriano, C., and Di Carlo, I. (2011) Petrography, mineralogy and geochemistry of a primitive pumice from Stromboli: implications for the deep feeding system. European Journal of Mineralogy, 23, 499–517.

Pownceby, M.I., and O'Neill, H.St.C. (1994) Thermodynamic data from redox reactions at high temperatures. III. Activity-composition relations in Ni-Pd alloys from EMF measurements at 850–1250 K and calibration of the NiO + Ni-Pd assemblage as a redox sensor. Contributions to Mineralogy and Petrology, 116, 327–339.

Robie, R.A., Hemingway, B.S., and Fisher, J.R. (1979) Thermodynamic properties of minerals and related substances at 298.15 K and 1 bar (10^5 pascals) pressure and at higher temperatures. U.S. Geological Survey Bulletin 1452.

Stern, C.R., and Wyllie, P.J. (1975) Effect of iron absorption by noble-metal capsules on phase boundaries in rock-melting systems. American Mineralogist, 60, 681–689.

Taylor, J.R., Wall, V.J., and Pownceby, M.I. (1992) The calibration and application of accurate redox sensors. American Mineralogist, 77, 284–295.

MANUSCRIPT RECEIVED AUGUST 14, 2014
MANUSCRIPT ACCEPTED MARCH 18, 2015
MANUSCRIPT HANDLED BY THOMAS SHEA

Yann-Aurélien BRUGIER

Magmatologie du Piton de la Fournaise (Ile de la Réunion)

Résumé :

Afin de parvenir à une meilleure compréhension des processus d'évolution des magmas réunionnais, nous avons réalisé une étude ayant pour objectifs principaux : (1) la simulation expérimentale du système d'alimentation du Piton de la Fournaise, à partir d'un matériel de départ de composition typique de Steady State Basalt et dans des conditions de pression, température, fO2 et de teneurs en volatils (H2O, CO2) réalistes ; (2) la détermination de la séquence de cristallisation d'échantillons représentatifs des roches plutoniques réunionnaises de façon à les comparer avec les résultats expérimentaux et (3) l'obtention d'une base de données volcanologiques, pétrologiques et géochimiques significative sur le groupe de laves anormales (« Abnormal Group ») permettant de confirmer son existence dans le système d'alimentation du Piton de la Fournaise.

La découverte de verres silicatés ayant des compositions caractéristiques de l'Abnormal Group confirme l'implication de ces magmas dans l'activité éruptive. Toutefois, les roches plutoniques n'enregistrent pour la plupart que des séquences de cristallisation témoignant d'une évolution superficielle des magmas. Cette dernière est simulée de façon satisfaisante par les expérimentations réalisées dans la gamme 0.1 à 50 MPa qui conduisent à des modèles pétrologiques et des pressions de stockage en accord avec les données géophysiques. Les expérimentations à plus forte pression démontrent l'existence de paliers au sein du système d'alimentation qui peuvent en grande partie expliquer les diverses compositions réunionnaises, mais posent la question de la composition des magmas parentaux.

Mots clés : Piton de la Fournaise, volcanologie, pétrologie, étude expérimentale, volatils, Steady State Basalts, Abnormal Group

Magmatic evolution of Piton de la Fournaise (La Réunion island)

Summary :

To better understand magmatic processes associated with the evolution of La Réunion magmas, we have carried out a multi-approach study aimed at (1) simulating experimentally the feeding system of the Piton de la Fournaise volcano, using a Steady State Basalt starting material and P-T-fO2-Volatiles (H2O, CO2) conditions compatible with the natural system; (2) determining crystallization sequences representative of La Réunion plutonic rocks for comparison with the experimental results and (3) constructing a volcanological, petrological and geochemical database for lavas of the Abnormal Group, to confirm the existence of Abnormal melts in the feeding system of the volcano.

The discovery of glasses having chemical characteristics similar to the Abnormal Group establishes the implication of Abnormal melts in eruptive processes. However, plutonic rocks record crystallization sequences that for the most part indicate a low pressure magmatic evolution. Experiments in the pressure range 0.1 to 50 MPa satisfactorily reproduce conditions in the shallow magmatic systems and lead to petrological models and magma storage depths in agreement with geophysical data. Experiments at higher pressures demonstrate transitions in magma fractionation mechanisms in the feeding system that can explain the range of erupted compositions, but call into question the compositions of parental magmas.

Keywords : Piton de la Fournaise, volcanology, petrology, experimental study, volatiles, SSB, AbG

Institut des Sciences de la Terre d'Orléans
1A, rue de la Férollerie
45071 ORLEANS Cedex 2